ACS SYMPOSIUM SERIES 1107

Functional Materials from Renewable Sources

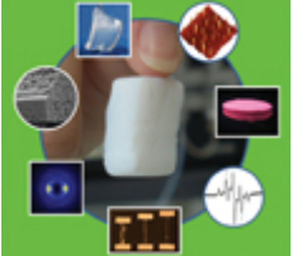

EDITED BY

Falk Liebner and Thomas Rosenau

Downloaded by 217.66.152.26 on August 23, 2012 | http://pubs.acs.org
Publication Date (Web): August 17, 2012 | doi: 10.1021/bk-2012-1107.fw001

Functional Materials from Renewable Sources

In Functional Materials from Renewable Sources; Liebner, F., et al.;
ACS Symposium Series; American Chemical Society: Washington, DC, 2012.

Downloaded by 217.66.152.26 on August 23, 2012 | http://pubs.acs.org
Publication Date (Web): August 17, 2012 | doi: 10.1021/bk-2012-1107.fw001

Downloaded by 217.66.152.26 on August 23, 2012 | http://pubs.acs.org
Publication Date (Web): August 17, 2012 | doi: 10.1021/bk-2012-1107.fw001

ACS SYMPOSIUM SERIES **1107**

Functional Materials from Renewable Sources

Falk Liebner, Editor
BOKU University
Vienna, Austria

Thomas Rosenau, Editor
BOKU University
Vienna, Austria

Sponsored by the
ACS Division of Cellulose and Renewable Materials

American Chemical Society, Washington, DC

Distributed in print by Oxford University Press, Inc.

Downloaded by 217.66.152.26 on August 23, 2012 | http://pubs.acs.org
Publication Date (Web): August 17, 2012 | doi: 10.1021/bk-2012-1107.fw001

Library of Congress Cataloging-in-Publication Data

Functional materials from renewable sources / Falk Liebner, editor, BOKU University, Vienna, Austria, Thomas Rosenau, editor, BOKU University, Vienna, Austria ; sponsored by the ACS Division of Cellulose and Renewable Materials.
pages cm. -- (ACS symposium series ; 1107)
Includes bibliographical references and index.
ISBN 978-0-8412-2788-0 (alk. paper)
1. Nanofibers. 2. Cellulose fibers. 3. Biomedical materials. 4. Renewable natural resources. I. Liebner, Falk, editor of compilation. II. Rosenau, Thomas, editor of compilation. III. American Chemical Society. Cellulose and Renewable Materials Division.
TA418.9.F5F86 2012
620.1′17--dc23
2012027854

The paper used in this publication meets the minimum requirements of American National Standard for Information Sciences—Permanence of Paper for Printed Library Materials, ANSI Z39.48n1984.

Copyright © 2012 American Chemical Society

Distributed in print by Oxford University Press, Inc.

All Rights Reserved. Reprographic copying beyond that permitted by Sections 107 or 108 of the U.S. Copyright Act is allowed for internal use only, provided that a per-chapter fee of $40.25 plus $0.75 per page is paid to the Copyright Clearance Center, Inc., 222 Rosewood Drive, Danvers, MA 01923, USA. Republication or reproduction for sale of pages in this book is permitted only under license from ACS. Direct these and other permission requests to ACS Copyright Office, Publications Division, 1155 16th Street, N.W., Washington, DC 20036.

The citation of trade names and/or names of manufacturers in this publication is not to be construed as an endorsement or as approval by ACS of the commercial products or services referenced herein; nor should the mere reference herein to any drawing, specification, chemical process, or other data be regarded as a license or as a conveyance of any right or permission to the holder, reader, or any other person or corporation, to manufacture, reproduce, use, or sell any patented invention or copyrighted work that may in any way be related thereto. Registered names, trademarks, etc., used in this publication, even without specific indication thereof, are not to be considered unprotected by law.

PRINTED IN THE UNITED STATES OF AMERICA

Downloaded by 217.66.152.26 on August 23, 2012 | http://pubs.acs.org
Publication Date (Web): August 17, 2012 | doi: 10.1021/bk-2012-1107.fw001

Foreword

The ACS Symposium Series was first published in 1974 to provide a mechanism for publishing symposia quickly in book form. The purpose of the series is to publish timely, comprehensive books developed from the ACS sponsored symposia based on current scientific research. Occasionally, books are developed from symposia sponsored by other organizations when the topic is of keen interest to the chemistry audience.

Before agreeing to publish a book, the proposed table of contents is reviewed for appropriate and comprehensive coverage and for interest to the audience. Some papers may be excluded to better focus the book; others may be added to provide comprehensiveness. When appropriate, overview or introductory chapters are added. Drafts of chapters are peer-reviewed prior to final acceptance or rejection, and manuscripts are prepared in camera-ready format.

As a rule, only original research papers and original review papers are included in the volumes. Verbatim reproductions of previous published papers are not accepted.

ACS Books Department

In Functional Materials from Renewable Sources; Liebner, F., et al.;
ACS Symposium Series; American Chemical Society: Washington, DC, 2012.

Downloaded by 217.66.152.26 on August 23, 2012 | http://pubs.acs.org
Publication Date (Web): August 17, 2012 | doi: 10.1021/bk-2012-1107.pr001

Preface

Functional materials have been always of interest for human beings, and the everlasting quest for novel, tailored materials has evidently been having a decisive impact on the survival, development, and prosperity of our mankind.

Looking back into distant human history, it appears to be nearly impossible for most people to imagine that there had been a period of about five million years in which people have lived almost exclusively from renewable resources. In this period, the human race learned to develop novel functional materials, driven by the demand to be more successful in hunting and gathering, to protect themselves from natural phenomena, to be more effective at fieldwork, to outmatch their enemies, to improve communication, or to realize higher prices for handcraft and special products.

Archeological collections or historical museums are places that are suitable to convey an impression of the multitude of functional materials that have been created driven by the genius and aptitude of human beings. Humans succeeded to manufacture knifes, axes, or arrows that had blades or tips from flintstone or obsidian, they found access to metals and invented alloys such as bronze, they manufactured tools, commodity, armor, and weapons from it, they used plant ash as fertilizer and charcoal as soil conditioner, they learned to prepare soap from potash and animal fat, to weave clothes from linen, wool, or silk, to tie ropes from hemp or sisal fibers, to caulk their fishing boats with oakum, and they discovered the hydraulic binding ability of puzzolanic soil that was from that point on used as a high-performance cement in combination with lime, quarrystone, and sheathings from highly porous tuff stone (*opus caementicium*, 40 B.C.). Early they discovered that a blue dye can be obtained from dyer's weed or the Indian Indigo plant by fermentation with urine and potash and subsequent air oxidation (ca. 4000 B.C.), that hides and skins are more durable and less susceptible to decomposition when tanned (2500 B.C.), and that charcoal powder in combination with saltpeter and sulfur can be used as gun powder. Felts tough enough to form construction materials were produced by matting, condensing, and pressing woolen fibers, linen sheaths soaked with chemicals or skins made from animal intestines were softened by treatment with sulfur and lye and used as condoms, aqueous suspensions of plant fibers were processed to paper, and celluloid – a mixture of cellulose nitrate and camphor – has been used as ivory substitute, as transparent carrier for photographic films, as liquid plaster, and is still used in high-quality table tennis balls.

Even though an incredible long list containing thousands and thousands of other examples could be compiled – some of them keystones in mankind´s advancement, others just minor proofs of men's unlimited ingenuity – functional

In Functional Materials from Renewable Sources; Liebner, F., et al.;
ACS Symposium Series; American Chemical Society: Washington, DC, 2012.

materials have always accompanied the development of the human race. Since the beginning of the industrial age about 200 years ago, evolution and design of novel materials has literally undergone a leap with respect to number, performance, and level of sophistication However, the breathtaking technical and technological development within this short period of human history has also led to a considerable depletion of fossil resources mainly caused by the global energy demand that rose simultaneously at a virtually explosive rate. The enormous annual exploration rates, which added up to 2,940 × 10^9 m^3 of natural gas, 4.22 × 10^9 tons of crude oil, and 6.38 × 10^9 tons of coal only for the year 2007, will in not-so-far future inevitably exhaust the remaining reserves and undermine the foundations of the current wealth of large proportion of our civilization. It is commonly acknowledged that the fossil reserves will be exhausted within a comparatively short period of time, which will be most likely not much longer than the time elapsed since the presentation of the first photographic image (Niepce 1826), the discovery of rubber vulcanisation (Goodyear 1839), or the development of the first synthetic dye (Perkin 1856).

After the turn of the millennium, we have now approached a time period where the public awareness for the finite nature of fossil resources and the necessity of using renewable sources has reached an encouraging level. Today, renewables are still being mainly used for energy production. However, it is safe to assume that the focus of future resource utilization strategies will increasingly move from energy to materials and platform chemicals; novel, more efficient energy technologies based on wind, water, solar energy or − controversially − nuclear power are at hand, while renewable resources are the only alternative to fossil ones as origin of organic carbon and thus the basis of chemicals and materials.

Today, the relatively young term “biorefinery” tries to encompass all approaches aiming on the production of chemicals or materials from aquatic or terrestrial biomass either by extraction, fractionation, modification, or physical, chemical, and biotechnological conversion processes. Furthermore, broad consensus exists that the operating efficiency of biorefinery units largely depends on the profitability of all product lines and the value of individual products. This implies that any sustainable biorefinery approach must use up not only one, but all plant constituents which would be cellulose, hemicelluloses, lignin, and extractives in the case of wood.

Following this concept, substantial advances have been recently made with respect to the development of innovative, biopolymer-based functional materials using both up-to-date synthetic and instrumental-analytical tools. Current research in this field − to name but a few examples − targets electronic, photonic, magnetic, and hemocompatible high-performance functional materials, is increasingly based on bionic principles and bioinspiration, and uses sophisticated methods for tailoring the properties for special applications. Nano (NEMS), micro (MEMS), and bio-micro electromechanical systems (bioMEMS) are further hot topics in functional material’s research as billions of such devices are already manufactured annually for sensing, ink jet printing, automotive applications, communications, and medicine.

The present book, “Novel Functional Materials from Renewable Resources”, has been prepared with the intention to convey an impression of the current state

Downloaded by 217.66.152.26 on August 23, 2012 | http://pubs.acs.org
Publication Date (Web): August 17, 2012 | doi: 10.1021/bk-2012-1107.pr001

of research in this field , and to reflect the ample activities in this field that are currently going on worldwide. The compilation of topics is based on presentations given during the 241 Annual Spring Meeting of the American Chemical Society, held in Anaheim in March 2011, at a series of sessions of the ACS Cellulose division.

May this book awake and sustain the curiosity of our readers to discover an old and new fascinating field of research that will hopefully contribute to the further wealth of future generations and to reasonable global resource management that will not be stopped by ignorance or lobbying.

> *Break-proof Pyrex glass was discovered twice in history with a time span of about 1900 years between the two events.*
>
> *When Tiberius, the second emperor of the Roman Empire, heard about the existence of a glass-maker about whom was said that he would be able to make break-proof glass, he urged the man to appear at his court. When the glass-maker arrived he presented a beautiful transparent vase made of Martiolum to the emperor. To demonstrate the intriguing properties of his functional material he threw the vase to the ground and − it did not shatter into sherds. While the spectators were stunned, frightened or even thought of wizardry, the emperor kept calm and just made inquiries about the material and the names of people that might also know the secrets of its manufacture. After having made sure that the glass-maker was the only secret-keeper of Pyrex glass production, the emperor had the glass-maker put to death and his factory destroyed to be the only owner of break-proof glassware. − Today, Pyrex is one of the most important source of lab glassware for the material's chemist.*
>
> *(based on John Emsley, Molecules at an Exhibition, Oxford University Press, Inc., New York, 1998)*

Falk Liebner and **Thomas Rosenau**, February 2012

Downloaded by 217.66.152.26 on August 23, 2012 | http://pubs.acs.org
Publication Date (Web): August 17, 2012 | doi: 10.1021/bk-2012-1107.pr001

Editors' Biographies

Falk Liebner

Falk Liebner, born 1962 in Dresden, Germany, is tenured assistant professor and head of the workgroup "Biomaterial Chemistry" at the Department of Chemistry, University of Natural Resources and Life Sciences Vienna (BOKU University). He graduated in organic chemistry from Dresden University of Technology, where he also obtained the Ph.D. in bio-organosilicon chemistry. After employments at the Research Institute for Post-mining Landscapes, Finsterwalde, Germany, and the Institute of Wood and Plant Chemistry, Dresden University of Technology, Germany, he joined BOKU University Vienna in 2006. Current research interests are biopolymer-based hydrogels and aerogels, supercritical carbon dioxide in biomaterial processing, and lignin chemistry. He has published more than 55 peer-reviewed papers, 70 conference contributions and 7 patents, and was visiting professor at renowned academic institutions in Japan and France.

Thomas Rosenau

Thomas Rosenau, born 1969 in Erfurt, Germany, is professor of Wood, Pulp and Fiber Chemistry at the Department of Chemistry, University of Natural Resources and Life Sciences Vienna (BOKU University), and head of the Division of Chemistry of Renewable Resources. After graduation from the Conservatory Franz Liszt Weimar (concert organ), he studied chemistry at Dresden University of Technology and received his doctoral degree in synthetic organic chemistry. After postdoctoral stays at North Carolina State University at Raleigh, North Carolina, U.S.A., he joined BOKU University Vienna in 1998, where he received the venia docendi in organic chemistry. He has published more than 220 SCI papers, 450 conference contributions and 14 patents, is Fellow Elect of the International Academy of Wood Science, and received several international awards in cellulose, fiber, and antioxidant chemistry.

Downloaded by COLUMBIA UNIV on August 28, 2012 | http://pubs.acs.org
Publication Date (Web): August 17, 2012 | doi: 10.1021/bk-2012-1107.ot001

In Functional Materials from Renewable Sources; Liebner, F., et al.;
ACS Symposium Series; American Chemical Society: Washington, DC, 2012.

Downloaded by 217.66.152.26 on August 23, 2012 | http://pubs.acs.org
Publication Date (Web): August 17, 2012 | doi: 10.1021/bk-2012-1107.ch001

Chapter 1

High-Modulus Oriented Cellulose Nanopaper

**Wolfgang Gindl-Altmutter,*,[1] Stefan Veigel,[1] Michael Obersriebnig,[1]
Christian Tippelreither,[1] and Jozef Keckes[2]**

**[1]Department of Materials Scvience and Process Engineering,
BOKU-University of Natural Resources and Life Science,
Konrad Lorenz Stzrasse 24, A-3430 Tulln, Austria
[2]Erich Schmid Institute of Materials Science, Austrian Academy of Sciences
and Institute of Metal Physics, University of Leoben, Jahnstrasse 12,
A-8700 Leoben, Austria
*E-mail: wolfgang.gindl@boku.ac.at**

Thin sheets of nanopaper were prepared from cellulose nanofibrils (CNF) obtained by means of high-pressure homogenisation of dissolving-grade beech pulp. Untreated pulp and pulp pre-treated by TEMPO-mediated surface oxidation were used, which resulted in significant differences in structure and mechanical performance of the nanopaper specimens. Overall, surface-oxidized CNF were characterized by reduced diameter, reduced crystallinity, and reduced crystallite thickness compared to untreated CNF. Nanopaper produced from surface-oxidized CNF showed better mechanical performance than untreated nanopaper with regard to tensile strength and modulus of elasticity, and also exhibited higher failure strain indicating better toughness. While stretching experiments with the aim of inducing preferred orientation failed with untreated nanopaper, surface-oxidized nanopaper could be stretched up to 30% elongation. Stretching resulted in a high degree of preferred orientation of CNF parallel to the direction of induced elongation as shown by wide-angle x-ray scattering and AFM. The mechanical performance of nanopaper improved to a tensile strength of up to 380 MPa and a modulus of elasticity up to 46 GPa parallel to the direction of preferred orientation.

In Functional Materials from Renewable Sources; Liebner, F., et al.;
ACS Symposium Series; American Chemical Society: Washington, DC, 2012.

Downloaded by 217.66.152.26 on August 23, 2012 | http://pubs.acs.org
Publication Date (Web): August 17, 2012 | doi: 10.1021/bk-2012-1107.ch001

Introduction

The tensile properties along the chain of the cellulose macromolecule are excellent. With a chain elastic modulus in the order of 140 GPa and a tensile strength of 7.5 GPa, as obtained from theoretical predictions and molecular simulations, cellulose I, the crystal allomorph which occurs naturally in plants, is well competitive with technical fibers such as glass, carbon and polyaramide (*1*). Plant tissue is porous and exhibits a complex hierarchical arrangement of its constituent polymers cellulose, hemicellulose, pectin, and lignin. Because of the inferior properties of non-cellulosic cell-wall building blocks such as lignin and hemicellulose compared to cellulose, the mechanical properties of plant fibers are obviously well below the maximum values inherent to pure cellulose (*2*). In order to exploit the full mechanical potential of cellulosic plant fibers, it is therefore necessary to remove non-cellulosic components. Subsequent mechanical disintegration of cellulosic plant material down to nano-scale further improves its suitability for reinforcement. Nano-scale cellulosic objects obtained in this procedure are termed cellulose nanofibrils (CNF) and cellulose nanocrystals (CNC). CNF are long and slender, ideally with diameters from 4-20 nm, but frequently also up to 100 nm, and have an aspect ratio in the order of 100 or more (*1*). The diameter of CNF, which depends on the source of cellulose and on the type of processing, is critical for the performance of materials produced thereof (*3*, *4*).

The modulus of cellulose I nanofibrils (bacterial cellulose) was measured directly by means of a three-point bending experiment in the AFM (*5*). For fibrils with diameters ranging from 35 to 90 nm, a value of 78 ± 17 GPa was obtained. By Raman spectroscopy, the modulus of elasticity of bacterial cellulose fiber networks was determined and an estimate of 114 GPa was inferred for single cellulose fibrils (*6*). In view of a reference value of 140 GPa for crystalline cellulose I (*7*), this value seems plausible considering the fact that CNF consist of both highly ordered crystalline domains and less ordered non-crystalline domains. Through an additional processing step involving hydrolysis of non-crystalline domains by strong acid, CNC are obtained (*8*). With the exception of CNC from tunicates, which can be up to 4 µm in length, CNC exhibit significantly lower aspect ratio than CNF. AFM three-point bending experiments showed a modulus of elasticity of 145 - 150 GPa for tunicate CNC with cross-sectional dimensions of 8 × 20 nm and several micrometers in length (*9*).

The excellent mechanical reinforcement potential of CNF and CNC, as well as other interesting features like low thermal expansion <8.5 ppm K^{-1} (*10*) and liquid crystalline properties of CNC (*11*) have recently inspired a high number of studies covering a very broad range of potential applications of nanocellulose (*12–16*). Owing to the nature of the production process of CNF- or CNC-reinforced composites, which is casting from suspension and subsequent evaporation of the liquid in the vast majority of studies, the fibril orientation is best approximated by in-plane random. According to micromechanical models (*17*), the in-plane elastic modulus in such a case is at best 3/8 of the fibril modulus scaled by the fibril volume fraction. Therefore it is desirable to orient the reinforcement in order to fully exploit its potential. In the case of CNC, this

In Functional Materials from Renewable Sources; Liebner, F., et al.;
ACS Symposium Series; American Chemical Society: Washington, DC, 2012.

goal has been achieved by means of two fundamentally different approaches, i.e. the use of strong electric or magnetic fields on the one hand, and the use of shear-based methods on the other hand. At field strengths above 1 kV cm^{-1} CNC align parallel to an AC electric field (*18*), whereas alignment perpendicular to the field is observed in a magnetic field of 7 T (*19*). Shear-based methods comprise spin-coating, where CNC orient parallel to the centrifugal forces on a rotating disc (*20*). In a rotating drum filled with CNC suspension, CNC orient parallel to the direction of rotation due to shear within the suspension along the inner wall of the drum (*21*). Finally, drawing leads to high orientation of CNC as shown for CNC-reinforced poly(vinyl alcohol) fibers (*22*) and cellulose self-reinforced films (*23*). In contrast to CNC, CNF are more difficult to align, because they are much longer and flexible, and thus more prone to entanglement than CNC, which are essentially short, rigid crystalline rods. However, CNF dispose of two major advantages with regard to polymer reinforcement compared to CNC. Firstly, both CNC and CNF are very stiff compared to the surrounding polymer matrix in composite applications. In such a case high aspect ratio as found for CNF ensures ample fiber-matrix contact area and thus optimum loading of the fiber through interfacial stress transfer. Secondly, CNF are easier to prepare than CNC, which require the additional processing step of acidic hydrolysis, and are thus less costly. Since drawing of moistened films proved a very successful approach for regenerated cellulose films (*24*), the present study aims at examining the possibility of producing CNF nanopaper sheets with high degree of preferred orientation according to this method.

Downloaded by 217.66.152.26 on August 23, 2012 | http://pubs.acs.org
Publication Date (Web): August 17, 2012 | doi: 10.1021/bk-2012-1107.ch001

Materials and Methods

Preparation of Cellulose Nanopaper

For the preparation of cellulose nanofibrils, never dried dissolving grade beech-wood pulp (Lenzing AG, Lenzing, Austria) with an initial solid content of about 50% was used as a starting material. Cellulose surface oxidation was carried out according to Saito et al. (*25*) with 2,2,6,6-tetramethylpiperidinyl-1-oxyl (TEMPO) as the catalyst and sodium chlorite as a primary oxidant under neutral conditions. Firstly, 2 g of never-dried pulp (i.e. 1 g of dry weight) was suspended in 0.05 M sodium phosphate buffer (90 ml) in an Erlenmeyer flask. Then, 0.016 g TEMPO and 1.13 g sodium chlorite were added. A 1.34 M solution of sodium hypochlorite was diluted to 0.1 M with 0.05 M sodium phosphate buffer, and 10 ml of the 0.1 M sodium hypochlorite solution were added to the flask. Thereafter, the flask was sealed and the pulp suspension was stirred at 60 °C for 2 h, 6 h, and 48 h. Finally, the oxidized cellulose was filtered off from the reaction solution and washed repeatedly with distilled water to remove the residues of the oxidizing agents. Samples of treated cellulose and untreated cellulose were diluted to a solid content of 0.5% and fibrillated with 20 passes in an APV high-pressure homogenizer at 800 bar. For the production of cellulose nanofibril sheets, cellulose suspension corresponding to 1.5 g cellulose was poured into a petri dish with a diameter of 195 mm. Water was evaporated at room temperature

In Functional Materials from Renewable Sources; Liebner, F., et al.;
ACS Symposium Series; American Chemical Society: Washington, DC, 2012.

after an evacuation step for the removal of air bubbles. After 48 h the films were ready to be transferred to standard climate (20 °C, 65 % relative humidity) for final conditioning before further processing and characterization.

Stretching and Mechanical Characterization

Strips with a width of 6 mm and a length of 60 mm were cut from dry sheets of nanopaper. Wood veneer patches were glued to the ends of the strips by means of hot-melt adhesive in order to protect the nanopaper specimens from damage by the grips of the universal testing machine, to which they were attached. Before stretching, the nanopaper samples were moistened by spraying them with distilled water. After a desired stretch of 15 % or 30 %, respectively, was attained, the samples were dried by means of hot air while still fixed in the testing machine. A higher degree of stretch could not be achieved due to specimen failure. Dry specimens, both stretched and unstretched, where prepared for mechanical testing by fixing wood veneer patches to the samples at a distance of 40 mm. Thus the tested length of 40 mm consisted only of nanopaper with desired stretch of 0 %, 15 %, and 30 %, respectively. The specimens were tested in tension parallel to the direction of stretch, using a Zwick-Roell universal testing machine equipped with a 2.5 kN load cell and a video extensometer for non-contacting measurement of extension. For each type of sample, at least ten specimens were tested.

Downloaded by 217.66.152.26 on August 23, 2012 | http://pubs.acs.org
Publication Date (Web): August 17, 2012 | doi: 10.1021/bk-2012-1107.ch001

Structural Characterization

Wide angle x-ray scattering was performed on a Bruker Nanostar. 2D detector image were acquired and evaluated by means of Fit2D software. The radial distribution of scattered intensity was used to calculate the crystallinity of the fibrillated material. The total area under the scattering intensity distribution curve was integrated numerically and the contribution of non-crystalline material (non-crystalline cellulose and potentially residual hemicellulose) was estimated according to ref. (*26*). The crystallinity X_c was then calculated according to equation 1

$$X_c = \frac{I_{tot} - I_a}{I_{tot}} \qquad (1)$$

where I_{tot} is the total area under the curve and I_a is the estimated area contributed by non-crystallin material. Furthermore the width of cellulose crystallites was evaluated using the full width at half maximum (FWHM) of the cellulose 200 reflection by means of Scherrer's formula (equation 2),

$$d = \frac{K\,\lambda}{FWHM\ cos\theta} \qquad (2)$$

where λ is the x-ray wavelength (0.154 nm), K is a shape factor with a typical value of 0.9, FWHM is the peak width at half maximum in radians and θ is the peak position. For the quantification of the degree of preferred orientation, the

Downloaded by 217.66.152.26 on August 23, 2012 | http://pubs.acs.org
Publication Date (Web): August 17, 2012 | doi: 10.1021/bk-2012-1107.ch001

azimuthal distribution of scattering intensity of the cellulose I 200 reflection, which is perpendicular to the direction of the cellulose chain, was evaluated by means of equation 3.

$$\cos^2\theta = \frac{\int_0^{\pi/2} \mathrm{I}(\theta)\cos^2\theta \, sin\theta d\theta}{\int_0^{\pi/2} \mathrm{I}(\theta)\sin\theta \, d\theta} \tag{3}$$

The orientation factor $\cos^2\theta$ obtained from equation (2) equals 1/3 at random orientation and 1 at unidirectional orientation parallel to the direction of reference. In order to evaluate the CNF geometry, in particular the fibril diameter, topography images of nanopaper surfaces were acquired by means of a Bruker AFM.

Results and Discussion

Structure and Properties of Random-Oriented Nanopaper

Sheets of cellulose nanopaper obtained from untreated CNF and CNF treated by TEMPO-mediated oxidation differed in their optical appearance, structure, and mechanical properties. The average thickness of both sets of nanopaper was 25 – 30 µm. Specimens consisting of untreated CNF showed little optical transparency, whereas excellent transparency was observed for sheets made from TEMPO-oxidized CNF (Figure 1). This difference in optical appearance closely correlates with a significant difference in CNF diameter as revealed by AFM (Figure 2).

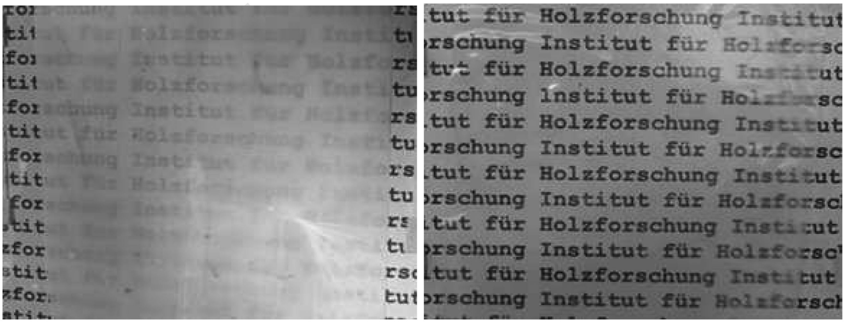

Figure 1. Different optical transparency of untreated cellulose nanopaper (left) and nanopaper prepared from CNF treated by means of TEMPO-mediated oxidation (right).

While the average diameter is 21±3.5 nm for untreated CNF, this value diminishes to 15±3.2 nm for TEMPO-oxidized CNF. As revealed by Nogi et al. (*27*), a low fibril diameter and small surface roughness is essential with regard to optical transparency. Wide-angle x-ray diffraction revealed further effects of TEMPO-oxidation on CNF structure apparent from diffractograms shown in Figure 3. Treatment resulted in a significant decrease in relative peak height of the strongest reflection (cellulose 200) indicating reduced crystallinity, and in a broadening of this peak indicating reduced crystallite size. Both effects were strong already after 2 h treatment (Table 1).

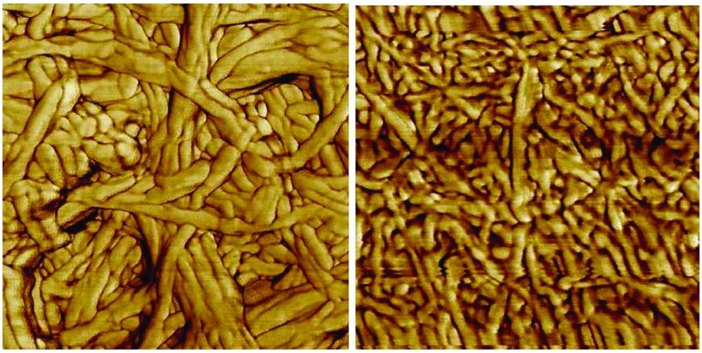

Figure 2. Flattened topography images (AFM) of untreated CNF (left), and TEMPO-oxidized CNF (right). Scan size was 500x500 nm.

Table 1. Crystallinity and crystallite width of different kinds of CNF

	Xc	d_{200} *(nm)*
Untreated	0.51	4.14
2h TEMPO-oxidized	0.38	2.83
6h TEMPO-oxidized	0.37	2.69
48h TEMPO-oxidized	0.36	2.68

Prolonged treatment only slightly enhanced this effect, indicating that TEMPO-mediated oxidation readily affects accessible cellulose at the surface of crystallites (*28*), thus diminishing their size, but probably proceeds much more slowly into the densely packed crystalline domains. Results of tensile tests with nanopaper specimens are summarized in Figure 4.

Downloaded by 217.66.152.26 on August 23, 2012 | http://pubs.acs.org
Publication Date (Web): August 17, 2012 | doi: 10.1021/bk-2012-1107.ch001

Downloaded by 217.66.152.26 on August 23, 2012 | http://pubs.acs.org
Publication Date (Web): August 17, 2012 | doi: 10.1021/bk-2012-1107.ch001

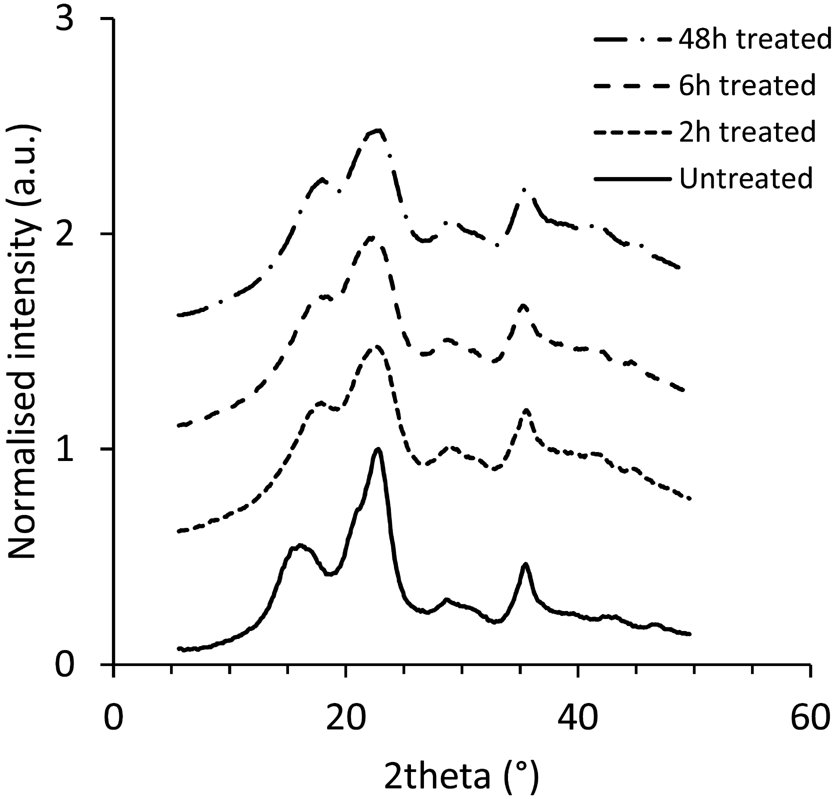

Figure 3. X-ray diffractograms for untreated CNF and CNF treated by TEMPO-mediated oxidation for different reaction times.

Overall, the mechanical performance of nanopaper specimens tested in the present study conforms well with the range of values of 6–15 GPa for the modulus of elasticity, 95–240 MPa for tensile strength, and 2–10 % failure strain compiled in a recent extensive review of the literature (*1*). With the exception of the tensile strength of specimens consisting of 48 h treated CNF, all values showed a trend towards improvement with treatment time. Improvements in strength and failure strain are best explained by the observed decrease in fibril diameter (*3*).

With regard to the modulus of elasticity, fibril diameter should not be of relevance at first view, because the modulus of elasticity of a polymer is determined by the intrinsic modulus of the polymer chain and the degree of preferred orientation of the chains (*29*). However, in paper-like networks also fibril-fibril interaction at points of overlap is critical (*30*). It is assumed that fibril interaction is facilitated by thinner fibrils in treated nanopaper, which therefore shows higher modulus.

Downloaded by 217.66.152.26 on August 23, 2012 | http://pubs.acs.org
Publication Date (Web): August 17, 2012 | doi: 10.1021/bk-2012-1107.ch001

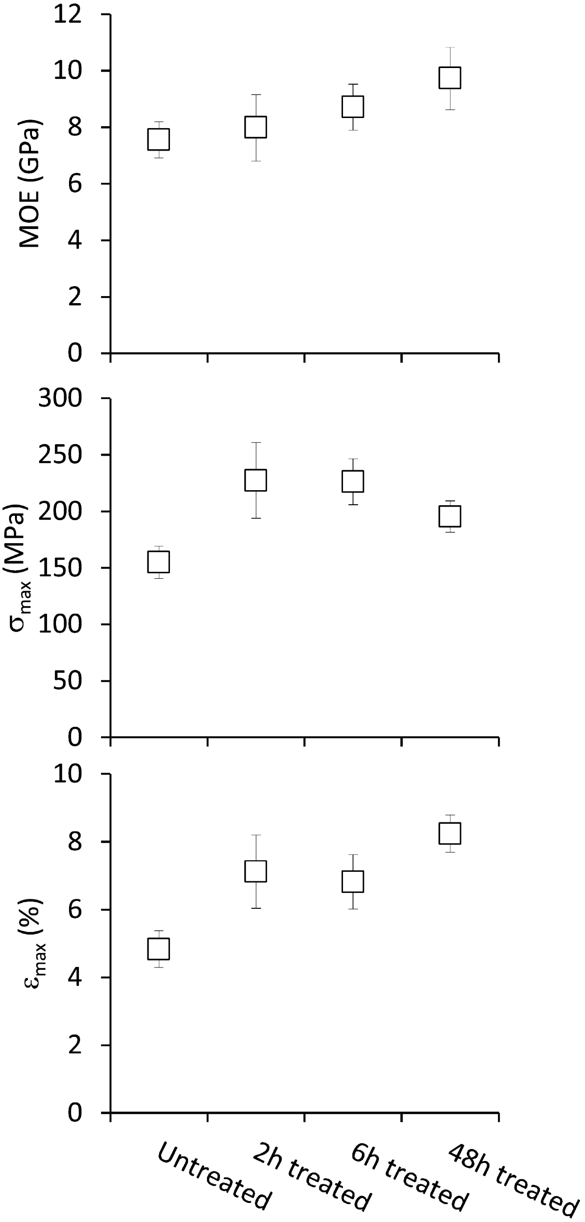

Figure 4. Results of tensile experiments with nanopaper from CNF and from CNF treated by TEMPO-mediated oxidation for different reaction times (average values and standard deviation).

Nanopaper with Preferred Orientation Due to Stretching

Stretching experiments were performed with nanopaper specimens consisting of untreated CNF and CNF treated by TEMPO-mediated oxidation. Untreated CNF nanopaper could not be stretched in moist condition, because it readily fractured at low strain. By contrast, nanopaper produced from TEMPO-oxidized CNF was stretchable up to 30% strain. (Figure 5).

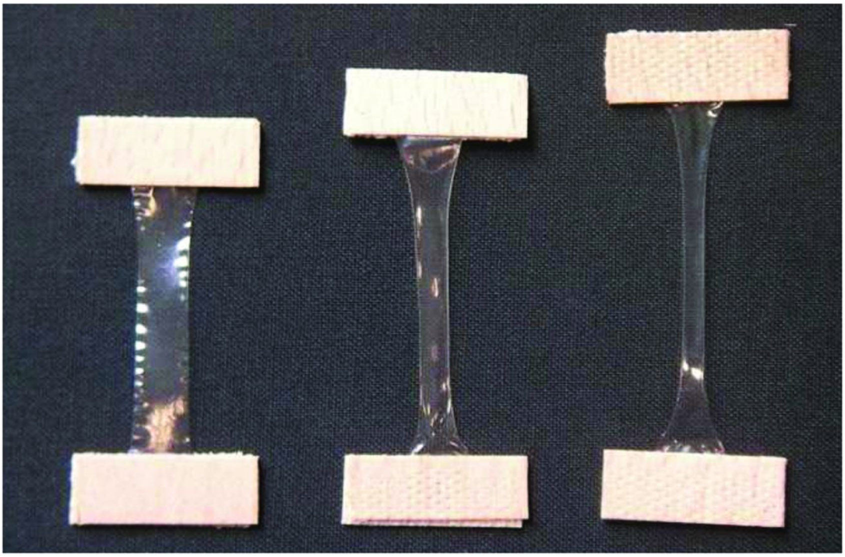

Figure 5. TEMPO-oxidized cellulose nanopaper specimens in unstretched condition (left) and after stretching to 15 % and 30 % elongation, respectively.

This remarkable difference indicates a higher degree of plasticity in the fibril-fibril interaction of TEMPO-oxidized CNF and corresponds well with the overall higher failure strain of TEMPO-oxidized nanopaper compared to nanopaper from untreated CNF (Figure 4). It is proposed that in dry nanopaper fibril-fibril hydrogen bonds between untreated CNF are more stable compared to hydrogen bonds between partially oxidized fibrils as found in nanopaper produced from CNF modified by TEMPO-mediated oxidation, which explains the higher plasticity found in the latter. The extensibility of oxidized nanopaper in moist condition may also be favoured by repulsive forces between CNF due to surface charge resulting from the treatment procedure (*28*). The degree of orientation and also ensuing mechanical properties after stretching did not show significant effects of the time of treatment by TEMPO oxidation, which is why average values of all three treatment groups are discussed in the following section. The specimens retained their initial optical transparency also after the stretching experiments (Figure 5).

Downloaded by 217.66.152.26 on August 23, 2012 | http://pubs.acs.org
Publication Date (Web): August 17, 2012 | doi: 10.1021/bk-2012-1107.ch001

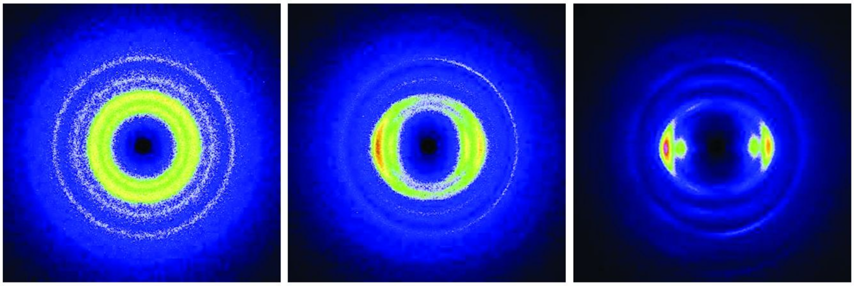

Figure 6. Wide angle x-ray scattering 2D detector images of nanopaper from TEMPO-oxidized CNF in unstretched condition (left), and after stretching to 15 % and 30 % elongation, respectively. Distinct intensity peaks of the cellulose 200 reflection indicate a high degree of preferred orientation.

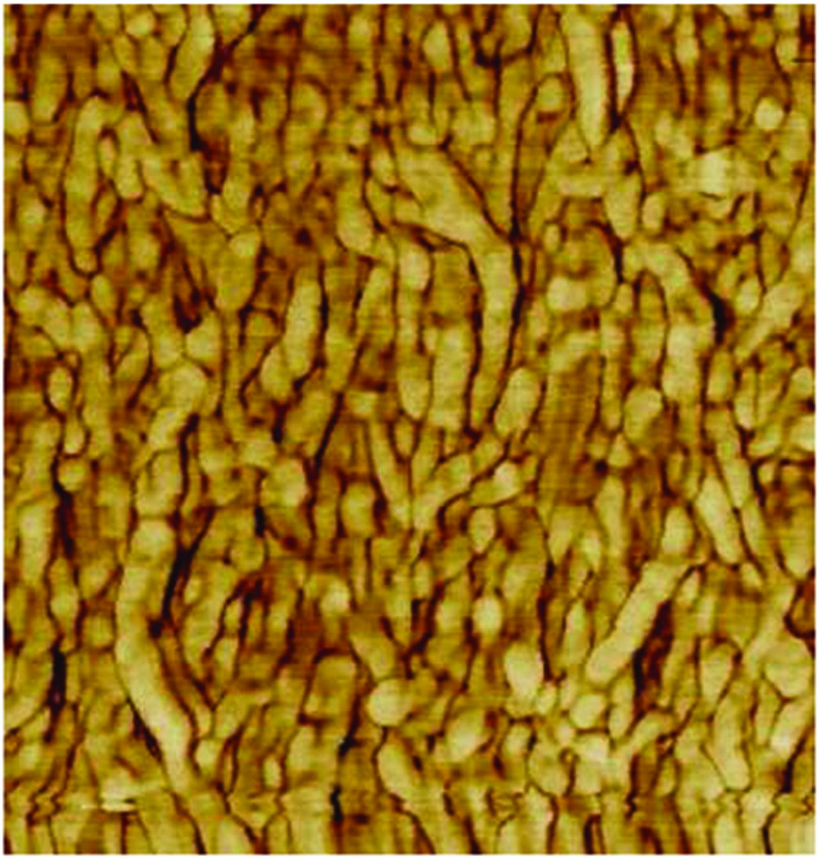

Figure 7. Flattened topography image of TEMPO-oxidized CNF nanopaper after stretching to 30% elongation in wet condition and subsequent drying. AFM scan size was 500x500 nm.

Downloaded by 217.66.152.26 on August 23, 2012 | http://pubs.acs.org
Publication Date (Web): August 17, 2012 | doi: 10.1021/bk-2012-1107.ch001

Wide-angle x-ray scattering revealed a significant degree of preferred orientation in the stretched nanopaper specimens (Figure 6). The orientation factor $\cos^2\theta$ increased from 1/3 in unstretched condition to 0.71 after 15% stretching and 0.83 after 30% stretching. This high degree of preferred orientation is quite remarkable in view of the fact that the average degree of orientation (considering both crystalline and non-crystalline domains) in a standard lyocell fiber is equivalent to a $\cos^2\theta$ value of 0.75 (*24*). An AFM-image of the surface of a specimen stretched to 30% elongation confirms the high degree of alignment achieved with the chosen stretching procedure (Figure 7).

The results of tensile tests with unstretched and stretched nanopaper reflect the changes in preferred orientation achieved by stretching in wet condition and subsequent drying (Figure 8). The modulus of elasticity and tensile strength increase strongly, whereas the strain at failure diminishes with increasing orientation. The average modulus of elasticity of 46 GPa measured for specimens stretched to 30% elongation is well superior to comparable materials, e.g. regenerated cellulose films (26 GPa, ref (*24*)) and regenerated cellulose films reinforced with undissolved cellulose I (33 GPa, ref (*23*)). The latter materials were stretched in an identical procedure as the one used in the present study, whereby a maximum degree of elongation of 50% was achieved, yet with significantly lower ensuing degree of orientation ($\cos^2\theta$ value of 0.75 vs. 83 in the present experiment). A similar stretching procedure was used by Bohn et al. (*31*) for never-dried bacterial cellulose films. They used a simple orientation parameter OG = (180-FWHM)/180 for the quantification of the degree of preferred orientation. The specimens with best performance in terms of elastic modulus achieved an average value of 25 GPa at OG = 0.62. This value of OG is modest compared to a value of OG = 0.79 calculated according to the procedure of Bohn et al. (*31*) for specimens stretched to 30% in the present study, thus explaining the low modulus of oriented bacterial cellulose sheets. Orientation of CNF from wood pulp was also achieved by direct spinning of an aqueous CNF suspension into acetone (*32*). At a degree of orientation OG = 0.72 the modulus of elasticity of hollow fibers obtained in this procedure was 24 GPa.

While the modulus of elasticity of stretched nanopaper clearly surpasses that of comparable cellulosic materials, the tensile strength is only in the same order of magnitude as found for stretched regenerated cellulose-based films (*23*, *24*), and spun CNF fibers (*32*). With an average value of 380 MPa for nanopaper stretched to 30%, the material prepared in the present study is clearly inferior to stretched bacterial cellulose films, which achieved average strength up to 450 MPa (*31*). Here it has to be considered that with regard to tensile strength, bacterial cellulose fibrils represent an optimum material because of their high inherent degree of polymerization (*33*) compared to dissolving-grade pulp used in the present study. Also, bacterial cellulose fibrils do not have to be treated by high-pressure homogenization, which is potentially damaging to tensile strength, because they are naturally synthesized in the form of nano-scale fibrils in a controlled biological process.

Downloaded by 217.66.152.26 on August 23, 2012 | http://pubs.acs.org
Publication Date (Web): August 17, 2012 | doi: 10.1021/bk-2012-1107.ch001

Downloaded by 217.66.152.26 on August 23, 2012 | http://pubs.acs.org
Publication Date (Web): August 17, 2012 | doi: 10.1021/bk-2012-1107.ch001

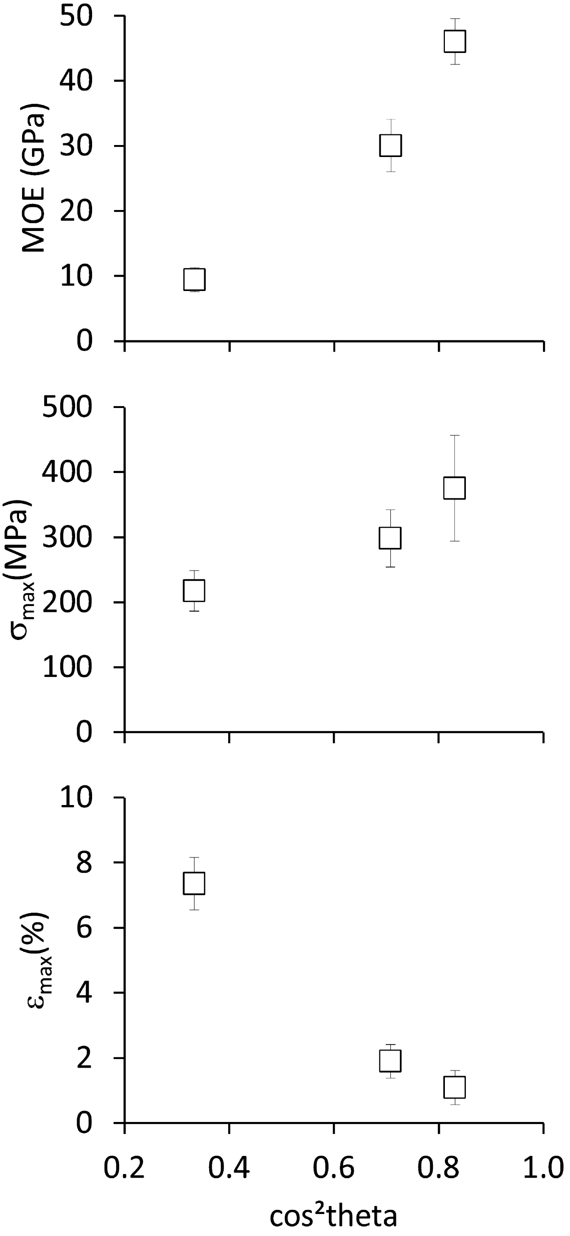

Figure 8. Results of tensile experiments with nanopaper from CNF treated by TEMPO-mediated oxidation in unstretched condition and after stretching to 15 % and 30 %, respectively, plotted over the degree of preferred orientation (average values and standard deviation).

Downloaded by 217.66.152.26 on August 23, 2012 | http://pubs.acs.org
Publication Date (Web): August 17, 2012 | doi: 10.1021/bk-2012-1107.ch001

Conclusion

The results presented in the section above demonstrate that TEMPO-mediated oxidation facilitates the stretching of CNF nanopaper in wet state. Stretching leads to a high degree of preferred orientation of CNF parallel to the direction applied strain. In dry state, stretched nanopaper is characterized by a superior modulus of elasticity, and good tensile strength, yet small strain at failure.

References

1. Moon, R. J.; Martini, A.; Nairn, J.; Simonsen, J.; Youngblood, J. *J. Chem. Soc. Rev.* **2011**, *40*, 3941–3994.
2. Hofstetter, K.; Hellmich, C.; Eberhardsteiner, J.; Mang, H. A. *Mech. Adv. Mater. Struct.* **2008**, *15*, 474–484.
3. Nakagaito, A. N.; Yano, H. *Appl. Phys. A: Mater. Sci. Process.* **2004**, *78*, 547–552.
4. Iwamoto, S.; Nakagaito, A. N.; Yano, H. *Appl. Phys. A: Mater. Sci. Process.* **2007**, *89*, 461–466.
5. Guhados, G.; Wan, W.; Hutter, J. L. *Langmuir* **2005**, *21*, 6642–6646.
6. Hsieh, Y. C.; Yano, H.; Nogi, M.; Eichhorn, S. J. *Cellulose* **2008**, *15*, 507–513.
7. Nishino, T.; Takano, K.; Nakamae, K. *J. Polym. Sci., Part B: Polym. Phys.* **1995**, *33*, 1647–1651.
8. Eichhorn, S. J. *Soft Matter* **2011**, *7*, 303–315.
9. Iwamoto, S.; Kai, W.; Isogai, A.; Iwata, T. *Biomacromolecules* **2009**, *10*, 2571–2576.
10. Nakagaito, A. N.; Nogi, M.; Yano, H. *MRS Bull.* **2010**, *35*, 214–218.
11. Lima, M. M. D.; Borsali, R. *Macromol. Rapid Commun.* **2004**, *25*, 771–787.
12. Azizi-Samir, A. S.; Alloin, F.; Dufresne, A. *Biomacromolecules* **2005**, *6*, 612–626.
13. Hubbe, M. A.; Rojas, O. J.; Luica, L. A.; Sain, M. *BioResources* **2008**, *3*, 929–980.
14. Eichhorn, S. J.; Dufresne, A.; Aranguren, M.; Marcovich, N. E.; Capadona, J. R.; Rowan, S. J.; Weder, C.; Thielemans, W.; Roman, M.; Renneckar, S.; Gindl, W.; Veigel, S.; Keckes, J.; Yano, H.; Abe, K.; Nogi, M.; Nakagaito, A. N.; Mangalam, A.; Simonsen, J.; Benight, A. S.; Bismarck, A.; Berglund, L. A.; Peijs, T. *J. Mater. Sci.* **2010**, *45*, 1–33.
15. Siqueira, G.; Bras, J.; Dufresne, A. *Polymers* **2010**, *2*, 728–765.
16. Klemm, D.; Kramer, F.; Moritz, S.; Lindström, T.; Ankerfors, M.; Gray, D.; Dorris, A. *Angew. Chem., Int. Ed.* **2011**, *50*, 5438–5466.
17. Garkhail, S. K.; Heijenrath, R. W. H.; Peijs, T. *Appl. Comp. Mater.* **2000**, *7*, 351–372.
18. Bordel, D.; Putaux, J. L.; Heux, L. *Langmuir* **2006**, *22*, 4899–4901.
19. Sugiyama, J.; Chanzy, H.; Maret, G. *Macromolecules* **1992**, *25*, 4232–4234.
20. Dugan, J. M.; Gough, J. E.; Eichhorn, S. J. *Biomacromolecules* **2010**, *11*, 2498–2504.

21. Nishiyama, Y.; Kuga, S.; Wada, M.; Okano, T. *Macromolecules* **1997**, *30*, 6395–6397.
22. Uddin, A. J.; Araki, J.; Gotoh, Y. *Biomacromolecules* **2011**, *12*, 617–624.
23. Gindl, W.; Keckes, J. *J. Appl. Polym. Sci.* **2007**, *103*, 2703–2708.
24. Gindl, W.; Martinschitz, K. J.; Boesecke, P.; Keckes, J. *Biomacromolecules* **2006**, *7*, 3146–3150.
25. Saito, T.; Nishiyama, Y.; Putaux, J. L.; Vignon, M.; Isogai, A. *Biomacromolecules* **2006**, *7*, 1687–1691.
26. Eichhorn, S. J.; Young, R. J. *Cellulose* **2001**, *8*, 197–207.
27. Nogi, M.; Iwamoto, S.; Nakagaito, A. N.; Yano, H. *Adv. Mater.* **2009**, *21*, 1595–1598.
28. Okita, Y.; Saito, T.; Isogai, A. *Biomacromolecules* **2010**, *11*, 1696–1700.
29. Northolt, M. G.; den Decker, P.; Picken, S. J.; Baltussen, J. J. M.; Schlatmann, R. *Adv. Polym. Sci.* **2005**, *178*, 1–108.
30. Cox, H. L. *Br. J. Appl. Phys.* **1952**, *3*, 72–79.
31. Bohn, A.; Fink, H-P.; Ganster, J.; Pinnow, M. *Macromol. Chem. Phys.* **2000**, *201*, 1913–1921.
32. Iwamoto, S.; Isogai, A.; Iwata, T. *Biomacromolecules* **2011**, *12*, 831–836.
33. Iguchi, M.; Yamanaka, S.; Budinho, A. *J. Mater. Sci.* **2000**, *35*, 261–70.

Downloaded by 217.66.152.26 on August 23, 2012 | http://pubs.acs.org
Publication Date (Web): August 17, 2012 | doi: 10.1021/bk-2012-1107.ch001

Chapter 2

Strategies for Preparation of Oriented Cellulose Nanowhiskers Composites

Elena Ten,*,[1] Long Jiang,[2] and Michael P. Wolcott[1]

[1]Composite Materials and Engineering Center, Washington State University,
P.O. Box 641806, Pullman, Washington 99163-1806
[2]Department of Mechanical Engineering, North Dakota State University,
P.O. Box 6050 Fargo, North Dakota 58108-6050
***E-mail: elena.ten@email.wsu.edu**

Downloaded by STANFORD UNIV GREEN LIBR on August 28, 2012 | http://pubs.acs.org
Publication Date (Web): August 17, 2012 | doi: 10.1021/bk-2012-1107.ch002

Due to hierarchical structure of cellulose, its building blocks known as "cellulose nanowhiskers" (CNW) have raised a great deal of research interest over the last decades. Natural affinity of CNW for self-assembly and structural anisotropy allow them to orient under external forces. This book chapter provides a review on the major developments in fabrication techniques of CNW alignment in polymers. First, we will present self-assembly phenomenon of CNW in aqueous medium. Following this, the book chapter will focus on discussion of major strategies reported in the literature on aligning CNW in polymer by external forces: mechanical and by applying electric and magnetic fields. Further, the chapter highlights recent developments in cellulose composite fibers and aligning CNWs by electrospinning and wet-spinning techniques. As insights are gained into CNW reinforcement mechanisms and processing options, future research directions and potential applications are anticipated. These potential application areas will be briefly introduced as well.

Downloaded by STANFORD UNIV GREEN LIBR on August 28, 2012 | http://pubs.acs.org
Publication Date (Web): August 17, 2012 | doi: 10.1021/bk-2012-1107.ch002

Introduction

Over the past century, increased production of plastics has raised serious concerns about their impact on the environment. Reduced capacities of landfills, environmental persistence, harm to marine mammals, greenhouse gas emission, and fossil fuel depletion are a few examples of environmental and economic concerns. Although today the proportion of plastics recycled or reused is gradually increasing, only part of the plastics produced can be recovered. Moreover, not all plastics are suitable for recycling or reuse (e.g., contamination of plastic by other materials and additives, non-reshaped properties of thermosetting materials, and poor compatibility of blends) (*1*, *2*). As a result, the volume of plastics discarded annually creates a substantial plastic waste disposal issue, and the concept of developing sustainable materials systems has gained great attention from scientists and engineers. Global sustainability relies on renewable sources of materials and energy; and use of natural polymers is of current interest.

By using biomass as a feedstock to produce renewable plastics we reduce our dependence on fossil fuels and materials. In addition, these biobased polymers often display enhanced biodegradability and biocompatibility, benefitting diverse applications ranging from packaging to medical devices.

Among naturally occurring renewable polymers, cellulose is the most abundant biopolymer on earth. Cellulose is a polydisperse linear polymer of β-(1,4)-D-glucose. One of the most promising uses of cellulose is in composites. The structure of cellulose is hierarchical: cellulose chains aggregate into the repeated crystalline structure to form microfibrils, which in turn aggregate into larger macroscopic fibers that comprise plant cell walls. These fibers consist of alternating crystalline and non-crystalline domains. Multiple mechanical shearing processes can be used to obtain individual microfibrils usually called "microfibrillated cellulose" (MFC). Network structure and high number of entanglements of MFC restrict the mobility of microfibrillated cellulose in polymer matrixes which in turn significantly influence mechanical properties of MFC composites (*3*). Therefore, the scope if this chapter is to give prospective on strategies of cellulose nanowhiskers orientation within polymer matrices. The non-crystalline domains are weak spots along MFC. They can be dissolved by a strong acid hydrolysis treatment. The remaining crystalline domains are commonly referred to as "cellulose nanowhiskers" (CNW) or "cellulose nanocrystals" (CNC) in the literature.

Cellulose nanowhiskers (CNWs) are needle-shaped highly crystalline fibrils that naturally occur in many plants (e.g. wood, hemp, sugar beet, sisal, cotton, and ramie), bacteria, and sea animals (e.g. tunicin). The most common method to harvest CNW from natural fibers is sulfuric acid hydrolysis followed by centrifugation. As already mentioned, the mechanism to isolate CNW is to destroy and remove non-crystalline or paracrystalline regions which are present between nanowhiskers through chemical reactions. The first report on the production of nanostructured cellulose in solution was published by Rånby in 1951 (*4*). It has been shown that CNW could be produced by controlled acid hydrolysis of native, viscose rayon and wood mercerized cellulose fibers. CNW formed stable suspensions of single crystals in water.

Typical transmission electron image of CNW prepared from microcrystalline cellulose is shown in Figure 1. Hydrolysis conditions such as temperature and time influence the size (*6–8*) and stiffness (*9*) of the resulting CNWs. The sulfuric acid treatment introduces sulfate groups to the surface of CNWs. The negative charges on the CNW surfaces lead to high stability of aqueous CNW suspensions (*10*). Most recent reviews summarize literature on cellulose nanoparticles in terms of particle morphology, crystal structure, and properties (*11*), isolation processes of CNW from wood and its application in nanocomposites (*12*) along with self-assembly phenomenon and surface modification (*13*).

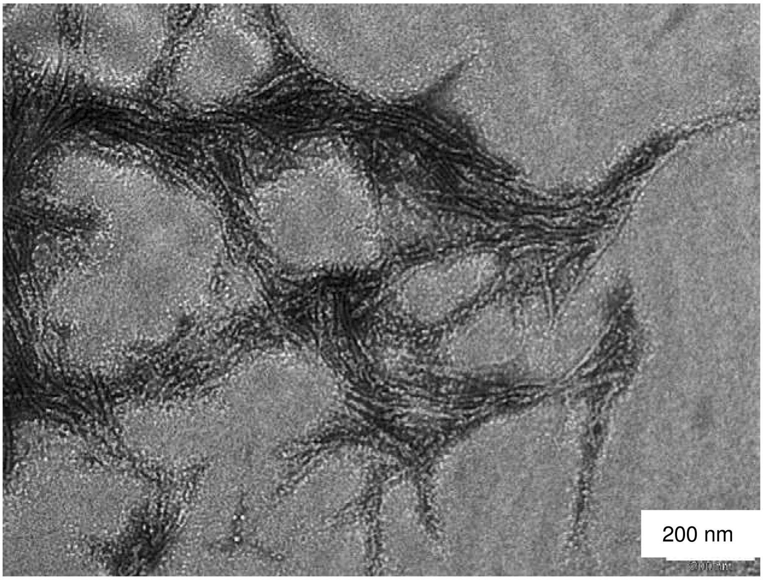

Figure 1. Transmission electron microscope image of cellulose nanowhiskers obtained from microcrystalline cellulose (5). Reproduced with permission from reference (5). Copyright 2010 Elsevier.

Since the first reports of using tunicate CNW as reinforcement for poly(styrene-*co*-butyl acrylate) latex by Favier *et al.* (*14*, *15*), cellulosic nanocomposites have received a great deal of research interest, because their environmental compatibility and superior mechanical and physical properties make them good alternatives to commodity petroleum-derived plastics. Due to abundance, low cost, high specific moduli (modulus over density), hierarchical structure, stiffness of about 100-143 GPa (*16–18*) and high aspect ratio, CNWs have found to be a good reinforcement agent for a wide variety of polymeric matrices (*19–41*).

Even though mechanical performance of cellulosic nanocomposites has been extensively investigated and many articles and review papers (*11–13*, *42–50*) have been published, industrial implementation of CNWs is still limited. The main reasons are high costs of isolation and challenges of homogeneous dispersion that require CNW surface modification. As a result, the reinforcing effect of cellulose nanowhiskers in polymer matrices is often not as high as expected (*5*,

Downloaded by STANFORD UNIV GREEN LIBR on August 28, 2012 | http://pubs.acs.org
Publication Date (Web): August 17, 2012 | doi: 10.1021/bk-2012-1107.ch002

Downloaded by STANFORD UNIV GREEN LIBR on August 28, 2012 | http://pubs.acs.org
Publication Date (Web): August 17, 2012 | doi: 10.1021/bk-2012-1107.ch002

41). One of the methods to control and tailor properties of nanocomposites is to manufacture unidirectional composites. Ultimately, highly reinforced composites can be manufactured by constructing several layers of unidirectional reinforced films alternating orientations. The quantity of available data on aligned CNW in polymer, however, is rather limited compared to randomly oriented composites. Thus, this book chapter will introduce current ways of aligning CNW in polymer matrices. The objective of this review is to present current developments in preparation of oriented cellulose nanowhisker composites. Such review will provide a useful guide in engineering cellulosic nanocomposites.

Self Assembly of CNW in Aqueous Solution

As mentioned earlier in the introduction, cellulose nanowhiskers prepared by acid hydrolysis easily form highly stable colloidal suspensions. Above a critical concentration, in order to minimize electrostatic interactions, the suspensions of rod-like particles spontaneously form an anisotropic chiral nematic or cholesteric liquid crystal phase (*51*).

These CNW suspensions self-organized into liquid crystalline arrangements can be observed between cross-polarizers (birefringence) or by polarized optical microscopy (typical fingerprint pattern indicative of a chiral nematic ordering). Examples of a birefringent pattern or "birefringent glassy phase" of the HCl hydrolyzed cellulose microcrystals followed by H_2SO_4 treatment (*52*) and fingerprint texture of the chiral nematic phase of H_2SO_4-hydrolyzed bleached hardwood pulp (*53*) are shown in Fig 2 (a) and (b), respectively.

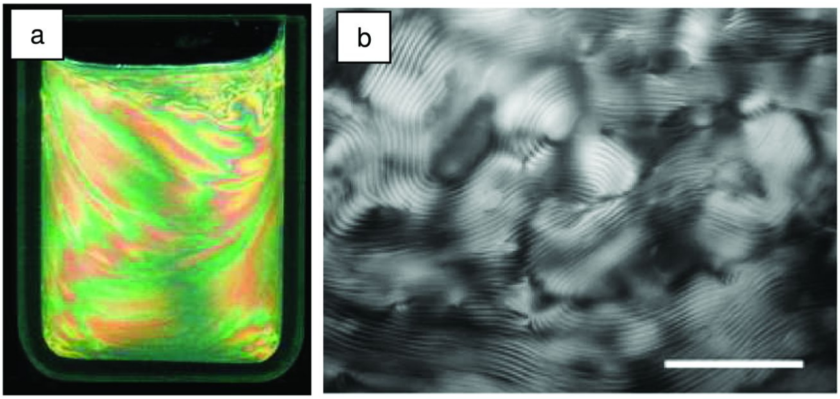

Figure 2. (a) Birefringent pattern of highly viscous suspension of cellulose nanocrystals prepared by postsulfating the HCl-hydrolyzed CNWs (7.1% solid content) (52); Reproduced with permission from references (52). Copyright 2000 American Chemical Society. (b) "fingerprint" texture in chiral nematic phase within the anisotropic region of a suspension of 10 wt% eucalyptus suspension viewed under optical polarized microscope. Scale bar is 200 µm. Chiral nematic pitch P = 17 µm (53). Reproduced with permission from references (53). Copyright 2005 American Chemical Society.

Downloaded by STANFORD UNIV GREEN LIBR on August 28, 2012 | http://pubs.acs.org
Publication Date (Web): August 17, 2012 | doi: 10.1021/bk-2012-1107.ch002

Marchessault *et al.* (*54*) were the first to describe formation of birefringent gels based on cellulose and chitin aqueous suspensions of crystallites. The concentration of cellulose in such gels was up to 13-15 wt%. The "liquid crystalline" character of these gels was ascribed to the presence of parallel alignments of the anisotropic cellulose crystallites (nematic order). Later, Revol *et al.* (*55*) reported *in vitro* self-organization of aqueous suspensions of cellulose crystallites into stable chiral nematic phases. These ordered suspensions solidified upon evaporation of the water to give helicoid structures. Further, the colloidal suspensions separation between upper isotropic and a lower anisotropic phase was typically observed at as low as 3 wt% (*55*) and 4 wt% (*56*) of cellulose in the suspension. The volume fractions of cellulose in the isotropic and anisotropic phases were estimated to be 0026 and 0.028, respectively (*56*). Even lower solid concentrations of cotton CNW (ca. 2-3%) were reported to be sufficient to form stable birefringent pattern without orientation by shear flow (*52*). Whereas, for bacterial cellulose (BC) suspensions, phase separation was observed at 0.3-1.2% (*57*). In this study (*57*) Araki and Kuga reported that BC nanowhiskers can undergo spontaneous nematic phase separation after complete desalination. Moreover, the addition of a trace electrolyte (0.1 mM NaCl) changed the phase separation behavior – the anisotropic phase became chiral nematic. The volume ratio of anisotropic phase for cellulose suspension decreased with NaCl concentration. The source of chiral interactions between CNWs was explained by the change of nanocrystals shape from cylindrical to twisted geometry that was induced by addition of an electrolyte. The same reason for twisted CNW structure was suggested when CNW suspensions were sterically stabilized by poly(ethylene glycol) polymer grafting (*58*). A later study (*59*) also demonstrated that aspect ratio, shape of the nanocrystals, and ionic strength of the suspensions are the most important factors governing the phase separation behavior. By altering the salt contents of the suspension for a given source of CNW and set of hydrolysis conditions, the films could be tailored to give different optical properties.

The chiral nematic microstructure of solid CNW films was studied by Roman and Gray (*60*). Characterized by polarized optical microscopy (POM) and atomic force microscopy (AFM), the microstructure revealed planar, polydomain areas and areas with parabolic focal conic (PFC) defect structure. PFC is a complex symmetrical structure of focal conic defects in which the line defects form a pair of perpendicular, antiparallel, and confocal parabolas (*61*). PFC structure of CNW chiral nematic films observed between two cross-polars is shown in Figure 3. To identify the local orientation of the quasi-nematic planes a full-wave retardation plate was inserted into the optical path of the POM. With a full-wave retardation plate, a blue color appeared where the slow axis of the birefringent sample was aligned with the slow axis of the wave plate and a yellow color appeared where the fast axis of the sample was aligned with the slow axis of the wave plate. By convention, the slow axis of the wave plate was oriented in the northeast-southwest direction.

Due to these unique structural and optical characteristics, CNW can be used as nontoxic, optically variable iridescent pigments in cosmetics and coating materials for decorative materials. Moreover, self-assembled chiral nematic films have potential applications as security papers.

Downloaded by STANFORD UNIV GREEN LIBR on August 28, 2012 | http://pubs.acs.org
Publication Date (Web): August 17, 2012 | doi: 10.1021/bk-2012-1107.ch002

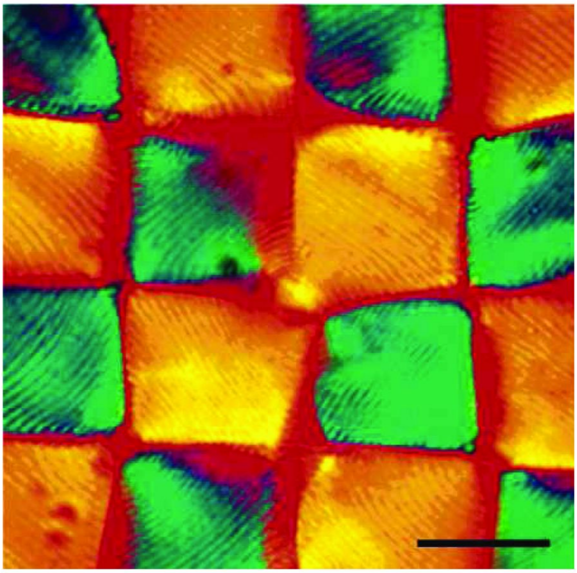

Figure 3. Parabolic focal conics in CNW chiral nematic films viewed between crossed polarizers with full-wave retardation plate inserted into the microscope. Scale bar 20 μm. Reproduced with permission from reference (60). Copyright 2005 American Chemical Society.

Methods for Preparation of Oriented CNW Composite Films

Conventionally fiber-reinforced composites often show higher mechanical properties in the direction of fiber orientation. Developing unidirectional fiber composite films is an essential step to the production of fiber composites/laminates for high-performance demanding applications. Attempts have been made to produce oriented CNW nanocomposites. Three methods have been reported in the literature to align CNW fibers, including applying mechanical forces (shearing and spin coating) (*62–67*), magnetic (*66*, *68–72*) and electric fields (*73–76*).

Owing to the rod-like shape of CNWs, they can orient themselves along the flow direction in flowing composite solutions. A method of shearing a suspension with simple equipment has been reported by Nishiyama *et al.* (*62*). A vial containing aqueous CNW suspension was kept in a horizontal position and rotated around its axis at 500 rpm at room temperature. The resulting film was found to be highly anisotropic and brittle in the direction perpendicular to the fiber orientation. Linearly oriented films were also obtained by shearing a drop of concentrated aqueous nanocrystal suspension along mica, glass or polystyrene surfaces (*63*). The same study demonstrated a radial arrangement of nanocrystals when the nanocrystals are spin-coated suspension onto a glass or mica surface. Under crossed polarizers light, the spin-coated samples displayed a Maltese cross suggesting that the nanocrystals were oriented radially in the direction of the shearing forces on the fluid during spin-coating (*63*).

Layer-by-layer (LbL) spin-coating technique was used to create polyelectrolyte multilayer (PEM) nanocomposites containing cellulose nanocrystals and poly(allylamine hydrochloride) (*64–66*). Similar to previous studies, CNWs were also radially oriented in spin-coated polyelectrolyte multilayer films. Films were assembled with up to 25 bilayers poly(allylamine hydrochloride)/CNW at 3000 rpm for 40 s. The observed birefringence was close to that of pure crystalline cellulose, indicating good flow-induced alignment of the nanocrystals (*65*).

Recently, Hoeger *et al.* (*67*) successfully aligned ramie CNW using convective and shear forces. The experimental set-up included a solid support and a moving or withdrawal plate (Figure 4). The effect of concentration of CNC in aqueous suspensions, type of solid support, relative humidity and rates of withdrawal of the deposition plate were determined by using atomic force microscopy (AFM) and ellipsometry. In particular, five different substrates were investigated: mica sheets with a high negative charge density, less negatively charged silica wafers, positively charged silicon wafers with pre-adsorbed poly(ethylene imine) (PEI), and high and low surface energy gold-based slides.

Downloaded by STANFORD UNIV GREEN LIBR on August 28, 2012 | http://pubs.acs.org
Publication Date (Web): August 17, 2012 | doi: 10.1021/bk-2012-1107.ch002

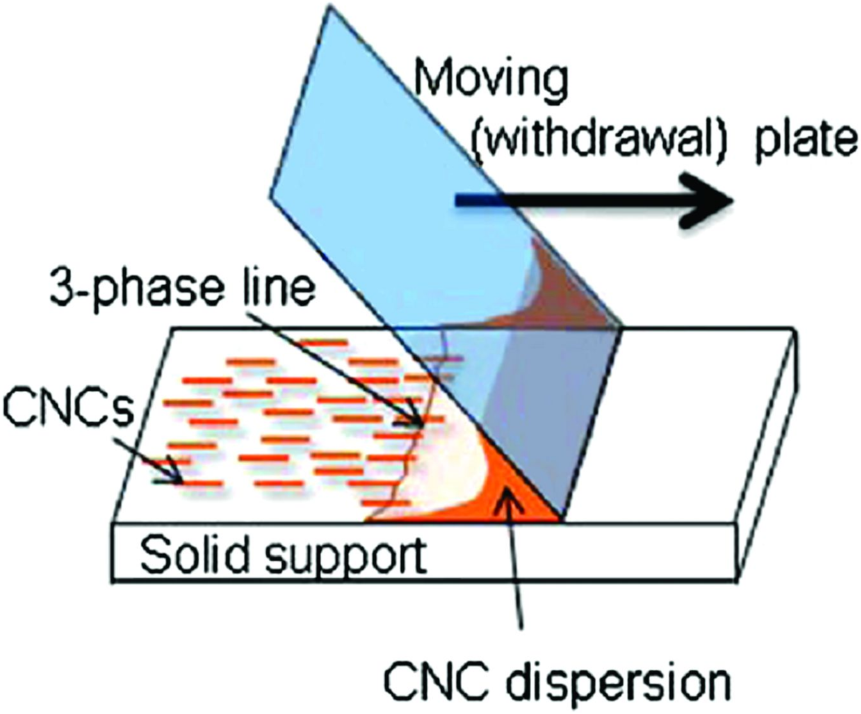

Figure 4. Experimental setup for assembly and deposition showing the CNW suspension, solid support, withdrawal plate and three-phase line (67). Reproduced by permission from reference (67). Copyright 2011 RSC.

Downloaded by STANFORD UNIV GREEN LIBR on August 28, 2012 | http://pubs.acs.org
Publication Date (Web): August 17, 2012 | doi: 10.1021/bk-2012-1107.ch002

It was reported that the poor alignment of CNW was observed in the case of the negatively charged solid support. The reasons for that were the dominant and counterbalancing effects of shear and capillary forces acting normal and parallel to the three phase contact line, respectively.

The best alignment of CNWs in the withdrawal direction, favored by shear effects, was achieved with gold and silica supports with a pre-adsorbed cationic polyelectrolyte layer and at a CNW suspension concentration above 2.5 wt%, below the critical concentration for chiral nematic phase separation. In fact, the induced orientation of CNW was determined by a complex balance of forces, mainly, hydrodynamic (shear and drag), Brownian, surface tension (capillary forces) and electrostatic interactions (between the negatively charged CNWs and between the CNWs and the substrate). Therefore, the bare solid support, nanoindentation of the obtained coatings of ultra-thin films of oriented CNW provided enhanced surface mechanical strength and wear resistance (*67*). Authors stated that this method of CNW alignment has a potential for scale up production considering that the degree of orientation of CNW comparable with those obtained after application of high electric fields. Up to 40–60% of CNW were aligned in angles between 0 and 20° with respect to the withdrawal direction.

Magnetic fields have been reported to orient CNW in both aqueous suspensions (*66*, *68–70*, *72*) and polymers (*71*). The first study on the production of aligned CNW in aqueous solutions using magnetic field was described by Sugiyama *et al.* (*68*). Tunicate nanocrystals were aligned using rather moderate magnetic field of 7 T. The orientation under magnetic field initiates from diamagnetic anisotropy of individual CNWs, specially, anisotropic magnetic susceptibility of the individual C-C, C-O, C-H, and O-H bonds and their relative orientation in the nanocrystal. Later, preliminary experiments relevant to layer-by-layer self-assembly of oriented cellulose nanocrystals were performed also in a 7 T magnetic field (*56*, *69*). A substantial orientation of CNW was observed under AFM only after long exposure to the magnetic field (24 hours) (*69*). The effect of magnetic field on chiral nematic phase of tunicate CNWs (*70*) showed that the helical axis of the chiral nematic phase aligned in the direction of the applied static field (1-28 T), resulting in highly regular monodomains. Exposure to the rotating (5 T, 10 rpm) magnetic field caused unwinding of the helical axes to form nematic-like alignment. These phenomena were interpreted in terms of aforementioned anisotropic diamagnetic susceptibility of the cellulose whisker. The diamagnetic susceptibility of the CNW is smaller in the direction parallel to the fiber axis than in the direction perpendicular to the fiber axis. Because the helical axis coincides with the direction normal to the fiber axis, the helical axis aligned parallel to the applied field. That's why the long axis of the nanocrystals is perpendicular to the magnetic field (*56*).

The first attempt to orient CNWs in polymeric matrix was reported by Kvien *et al.* (*71*). Cellulose nanowhiskers (2 wt%) were incorporated in a polyvinyl alcohol (PVA) matrix using solution casting with water as the solvent. The water evaporated while a ~7 T homogeneous magnetic field was applied. Dynamic mechanical thermal analysis (DMTA) showed that the dynamic modulus of the nanocomposite was ~47% higher in the transverse direction than in the field direction, an indication of CNW orientation in the transverse direction

(*71*). Relevant to large-scale production of paper, all cellulose composites were prepared by mixing CNW fabricated by H_2SO_4 treatment of microcrystalline cellulose and wood pulp fibers (*72*). The mixture was vacuum filtered through filter paper under magnetic field of 1.2 T followed by compression and drying at 100 °C for 15 min. The DMTA results showed that the magnetic field aligned the nanowhisker in the fabricated all-cellulose nanocomposite, while it did not have any influence on the orientation distribution of the cellulose pulp fibers. Large pulp fibers prevented free movement and limited the realignment of pulp fibers. The rotation force generated by the diamagnetic susceptibility was not large enough to rotate the pulp fibers, but it was sufficient to promote the rotation of the nanowhiskers. The presence of 5 wt% cellulose nanowhiskers in the composites increased the storage modulus almost by one order of magnitude, from 652 MPa for the paper sheet to 4.88 GPa for the nanocomposite along the direction perpendicular to the applied magnetic field direction at 20 °C (*72*).

An alternative method for CNW orientation reported in the literature is to use strong electric fields. Most studies on the orientation of suspended particles in electric field have dealt with aqueous suspensions, which exhibit limitations arising mainly from the high conductivity of water. Bordel *et al.* successfully demonstrated for the first time the ability to align ramie cellulose fibers and tunicin whiskers at macroscopic and colloidal levels when they were dispersed in chloroform and cyclohexane, respectively (*73*). Both suspensions were introduced into a Kerr cell consisting of a Teflon container and two parallel stainless steel plates. Electric filed of 2000 V/cm was applied at 1 kHz. The effect of applied electric field on cellulose fibers and whiskers is shown in Fig 5. The ramie fibers and whiskers aligned perpendicular to the electrodes (Figure 5 b,c) pointing in the direction of the electric field. However, this pioneer study did not investigate the influence of the alternating electric field, e.g. frequency and amplitude on the fiber orientation. Habibi *et al.* reported a highly reproducible, efficient and quick method to create anisotropic films from aqueous suspensions of tunicate and ramie CNW (*74*).

Cellulose nanocrystals orientation was strongly dependent on the strength and the frequency of the electric field. The applied electric field ranged between 250 and 10^4 V/cm while frequency from 1 kHz to 1 MHz.

Compared to tunicate CNW, ramie CNW did not demonstrate the similarities in the alignment capabilities under AC electric fields. This is probably attributed to the lowest polarizability of ramie whiskers since their shorter length does not favor the counter ion cloud deformation. Interactions between cellulose nanocrystals and ammonium groups grafted on the surface are also suggested to play a role. These interactions are stronger for ramie nanocrystals than tunicate. In the case of tunicate cellulose nanocrystals, there was no obvious alignment in the samples exposed to AC electric field with electric field lower than 2000 V/cm for all frequencies. A better orientation percentage was observed for starting electric field of 2500 V/cm but it seems to be affected by electric field frequency. Surprisingly, perfect orientation is observed for frequencies ranging between 10^4 and 10^6 Hz. Results demonstrate that the cellulose nanocrystals degree of alignment is gradually reduced with the decrease ($<10^4$ Hz) or the increase ($>10^6$ Hz) of the electric field frequency. Interestingly, when the electric field frequency

Downloaded by STANFORD UNIV GREEN LIBR on August 28, 2012 | http://pubs.acs.org
Publication Date (Web): August 17, 2012 | doi: 10.1021/bk-2012-1107.ch002

Downloaded by STANFORD UNIV GREEN LIBR on August 28, 2012 | http://pubs.acs.org
Publication Date (Web): August 17, 2012 | doi: 10.1021/bk-2012-1107.ch002

is decreased, cellulose nanocrystals tend to aggregate within the electrode gaps suggesting electrostatic interactions between sulfate groups (electrostatic repulsion) is not strong enough to counter electric field induced aggregation. By contrast, when the electric field frequency is increased, cellulose nanocrystals are attracted toward the electrodes suggesting that electrostatic forces influence whisker alignment dynamics. In both cases, high orientation was observed only near to the electrodes (*74*). A high percentage of fiber orientation was observed under the electric field of 2 kV/cm and higher (Figure 6).

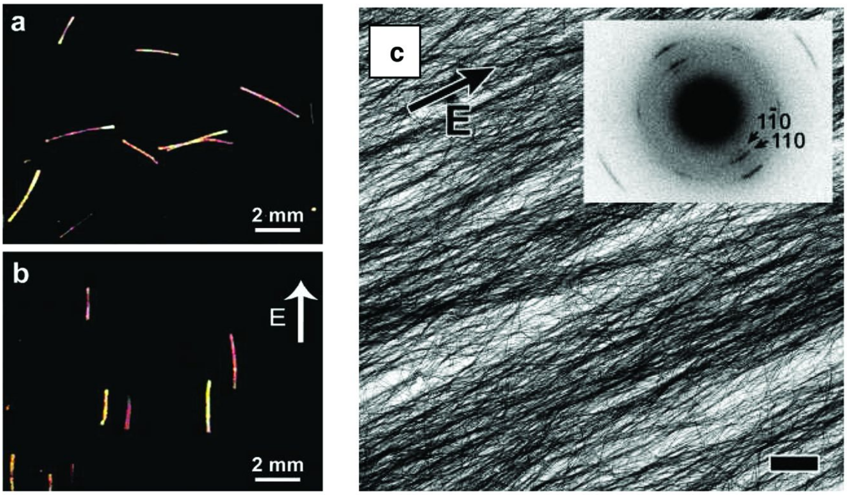

Figure 5. Optical micrograph in polarized light of ramie fiber fragments (a) in the absence of field and (b) in the presence of a 1 kHz electric field of 1200 V/cm. (c) TEM image of a film of 0.5 wt% tunicin whisker suspension in cyclohexane oriented with a 1 kHz electric field of 2000 V/cm (scale bar 2 μm). (Insert) electron diffraction pattern correctly oriented with respect to the specimen, recorded on 1 μm^2 of the specimen. The arrow indicates the direction of the electric field (73). Reproduced with permission from references (73). Copyright 2006 American Chemical Society.

Much lower electric field strength of 56.25 kV/m and DC conditions have been shown to be sufficient to align CNW in non-water soluble poly(3-hydroxybutyrate-*co*-3-hydroxyvalerate) (PHBV) (*75*, *76*). After harvesting CNW from microcrystalline cellulose by H_2SO_4 treatment, CNW were transferred to *N,N*-dimethylformamide by solvent exchange. PHBV was further dissolved in DMF/CNW suspension and cast on a glass substrate, which was placed between a pair of electrodes. The storage E′ moduli were determined below and above the glass transition temperature of PHBV: at -10 and 60 °C, respectively. Due to aligned CNW, nanocomposites demonstrated highly anisotropic behavior: E′ was increased by 78% and 63% for 1.5 and 3wt% of CNW, respectively, at -10 °C, while the increase was 45% and 38% at +60 °C (*75*). Furthermore, the authors analytically evaluated anisotropic properties

Downloaded by STANFORD UNIV GREEN LIBR on August 28, 2012 | http://pubs.acs.org
Publication Date (Web): August 17, 2012 | doi: 10.1021/bk-2012-1107.ch002

of PHBV/CNW composites by using micromechanics model. The effect of CNW volume fraction and orientation angle on storage moduli of PHBV/CNW composites was predicted by Cox "shear lag" model (*76*).

The reviewed literature shows that the development and property studies of the oriented CNW composites are still in their early stages. Although many successful results have been reported, producing polymer/CNWs nanocomposites with desirable polymer matrix and CNW orientations remains a technical and scientific challenge.

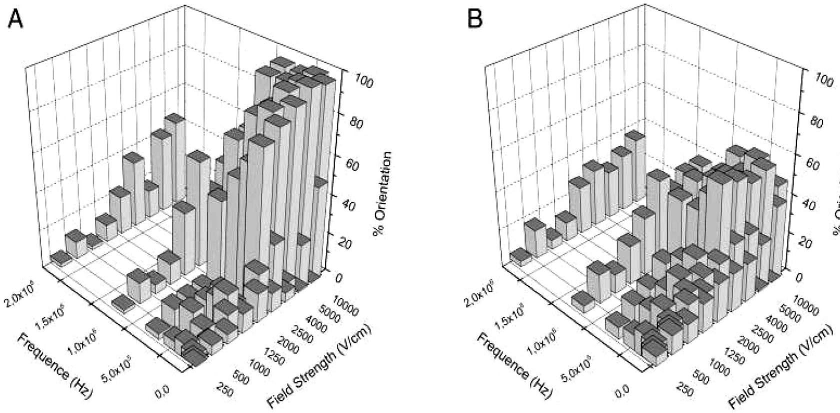

Figure 6. Effect of AC electric field force and frequency on the orientation of tunicin (A) and ramie (B) cellulose nanocrystal films (74). Reproduced with permission from references (74). Copyright 2008 Wiley Periodicals Inc.

Aligned CNW Microfibers by Electrospinning and Wet-Spinning Techniques

Given the biocompatibility of cellulose nanowhiskers and their ability to align under shear and electrostatic forces, a wide range of applications, predominantly biomedicine, sees an increasing demand for wet-spun and electrospun cellulosic mats, marco- and nanofibers.

"Electrospinning" is a versatile method to fabricate fibers with diameters ranging from several microns to 100 nm or less. During the electrospinning process, a charged fluid jet from a polymer solution is extruded under an applied electric field between two electrodes. As solvent in the jet solution evaporates, the polymer is collected onto a grounded substrate to form a nonwoven mat or network with large surface-to-volume ratios. Processing parameters such as the voltage, flow rate and distance between the spinning tip and the collector can drastically change properties of the final mat. The intrinsic properties of the polymer solution including conductivity, viscosity, net charge density, and surface tension are other important factors to consider during the electrospinning process. The first electrospun fibers were in fact fabricated from cellulose acetate/acetone/alcohol solution with patent dating back to Formhals in 1934 (*77*). Since then, numerous studies have been reported on electrospinning cellulose and derivatives using

Downloaded by STANFORD UNIV GREEN LIBR on August 28, 2012 | http://pubs.acs.org
Publication Date (Web): August 17, 2012 | doi: 10.1021/bk-2012-1107.ch002

various solvents, e.g. acetic acid/*N.N*-dimethylacetamide (CH_3COOH/DMAc), acetic acid/acetone (*78*), lithium chloride/*N.N*-dimethylacetamide (LiCl/DMAc) (*79–82*), *N*-methyl-morpholine *N*-oxide/water (NMMO/H_2O) (*10–85*), ionic liquids (*86*), DMAc/acetone (*87*), acetic acid/water (CH_3COOH/H_2O) (*88*), and NaOH/urea (*89*). The concentration of cellulose in solutions depends on both the cellulose molecular weight (degree of polymerization (DP)) and the solvent composition. The source of the cellulose, from wood pulps, cotton linters, or cotton fibers, does not appear to have a significant effect (*90*). In order to improve quality of electrospun fibers, researchers have added coagulant baths to the spinning line to remove components that do not volatilize in the spinning air gap and have incorporated temperature control at the spinneret, the collector, or the coagulation bath. These nanofibers can be used for a wide variety of applications such as separation filters, wound dressing materials, tissue scaffold, biosensors, drug delivery systems, etc.

Cellulose nanowhiskers themselves has been used as reinforcing materials for electrospun fibers such as polystyrene (*91*), poly(vinyl alcohol) (*92–94*), poly(lactic acid) (*95*), cellulose acetate (*38*), poly(acrylic acid) (*96*), polystyrene-*block*-poly(ethylene-*ran*-butylene)-*block*-polystyrene-*graft*-maleic anhydride (*97*), poly(ethylene oxide) (*98*) and polyethylene–polyvinyl alcohol (*99*).

Rojas, *et al.* pointed out increased tendency of bead formation with an increase of CNW in polystyrene/CNW nanofibers (*92*). This was ascribed to poor dispersion or compatibility of CNW with polystyrene. Sorbitan monostearate used as surfactant to improve the dispersion and compatibility of the hydrophilic cellulose nanowhiskers with the hydrophobic polystyrene matrix minimized the presence of beads. An increase in CNW loadings resulted in decrease of fiber's diameter. The reduction in the microfiber diameter was explained by the improved interaction between PS-chains and the CNWs in the presence of surfactant and also by the reduction in surface tension. Similar results of decreased fiber diameter have been reported for poly(lactic acid) (PLA) in *N,N*-dimethylformamide (DMF) (*95*), aqueous poly(vinyl alcohol) (PVOH) (*93*) and poly(acrylic acid) (PAA)/ethanol mixtures loaded with CNW (*96*). In a latter study (*96*), the Young's modulus and tensile strength were significantly improved with increasing CNW loadings in poly(acrylic acid) nanocomposite fibers by up to 35-fold and 16-fold, respectively, with 20% CNW. Enhancement in the dynamic storage modulus (E′) was also observed for the composites in both glassy and rubbery regions of poly(vinyl alcohol)/cotton CNW fibers was observed with increasing CNWs, even at a low CW content. For example, the addition of only 5 wt.% of CWs led to 100% and 165% E′ increase respectively in the glassy and rubbery regions of the composites (*94*). Drastic improvement in mechanical performance of electrospun polymer/CNW fibers arises from the efficient stress transfer between polymer and CNWs originating from their strong interactions, relatively uniform dispersion and high alignment of CNWs in the electrospun fibers (Figure 7).

Regarding thermal properties, differential scanning calorimetry (DSC) showed slight (2 °C) increase in melting temperature for PVOH/ramie CNW and reduced degree of crystallinity (*93*). These effects were explained by undermined

Downloaded by STANFORD UNIV GREEN LIBR on August 28, 2012 | http://pubs.acs.org
Publication Date (Web): August 17, 2012 | doi: 10.1021/bk-2012-1107.ch002

crystallization upon addition of CNWs. Disorder of PVOH nucleation in the presence of CNWs may have taken place during the short time allowed during electrospinning.

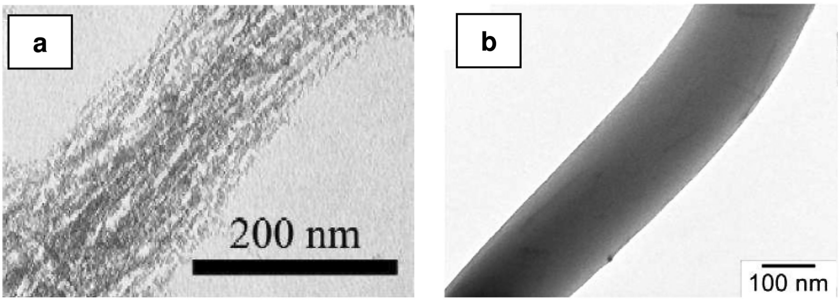

Figure 7. TEM micrographs of as-spun (a) polyethylene oxide/20wt%CNW (98) and (b) poly(acrylic acid)/5wt%CNW nanocomposite fibers (96). Reproduced with permission from reference (98). Copyright 2011 American Chemical Society. Reproduced with permission from references (96). Copyright 2009 IOP Publishing.

Magalhaes *et al.* described the fabrication of all-cellulose nanocomposites by co-electrospinning technique (Figure 8) (*100*, *101*). The authors used regenerated cellulose (type II and amorphous) as the shell solution (neat cellulose-doped solution consisted of 1.5 wt % of cellulose in *N*-methylmorpholine *N*-oxide (NMMO)/H_2O with dimethylsulfoxide (DMSO)) and aqueous cellulose whiskers (type I) suspension as core material.

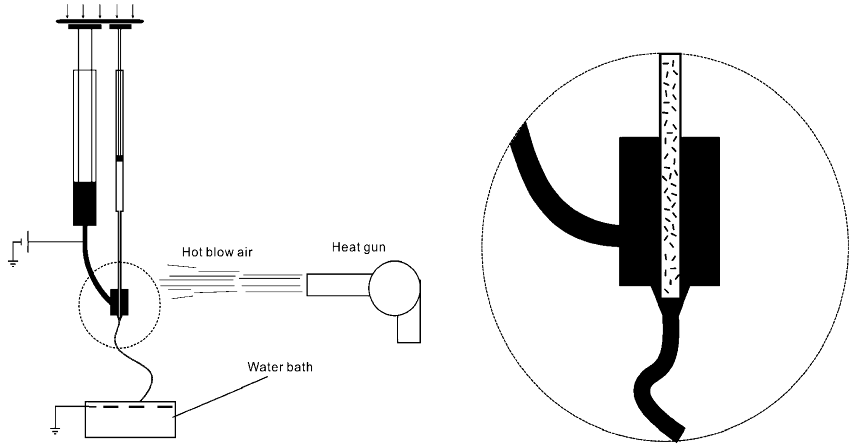

Figure 8. Schematic drawing of the co-electrospinning apparatus (100). Reproduced with permission from reference (100). Copyright 2009 American Chemical Society.

Several volume ratios between the shell and core, four flow rates for the shell dope solution, and four high voltages were tested. By decreasing the shell-to-core volume ratio, it was found that precise control of the voltage and flow rate promoted individual fiber formation. Moreover, CNWs suspensions were found to be easily electrospun when using solely NMMO/H_2O as the carrier likely because of its higher viscosity relative to a NMMO/DMSO dual solvent carrier. Finally, during the electrospinning of a neat cellulose solution, any increases in the flow rate slightly increased the cellulose crystallinity, but no effect was observed during co-electrospinning (*100*).

Since orientation of nanowhiskers is one of the main factors governing improved mechanical performance of CNW composites, the characterization of CNW alignment within polymer and its correlation to mechanical properties is of great importance. Wide-angle X-ray diffraction (WAXD) is a powerful technique commonly used to describe the crystalline structure of materials. It is commonly used to determinate degree of crystallinity, orientation of crystalline regions, concentration of a solid phase, etc. in polymer composites.

Recently, it was demonstrated that a simple variation in wet spinning processing conditions can be used to tune the mechanical properties of cellulose-based nanocomposites, which directly correlate with CNC orientation (*102*). The calcium alginate fibers filled with CNW were prepared by wet spinning an aqueous suspension of the CNC and sodium alginate into a $CaCl_2$ coagulating bath. Apparent jet stretch J_A defined as the tangential velocity of the first roller divided by the linear extrusion velocity (*103*) was varied and the diffraction patterns were used to study the effects of CNC and processing conditions on the alginate structure and CNC orientation. The orientation of the CNC was studied from the azimuthal intensity distribution of the (2 0 0) reflection by WAXD. The spread of the orientation increased with higher loads until the nanoparticles within the matrix spiraled around the longitudinal axis (Figure 9), which resulted in a reduction in tenacity and modulus and an increase in elongation at break and toughness. This spiral orientation is also observed in native cellulose fibers and is deterministic of their mechanical properties. This is evidenced by the formation of previously mentioned chiral nematic aqueous suspensions of CNWs.

The wet-spinning technique was also employed to obtain silk fibroin (SF)/cellulose nanowhisker hybrid fibers as a new material for the clothing industry (*104*). The rheological behavior of SF/CNW solution was tested to evaluate its spinnability. Compared with the pure silk fiber, the tensile strength and Young's modulus of the SF/CNW hybrid fibers containing 5 wt% CNWs were increased from 135.78±12.73 MPa and 5.74±0.43 GPa to 438.68±22.63 MPa and 17.36±2.04 GPa, respectively.

Biobased bacterial polyester poly(3-hydroxybutyrate-*co*-3-hydroxyvalerate) (PHBV) can be also wet-spun with CNWs, as shown by our group (*105*). Two-step solvent exchange process was used to obtain PHBV/CNW solution in chloroform. Fibers with diameter of ca. 100-150 μm (Figure 10) were spun into ethanol coagulation bath. The fibers were hot drawn to improve CNW orientation, hence increase mechanical properties.

Tenacity of drawn fibers was significantly improved, e.g. compared to as-spun fibers, neat PHBV showed 4-fold improvement in tenacity and PHBV/1

Downloaded by STANFORD UNIV GREEN LIBR on August 28, 2012 | http://pubs.acs.org
Publication Date (Web): August 17, 2012 | doi: 10.1021/bk-2012-1107.ch002

Downloaded by STANFORD UNIV GREEN LIBR on August 28, 2012 | http://pubs.acs.org
Publication Date (Web): August 17, 2012 | doi: 10.1021/bk-2012-1107.ch002

wt% CNW showed 2.5-fold enhancement. Detailed study is under way into the characterization of morphology of PHBV/CNW fibers and CNW orientation, as well as mechanical properties evaluation.

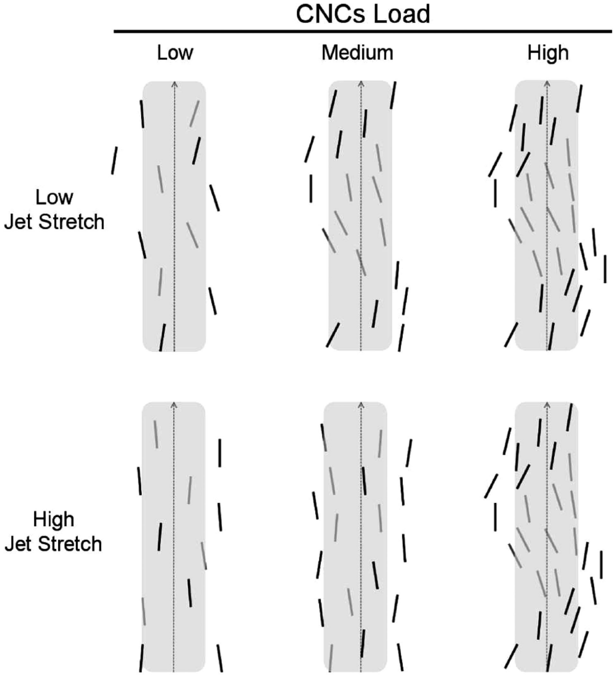

Figure 9. Schematic representation of the assembly of CNC in a calcium alginate fiber (102). The nanocrystals are incorporated within the alginate matrix and spiral around the fiber axis as the load is increased. Reproduced with permission from reference (102). Copyright 2011 American Chemical Society.

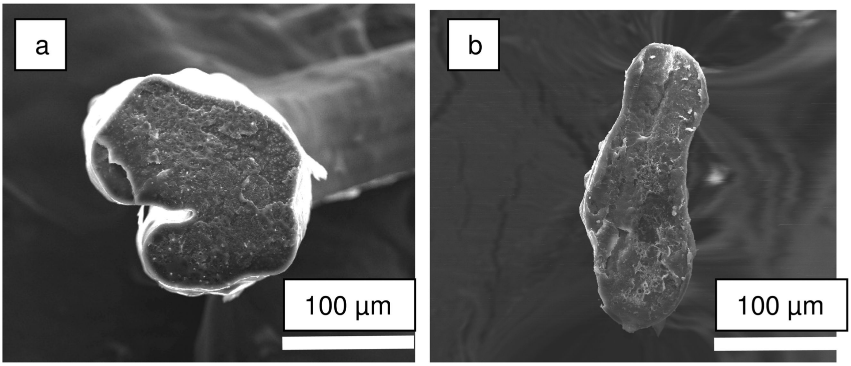

Figure 10. SEM micrographs of PHBV/4 wt% CNW (a) as-spun (b) after hot drawing.

Downloaded by STANFORD UNIV GREEN LIBR on August 28, 2012 | http://pubs.acs.org
Publication Date (Web): August 17, 2012 | doi: 10.1021/bk-2012-1107.ch002

Summary and Concluding Remarks

Development of nanotechnologies and increasing demand for an alternative to petroleum-based plastics encourage the use of forestry-derived nanocomposites. The wide availability, renewable and biocompatible nature, reactivity, high intrinsic strength and modulus make cellulose nanowhiskers superior to other traditional nanomaterials. It has already been shown that CNWs are viable reinforcements for a wide range of polymers. Based on reported literature, there is an ever-increasing interest to consolidate CNW use in "smart" packaging, drug delivery, biosensors, tissue engineering, inks for security paper, and structural composite platforms. For most of the potential applications the ability to orient nanowhiskers and further development of relevant fabrication method of unidirectional composites are of fundamental importance.

This study provided a short review of current methods to fabricate anisotropic CNW-reinforced composite films and fibers. The inherent anisotropy of cellulose crystals allows CNW to orient under magnetic, electric fields and shear forces. Tremendous ongoing work makes CNW to enable special functionalities and precise control over properties of the resulting composites. Overall, this effort is anticipated to inspire new opportunities for cellulose nanowhiskers in nanocomposites.

References

1. Howell, S. G. *J. Hazard. Mater.* **1992**, *29*, 143–164.
2. Cao, A. M. *China Environmental Protection Industry* **2002**, *1*, 86.
3. Siqueira, G.; Bras, J; Dufresne, A. *Biomacromol.* **2009**, *10*, 425–432.
4. Rånby, B. G. *Discuss. Faraday Soc.* **1951**, *11*, 158–164.
5. Ten, E.; Turtle, J.; Bahr, D.; Jiang, L.; Wolcott, M. P. *Polym. J.* **2010**, *51*, 2652–2660.
6. Dong, X. M.; Revol, J. F.; Gray, D. G. *Cellulose* **1998**, *5* (1), 19–32.
7. Bondeson, D.; Mathew, A.; Oksman, K. *Cellulose* **2006**, *13*, 171–180.
8. Elazzouzi-Hafraoui, S.; Nishiyama, Y.; Putaux, J-L.; Heux, L.; Dubreuil, F.; Rochas, C. *Biomacromol.* **2008**, *9*, 57–65.
9. Rusli, R.; Eichhorn, S. J. *Appl. Phys. Lett.* **2008**, *93*, 033111–033113.
10. Bondeson, D.; Kvien, I.; Oksman, K. Strategies for Preparation of Cellulose Whiskers from Microcrystalline Cellulose as Reinforcement in Nanocomposites. In *Cellulose Nanocomposites Processing: Characterization, and Properties*; Oksman, K., Mohini, S., Eds.; ACS Symposium Series 938; American Chemical Society: Washington, DC, 2006; pp 10−25.
11. Moon, R. J.; Martini, A.; Nairn, J.; Simonsenf, J.; Youngblood, J. *Chem. Soc. Rev.* **2011**, *40*, 3941–3994.
12. Klemm, D.; Kramer, F.; Moritz, S.; Tom Lindstrm, T.; Ankerfors, M.; Gray, D.; Dorris, A. *Angew. Chem., Int. Ed.* **2011**, *50*, 5438–5466.
13. Habibi, Y.; Lucia, L. A.; Rojas, O. J. *Chem. Rev.* **2010**, *110* (6), 3479–3500.
14. Favier, V.; Chanzy, H.; Cavaille, J. Y. *Macromol.* **1995**, *28*, 6365–6367.

15. Favier, V.; Canova, G. R.; Cavaille, J. Y.; Chanzy, H.; Dufresne, A.; Gauthier, C. *Polym. Adv. Technol.* **1995**, *6*, 351–371.
16. Sakurada, I.; Nukushina, Y.; Ito, T. *J. Polym. Sci.* **1962**, *57*, 651–660.
17. Matsuo, M.; Sawatari, C.; Iwai, Y.; Ozaki, F. *Macromol.* **1990**, *23*, 3266–75.
18. Stucova, A.; Davies, G.; Eichhorn, S. J. *Biomacromol.* **2005**, *6*, 1055–1061.
19. Kvien, I.; Oksman, K. *Appl. Phys. A.* **2007**, *87*, 641–643.
20. Roohani, M.; Habibi, Y.; Belgacem, N. M.; Ebrahim, G.; Karimi, A. N.; Dufresne, A. *Eur. Polym. J.* **2008**, *44*, 2489–2498.
21. Paralikar, S. A.; Simonsen, J.; Lombardi *J. Membr. Sci.* **2008**, *320*, 248–258.
22. Wang, Y.; Chang, C.; Zhang, L. *Macromol. Mater. Eng.* **2010**, *295*, 137–145.
23. Ibnyaich, A. M.S. Thesis, Lulea University of Technology, Lulea, Sweden, 2010; 061 – ISSN: 1653-0187.
24. Helbert, W.; Cavaille´, J. Y.; Dufresne, A. *Polym. Compos.* **1996**, *17*, 604–611.
25. Hajji, P.; Cavaille´, J. Y.; Favier, V.; Gauthier, C.; Vigier', G. *Polym. Compos.* **1996**, *4*, 612–619.
26. Anglés, M.; Dufresne, A. *Macromol.* **2001**, *34*, 2921–2931.
27. Chen, Y.; Liu, C.; Chang, P.; Cao, X.; Anderson, D. *Carbohydr. Polym.* **2009**, *76*, 607–615.
28. Garcı´a, N. L.; Ribba, L.; Dufresne, A.; Aranguren, M. I.; Goyanes, S. *Macromol. Mater. Eng.* **2009**, *294*, 169–177.
29. Azizi Samir, M.; Alloin, F.; Sanchez, J.; Dufresne, A. *Polym. J.* **2004**, *45*, 4149–4157.
30. Zheng, H.; Ai, F.; Chang, P. R.; Huang, J.; Dufresne, A. *Polym. Compos.* **2009**, *30*, 474–480.
31. de Menezes, A. J.; Siqueira, G.; Curvelo, A.; Dufresne, A. *Polym. J.* **2009**, *50*, 4552–4563.
32. Ljungberg, N.; Bonini, C.; Bortolussi, F.; Boisson, C.; Heux, L.; Cavaille, J. Y. *Macromol.* **2005**, *6*, 2732–2739.
33. Ljungberg, N.; Cavaille´, J. Y.; Heux, L. *Polym. J.* **2006**, *47*, 6285–6292.
34. Siqueira, G.; Bras, J.; Dufresne, A. *Biomacromol.* **2009**, *10*, 425–432.
35. Pandey, J. K.; Chu, W. S.; Kim, S. C.; Lee, C. S.; Ahn, S. H. *Composites, Part B* **2009**, *40*, 676–680.
36. Sanchez-Garcia, M. D.; Lagaron, J. M. *Cellulose* **2010**, *17*, 987–1004.
37. Pei, A.; Zhou, Q.; Berglund, L. A. *Compos. Sci. Technol.* **2010**, *70*, 815–821.
38. Herrera Vargas, N. M.S. Thesis, Lulea University of Technology, Lulea, Sweden, 2010; 053 – ISSN: 1653-0187.
39. Cao, X.; Dong, H.; Li, C. *Biomacromol.* **2007**, *8*, 899–904.
40. Ruiz, M.; Cavaille, J. Y.; Dufresne, A.; Granillat, C.; Gerard, J. *Macromol. Symp.* **2001**, *169*, 211–222.
41. Jiang, L.; Morelius, E.; Zhang, J.; Wolcott, M. P.; Holbery, J. *J. Compos. Mater.* **2008**, *42*, 2629–2645.
42. Berglund, L. In *Natural Fibers, Biopolymers, and Biocomposites*; Mohanty, A., Misra, M., Drzal, L., Eds.; CRC Press Taylor & Francis: Boca Raton, FL, 2005; pp 807−832, ISBN 0-8493-1741-X.
43. Zimmermann, T.; Pöhler, E.; Geiger, T. *Adv. Eng. Mater.* **2004**, *5*, 754–761.

Downloaded by STANFORD UNIV GREEN LIBR on August 28, 2012 | http://pubs.acs.org
Publication Date (Web): August 17, 2012 | doi: 10.1021/bk-2012-1107.ch002

Downloaded by STANFORD UNIV GREEN LIBR on August 28, 2012 | http://pubs.acs.org
Publication Date (Web): August 17, 2012 | doi: 10.1021/bk-2012-1107.ch002

44. Eichhorn, S. J.; Dufresne, A.; Aranguren, M.; Marcovich, N. E.; Capadona, J. R.; Rowan, S. J.; Weder, C.; Thielemans, W.; Roman, M.; Renneckar, S.; Gindl, W.; Veigel, S.; Keckes, J.; Yano, H.; Abe, K.; Nogi, M.; Nakagaito, A. N.; Mangalam, A.; Simonsen, J.; Benight, A. S.; Bismarck, A.; Berglund, L. A.; Peijs, T. *J. Mater. Sci.* **2010**, *45*, 1–33.
45. Cheng, Q.; DeVallance, D.; Wang, J.; Wang, S. Advanced Cellulosic Nanocomposite Materials. In *Advances in Composite Materials for Medicine and Nanotechnology*; Attaf, B., Ed.; InTech: Rijeka, Croatia, 2011; pp 547−564, ISBN: 978-953-307-235-7.
46. Dufresne, A. *Molecules* **2010**, *15*, 4111–4128.
47. Azizi Samir, M.; Alloin, F.; Dufresne, A *Biomacromol.* **2005**, *6*, 612–626.
48. Ioelovich, M. *BioResources* **2008**, *3*, 1403–1418.
49. Eichhorn, S. J. *Soft Matter* **2011**, *7*, 303–315.
50. Dufresne, A. In *Natural Fibre Reinforced Polymer Composites: From Macro to Nanoscale*; Thomas, S., Pothan, L. A., Eds.; Old City Publishing: Philadelphia, PA, 2008; pp 142−170, ISBN: 9781933153094.
51. Onsager, L. *Ann. N.Y. Acad. Sci.* **1949**, *51*, 627–659.
52. Araki, J.; Wada, M.; Kuga, S.; Okano, T. *Langmuir* **2000**, *16*, 2413–2415.
53. Beck-Candanedo, S.; Roman, M.; Gray, D. G. *Biomacromolecules* **2005**, *6*, 1048–1054.
54. Marchessault, R. H.; Morehead, F. F.; Walter, N. M. *Nature* **1959**, *184*, 632–633.
55. Revol, J.-F.; Bradford, H.; Giasson, J.; Marchessault, R. H.; Gray, D. G. *Int. J. Biol. Macromol.* **1992**, *14*, 170–172.
56. Revol, J.-F.; Godbout, L.; Dong, X.-M.; Gray, D. G.; Chanzy, H.; Maret, G. *Liq. Cryst.* **1994**, *16*, 127–134.
57. Araki, J.; Kuga, S. *Langmuir* **2001**, *17*, 4493–4496.
58. Araki, J.; Wada, M.; Kuga, S. *Langmuir* **2001**, *17*, 21–27.
59. Hirai, A.; Inui, O.; Horii, F.; Tsuji, M. *Langmuir* **2009**, *25*, 497–502.
60. Roman, M.; Gray, D. G. *Langmuir* **2005**, *21*, 5555–5561.
61. Rosenblatt, C. S.; Pindak, R.; Clark, N. A.; Meyer, R. B. *J. Phys.* **1977**, *38*, 1105.
62. Nishiyama, Y.; Kuga, S.; Wada, M.; Okano, T. *Macromolecules* **1997**, *30*, 6395–6397.
63. Edgar, C. D.; Gray, D. G. *Cellulose* **2003**, *10*, 299–306.
64. Cranston, E. D.; Gray, D. G. *Biomacromolecules* **2006**, *7*, 2522–2530.
65. Cranston, E. D.; Gray, D. G. *Colloids Surf., A* **2008**, *325*, 44–51.
66. Cranston, E. D.; Gray, D. G.; Rutland, M. W. *Langmuir* **2010**, *26*, 17190–17197.
67. Hoeger, I.; Rojas, O. J.; Efimenko, K.; Velev, O. D.; Kelley, S. S. *Soft Matter* **2011**, *7*, 1957–1967.
68. Sugiyama, J.; Chanzy, H.; Maretg, G. *Macromolecules* **1992**, *25*, 4232–4234.
69. Cranston, E. D.; Gray, D. G. *Sci. Technol. Adv. Mater.* **2006**, *7*, 319–321.
70. Kimura, F.; Kimura, T.; Tamura, M.; Hirai, A.; Ikuno, M.; Horii, F. *Langmuir* **2005**, *21*, 2034–2037.
71. Kvien, I.; Oksman, K. *Appl. Phys. A* **2007**, *87*, 641–643.

72. Li, D.; Liu, Z.; Al-Haik, M.; Tehrani, M.; Murray, F.; Tannenbaum, R.; Garmestani, H. *Polym. Bull.* **2010**, *65*, 635–642.
73. Bordel, D.; Putaux, J-L.; Heux, L. *Langmuir* **2006**, *22*, 4899–4901.
74. Habibi, Y.; Heim, T.; Douillard, R. *J. Polym. Sci., Part B: Polym. Phys.* **2008**, *46*, 1430–1436.
75. Ten, E.; Jiang, L.; Wolcott, M. P. *Abstracts of Papers*; 241st ACS National Meeting, Anaheim, CA, March 27−31, 2011.
76. Ten, E.; Jiang, L.; Wolcott, M. P. Proceedings of Nanotechnology in Wood Composite Symposium, Madison, WI, May 16−18, 2011.
77. Formhals, A.; Gastell, R. S. U.S. Patent 1,975,504, 1934.
78. Liu, H.; Hsieh, Y. L. *J. Polym. Sci., Part B: Polym. Phys.* **2002**, *40*, 2119–2129.
79. Kim, C.-W.; Kim, D.-S.; Kang, S.-Y.; Marquez, M.; Joo, Y. L. *Polym. J.* **2006**, *47*, 5097–5107.
80. Frenot, A.; Henriksson, M. W.; Walkenstrom, P. *J. Appl. Polym. Sci.* **2007**, *103*, 1473–1482.
81. Kim, C. W.; Frey, M. W.; Marquez, M.; Joo, Y. L. *J. Polym. Sci., Part B: Polym. Phys.* **2005**, *43*, 1673–1683.
82. Walkenstrom, P.; Frenot, A.; Henriksson, M. W. *J. Appl. Polym. Sci.* **2007**, *103*, 1473–1482.
83. Huang, Z. H.; Kang, F. Y.; Zheng, Y. P.; Yang, J. B.; Liang, K. M. *Carbon* **2002**, *40*, 1363–1367.
84. Khil, M. S.; Kim, H. Y.; Kang, Y. S.; Bang, H. J.; Lee, D. R.; Doo, J. K. *Macromol. Res.* **2005**, *13*, 62–67.
85. Kulpinski, P. *J. Appl. Polym. Sci.* **2005**, *98*, 1855–1859.
86. Viswanathan, G.; Murugesan, S.; Pushparaj, V.; Nalamasu, O.; Ajayan, P. M.; Linhardt, R. J. *Biomacromolecules* **2006**, *7*, 415–418.
87. Liu, H.; Tang, C. *Polym. J.* **2007**, *39*, 65–72.
88. Han, S. O.; Youk, J. H.; Min, K. D.; Kang, Y. O.; Park, W. H. *Mater. Lett.* **2008**, *62*, 759–762.
89. Qi, H.; Sui, X.; Yuan, J.; Wei, Y.; Zhang, L. *Macromol. Mater. Eng.* **2010**, *295*, 695–700.
90. Frey, M. W. *Polym. Rev.* **2008**, *48*, 378–391.
91. Rojas, O. J.; Montero, G. A.; Habibi, Y. *J. Appl. Polym. Sci.* **2009**, *113*, 927–935.
92. Junkasem, J.; Rujiravanit, R.; Supaphol, P. *J. Nanotechnology* **2006**, *17*, 4519–4528.
93. Peresin, M. S.; Habibi, Y.; Zoppe, J. O.; Rojas, J. J.; Pawlak, O. J. *Biomacromolecule* **2010**, *11*, 674–681.
94. Uddin, A. J.; Araki, J.; Gotoh, Y. *Composites, Part A* **2011**, *42*, 741–747.
95. Xiang, C. H.; Joo, Y. L.; Frey, M. W. *J. Biobased Mater. Bioenergy* **2009**, *3*, 147–155.
96. Lu, P.; Hsieh, Y. L. *J. Nanotechnology* **2009**, *20*, 1–9.
97. Ucar, N.; Ayaz, O.; Oksuz, M.; Onen, A.; Bbahar, E.; Ucar, M.; Demer, A.; Wang, Y. *Composite Nanofibers Produced by Electrospinning Technique*; Proceeding of the 8th Saudi Engineering Conference (SEC8), Buraydah, Saudi Arabia, November 17−20, 2011.

Downloaded by STANFORD UNIV GREEN LIBR on August 28, 2012 | http://pubs.acs.org
Publication Date (Web): August 17, 2012 | doi: 10.1021/bk-2012-1107.ch002

98. Zhou, C.; Chu, R.; Wu, R.; Wu, Q. *Biomacromolecule* **2011**, *12*, 2617–2625.
99. Martinez-Sanz, M.; Olsson, R. T.; Lopez-Rubio, A.; Lagaron, J. M. *Cellulose* **2011**, *18*, 335–347.
100. Magalhaes, W. L. E.; Cao, X.; Lucia, L. A. *Langmuir* **2009**, *25*, 13250–13257.
101. Magalhaes, W. L. E.; Cao, X.; Ramires, M. A.; Lucia, L. A. *TAPPI J.* **2011**, *10*, 19–25.
102. Urena-Benavides, E. E.; Kitchens, C. L. *Macromolecule* **2011**, *44*, 3478–3484.
103. Urena-Benavides, E. E.; Brown, P. J.; Kitchens, C. L. *Langmuir* **2010**, *26*, 14263–14270.
104. Liu, L.; Yao, J. *Adv. Mater. Res.* **2011**, *175-176*, 272–275.
105. Turtle, J., Ten, E.; Jiang, L.; Wolcott, M. P. *Fabrication of PHBV-CNW Nanocomposite Fibers by Wet-Spinning*, Summer REU Poster Session, Pullman, WA, July 31, 2009.

Downloaded by STANFORD UNIV GREEN LIBR on August 28, 2012 | http://pubs.acs.org
Publication Date (Web): August 17, 2012 | doi: 10.1021/bk-2012-1107.ch002

Downloaded by COLUMBIA UNIV on August 28, 2012 | http://pubs.acs.org
Publication Date (Web): August 17, 2012 | doi: 10.1021/bk-2012-1107.ch003

Chapter 3

Preparation of Cellulose-Based Honeycomb-Patterned Films with ATRP-Active Surfaces

Ana F. Xavier* and John F. Kadla*

Advanced Biomaterials Chemistry Laboratory,
University of British Columbia, Faculty of Forestry,
Department of Wood Science, 2424 Main Mall 4330,
Vancouver, British Columbia, Canada V6T1Z4
***E-mail: afxavier@interchange.ubc.ca, john.kadla@ubc.ca**

Honeycomb-patterned films were prepared with novel cellulosic macroinitiators. Both regiochemistry and degree of substitution (DS) were found to dramatically affect the ability to form honeycomb films. 3-*O*-(2-bromoisobutyryl)-2,6-TDMS-*O*-cellulose did not produce uniform honeycomb-patterned films, while 2,3-*O*-(2-bromoisobutyryl)-2,6-TDMS-*O*-cellulose was able to form honeycomb-patterned films with a narrow distribution of pore sizes of around 1 μm. Poly(*N*-isopropylacrylamide) (pNIPAm) was grafted from the surface of these films with different degrees of polymerization (DP) by surface-initiated atom transfer radical polymerization (ATRP) and it was found that the pNIPAm DP had a significant impact on the morphology of the films. At high DP, the films exhibited very hydrophilic surfaces at room temperature, however the honeycomb-patterned was lost. At lower DPs, the honeycomb pattern was maintained and the surface hydrophobicity/hydrophilicity was tailored by manipulating the DP. However, the pore size distribution of the modified surface varied between 0.4 to 1 μm, likely due to poor control of the polymerization process.

In Functional Materials from Renewable Sources; Liebner, F., et al.;
ACS Symposium Series; American Chemical Society: Washington, DC, 2012.

Downloaded by COLUMBIA UNIV on August 28, 2012 | http://pubs.acs.org
Publication Date (Web): August 17, 2012 | doi: 10.1021/bk-2012-1107.ch003

Introduction

Cellulose is a unique biopolymer with characteristic properties, such as hydrophilicity, chirality, chain stiffness and 3 hydroxyl groups with distinct reactivity. Developments in synthetic modification of cellulose using protecting group chemistry allowed for preparation of cellulose derivatives with different functionalization pattern (*1*, *2*). These regioselective cellulosics have a pattern of substitution which yields new materials with special properties (*3–6*). For example, it was found that increasing the degree of substitution with acetyl groups in position C6 promotes the solubility in organic solvents, whereas free OH groups in position C6 favor the solubility in aqueous systems (*6*). Nowadays, demand for innovative, environmentally friendly materials has driven the synthesis of new cellulosics and its application in the preparation of new materials.

Micropatterned films are highly attractive materials owing to the wide range of applications, such as: micro-lens arrays (*7*), superhydrophobic surfaces (*8*), or solar cells (*9*). Honeycomb-patterned films are easily produced according to the breath figures method (*10*, *11*). Aitken (*12*) first observed the formation of ordered arrays upon the condensation of water droplets on cold surfaces. Francois et al. (*13*) later used the arrays of water droplets on the surface of a solution as templates to produce honeycomb-patterned films. A typical process for the fabrication of such films consists on casting a dilute polymer solution on a solid substrate in a humid environment under an adequate gas-flow. As the solvent evaporates water droplets are formed on the surface of the cold solution. Surface tension and simultaneous cooling of the surface and rapid heating of the bottom of the thin layer of liquid (Benard-Marangoni convection) (*14*, *15*) allows the water droplets to assemble in a hexagonal patterned. Once the solvent and the water evaporate, the polymer, previously assembled in between the water droplets, forms a honeycomb-patterned film (*16*).

Cellulose derivatives have been used to fabricate honeycomb-patterned materials. One of the first reports was using polystyrene comb polymers built on hydroxyisopropyl cellulose (*17*, *18*). It was found that the regularity of the porous films increased with the density of branches and with the increasing length of each branch; however, poor quality films with low regularity were obtained. Similarly, honeycomb-shaped films were also reported based on cellulose acetates (*19–21*), but again the corresponding films were extremely irregular with pore sizes varying between 1 to 100 µm. Recently we (*3*) prepared honeycomb thin films from 2,6-(dimethylthexylsilyl) cellulose in which a hydrophilic substituent (polyethylene glycol) was regioselectively introduced in the C3 position of the AGU. Film formation was found to depend on the casting conditions and polymer amphiphilicity. Flow and humidity were optimized and toluene was found to be most suitable solvent for honeycomb film formation. The polymer's amphiphilicity was varied by introducing polyethylene glycol (EG) with different degree of polymerization (DP_{EG}) from 3 to 16. It was found that the DP=16 derivative, 3-*O*-EG_{16}2,6-TDMS-cellulose, formed a uniform structure with approximately 2 µm diameter pore size.

The use of micropatterned films for tissue growth has also been in the focus of recent studies (*22–26*). These films provide the necessary conditions for the tissue growth without affecting adhesion and proliferation of the cells. Furthermore, cell morphology is affected by the architecture of the films. Flattened films produced flat chondrocyte and hepatocyte cells which makes unfeasible its use in tissue engineering. On the other hand, micropatterned films formed cells with a spherical shape which exhibits potential use in tissue engineering (*24*, *25*).

Poly(*N*-isopropylacrylamide) (pNIPAm) is a thermoresponsive polymer that exhibits a phase transition temperature (lower critical solution temperature, LCST) in water at 32 °C. Below this temperature, the polymer is hydrophilic and water soluble, however, increasing temperature beyond the LCST it undergoes a corresponding coil-to-globule transition, becoming hydrophobic and precipitates out of solution. This phenomenon has been shown to be beneficial for cell growth. Yamada et al. (*27*) grafted pNIPAm from the surface of polystyrene dishes and were able to grow bovine hepatocytes from its surface. Utilizing pNIPAm's thermoresponsive behavior they decreased the culture temperature to below 32 °C which resulted in the cells detaching from the surface and being readily recovered.

Atom transfer radical polymerization (ATRP) reactions are one of the most effective and most widely used methods of controlled radical polymerization (CRP) (*28*, *29*). In ATRP-copolymerization, chemical modification and functionalization with 2-bromoisobutyryl is commonly used to introduce initiation sites in macromolecules. In the present work, regioselective 3-*O*-(2-bromoisobutyryl)-2,6-(TDMS) cellulose and non-regioselective 2,3-*O*-(2-bromoisobutyryl)-2,6-(TDMS) cellulose were synthesized, and the synthesis optimized to obtain the highest DS without extensively degrading the cellulose. The effect of DS and substitution pattern on the ability of these compounds to form honeycomb-patterned films was investigated. Copolymers were then prepared by grafting poly(*N*-isopropylacrylamide) from the honeycomb-patterned films by surface initiated atom transfer radical polymerization and the resulting surface morphology was analyzed. This study serves to set the grounds for future work looking into thermoresponsive cellulose-pNIPAm copolymer honeycomb films for cell culture.

Experimental

Materials

Cellulose acetate (30K, 39.8 wt% acetyl content), potassium hydroxide, thexyldimethylsilyl chloride (TDMS-Cl), imidazole, pyridine, 2-bromoisobutyryl bromide, triethylamine (TEA), copper (I) chloride, copper (II) chloride, copper, tris(aminoethyl)amine (TREN) were purchased from Sigma-Aldrich and used as received unless otherwise indicated. CuCl was purified in glacial acetic acid and washed with ethanol according to previous work (*30*). NIPAm was recrystallized from toluene:hexane (65:35) solution. Tris(2-dimethylaminoethyl)amine (Me_6TREN) was prepared from TREN by a procedure similar to that of Ciampolini and Nardi (*31*). *N,N*-Dimethylacetamide (DMA), lithium chloride (LiCl), potassium phosphate monobasic (KH_2PO4), potassium phosphate

Downloaded by COLUMBIA UNIV on August 28, 2012 | http://pubs.acs.org
Publication Date (Web): August 17, 2012 | doi: 10.1021/bk-2012-1107.ch003

dibasic (K_2HPO_4) and tetrahydrofuran (THF) were purchased from Fisher Scientific and used as received to the exception of THF which was distilled over sodium-benzophenone prior to use.

Methods

Fourier-Transform Infrared (FTIR) spectroscopy spectra were recorded on a Perkin Elmer Spectrum One FTIR spectrometer. For chloroform soluble polymers thin films were deposited on ZnSe plates using 2-3 drops of 5% w/w chloroform solutions. Spectra were collected over the wavenumber range of 4000-600 cm^{-1} at a resolution of 4 cm^{-1} and a minimum of 16 scans were recorded.

^{1}H, ^{13}C and quantitative ^{13}C nuclear magnetic resonance (NMR) spectra were recorded using a 300 MHz Bruker Avance Ultrashield NMR spectrometer at 25°C in deuterated chloroform ($CDCl_3$), as per reference (*32*). Chemical shifts were referenced to tetramethyl silane (TMS; 0 ppm). Chromium(III) acetylacetonate (Cr(III)acac) was used as relaxation agent in deuterated chloroform, 0.1M.

Gel permeation chromatography (GPC) was performed using an Agilent 1100 Series GPC Analysis System equipped with a Wyatt Dawn Heleos-II multiangle light scattering (MALS) to determine number average and weight average molecular weight and polydispersity index. Styragel HR-1, HR-2 and HR-5E columns (Waters Corp., Milford, USA) were used with THF as the eluting solvent at a flow rate of 0.5 ml/min at 35°C. The injection volume was 100 µL, and polymers were dissolved in HPLC-grade THF at concentrations of 1.5 mg/ml.

Contact angles were measured using a KSV CAM 101 instrument (KSV Instruments Ltd., Finland). A 5 µL droplet of distilled water was placed on the surface of the honeycomb film and the contact angle was measured after 20 seconds.

Optical microscopy images were obtained from BX41 - Olympus and scanning electron microscopy images from JEOL JSM-5900LV.

Synthesis

2,6-O-TDMS-cellulose

60 g of cellulose acetate, (Mw=30,000; DS=2.5) was suspended in a solution of methanol (1.4 L) and potassium hydroxide (84 g) and stirred overnight at room temperature. The alkaline mixture was then neutralized with 70 mL of hydrochloric acid and filtered. The residue was washed with water and methanol (2 × 500 mL), stirred in water for 30 min and washed with 500 mL of ethyl ether. The residue was dried under vacuum (635 mmHg) at 30 °C. The isolated cellulose was then activated prior to use by solvent exchange with water, followed by methanol and finally DMA. The activated cellulose (1g, 6 mmol) was suspended in 25 mL of DMA and stirred at 120 °C for 2 hours. The reaction mixture was allowed to cool to 100 °C, and 1.5 g (35.4 mmol) of LiCl was added and the reaction cooled to room temperature. The cellulose dissolved over-night after constant stirring under an argon atmosphere. 2.0 g (30 mmol) of imidazole was then added to the mixture and stirred for 15

Downloaded by COLUMBIA UNIV on August 28, 2012 | http://pubs.acs.org
Publication Date (Web): August 17, 2012 | doi: 10.1021/bk-2012-1107.ch003

minutes, followed by the addition of 4.7 mL (24 mmol) of thexyldimethylsilyl chloride (TDMS-Cl). The reaction mixture was heated to 100 °C for 24 hours under an argon atmosphere and constant stirring. The reaction mixture was then poured into buffer solution (7.14g K_2HPO_4 and 3.54g KH_2PO4 in 1000mL of distilled water). The precipitate was then collected and washed with distilled water and ethanol and dried under vacuum (635 mmHg) at 30 °C. The crude product was purified by dissolving it into a minimal amount of chloroform ($CHCl_3$) and precipitating it from methanol (MeOH). The purified colorless compound was recovered by filtration and dried as previously described. Yield 2.5g (91%). FTIR ($CHCl_3$, cm^{-1}), 3517 ($\upsilon_{\text{O-H}}$); 2957, 2871 (υ_{CH3}, υ_{CH2}); 1465, 1377 (δ_{CH3}); 1252 ($\delta_{\text{Si-C}}$); 1116, 1078 ($\upsilon_{\text{C-O-C}}$); 835 ($\upsilon_{\text{Si-C}}$); 777 ($\gamma_{\text{Si-CH3}}$). ^{1}H NMR (10% in $CDCl_3$, ppm, 313 K): δ=0.15 ($\text{Si-C}\underline{\text{H}_3}$), δ=0.89 ($\text{Si-C(C}\underline{\text{H}_3}\text{)}_2\text{CH(C}\underline{\text{H}_3}\text{)}_2$), δ=1.66 ($\text{Si-C(CH}_3\text{)}_2\text{C}\underline{\text{H}}\text{(CH}_3\text{)}_2$), δ=3.34 (OH), δ=3.71 (H-6), δ=3.8 (H-2), δ=3.9 (H-5,4,3), δ=4.4 (H-1). ^{13}C NMR (10% in $CDCl_3$, ppm, 313 K): δ=-2.5 ($\text{Si-(}\underline{\text{C}}\text{H}_3\text{)}_2$), δ=18.6 ($\text{Si-C(}\underline{\text{C}}\text{H}_3\text{)}_2\text{CH(CH}_3\text{)}_2$), δ=20.4 ($\text{Si-C(CH}_3\text{)}_2\text{CH(}\underline{\text{C}}\text{H}_3\text{)}_2$), 25.2 ($\text{Si-}\underline{\text{C}}\text{(CH}_3\text{)}_2\text{CH(CH}_3\text{)}_2$), δ=34.3 ($\text{Si-C(CH}_3\text{)}_2\underline{\text{C}}\text{H(CH}_3\text{)}_2$), δ=60.3 (C-6), δ=75.02 (C-4), δ=101.9 (C-1).

3-O-(2-Bromoisobutyryl)-2,6-O-TDMS-cellulose

1 g (2.2 mmol) of 2,6-*O*-TDMS-cellulose was suspended in 25 ml of freshly distilled THF and 3.7 mL (46.2 mmol) of anhydrous pyridine under an argon atmosphere. The reaction solution was cooled to 0 °C with an ice/water bath and 5.4 g (44 mmol) of 2-bromo isobutyryl bromide was added dropwise. The ice/water bath was removed and the reaction mixture was allowed to react for 19 hours at room temperature. The reaction mixture was precipitated from methanol, filtered and dried in a vacuum oven (635 mmHg) at 30 °C. The crude product was purified in $CHCl_3$, precipitated from MeOH and dried under vacuum (635 mmHg, 30°C). Yield: 1.25g (82%). FTIR ($CHCl_3$, cm^{-1}), 3530 (υ_{OH}); 2957, 2871 (υ_{CH3}, υ_{CH2}); 1751 ($\upsilon_{\text{C=O}}$); 1465, 1377 (δ_{CH3}); 1252 ($\delta_{\text{Si-C}}$); 1117, 1075 ($\upsilon_{\text{C-O-C}}$); 835 ($\upsilon_{\text{Si-C}}$); 777 ($\gamma_{\text{Si-CH3}}$). ^{1}H NMR (10% in $CDCl_3$, ppm, 313 K): δ=0.15 ($\text{Si-C}\underline{\text{H}_3}$), δ=0.89 ($\text{Si-C(C}\underline{\text{H}_3}\text{)}_2\text{CH(C}\underline{\text{H}_3}\text{)}_2$), δ=1.66 ($\text{Si-C(CH}_3\text{)}_2\text{C}\underline{\text{H}}\text{(CH}_3\text{)}_2$), δ=1.95 ($\text{C(C}\underline{\text{H}_3}\text{)}_2\text{Br}$), δ=3.3 (OH), δ=3.7 (H-6), δ=3.8 (H-2, 5), δ=4.0 (H-4), δ=4.4 (H-1, 3). ^{13}C NMR (10% in $CDCl_3$, ppm, 313 K): δ=-2.5 ($\text{Si-(}\underline{\text{C}}\text{H}_3\text{)}_2$), δ=18.6 ($\text{Si-C(}\underline{\text{C}}\text{H}_3\text{)}_2\text{CH(CH}_3\text{)}_2$), δ=20.4 ($\text{Si-C(CH}_3\text{)}_2\text{CH(}\underline{\text{C}}\text{H}_3\text{)}_2$), 25.2 ($\text{Si-}\underline{\text{C}}\text{(CH}_3\text{)}_2\text{CH(CH}_3\text{)}_2$), δ=34.3 ($\text{Si-C(CH}_3\text{)}_2\underline{\text{C}}\text{H(CH}_3\text{)}_2$), δ=60.3 (C-6), δ=75.02 (C-4), δ=101.9 (C-1).

2,3-O-(2-Bromoisobutyryl)-2,6-di-O-(thexyldimethylsilyl)-cellulose

1 g (2.2 mmol) of 2,6-*O*-TDMS-cellulose with a total DS of ~1.3 was suspended in 25 ml of freshly distilled THF and 3.7 mL (46.2 mmol) of anhydrous pyridine under an argon atmosphere. The reaction solution was cooled to 0 °C with an ice/water bath and 5.4 g (44 mmol) of 2-bromo isobutyryl bromide was added dropwise. The ice/water bath was removed and the reaction mixture was

Downloaded by COLUMBIA UNIV on August 28, 2012 | http://pubs.acs.org
Publication Date (Web): August 17, 2012 | doi: 10.1021/bk-2012-1107.ch003

Downloaded by COLUMBIA UNIV on August 28, 2012 | http://pubs.acs.org
Publication Date (Web): August 17, 2012 | doi: 10.1021/bk-2012-1107.ch003

allowed to react for 19 hours at room temperature. The reaction mixture was precipitated from methanol, filtered and dried in a vacuum oven (635 mmHg) at 30 °C. The crude product was purified in $CHCl_3$, precipitated from MeOH and dried under vacuum (635 mmHg, 30°C). Yield: 1.25g (82%). FTIR ($CHCl_3$, cm^{-1}), 3530 (υ_{OH}); 2957, 2871 (υ_{CH3}, υ_{CH2}); 1751 ($\upsilon_{C=O}$); 1465, 1377 (δ_{CH3}); 1252 ($\delta_{Si\text{-}C}$); 1117, 1075 ($\upsilon_{C\text{-}O\text{-}C}$); 835 ($\upsilon_{Si\text{-}C}$); 777 ($\gamma_{Si\text{-}CH3}$). ^{1}H NMR (10% in $CDCl_3$, ppm, 313 K): δ=0.15 ($Si\text{-}C\underline{H_3}$), δ=0.89 ($Si\text{-}C(C\underline{H_3})_2CH(C\underline{H_3})_2$), δ=1.66 ($Si\text{-}C(CH_3)_2C\underline{H}(CH_3)_2$), δ=1.95 ($C(C\underline{H_3})_2Br$), δ=3.3 ($\overline{OH}$), δ=3.7 (H-6), δ=3.8 (H-2, 5), δ=4.0 (H-4), δ=4.3 (H-3 if TDMS in C-2 and 2-bromoisobutyryl in C-3), δ=4.7 (H-1 if 2-bromoisobutyryl in position C-2), δ=4.8 (H-1 if TDMS in position C-2), δ=5.0 (H-2 if 2-bromoisobutyryl in position C-2), δ=5.2 (H-3 if 2-bromoisobutyryl in position C-2). ^{13}C NMR (10% in $CDCl_3$, ppm, 313 K): δ=-2.5 ($Si\text{-}(\underline{C}H_3)_2$), δ=18.6 ($Si\text{-}C(\underline{C}H_3)_2CH(CH_3)_2$), δ=20.4 ($Si\text{-}C(CH_3)_2CH(\underline{C}H_3)_2$), 25.2 ($Si\text{-}\underline{C}(CH_3)_2CH(CH_3)_2$), δ=34.3 ($Si\text{-}C(CH_3)_2\underline{C}H(CH_3)_2$), δ=60.3 (C-6), δ=75.02 (C-4), δ=101.9 (C-1), δ=169.6 (C-13, if 2-bromoisobutyyrl in position C-2), δ=170.8 (C-13, if 2-bromoisobutyryl in position C-3).

Film Preparation

Cellulose derivatives 3-*O*-(2-bromoisobutyryl 2,6-*O*-TDMS-cellulose and 2,3-*O*-(2-bromoisobutyryl) 2,6-*O*-TDMS-cellulose were dissolved in toluene at a specific concentration, and 10 µL of the solution was cast onto a glass slide under a relative humidity of 75% and a temperature of 22 ± 2 °C.

Surface-Initiated ATRP

10 mL of a 10 wt % (NIPAm/H_2O) solution was added to a Schlenk flask and degassed through 4 freeze-pump-thaw (FPT) cycles. CuCl (3.6 mg, 2.5 µmol/mL), $CuCl_2$ (8.3 mg, 3.7 µmol/mL), Cu (0.95 mg, 1.5 µmol/mL) and Me_6TREN were added to the Schlenk flask and mixed well. To initiate the reaction the honeycomb-patterned film was then inserted into the solution. The reaction proceeded at room temperature overnight under an argon atmosphere after which the films were thoroughly washed with distilled water.

Results and Discussion

The regioselective modification of cellulose was performed according to Koschella et al (*2*) where cellulose was reacted with TDMS-Cl in DMA/LiCl. The resulting 2,6-*O*-TDMS-cellulose was analyzed by quantitative ^{13}C NMR (Figure 1). The degree of substitution of the TDMS group was determined by setting the integral value for the C1 carbon of the AGU to 1.00. The corresponding TDMS carbon integrals at C7 ($Si\text{-}\underline{C}H_3$), C8 and C9 ($C\text{-}\underline{C}H_3$) were 4.07, 4.46 and 4.31, respectively and 2.02 and 2.11 for C11 and C12, corresponding to a TDMS DS of ~2.1.

Downloaded by COLUMBIA UNIV on August 28, 2012 | http://pubs.acs.org
Publication Date (Web): August 17, 2012 | doi: 10.1021/bk-2012-1107.ch003

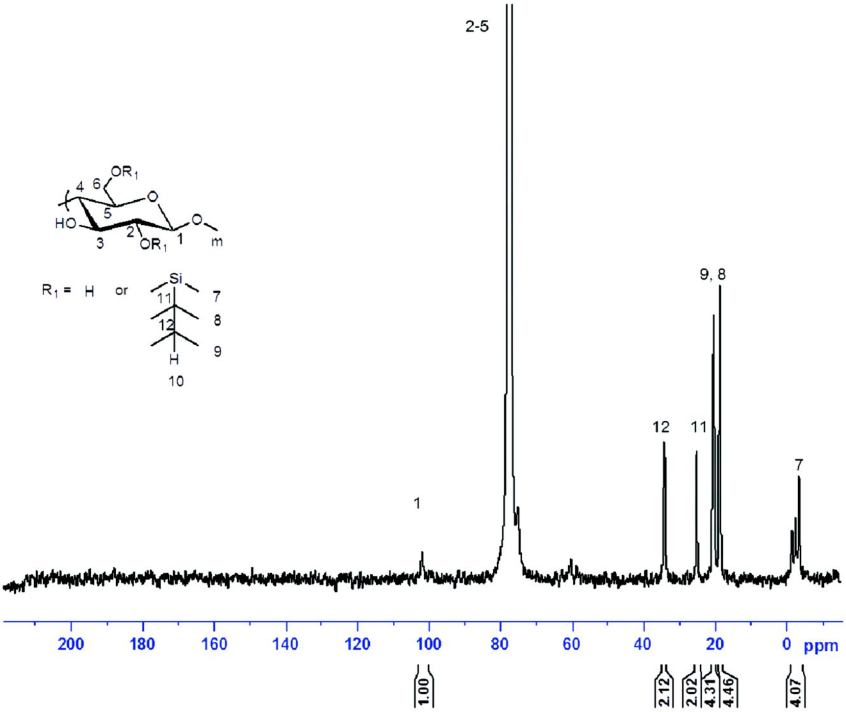

Figure 1. Quantitative ${}^{13}C$ NMR of 2,6-O-TDMS-cellulose with DS ~ 2.1.

Synthesis of 3-*O*-(2-Bromoisobutyryl)-2,6-*O*-TDMS-cellulose

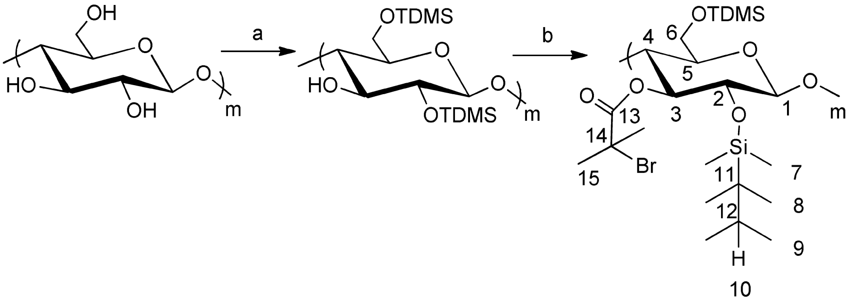
OH
O
HO
OH
O
m
a
OTDMS
O
HO
OTDMS
O
m
b
OTDMS
4
6
O
5
O
O
13
3
2
1
O
m
14
Br
15
O
Si
11
7
12
8
9
H
10

Scheme 1. Synthetic scheme to synthesize 3-O-(2-bromoisobutyryl)-2,6-O-TDMS-cellulose. a) DMA/LiCl, TDMS-Cl, imidazole b) pyridine, 2-bromoisobutyryl bromide, THF.

Downloaded by COLUMBIA UNIV on August 28, 2012 | http://pubs.acs.org
Publication Date (Web): August 17, 2012 | doi: 10.1021/bk-2012-1107.ch003

In the present study, the regioselective macroinitiator 3-*O*-(2-bromoisobutyryl)-2,6-*O*-TDMS-cellulose was prepared by reacting 2-bromoisobutyryl bromide with 2,6-*O*-TDMS-cellulose in the presence of a base and THF (Scheme 1). The reaction conditions were optimized to maximize the 2-bromoisobutyryl DS while minimizing the extent of degradation of the cellulose backbone. Table 1 lists the optimization conditions, which included the ratio of base and 2-bromoisobutyryl bromide, as well as temperature, time and base used.

Table 1. Optimization parameters used for the synthesis of 3-*O*-(2-bromoisobutyryl)-2,6-*O*-TDMS-cellulose

	Temp (°C)	*Time (hour)*	*Base*	*Ratio*	*DS*	*Mn*	*DP*	*PDI*
	2,6-*O*-TDMS-cellulose					39,480	88	2.5
1	RT	19	Pyr	1:11:10:0	0.16	32,910	70	1.24
2	RT	19	Pyr	1:21:20:0	0.21	30,190	63	1.22
3	Refl	19	Pyr	1:11:10:0	0.22	26,350	55	1.29
4	RT	48	Pyr	1:11:10:0	0.28	30,014	61	1.27
5	RT	19	Im	1:11:10:0	<0.1	30,690	67	1.21
6	Refl	19	Pyr	1:20:20:0.05	0.26	N/A	N/A	N/A

(RT = room temperature; Refl = Reflux; Pyr=pyridine; Im=imidazole; Ratio= 2,6-*O*-TDMS-cellulose:base:2-bromoisobutyryl bromide: *N,N*-dimethyl-4-aminopyridine).

The degree of substitution of 2-bromoisobutyryl was calculated based on the ^{1}H NMR spectrum by comparing the integral areas of the signals for the methyl proton of isobutyryl group, around 2.0 ppm with the anhydroglucopyranose unit protons at 3.0-5.5 ppm which was calibrated to 7. Figure 2 shows a representative ^{1}H NMR spectrum for a 3-*O*-(2-bromoisobutyryl)-2,6-*O*-TDMS-cellulose macroinitiator. Despite varying the reaction parameters and conditions, the highest DS was found only to be ~0.3, substantially lower than anticipated. In fact the use of a stronger base such as *N,N*-dimethylaminopyridine (experiment 6) did not improve the DS, under extreme conditions of 1:20:20:0.05, 2,6-TDMS-cellulose:2-bromoisobutyryl bromide: pyridine:*N,N*-dimethyl-4-aminopyridine under reflux for 19 hours, a DS of 0.26 was still achieved.

Downloaded by COLUMBIA UNIV on August 28, 2012 | http://pubs.acs.org
Publication Date (Web): August 17, 2012 | doi: 10.1021/bk-2012-1107.ch003

The unexpectedly poor reactivity of the regioselective 2,6-*O*-TDMS-cellulose may be a result of steric and electronic effects arising from the bulky thexyldimethylsilyl protecting groups, particularly that at position 2 of the AGU. Therefore, we attempted to reduce these effects by decreasing the DS of the TDMS group at the C-2 position. To decrease the DS at the C-2 position the TDMS-Cl – cellulose reaction was modified by using lower equivalents of TDMS-Cl in the presence of imidazole in a ratio of 2:3:1 (TDMS-Cl:imidazole:cellulose) and at a lower temperature, 90 °C instead of 100 °C, as described in the literature (*2*). A 2,6-*O*-TDMS-cellulose with a lower DS of TDMS (approximately 1.3) and higher molecular weight was obtained (Table 2). The DS was calculated from the quantitative ^{13}C NMR analysis (Figure 3) as described above.

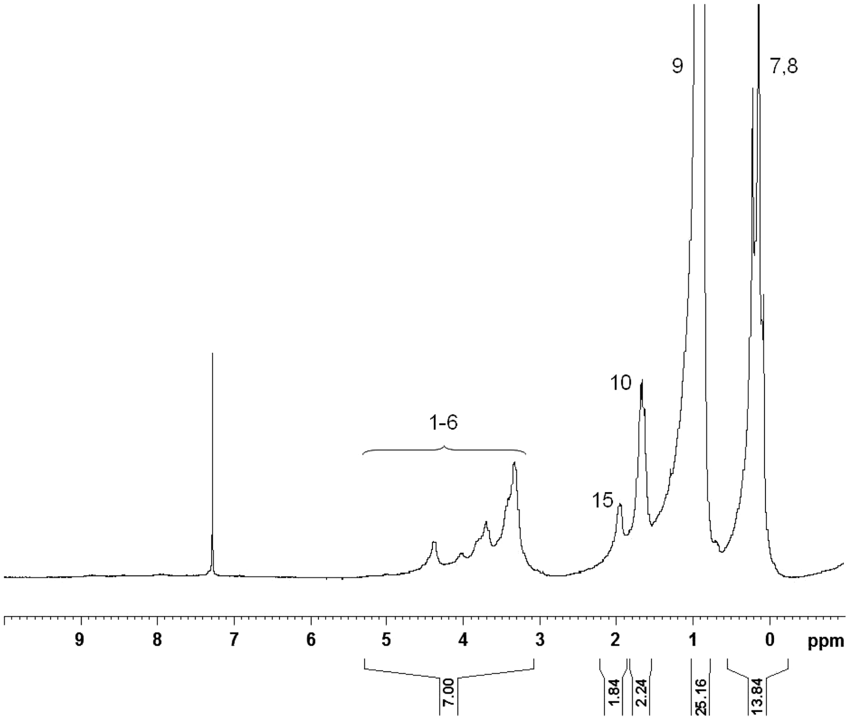

Figure 2. ^{1}H NMR spectrum of 3-O-(2-bromoisobutyryl)-2,6-O-TDMS-cellulose.

Downloaded by COLUMBIA UNIV on August 28, 2012 | http://pubs.acs.org
Publication Date (Web): August 17, 2012 | doi: 10.1021/bk-2012-1107.ch003

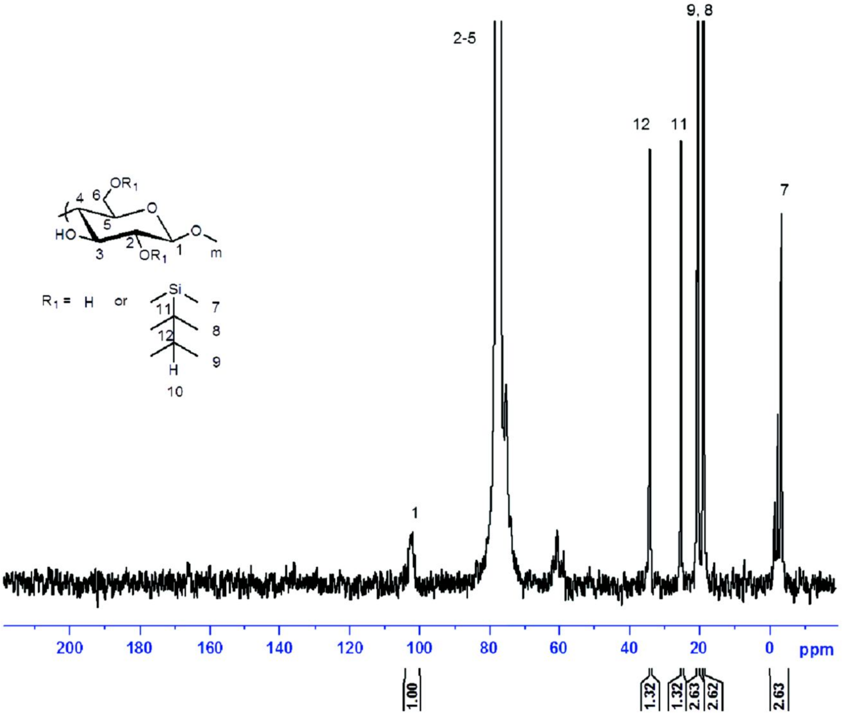

Figure 3. Quantitative ^{13}C NMR of 2,6-O-TDMS-cellulose with DS ~ 1.3.

Synthesis of 2,3-*O*-(2-Bromoisobutyryl)-2,6-*O*-TDMS-cellulose

As per the synthesis of the regioselective 3-*O*-(2-bromoisobutyryl) 2,6-*O*-TDMS-cellulose the 2-bromoisobutyrylation of the lower DS (~1.3) 2,6-*O*-TDMS-cellulose was optimized. The first parameter varied was base. Three different bases were investigated: pyridine, imidazole and triethylamine, and the result on DS of the 2-bromoisobutyryl moiety as well as polymer molecular weight are shown in Table 2. Reactions run with pyridine obtained the highest 2-bromoisobutyryl DS, accompanied with a slight decrease in molecular mass. Imidazole and triethylamine produced very low 2-bromoisobutyryl DS products, with 0.10 and 0.13 DS respectively. The molecular weight did not significantly decrease in the reactions with imidazole, whereas that with TEA causes a somewhat large drop in molecular weight relative to the degree of substitution.

Downloaded by COLUMBIA UNIV on August 28, 2012 | http://pubs.acs.org
Publication Date (Web): August 17, 2012 | doi: 10.1021/bk-2012-1107.ch003

Table 2. Effect of base on the synthesis of 2,3-*O*-(2-bromoisobutyryl)-2,6-*O*-TDMS-cellulose

	Base	*Ratio*	*DS*	*Mn*	*DP*	*PDI*
2,6-*O*-TDMS-cellulose				54,000	121	2.4
1	Pyridine	1:5:5	0.30	46,000	94	2.4
2	Imidazole	1:5:5	0.10	53,000	115	2.2
3	Triethylamine	1:5:5	0.13	46,000	99	2.2
4	Pyridine	1:5:10	0.35	53,000	115	1.9

(all samples were run at room temperature for 19 hours; Ratio= 2,6-*O*-TDMS-cellulose:base:2-bromoisobutyryl bromide).

We then examined the effect of increasing the ratio of base:2-bromoisobutyryl bromide (experiment 1 vs. 4). We observed a similar DS (0.3-0.35) but a slightly higher Mn. When we increased the temperature of the reaction we saw a substantial increase in DS, but a significant drop in Mn was observed (Table 3). Refluxing the reaction mixture for 48 hours produced a 2,3-*O*-(2-bromoisobutyryl) 2,6-*O*-TDMS-cellulose with the highest DS of 0.83, but also the lowest Mn.

Table 3. Effect of time and temperature on the synthesis of 2,3-*O*-(2-bromoisobutyryl)-2,6-*O*-TDMS-cellulose

	Temp (°C)	*Time (hour)*	*Ratio*	*DS*	*Mn*	*DP*	*PDI*
4	RT	19	1:5:10	0.35	53000	115	1.9
5	Reflux	6	1:5:10	0.43	31000	61	2.2
6	Reflux	19	1:5:10	0.53	27000	51	2.4
7	Reflux	48	1:5:10	0.83	21000	37	3.4
8	Reflux	19	1:5:10	0.53	27000	51	2.4

(RT = room temperature; Ratio= 2,6-*O*-TDMS-cellulose:base:2-bromoisobutyryl bromide).

The impact of the various reaction parameters was further investigated by varying the equivalents of 2-bromoisobutyryl bromide to 2,6-*O*-TDMS-cellulose from 1 to 20 equivalents (Table 4). Increasing the molar equivalents increased the DS (experiment 9-12), with the highest equivalents, 1:20 (experiment 12) showing the best results with regards to DS, however again a decrease in Mn was observed. A further increase in DS was observed when the molar equivalents of pyridine was increased to 20 molar equivalents relative to 2,6-*O*-TDMS-cellulose (experiment 13). The result was a DS of 0.8 and a PDI of 2.1 with a further drop in Mn to $3.7*10^4$ g/mol.

Downloaded by COLUMBIA UNIV on August 28, 2012 | http://pubs.acs.org
Publication Date (Web): August 17, 2012 | doi: 10.1021/bk-2012-1107.ch003

Table 4. Effect of changing the mole equivalents of 2-bromoisobutyryl bromide and pyridine in the synthesis of 2,3-(2-bromoisobutyryl)-2,6-*O*-TDMS-cellulose

	Base	*Ratio*	*DS*	*Mn*	*DP*	*PDI*
9	Pyridine	1:10:1	0.39	54000	107	2.6
10	Pyridine	1:10:5	0.35	53000	106	2.4
11	Pyridine	1:10:10	0.58	51000	96	2.6
12	Pyridine	1:10:20	0.67	42000	77	2.8
13	Pyridine	1:20:20	0.78	37000	66	2.1

(all samples were run at room temperature for 19 hours; Ratio=2,6-*O*-TDMScellulose:base:2-bromoisobutyryl bromide).

Although the DS obtained using the 2,6-*O*-TDMS-cellulose:Base:2-Bromoisobutyryl bromide of 1:20:20 significantly increased the DS, to ~0.8, a significant number of hydroxyl groups were still unreacted, ~0.9 based on a 2,6-*O*-TDMS-cellulose with a DS of ~1.3. Therefore the effect of sequential reaction cycles on the DS was evaluated, and the results obtained are presented in Table 5.

Table 5. Effect of 2nd reaction cycle on the synthesis of 2,3-*O*-(2-bromoisobutyryl) 2,6-*O*-TDMS-cellulose

	1st cycle	*2nd cycle*	*DS*	*Mn*	*DP*	*PDI*
14	19h, RT	19h, RT	0.84	24000	42	2.6
15	19h, RT	3h, reflux	0.82	23000	40	1.9

(RT = room temperature; Ratios = 2,6-*O*-TDMS-cellulose : base : 2-bromoisobutyryl bromide, 1:20:20).

The addition of a second reaction cycle, whether at room temperature (RT) or at reflux did not improve the DS, but dramatically decreased the Mn. Thus, the highest DS (~0.8) 2,3-*O*-(2-bromoisobutyryl) 2,6-*O*-TDMS-cellulose with an acceptable Mn (~$3.7*10^4$ g/mol) was obtained by reacting 2,6-*O*-TDMS-cellulose with 2-bromoisobutyryl bromide for 19 hours in the presence of pyridine, at room temperature with a 2,6-*O*-TDMS-cellulose:pyridine:2-bromoisobutyryl bromide ratio of 1:20:20.

Downloaded by COLUMBIA UNIV on August 28, 2012 | http://pubs.acs.org
Publication Date (Web): August 17, 2012 | doi: 10.1021/bk-2012-1107.ch003

As mentioned above, 50% of the available hydroxyl groups were not derivatized even under the most extreme conditions investigated; high temperature, base and time. In the regioselective 3-*O*-(2-bromoisobutyryl) 2,6-*O*-TDMS-cellulose a maximum DS of 0.3 or 30% conversion was obtained. Therefore we investigated the allocation of the 2-bromoisobutyryl groups at the C-2 and C-3 positions of the AGU to see if there was an increase in DS at the C-3 by decreasing the steric and electronic effects of the C-2-TDMS groups. Figure 4 shows the ^{1}H NMR of 2,3-*O*-(2-bromoisobutyryl) 2,6-*O*-TDMS-cellulose. In addition to the various signals associated with the 2,6-*O*-TDMS-cellulose and with the methyl protons from 2-bromoisobutyrl moiety, two new signals were detected at 5 and 5.2 ppm. These signals can be assigned to protons at C-2 and C-3, respectively, when they are substituted with 2-bromoisobutyryl groups.

Similarly, from the ^{13}C NMR spectrum (Figure 5) the two different carbonyl peaks associated with 2-bromoisobutyryl substitution of the C-2 and C-3 positions can be clearly seen (peak 13). Analysis of the two peaks at ~170 ppm reveals the DS of the C-2 (~0.5) > C-3 (~0.3), and indicates that the increase in DS is completely due to substitution at the C-2 position. Thus steric and electronic effects arising from the C-2 position are not responsible for the low DS achievable at the C-3 position.

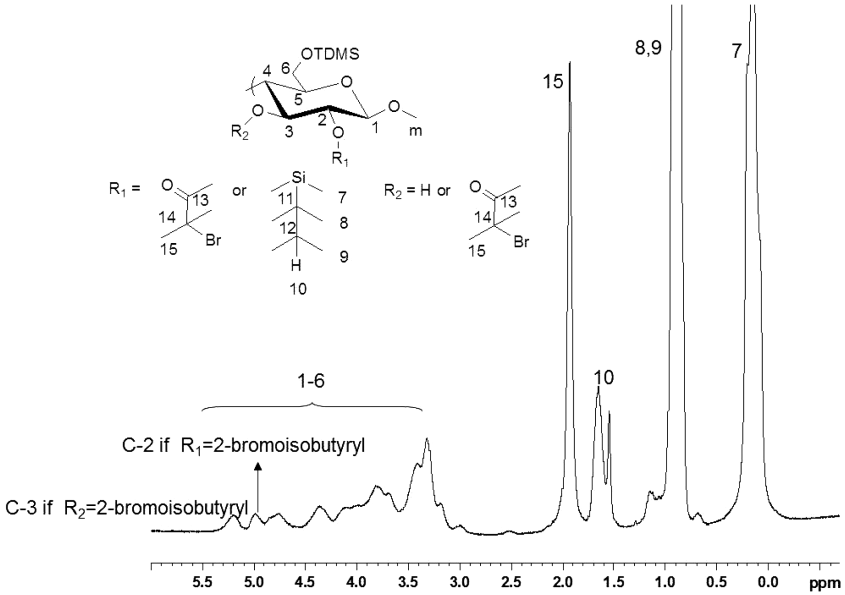

Figure 4. ^{1}H NMR spectrum of 2,3-O-(2-bromoisobutyryl)-2,6-O-TDMS-cellulose in chloroform.

Downloaded by COLUMBIA UNIV on August 28, 2012 | http://pubs.acs.org
Publication Date (Web): August 17, 2012 | doi: 10.1021/bk-2012-1107.ch003

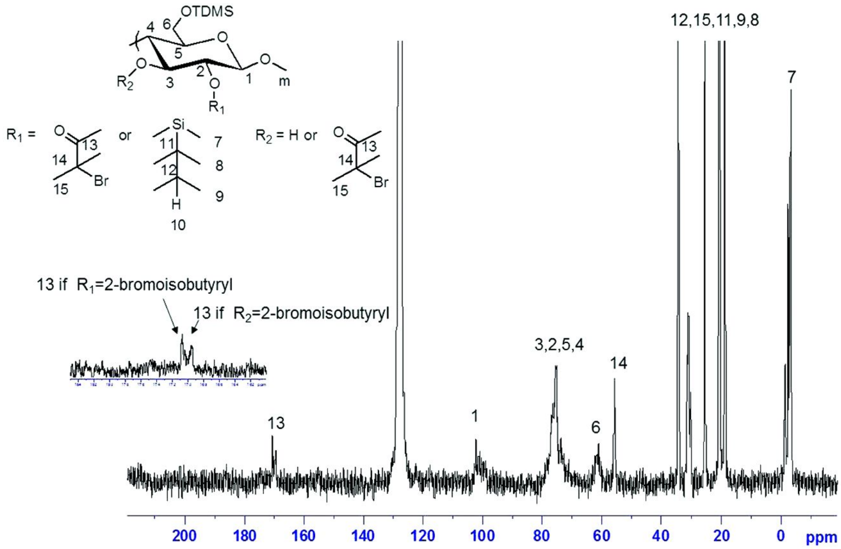

Figure 5. ^{13}C NMR spectrum of 2,3-O-(2-bromoisobutyryl)-2,6-O-TDMS-cellulose in benzene.

Honeycomb Film Formation

Honeycomb films were prepared from both 3-*O*-(2-bromoisobutyryl)-2,6-*O*-TDMS-cellulose and 2,3-*O*-(2-bromoisobutyryl)-2,6-*O*-TDMS-cellulose. It should be noted that both polymers have the same C-3 DS ~0.3; the 2,3-*O*-(2-bromoisobutyryl) 2,6-*O*-TDMS-cellulose has a total 2-bromoisobutyryl DS~0.8 ($DS_{C\text{-}3}$~0.3, $DS_{C\text{-}2}$~0.5). As with our previously reported ethyleneglycol-modified 2,6-*O*-TDMS cellulosics both 3-*O*-(2-bromoisobutyryl)-2,6-*O*-TDMS-cellulose and 2,3-*O*-(2-bromoisobutyryl)-2,6-*O*-TDMS-cellulose were soluble in toluene (*3*). Figure 6 shows optical microscope images of the films obtained for 3-*O*-(2-bromoisobutyryl)-2,6-*O*-TDMS-cellulose and 2,3-*O*-(2-bromoisobutyryl)-2,6-*O*-TDMS-cellulose using the optimized conditions: 3 mg/mL in toluene, 75 % relative humidity (RH), and an air flow to film surface of 5 mm.

Unlike the 2,6-*O*-TDMS-cellulose which did not form honeycomb-patterned films, (*3*) both 3-*O*-(2-bromoisobutyryl)- and 2,3-*O*-(2-bromoisobutyryl)-2,6-*O*-TDMS cellulosics did form patterned films. However, despite our best efforts, the regioselective 3-*O*-(2-bromoisobutyryl)-2,6-*O*-TDMS-cellulose did not produce a uniform honeycomb like structure. In 2,6-*O*-TDMS-cellulose the hydroxyl group in the C-3 position is available to interact through hydrogen bonding with the pyranose ring C-5 oxygen, thereby affecting the rigidity and perhaps the ability to form the necessary spherical shape required for honeycomb film formation (*16*). By substituting the C-3 position these intramolecular interactions may be reduced and honeycomb-like structures thus produced. However, the limiting DS may preclude uniform film formation. By contrast the 2,3-*O*-(2-bromoisobutyryl)-2,6-*O*-TDMS-cellulose formed more regular honeycomb-structured films. Perhaps changing the substitution pattern at the C-2 from TDMS to 2-bromoisobutyryl further impacted the intra- and intermolecular interactions and thus molecular shape, resulting in better pattern formation. Figure 7 shows the SEM images of 2,3-*O*-(2-bromoisobutyryl)-2,6-*O*-TDMS-cellulose honeycomb films; the pores are approximately 1 μm in diameter.

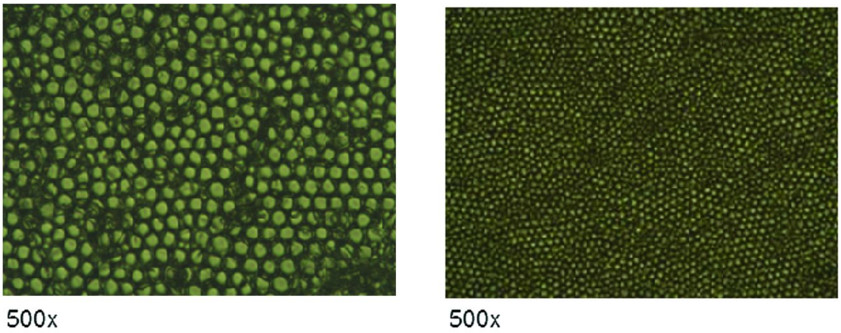

Figure 6. Optical microscope images of the thin films formed from regioselective 3-O-2-(bromoisobutyryl)-2,6-O-TDMS-cellulose (left) and 2,3-O-(2-bromoisobutyryl)-2,6-O-TDMS-cellulose (right).

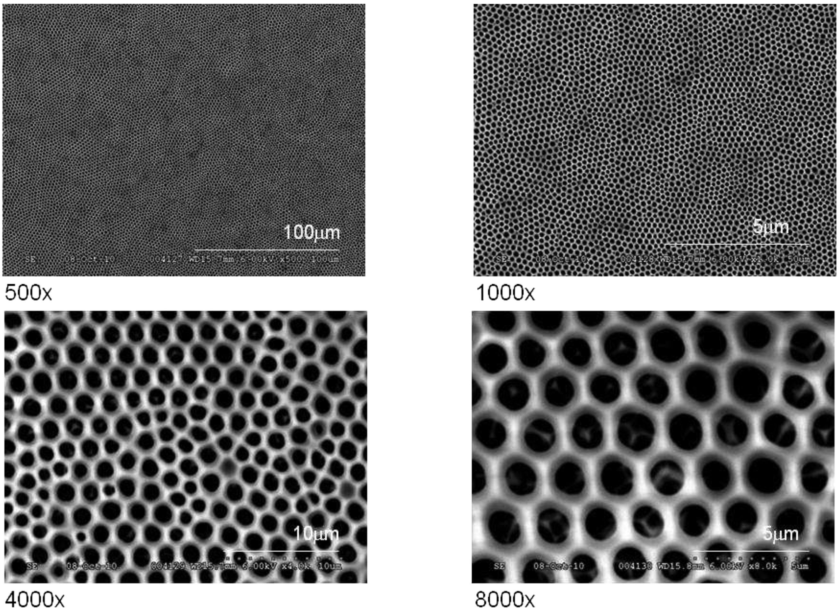

Figure 7. SEM images of the 2,3-O-(2-bromoisobutyryl)-2,6-O-TDMS-cellulose honeycomb films.

Downloaded by COLUMBIA UNIV on August 28, 2012 | http://pubs.acs.org
Publication Date (Web): August 17, 2012 | doi: 10.1021/bk-2012-1107.ch003

Downloaded by COLUMBIA UNIV on August 28, 2012 | http://pubs.acs.org
Publication Date (Web): August 17, 2012 | doi: 10.1021/bk-2012-1107.ch003

Surface-Initiated ATRP

The 2,3-*O*-(2-bromoisobutyryl)-2,6-*O*-TDMS-cellulose honeycomb-patterned films were modified by surface initiated ATRP of NIPAm. The experimental conditions were based in previous work (*33*) and are described in Table 6.

Table 6. Experimental conditions used in the surface initiated ATRP

NIPAm/H_2O	*CuBr*	*$CuBr_2$*	*Cu °*	*Me_6TREN*
1:10	2.5μmol/ml	3.7μmol/ml	1.5μmol/ml	8.7μmol/ml
0.1:10	2.5μmol/ml	3.7μmol/ml	1.5μmol/ml	8.7μmol/ml

Two conditions were run, one with a solution of 10 wt % and the other with 1 wt % NIPAm/H_2O. At the higher monomer content the grafted pNIPAm polymer chains covered the honeycomb film surface, completely obscuring the honeycomb film pattern (Figure 8 bottom). On the other hand, reducing the amount of NIPAm lead to the surface morphology being preserved (Figure 8 top). However, the pore size decreased and the pore size distribution increased as compared to the original film. Pore sizes varied between 0.4 to 1 μm.

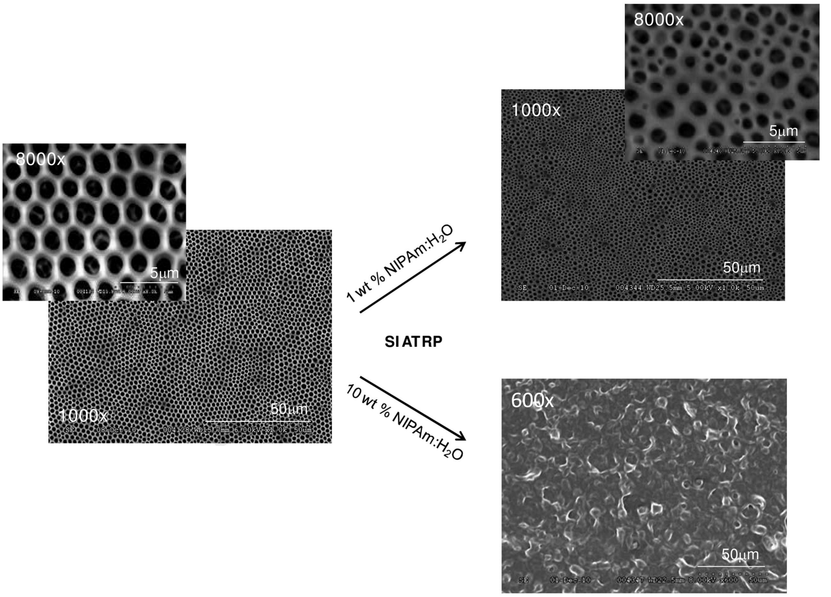

Figure 8. SEM images of thin film from 2,3-O-(2-bromoisobutyryl)-2,6-O-TDMS-cellulose before (left) and after SI ATRP (right) with 1 wt % (top) and 10 wt % (bottom) of NIPAm/H_2O.

Downloaded by COLUMBIA UNIV on August 28, 2012 | http://pubs.acs.org
Publication Date (Web): August 17, 2012 | doi: 10.1021/bk-2012-1107.ch003

In addition to microscopic analysis of the pNIPAm surface grafted honeycomb-patterned films, the effect of pNIPAm on the surface hydrophilicity was measured by contact angle (Figure 9). As expected the originally hydrophobic 2,3-*O*-(2-bromoisobutyryl) 2,6-*O*-TDMS-cellulose surfaces became more hydrophilic after SI ATRP with NIPAm. Again, increasing the amount of pNIPAm on the surface more dramatically changed the surface energy and resulting contact angle.

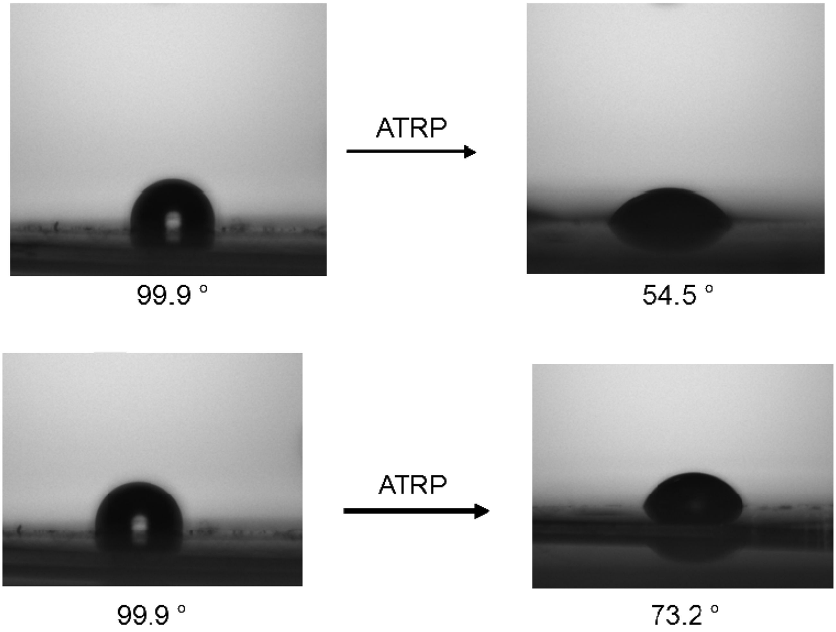

Figure 9. Contact angle measurements of thin films from 2,3-O-(2-bromoisobutyryl)-2,6-O-TDMS-cellulose before (left) and after SI ATRP (right) with 100 (top) and 10 (bottom) equivalents of NIPAm.

Conclusions

In this paper we explored the 2-bromoisobutyration of 2,6-*O*-TDMS-cellulose for the fabrication of honeycomb films. The maximum DS of 2-bromoisobutyryl groups in 3-*O*-(2-bromoisobutyryl)-2,6-*O*-TDMS-cellulose was 0.3. However, by decreasing the TDMS substitution at the C-2 position of the 2,6-*O*-TDMS-cellulose enabled higher 2-bromoisobutyryl DS values to be obtained (max ~0.8), but the enhancement was only due to substitution of the vacated C-2 position hydroxyl groups. Both compounds produced honeycomb-patterned films, however the latter 2,3-*O*-(2-bromoisobutyryl)-2,6-*O*-TDMS-cellulose films were much more uniform. Surface-initiated ATRP was successfully performed on the 2,3-*O*-(2-bromoisobutyryl)-2,6-*O*-TDMS-cellulose honeycomb films. pNIPAm polymer brushes where successfully grafted from the surfaces, the properties of which depended on the monomer concentration used. At high NIPAm loadings

(10 wt % NIPAm/H_2O) the porous honeycomb structure was lost, and a rough continuous hydrophilic surface was formed. At much lower NIPAm loadings (1 wt % NIPAm/H_2O) the honeycomb structure was maintained, albeit much less regular in structure. SI ATRP with NIPAm decreased the contact angle of the 2,3-*O*-(2-bromoisobutyryl)-2,6-*O*-TDMS-cellulose films from 99.9° to 73.2° (1 wt % NIPAm/H_2O) to 54.5° (10 wt % NIPAm/H_2O). We believe this system may serve as scaffold for cell growth with the ability to control the attachment and detachment of cultured cells. Furthermore, the honeycomb-patterned films can also be used as a platform with which to develop novel cellulosic films and membranes with tailorable properties through the grafting-from technique of specific polymers.

Downloaded by COLUMBIA UNIV on August 28, 2012 | http://pubs.acs.org
Publication Date (Web): August 17, 2012 | doi: 10.1021/bk-2012-1107.ch003

References

1. Gómez, J. A. D.; Erler, U. W.; Klemm, D. O. *Macromol. Chem. Phys.* **1996**, *197*, 953–964.
2. Koschella, A.; Heinze, T.; Klemm, D. *Macromol. Biosci.* **2001**, *1*, 49–54.
3. Kadla, J. F.; Asfour, F. H.; Bar-Nir, B. *Biomacromolecules* **2007**, *8*, 161–165.
4. Ifuku, S.; Nakai, S.; Kamitaka, H.; Takano, T.; Tsujii, Y.; Nakatsubo, F. *Biomacromolecules* **2005**, *6*, 2067–2073.
5. Sakakibara, K.; Nakatsubo, F. *Macromol. Rapid Commun.* **2007**, *28*, 1270–1275.
6. Klemm, D.; Heinze, T.; Philipp, B.; Wagenknecht, W. *Acta Polym.* **1997**, *48*, 277–297.
7. Yabu, H.; Shimomura, M. *Langmuir* **2005**, *21*, 1709–1711.
8. Yabu, H.; Takebayashi, M.; Tanaka, M.; Shimomura, M. *Langmuir* **2005**, *21*, 3235–3237.
9. Tsai, H.; Xu, Z.; Pai, R. K.; Wang, L.; Dattelbaum, A. M.; Shreve, A. P.; Wang, H.-L.; Coltlet, M. *Chem. Mater.* **2011**, *23*, 759–761.
10. Srinivasarao, M.; Collings, D.; Philips, A.; Patel, S. *Science* **2001**, *292*, 79–83.
11. Bunz, U. H. F. *Adv. Mater.* **2006**, *18*, 973–989.
12. Aitken, J. *Nature* **1911**, *86*, 516–517.
13. Widawski, G.; Rawiso, M.; Francois, B. *Nature* **1994**, *369*, 387.
14. Tan, K. K.; Thorpe, R. B. *Chem. Eng. Sci.* **1999**, *54*, 775–783.
15. Tokaruku, W. A.; Molteno, T. C. A.; Morris, S. W. *Phys. Rev. Lett.* **2000**, *84*, 3590–3593.
16. Stenzel, M. H. *Aust. J. Chem.* **2002**, *55*, 239.
17. Hernandez-Guerrero, M.; Davis, T. P.; Barner-Kowollik, C.; Stenzel, M. H. *Eur. Polym. J.* **2005**, *41*, 2264–2277.
18. Stenzel, M. H.; Davis, T. P.; Fane, A. G. *J. Mater. Chem.* **2003**, *13*, 2090–2097.
19. Nemoto, J.; Uraki, Y.; Kishimoto, T.; Sano, Y.; Funada, R.; Obata, N.; Yabu, H.; Tanaka, M.; Shimomura *Bioresour. Technol.* **2005**, *96*, 1955–1958.
20. Kasai, W.; Kondo, T. *Macromol. Biosci.* **2004**, *4* (1), 17–21.

21. Nemoto, J.; Uraki, Y.; Kishimoto, T.; Sano, Y.; Funada, R.; Obata, N.; Yabu, H.; Tanaka, M.; Shimomura *Bioresour. Technol.* **2005**, *96* (17), 1955–1958.
22. Donati, I.; Stredanska, S.; Silvestrini, G.; Vetere, A.; Marcon, P.; Marsich, E.; Mozetic, P.; Gamini, A.; Paoletti, S.; Vittur, F. *Biomaterials* **2005**, *26*, 987–998.
23. Lee, C. T.; Huang, C. P.; Lee, Y. D. *Biomacromolecules* **2006**, *7*, 2200.
24. Fukuhira, Y.; Kaneko, H.; Yamagaa, M.; Tanaka, M.; Yamamoto, S.; Shimomura, M. *Colloids Surf., A* **2008**, *313–314*, 520–525.
25. Tanaka, M.; Nishikawa, K.; Okubo, H.; Kamachi, H.; Kawai, T.; Matsushita, M.; Todo, S.; Shimomura, M. *Colloids Surf., A* **2006**, *284–285*, 464–469.
26. Chaudhuri, J. B.; Davidson, M. G.; Ellis, M. J.; Jones, M. D.; Wu, X. J. *Macromol. Symp.* **2008**, *272*, 52–57.
27. Yamada, N.; Okano, T.; Sakai, H.; Harikusa, F.; Sawasaki, Y.; Sakurai, Y. *Makromol. Chem., Rapid Commun.* **1990**, *11*, 571–576.
28. Wang, S.-H.; Matyjaszewsky, K. *J. Am. Chem. Soc.* **1995**, *117*, 5614–5615.
29. Kato, M.; Kamigaito, M.; Sawamoto, M.; Higashimura, T. *Macromolecules* **1995**, *28*, 1721–1723.
30. Keller, R. N.; Wycoff, H. D. *Inorg. Synth.* **1946**, *2*, 1.
31. Ciampolini, N.; Nardi, N. *Inorg. Chem.* **1996**, *5*, 41.
32. Bar-Nir, B.; Kadla, J. F. *Carbohydr. Polym.* **2009**, *76*, 60–67.
33. Zou, Y.; Kizhakkedathu, J.; Brooks, D. E. *Macromolecules* **2009**, *42*, 3258–3268.

Downloaded by COLUMBIA UNIV on August 28, 2012 | http://pubs.acs.org
Publication Date (Web): August 17, 2012 | doi: 10.1021/bk-2012-1107.ch003

Downloaded by OHIO STATE UNIV LIBRARIES on August 28, 2012 | http://pubs.acs.org
Publication Date (Web): August 17, 2012 | doi: 10.1021/bk-2012-1107.ch004

Chapter 4

Bacterial Cellulose Aerogels: From Lightweight Dietary Food to Functional Materials

Falk Liebner,[*] Nikita Aigner, Christian Schimper, Antje Potthast, and Thomas Rosenau

University of Natural Resources and Life Sciences, Vienna, Austria
Department of Chemistry, UFT Campus Tulln, Konrad-Lorenz-Straße 24,
A-3430 Tulln, Austria
[*]E-mail: falk.liebner@boku.ac.at

Aerogels are highly porous, extremely lightweight materials that have a huge application potential. Following their inorganic and organic predecessors, such as the "famous" silica-based materials, aerogels from renewables, in particular cellulose, are sometimes regarded as the third, "young" generation of aerogels, and research in this field has literally undergone a boom at the turn of the millennium. This book chapter introduces a subclass of cellulosic aerogels: Bacterial cellulose (BC) aerogels. Compared to mechanically, chemically or enzymatically processed plant celluloses, BC features some outstanding properties, such as high purity, high molecular weight and high gelation that render this natural source an excellent candidate for biomedical applications. Following a brief introduction of the natural resource bacterial cellulose, the chapter describes in detail the preparation of BC aerogels and comprehensively discusses their properties, in particular their pore features and their response to mechanical stress. Furthermore, the loading of BC aerogels with bioactive compounds is reported, revealing the potential for controlled release applications. The preparation of interpenetrating networks that consists of BC and a second polymer, such as cellulose acetate, is shown to have a strong mechanical reinforcement effect. Based on their recent work, the authors finally propose a new definition that might help to describe "aerogels" more precisely.

Downloaded by OHIO STATE UNIV LIBRARIES on August 28, 2012 | http://pubs.acs.org
Publication Date (Web): August 17, 2012 | doi: 10.1021/bk-2012-1107.ch004

Introduction

Nata de coco is a well-known chewy, translucent dessert originating from the Philippines, produced by bacterial fermentation of coconut liquid. It can be found as a food additive in drinks, ice cream, puddings or as small, cubic pieces in aromatized, sweetened jellies that are sold in Asian supermarkets around the world. As the fibrous base of nata de coco consists of pure bacterial cellulose it would be tasteless without being aromatized. Furthermore, it is indigestible and therefore used as a dietary food.

However, nata de coco features some other properties that render this natural product an interesting source for the development of functional materials. Provided that the water filling the open-porous voids between the cellulose microfibrils would be replaced by air, extremely lightweight, materials could be obtained. Similarly as with other types of aerogels there would be a wide range of technical applications for such materials, such as in tissue engineering, high-performance thermal or acoustic insulation, advanced filter techniques, controlled release of bioactive compounds, catalysis, or electrochemical applications.

Along with the increasing societal interest in valorization of biomaterials, research on biopolymer-based hydro- and aerogels has been considerably advanced over the past few years. In particular cellulosic aerogels are currently a "hot topic" in material research due to both the vast quantities of cellulose produced by terrestrial vegetation and its intriguing properties, such as high fiber strength.

Next to plants with cellulose being an integral constituent of their cell walls, there is also a variety of bacteria that have the ability to produce cellulose as a byproduct of their metabolism, e.g. strains of *Pseudomonas, Achromobacter, Alcaligenes, Aerobacter, Rhizobium, Agrobacterium, Azotobacter and Acetobacter* (*1*). The driving force for bacteria to synthesize cellulose is preservation and survival of their species since cellulose production enables them to better adapt to a broad variety of habitats.

Acetobacter xylinum – a strain that is nowadays widely used for commercial as well as scientific purposes – produces cellulose pellicles that keep the strain floating on the surface of the culture medium for maintaining sufficient oxygen supply. Other bacteria as for example *Agrobacterium tumefaciens* that are plant pathogens use cellulose for better attachment to plants, similar to the symbiotic *Rhizobium spp*. Another kind - *Sarcina ventriculi* - aggregates to packets and protects itself with a cellulose hull (*2*). Many further examples for environmental adaption exist, and the comparatively recent discovery of *Enterobacter* by Fujiwara et al. (*3*) in 2001 or the isolation of a cellulose-producing *Enterobacter* stem from rotten apple by Hungund and Gupta (*4*) may serve as indicators for both – the still ongoing discovery of cellulose producing bacteria and the frequent occurrence of such bacteria in our environment.

In contrast to plant cells, bacteria produce cellulose as an extracellular substance. At the end of a complex biosynthetic pathway (see e. g. Ross et al. (*2*)), cellulosic elementary fibrils are released into the environment through a number of rosette-type "biological spinnerets" lined up in the terminal endoplasmatic complexes of the bacterium, and eventually aggregate into ribbons typical for bacterial cellulose. An interesting aspect of cellulose generation by bacteria is cell division as it contributes to the microstructure of the cellulose pellicle. The cellulose synthesizing sites are also duplicated during cell division (*5*), and when this process is finished, mother and daughter cell are connected to the same cellulose ribbon which contributes to interconnections and entanglement in the framework.

As soon as a suitable cellulose producing stem is isolated, it needs the right conditions in terms of temperature, oxygen supply and nutrients to be able to synthesize cellulose. As a nutrient source, several growth media exist, one that is very common is a mixture introduced by Schramm and Hestrin in 1954 (*6*) and thus referred to as "Hestrin-Schramm growth medium", which consists of 20 g l^{-1} glucose, 5 g l^{-1} peptone, 5 g l^{-1} yeast extract, 1.15 g l^{-1} citric acid monohydrate and 6.8 g l^{-1} $Na_2HPO_4 \times 12\ H_2O$. Other growth media include the very easily prepared Waterman's sucrose beer solution which is obtained by "adding 40 grams of sucrose to a liter of beer" (*7*) or coconut milk that is the source of the above-mentioned indigenous dessert *nata de coco*.

Fermentation can be accomplished in different types of fermenters. The most straightforward construction is static cultivation involving a vessel filled with an adequate growth medium (*8*, *9*). The medium is inoculated with the respective bacteria which, after a lag phase, begin to produce cellulose. A problem with static cultivation is that the possible maximum thickness of the cellulose pellicle is limited by the fact that the aerobic bacteria reside on top of it and the growth medium has to diffuse through an increasingly thick barrier of cellulose. To overcome this problem, agitated fermenters can be used providing better contact with oxygen and growth medium. However, the oxygen abundance leads to increased survival of non-cellulose producing mutants (Cel-) (*10*). Also, shear forces caused by agitation negatively influence the product on a microstructural level, by reducing the content of I_α-type crystallites and hence lowering the E-moduli for sheets pressed from this product, though a higher water holding capacity compared to static cultivation was determined (*11*). Similar results with respect to structural properties were obtained for cellulose produced in rotary disk fermenters by Krystynowicz et al. (*12*), but the generation of Cel- mutants could be inhibited by adding ethanol. In more recent approaches, the continuous production of bacterial cellulose is investigated, for example in the horizontal lift reactor (HoLiR) concept. This device slowly pulls a BC sheet off a basin with a growth medium allowing for producing BC sheets of variable length and adjustable thickness (*13*).

Generally, the bacteria type will determine the best fermenter/growth medium combination which has to be separately determined for each of the different strains to achieve satisfying results. However, the strong dependence on environmental conditions, such as the composition of the culture medium, can be also utilized to tailor the properties (porosity, composition and size of nanofibrils, mechanical parameters etc.) of bacterial cellulose by adding modifiers to the culture medium (*cf.* this chapter, below).

Downloaded by OHIO STATE UNIV LIBRARIES on August 28, 2012 | http://pubs.acs.org
Publication Date (Web): August 17, 2012 | doi: 10.1021/bk-2012-1107.ch004

Downloaded by OHIO STATE UNIV LIBRARIES on August 28, 2012 | http://pubs.acs.org
Publication Date (Web): August 17, 2012 | doi: 10.1021/bk-2012-1107.ch004

BC Aerogels as a Sub-Class of Cellulosic Aerogels: Preparation, Properties, and Application Potential

Complementary to regenerated cellulose (cellulose II polymorph) that has been the main source of cellulosic aerogels since their early days about 10 years ago (see the previous chapter), native cellulose (cellulose I polymorph) has only recently moved into the limelight of research within this comparatively young field.

Correspondingly, cellulose aerogels are nowadays distinguished by their type of cellulose crystal structure that dominates the final product. It is affected by both the technique of aerogel preparation and the type and origin of cellulose used:

1) **Cellulose II aerogels**: Molecularly disperse dissolution and subsequent regeneration/coagulation of cellulose or commercial pulps inevitably affords the thermodynamically more stable cellulose II polymorph to be formed – regardless of whether the cellulose dissolved originates from plants or bacteria (*14–24*).
2) **Cellulose I aerogels (I_α, I_β)**: The different cellulose I crystal phases (I_α, triclinic, P1: dominating in bacterial cellulose; I_β, monoclinic, $P2_1$: dominating in plant cellulose) are preserved as the preparation protocols circumvent dissolution and subsequent coagulation. While BC is mostly used without further pre-treatment (*25*, *26*) plant cellulose for cellulose I aerogels is commonly subjected to mechanical disintegration and/or enzymatic or chemical degrading procedures (nano- or microfibrillated cellulose, NFC, MFC (*27*), nanocrystalline cellulose NCC (*28*)) to increase the portion of crystalline domains or to obtain a preferred fibril aspect ratio.

The considerable interest in cellulose I sources such as BC, NFC, MFC, or NCC is due to the high portion of crystalline domains that adds considerable strength to the cellulose network structure. A certain fibril aspect ratio provided, some of the cellulose I lyogels (gels in which the pores are filled with a liquid) have been successfully converted into lightweight aerogels already by conventional drying as the “reinforced” cellulosic scaffolds much better resist capillary forces. In contrast, in the case of (regenerated) cellulose II gels of comparable cellulose content, supercritical drying is commonly the only choice to preserve the fragile cellulose network structure.

Bacterial cellulose features not only high average molecular weight, crystallinity, and mechanical stability (*29*). Its high purity and bio-compatibility (*30–32*) are some of the additional features that render bacterial cellulose an interesting source for highly porous scaffolds with considerable application potential in biomedicine and health care (*33*, *34*). Cosmetic applications can already be found in the different fields of skin care where BC is used as light scatterer for sunscreen applications (*35*) or as a stimulant for skin tissue regeneration (*36*). Biomedical applications comprise the utilization of open-porous BC scaffolds for production of artificial blood vessels (*37*, *38*), as matrices for slow-release applications of bioactive compounds (*39*), and in wound dressings for patients with burns, chronic skin ulcers or other extensive loss of tissue (*40*), where such gels act as temporary skin substitutes with high mechanical strength in wet state. The high water retention capacity of the oxygen-permeable BC along with the high abundance of surface hydroxyl groups seems to stimulate re-growth of skin tissue, while at the same time limiting infection (*36*). Reinforced, yet biodegradable bacterial cellulose aerogels of appropriate porosity are considered as a potential alternative to organ or tissue transplantation as these materials are able to direct tissue generation from culture cells (*41*).

Downloaded by OHIO STATE UNIV LIBRARIES on August 28, 2012 | http://pubs.acs.org
Publication Date (Web): August 17, 2012 | doi: 10.1021/bk-2012-1107.ch004

Preparation of Bacterial Cellulose Aerogels

Static cultivation of bacterial cellulose has been accomplished in aquarium-type glass tanks in Hestrin-Schramm culture medium (see above). After inoculating the growth medium with a suspension of *Gluconacetobacter xylinum* X5 wild type strain and a certain lag phase, extracellular expression of cellulose I on the surface of the growth medium sets in. After 30 days of cultivation at 30°C, most of the glucose is consumed and the thickness of the cellulose layer amounts to about 3-4 cm. The harvested cellulose mats are than cut into pieces or sheets of desired size, subjected to repeated alkaline treatment (0.1 M aqueous NaOH at 90°C, 20 min, three times) to get rid of protein residues and by-products, and finally neutralized by rinsing with deionized water for 24 h. For further use the material can be stored in 70% aqueous ethanol.

BC aquogels can be easily converted into the corresponding aerogels by freeze-drying. However, it was shown that freeze-drying can reduce the re-wettability of BC aerogels by up to 10%, suggesting collapsing of some weaker cellulose pore walls during drying. Supercritical drying as the most gentle drying technique is therefore preferred if full preservation of porosity is imperative.

The first report on bacterial cellulose aerogels can be found in the Japanese Journal of Polymer Science and Technology. Maeda et al. (*42*) converted BC aquogels into the corresponding aerogels using supercritical ethanol and obtained ultra-lightweight (≥ 6 mg cm^{-3}), open-porous materials composed of 20-60 nm thick, network forming microfibrils that had a porosity of more than 99%. However, it must be assumed that the chemical integrity of cellulose had largely suffered from hornification processes due to the rather harsh drying conditions used (6.38 MPa, 243°C). The strong increase of stress measured at 60% strain ($\sigma_{60\%}$) from 20 kPa (hydrogel) to 54 kPa (aerogel) (*42*) may support this assumption. It is known that thermal drying of lignocellulosic material beyond 180-200°C causes considerable stiffening of the polymer structure (*43*) and negatively affects both hydrophilicity and re-wettability. These drawbacks can be circumvented if ethanol is replaced by supercritical carbon dioxide (scCO$_2$ (*26*, *42*); due to its low critical point (31.1°C, 7.38 MPa). Thorough replacement of the pore water of BC aquogels by an appropriate organic solvent – preferably ethanol – prior to scCO$_2$ drying is the only pre-condition as water is immiscible with scCO$_2$. Solvent exchange is accomplished by gently shaking the aquogels

Downloaded by OHIO STATE UNIV LIBRARIES on August 28, 2012 | http://pubs.acs.org
Publication Date (Web): August 17, 2012 | doi: 10.1021/bk-2012-1107.ch004

in the twenty-fold volume of absolute ethanol. After 6 and 12 h, the gels are transferred to a second and third bath with the same amount of fresh solvent.

The $scCO_2$ drying step was performed in a laboratory-scale autoclave (Alltech Grom GmbH, Germany) at 40°C. The alcogel was placed on a stainless steel filter plate inside the autoclave. After equilibrating the closed autoclave at 40°C for 15 min, the system was pressurized over the bottom valve with liquid, pre-heated CO_2 by a HPLC pump until a final pressure of 100 bar was reached. This state was maintained for 15 min before the top valve was opened. The bottom valve was subsequently switched to the separator, where ethanol and CO_2 were separated by an isothermal flush. In a first step, the ethanol-rich phase was flushed out of the autoclave. Then, ethanol was drained from the gel pores at constant CO_2 flow rate of 1 g min^{-1} (*26*). After 60 min, the top valve was closed and the autoclave was depressurized over the separator. Prior and after $scCO_2$ drying, mass (±1 mg) and volume (±1 μm^3) of the block-shaped cellulose aquogels and aerogels, respectively, were recorded to calculate the density of the materials and the extent of shrinking upon the drying step.

Properties of Bacterial Cellulose Aerogels

Figure 1 (left) shows a BC aquogel before and after drying with $scCO_2$ (40°C; 10 MPa; 2 h). The far-reaching preservation of the BC aquogel's shape and porosity throughout solvent replacement and subsequent $scCO_2$ drying was obviously the most unexpected result of the first $scCO_2$ drying experiments in view of the very low cellulose content of the aquogels (1 w%). The observed low shrinkage clearly distinguishes BC aerogels from their cellulose II-derived counterparts that were previously obtained by dissolution/coagulation of different commercial pulps according to the Lyocell approach (regeneration of cellulose from solutions in *N*-methylmorpholine *N*-oxide monohydrate). In those cases, strong shrinkage in the range of about 30% (*18*) and more (*15*) had been reported for supercritical drying of the aerogels, even for solutions with the threefold concentration of cellulose. For dopes that contained 1 w% of cellulose – about the cellulose weight fraction of BC aquogels – shrinking even exceeded 60% (*15*). While the densities of the cellulose II aerogels were consequently high, ultra-lightweight cellulose bodies of an average density of 8.25 ± 0.7 mg cm^{-3} (n = 10 (*26*);) have been obtained from the respective BC aquogels. Similar to the most lightweight expanded polystyrene foams (16 mg cm^{-3} (*44*);), electrostatic attraction or surface effects suffice to keep a larger piece of BC aerogel in suspense on a fingertip (see insert of Figure 1, right).

Bacterial cellulose aerogels were furthermore shown to resist shrinking during long-term storage even under humid conditions. Whereas cellulose II aerogels suffer a significant volume reduction of 15.5% at 30% relative humidity (r.h.), 50.9% at 65% r.h. and 84.2% at 98% r.h. throughout 14 days of storage, BC aerogels were confirmed to resist shrinking completely even at 98% r.h. for at least several days. The almost zero shrinkage during $scCO_2$ drying and open-air storage is supposed to be mainly due to the high portion of crystalline domains present in bacterial cellulose. According to Zugenmaier (*45*) the crystallinity index of BC is

Downloaded by OHIO STATE UNIV LIBRARIES on August 28, 2012 | http://pubs.acs.org
Publication Date (Web): August 17, 2012 | doi: 10.1021/bk-2012-1107.ch004

in the range of 65-79% whereas regenerated cellulose, such as Lyocell fibers, has about 35% only. Also the molecular weight average of the cellulose sources has to be considered as a reason for the intriguingly different dimensional stability of the cellulose aerogels. Even though the degree of polymerization (DP) of BC does not seem to be particularly high (4000-6000) compared to cotton (≤ 15000) or wood (≤ 10000), separation (pulping), purification (bleaching), and the dissolving step for gel preparation (NaOH, NMMO, e.g.) lead to a much lower effective DP for such plant-derived pulps (commonly ≤ 1000) whereas the DP of BC can be fully preserved as all of the above-mentioned treatments are not required in BC aerogel manufacture.

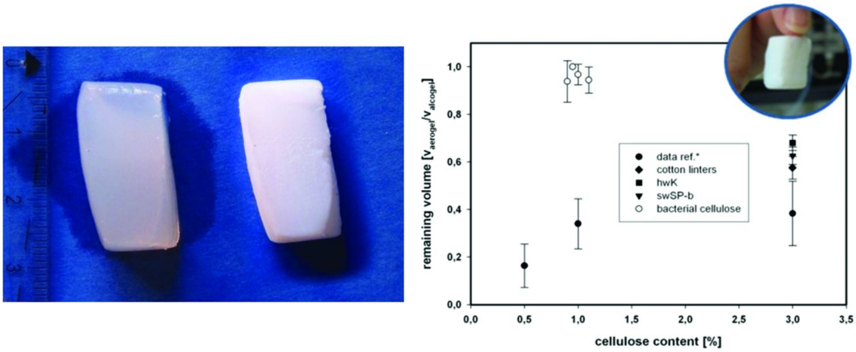

Figure 1. Left: BC aquogel before (left) and after solvent exchange to ethanol and subsequent scCO₂ drying (right). Right: shrinkage of BC aquogels (empty circles) and Lyocell dopes of different cellulose content (solid symbols, date taken from (5, 18)) upon converting them into aerogels by scCO₂ drying.

The full preservation of the pore features during solvent exchange from water to ethanol and subsequent $scCO_2$ drying and the high resistance towards shrinking in aqueous environment are the factors that explain the surprising complete re-wettability of BC aerogels. This special feature of BC aerogels - along with other properties such as high purity, interconnected porosity and pore surface area - renders them ideal materials for slow-release applications where a predictable loading/unloading of active compounds is required (see below).

Porosity and Mechanical Properties

Characterization of ultra-lightweight soft materials, such as bacterial cellulose aerogels, in terms of porosity, solid cellulose aggregate structure, and mechanical properties is a challenging task. For porosity studies usually segments of the inner parts of a sample are used as solvent exchange during preparation and the applied drying techniques can easily alter the surface of specimen for example by diffusion effects (*46*). However, standard sample preparation techniques, such as cutting with a microtome cutter or - more simply - razor blades, are considered to bear a high artefact-generating potential. Even after deep-freezing in liquid nitrogen the problem remains due to the high elasticity and tensile strength of individual BC cellulose ribbons on the one hand, and the very low solid volume fraction (and

Downloaded by OHIO STATE UNIV LIBRARIES on August 28, 2012 | http://pubs.acs.org
Publication Date (Web): August 17, 2012 | doi: 10.1021/bk-2012-1107.ch004

hence density) of the aerogels on the other hand. The same applies to dissection by notching and subsequent transversal breaking by applying a combination of tension and bending (*18*).

Scanning electron micrographs (SEM) confirm that the dense network of bacterial cellulose nanofibers as present in BC aquogels is largely preserved throughout the solvent exchange and $scCO_2$ drying steps (see Figure 2). The results of small-angle X-ray scattering (SAXS), nitrogen sorption at 77K (calculation of the specific pore surface area by applying the models developed by Brunauer, Emmett, and Teller, BET, and Benjamin, Johnson and Hui, BJH), and thermoporosimetry with *o*-xylene as "confined" solvent confirmed that the dimension of the voids between the nanofibers correspond to interconnected micro-, meso-, and macropores. In particular smaller macropores of around 100 nm in diameter contribute mostly to the BC aerogel's overall porosity which is in good agreement with different series of SEM and ESEM pictures (Figure 2).

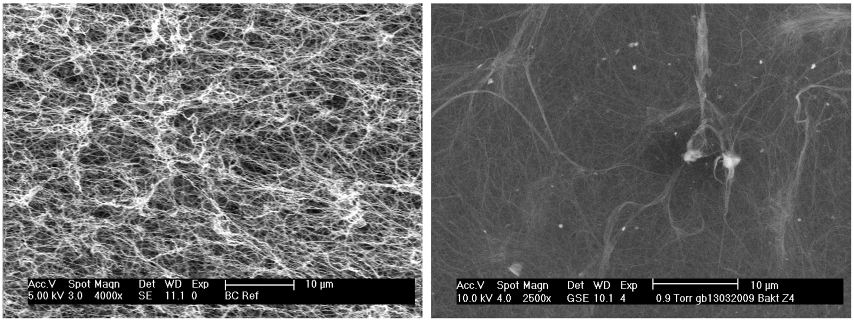
Acc.V Spot Magn Det WD Exp 10 µm
5.00 kV 3.0 4000x SE 11.1 0 BC Ref
Acc.V Spot Magn Det WD Exp 10 µm
10.0 kV 4.0 2500x GSE 10.1 4 0.9 Torr gb13032009 Bakt Z4

Figure 2. SEM (left) and ESEM (right) pictures of BC aerogels obtained by solvent exchange (water → ethanol) and subsequent $scCO_2$ drying at 40°C (10 MPa).

However, the occurrence of larger voids ("macropores") is difficult to investigate as thermoporosimetry – even though a powerful tool for multi-scale pore characterisation of soft matter – has its upper detection limit at about 1-5 µm pore diameter. Larger macropores are thus not considered by this method which is due to the underlying principles of differential scanning calorimetry, with "confined" solvent in small pores causing a second peak in the DSC curve at lower T relative to the freezing point of "free" solvent. The pore size distribution of small pores that have a high "shielding" potential for the "confined" solvent can be calculated from the relative shift (size) and peak area (percentage) of this second peak, whereas the solvent in larger pores ($Ø \geq 1...5$ µm) can be hardly distinguished from "free solvent".

Mercury intrusion – commonly the method of choice for studying macropores – cannot be applied as the structure of the cellulosic aerogels completely collapses under the applied high pressure. This is not only the case for BC aerogels, but has also been reported for aerogels from plant cellulose (*47*), cellulose acetate (*48*), polyurethane (*49*), and silica (*50*, *51*).

The mechanical response profiles to uniaxial compressive stress confirmed that bacterial cellulose aerogels behave very much like cellular solids as the different regions shown in Figure 3 correspond very well with those in the work on cellular solids conducted by Gibson and Ashby (1982).

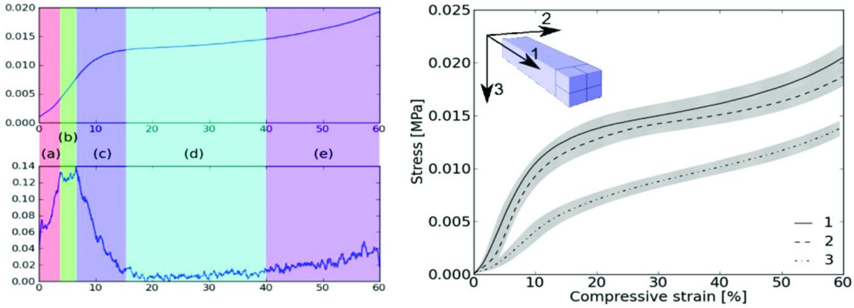

Figure 3. Left: sample stress-strain curve of a BC aerogel (a: adjustment region, b: linear elastic deformation, c: non-linear elastic and plastic deformation, d: plateau region, e: densification). Right: stress-strain curves under compression in three orthogonal directions (direction 3: direction of growth; lines are mean values of stress, grey background represents standard deviation, sample size n=5).

The region within the first 3% of strain (Figure 3 left, a) is considered to be an adjustment region where mainly irregularities in specimen geometry are evened out. At around 5% strain the stress-strain relation is linear with a relatively constant slope (b). This region is used to calculate the E-modulus under compression. At higher compressive strain, the slope decreases (c) which is due to non-linear elastic deformation (cell wall buckling) and beginning plastic deformation (cell collapse). Subsequently, the stress-strain curve passes a plateau region (d) which is of considerable size (from 15% to 40% strain). Eventually the material densifies (e) leading to an exponential increase of stress over strain. The overall smoothness of the curve and the absence of a peak after the linear elastic region indicate that the material deforms in a ductile way on the microscale, in contrast to brittle foams and silica aerogels.

Interestingly, no sample buckling was observed during compression. The Poisson ratio, which describes the change of the cross-section area upon application of mechanical stress, being in the range of 0.1 to 0.3 for silica aerogels, was approximately zero for BC aerogels independent of the loading direction. This is in good agreement with Sescousse et al. (*52*) who also reported a zero Poisson ratio for cellulosic aerogels from EMIMAc solution, similar to cork.

Compression tests along the three orthogonal spatial directions revealed that BC aerogels are transversely isotropic. Thus, unlike a unidirectional fiber-reinforced composite, it features two directions with higher stiffness and strength and a third direction with lower values, the latter being the growth direction of the bacterial cellulose which is perpendicular to the interface between culture medium and air. The E-moduli for the two stiffer directions 1 and 2 were determined to be 0.149 MPa and 0.140 MPa, respectively. The third direction

Downloaded by OHIO STATE UNIV LIBRARIES on August 28, 2012 | http://pubs.acs.org
Publication Date (Web): August 17, 2012 | doi: 10.1021/bk-2012-1107.ch004

featured an E-modulus which was some 60% less (0.057 MPa). Strength behaved similarly, being 7.05 kPa and 7.84 kPa for the two stronger directions 1 and 2, respectively, and 4.65 kPa for the weaker direction 3.

Reinforcement of BC Aerogels

The extremely low density of BC-based aerogels is certainly one of their most intriguing features. However, reinforcement is required for some applications due to the relatively low mechanical strength and stiffness. Composite materials and, in particular, interpenetrating networks are considered to be promising approaches in this respect, and both inorganic (e.g. silica (*53*),) and organic polymers (e.g. poly(methylmethacrylate) (*54*),) have been used for this purpose.

For formation of interpenetrating networks, simultaneous generation of the two network components, subsequent gelation of a second component inside the open-porous parent BC matrix, or loading and subsequent precipitation of the reinforcing compound within the BC are possible approaches. $ScCO_2$ is an elegant means of preparing composites by loading/precipitation as different variants can be applied: 1) Compounds that are soluble in $scCO_2$ can be pre-dissolved in the supercritical fluid and homogeneously distributed inside the porous matrix. Subsequent depressurization into the subcritical region causes precipitation; 2) Other compounds, insoluble in $scCO_2$ but soluble in solvents that are extractable with $scCO_2$, can be precipitated directly during the drying procedure with CO_2 as the anti-solvent, as flushing of the CO_2-expanded solvent phase causes supersaturation and precipitation of the solute.

Following the second approach, bacterial cellulose/cellulose acetate (BC-CA) composite aerogels have been prepared. The comparatively facile procedure comprised 1) immersion of BC lyogels in cellulose acetate (CA; DS 2.5) solutions of different concentration (10, 20, 30, 40, and 50 mg ml^{-1}) in acetone, 2) precipitation of CA from solution into the BC network with CO_2 as the anti-solvent, and 3) replacing the CO_2-expanded organic solvent by $scCO_2$ (see Figure 4).

Anti-solvent precipitation is based on the effect that the solvent power of a $scCO_2$-miscible solvent and CO_2 sharply decreases close to the critical pressure of the binary mixture at a given temperature and turns CO_2 to act as an anti-solvent (*55*). For mixtures of CO_2 and acetone, the critical pressure is reached at around 8 MPa (*56*) at 40°C, and further pressurization causes solute precipitation inside the porous matrix. The advantage of this method is that immediately after precipitation the composite lyogel can be converted into the corresponding aerogel, virtually using the same conditions as the interfacial tension between liquid and supercritical phase is here close to zero (*57*) which is a pre-requisite for supercritical drying (*58*). To ensure supercritical conditions throughout the drying step a slightly higher CO_2 pressure (10 MPa) than required for anti-solvent precipitation is used.

A strong correlation was observed between the CA concentration in the loading bath and the apparent density of the resulting BC aerogels (R^2=0.998, see Figure 4, left). The intercept of the regression line is at about 10 mg cm^{-3} which is in good agreement with the apparent density of the unmodified BC aerogels

Downloaded by OHIO STATE UNIV LIBRARIES on August 28, 2012 | http://pubs.acs.org
Publication Date (Web): August 17, 2012 | doi: 10.1021/bk-2012-1107.ch004

Downloaded by OHIO STATE UNIV LIBRARIES on August 28, 2012 | http://pubs.acs.org
Publication Date (Web): August 17, 2012 | doi: 10.1021/bk-2012-1107.ch004

obtained from respective acetone lyogels (9.63 mg cm^{-3}). Mechanical properties also scaled well with apparent density. The E-modulus (under compression) increased by a factor of 15 from 0.235 MPa to 3.561 MPa over the probed density range (Figure 4, right). Yield strength calculated at 0.2% offset strain behaved in a similar manner by increasing from 13 kPa to 123 kPa (see Table 1 for detailed values).

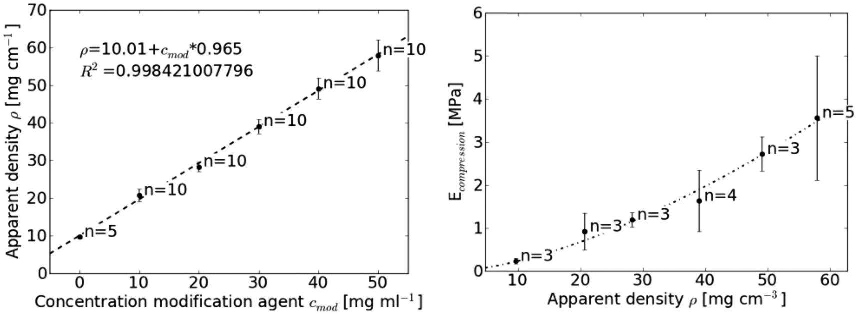

Figure 4. Left: apparent density of BC aerogels vs. concentration of CA in the loading bath. Right: E-modulus under compression vs. apparent density. Full circles and whiskers indicate mean values (n = sample number) and standard deviation, respectively. The dashed line in the right diagram represents a power-law fitting of the data points.

Table 1. Apparent densities, Young's modulus and yield strength of BC aerogels modified with various concentrations of CA

	E *[MPa]*	*$Rp_{0.2}$* *[kPa]*	*R* *[mg cm^{-3}]*
0	9.63	0.235	0.013
10	20.69	0.921	0.024
20	28.31	1.193	0.051
30	39.05	1.634	0.070
40	49.12	2.722	0.101
50	57.94	3.561	0.123

The reinforcing effect of CA can be nicely demonstrated by means of both unmodified and reinforced BC aerogels subject to scCO$_2$ drying under inappropriate conditions. Short drying periods and fast depressurization are factors that easily cause pore collapsing and formation of larger voids of up to 100 µm in one spatial orientation for the unmodified BC aerogels (see left SEM picture in Figure 5). However, if the bacterial cellulose network is homogeneously reinforced with CA prior to drying, the reinforced BC network resist much better the capillary forces, hence minimizing or avoiding pore collapsing and formation of the above-mentioned large macropores (Figure 5, middle and right SEM pictures).

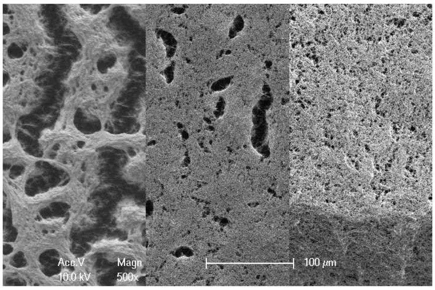

Figure 5. SEM images of rapidly depressurized BC aerogels prior to (left) and after reinforcement with cellulose acetate corresponding to a BC:CA ratio of about 1:1 (w/w; middle) and 1:3 (w/w, right).

Bacterial Cellulose Aerogels: Highly Porous Scaffolds for Controlled Release Applications

The high molecular weight and the high percentage of crystalline domains are factors that lead to an outstanding high dimensional stability of bacterial cellulose throughout both solvent exchange from water to ethanol, and scCO_2 drying. Thus, the entire volume fraction formed by the voids between the nanofibrils of bacterial cellulose remains fully accessibility for gases and liquids after converting BC aquogels into the respective aerogels. The resulting quantitative rewettability renders BC aerogels attractive matrices for controlled release applications in cosmetics and medicine.

Haimer et al. (*39*) have shown that bioactive compounds such as D-panthenol or L-ascorbic acid can be homogenously deposited onto the inner surface of purified and sterilized bacterial cellulose under full preservation of their pore features. The proposed facile procedure comprises the same steps as described for reinforcement of BC aerogels with cellulose acetate, i.e. 1) thorough replacement of water that originally fills the voids of bacterial cellulose by ethanol, 2) immersing the resulting alcogels in an ethanolic solution of the respective bioactive compounds, 3) homogeneous anti-solvent precipitation (loading) of the bioactive compounds on the surface of the nanofibrils that form the “pore walls” of the bacterial cellulose alcogels using carbon dioxide, and 4) subsequent scCO_2 drying which affords the respective “loaded” aerogels (see above).

If the dry, loaded monolithic aerogel is then re-wetted by water for example, and the bioactive compound is slowly released depending on solubility of the compound and the diffusion rate.

Loading isotherms evidenced that loading of BC alcogels with D-panthenol or L-ascorbic acid (Figure 6, left) is mostly driven by diffusion of the solution into the porous matrix and not by specific interactions between solid matrix and solute. This is supported by a) the shape of the loading isotherms that remained largely linear even at very high solute concentrations close to the saturation limit in ethanol

Downloaded by OHIO STATE UNIV LIBRARIES on August 28, 2012 | http://pubs.acs.org
Publication Date (Web): August 17, 2012 | doi: 10.1021/bk-2012-1107.ch004

Downloaded by OHIO STATE UNIV LIBRARIES on August 28, 2012 | http://pubs.acs.org
Publication Date (Web): August 17, 2012 | doi: 10.1021/bk-2012-1107.ch004

and b) the similar slopes of the loading isotherms expressed as correlation between solute weight fraction in the aerogel and solute concentration in the loading bath (D-panthenol: 0.026 ml mg^{-1}; L-ascorbic acid: 0.029 ml mg^{-1}).

Similarly, the exponential shape of the experimentally determined release curves (Figure 6, right) suggested purely diffusion-driven release kinetics which would be independent of the amount of loaded substance. Hence, unloading of bacterial cellulose aerogels, i.e. the release of bioactive compounds from loaded bacterial cellulose aerogels into water, and hence the solute concentration should be primarily controllable by the thickness of the gel layer, but also by pore features, such as pore geometry and pore size.

This was confirmed by Haimer et al. (*39*) who tried to predict the release of D-panthenol and L-ascorbic acid from loaded bacterial cellulose aerogels of different thickness according to the diffusion-based Korsmeyer model. The advantage of this mathematical model is that it allows for simultaneous consideration of both the diffusion of water into an open-porous matrix and of a given organic compound out of it.

Starting with the initial content of bioactive compound that can be calculated from the loading isotherm and based on a time- and location-independent effective diffusion coefficient $D_{eff,water}$ of $5\cdot10^{2}$ cm^2 min^{-1} that was experimentally determined, the applied models were confirmed to be well suited to calculate the release of the studied compounds by adjusting only one parameter, namely the effective diffusion coefficient of the respective bioactive compound $D_{eff,drug}$.

$D_{eff,drug}$ values of 6.9 10^{-4} cm^2 min^{-1} and $5.94\cdot10^{-4}$ cm^2 min^{-1} were determined for the release of D-panthenol and L-ascorbic acid from gel layers of a thickness of 4.5 and 3 mm, respectively. Based on these effective diffusion coefficients the release from gel layers of different thicknesses were calculated and compared with the experimental values. The obtained release profiles confirmed that the release of the bioactive compounds D-panthenol and L-ascorbic acid is basically diffusion-controlled and can be adjusted by respective parameters, such as gel layer thickness or porosity.

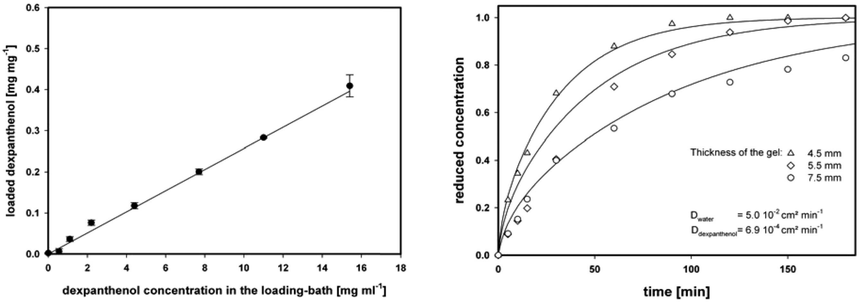

Figure 6. Left: loading and release of D-panthenol on/from BC aerogels: Loading isotherms (25°C). Right: release of the active substances from loaded gels of different layer thickness into water; experimental values (data points) and mathematical modeling (solid line). Reproduced with permission from reference (39). Copyright 2010 John Wiley and Sons.

Downloaded by OHIO STATE UNIV LIBRARIES on August 28, 2012 | http://pubs.acs.org
Publication Date (Web): August 17, 2012 | doi: 10.1021/bk-2012-1107.ch004

Revisiting the Definition of Aerogels

Quid hoc est? – What is it?

That is what the Old Romans would have asked in astonishment if they ever put their hands onto a piece of ultra-lightweight, highly porous, fluorescent bacterial cellulose aerogel as it is shown in Figure 7 (left).

The explanation is not as trivial as it might seem at a first glance. Even today - about 80 years after the preparation of the first aerogels by Samuel Stephen Kistler (*59*) – we rather tend to describe this comparatively young class of materials by enumerating their intriguing, outstanding properties instead of providing a clear general definition - which is due to the fact that to date no commonly accepted definition exists.

Accompanying the strongly advancing aerogel research that had been triggered by the advances of sol-gel chemistry in the 70ies, emerging $scCO_2$ technologies in the 80ies, and the revival of polymer chemistry in the 90ies, a considerable number of scientific papers has been devoted to aerogels and has producedseveral attempts to define the term "aerogel". Gesser and Goswami (*60*) limited the base material to a colloidal gel, i.e. a mixture of two continuous phases on a microscopic level. Fricke and Emmerling (*61*) did not mention this particular structural feature, however restricted aerogels to "...sol-gel derived nanostructured materials...". While the term nanostructured is applicable to bacterial cellulose aerogels, the latter are neither sol-gel derived nor colloidal, as shown above. Hüsing and Schubert (*62*) defined aerogels in a more general way through the production process: "Materials in which the typical pore structure and network are largely maintained when the pore fluid of a gel is replaced by air...", immediately mentioning a somewhat problematic point of their definition: "However, it is not always clear to what extent the structure is maintained." And indeed, the claim that the structure of the wet gel remains intact throughout the drying process is difficult to maintain because certain structural investigations simply cannot be performed on wet gels, in particular for soft matter such as cellulose. This makes the validation of the latter definition impossible in many cases. Kistler (*63*) already concluded that one of the benefits of the ability to replace the liquid phase in a gel by a gas is a better investigation of the gel structure. To circumvent the weaknesses of the above mentioned definitions, the authors believe that it would be more convenient to define aerogels by properties that most of the published work agrees on. Based on their work with different types of aerogels from renewable sources the authors would like to suggest the following modified definition of aerogels:

Aerogels are solids that feature very low density, high specific surface area and consist of a coherent open-porous network of loosely packed, bonded particles or fibers.

This definition enables to distinguish aerogels from liquid foams (e.g. whipped cream), packed beds (freshly fallen snow) and open porous metal foams and gives them a particular place within the group of cellular solids.

Worth mentioning is the metaphor to describe the nature of aerogels rather than a definition by Long and Rolison (*64*) – they compared aerogels to buildings and look at the material from an architectural point of view. A building consists

Downloaded by OHIO STATE UNIV LIBRARIES on August 28, 2012 | http://pubs.acs.org
Publication Date (Web): August 17, 2012 | doi: 10.1021/bk-2012-1107.ch004

of a comparably little amount of walls (solid volume fraction) compared to the volume occupied by rooms (void volume fraction). Doors and windows make a building open porous and people moving through them are a good metaphor for substances diffusing through an aerogel. Considering for instance Fritz Wotruba's Church of the Holy Trinity (Figure 7, right), even the packed particles constraint seems met. The only difference that remains between buildings and aerogels is the scale; while the appropriate unit for measuring buildings is obviously meters, that for aerogels is six to nine orders of magnitude lower, namely on the µm to nm scale. Nevertheless, this metaphor is not only interesting as a means of explaining the nature of aerogels to laymen, but it can also help to visualize the role of the chemist or materials scientist. Whoever designs the structure of an aerogel or modifies its surface characteristics can be considered some kind of architect of the material at the nanoscale level.

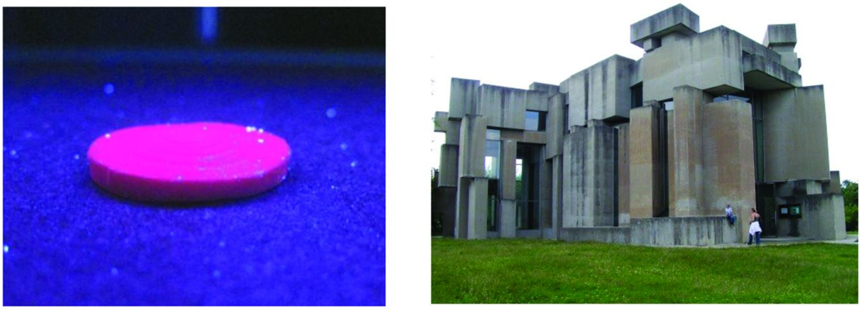

Figure 7. Left: ultra-lightweight, highly porous, fluorescent bacterial cellulose aerogel homogeneously loaded with dodecyl-capped $CuInS_2$ quantum dots and dried with $scCO_2$. Right: a macroscopic aerogel?! Fritz Wotruba's Church of the Holy Trinity in Vienna, Austria (anonymous photograph, 2005).

Summary and Concluding Remarks

We have approached a time period where the public awareness of the limitation of fossil resources and the necessity of using renewable sources has reached an encouraging level. Nowadays, renewables are still being mainly used for energy production. However, it is safe to assume that the focus of future resource utilization strategies will increasingly move from energy to materials/chemicals as novel and more efficient energy production based on wind, water, solar or nuclear energy will be provided, but no alternative sources to chemical/material utilization exist.

The development of novel functional materials from renewable sources is a fascinating field and a challenge to scientists of many disciplines. Ultra-lightweight, highly porous cellulosic aerogels are representatives of such a novel class of renewable-based materials, with their intriguing properties and wide application potential being largely affected by the particular properties of the biopolymer cellulose.

Downloaded by OHIO STATE UNIV LIBRARIES on August 28, 2012 | http://pubs.acs.org
Publication Date (Web): August 17, 2012 | doi: 10.1021/bk-2012-1107.ch004

Over the past few years cellulosic aerogels have been proven to be promising materials that could be used in a large variety of technical applications such as high-performance sound and heat insulation, gas sorption, filtration, or catalysis. Recent approaches that have been succeeded to convert cellulosic aerogels into electro-conductive, magnetic, or fluorescing, ultra-lightweight, porous matrices of tailored properties further contributed to the awakening curiosity and interest by the respective industrial sectors.

The high purity of bacterial cellulose and several outstanding mechanical and surface properties render aerogels promising materials for cosmetic, biomedical as well as even construction, insulation and building applications. Their use as matrices for controlled release of bioactive compounds, as cell scaffolding materials in tissue engineering for bone and cartilage repair are just a few examples of the committed research in this field.

References

1. Deinema, M. H.; Zevenhuizen, L. P. T. M. *Arch. Microbiol.* **1971**, *78* (1), 42–57.
2. Ross, P.; Mayer, R.; Benziman, M. *Microbiol. Rev.* **1991**, *55* (1), 35–58.
3. Fujiwara, K.; Otsuka, M.; Enomoto, H.; Fen, S. 1991.
4. Hungund, B. S.; Gupta, S. G. *Asian J. Microbiol., Biotechnol. Environ. Sci.* **2010**, *12*, 517–522.
5. Brown, R. M., Jr.; Willison, J. H.; Richardson, C. L. *Proc. Natl. Acad. Sci. U.S.A.* **1976**, *73*, 4565–9.
6. Hestrin, S.; Schramm, M. *Biochem. J.* **1954**, *58*, 345–352.
7. Mühlethaler, K. *Biochim. Biophys. Acta* **1949**, *3* (0), 527–535.
8. Bungay, H. R.; Serafica, G. C. Production of Microbial Cellulose. United States Patent 6071727,1997.
9. Geyer, U.; Heinze, T.; Stein, A.; Klemm, D.; Marsch, S.; Schumann, D.; Schmauder, H. P. *Int. J. Biol. Macromol.* **1994**, *16* (6), 343–347.
10. Valla, S.; Kjosbakken, J. *J. Gen. Microbiol.* **1982**, *128* (7), 1401–1408.
11. Watanabe, K.; Tabuchi, M.; Morinaga, Y.; Yoshinaga, F. *Cellulose* **1998**, *5* (3), 187–200.
12. Krystynowicz, A.; Czaja, W.; Wiktorowska-Jezierska, A.; Gonçalves-Miśkiewicz, M.; Turkiewicz, M.; Bielecki, S. *J. Ind. Microbiol. Biotechnol.* **2002**, *29* (4), 189–195.
13. Kralisch, D.; Hessler, N.; Klemm, D.; Erdmann, R.; Schmidt, W. *Biotechnol. Bioeng.* **2010**, *105* (4), 740–747.
14. Jin, H.; Nishiyama, Y.; Wada, M.; Kuga, S. *Colloids Surf., A* **2004**, *240* (1–3), 63–67.
15. Innerlohinger, J.; Weber, H. K.; Kraft, G. *Macromol. Symp.* **2006**, *244* (1), 126–135.
16. Gavillon, R.; Budtova, T. *Biomacromolecules* **2008**, *9*, 269–277.
17. Liebner, F.; Potthast, A.; Rosenau, T.; Haimer, E.; Wendland, M. *Holzforschung* **2008**, *62*, 129–135.

18. Liebner, F.; Haimer, E.; Potthast, A.; Loidl, D.; Tschegg, S.; Neouze, M.-A.; Wendland, M.; Rosenau, T. *Holzforschung* **2009**, *63* (1).
19. Tsioptsias, C.; Stefopoulos, A.; Kokkinomalis, I.; Papadopoulou, L.; Panayiotou, C. *Green Chem.* **2008**, *10*, 965–971.
20. Sescousse, R.; Budtova, T. *Cellulose* **2009**, *16* (3), 417–426.
21. Deng, M.; Zhou, Q.; Du, A.; van Kasteren, J.; Wang, Y. *Mater. Lett.* **2009**, *63*, 1851–1854.
22. Aaltonen, O.; Jauhiainen, O. *Carbohydr. Polym.* **2009**, *75* (1), 125–129.
23. Duchemin, B. J. C.; Staiger, M. P.; Tucker, N.; Newman, R. H. *J. Appl. Polym. Sci.* **2010**, *115* (1), 216–221.
24. Sescousse, R.; Gavillon, R.; Budtova, T. *J. Mater. Sci.* **2011**, *46* (3), 759–765.
25. Maeda, H. *Cellul. Commun.* **2006**, *13* (4), 169–172.
26. Liebner, F.; Haimer, E.; Wendland, M.; Neouze, M.-A.; Schlufter, K.; Miethe, P.; Heinze, T.; Potthast, A.; Rosenau, T. *Macromol. Biosci.* **2010**, *10* (4).
27. Pääkko, M.; Vapaavuori, J.; Silvennoinen, R.; Kosonen, H.; Ankerfors, M.; Lindstrom, T.; Berglund, L. A.; Ikkala, O. *Soft Matter* **2008**, *4* (12), 2492–2499.
28. Edgar, C. D.; Gray, D. G. *Macromolecules* **2002**, *35* (19), 7400–7406.
29. Bodin, A.; Bäckdahl, H.; Fink, H.; Gustafsson, L.; Risberg, B.; Gatenholm, P. *Biotechnol. Bioeng.* **2007**, *97* (2), 425–434.
30. Helenius, G.; Bäckdahl, H.; Bodin, A.; Nannmark, U.; Gatenholm, P.; Risberg, B. *J. Biomed. Mater. Res., Part A* **2006**, *76A* (2), 431–438.
31. Jonas, R.; Farah, L. F. *Polym. Degrad. Stab.* **1998**, *59* (1−3), 101–106.
32. Yamanaka, S.; Watanabe, K.; Kitamura, N.; Iguchi, M.; Mitsuhashi, S.; Nishi, Y.; Uryu, M. *J. Mater. Sci.* **1989**, *24* (9), 3141–3145.
33. Barud, H. S.; Barrios, C.; Regiani, T.; Marques, R. F. C.; Verelst, M.; Dexpert-Ghys, J.; Messaddeq, Y.; Ribeiro, S. J. L. *Mater. Sci. Eng. C* **2008**, *28*, 515–518.
34. Sheridan, R. L.; Morgan, J. R.; Mohamed, R. In *Handbook of Polymeric Biomaterials*, 1st ed.; Severian, D., Ed.; Marcel Dekker: New York, 2002; Vol. XVII.
35. Tabuchi, M. *Nat. Biotechnol.* **2007**, *25* (4), 389–390.
36. Sutherland, I. W. *Trends Biotechnol.* **1998**, *16* (1), 41–46.
37. Klemm, D.; Schumann, D.; Udhardt, U.; Marsch, S. *Prog. Polym. Sci.* **2001**, *26* (9), 1561–1603.
38. Schumann, D.; Wippermann, J.; Klemm, D.; Kramer, F.; Koth, D.; Kosmehl, H.; Wahlers, T.; Salehi-Gelani, S. *Cellulose* **2009**, *16* (5), 877–885.
39. Haimer, E.; Wendland, M.; Schlufter, K.; Frankenfeld, K.; Miethe, P.; Potthast, A.; Rosenau, T.; Liebner, F. *Macromol. Symp.* **2010**, *294* (2), 64–74.
40. Czaja, W.; Krystynowicz, A.; Bielecki, S.; Brown, J. R. M. *Biomaterials* **2006**, *27* (2), 145–151.
41. Nge, T. T.; Nogi, M.; Yano, H.; Sugiyama, J. *Cellulose* **2010**, *17* (2), 349–363.
42. Maeda, H.; Nakajima, M.; Hagiwara, T.; Sawaguchi, T.; Yano, S. *Jpn. J. Polym. Sci. Technol.* **2006**, *63*, 135–137.

Downloaded by OHIO STATE UNIV LIBRARIES on August 28, 2012 | http://pubs.acs.org
Publication Date (Web): August 17, 2012 | doi: 10.1021/bk-2012-1107.ch004

Downloaded by OHIO STATE UNIV LIBRARIES on August 28, 2012 | http://pubs.acs.org
Publication Date (Web): August 17, 2012 | doi: 10.1021/bk-2012-1107.ch004

43. Diniz, J. M. B. F.; Gil, M. H.; Castro, J. A. A. M. *Wood Sci. Technol.* **2004**, *37*, 489–494.
44. Maul, J.; Frushour, B. G.; Kontoff, J. R.; Eichenauer, H.; Ott, K.-H.; Schade, C. Polystyrene and Styrene Copolymers. In *Ullmann's Encyclopedia of Industrial Chemistry*; Wiley-VCH Verlag GmbH & Co. KGaA: Weinheim, Germany, 2000.
45. Zugenmaier, P. *History of Cellulose Research Crystalline Cellulose and Derivatives*; Springer Berlin, Heidelberg, 2008; pp 7−51.
46. Moss, C. E.; Butler, M. F.; Müller, M.; Cameron, R. E. *J. Appl. Polym. Sci.* **2002**, *83* (13), 2799–2816.
47. Sescousse, R.; Gavillon, R.; Budtova, T. *Carbohydr. Polym.* **2010**.
48. Fischer, F.; Rigacci, A.; Pirard, R.; Berthon-Fabry, S.; Achard, P. *Polymer* **2006**, *47*, 7636–7645.
49. Pirard, R.; Rigacci, A.; Maréchal, J. C.; Quenard, D.; Chevalier, B.; Achard, P.; Pirard, J. P. *Polymer* **2003**, *44* (17), 4881–4887.
50. Scherer, G. W.; Smith, D. M.; Qiu, X.; Anderson, J. M. *J. Non-Cryst. Solids* **1995**, *186*, 316–320.
51. Majling, J.; Komarneni, S.; Fajnor, V. S. *J. Porous Mater.* **1995**, *1* (1), 91–95.
52. Sescousse, R.; Gavillon, R.; Budtova, T. *Carbohydr. Polym.* **2011**, *83* (4), 1766–1774.
53. Litschauer, M.; Neouze, M.-A.; Haimer, E.; Henniges, U.; Potthast, A.; Rosenau, T.; Liebner, F. *Cellulose* **2010**.
54. Sakaguchi, M.; Ohura, T.; Iwata, T.; Takahashi, S.; Akai, S.; Kan, T.; Murai, H.; Fujiwara, M.; Watanabe, O.; Narita, M. *Biomacromolecules* **2010**, *11* (11), 3059–3066.
55. Mukhopadhyay, M. *J. Supercrit. Fluids* **2003**, *25* (3), 213–223.
56. Knez, Ž.; Škerget, M.; Ilič, L.; Lütge, C. *J. Supercrit. Fluids* **2008**, *43* (3), 383–389.
57. Dittmar, D.; Bijosono Oei, S.; Eggers, R. *Chem. Eng. Technol.* **2002**, *25* (1), 23–27.
58. Smirnova, I. *Synthesis of Silica Aerogels and Their Application as a Drug Delivery System*; Technical University of Berlin, Berlin, 2002.
59. Kistler, S. S. *Nature* **1931**, *127*.
60. Gesser, H. D.; Goswami, P. C. *Chem. Rev.* **1989**, *89* (4), 765–788.
61. Fricke, J.; Emmerling, A. *J. Sol-Gel Sci. Technol.* **1998**, *13* (1), 299–303.
62. Hüsing, N.; Schubert, U. *Angew. Chem., Int. Ed.* **1998**, *37*, 22–45.
63. Kistler, S. S. *J. Phys. Chem.* **1932**, *36*, 2948–66.
64. Long, J. W.; Rolison, D. R. *Acc. Chem. Res.* **2007**, *40* (9), 854–862.

Downloaded by PENNSYLVANIA STATE UNIV on August 28, 2012 | http://pubs.acs.org
Publication Date (Web): August 17, 2012 | doi: 10.1021/bk-2012-1107.ch005

Chapter 5

Cellulose Nanowhiskers in Electrochemical Applications

Soon Yee Liew,[a] Sara Shariki,[b] Anne Vuorema,[c] Darren A. Walsh,[a,d] Frank Marken,[b] and Wim Thielemans*,[a,d]

**[a]Process and Environmental Research Division, Faculty of Engineering,
University of Nottingham, University Park,
Nottingham NG7 2RD, United Kingdom
[b]Department of Chemistry, University of Bath, Claverton Down,
Bath BA2 7AY, United Kingdom
[c]Laboratory of Green Chemistry, Lappeenranta University of Technology,
Patteristonkatu 1, 50100 Mikkeli, Finland
[d]School of Chemistry, University of Nottingham, University Park,
Nottingham NG7 2RD, United Kingdom
*E-mail: Wim.thielemans@nottingham.ac.uk**

Over the past couple of years, we have been investigating the use of nanocellulose, in the form of nanocrystals or nanowhiskers, for applications in electrochemical sensor development, for the creation of percolated conducting polymer networks, in supercapacitor material design, and in the preparation of novel electrocatalyst structures. We will give a concise summary of important results from our past work and lay important connections with the different parts. This overview shows the versatility and great potential cellulose nanoparticles have in electrochemical applications while employing straightforward techniques for device assembly and fabrication. Extension of this work towards free-standing functional membranes is also discussed where appropriate.

In Functional Materials from Renewable Sources; Liebner, F., et al.;
ACS Symposium Series; American Chemical Society: Washington, DC, 2012.

Downloaded by PENNSYLVANIA STATE UNIV on August 28, 2012 | http://pubs.acs.org
Publication Date (Web): August 17, 2012 | doi: 10.1021/bk-2012-1107.ch005

Introduction

The market demand for chemical sensors that are inexpensive, highly selective and accurate has grown exponentially in recent years, especially in fields of clinical studies and environmental monitoring (*1–6*). The production of more cost effective electrochemical sensors with a high selectivity for a specific analyte or class of analytes has been the major goal for researchers for years. One way to modify electrodes to that purpose is to coat them with materials such as Nafion (*7*, *8*), PVC (*9*), and sol gel materials (*10*). The coatings either function as a permselective barrier based on size (*11*, *12*), charge (*13*, *14*) or chirality (*15*, *16*), or as platforms for immobilization of enzymes (*17*, *18*) in biosensors. Commonly, the coating materials are expensive and/or difficult to prepare. The use of materials that allow inexpensive, easy and versatile modification of electrode surfaces would offer a major advantage over existing materials. Equally, methods to modify electrode surfaces can be used to create functional conducting networks, electrocatalysts, and supercapacitor materials on electrode surfaces. Current commercial supercapacitors display specific energies of 2-12 Wh kg^{-1} and specific power supply of 4-50 kW kg^{-1}, as target values for future development, with required charge-discharge cycle times variable between milliseconds and hours depending on the application (*19*).

Cellulose, the most abundant natural material in the world, has much to offer as a surface coating for electrodes. For example, it has the potential to improve the selectivity and sensitivity of electrochemical sensors at a relatively small cost. As a result, the use of cellulose films to modify electrode surfaces is well established. Most reports however come from commercial sources in the form of patents rather than scientific journal articles. This existing work, as will be reviewed briefly below, is largely based on molecular cellulose films.

In a first example, cellulose acetate and cellulose acetate propionate membranes have been used to immobilize glucose oxidase in a glucose biosensor (*20*, *21*). In this device, the protein immobilization method was instrumental in the device performance (*22*). A nitrocellulose membrane has also been reported to immobilize glucose oxidase for glucose sensing (*23*). Cellulose membranes in cancer detection sensors have also been reported using two approaches: Monoclonal capture antibodies were immobilized with horseradish peroxidase on a hydroxyethyl cellulose-rhodinised carbon working electrode and umbilical vein endothelial cells were seeded across an asymmetric cellulose triacetate membrane of an ion selective electrode (*24*, *25*). These devices were then used to determine differences in potassium levels between healthy blood serum and that of cancerous patients. Creatinine levels in the blood and urine are a good indicator of renal and muscle function (*26*). By covering a creatinine-sensing electrode based on immobilized creatine amidinohydrolase in hydrophilic polyurethane with a cellulose acetate membrane, its working life was increased from one to five days (*27*, *28*). The cellulose acetate membrane prevented silver ions leaching from the reference electrode from reaching the immobilized enzyme. As silver is an effective inhibitor of creatine amidinohydrolase, the cellulose acetate barrier was key in prolonged device performance.

Downloaded by PENNSYLVANIA STATE UNIV on August 28, 2012 | http://pubs.acs.org
Publication Date (Web): August 17, 2012 | doi: 10.1021/bk-2012-1107.ch005

Thiomethyl- and thiosulfate-modified carboxymethyl cellulose onto which biotin was immobilized was found to form stable monolayers onto gold surfaces and to bind the protein streptavidin irreversibly (*29*). Immobilisation of DNA or oligodeoxynucleotide fragments in a nitrocellulose matrix was used to study DNA hybridization (*30*) and to determine heavy metal levels in blood serum and environmental samples (*31*). A H_2O_2 sensor based on hemin-catalysed H_2O_2 reduction has been reported (*32*). This device used a hemin impregnated poly(ethyleneimine)/carboxymethyl cellulose film on a glassy carbon electrode. Immobilisation of anti-gentamicin antibodies on a nitrocellulose strip allowed the determination of gentamicin, an antibiotic used to treat infections in dairy cattle. Gentamicin in milk samples was determined by competitive binding of a gentamicin-glucose oxidase with the gentamicin in the samples followed by measurement of the H_2O_2 produced by the glucose oxidase-gentamicin conjugate when glucose solution was injected (*33*). A galactose sensor using immobilized galactose oxidase on a cellulose acetate membrane gave a quick and reliable indication of galactose levels in plasma and blood (*34*). Similar work on sucrose determination in food used three enzymes, glucose oxidase, invertase and mutarotase, in cellulose acetate as well as in other polymers and found poly(tetrafluoroethylene) to be the better material of the investigated polymers (*35*).

Cellulose compounds have also been used as size selective barrier membranes by blocking larger electroactive species that interfere with the analyte. Cellulose acetate hydrolysed to various extents was found to improve dopamine selectivity over epinephrine, norepinephrine and serotonin when used as a coating over electrodes coated with a perfluorinated ionomer (*36*). This was later followed up with a dopamine sensor having a nanoscale cerium(IV) oxide selective carboxymethyl cellulose membrane employing the Belousov-Zhabotinsky oscillating chemical reaction (*37*). Cellulose acetate membranes have also been used as a size exclusion barrier to inhibit electrode fouling or poisoning (*38–40*). Cobalt phthalocyanine was included to improve electron transfer kinetics. Cellulose acetate membranes were further shown to display a higher permeability for smaller neurochemicals (*41*). They were further investigated as a phase inversion process membrane, similar to reverse osmosis membranes, whereby the membrane protected the electrode from fouling but molecules smaller than 1500 Da still gave a fast response time (*42*). Using ultrathin cellulose acetate coatings formed by electrospraying further improved the performance (*43*). Coating silver/silver chloride electrodes with cellulose acetate has also been reported to eliminate bromide and uric acid interference in chloride detection (*44*).

Combining carboxymethyl cellulose with alginic acid and poly(allylamine hydrochloride) on a gold electrode enabled immobilization of ferricyanide ions $[Fe(CN)_6]^{3-}$ which could also catalyse the oxidation of ascorbic acid (*45*). The same composite films were also made with poly(ethyleneimine) (PEI) and poly(diallyldimethylammonium chloride) (PDDAC) as the cationic polymer. These composite membranes showed ferricyanide binding on PDDAC to be almost pH independent, while ferricyanide binding on PEI was enhanced in more acidic media (*46*).

Downloaded by PENNSYLVANIA STATE UNIV on August 28, 2012 | http://pubs.acs.org
Publication Date (Web): August 17, 2012 | doi: 10.1021/bk-2012-1107.ch005

Cellulose in the actual electrode material was shown to work by saturating filter paper with an aqueous solution able to oxidize metals on a surface which then diffuse into this *cellulose electrode* to be analyzed after extraction (*47*). Solid-state reference electrodes were also prepared by a 3/7 weight ratio of cellulose acetate/polyurethane offering a well characterized path for electrolyte and water diffusion, a fast preconditioning and a strong adherence to solid substrates (*48*). This composite also limits diffusion of internal electrolytes, resulting in a stable reference potential over an extended time (*48*).

In our work, we moved away from using cellulose derivatives and focused on cellulose nanowhiskers or nanocrystals (CNXLs), monocrystalline ribbon-like rods, obtained from pure cellulose by acid hydrolysis (Figure 1). When using sulfuric acid, a small amount of sulfate half esters ($ROSO_3^-$) are grafted on the CNXL surface enabling the formation of stable aqueous dispersions. As is well known in nanocomposite fabrication, these nanowhiskers form percolated networks held together by interparticle hydrogen bonds (*49–52*). We have over the last couple of years used these two effects to prepare cellulose nanowhisker films on electrode surfaces by themselves or in a layer-by-layer deposition approach with cationic polymer for sensing applications, with metal/metal oxide nanoparticles or larger metal structures for electrocatalysis and sensing applications, and with electrically conducting polymers. We have also used CNXLs to form thin carbon coats onto metallic nanoparticles after pyrolysis. Important findings from this work are combined in the ensuing sections.

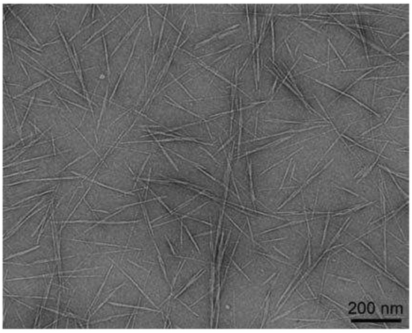

Figure 1. Transmission electron micrograph of cellulose nanocrystals derived from sisal (53). Reproduced with permission from reference (53) Copyright 2006 Springer.

Cellulose Nanowhiskers in Electrochemical Sensing Applications

As mentioned before, chemical sensors for large scale application should be inexpensive, highly selective and accurate. They should also give results in as short a timeframe as possible. Development of new electrochemical sensors should thus take into account all of these issues. Electrochemical sensors work through the signal generated by a redox process at the surface of an electrode. The oxidation-reduction reaction can be the result of direct oxidation/reduction of the analyte, changes in concentration of redox-active species at the surface due to competitive binding with a redox-inactive analyte, or can come from oxidation/reduction of a reaction product formed from the analyte near the electrode surface. When modifying electrode surfaces, care needs to be taken to retain full and unhindered access of the analyte, or the analyte reaction product, to the electrode surface to preserve fast response times. Deposition of polymer films thus needs to be very carefully controlled to achieve diffusion pathways from the bulk solution containing the analyte to the electrode surface. To achieve a high selectivity for a specific analyte, or a class of analytes, these diffusion pathways will need to be selective, further complicating membrane deposition. Inclusion of selective binding sites, or catalysts or enzymes to convert analytes to redox-active species requires further optimization and control to be achieved.

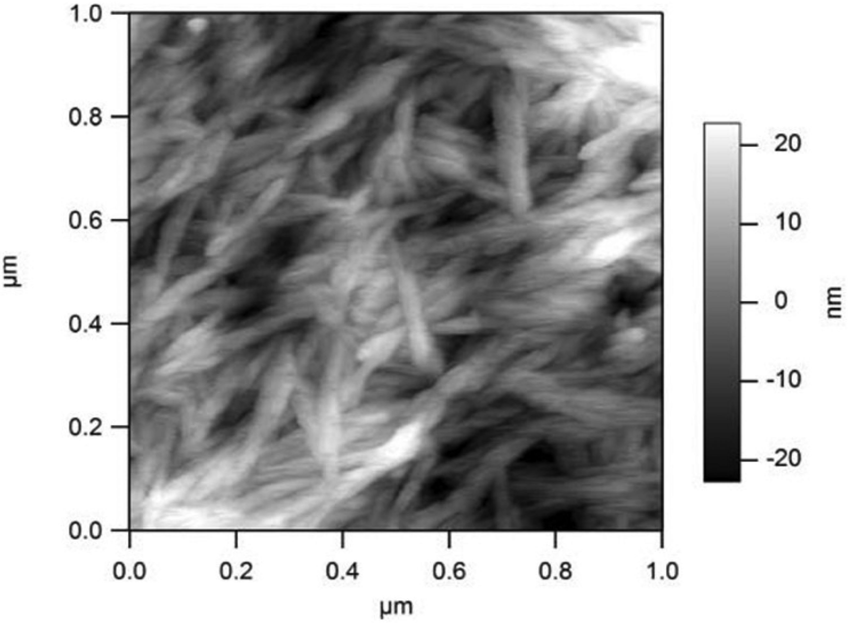

Figure 2. Tapping-mode AFM image of a cellulose nanowhisker film on a glassy carbon electrode prepared by drop coating with 10mL of a 1.5wt% aqueous nanowhisker dispersion and drying at 40°C form 45 mins (54). Reproduced with permission from reference (54). Copyright 2009 The Royal Society of Chemistry.

CNXLs form porous networks (Figure 2) which, once dried, retain their integrity in aqueous solutions. This open porous network can be expected to enable easy transport of species through the pores in the percolated network. The high amount of hydroxyl groups of CNXLs can be further modified to introduce binding sites for analytes, while codeposition with polymers can form

In Functional Materials from Renewable Sources; Liebner, F., et al.;
ACS Symposium Series; American Chemical Society: Washington, DC, 2012.

Downloaded by PENNSYLVANIA STATE UNIV on August 28, 2012 | http://pubs.acs.org
Publication Date (Web): August 17, 2012 | doi: 10.1021/bk-2012-1107.ch005

an even easier and less expensive method to introduce these required binding sites. Surface modifications or codeposition with polymers can thus be expected to introduce selectivity in a relatively direct way without the need to redesign the sensor assembly process. Such versatility could prove a significant advance on current technology.

Therefore, initial investigations on CNXL electrode surface modifications looked at the ability of CNXL membranes to immobilize analytes and to alter access to the electrode surface. The potential of these membranes in sensor development were investigated for a variety of potential applications.

Downloaded by PENNSYLVANIA STATE UNIV on August 28, 2012 | http://pubs.acs.org
Publication Date (Web): August 17, 2012 | doi: 10.1021/bk-2012-1107.ch005

Pure Cellulose Nanocrystal Films

To investigate the potential of unmodified CNXL films, pure CNXL films were formed by drop-depositing sulfuric acid-extracted CNXLs from cotton from a 1.5 wt% aqueous dispersion onto a glassy carbon electrode (*54*). After drying at 40°C for 45 min, a 2 μm ± 0.5 μm film with 50-100 nm pores was formed (Figure 2). This film retained mechanical integrity upon immersion in water and remained attached to the glassy carbon electrode surface. The sulfate half esters ($ROSO_3^-$) on the CNXL surface, bestow a negative charge onto the deposited film covering the electrode surface (Figure 3). Indeed, the anodic and cathodic peak currents $i_{p,a}$ and $i_{p,c}$, for potassium hexachloroiridate ($[IrCl_6]^{3-}$) and ruthenium hexammin ($[Ru(NH_3)_6]^{3+}$) were found to decrease (to 34%) and to increase (to 216%) respectively, when compared to their peak currents at a bare glassy carbon electrode. The peak currents for neutral ferrocene-methanol (FcOH) were virtually unchanged with only a small reduction (to 81%) due to physical blocking showing that physical access to the electrode surface was not significantly encumbered. Mediator size was not a factor as they were all similar in size.

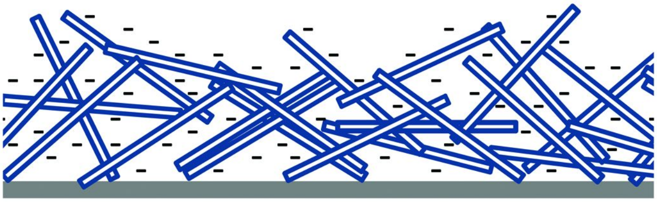

Figure 3. Schematic of a film of rod-like CNXLs with negatively surface charge creating a negatively charged cover over the electrode surface without significantly blocking physical transport.

Further confirmation of the mediator size not being the driver for this behavior was obtained with anionic ferrocene carboxylate ($FcOO^-$), resulting in a peak current with the cellulose film only 40% of the bare electrode. This shows that charge-based exclusion can easily be instilled by deposition of a film of charged CNXLs. Determination of the apparent diffusion constants of the mediators further showed that the diffusion of the cationic and neutral mediators ($[Ru(NH_3)_6]^{3+}$ and FcOH, respectively) was not hindered in the cellulose nanowhisker film, unlike the anionic mediator $[IrCl_6]^{3-}$, which showed a reduction of the apparent diffusion coefficient by a factor of 10 when compared to the solution diffusion coefficient. This confirms electrostatic blocking of the electrode surface by the negatively charged nanowhisker film, which was further corroborated by the mediator partition constants in the film.

$Ru(NH_3)_6^{3+}$ was also shown to follow Langmuir adsorption behavior into the negatively charged film (binding by electrostatic interactions) with a binding constant of 1.57 x 10^3 mol^{-1} dm^3 and a Gibbs free energy of binding from a dilute aqueous solution of -28.2 kJ mol^{-1}, measured at room temperature.

Downloaded by PENNSYLVANIA STATE UNIV on August 28, 2012 | http://pubs.acs.org
Publication Date (Web): August 17, 2012 | doi: 10.1021/bk-2012-1107.ch005

Cellulose Nanocrystal-Polymer and -Metal Nanoparticle Composite Films

Instead of using surface groups of CNXLs to induce perm-selectivity or immobilization functionalities, it is also possible to co-deposit CNXLs with functional polymers or other nanoparticles. A straightforward method is the layer-by-layer (LbL) approach with polymers or metallic nanoparticles having an opposite surface charge to the nanowhiskers. We have shown this approach to be very effective using CNXLs bearing deprotonated (negatively charged) sulfate surface groups and positively charged TiO_2 nanoparticles (*55*) as well as poly(diallyldimethylammonium chloride) (PDDAC) (*56*) and chitosan (*57*). This approach has been proven to be extremely versatile and could be used to introduce virtually any desired functionality within the CNXL film. Variation in binding sites can easily be achieved by varying concentrations of the constituents or through deposition of successive layers until the desired amount is achieved. The porosity of the obtained composite, resulting from the ribbon-like rigid CNXLs, is retained and guarantees access of analytes to the binding sites. The versatility of this co-deposition approach will become clear from the ensuing examples.

The cellulose nanowhisker/TiO_2 nanocomposite films were prepared in a LbL approach on indium tin oxide (ITO) with CNXLs derived from sisal by submerging an ITO coated glass electrode in aqueous dispersion of the respective composite components (*55*). The aim of this work was to create a film in a straightforward manner with the same characteristics of mesoporous TiO_2 films, but with a more open pore structure which permits sensing of larger analytes. The sisal nanowhiskers used had average cross-sectional dimension of around 4 nm and lengths around 250 nm (*53*). Drying of the film after each deposition sequence at 50°C in air resulted in a mechanically stable film with a thickness increase upon each deposition sequence of 16 nm. Figure 4 shows the comparison of a pure cellulose nanowhisker film and a film formed by 20 subsequent layers of TiO_2-CNXLs. Importantly, the electrochemical behaviour of cellulose nanowhisker/TiO_2 films was similar to porous TiO_2 films, with a current response at -0.8 C *vs* SCE consistent with the sequential filling of the TiO_2 electronic states (*58*). Therefore, inclusion of TiO_2 in the CNXL film created conductive pathways enabling analyte sensing while the CNXLs ensured an open pore structure which permitted diffusion, and thus sensing, of larger analytes.

Downloaded by PENNSYLVANIA STATE UNIV on August 28, 2012 | http://pubs.acs.org
Publication Date (Web): August 17, 2012 | doi: 10.1021/bk-2012-1107.ch005

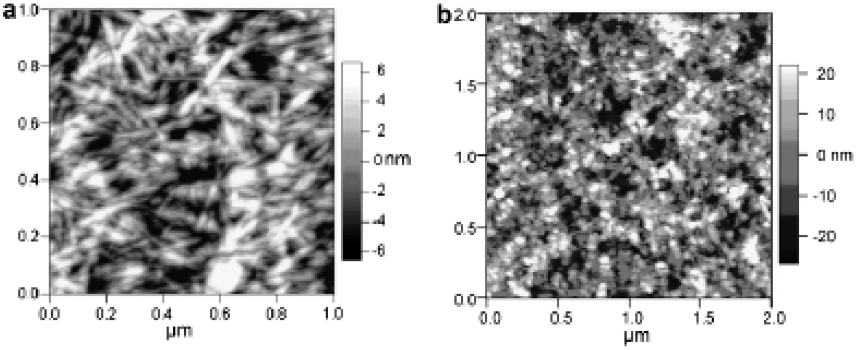

Figure 4. AFM images of film of (a) cellulose nanowhisker derived from sisal, drop deposited in an ITO surface from aqueous solution and (b) a 20-layer TiO_2-cellulose nanowhisker composite film (55). Reproduced with permission from reference (55). Copyright 2007 Elsevier.

Immersion of the coated electrode in a solution of bovine methemoglobin protein, resulted in immobilization of this protein into the composite film. The immobilized amount was found to increase linearly with increasing film thickness. Methemoglobin can easily be perceived as a test redox system for other large protein binding within the nanowhisker/TiO_2 composite film and it has been used widely in many types of film electrodes (e.g. in clay films (*59*), mesoporous silica and TiO_2 (*60*, *61*), ZrO_2–collagen composites (*62*), gold nanoparticle assemblies (*63*), Fe_3O_4 nanoparticle composites (*64*), and hydroxyethylcellulose films (*65*)). The behavior of the methemoglobin in the composite cellulose nanowhisker/TiO_2 film depended on the immobilisation environment and the electrolyte during potential cycling. In a pH 5.5 phosphate buffer solution for immobilisation, spontaneous demetallation occurred, transforming methemoglobin into a metal-free protein. In the case of methemoglobin immobilisation ina pH 5.5 acetate buffer, no demetallation occurred and a methemoglobin/hemoglobin redox process with potential cycling occurred only close to the electrode surface due to insufficient TiO_2 electron conduction and transfer within the film. Facile immobilisation of large proteins is thus possible while also exerting control over the immobilised protein form.

Cellulose nanowhisker/PDDAC composite films were prepared in a similar fashion to the TiO_2 composite films, resulting in positively charged porous films capable of binding negatively charged species (*56*). The cationic polymer can be expected to coat the anionic CNXL surface during the LbL deposition leading to an overall cationic electrode modification (Figure 5). These can be used as free standing films or to accumulate anionic analytes at sensor electrode surfaces for increased sensitivity. The use of PDDAC also introduces selectivity towards hydrophobic anions. The critical aspect is to investigate whether sufficient binding sites remain after LbL deposition and whether the porous CNXL membrane structure is retained, i.e. the polymer does not form a continuous film and closes the pores.

Downloaded by PENNSYLVANIA STATE UNIV on August 28, 2012 | http://pubs.acs.org
Publication Date (Web): August 17, 2012 | doi: 10.1021/bk-2012-1107.ch005

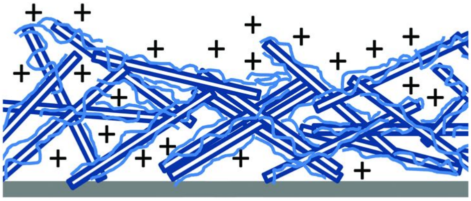

Figure 5. Schematic of coating of negatively charged CNXL with positively charge polymer leading to an overall positively charged coating on the electrode surface (larger amount of cationic polymer charge relative to anionic CNXL surface charge).

By small-angle X-ray scattering (SAXS) measurements, the radius of gyration of CNXLs was found to increase slightly upon co-deposition with PDDAC compared to pure nanowhisker films accounting for the polymer layer between nanowhiskers. Studying the ion permeability of these films (5µm thick) deposited on a glassy carbon with the anionic $[Fe(CN)_6]^{3-/4-}$ redox system in aqueous 0.1 M KCl, the pure cellulose nanowhisker film showed a reduction of the peak current for the $[Fe(CN)_6]^{4-/3-}$ compared to a bare electrode, similar to the earlier described behavior for $[IrCl_6]^{3-}$. Inclusion of 20% PDDAC into the film reversed this effect with a substantial increase in peak current when compared to the bare electrode response. The voltammetric response also changed from 0.21 V *vs* SCE (bare electrode and pure nanowhisker film-covered electrode) to 0.11 V *vs* SCE (nanowhisker/PDDAC-covered electrode), indicative of the move of the one-electron redox system $[Fe(CN)_6]^{3-/4-}$ from unhindered aqueous solution to a membrane (*66*). Diffusion (both anionic diffusion along the polycationic polymer and electron hopping between immobilized redox centers) was found to be the dominating transport process in the membrane with a diffusion coefficient estimated to be on the order of 10^{-15} m^2 s^{-1}, which is about 6 orders of magnitude slower than that in water. Immobilisation of anionic $[Fe(CN)_6]^{3-/4-}$ followed Langmuirian behavior with a binding constant of K = 12.000 mol^{-1} dm^3 in aqueous KCl. Therefore, sufficient binding sites remain and the open CNXL structure is retained, opening up a wide range of possible composites.

The application range of cellulose nanowhisker/PDDAC can also be extended into detection of oxidisable organic compounds such as triclosan, a polychlorinated aromatic phenolic biocide (*56*). Quantitative triclosan detection by measurement of its oxidative anodic peak current has been reported on mercury electrodes, at carbon microfibers, screen printed electrodes and carbon-PDDAC thin-film electrodes (*67–69*). Triclosan was found to immobilise from a pH 9.5 phosphate buffer into the CNXL-PDDAC film, whereas no triclosan is detected in the pure nanowhisker film. Irreversible triclosan oxidation in the nanowhisker/PDDAC film which leads to polymer formation (Figure 6), limited diffusion into the film and suppressed electron hopping contributions to charge transport. This resulted in a linear dependence of the oxidative peak current on scan rate. The cellulose nanowhisker/PDDAC film could easily detect triclosan down to the micromolar level and displayed Langmuirian adsorption characteristics with a binding constant K = 21.000 mol^{-1} dm^3.

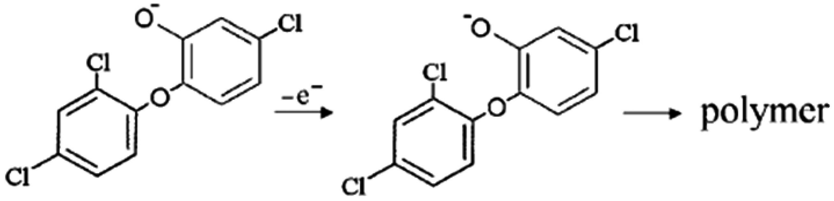

Figure 6. Irreversible triclosan oxidation causing polymerisation (57). Reproduced with permission from reference (57). Copyright 2008 Wiley-VCH Verlag GmbH & Co.

Downloaded by PENNSYLVANIA STATE UNIV on August 28, 2012 | http://pubs.acs.org
Publication Date (Web): August 17, 2012 | doi: 10.1021/bk-2012-1107.ch005

A completely nature-derived alternative to the cellulose nanowhisker/PDDAC system can be obtained with chitosan instead of PDDAC. Chitosan displays ammonium functionalities at pH < 7 with a pK_a reported in the range of 6-7 (*70*, *71*). A composite of 50 wt% sisal-derived CNXLs and 50 wt% low-molecular weight chitosan (75-85% deacetylation) showed similar behavior to the PDDAC composite for the anionic $[Fe(CN)_6]^{3-/4-}$ redox system in 0.1 M phosphate buffer at pH 6 (*57*), i.e. a shift to more positive potential of the redox process compared to pure cellulose film due to membrane immobilization, binding of the anion into the composite film, and slow diffusion of the anion within the membrane. However, unlike the PDDAC film, the influence of the chitosan containing composite was pH dependent with a significant reduction of anion binding capacity above pH 7, in agreement with the deprotonation of the ammonium functionality at basic pH. An approximate Langmuirian binding constant value in a highly simplified description of the process for $[Fe(CN)_6]^{4-}$ binding in the cellulose nanowhisker/chitosan composite film was obtained as 2200 mol^{-1} dm^3. The $[Fe(CN)_6]^{4-}$ concentration was further found to vary linearly with chitosan content in the composite and the diffusion zone extended to about 200 nm from the electrode surface (at a scan rate of 50 mV s^{-1}).

In the case of competitive binding, the $[Fe(CN)_6]^{3-/4-}$ redox system can also be used to determine the concentration of non-electrochemically active anionic species. Anionic surfactants are widely used in emulsifications and an accurate non-invasive method to determine their concentration in waste, food and drink items would be very beneficial. Sodium dodecyl sulfate (SDS) is a widely used anionic surfactant and is known to bind well to chitosan (*72*). The voltammetric signal from a chitosan/cellulose nanowhisker composite films exposed to 1 mM $Fe(CN)_6^{4-}$ (15 min, phosphate buffer at pH 6) with and without 100 μM SDS, showed a reduced redox signal when SDS was present. This indicated preferential binding of SDS to the chitosan, opening up the possibility to use this effect to determine the SDS concentration. Based on the Langmuir isotherm for competitive binding (Equation 1), the binding constant for SDS on chitosan can be determined:

$$\Phi_{coverage} = \frac{K_{[Fe(CN)_6]^{4-}}\left[[Fe(CN)_6]^{4-}\right]}{1 + K_{[Fe(CN)_6]^{4-}}\left[[Fe(CN)_6]^{4-}\right] + K_{SDS}[SDS]} \qquad (1)$$

with $K_{[Fe(Cn)_6]^{4-}}$ the binding constant for ferrocyanide determined without SDS competition, $[[Fe(Cn)_6]^{4-}]$ the concentration of ferrocyanide in the pretreatment solution, KSDS the unknown SDS binding constant, and [SDS] the SDS concentration in the pretreatment solution. At different SDS concentrations, which result in a lower $[Fe(CN)_6]^{4-}$ oxidation response, K_{SDS} was determined to be 3.3 x 10^4 mol^{-1} dm^3. With this binding constant known, SDS concentration in unknown samples could be determined by choice of the appropriate ferrocyanide concentration.

Triclosan detection in the cellulose nanowhisker/chitosan was again similar to the cellulose nanowhisker/PDDAC composites with triclosan oxidation only occurring very close to the electrode surface and with a lack of diffusion (*57*). The estimated Langmuir binding constant was significantly lower at 2600 mol^{-1} dm^3 at alkaline pH of 9.5 in a 0.1 M phosphate buffer. This indicated that the electrostatic and hydrophobic interactions were significantly weaker.

Having proven the ability to use polycationic polymers to detect electrochemically and non-electrochemically active anions, we also studied cellulose nanowhisker composite films containing boronic acid binding sites (*73*).

Stable composite membranes were formed by solvent casting a solution of boronic acid appended poly(amidoamine) dendrimer (generation 1, Figure 7) and CNXLs from a 10:1 methanol/water mixture and drying at 60°C for 1 h. Incorporation of the boronic acid-appended dendrimer resulted in an increase in the apparent nanowhisker radius of gyration from 11.4 nm (pure nanowhisker film) to 15.3 nm (composite membrane) as determined by SAXS, showing that the dendrimer opens up the structure of the film. The increase in the radius of gyration is also consistent with the dendrimer's diameter of approximately 4 nm.

Boronic acid is well known to bind to various diols, carbohydrates and amino acids and has also been shown to display stereospecific receptor-like binding (*74*, *75*). They have also been proposed as in vivo-sensing functionalities for D-glucose and similar physiological analytes (*76*). Any redox-active molecule binding to boronic acid sites could be used to easily determine active sites within the membrane cast onto an electrode surface. We used anionic Alizarin Red S, the sulfonated form of Alizarin (1,2-dihydroxy-9,10-anthracenedione). Alizarine Red S is used as fluorescent probe for metal ions (*77*), analytical dye molecules (*78*), and calcium stains in tissue (*79*, *80*). Alizarine Red S has both spectrophotometric and electrochemical activity (in aqueous media a 2-electron 2-proton reversible reduction occurs (*81*), Figure 8) and is known to bind to boronic acid (*77*). Since the pK_a for the first deprotonation of Alizarine Red S is about 4 (*82*) (Figure 9), binding was studied using a 0.1 mM acetate buffer at pH 3 and pH 7by UV spectroscopy and electrochemical techniques.

Alizarin Red S in pH 3 solution shows a maximum UV absorbance at 420 nm, which shifts to 520 nm at pH 7. The Langmuirian binding constant K was found to be 6000 ± 1000 mol^{-1} dm^3 for Alizarin Red S at pH 3 and pH 7 (Alizarin Red S undergoes phenolic protonation/deprotonation between these pH values as shown in Figure 9). While similar results were obtained at both pH values, as confirmed by electrochemical determination of Alizarin Red S as well by investigating its redox behavior (see below), some of the error bar in the binding constant may be due to small differences in boronic acid binding with Alizarin Red S in its phenolic

Downloaded by PENNSYLVANIA STATE UNIV on August 28, 2012 | http://pubs.acs.org
Publication Date (Web): August 17, 2012 | doi: 10.1021/bk-2012-1107.ch005

protonated and deprotonated forms. No significant binding was noticed without boronic acid dendrimer. Comparison of the redox behavior of Alizarin Red S in the cellulose nanowhisker/boronic acid-appended dendrimer composite compared to bare electrode response revealed significant differences. For a bare glassy carbon electrode, a reversible voltammetric response at pH 3 (0.1 mM acetate buffer) at a potential around -0.37 *vs* SCE was obtained. In a 4 wt% boronic acid dendrimer 96 wt% cellulose nanowhisker composite, three peaks were seen; a cathodic peak at -0.47 V *vs* SCE, followed by two anodic peaks at -0.32 and -0.17 V *vs* SCE.

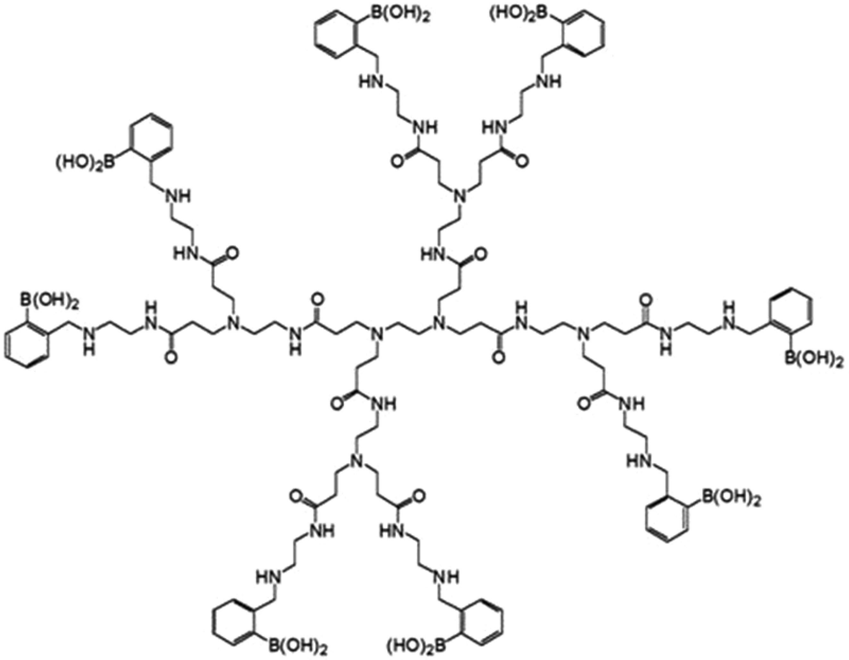

Figure 7. Boronic acid dendrimer used in co-deposition with CNXLs extracted from sisal (73). Reproduced with permission from reference (73). Copyright 2010 The Royal Society of Chemistry.

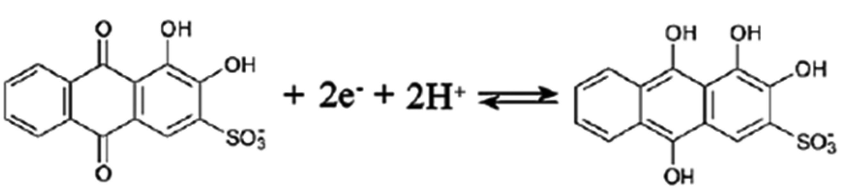

Figure 8. 2-Electron 2-proton reversible reduction for free aqueous Alizarin Red S (73). Reproduced with permission from reference (73). Copyright 2010 The Royal Society of Chemistry.

Downloaded by PENNSYLVANIA STATE UNIV on August 28, 2012 | http://pubs.acs.org
Publication Date (Web): August 17, 2012 | doi: 10.1021/bk-2012-1107.ch005

Downloaded by PENNSYLVANIA STATE UNIV on August 28, 2012 | http://pubs.acs.org
Publication Date (Web): August 17, 2012 | doi: 10.1021/bk-2012-1107.ch005

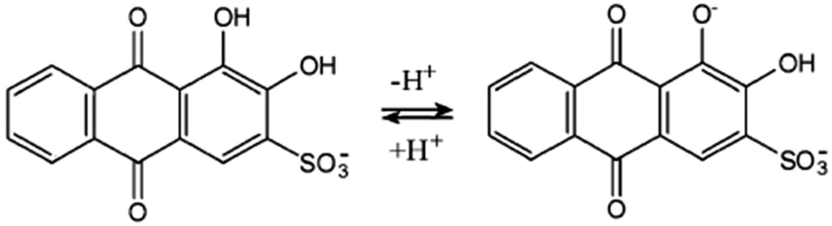

Figure 9. First deprotonation step of phenolic OH for Alizarin Red S (73). Reproduced with permission from reference (73). Copyright 2010 The Royal Society of Chemistry.

While the process for the bound Alizarin Red S was still a 2-electron 2-proton reversible reduction (Figure 10), the appearance of a second oxidation peak points towards the formation of two species: a less strongly bound form binding as shown in Figure 10, and a more strongly bound form with 3 or 4 B-O bonds due to participation of the phenolic OH groups in the binding. It was further found that only about 1% of the cellulose film was electrochemically active (~ 60 nm) due to poor charge carrier mobility as Alizarin Red S molecules did not transfer charge. Furthermore, only films containing up to 8 wt% boronic acid dendrimer were found to remain stable during analysis. Inclusion of metallic nanoparticles may improve film activity away from the electrode by providing charge transfer pathways.

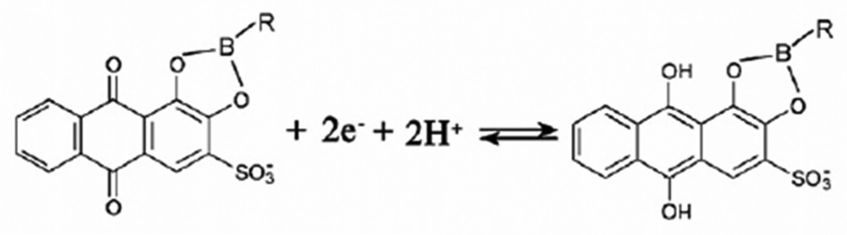

Figure 10. 2-electron 2-proton reversible reduction for boronic acid bound Alizarin Red S (73). Reproduced with permission from reference (73). Copyright 2010 The Royal Society of Chemistry.

These examples clearly show the potential to use cellulose nanowhiskers to create membranes with specific binding functionalities capable of immobilizing a wide variety of molecular species. Both positively and negatively charged polymers as well as metallic nanoparticles have been incorporated while retaining the porous CNXL membrane structure. Selective binding sites in the form of boronic acids were also successfully introduced. This creates an extremely versatile platform for the creation of electrochemical sensors for virtually any analyte, or for the production of free-standing porous membranes with immobilized species. Electrochemical techniques can be used to probe the binding characteristics while the combination of electrochemical characterization and the binding capability of the films can lead to efficient and selective sensors.

Downloaded by PENNSYLVANIA STATE UNIV on August 28, 2012 | http://pubs.acs.org
Publication Date (Web): August 17, 2012 | doi: 10.1021/bk-2012-1107.ch005

Cellulose Nanowhisker/Electronically Conducting Polymer Composites

We have also used cellulose nanowhisker membranes as a backbone to template electronically conducting polymers resulting in porous conducting membranes and highly stable supercapacitor materials. These composites were mesoporous membranes rather than the more common solid cellulose nanowhisker/reinforced polymers. Two methods have been used to create these porous membranes: LbL deposition to create cellulose nanowhisker/polyaniline conducting networks and electrochemical co-deposition for the fabrication of cellulose nanowhisker stabilized polypyrrole supercapacitor materials. It was critical to optimize the deposition conditions to retain the porous CNXL network while ensuring sufficient continuity of the conducting polymer coating the CNXLs to create a conducting network.

Cellulose Nanowhisker/Polyaniline Conducting Networks

To look at the potential to create CNXL-polyaniline membranes through a LbL approach, films were created using sisal-derived CNXLs (aqueous dispersion) and low molecular weight polyaniline (~10 kDa, aqueous solution at pH 2.5-4 using HCl) by simply dipping an ITO electrode into the solutions followed by rinsing and air-drying (*83*). The blue color of the film was found to darken with each deposition cycle (Figure 11a) which increased the membrane thickness with *ca.* 4 nm. SAXS measurements on pure cellulose nanowhisker films showed a radius of gyration of 11 nm, consistent with earlier results, increasing to 14 nm for the nanowhisker/polyaniline composite. The increase in radius of gyration indicated an arrangement of polyaniline binder in between the cellulose nanowhiskers on the order of 3 nm, while AFM images also showed the formation of spherical polyaniline beads on the surface (Figure 11c).

As the film thickness increased, and polyaniline content increased, the charge under the oxidation peak with voltammetric cycling increased linearly with an estimated apparent diffusion coefficient for charge transport $D_{app} = 6 \times 10^{14}$ m^2 s^{-1}.

Cellulose/polyaniline films were then deposited over an ITO pattern machined out of an active part of the electrode (~ 700 nm wide) to form an ITO junction electrode (Figure 12). This cellulose nanowhisker/polyaniline film produced a conductive connection across the junction and the diffusion coefficient for charge to bridge the junction through the cellulose/polyaniline composite was estimated to be 6×10^{-14} m^2 s^{-1} (results obtained with 5 and 10 layer films). A jump in electrical conductivity was seen at 0.2 V *vs* SCE. Compared to studies on pure polyaniline in the conducting emeraldine phase, switching between conducting and non-conducting polymer states was two orders of magnitudes faster for pure polyaniline than for the cellulose nanowhisker/polyaniline composites (*84*). Therefore, charge propagation was roughly 2 orders of magnitudes faster in pure polyaniline than in our composites, indicating that the charge propagation rate can be tuned by controlling the polyaniline content and the nanoarchitecture.

Downloaded by PENNSYLVANIA STATE UNIV on August 28, 2012 | http://pubs.acs.org
Publication Date (Web): August 17, 2012 | doi: 10.1021/bk-2012-1107.ch005

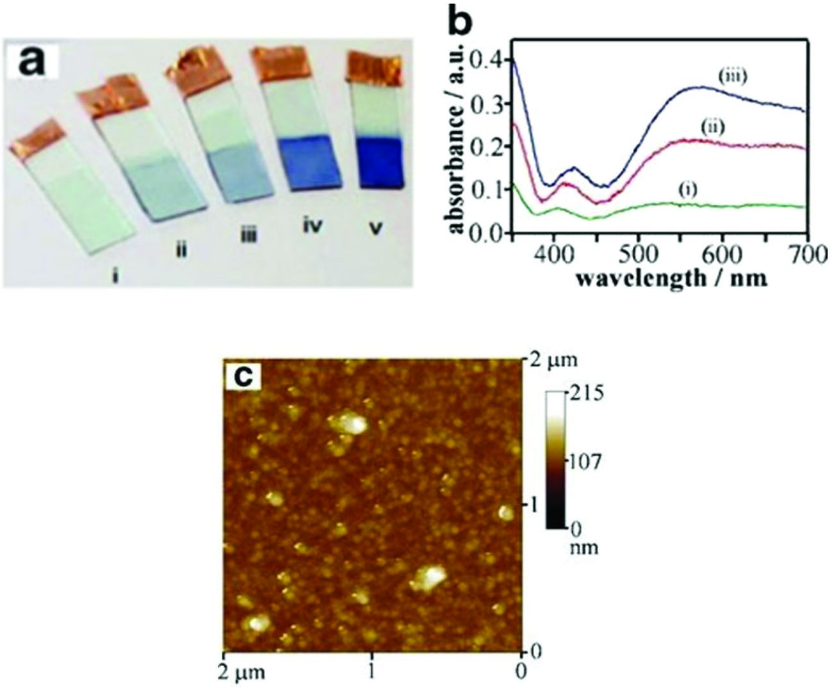

Figure 11. ***a*** *Cellulose nanowhisker/polyaniline membranes on ITO electrodes consisting of (i) 0, (ii) two, (iii) five, (iv) 10, and (v) 15 layers.* ***b*** *UV-visible spectrum of ITO electrodes with (i) two-, (ii) 10- and (iii) 15-layer polyaniline–nanocellulose film deposits.* ***c*** *AFM image showing the surface topography for a 10-layer polyaniline/nanocellulose film with spherical polyaniline and cellulose nanowhiskers clearly visible. Reproduced with permission from reference (83). Copyright 2011 Springer.*

Cellulose Nanowhisker-Stabilized Polypyrrole Supercapacitor Materials

Apart from simply being a support for porous functional membrane synthesis, it is also possible to use functionality introduced on the cellulose nanowhisker surface to improve performance of the composite membrane. An example of this approach was the development of cellulose nanowhisker-supported polypyrrole (PPy) for supercapacitor applications (*85*). PPy can exist in two states: a neutral state (reduced state) and a positively charged state (oxidized state) where approximately one electron per three pyrrole units has been removed. PPy is electron-conductive in the oxidized state, and non-electron-conductive in the reduced state. Oxidation or reduction of the polymer removes or adds electrons respectively to the polymer and this process can be used to store charge, making them interesting materials for supercapacitor materials (Figure 13).

Downloaded by PENNSYLVANIA STATE UNIV on August 28, 2012 | http://pubs.acs.org
Publication Date (Web): August 17, 2012 | doi: 10.1021/bk-2012-1107.ch005

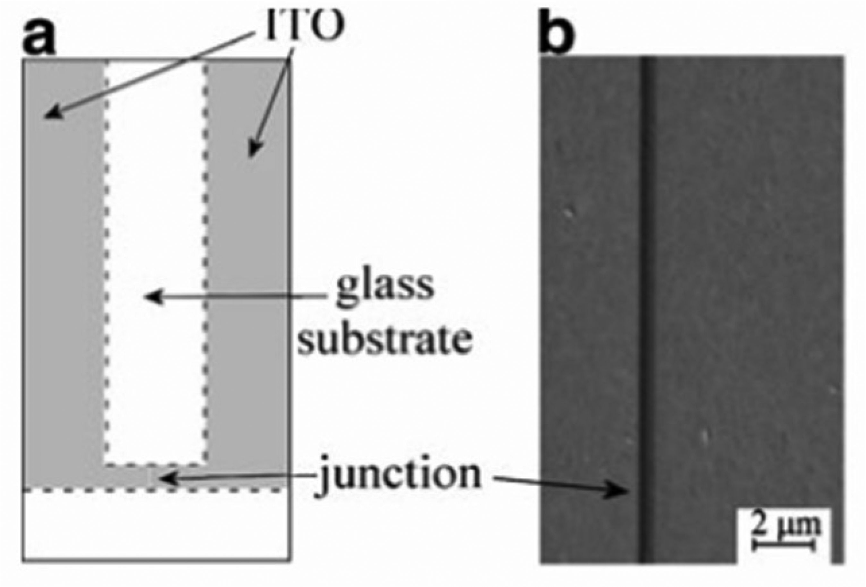

Figure 12. (a) Schematic drawing of the glass slide with ITO coating patterned by a focussed ion beam (FIB) and (b) SEM image of the actual patterned slide showing the ~700 nm wide cut out of the ITO layer. Reproduced with permission from reference (83). Copyright 2011 Springer.

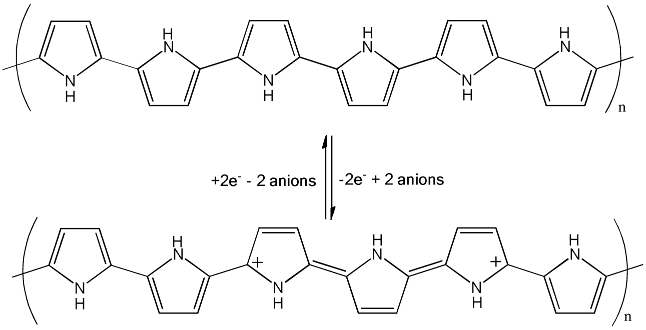

Figure 13. Reversible redox behavior of polypyrrole causing charging and discharging.

However, when the polymer is oxidized, anions from the electrolyte solution need to diffuse into the polymer to balance the positive charge (and diffuse out upon reduction) leading to significant polymer degradation with each charge-discharge cycle (Figure 14). Use of a support material bearing

Downloaded by PENNSYLVANIA STATE UNIV on August 28, 2012 | http://pubs.acs.org
Publication Date (Web): August 17, 2012 | doi: 10.1021/bk-2012-1107.ch005

anionic surface groups which may act as charge-balancing functionalities, can reduce PPy degradation as less ion movement occurs. This has been shown with oxidized carbon nanotubes (CNTs) (*86*). For the case of CNXLs, we wanted to investigate whether a conductive backbone is really required for high-performance supercapacitor materials.

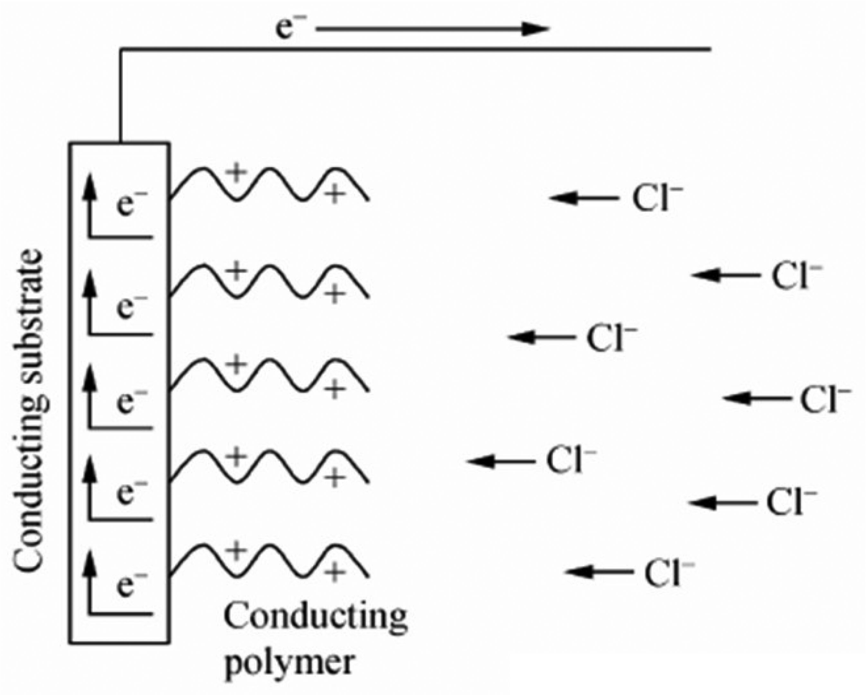

Figure 14. Schematic showing the need for electrolyte ion to diffusion into the polymer to balance charge (87). Reproduced with permission from reference (87). Copyright 2008 Elsevier.

During electropolymerisation, pyrrole is oxidized and forms a cationic conducting PPy polymer. However, when negatively charged CNXLs (formed by controlled surface oxidation of primary hydroxyl groups to carboxylic acids (*88*), O-CNXL) were used instead of a salt in the electrodeposition solution, a highly porous network is formed by interconnected O-CNXLs coated with a PPy layer of approximately 15 nm (Figure 15). All porosity in pure O-CNXL membrane structures consists of open pores, and this appeared to be transferred to the PPy/O-CNXL composite as evidenced by excellent electrolyte transport through the film (*vide infra*). The mesoporous film was robust enough to be peeled off the deposition electrode with tweezers. By charging the polypyrrole in the film with electrons, the polymer attained a neutral, non-conducting state.

Downloaded by PENNSYLVANIA STATE UNIV on August 28, 2012 | http://pubs.acs.org
Publication Date (Web): August 17, 2012 | doi: 10.1021/bk-2012-1107.ch005

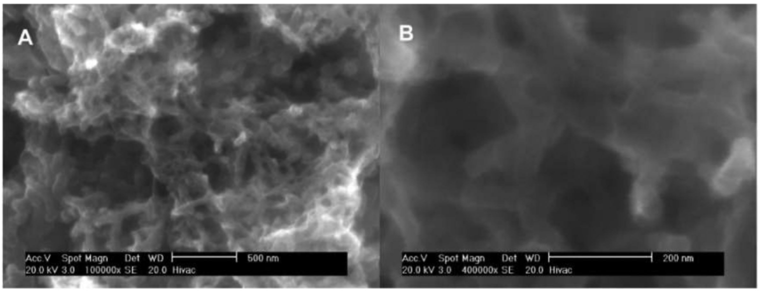
A
Acc.V Spot Magn Det WD 500 nm
20.0 kV 3.0 100000x SE 20.0 Hivac
B
Acc.V Spot Magn Det WD 200 nm
20.0 kV 3.0 400000x SE 20.0 Hivac

Figure 15. SEM images of the porous structure formed by co-electrodeposition of pyrrole with TEMPO-oxidised cellulose nanocrystals (85). Reproduced with permission from reference (85). Copyright 2010 American Chemical Society.

Despite the non-conductive nature of cellulose, the composite was found to remain conductive over the charge-discharge cycle (potential limits -0.5 V and 0.7 V vs Ag/AgCl at 0.25 V.s^{-1} in 0.1 M aqueous KCl), even at negative potentials where pure PPy exists in the reduced (neutral) and thus, non-conductive, state. In previous work with surface-oxidized CNTs in a similar fashion to O-CNXLs, this behavior was attributed to the conductivity of the CNTs (*86*). However, given the non-conductive nature of the O-CNXLs, the high conductivity of the composite when PPy was in the non-conducting state was shown to be due to cation ingress into polypyrrole to charge-balance the nanowhisker negative surface charge. This clearly proved that a conducting support is not required for the fabrication of high-performance supercapacitor materials.

The cellulose nanowhisker/PPy composites showed fast charging and discharging behavior due to the porous nature of the composite and the thin polypyrrole coating on the nanowhiskers. Comparison of PPy/CNT composites with PPy/cellulose nanowhisker composites prepared under exactly the same conditions, demonstrated a thicker PPY layer on the CNTs (~ 60 nm) compared to the PPy layer on O-CNXLs (~ 15 nm), while the specific capacitance was comparable (316 F.g^{-1} for CNT/PPy *vs* 336 F.g^{-1} for O-CNXL/PPy). After 5000 charge-discharge cycles (between +0.5 V and 0.5 V at 0.25 V.s^{-1}), the capacitance decrease due to PPy degradation was seen to be larger for the PPy/CNT composite than for the PPy/O-CNXL composite, while the capacitance for pure PPy/Cl was negligible due to severe degradation. The faster PPy degradation in the PPy/CNT composite is believed to be due to the thicker PPy coating on the CNTs. A thicker polymer layer increases required ion diffusion through the polymer layer which results in increased stress generation during charging and discharging ensuing in faster polymer degradation. The PPy/O-CNXL system was thus found to be more durable than the equivalent composite using CNTs as a thinner PPy coating was achieved in the PPy/O-CNXL composite.

Downloaded by PENNSYLVANIA STATE UNIV on August 28, 2012 | http://pubs.acs.org
Publication Date (Web): August 17, 2012 | doi: 10.1021/bk-2012-1107.ch005

Cellulose Nanowhiskers and Electrocatalysis

The use of CNXLs in electrocatalysis was restricted to a secondary role with either aiding the formation or structuring of the electrocatalytic substrate, or acting as the modification agent for the modification of the active surfaces.

In a first approach, the electrocatalytic activity of CNXL/polyaniline porous membranes prepared by LbL deposition, as described above, were investigated. Polyaniline is known to exhibit electrocatalytic activity (*89*) and in particular to electrocatalyse the oxidation of hydroquinone (*90*, *91*). Cellulose nanowhisker/polyaniline composite membranes showed the same electrocatalytic activity towards hydroquinone oxidation as pure polyaniline with thicker films (more layers) having higher activity, and with the reactivity limited by hydroquinone diffusion (*83*). This work further proved that LbL deposition of CNXL with polyaniline retains the CNXL membrane porous structure, similar to the co-deposition used to create sensors.

Metal Electrocatalysts

Nanostructured metals are interesting materials because of unique catalytic (*92*, *93*), magnetic (*94*), electrochemical (*95*), and photonic properties (*96*). The preparation of metal nanoparticles with the help of bio-derived substrates as reducing agents is an attractive option because of sustainability and minimal environmental impact (*97*). Cellulose is particularly useful as it does not compete with food production and can be extracted from a variety of sources including biomass waste. CNXLs offer the advantage of being easily dispersible in water, wherein cellulose is insoluble. Aqueous reduction of metal salts by cellulose thus becomes possible. We used the reductive capability of cellulose nanocrystals to reduce silver and platinum metal salts to form active electrocatalysts (*98*, *99*). In all metal salt reductions discussed here, surface-oxidised cellulose nanocrystals (O-CNXLs) were used in which the primary hydroxyl groups were selectively converted to carboxylic acids by TEMPO oxidation to improve dispersibility in the presence of metal salts (*88*).

Silver Electrocatalysts

Templating of reduced silver on cellulose fibers has been well established and used to prepare silver nanoparticles for antibacterial purposes (*100*, *101*). However, an additional reducing agent such as $NaBH_4$ is commonly used. In contrast, we used direct reduction of $AgNO_3$, employing the reductive power of cellulose by adding O-CNXLs to an aqueous $AgNO_3$ solution. After 5 min at 80°C, metallic silver formed, visible by a yellow discoloration of the solution. A yellow precipitate formed which became denser with increasing $[AgNO_3]$:[O-CNXL] ratio (Figure 16). UV spectroscopy confirmed the formation of nanostructured silver by a silver surface plasmon peak located at 404 nm and shifting to 420 nm for higher $[AgNO_3]$:[O-CNXL] ratios indicating increasing particle size (*102*, *103*). No discoloration occurred for aqueous $AgNO_3$, even over a period of 2 h.

In Functional Materials from Renewable Sources; Liebner, F., et al.;
ACS Symposium Series; American Chemical Society: Washington, DC, 2012.

Downloaded by PENNSYLVANIA STATE UNIV on August 28, 2012 | http://pubs.acs.org
Publication Date (Web): August 17, 2012 | doi: 10.1021/bk-2012-1107.ch005

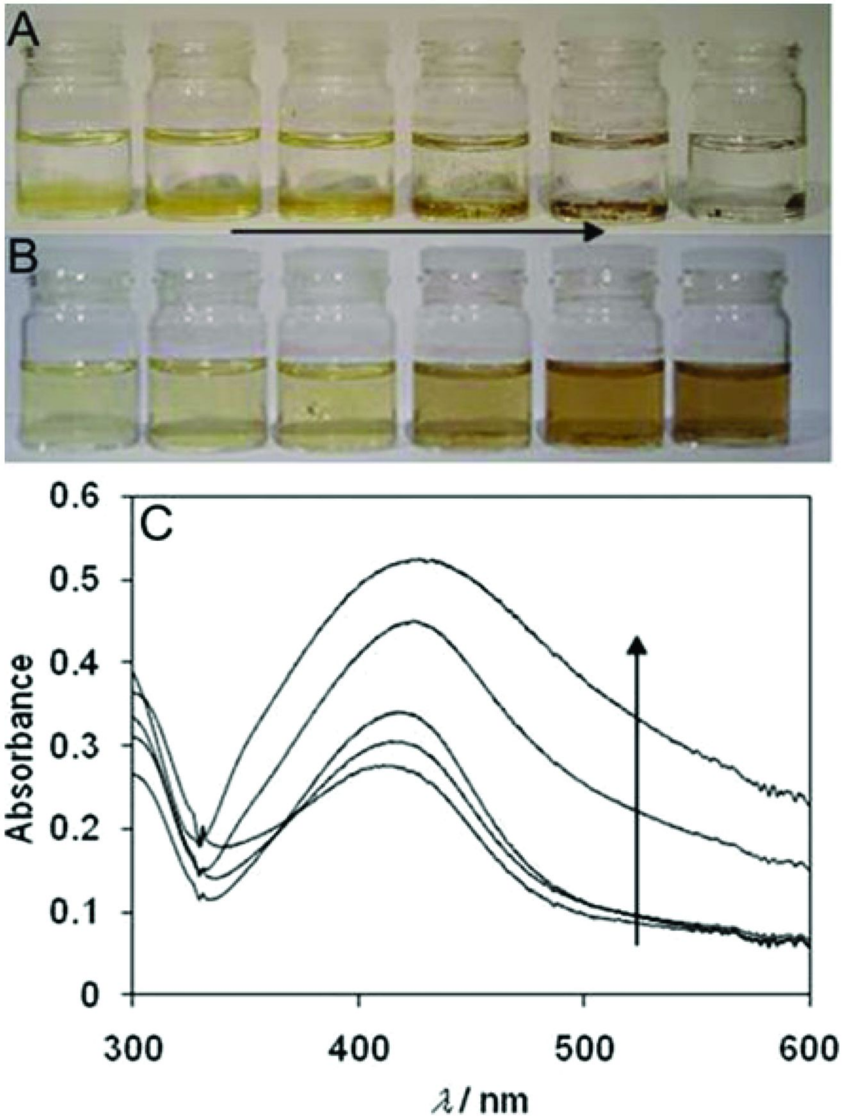

Figure 16. (A) Photographs of the reaction products obtained by heating 5 mL of (left to right) 0.10 wt%, 0.05 wt%, 0.02 wt%, 0.01 wt%, 0.005 wt% and 0.0023 wt% CNXL suspensions containing 20 mg $AgNO_3$ at 80° C for 2 h. (B) Photographs obtained after dispersing each product suspension ultrasonically for 5 min. (C) UV/Visible spectra of the first 5 solutions (from left to right) in part B arranged in order of (from bottom to top) decreasing amounts of CNXL. The arrows in each figure indicate increasing [$AgNO_3$]:[CNXL] ratios (98). Reproduced with permission from reference (98). Copyright 2010 The Royal Society of Chemistry.

Downloaded by PENNSYLVANIA STATE UNIV on August 28, 2012 | http://pubs.acs.org
Publication Date (Web): August 17, 2012 | doi: 10.1021/bk-2012-1107.ch005

Deposition of the Ag covered O-CNXLs on a surface from a suspension of sufficiently high concentration gave rise to particle agglomeration and the formation of silver dendritic structures on the order of several 100 nm to µm (Figure 17). At low concentration however, silver nanoparticles remained individualised with sizes of 10-50 nm. Drop coating the suspension on a surface followed by heating at 70°C (drying) on the other hand, lead to non-dendritic silver deposits. At high O-CNXL concentration, silver nanostructures were retained, while at low O-CNXL concentrations the deposits took on the form of bulk silver. Deposition followed by drying of a larger amount of $AgNO_3$ (20 µL of a suspension prepared by adding 211 mg $AgNO_3$ to 5 mL of 0.29 wt% cotton-derived O-CNXLs) on a glassy carbon electrode lead to smooth silver deposit with nanoparticulate features. This film showed stable electrocatalytic activity towards the reduction of O_2 in an O_2 saturated NaOH solution, comparable to a pure silver electrode. It was further shown that the Ag/O-CNXL composite reduced O_2 *via* direct 4-electron reduction forming 2 OH^-, rather than the 2-electron route which leads to peroxide formation.

This work showed the potential to use CNXLs′ reducing capability to form stable, highly active electrocatalysts. The advantage of CNXLs is their easy removal through burning them off, resulting in nanoscale channels within the metallic suprastructure.

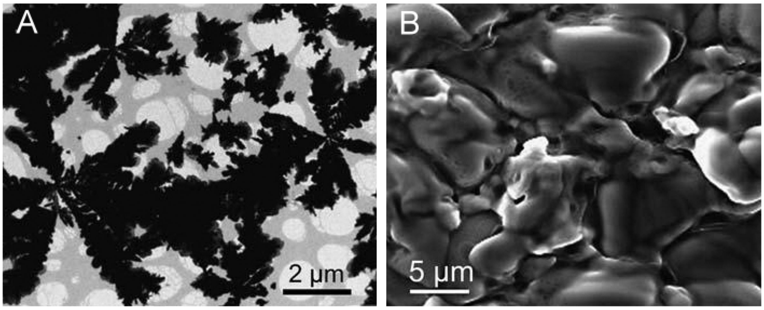

*Figure 17. **A** TEM image of silver formed by dissolving 211 mg $AgNO_3$ in 5 mL of 0.29 wt% CNXL suspension and heating for 2 h at 80°C. **B** SEM images of the surface of Ag/CNXL-modified glassy carbon electrodes formed by drop coating with 5ml suspensions containing 20 mg $AgNO_3$ and 0.0023 wt% CNXLs (heated to 80°C for 2h) and drying at 70°C for 30 min (98). Reproduced with permission from reference (98). Copyright 2010 The Royal Society of Chemistry.*

Platinum Electrocatalysts

In a way similar to the preparation of silver nanoparticles, platinum ions can also be reduced by CNXLs. Platinum is used as a catalyst in a variety of reactions and also finds applications as the cathode electrocatalyst in low temperature fuel cells (*104–107*). However, Pt is more difficult to reduce than is Ag such that longer reaction times, or higher temperatures, are required. Keeping an aqueous mixture of H_2PtCl_6 and O-CNXLs at 80°C for 24 h resulted in the formation of a black suspension due to Pt nanoparticle formation. No discoloration of the mixture was seen before 12 h. Industrially relevant Pt/C catalysts used in fuel cell electrodes were prepared by adding carbon black to the reduction solution followed by heating the composite in air at 445°C to remove the CNXLs without decomposing the carbon black. The Pt nanoparticles formed had diameters in the range of 2.3 ± 0.4 nm both in the presence of and in the absence of carbon black, which increased to 2.5 ± 0.9 nm after heating to 445°C (Figure 18).

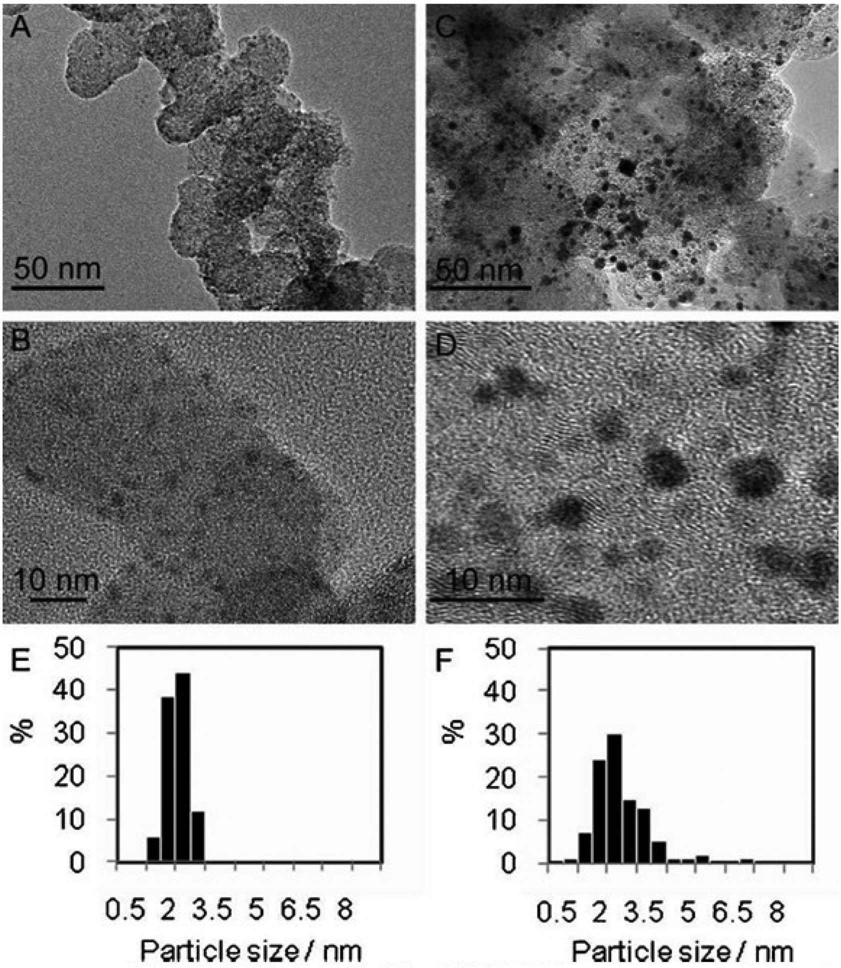

Figure 18. (A and B) TEM images of Pt/C/CNXL, obtained from heating a mixture of H_2PtCl_6(100 mM) and CNXLs (3 mg) and Vulcan XC72R (5 mg) in water (1 mL). (C and D) TEM images of the product after heating it in air at 445° C. (E and F) Particle size distributions of the Pt nanoparticles on carbon before (E) and after (F) heating. Particle size distributions were obtained from analysis of at least 100 particles shown in the TEM images (99). Reproduced with permission from reference (99). Copyright 2011 The Royal Society of Chemistry.

Downloaded by PENNSYLVANIA STATE UNIV on August 28, 2012 | http://pubs.acs.org
Publication Date (Web): August 17, 2012 | doi: 10.1021/bk-2012-1107.ch005

Downloaded by PENNSYLVANIA STATE UNIV on August 28, 2012 | http://pubs.acs.org
Publication Date (Web): August 17, 2012 | doi: 10.1021/bk-2012-1107.ch005

By electrochemical characterisation, the Pt/C nanoparticles were shown to be free of organic contaminants, which is important for catalysis. All cellulose traces were thus removed. The electrocatalytic activity towards the oxygen reduction reaction of the CNXL-prepared Pt/C was similar to commercial state-of-the-art Johnson-Matthey (JM) Pt/C. However, the performance of CNXL generated Pt/C was lower due to larger Pt nanoparticles versus JM's Pt nanoparticles, leading to a specific Pt surface area of 18.4 ± 4.0 m^2 g_{Pt}^{-1} versus 73.3 ± 9.7 m^2 g_{Pt}^{-1} respectively. The oxygen reduction occurred almost exclusively by the preferable 4-electron reduction route for both catalysts. Optimisation of Pt nanoparticle formation to reduce their size by 0.5 nm would lead to bio-reduced Pt nanoparticles with the same performance as JM's reference material.

Cellulose nanowhiskers thus offer a new sustainable tool to the fabrication of active electrocatalysts with the same performance as existing state-of-the-art materials while allowing easy reduction in aqueous environment and the potential to create nanostuctured metallic catalysts.

Cellulose Nanowhiskers as Precursor for Ultrathin Carbon Films

Cellulose has been used extensively to create carbonaceous materials through pyrolysis (*108*, *109*). The formation of thin carbon films on the surface of metal or metal oxide surfaces has the potential to control the electron transfer rate at the surface by varying the carbon layer thickness. While this can readily be done on flat surfaces, the potential of nanostructured materials in catalysis, electrocatalysis and photocatalysis requires extension of this ability into mesopores. Furthermore, to attain a uniform effect, the carbon layer needs to have a uniform thickness and coverage everywhere on the surface. The previously shown ability to co-deposit CNXLs with TiO_2 nanoparticles opens up the possibility to create homogeneous composites which after pyrolysis should result in uniformly carbon-coated TiO_2 in a very direct manner, which can easily be extended to other metal and metal oxide materials.

Initial work on the use of CNXLs as a method to coat surfaces with an ultrathin carbon film was performed on flat ITO surfaces (*110*). Films of various thicknesses were prepared by an LbL approach with CNXLs bearing surface sulfate groups from H_2SO_4 hydrolysis of sisal and PDDAC by subsequently dipping the ITO substrate in aqueous solutions of each component with rinsing and drying in-between. Subsequent carbonization under vacuum resulted in a thin carbon layer covering the ITO surface. A single cellulose-PDDAC layer resulted in a carbon layer showing pore imperfections, while 10 to 40 layers gave rise to more uniform carbon films (Figure 19) still retaining the transparency of the ITO substrate. The carbonized films showed signs of nanocrystalline graphite and aromatic cluster formation with apparent disorder in the graphite structure.

Increasing the thickness of the film (more layers) was found to enhance the peak current for the hydroquinone-benzoquinone redox system. The vacuum-carbonized film was also found to significantly increase the rate of electron transfer at the ITO surface. The carbon film appeared to be stable over prolonged use.

In Functional Materials from Renewable Sources; Liebner, F., et al.;
ACS Symposium Series; American Chemical Society: Washington, DC, 2012.

Downloaded by PENNSYLVANIA STATE UNIV on August 28, 2012 | http://pubs.acs.org
Publication Date (Web): August 17, 2012 | doi: 10.1021/bk-2012-1107.ch005

More detailed analysis determined a decrease in charge transfer resistance at the ITO surface of two orders of magnitude without affecting the capacitance. With these systems it is thus possible to directly improve electron transfer at surfaces without affecting the optical window or transparency of the substrate.

This work was further extended to the modification of TiO_2 anatase nanoparticle surfaces (*111*, *112*). The electrochemical characteristics of carbon coated TiO_2 and pure TiO_2 surface were determined by comparing air- and vacuum-carbonized films of anatase nanoparticles (schematic shown in Figure 20).

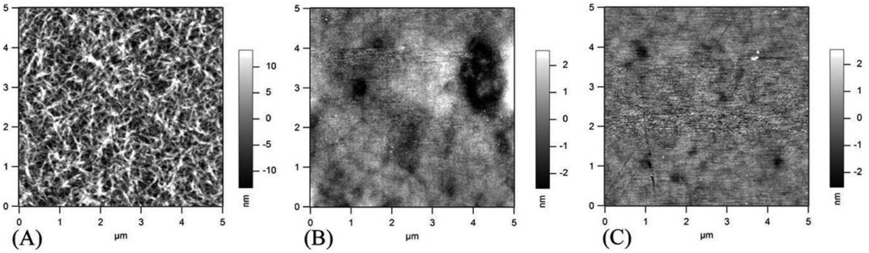
(A)
(B)
(C)
0
1
2
3
4
5
µm
nm
10
5
0
-5
-10
2
1
0
-1
-2

Figure 19. AFM images of (A) 10 layers of a cellulose nanofibril-PDDAC film on ITO, (B) a 1-layer film of cellulose nanofibril-PDDAC on ITO after vacuum carbonization, and (C) a 10-layer film of cellulose nanofibril-PDDAC on ITO after vacuum carbonization. Reproduced with permission from reference (110). Copyright 2010 John Wiley and Sons.

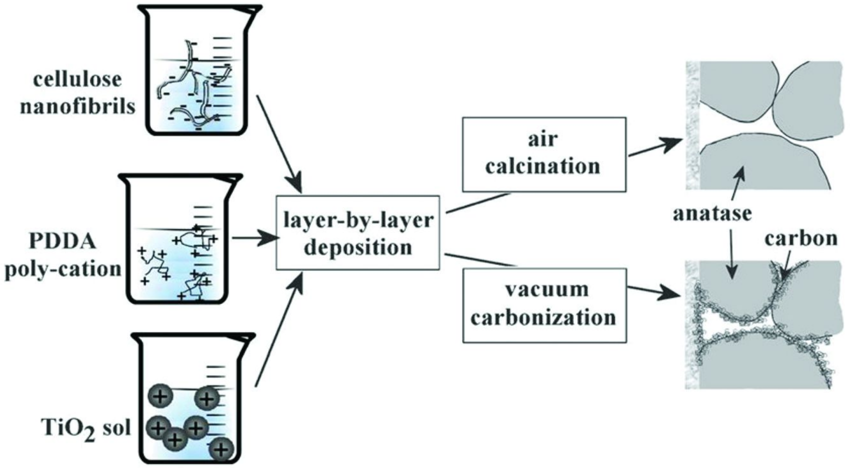
cellulose nanofibrils
PDDA poly-cation
TiO2 sol
layer-by-layer deposition
air calcination
vacuum carbonization
anatase
carbon

Figure 20. Schematic of the preparation of anatase mesoporous films with and without a fine carbon coat (111). Reproduced with permission from reference (111). Copyright 2011the PCCP Owner Societies.

All films contained 10 layers of TiO_2 but, between them, cellulose-PDDAC was varied from 1 to 4 layers (Figure 21). After heat treatment at 500°C, film thicknesses of 150 nm were obtained by a 10-layer TiO_2 LbL deposition. Vacuum-carbonized films showed TiO_2 nanoparticles as 40-70 nm agglomerates, which were slightly bigger for air calcined samples believed to be due to some sintering (*110*). Carbon deposits did not show any measurable crystallinity, but appeared to reduce the anatase crystal size (20 nm *vs* 7 nm) (*111*, *112*). Carbon-modified TiO_2 films on ITO were transparent albeit with a brown tinge at higher carbon levels (Figure 22).

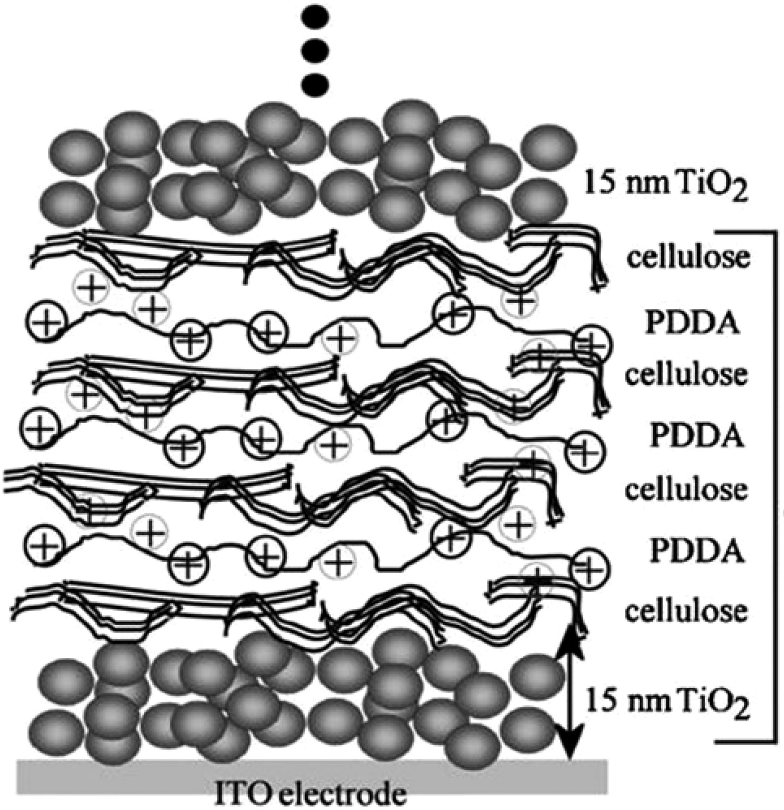

Figure 21. Schematic of layering of cellulose nanowhiskers, PDDAC and TiO_2 nanoparticles before carbonization. Reproduced with permission from reference (112). Copyright 2012 Elsevier Ltd.

The carbon modification of the TiO_2 surface allowed for a larger surface area to be directly reduced and oxidized for a given scan rate than possible for a pure TiO_2 film. This was also scan rate-dependent, indicating mixed surface conductivity and surface structure effects. The carbon modification also resulted in the hydroquinone-benzoquinone redox system becoming more and

Downloaded by PENNSYLVANIA STATE UNIV on August 28, 2012 | http://pubs.acs.org
Publication Date (Web): August 17, 2012 | doi: 10.1021/bk-2012-1107.ch005

more reversible with increasing carbon modification. With carbon modification, the charge transfer resistance at the TiO_2 surface in aqueous environment also decreased while the capacitance was seen to increase. The latter indicated an increase in active area. Dopamine, a redox-active neurotransmitter, was used to probe the effect of the carbon modification, since dopamine oxidation on pure TiO_2 is inhibited due to the lack of conductivity. Because of improved surface conductivity (Fig. 23) and a high Langmuirian binding constant (~ 10^6 mol^{-1} dm^3), carbon-modified TiO_2 films were able to detect dopamine with a concentration sensitivity to below 100 nM, similar to carbon nanotube network electrodes.

Downloaded by PENNSYLVANIA STATE UNIV on August 28, 2012 | http://pubs.acs.org
Publication Date (Web): August 17, 2012 | doi: 10.1021/bk-2012-1107.ch005

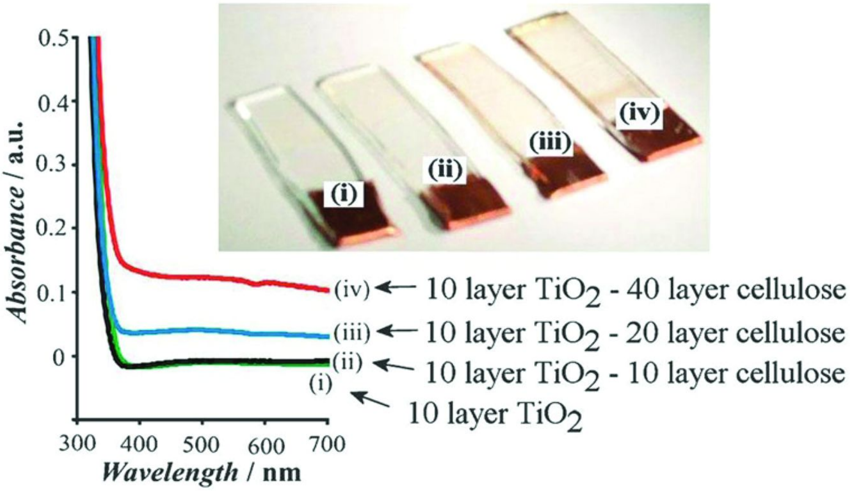

Figure 22. UV/Vis absorption spectra for electrodes with (i) 10-layer TiO_2, (ii) 10-layer TiO_2 10-layer cellulose carbonised in 500°C vacuum, (iii) 10-layer TiO_2 20-layer cellulose carbonised in 500°C vacuum, and (iv) 10-layer TiO_2 40-layer cellulose carbonised in 500°C vacuum. Also shown is a photographic image of the transparent electrodes. Reproduced with permission from reference (111). Copyright 2011 the PCCP Owner Societies.

Carbon modification of TiO_2 can also be used to suppress the TiO_2 photoreactivity which may be beneficial for example for protection against UV light or prevention of photodegradation of sensor films. The photocurrent responses for the photo-oxidation of iodide to tri-iodide ($I^- \rightarrow I_3^-$) were strongly suppressed by the carbon modification. As UV/vis spectra were virtually unaffected, this suppression was not due to light filtering. Quenching of photoactivity also increased with increasing carbon deposition. This indicates that the thin carbon layer aided the recombination of holes (oxidizing surface states) and electrons from the ITO substrate.

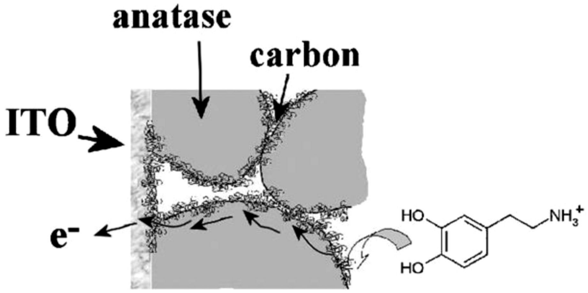

Figure 23. Schematic diagram of the binding of dopamine onto the carbon –modified TiO_2 electrode and electron conduction through the carbon film. Reproduced with permission from reference (111). Copyright 2011 the PCCP Owner Societies.

The LbL deposition technique of CNXLs thus enables the uniform surface coating of complex objects with very good control over thickness and ensuing behavior. While used here solely for TiO_2, it can easily be extended to other metals and metal oxides.

Conclusions

Cellulose nanowhiskers, or nanocrystals, can be used to form strong hydrogen-bonded porous films. Through targeted surface modification and layer-by-layer deposition with polymers and dendrimers, specific functionalities can be introduced into the films. Several examples have been discussed where these functionalities were used to bind analytes or classes of analytes to create electrochemical sensors for redox-active metal and organic compounds, but also for redox-inactive species through the use of a competitive binding model between the analyte and redox-active species immobilized in the film. The versatility of the LbL deposition approach together with the retention of the open pore structure of the CNXL film represents a very versatile technology platform for the creation of sensors and free-standing functionalized membranes. There is a high potential for further development by using function polymers which increase binding selectivity. The creation of free-standing membranes with immobilized species may find applications in combined separation and catalysis applications. The use of CNXL surface modifications has been extensively used in our group (*113*)–(*115*) and offers further possibilities to construct functional free-standing membranes and surface modifications with or without the co-deposition with functional polymers to introduce further functionality.

The co-deposition with TiO_2 has shown that CNXLs can be used to create open porous structures with metallic nanoparticles without loss of conductivity throughout the film. Extension of this work with other metal and metal oxide structures could lead to interesting composite films while further research on enzyme immobilization in these films could also result in very promising materials.

Downloaded by PENNSYLVANIA STATE UNIV on August 28, 2012 | http://pubs.acs.org
Publication Date (Web): August 17, 2012 | doi: 10.1021/bk-2012-1107.ch005

Co-deposition with electronically conducting polymers resulted in percolated conducting porous membranes which were used as electrocatalysts or showed very high stability as supercapacitor materials due to specific cellulose nanoparticle-polymer interactions. Improvements in their performance and extension to other conducting polymers are obvious targets for future work with the current results being quite promising.

The reducing capability of cellulose nanowhiskers has been shown to create metal nanoparticles which can form conducting networks when deposited in films, or the cellulose can be burned off to form surface-clean metal nanoparticles. The extension of this work to other metals, control over metal loading and size of the nanoparticles formed, and optimization of the reduction conditions to reduce energy consumptions should lead to interesting advancements and better control over the obtained structures.

Finally, cellulose nanowhiskers have also been shown to be a great material to surface-coat metal and metal oxide nanostructures with a fine carbon layer through vacuum carbonization, which can be used to alter the electrochemical and photocatalytic activity of the metallic nanostructures. Its potential to coat nanostructured metals and metal oxides is vast, and exploration of various structures and metal/metal oxides may further offer some interesting advancements.

To conclude, the versatility and relative ease of the usage of cellulose nanoparticle in a variety of electrochemical applications make it a great and adaptable building block with many avenues still left unexplored.

Downloaded by PENNSYLVANIA STATE UNIV on August 28, 2012 | http://pubs.acs.org
Publication Date (Web): August 17, 2012 | doi: 10.1021/bk-2012-1107.ch005

References

1. McQuade, D. T.; Pullen, A. E.; Swager, T. M. *Chem. Rev.* **2000**, *100* (7), 2537–2574.
2. Huang, X.-J.; Choi, Y.-K. *Sens. Actuators, B* **2007**, *122* (2), 659–671.
3. Shao, Y.; Wang, J.; Wu, H.; Liu, J.; Aksay, I. A.; Lin, Y. *Electroanalysis* **2010**, *22* (10), 1027–1036.
4. Bakker, E.; Qin, Y. *Anal. Chem.* **2006**, *78* (12), 3965–3984.
5. Privett, B. J.; Shin, J. H.; Schoenfisch, M. H. *Anal. Chem.* **2008**, *80* (12), 4499–4517.
6. Zhang, X.; Ju, H.; Wang, J. *Electrochemical Sensors, Biosensors and Their Biomedical Applications*; Academic Press: San Diego, CA, 2007.
7. Selvaraju, T.; Ramaraj, R. *J. Electroanal. Chem.* **2005**, *585* (2), 290–300.
8. Chen, S.-M.; Chen, J.-Y.; Thangamuthu, R. *Electroanalysis* **2008**, *20* (14), 1565–1573.
9. Momma, T.; Komaba, S.; Yamamoto, M.; Osaka, T.; Yamauchi, S. *Sens. Actuators, B* **1995**, *25* (1–3), 724–728.
10. Aurobind, S. V.; Amirthalingam, K. P.; Gomathi, H. *Adv. Colloid Interface Sci.* **2006**, *121* (1–3), 1–7.
11. Hoshi, T.; Saiki, H.; Kuwazawa, S.; Tsuchiya, C.; Chen, Q.; Anzai, J.-i. *Anal. Chem.* **2001**, *73* (21), 5310–5315.

12. Muguruma, H.; Itazu, N.; Miura, S. *J. Phys. Chem. B* **2005**, *109* (40), 18839–18845.
13. Elliott, J. M.; Cabuché, L. M.; Bartlett, P. N. *Anal. Chem.* **2001**, *73* (13), 2855–2861.
14. Khramov, A. N.; Munos, J.; Collinson, M. M. *Langmuir* **2001**, *17* (26), 8112–8117.
15. Okuno, H.; Kitano, T.; Yakabe, H.; Kishimoto, M.; Siigi, H.; Nagaoka, T. *Anal. Chem.* **2002**, *74* (16), 4184–4190.
16. Cichelli, J.; Zharov, I. *J. Am. Chem. Soc.* **2006**, *128* (25), 8130–8131.
17. Camacho, C.; Matías, J. C.; Cao, R.; Matos, M.; Chico, B.; Hernández, J.; Longo, M. A.; Sanromán, M. A.; Villalonga, R. *Langmuir* **2008**, *24* (15), 7654–7657.
18. Crespilho, F. N.; Ghica, M. E.; Gouveia-Caridade, C.; Oliveira, O. N., Jr; Brett, C. M. A. *Talanta* **2008**, *76* (4), 922–928.
19. Conte, M. *Fuel Cells* **2010**, *10* (5), 806–818.
20. Sternberg, R.; Bindra, D. S.; Wilson, G. S.; Thevenot, D. R. *Anal. Chem.* **1988**, *60* (24), 2781–2786.
21. Guiomar, A. J.; Evans, S. D.; Guthrie, J. T. *Supramol. Sci.* **1997**, *4* (3–4), 279–291.
22. Portaccio, M.; Durante, D.; Viggiano, A.; Di Martino, S.; De Luca, P.; Di Tuoro, D.; Bencivenga, U.; Rossi, S.; Canciglia, P.; De Luca, B.; Mita, D. G. *Electroanalysis* **2007**, *19* (17), 1787–1793.
23. Cui, G.; Yoo, J. H.; Yoo, J.; Lee, S. W.; Nam, H.; Cha, G. S. *Electroanalysis* **2001**, *13* (3), 224–228.
24. Sarkar, P.; Pal, P. S.; Ghosh, D.; Setford, S. J.; Tothill, I. E. *Int. J. Pharm.* **2002**, *238* (1–2), 1–9.
25. Ghosh, G.; Bachas, L.; Anderson, K. *Anal. Bioanal. Chem.* **2008**, *391* (8), 2783–2791.
26. Anderson, D. J.; Van Lente, F.; Apple, F. S.; Kazmierczak, S. C.; Lott, J. A.; Gupta, M. K.; McBride, N.; Katzin, W. E.; Scott, R. E. *Anal. Chem.* **1991**, *63* (12), 165R–270R.
27. Berberich, J. A.; Chan, A.; Boden, M.; Russell, A. J. *Acta Biomater.* **2005**, *1* (2), 193–199.
28. Berberich, J. A.; Yang, L. W.; Bahar, I.; Russell, A. J. *Acta Biomater.* **2005**, *1* (2), 183–191.
29. Wenz, G.; Liepold, P. *Cellulose* **2007**, *14* (2), 89–98.
30. Babkina, S. S.; Palecek, E.; Jelen, F.; Fojta, M. *J. Anal. Chem.* **2005**, *60* (6), 567–572.
31. Babkina, S. S.; Ulakhovich, N. A. *Bioelectrochemistry* **2004**, *63* (1–2), 261–265.
32. Wang, B.; Du, X.; Wang, M.; Gong, W.; Anzai, J.-i. *Electroanalysis* **2008**, *20* (9), 1028–1031.
33. Van Es, R. M.; Setford, S. J.; Blankwater, Y. J.; Meijer, D. *Anal. Chim. Acta* **2001**, *429* (1), 37–47.
34. Taylor, P. J.; Kmetec, E.; Johnson, J. M. *Anal. Chem.* **1977**, *49* (6), 789–794.
35. Xu, Y.; Guilbault, G. G.; Kuan, S. S. *Anal. Chem.* **1989**, *61* (7), 782–784.
36. Wang, J.; Tuzhi, P. *Anal. Chem.* **1986**, *58* (14), 3257–3261.

Downloaded by PENNSYLVANIA STATE UNIV on August 28, 2012 | http://pubs.acs.org
Publication Date (Web): August 17, 2012 | doi: 10.1021/bk-2012-1107.ch005

37. Gao, J.; Zhao, G.; Zhang, Z.; Zhao, J.; Yang, W. *Microchim. Acta* **2007**, *157* (1), 35–40.
38. Wang, J.; Golden, T.; Li, R. *Anal. Chem.* **1988**, *60* (15), 1642–1645.
39. Wang, J.; Hutchins, L. D. *Anal. Chem.* **1985**, *57* (8), 1536–1541.
40. Aldstadt, J. H.; Dewald, H. D. *Anal. Chem.* **1993**, *65* (7), 922–926.
41. Wang, J.; Rayson, G. D.; Lu, Z.; Wu, H. *Anal. Chem.* **1990**, *62* (18), 1924–1927.
42. Kuhn, L. S.; Weber, S. G.; Ismail, K. Z. *Anal. Chem.* **1989**, *61* (4), 303–309.
43. Hoyer, B.; Sørensen, G.; Jensen, N.; Christensen, M. K. *Electroanalysis* **1999**, *11* (13), 940–944.
44. Sandifer, J. R. *Anal. Chem.* **1981**, *53* (8), 1164–1170.
45. Noguchi, T.; Anzai, J.-i. *Langmuir* **2006**, *22* (6), 2870–2875.
46. Wang, B.; Anzai, J.-i. *Langmuir* **2007**, *23* (13), 7378–7384.
47. Charleton, K.; Buffie, T.; Goltz, D. M. *Talanta* **2007**, *74* (1), 7–13.
48. Ha, J.; Martin, S. M.; Jeon, Y.; Yoon, I. J.; Brown, R. B.; Nam, H.; Cha, G. S. *Anal. Chim. Acta* **2005**, *549* (1–2), 59–66.
49. Eichhorn, S. J.; Dufresne, A.; Aranguren, M.; Marcovich, N. E.; Capadona, J. R.; Rowan, S. J.; Weder, C.; Thielemans, W.; Roman, M.; Renneckar, S.; Gindl, W.; Veigel, S.; Keckes, J.; Yano, H.; Abe, K.; Nogi, M.; Nakagaito, A. N.; Mangalam, A.; Simonsen, J.; Benight, A. S.; Bismarck, A.; Berglund, L. A.; Peijs, T. *J. Mater. Sci.* **2010**, *45* (1), 1–33.
50. Eichhorn, S. J. *Soft Matter* **2011**, *7* (2), 303–315.
51. Moon, R. J.; Martini, A.; Nairn, J.; Simonsen, J.; Youngblood, J. *Chem. Soc. Rev.* **2011**, *40* (7), 3941–3994.
52. Dufresne, A. *Can. J. Chem.-Rev. Can. Chim.* **2008**, *86* (6), 484–494.
53. de Rodriguez, N. L. G.; Thielemans, W.; Dufresne, A. *Cellulose* **2006**, *13* (3), 261–270.
54. Thielemans, W.; Warbey, C. R.; Walsh, D. A. *Green Chem.* **2009**, *11* (4), 531–537.
55. Bonne, M. J.; Milsom, E. V.; Helton, M.; Thielemans, W.; Wilkins, S.; Marken, F. *Electrochem. Commun.* **2007**, *9* (8), 1985–1990.
56. Bonne, M. J.; Edler, K. J.; Buchanan, J. G.; Wolverson, D.; Psillakis, E.; Helton, M.; Thielemans, W.; Marken, F. *J. Phys. Chem. C* **2008**, *112* (7), 2660–2666.
57. Tsourounaki, K.; Bonne, M. J.; Thielemans, W.; Psillakis, E.; Helton, M.; McKee, A.; Marken, F. *Electroanalysis* **2008**, *20* (22), 2395–2402.
58. Fabregat-Santiago, F.; Mora-Seró, I.; Garcia-Belmonte, G.; Bisquert, J. *J. Phys. Chem. B* **2002**, *107* (3), 758–768.
59. Chen, X.; Hu, N.; Zeng, Y.; Rusling, J. F.; Yang, J. *Langmuir* **1999**, *15* (20), 7022–7030.
60. Liu, Y.; Xu, Q.; Feng, X.; Zhu, J.-J.; Hou, W. *Anal. Bioanal. Chem.* **2007**, *387* (4), 1553–1559.
61. Topoglidis, E.; Campbell, C. J.; Cass, A. E. G.; Durrant, J. R. *Electroanalysis* **2006**, *18* (9), 882–887.
62. Zong, S.; Cao, Y.; Zhou, Y.; Ju, H. *Anal. Chim. Acta* **2007**, *582* (2), 361–366.
63. Wang, G.-f.; Deng, X.-h.; Zhang, W.-z.; Fang, B. *Ann. Chim.* **2006**, *96* (3-4), 247–252.

Downloaded by PENNSYLVANIA STATE UNIV on August 28, 2012 | http://pubs.acs.org
Publication Date (Web): August 17, 2012 | doi: 10.1021/bk-2012-1107.ch005

64. Cao, D.; Hu, N. *Biophys. Chem.* **2006**, *121* (3), 209–217.
65. Liu, X.; Chen, T.; Liu, L.; Li, G. *Sens. Actuators, B* **2006**, *113* (1), 106–111.
66. McKenzie, K. J.; King, P. M.; Marken, F.; Gardner, C. E.; Macpherson, J. V. *J. Electroanal. Chem.* **2005**, *579* (2), 267–275.
67. Safavi, A.; Maleki, N.; Shahbaazi, H. R. *Anal. Chim. Acta* **2003**, *494* (1–2), 225–233.
68. Pemberton, R. M.; Hart, J. P. *Anal. Chim. Acta* **1999**, *390* (1–3), 107–115.
69. Wang, L.-H.; S.-C., C.; Chin, C.-Y. *Bull. Electrochem.* **2004**, *20* (5), 225–230.
70. Sashiwa, H.; Shigemasa, Y.; Roy, R. *Chem. Lett.* **2000**, *29* (6), 596–597.
71. Kas, H. S. *J. Microencapsul.* **1997**, *14* (6), 689–711.
72. Barreiro-Iglesias, R.; Alvarez-Lorenzo, C.; Concheiro, A. *J. Therm. Anal. Calorim.* **2005**, *82* (2), 499–505.
73. Bonne, M. J.; Galbraith, E.; James, T. D.; Wasbrough, M. J.; Edler, K. J.; Jenkins, A. T. A.; Helton, M.; McKee, A.; Thielemans, W.; Psillakis, E.; Marken, F. *J. Mater. Chem.* **2010**, *20* (3), 588–594.
74. Lorand, J. P.; Edwards, J. O. *J. Org. Chem.* **1959**, *24* (6), 769–774.
75. James, T. D.; Sandanayake, K. R. A. S.; Shinkai, S. *Angew. Chem., Int. Ed. Engl.* **1996**, *35* (17), 1910–1922.
76. Bosch, L. I.; Fyles, T. M.; James, T. D. *Tetrahedron* **2004**, *60* (49), 11175–11190.
77. Kubo, Y.; Ishida, T.; Kobayashi, A.; James, T. D. *J. Mater. Chem.* **2005**, *15* (27-28), 2889–2895.
78. Sun, W.; Jiao, K. *Talanta* **2002**, *56* (6), 1073–1080.
79. Schour, I.; Hoffman, M. M.; Sarnat, B. G.; Engel, M. B. *J. Dent. Res.* **1941**, *20* (5), 411–418.
80. Vilmann, H. *J. Anat.* **1969**, *105* (Pt. 3), 533–545.
81. Filho, V. E. M.; Marques, A. L. B.; Zhang, J. J.; Chierice, G. O. *Electroanalysis* **1999**, *11* (15), 1130–1136.
82. Yan, J.; Springsteen, G.; Deeter, S.; Wang, B. *Tetrahedron* **2004**, *60* (49), 11205–11209.
83. Shariki, S.; Liew, S.; Thielemans, W.; Walsh, D.; Cummings, C.; Rassaei, L.; Wasbrough, M.; Edler, K.; Bonné, M.; Marken, F. *J. Solid State Electrochem.* **2011**, *15* (11), 2675–2681.
84. Aoki, K.; Kawase, M. *J. Electroanal. Chem.* **1994**, *377* (1–2), 125–129.
85. Liew, S. Y.; Thielemans, W.; Walsh, D. A. *J. Phys. Chem. C* **2010**, *114* (41), 17926–17933.
86. Hughes, M.; Chen, G. Z.; Shaffer, M. S. P.; Fray, D. J.; Windle, A. H. *Chem. Mater.* **2002**, *14* (4), 1610–1613.
87. Peng, C.; Zhang, S.; Jewell, D.; Chen, G. Z. *Prog. Nat. Sci.* **2008**, *18* (7), 777–788.
88. Habibi, Y.; Chanzy, H.; Vignon, M. R. *Cellulose* **2006**, *13* (6), 679–687.
89. Albertas, M. *Synth. Met.* **1999**, *107* (2), 75–83.
90. Duić, L.; Grigić, S. *Electrochim. Acta* **2001**, *46* (18), 2795–2803.
91. Büttner, E.; Holze, R. *J. Electroanal. Chem.* **2001**, *508* (1–2), 150–155.
92. Min, M.-k.; Cho, J.; Cho, K.; Kim, H. *Electrochim. Acta* **2000**, *45* (25–26), 4211–4217.

Downloaded by PENNSYLVANIA STATE UNIV on August 28, 2012 | http://pubs.acs.org
Publication Date (Web): August 17, 2012 | doi: 10.1021/bk-2012-1107.ch005

93. Shiju, N. R.; Guliants, V. V. *Appl. Catal. A: Gen.* **2009**, *356* (1), 1–17.
94. Goncharov, A.; Zhukov, A. A.; Bartlett, P. N.; Ghanem, M. A.; Boardman, R.; Fangohr, H.; de Groot, P. A. J. *J. Magn. Magn. Mater.* **2005**, *286* (0), 1–4.
95. Sun, X.; Li, R.; Villers, D.; Dodelet, J. P.; Désilets, S. *Chem. Phys. Lett.* **2003**, *379* (1–2), 99–104.
96. Lim, Y. T.; Kim, J. K.; Shin, Y. B.; Chung, B. H. *Adv. Funct. Mater.* **2006**, *16* (8), 1015–1021.
97. Murphy, C. J. *J. Mater. Chem.* **2008**, *18* (19), 2173–2176.
98. Johnson, L.; Thielemans, W.; Walsh, D. A. *J. Mater. Chem.* **2010**, *20* (9), 1737–1743.
99. Johnson, L.; Thielemans, W.; Walsh, D. A. *Green Chem.* **2011**, *13* (7), 1686–1693.
100. He, J.; Kunitake, T.; Watanabe, T. *Chem. Commun.* **2005** (6), 795–796.
101. Dankovich, T. A.; Gray, D. G. *Environ. Sci. Technol.* **2011**, *45* (5), 1992–1998.
102. Cai, J.; Kimura, S.; Wada, M.; Kuga, S. *Biomacromolecules* **2008**, *10* (1), 87–94.
103. Bhui, D. K.; Bar, H.; Sarkar, P.; Sahoo, G. P.; De, S. P.; Misra, A. *J. Mol. Liq.* **2009**, *145* (1), 33–37.
104. Blaser, H.-U.; Jalett, H.-P.; Müller, M.; Studer, M. *Catal. Today* **1997**, *37* (4), 441–463.
105. Li, W.; Liang, C.; Zhou, W.; Qiu, J.; Zhou; Sun, G.; Xin, Q. *J. Phys. Chem. B* **2003**, *107* (26), 6292–6299.
106. Marković, N. M.; Schmidt, T. J.; Stamenković, V.; Ross, P. N. *Fuel Cells* **2001**, *1* (2), 105–116.
107. Stamenkovic, V. R.; Fowler, B.; Mun, B. S.; Wang, G.; Ross, P. N.; Lucas, C. A.; Marković, N. M. *Science* **2007**, *315* (5811), 493–497.
108. Babu, B. V. *Biofuels, Bioprod. Biorefin.* **2008**, *2* (5), 393–414.
109. Shen, D. K.; Xiao, R.; Gu, S.; Luo, K. H. *RSC Adv.* **2011**, *1* (9), 1641–1660.
110. Vuorema, A.; Sillanpaa, M.; Rassaei, L.; Wasbrough, M. J.; Edler, K. J.; Thielemans, W.; Dale, S. E. C.; Bending, S.; Wolverson, D.; Marken, F. *Electroanalysis* **2010**, *22* (6), 619–624.
111. Vuorema, A.; Shariki, S.; Sillanpaa, M.; Thielemans, W.; Nelson, G. W.; Foord, J. S.; Dale, S. E. C.; Bending, S.; Marken, F. *Phys. Chem. Chem. Phys.* **2011**, *13* (20), 9857–9862.
112. Vuorema, A.; Walsh, J. J.; Sillanpää, M.; Thielemans, W.; Forster, R. J.; Marken, F. *Electrochim. Acta* **2012**, 10.1016/j.electacta.2011.10.025.
113. Morandi, G.; Heath, L.; Thielemans, W. *Langmuir* **2009**, *25* (14), 8280–8286.
114. Nielsen, L. J.; Eyley, S.; Thielemans, W.; Aylott, J. W. *Chem. Commun.* **2010**, *46* (47), 8929–8931.
115. Eyley, S.; Thielemans, W. *Chem. Commun.* **2011**, *47* (14), 4177–4179.

Downloaded by PENNSYLVANIA STATE UNIV on August 28, 2012 | http://pubs.acs.org
Publication Date (Web): August 17, 2012 | doi: 10.1021/bk-2012-1107.ch005

Downloaded by NORTH CAROLINA STATE UNIV on August 28, 2012 | http://pubs.acs.org
Publication Date (Web): August 17, 2012 | doi: 10.1021/bk-2012-1107.ch006

Chapter 6

Synthesis and Properties of Cellulose Graft Copolymers with Well-Defined Architecture

Hongliang Kang,[1] Xia Gao,[2] Ruigang Liu,[*,1] and Yong Huang[1]

**[1]Labortory of Polymer Physics and Chemistry,
Beijing National Laboratory of Molecular Sciences,
Institute of Chemistry, Chinese Academy of Sciences,
2 Zhongguancun North 1st Street, Beijing 100190, China
[2]Beijing Centre of Physical and Chemical Analysis,
Beijing Academy of Sciences and Technology,
27 North-West 3rd Ring Road, Beijing 100089, China
[*]E-mail: rgliu@iccas.ac.cn**

Cellulose graft copolymers with well-defined architecture are synthesized by atom transfer radical polymerization (ATRP). Kinetic studies indicate that the ATRP graft copolymerization is living and controllable. The properties of the cellulose graft copolymers can be tailored by varying the structure of the cellulosic backbone, the chemical structure and length of the side chains, and the graft density. The cellulose graft copolymers can self-assemble into spherical micelles in selective solvents or can self-assemble with the trigger of temperature, pH, and ionic strength. The structure of the micelles depends on the medium, temperature and/or pH of the medium, and the chemical structure of the cellulosic backbone and the side chains. The cellulose graft copolymers have the promising applications as the carriers for drug control target delivery and biosensors.

In Functional Materials from Renewable Sources; Liebner, F., et al.;
ACS Symposium Series; American Chemical Society: Washington, DC, 2012.

Introduction

Cellulose is the most abundant natural resourced polymer that is mainly produced by photosynthesis in high plants (*1*). As biocompatible, biodegradable, renewable, and environmental friendly materials (*2–7*), cellulose and its derivatives have been widely used in industry, medical products, and domestic commodities. Cellulose cannot be melted or be dissolved in most organic solvents due to the intrinsically strong intra- and inter-molecular hydrogen bonds. Regenerated cellulose products, e.g. fibers and membranes, are mainly produced by the tedious and environmentally challenging viscose process. The efforts to find environmentally friendly processes to replace the viscose process for producing alternative cellulose products have never stopped. The studies on finding new solvent systems for dissolving cellulose have made a great progress. New cellulose solvent systems have been found, including *N*-methylmorpholine-*N*-oxide/water (NMMO/H_2O) (*1*, *8*), ionic liquids (*9–12*), and NaOH/urea (*13–15*), solvent systems for dissolving cellulose and manufacturing cellulosic products. The Lyocell process based on NMMO/H_2O as the direct solvent for cellulose for the production of cellulosic fibers has been commercialized in the 1990s.

Besides the progress on new solvent systems, cellulose functional materials based on cellulose derivatives and graft copolymers are also attracting increasing attention both in scientific research and industrial applications. Cellulose derivatives have been traditionally synthesized in heterogeneous systems. The finding of new solvent systems for dissolving cellulose also provides opportunities for synthesis of cellulose derivatives and graft copolymers in homogeneous systems (*16–21*). In the case of synthesis of cellulose graft copolymers, free radical graft copolymerization induced by radiation (*22–24*), sodium periodate (*25*), ceric ions (*26–28*) etc. have been used since the 1960s. The free radical graft copolymerization has the disadvantages of producing homopolymers, and the molecular weight and its distribution of the graft chains are uncontrollable. The macromolecular reaction has low reaction activity and graft efficiency.

The development of controllable/living radical polymerizations (CRP) (*29*), such as nitroxide-mediated polymerization (NMP) (*30*), atom transfer radical polymerization (ATRP) (*31–34*) and reversible addition-fragmentation chain transfer polymerization (RAFT) (*35*, *36*), offers versatile approaches for the synthesis of polymers with well-defined architecture. The CRP have been extended to synthesis of polysaccharide block and graft copolymers in homogeneous medium (*37–43*) or surface modification of polysaccharides substrates in heterogeneous medium (*7*, *37*, *44–54*). The application of ATRP for the modification of cellulose was first reported by Carlmark et al. (*7*, *55*) and were then expanded to surface modification of cellulosic materials (*44–47*, *56–60*) and the synthesis cellulose graft copolymers with well-defined architecture (*38–40*, *51–54*). In this chapter, the progress of the synthesis of cellulose graft copolymers by ATRP, the self-assembly behaviors, and the possible applications of the resultant cellulose graft copolymers will be reviewed.

Downloaded by NORTH CAROLINA STATE UNIV on August 28, 2012 | http://pubs.acs.org
Publication Date (Web): August 17, 2012 | doi: 10.1021/bk-2012-1107.ch006

Downloaded by NORTH CAROLINA STATE UNIV on August 28, 2012 | http://pubs.acs.org
Publication Date (Web): August 17, 2012 | doi: 10.1021/bk-2012-1107.ch006

Controllable Synthesis of Cellulose Graft Copolymers by ATRP

The typical synthesis route to cellulose graft copolymers with well-defined architecture is shown in Scheme 1. The cellulosic backbones can be cellulose or its derivatives, such as ethyl cellulose (EC), hydroxypropyl cellulose (HPC), diacetate cellulose (CDA), etc. Briefly, active sites for initiating ATRP reaction are first introduced onto the cellulose backbone, which is generally achieved by the esterification of hydroxyl on cellulose backbones with components that contain bromide groups, e.g. 2-bromoisobutyryl bromide. The graft density of the final graft copolymer is determined by the substitution degree of bromide groups (*DS*–$_{\mathrm{Br}}$). *DS*–$_{\mathrm{Br}}$ is defined as the number of active bromide groups per glucose ring, which can be tailored by varying the feeding ratio of 2-bromoisobutyryl bromide to the hydroxyl groups of cellulose or its derivatives. The ATRP graft copolymerization can be carried out by using Cu(I) as the catalyst. The ligands could be *N*,*N*,*N*′,*N*″,*N*″-pentamethyldiethylenetriamine (PMDETA), 2,2′-bipyridine, 1,1,4,7,10,10-hexamethyl-triethylenetetramine (HMTETA), tris[2-(dimethylamino)ethyl]amine (Me_6-TREN), and 4,4′-dinonyl-2,2′-dipyridyl (dNbpy), depending on the monomer and the reaction media that are used.

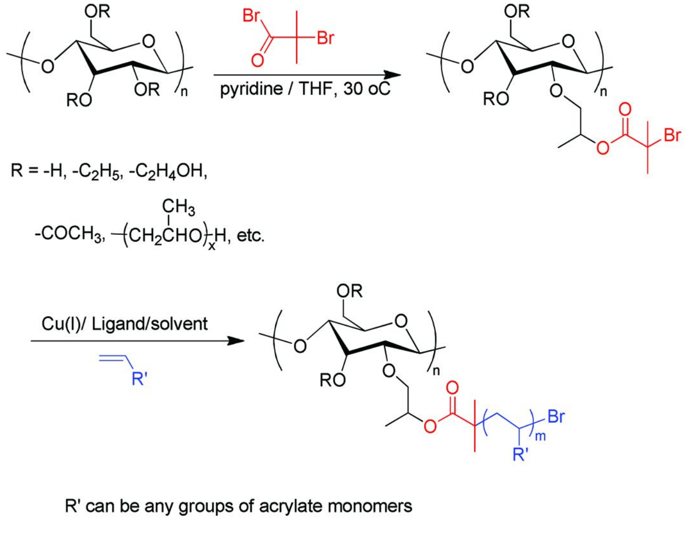

Scheme 1. Synthesis route to cellulose graft copolymers via ATRP.

Figure 1 shows the kinetics data for the synthesis of hydroxypropyl cellulose graft poly(*N*,*N*-dimethyl aminoethyl methacrylate) (HPC-*g*-PDMAEMA), which is typical for the ATRP graft copolymerization. The linear relationship of $\ln([M_0]/[M_t])$ versus the reaction time t indicates that the graft copolymerization follows first-order kinetics and the concentration of propagating radicals keeps constant (Figure 1a). Moreover, M_n of the PDMAEMA side chains, estimated by the combination of ^{1}H NMR and elemental analysis (EA), increases linearly with the monomer conversion during the polymerization of HPC-*g*-PDMAEMA (Figure 1b). These results suggest that the graft copolymerization is living and controllable (*61*).

In Functional Materials from Renewable Sources; Liebner, F., et al.;
ACS Symposium Series; American Chemical Society: Washington, DC, 2012.

Downloaded by NORTH CAROLINA STATE UNIV on August 28, 2012 | http://pubs.acs.org
Publication Date (Web): August 17, 2012 | doi: 10.1021/bk-2012-1107.ch006

By ATRP graft copolymerization, cellulose graft copolymers with well-defined architecture have been successfully synthesized. These graft copolymers are cellulose graft polystyrene (EC-*g*-PS) (*62–65*), ethyl cellulose graft poly (methyl methacrylate) (EC-*g*-PMMA) (*63*, *66*), ethyl cellulose grafting poly(acrylic acid) (EC-*g*-PAA) (*67*), ethyl cellulose graft poly(2-hydroxyethyl methacrylate) (EC-*g*-PHEMA) (*68*), ethyl cellulose graft poly(poly(ethylene glycol) methyl ether methacrylate) (EC-*g*-P(PEGMA)) (*69*, *70*), hydroxypropyl cellulose graft poly(*N*,*N*-dimethyl aminoethyl methacrylate) (HPC-*g*-PDMAEMA) (*61*), hydroxypropyl cellulose graft poly(4-vinyl pyridine) (HPC-*g*-P4VP) (*71*), poly(2-(diethylamino) ethyl methacrylate) (EC-*g*-PDEAEMA) (*72*). The kinetics of these cellulose graft copolymerizations also confirm the living and controllable ATRP reaction. The success of the synthesis of the graft copolymers can be confirmed by IR and ^{1}H NMR.

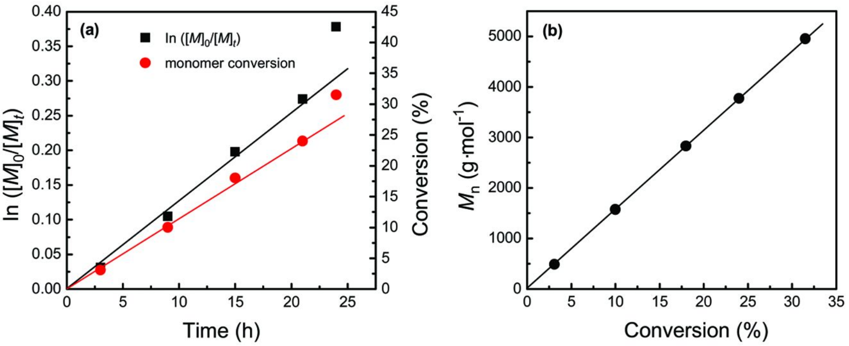

Figure 1. (a) Ln([M_0]/[M_t]) and monomer conversion versus reaction time for the ATRP of DMAEMA initiated by HPC-Br (DS = 0.1); (b) M_n of the PDMAEMA side chains versus the monomer conversion, feeding ratio [M]:[I]:[CuCl]:[HMTETA] = 100:1:1:1 at 30 °C. (Reproduced with permission from reference (61). Copyright 2010 ACS.)

Self-Assembly and Stimuli-Responsive Properties of Cellulose Graft Copolymers

The synthesized cellulose graft copolymers with different properties between the backbone and side chains can self-assemble into micelles with different structure and morphology. The core of the micelles can be the cellulose backbone with the side chains mainly staying on the surface of the micelles, or vice versa, depending on the properties of the graft copolymer, the medium, and the pH and temperature of the medium. The amphiphilic cellulose graft copolymers have been synthesized including EC-*g*-PAA, EC-*g*-PHEMA, EC-*g*-P(PEGMA), and EC-*g*-PDEAEMA. These graft copolymers can self-assemble into micelles with hydrophobic core that stabilized with hydrophilic side chains as the shell. When hydroxypropyl cellulose (HPC) was used as the backbone, the HPC itself is thermo-sensitive, which is generally applied for the synthesis of dual stimuli responsive cellulose graft copolymers, such as HPC-*g*-PDMAEMA and HPC-*g*-P4VP. These cellulose graft copolymers can form micelles with different architecture depending the temperature and pH of the medium.

Figure 2 shows the self-assembly of the dense graft copolymers EC-*g*-PS in acetone. The micelles are of spherical shape. The size of the resultant micelles increases with increasing the copolymer concentration and the PS side-chain length. Due to the fact that acetone is a relatively good solvent for ethyl cellulose, the micelles have a core-shell structure with the ethyl cellulose main chains in the shell and the side polystyrene chains in the core of the micelles.

Downloaded by NORTH CAROLINA STATE UNIV on August 28, 2012 | http://pubs.acs.org
Publication Date (Web): August 17, 2012 | doi: 10.1021/bk-2012-1107.ch006

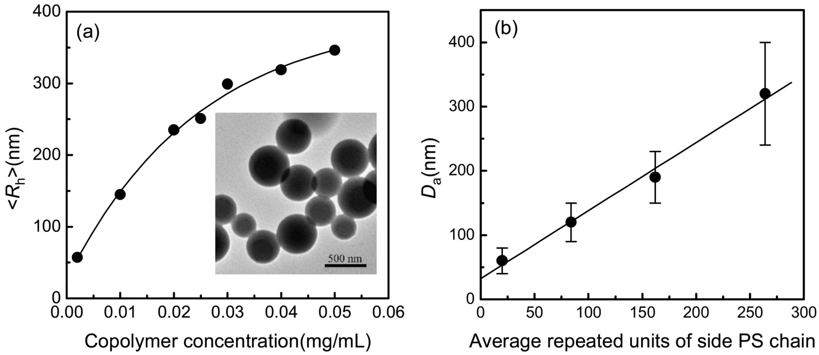

Figure 2. Core-shell micelles of EC-g-PS self-assemble in acetone. (a) <R_h> as a function of polymer concentration (DLS data, $EC_{0.5}$-g-PS_{128}) and (b) dependence of the micelles size on the side chain length (TEM data, graft density: 0.5 PS chains per glucose ring of the cellulose backbone). Inset: typical TEM image of the micelles. (Reproduced with permission from reference (64). Copyright 2009 Elsevier.)

With hydrophilic side chains and the hydrophobic cellulosic backbones, the graft copolymers can self-assemble into micelles in aqueous medium, in which the hydrophobic cellulosic backbones are located in the core of the micelles and the hydrophilic side chains are mainly on the surface of the micelles. A typical example are ethyl cellulose graft poly(poly(ethylene glycol) methyl ether methacrylate) (EC-*g*-P(PEGMA)) copolymers, which can self-assemble into spherical micelles in water (*69*). The size of the micelles increases with the increase of the side chain length. The spherical micelles show thermo-sensitive properties with a lower critical solution temperature around 65 °C, which is almost independent of the graft density and the length of the side chains (*69*). Figure 3 shows the hydrodynamic radius (<R_h>) and the transmittance of copolymers $EC_{0.2}$-*g*-P(PEGMA)$_{27}$ and $EC_{0.02}$-*g*-P(PEGMA)$_{185}$ as a function of the temperature. Both <R_h> and transmittance curves show a sharp transition during heating, and the transition occurs at almost the same temperature. The phase transition attributes to a subtle hydrophilic-hydrophobic equilibrium for the hydrogen bonding interaction between the copolymers and water molecules. When the temperature increased above the LCST, hydrogen bonds between ether oxygen atoms of P(PEGMA) and water are broken, and the P(PEGMA) side

Downloaded by NORTH CAROLINA STATE UNIV on August 28, 2012 | http://pubs.acs.org
Publication Date (Web): August 17, 2012 | doi: 10.1021/bk-2012-1107.ch006

chains collapse and become hydrophobic. So, the intermolecular hydrophobic attractions are thermodynamically favored and micelle aggregates occur, which result in the increase in <R_h> and a visible turbidity. Moreover, the profiles of the transmittance of heating and cooling processes are overlapping each other, which indicates that the phase transition of the micelles is reversible. The inter-chain interactions from the weaker van der Waals forces stabilize the aggregates, which provide the reversible phase transition. The results indicate that the LCSTs of the dense graft copolymers are slightly lower than that of sparse graft copolymers and almost independent of the length of side chain (*69*).

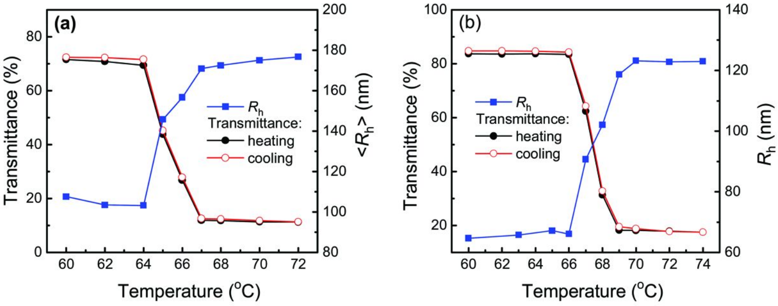

Figure 3. <R_h> and transmittance as a function of temperature. (a) $EC_{0.2}$-g-$P(PEGMA)_{27}$ and (b) $EC_{0.02}$-g-$P(PEGMA)_{185}$. Polymer concentration: 1.0 mg/mL in water. (Reproduced with permission from reference (69). Copyright 2008 Wiley.)

For the cellulose graft copolymers with dual stimuli-responsive properties, micelles with different structure can self-assemble and the resultant micelles show stimuli-responsive properties. Figure 4 shows the transmittance of the $HPC_{0.1}$-*g*-$PDMAEMA_{20}$ aqueous solution at different pH values as a function of temperature and the LCST as a function of pH values (*61*). It is known that PDMAEMA (p*K*a ≈ 8.0) (*73*) can be protonated in acidic aqueous solution, which leads to the increase in the electrostatic repulsive forces and prevents phase separation (*74*). Therefore, the LCST of $HPC_{0.1}$-*g*-$PDMAEMA_{20}$ copolymer shifts to a higher temperature with decreasing pH values of the solutions (Figure 4b), which is similar to tendency of the LCST of $PDMAEMA_{108}$ homopolymer reported in literature (*73*). However, the change of LCST of the graft copolymer is not as obvious as that of the homopolymer, which may be due to the fact that the side chains only have an average of 20 repeating units, which is much shorter than the PDMAEMA108. Moreover, in copolymer solutions at a low pH value, e.g. 3.0 and 6.5, the transmittance of the solutions only decreases to around 90% and 80%, respectively (Figure 4a), which is due to stable micelles forming at low pH, in which the protonated PDMAEMA side chains are in the shell of the micelles (*61*).

Downloaded by NORTH CAROLINA STATE UNIV on August 28, 2012 | http://pubs.acs.org
Publication Date (Web): August 17, 2012 | doi: 10.1021/bk-2012-1107.ch006

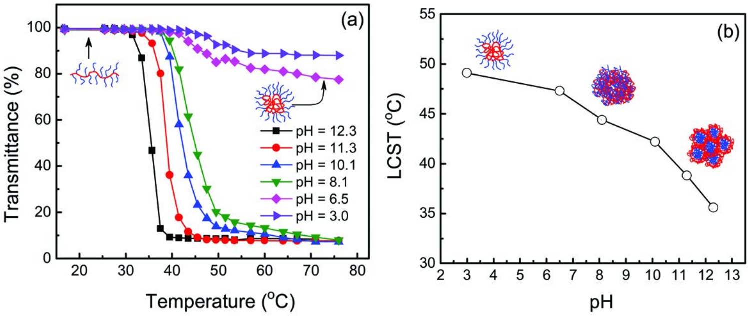

Figure 4. Transmittance of HPC$_{0.1}$-g-PDMAEMA$_{20}$ in aqueous solution at different pH values as a function of temperature (a). LCST of HPC$_{0.1}$-g-PDMAEMA$_{20}$ graft copolymer as a function of the pH value (b). (Reproduced with permission from reference (61). Copyright 2010 ACS.)

Solution ^{1}H NMR has been used to study the core-shell structure of block copolymer micelles (*75–77*). As the core of the micelles is in an aggregated state, the signals of the core-forming block chains are weakened or even disappear, depending on the density of the cores. Figure 5 shows ^{1}H NMR spectra of the HPC$_{0.1}$-*g*-PDMAEMA$_{20}$ graft copolymer in D_2O at different temperatures at pH 3.0, 8.1, and 12.3. At low pH values, e.g. pH 3.0, the intensity of the peaks for HPC backbone (***e*** and the glucose ring in Figure 5a) decreases at 45 °C, near the LCST of HPC, compared to the peaks at 25 °C, and disappears at further rising the temperature to 60 °C, whereas the peaks for the PDMAEMA side chains remains unchanged at all the temperatures (***a, b, c, d*** in Figure 4a). It is known that PDMAEMA (p*K*a ≈ 8.0) is a weak polyelectrolyte and can be protonated in acidic aqueous solutions (*73*, *74*). The LCST of PDMAEMA shifts to higher temperature with decreasing pH due to the protonation of PDMAEMA chains, which leads to an increase in the electrostatic repulsive force and prevent the phase separation. The protonated PDMAEMA will not possess an LCST anymore (*73*, *78*). Therefore, when the HPC$_{0.1}$-*g*-PDMAEMA$_{20}$ acid aqueous solutions are heated, the HPC backbone collapse to form the core of the micelles that is stabilized by the hydrophilic PDMAEMA side chains as the shell. When HPC$_{0.1}$-*g*-PDMAEMA$_{20}$ copolymers were directly dissolved in deuterated water at pH 8.1, the intensity of the peaks for both HPC backbone and PDMAEMA side chain decreases simultaneously upon heating (Figure 5b), which indicates that both the HPC backbone and the PDMAEMA side chain collapse with increasing temperature. We also observed that the solution is unstable and precipitates are formed during heating. At high pH value, pH 12.3, the intensity of the peaks for PDMAEMA side chain disappeared at 37 °C, whereas the intensity of the peaks of HPC backbone decreased slightly (Figure 5c), indicating that PDMAEMA side chain aggregated to the core of micelles and the HPC backbone mainly as the shell to stabilize the micelles. At an even higher temperature above the LCST of HPC, e.g. 60 °C, the peaks for both HPC and PDMAEMA disappeared, which indicates that the shell HPC aggregated and lost the ability to stabilize the micelles (*61*).

Downloaded by NORTH CAROLINA STATE UNIV on August 28, 2012 | http://pubs.acs.org
Publication Date (Web): August 17, 2012 | doi: 10.1021/bk-2012-1107.ch006

Figure 6 shows the R_h of HPC$_{0.1}$-*g*-PDMAEMA$_{20}$ in aqueous solution at a concentration of 2 mg/mL at various temperatures. At the lower pH value (pH 3.0), the R_h value increases slightly, and the turning point is about 42 °C. Further increase in temperature leads to a slight decrease of R_h, which might be due to the shrinkage of the HPC core upon heating. In contrast, the R_h increases sharply and the turning point shifts to lower temperature with the increase in pH value. DLS experiments confirm the results of the transmittance experiments. The dual stimuli responsive properties of the HPC-*g*-PDMAEMA graft copolymers can be summarized schematically as in the right of Figure 6. In summary, at low pH, e.g. 3.0, the HPC backbone of the copolymer collapse to form the core of micelles stabilized with protonated PDMAEMA side chains on the surface of the micelles upon heating. At the medium pH, e.g. 8.1, both HPC backbone and PDMAEMA side chains collapse upon heating to form unstable aggregates. At high pH, e.g. 12.3, PDMAEMA side chains collapse first to form the core of micelles stabilized with HPC chains upon heating. Further heating the copolymer solution at this pH leads to the aggregation of the micelles due to the collapse of the shell HPC chains. The thermal sensitivity of the HPC-*g*-PDMAEMA copolymers is reversible (*61*).

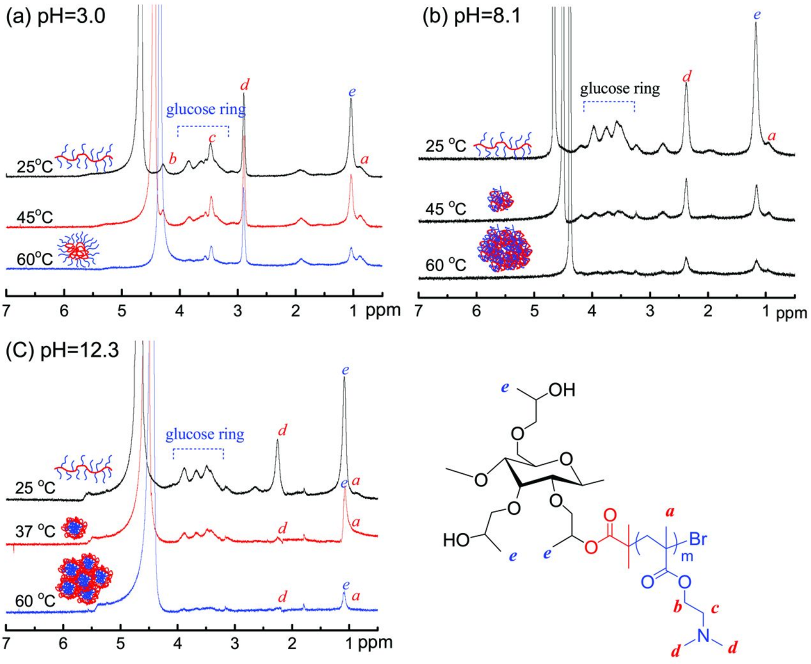

Figure 5. Temperature dependence of ^1H NMR spectra of the HPC$_{0.1}$-g-PDMAEMA$_{20}$ solutions in D$_2$O at pH (a) 3.0, (b) 8.1, and 12.3. (Reproduced with permission from reference (61). Copyright 2010 ACS.)

Downloaded by NORTH CAROLINA STATE UNIV on August 28, 2012 | http://pubs.acs.org
Publication Date (Web): August 17, 2012 | doi: 10.1021/bk-2012-1107.ch006

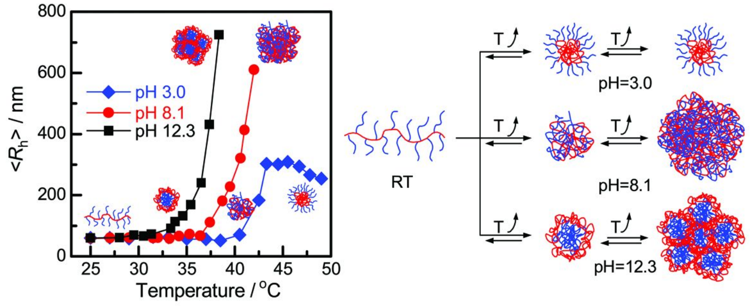

Figure 6. Temperature dependence of the average hydrodynamic radius R_h of $HPC_{0.1}$-g-$PDMAEMA_{20}$ in aqueous solution at different pH values. (Reproduced with permission from reference (61). Copyright 2010 ACS.)

HPC-*g*-P4VP graft copolymers also show thermal and pH stimuli-responsive properties (*71*). Figure 7 show the dependence of the transmittance of the graft copolymer and P4VP solutions on the pH values of the solutions. All the solutions are clear at a pH below 4, whereas the transmittance of the solutions of $HPC_{0.05}$-*g*-$P4VP_{35}$ and P4VP start to decrease sharply at pH of 4.5 and 4, respectively. However, P4VP precipitated at pH of 4.8, whereas the $HPC_{0.05}$-*g*-$P4VP_{35}$ solution becomes bluish and its transmittance was independent on the pH value at pH ≥ 6, which indicates micelle formation at pH > 6.0. The P4VP side chains become hydrophobic due to the deprotonation, while the HPC backbones are still hydrophilic. Therefore, stable micelles were formed by the aggregation of the hydrophobic P4VP side chains as the core and the hydrophilic HPC backbones are in the shell of the micelles. For comparison, graft copolymers with very short side chains, e.g. $HPC_{0.05}$-*g*-$P4VP_3$ were also investigated by transmittance experiments. The solution was highly transparent and no obvious cloud point was observed. This is due to the short P4VP side chain and the low molar content of the P4VP side chains which cannot form efficiently large aggregates.

Dynamic light scattering results are shown in Figure 8. It can be seen that $<R_h>$ and I_1/I_0 are very low and remain invariant at the pH < 4.While both I_1/I_0 and $<R_h>$ jump sharply at around pH of 5.1. I_1/I_0 increases by about a factor of 30, and $<R_h>$ rises to about 190 nm when pH increases to 6, which is due to the P4VP side chains becoming hydrophobic with rising pH value and aggregating into the core of micelles that are stabilized with the hydrophilic HPC backbones. Both the I_1/I_0 and $<R_h>$ stay invariant over a wide pH range of 6-12, which demonstrates that the hydrophilic HPC backbone can efficiently stabilize the hydrophobic P4VP core and prevent the aggregates from precipitating.

The structure of the pH-induced micelles was investigated by ^1H NMR (Figure 9). At low pH (pH 1.2), the characteristic peaks of both P4VP side chains at 8.3, 6.6 and 1.5 ppm and HPC back bones at 3-5 and 1.1 ppm appear in the ^1H NMR spectrum of the HPC-*g*-P4VP graft copolymers (Figure 9a), which indicates that both the HPC back bones and P4VP side chains are soluble at a pH below the pK_a of P4VP. The peaks coming from the protons of P4VP side chains at 8.3, 6.6 and 1.5 ppm decrease with increasing pH of the solution. These peaks become quite weak at pH 4.8 (Figure 9b) and totally disappear at pH 7.4 (Figure 9c). However, no obvious change can be observed for the peaks from the protons of HPC backbone at 3-5 and 1.1 ppm. The results suggest that P4VP side chains collapse to form the core of the micelles and the HPC backbones stay in the shell to stabilize the micelles. The pH-induced micelles is quite stable. The size and the size distribution of the micelles remained unchanged after the micelles of the graft copolymer at pH 7.4 were stored at 25 °C for one month (Figure 10).

Downloaded by NORTH CAROLINA STATE UNIV on August 28, 2012 | http://pubs.acs.org
Publication Date (Web): August 17, 2012 | doi: 10.1021/bk-2012-1107.ch006

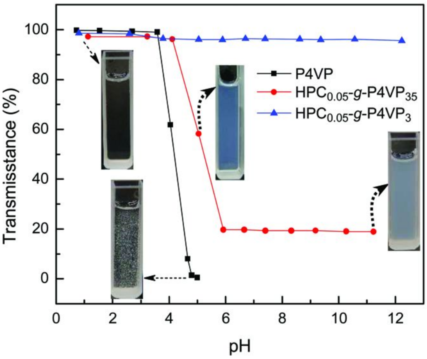

Figure 7. Transmittance of HPC$_{0.05}$-g-P4VP graft copolymers and P4VP aqueous solution at different pH values. (Reproduced with permission from reference (71). Copyright 2010 ACS.)

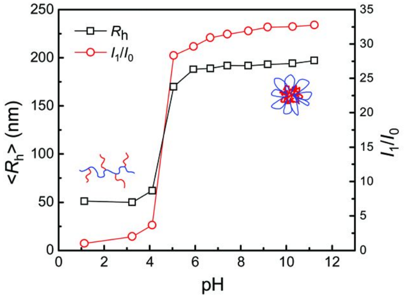

Figure 8. I_1/I_0 and $<R_h>$ of HPC$_{0.05}$-g-P4VP$_{35}$ as a function of pH at 25 °C. (Reproduced with permission from reference (71). Copyright 2010 ACS.)

Downloaded by NORTH CAROLINA STATE UNIV on August 28, 2012 | http://pubs.acs.org
Publication Date (Web): August 17, 2012 | doi: 10.1021/bk-2012-1107.ch006

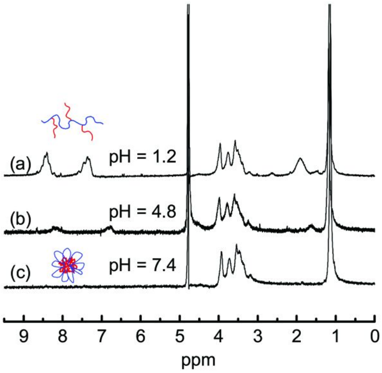

Figure 9. ^{1}H NMR spectra of HPC$_{0.05}$-g-P4VP$_{35}$ aqueous solutions (1 mg/mL) at pH of (a) 1.2, (b) 4.8, and (c) 7.4. The spectra were recorded at 25 °C. (Reproduced with permission from reference (71). Copyright 2010 ACS.)

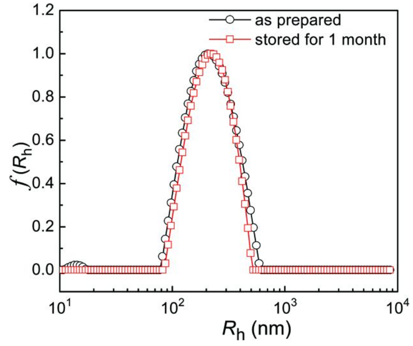

Figure 10. Size distributions of the as-prepared micelles and the micelle solution stored at 25 °C and pH of 7.4 for one month, concentrations 1 mg/mL. (Reproduced with permission from reference (71). Copyright 2010 ACS.)

The thermally induced micelle formation of HPC-*g*-P4VP has also been investigated systematically (*71*). Figure 11a shows the transmittance of HPC-g-P4VP copolymers in aqueous solution as a function of temperature at pH 1.2. The transmittance of the HPC-*g*-P4VP solutions decreases at a temperature above the LCST of HPC. Moreover, the solutions become less opaque with the increase in the length of P4VP side chains. The cloud point of all the graft copolymers is higher than that of HPC and shifts to a higher temperature with

Downloaded by NORTH CAROLINA STATE UNIV on August 28, 2012 | http://pubs.acs.org
Publication Date (Web): August 17, 2012 | doi: 10.1021/bk-2012-1107.ch006

increasing the graft length (Figure 11b). DLS results indicate that the sharp increase in <R_h> and the scattering intensity occur at about the cloud point of the graft copolymers HPC$_{0.05}$-*g*-P4VP$_{35}$ (Figure 12). The <R_h> increases from 40 nm to about 180 nm, and I_1/I_0 increases by about a factor of 50. The <R_h> and I_1/I_0 remain at a constant value with further increase of the temperature of the solution, which indicates that P4VP can effectively stabilize the micelles in acidic solution. The structure of the thermally induced micelles of HPC-*g*-P4VP graft copolymers was investigated by ^{1}H NMR in D_2O. It was found that the peaks from protons on the HPC backbones (around 1.1, 3.0-5.0 ppm) are largely shielded due to the phase transition of HPC backbone above its LCST. However, the peaks from the protons of P4VP side chains (at about 8.3, 6.6, and 1.5 ppm) are clear over the measured temperature range (Figure 13). The ^{1}H NMR results suggest that HPC collapsed to form the core of the micelles that are stabilized with the protonated P4VP side chains in the shell.

For HPC-*g*-P4VP graft copolymer with short side P4VP chains, e.g. HPC$_{0.05}$-*g*-P4VP$_3$, the cloud point depends on the pH value. The cloud point of the copolymer shifts to lower temperature with the increase in pH, which may attribute to the deprotonation of P4VP side chains (Figure 14). The HPC$_{0.05}$-*g*-P4VP$_{35}$ copolymer shows both pH- and thermo-induced micelle formation in aqueous solution, in which P4VP side chains are the core and HPC backbones the shell, or vice versa. The pH- or thermo-induced micelles are prospected to have thermal or pH sensitivity.

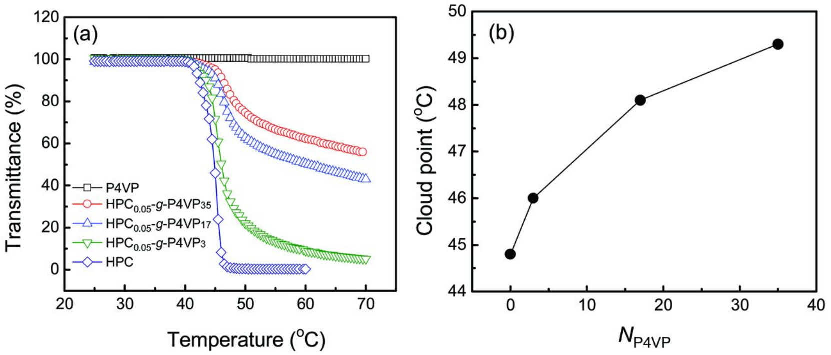

Figure 11. (a) Transmittance of HPC$_{0.05}$-g-P4VP, HPC and P4VP aqueous solutions as a function of temperature at pH 1.2 and (b) the cloud point as a function of the length of P4VP side chains. (Reproduced with permission from reference (71). Copyright 2010 ACS.)

Downloaded by NORTH CAROLINA STATE UNIV on August 28, 2012 | http://pubs.acs.org
Publication Date (Web): August 17, 2012 | doi: 10.1021/bk-2012-1107.ch006

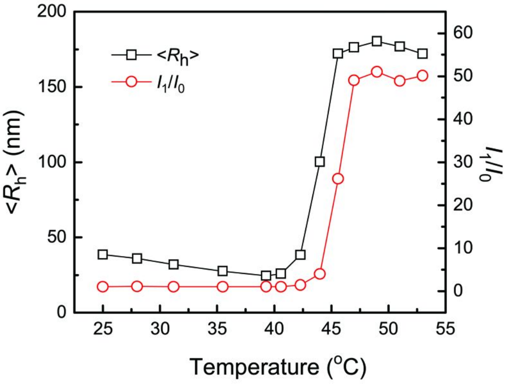

Figure 12. I_1/I_0 and <R_h> of $HPC_{0.05}$-g-$P4VP_{35}$ as a function of temperature at pH 1.2. (Reproduced with permission from reference (71). Copyright 2010 ACS.)

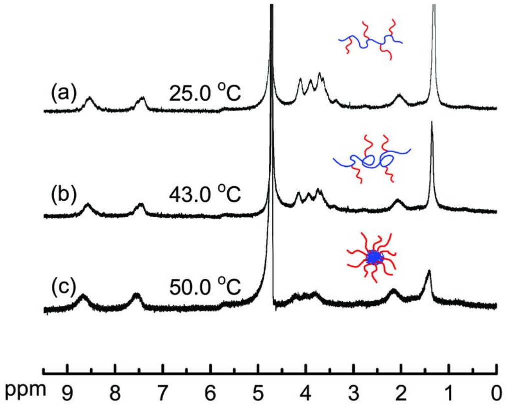

Figure 13. ^1H NMR spectra of $HPC_{0.05}$-g-$P4VP_{35}$ at pH 7.4 at temperature (a) 25, (b) 41, (c) 43, and (d) 47 °C. (Reproduced with permission from reference (71). Copyright 2010 ACS.)

Downloaded by NORTH CAROLINA STATE UNIV on August 28, 2012 | http://pubs.acs.org
Publication Date (Web): August 17, 2012 | doi: 10.1021/bk-2012-1107.ch006

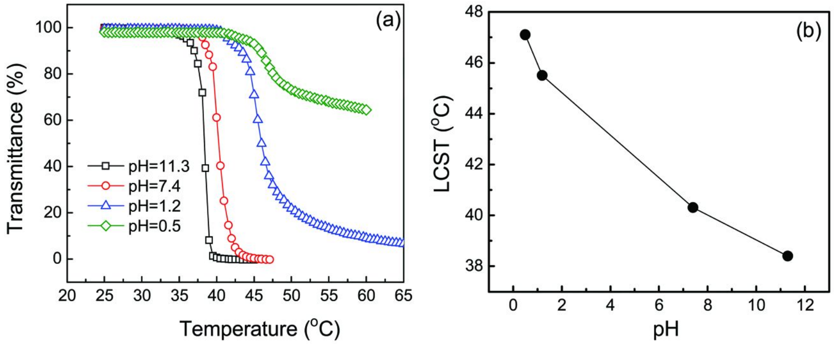

Figure 14. (a) Transmittance of $HPC_{0.05}$-g-P4VP3 aqueous solutions as a function of temperature at different pH values and (b) cloud point as a function of pH values. (Reproduced with permission from reference (71). Copyright 2010 ACS.)

Potential Applications of the Cellulose Graft Copolymers

Cellulose graft copolymers have some potential applications, e.g. ordered microporous thin films, micelles for controlled drug release. Figure 15 shows the morphology of the microporous films prepared from copolymer $EC_{0.5}$-*g*-PS_{84}/CS_2 solutions with a different polymer concentration. The RH of the atmosphere was adjusted at 72%. The results show that the average pore size of the obtained film decreased from 4.0 μm to 100 nm when the polymer concentration increased from 1 to 20 g/L. The porous size of the porous films is also dependent on the length of the side chain of EC-*g*-PS. Figure 16 shows the SEM images of the microporous films prepared from the solutions of EC-*g*-PS copolymers with different side chain length (DP_{St}). The copolymer concentration in CS_2 solutions was set at 10 g/L and the RH was set at 72%. In the case of the copolymer with the longest side chain, $EC_{0.5}$-*g*-PS_{256} (DP_{st} = 256), the disordered porous film can be obtained and the pore size has a wide distribution. The relative ordered structure could be obtained from the copolymer $EC_{0.5}$-*g*-PS_{162} with relative shorter side chain (DP_{st} = 162) than that of copolymer $EC_{0.5}$-*g*-PS_{256} and the average diameter of pore is about 700 nm. Specifically, hexagonal pore morphology was observed (Figure 16d) in the film prepared from the copolymer $EC_{0.5}$-*g*-PS_{20} with the shortest side chain (DP_{st} = 20), which is different from the circular pores in the films prepared from copolymer $EC_{0.5}$-*g*-PS_{256}, $EC_{0.5}$-*g*-PS162, and $EC_{0.5}$-*g*-PS_{84}. The micro-pores are well arranged and the pores have an average size of 1.65 μm (*65*).

As discussed in the previous section, amphiphilic cellulose graft copolymers, such as EC-*g*-PPEGMA, can self-assemble into core-shell micelles in aqueous media. Such micelles can be used as the carrier for controlled drug release. Table 1 lists the loading of pyrene as the model drug in EC-*g*-PPEGMA micelles. Generally, the copolymers with lower graft density or shorter side chains have a higher loading efficiency and probe content, which attributes to the relatively higher content of the hydrophobic EC backbone that has a better compatibility

Downloaded by NORTH CAROLINA STATE UNIV on August 28, 2012 | http://pubs.acs.org
Publication Date (Web): August 17, 2012 | doi: 10.1021/bk-2012-1107.ch006

with pyrene at lower graft density. Moreover, higher graft density is the dominant factor of loading efficacy and probe content. For example, the graft copolymers $EC_{0.15}$-*g*-$PPEGMA_{13.4}$ and $EC_{0.04}$-*g*-$PPEGMA_{12.8}$ with almost the same side chain length and different graft density showed an obvious difference in the loading efficiency and probe content which may attribute to the higher flexibility, hydrophobicity and compatibility with pyrene for the EC backbone chains at lower DS. Besides the structure of the graft copolymers, the loading efficiency also depends on the feeding ratio of the graft copolymer to pyrene. For the graft copolymer of $EC_{0.04}$-g-$PPEGMA_{6.6}$ - when the feeding ratio of graft copolymer to pyrene is changed from 5:1 to 10:1 - the loading efficiency is increased from 17.7% to 24.4%. For the copolymer of $EC_{0.04}$-g-$PPEGMA_{12.8}$, the loading efficiency is increased from 16.3% to 28.3% when the feeding ratio of copolymer to pyrene is changed from 5:1 to 10:1. However, the increase in the feeding ratio of the graft copolymer to pyrene has no obvious effect on the loading capacity in the micelles. The loading efficiency increases with increasing polymer-to-pyrene ratio. However, the loading capacity in the micelles was mainly determined by the structure and the property of the graft copolymer and partition coefficient of pyrene in the micelles (*70*).

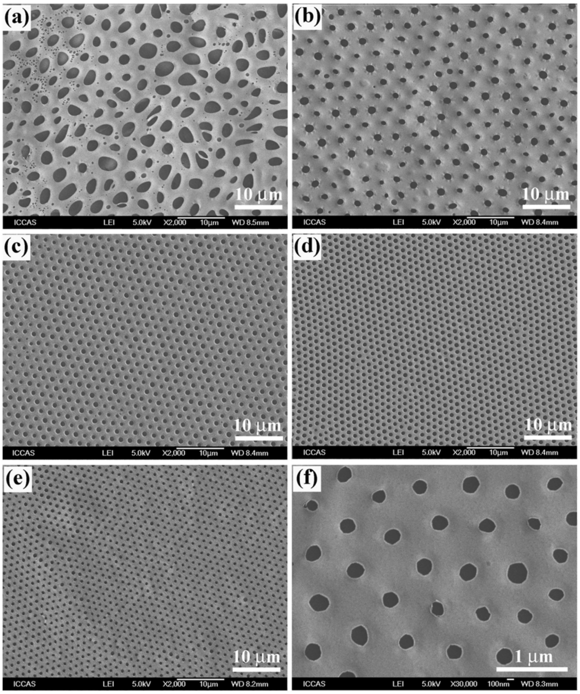
(a)
10 µm
ICCAS LEI 5.0kV X2,000 10µm WD 8.5mm
(b)
10 µm
ICCAS LEI 5.0kV X2,000 10µm WD 8.4mm
(c)
10 µm
ICCAS LEI 5.0kV X2,000 10µm WD 8.4mm
(d)
10 µm
ICCAS LEI 5.0kV X2,000 10µm WD 8.4mm
(e)
10 µm
ICCAS LEI 5.0kV X2,000 10µm WD 8.2mm
(f)
1 µm
ICCAS LEI 5.0kV X30,000 100nm WD 8.3mm

Figure 15. SEM images of porous films prepared from copolymer $EC_{0.5}$-g-PS_{84}/CS_2 solutions with a copolymer concentration of (a) 1, (b) 2, (c) 5, (d) 10, (e) 15, and (f) 20 g/L at RH of 72%. (Reproduced with permission from reference (65). Copyright 2009 Elsevier.)

Downloaded by NORTH CAROLINA STATE UNIV on August 28, 2012 | http://pubs.acs.org
Publication Date (Web): August 17, 2012 | doi: 10.1021/bk-2012-1107.ch006

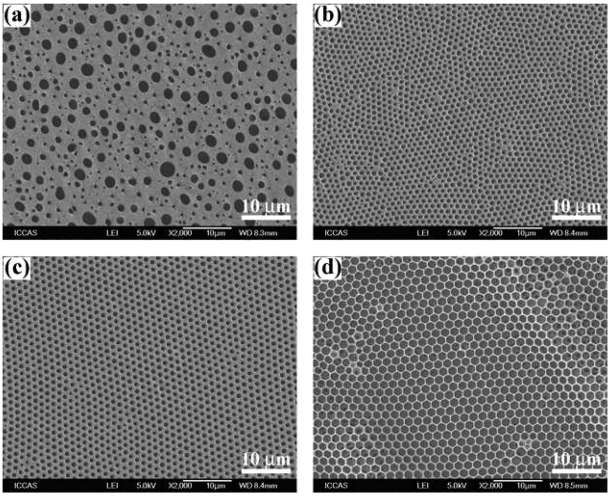

Figure 16. SEM images of porous films prepared from copolymer (a) $EC_{0.5}$-g-PS_{256}, (b) $EC_{0.5}$-g-PS_{162}, (c) $EC_{0.5}$-g-PS_{84}, and (d) $EC_{0.5}$-g-PS_{20} CS_2 solutions at RH of 72%. The copolymer concentration is kept at 10 g/L. (Reproduced with permission from reference (65). Copyright 2009 Elsevier.)

Table 1. Details of EC-g-PPEGMA copolymers, loading efficiency and probe content of EC-g-PPEGMA micelles

Sample	*Graft density* [a]	*Side chain length* [b]	W_{polym}/W_{py}[c]	*Loading eff. (%)*	*Probe cont. (%)*
$EC_{0.15}$-g-$PPEGMA_{2.9}$	0.15	2.9	5:1	7.6	1.5
$EC_{0.15}$-g-$PPEGMA_{13.4}$	0.15	13.4	5: 1	4.3	0.6
$EC_{0.04}$-g-$PPEGMA_{6.6}$	0.04	6.6	5:1 10:1	17.7 24.4	4.4 4.2
$EC_{0.04}$-g-$PPEGMA_{12.8}$	0.04	12.8	5:1 10:1	16.3 28.3	2.8 4.1

[a] Average graft of side chains. [b] Average repeating unit method. [c] Mass feeding ratio of graft copolymer to pyrene in the preparation of pyrene-loaded micelles by dialysis, chains per glucose ring of EC backbone.

Figure 17 shows the hydrodynamic radius ($<R_h>$) distribution of the pure micelles and pyrene-loaded micelles of the graft copolymer $EC_{0.04}$-*g*-$PPEGMA_{12.8}$ and $EC_{0.04}$-*g*-$PPEGMA_{6.6}$. The results indicate that all the micelles have the good unimodal size distribution. For the sample $EC_{0.04}$-*g*-$PPEGMA_{12.8}$, the average hydrodynamic radius $<R_h>$ of the pure micelle is about 31 nm , while $<R_h>$ of the pyrene-loaded micelles is 52 nm and 62 nm, for a pyrene content of 2.8% and 4.1%, respectively, which is much larger than that of the pure micelles. For the sample $EC_{0.04}$-*g*-$PPEGMA_{12.8}$, the average hydrodynamic radius $\langle R_h \rangle$ of the pure micelle is about 54 nm and $\langle R_h \rangle$ of the pyrene-loaded micelles is 156nm for a pyrene content of 4.2%. The increase of the $\langle R_h \rangle$ of the micelle with increasing pyrene content results from the solubilized pyrene in the hydrophobic core of the micelle. Moreover, whatever the blank micelles and pyrene loading micelles, the side chain length of the graft copolymer evidently affects the $\langle R_h \rangle$ of the micelles. The $\langle R_h \rangle$ of micelles of $EC_{0.04}$-*g*-$PPEGMA_{6.6}$ is larger than the micelles of $EC_{0.04}$-*g*-$PPEGMA_{12.8}$. Therefore, the $EC_{0.04}$-*g*-$PPEGMA_{6.6}$ micelles contain more molecules of copolymer.

Downloaded by NORTH CAROLINA STATE UNIV on August 28, 2012 | http://pubs.acs.org
Publication Date (Web): August 17, 2012 | doi: 10.1021/bk-2012-1107.ch006

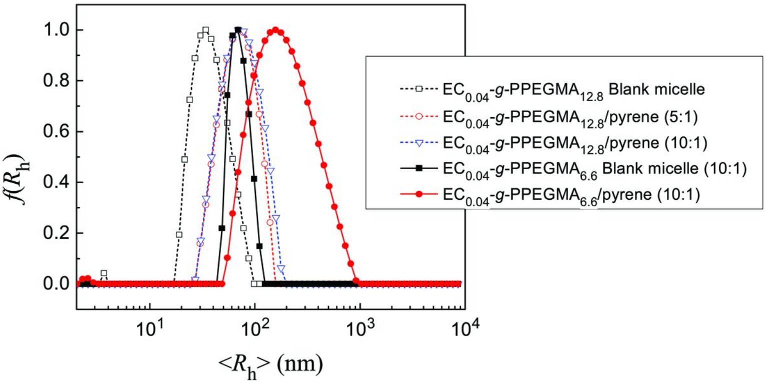

Figure 17. Hydrodynamic radius distribution of the self-assembled blank micelle and pyrene-loaded micelle at copolymer to pyrene ratio of 5:1 and 10:1. All the measurements were carried out at a scattering angle of 90° and at a temperature of 25 °C. (Reproduced with permission from reference (70). Copyright 2010 Elsevier.)

The release of pyrene from copolymer micelles (average graft density of 0.04) with different graft length and at a ratio of W_{polym}/W_{py} was investigated in PBS solutions at 37°C under constant stirring. The release of pyrene to the PBS solution as a function of time is shown in Figure 18. When the pyrene-loaded micelles was dialyzed against PBS solution, pyrene will diffuse into the PBS solution due to concentration gradient. All pyrene-loaded micelles show a two-step release profile, i.e. an initial burst release in the 1st hour and then a sustained release for a long time. The burst release of pyrene may be caused by the diffusion of absorbed pyrene from the hydrophilic corona of the micelle and then the followed sustained release may be dominated by the pyrene from the hydrophobic core of the micelles. The pyrene in the micelle of $EC_{0.04}$-*g*-$PPEGMA_{6.6}$ showed a slower release than that in the micelle of $EC_{0.04}$-*g*-$PPEGMA_{12.8}$, which is due to the higher pyrene probe content in the $EC_{0.04}$-*g*-$PPEGMA_{6.6}$ micelles. The release rate can be controlled by changing the ratio of copolymer to pyrene for a graft copolymer with same graft length. The results mentioned above suggest that EC-*g*-PPEGMA copolymers might be used as a good carrier material for the sustained release of hydrophobic drugs (*70*).

Downloaded by NORTH CAROLINA STATE UNIV on August 28, 2012 | http://pubs.acs.org
Publication Date (Web): August 17, 2012 | doi: 10.1021/bk-2012-1107.ch006

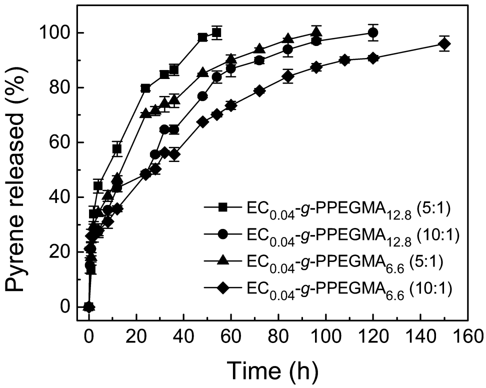

Figure 18. The release profile of pyrene from EC-g-PPEGMA micelles to phosphate buffer solution (PBS) (pH 7.4) as a function of time at 37 °C. (Reproduced with permission from reference (70). Copyright 2010 Elsevier.)

EC-*g*-PDEAEMA graft copolymer micelles can also be used as the drug carrier. The cumulated release of the model rifampicin (RIF) in the buffer solution at pH 6.6 is higher than that at pH 7.4 (*72*).

Redox groups can be introduced in the cellulose graft copolymers, which can be used for application as functional materials for the decoration of electrodes that can be used as biosensors. Figure 19 shows the HPC-*g*-P4VP copolymers conjugated with Os(bipyridine) (HPC-*g*-P4VP-Os(bpy). The copolymers have pH-dependent redox properties and have a wide working window. The cyclic voltammograms of the HPC-*g*-P4VP-Os(bpy) modified electrode shows switchable property and is reproducible for several circles. At low pH (e.g. 5.6), the electrochemical activity of the HPC-*g*-P4VP-Os(bpy) modified electrode is better than that at higher pH (e.g. 10), which is due to collapse of the P4VP side chain, and the electrochemical activity of the electrode is reduced as a result. However, the hydrophilic property of backbone still maintains the electrochemical process.

Figure 20a shows the cyclic voltammograms of HPC-*g*-P4VP-Os(bpy) modified electrode in the solutions with and without glucose. The oxidation of glucose is catalyzed by glucose oxidase (GOx). It is shown that the anodic electrocatalytic current corresponds to the oxidation of glucose biocatalyzed by GOx and mediated by HPC-*g*-P4VP-Os(bpy) graft copolymer. Figure 20b shows the amperometric response of the GOX/HPC-*g*-P4VP-Os(bpy) biosensor to different concentrations of glucose in PBS (0.1 M, pH 7.0) at an applied potential of 0.4 V. The results indicate that the biosensor is sensitive to the concentration of glucose and that the current obviously increases with the increasing concentration of glucose. The results show that the current of the GOX/HPC-*g*-P4VP-Os(bpy) modified electrode is linear to the glucose concentration with a limit of detection of 0.2 mM. The above results confirm that HPC-*g*-P4VP-Os(bpy) graft copolymers can be used as a matrix that provides a good environment for enzyme activity to enhance the sensitivity of the modified electrode for glucose detection.

Downloaded by NORTH CAROLINA STATE UNIV on August 28, 2012 | http://pubs.acs.org
Publication Date (Web): August 17, 2012 | doi: 10.1021/bk-2012-1107.ch006

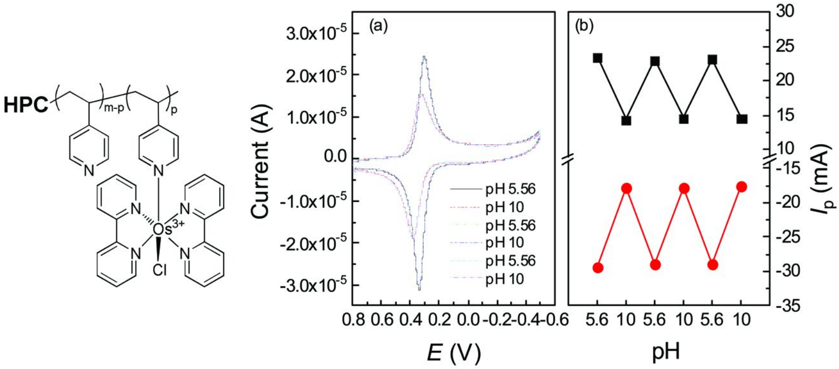

Figure 19. The chemical structure and (a) cyclic voltammograms of the HPC-g-P4VP-Os(bpy) modified electrode obtained upon stepwise measurements performed at pH 5.56 and at pH 10 solutions; (b) reversible switching of the HPC-g-P4VP-Os(bpy) modified electrode activity. Measurements were performed in 0.1 M phosphate buffer with a potential scan rate of 100 mV/s. (Reproduced with permission from reference (79). Copyright 2011 ACS.)

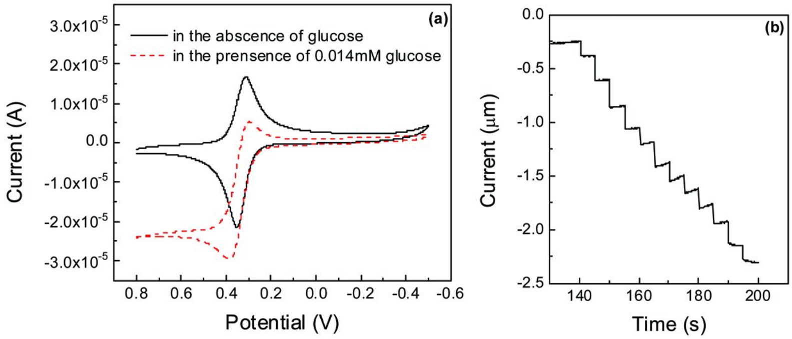

Figure 20. (a) Cyclic voltammograms corresponding to the oxidation of glucose catalyzed by glucose oxidase (GOX), 0.014 mM. The measurements were performed in 0.1 M phosphate buffer (pH 7.0) with a potential scan rate of 50 mV/s. (b) Amperometric response of the GOX/ HPC-g-P4VP-Os(bpy) biosensor to different concentrations of glucose in PBS (0.1 M, pH 7.0) at an applied potential of 0.4 V. (Reproduced with permission from reference (79). Copyright 2011 ACS.)

Downloaded by NORTH CAROLINA STATE UNIV on August 28, 2012 | http://pubs.acs.org
Publication Date (Web): August 17, 2012 | doi: 10.1021/bk-2012-1107.ch006

Summary and Perspective

As one of the most abundant renewable natural polymers, it is undoubted that cellulose is the un-replaceable material in both polymer science and materials. However, efficient applications of cellulose are still limited due to the strong inter- and intra-molecular hydrogen bonds. The general investigations of synthesis and properties of cellulose graft copolymers by ATRP are helpful for the understanding of the structure and properties relationships of cellulosic functional materials. The cellulose graft copolymers synthesized by ATRP have a well-defined architecture without homopolymer chains formed during the ATR reaction. The possible tuning of cellulose functional materials based on cellulose graft copolymers can be achieved by variation of the chemical structure of both cellulosic backbone and side chain, the graft density, and the length of the side chain. The disadvantages of the ATRP graft copolymerization are that it is undesirable to carry out ATRP graft copolymerization at large scale. Moreover, the cellulose backbone is from nature and has a wide molecular weight distribution.

In personal view, the most important problems for the applications of cellulose is to understand the inter- and intra-molecular interactions of cellulose, the basic information of the interactions between cellulose and other small molecules for the purpose to find common methods for processing cellulose. The other problem is to understand surfaces and interfaces of cellulose, lignin, hemicellulose and other component in the natural state. It is known that wood itself is the most optimized composites with the most reasonable structure and properties in nature. The understanding of the surface and the interface problems of cellulose could help us to setup reasonable methods for the preparation of composites.

References

1. Klemm, D.; Heublein, B.; Fink, H. P.; Bohn, A. *Angew. Chem., Int. Ed.* **2005**, *44*, 3358–3393.
2. Tang, X. D.; Gao, L. C.; Fan, X. H.; Zhou, Q. F. *J. Polym. Sci., Part A: Polym. Chem.* **2007**, *45*, 1653–1660.
3. Sturcova, A.; His, I.; Apperley, D. C.; Sugiyama, J.; Jarvis, M. C. *Biomacromolecules* **2004**, *5*, 1333–1339.
4. Gupta, K. C.; Khandekar, K. *Biomacromolecules* **2003**, *4*, 758–765.
5. Hinterstoisser, B.; Akerholm, M.; Salmen, L. *Biomacromolecules* **2003**, *4*, 1232–1237.
6. Wada, M.; Heux, L.; Sugiyama, J. *Biomacromolecules* **2004**, *5*, 1385–1391.
7. Carlmark, A.; Malmstrom, E. E. *Biomacromolecules* **2003**, *4*, 1740–1745.
8. Liu, R. G.; Shen, Y. Y.; Shao, H. L.; Wu, C. X.; Hu, X. C. *Cellulose* **2001**, *8*, 13–21.
9. Swatloski, R. P.; Spear, S. K.; Holbrey, J. D.; Rogers, R. D. *J. Am. Chem. Soc.* **2002**, *124*, 4974–4975.
10. Zhu, S. D.; Wu, Y. X.; Chen, Q. M.; Yu, Z. N.; Wang, C. W.; Jin, S. W.; Ding, Y. G.; Wu, G. *Green Chem.* **2006**, *8*, , 325–327.
11. Zhang, H.; Wu, J.; Zhang, J.; He, J. S. *Macromolecules* **2005**, *38*, 8272–8277.

Downloaded by NORTH CAROLINA STATE UNIV on August 28, 2012 | http://pubs.acs.org
Publication Date (Web): August 17, 2012 | doi: 10.1021/bk-2012-1107.ch006

12. Turner, M. B.; Spear, S. K.; Holbrey, J. D.; Rogers, R. D. *Biomacromolecules* **2004**, *5*, 1379–1384.
13. Lu, A.; Zhang, L. N. *Acta Polym. Sin.* **2007**, 937–944.
14. Li, R.; Chang, C. Y.; Zhou, J. P.; Zhang, L. N.; Gu, W. Q.; Li, C. T.; Liu, S. L.; Kuga, S. *Ind. Eng. Chem. Res.* **2010**, *49*, 11380–11384.
15. Ruan, D.; Zhang, L. N.; Lue, A.; Zhou, J. P.; Chen, H.; Chen, X. M.; Chu, B.; Kondo, T. *Macromol. Rapid Commun.* **2006**, *27*, 1495–1500.
16. Wu, J.; Zhang, J.; Zhang, H.; He, J. S.; Ren, Q.; Guo, M. *Biomacromolecules* **2004**, *5*, 266–268.
17. Heinze, T.; Schwikal, K.; Barthel, S. *Macromol. Biosci.* **2005**, *5*, 520–525.
18. Cao, Y.; Wu, J.; Meng, T.; Zhang, J.; He, J. S.; Li, H. Q.; Zhang, Y. *Carbohydr. Polym.* **2007**, *69*, 665–672.
19. El Seoud, O. A.; Koschella, A.; Fidale, L. C.; Dorn, S.; Heinze, T. *Biomacromolecules* **2007**, *8*, 2629–2647.
20. Li, Y. X.; Liu, R. G.; Huang, Y. *J. Appl. Polym. Sci.* **2008**, *110*, 1797–1803.
21. Li, Y. X.; Wu, M.; Liu, R. G.; Huang, Y. *Sol. Energy Mater. Sol. Cells* **2009**, *93*, 1321–1328.
22. Kaeppner, W. M.; Huang, R. Y. M. *Text. Res. J.* **1965**, *35*, 504–516.
23. Huang, R. Y. M. *J. Appl. Polym. Sci.* **1966**, *10*, 325–341.
24. Nakamura, Y.; Hinojosa, O.; Arthur, J. C. *J. Appl. Polym. Sci.* **1969**, *13*, 2633–2641.
25. Toda, T. *J. Polym. Sci.* **1962**, *58*, 411–427.
26. Kubota, H.; Ogiwara, Y. *J. Appl. Polym. Sci.* **1970**, *14*, 2611–2618.
27. Iwakura, Y.; Kurosaki, T.; Imai, Y. *J. Polym. Sci., Part A: Gen. Pap.* **1965**, *3*, 1185–1193.
28. Huang, R. Y. M.; Chandramouli, P. *J. Appl. Polym. Sci.* **1968**, *12*, 2549–2562.
29. Braunecker, W. A.; Matyjaszewski, K. *Prog. Polym. Sci.* **2007**, *32*, 93–146.
30. Hawker, C. J.; Bosman, A. W.; Harth, E. *Chem. Rev.* **2001**, *101*, 3661–3688.
31. Matyjaszewski, K. *Macromolecules* **2012**, *45*, 4015–4039.
32. Wang, J. S.; Matyjaszewski, K. *J. Am. Chem. Soc.* **1995**, *117*, 5614–5615.
33. Patten, T. E.; Matyjaszewski, K. *Adv. Mater.* **1998**, *10*, 901+.
34. Matyjaszewski, K.; Xia, J. H. *Chem. Rev.* **2001**, *101*, 2921–2990.
35. Moad, G.; Rizzardo, E.; Thang, S. H. *Polymer* **2008**, *49*, 1079–1131.
36. Chiefari, J.; Chong, Y. K.; Ercole, F.; Krstina, J.; Jeffery, J.; Le, T. P. T.; Mayadunne, R. T. A.; Meijs, G. F.; Moad, C. L.; Moad, G.; Rizzardo, E.; Thang, S. H. *Macromolecules* **1998**, *31*, 5559–5562.
37. Tizzotti, M.; Charlot, A.; Fleury, E.; Stenzel, M.; Bernard, J. *Macromol. Rapid Commun.* **2010**, *31*, 1751–1772.
38. Zhong, J. F.; Chai, X. S.; Fu, S. Y. *Carbohydr. Polym.* **2012**, *87*, 1869–1873.
39. Hiltunen, M.; Siirila, J.; Aseyev, V.; Maunu, S. L. *Eur. Polym. J.* **2012**, *48*, 136–145.
40. Raus, V.; Stepanek, M.; Uchman, M.; Slouf, M.; Latalova, P.; Cadova, E.; Netopilik, M.; Kriz, J.; Dybal, J.; Vlcek, P. *J. Polym. Sci., Part A: Polym. Chem.* **2011**, *49*, 4353–4367.
41. Semsarilar, M.; Ladmiral, V.; Perrier, S. *J. Polym. Sci., Part A: Polym. Chem.* **2010**, *48*, 4361–4365.

42. Dupayage, L.; Nouvel, C.; Six, J. L. *J. Polym. Sci., Part A: Polym. Chem.* **2011**, *49*, 35–46.
43. Dupayage, L.; Save, M.; Dellacherie, E.; Nouvel, C.; Six, J. L. *J. Polym. Sci., Part A: Polym. Chem.* **2008**, *46*, 7606–7620.
44. Zoppe, J. O.; Habibi, Y.; Rojas, O. J.; Venditti, R. A.; Johansson, L. S.; Efimenko, K.; Osterberg, M.; Laine, J. *Biomacromolecules* **2010**, *11*, 2683–2691.
45. Xiao, M. M.; Li, S. Z.; Chanklin, W.; Zheng, A. N.; Xiao, H. N. *Carbohydrate Polymers* **2011**, *83*, 512–519.
46. Wei, Y. T.; Zheng, Y. M.; Chen, J. P. *Langmuir* **2011**, *27*, 6018–6025.
47. Li, S. Z.; Xiao, M. M.; Zheng, A.; Xiao, H. N. *Biomacromolecules* **2011**, *12*, 3305–3312.
48. Tastet, D.; Save, M.; Charrier, F.; Charrier, B.; Ledeuil, J. B.; Dupin, J. C.; Billon, L. *Polymer* **2011**, *52*, 606–616.
49. Westlund, R.; Carlmark, A.; Hult, A.; Malmstrom, E.; Saez, I. M. *Soft Matter* **2007**, *3*, 866–871.
50. Roy, D.; Guthrie, J. T.; Perrier, S. *Macromolecules* **2005**, *38*, 10363–10372.
51. Porsch, C.; Hansson, S.; Nordgren, N.; Malmstrom, E. *Polym. Chem.* **2011**, *2*, 1114–1123.
52. Meng, T.; Gao, X.; Zhang, J.; Yuan, J. Y.; Zhang, Y. Z.; He, J. S. *Polymer* **2009**, *50*, 447–454.
53. Vlcek, P.; Janata, M.; Latalova, P.; Dybal, J.; Spirkova, M.; Toman, L. *J. Polym. Sci., Part A: Polym. Chem.* **2008**, *46*, 564–573.
54. Sui, X. F.; Yuan, J. Y.; Zhou, M.; Zhang, J.; Yang, H. J.; Yuan, W. Z.; Wei, Y.; Pan, C. Y. *Biomacromolecules* **2008**, *9*, 2615–2620.
55. Carlmark, A.; Malmstrom, E. *J. Am. Chem. Soc.* **2002**, *124*, 900–901.
56. Eichhorn, S. J. *Soft Matter* **2011**, *7*, 303–315.
57. Liu, P. S.; Chen, Q.; Wu, S. S.; Shen, J.; Lin, S. C. *J. Membr. Sci.* **2010**, *350*, 387–394.
58. Zampano, G.; Bertoldo, M.; Bronco, S. *Carbohydr. Polym.* **2009**, *75*, 22–31.
59. Morandi, G.; Heath, L.; Thielemans, W. *Langmuir* **2009**, *25*, 8280–8286.
60. Liu, P. S.; Chen, Q.; Liu, X.; Yuan, B.; Wu, S. S.; Shen, J.; Lin, S. C. *Biomacromolecules* **2009**, *10*, 2809–2816.
61. Ma, L.; Liu, R. G.; Tan, J. J.; Wang, D. Q.; Jin, X.; Kang, H. L.; Wu, M.; Huang, Y. *Langmuir* **2010**, *26*, 8697–8703.
62. Shen, D.; Yu, H.; Huang, Y. *Cellulose* **2006**, *13*, 235–244.
63. Shen, D. W.; Yu, H.; Huang, Y. *J. Polym. Sci., Part A: Polym. Chem.* **2005**, *43*, 4099–4108.
64. Liu, W. Y.; Liu, R. G.; Li, Y. X.; Kang, H. L.; Shen, D.; Wu, M.; Huang, Y. *Polymer* **2009**, *50*, 211–217.
65. Liu, W. Y.; Liu, R. G.; Li, Y. X.; Wang, W.; Ma, L.; Wu, M.; Huang, Y. *Polymer* **2009**, *50*, 2716–2726.
66. Shen, D. W.; Yu, H.; Wu, Z. H.; Huang, Y. *High Energy Phys. Nucl. Phys., Chin. Ed.* **2005**, *29*, 8–11.
67. Kang, H.; Liu, W.; He, B.; Shen, D.; Ma, L.; Huang, Y. *Polymer* **2006**, *47*, 7927–7934.

Downloaded by NORTH CAROLINA STATE UNIV on August 28, 2012 | http://pubs.acs.org
Publication Date (Web): August 17, 2012 | doi: 10.1021/bk-2012-1107.ch006

68. Kang, H. L.; Liu, W. Y.; Liu, R. G.; Huang, Y. *Macromol. Chem. Phys.* **2008**, *209*, 424–430.

69. Li, Y. X.; Liu, R. G.; Liu, W. Y.; Kang, H. L.; Wu, M.; Huang, Y. *J. Polym. Sci., Part A: Polym. Chem.* **2008**, *46*, 6907–6915.

70. Tan, J. J.; Li, Y. X.; Liu, R. G.; Kang, H. L.; Wang, D. Q.; Ma, L.; Liu, W. Y.; Wu, M.; Huang, Y. *Carbohydr. Polym.* **2010**, *81*, 213–218.

71. Ma, L.; Kang, H. L.; Liu, R. G.; Huang, Y. *Langmuir* **2010**, *26*, 18519–18525.

72. Wang, D. Q.; Tan, J. J.; Kang, H. L.; Ma, L.; Jin, X.; Liu, R. G.; Huang, Y. *Carbohydr. Polym.* **2011**, *84*, 195–202.

73. Plamper, F. A.; Ruppel, M.; Schmalz, A.; Borisov, O.; Ballauff, M.; Muller, A. H. E. *Macromolecules* **2007**, *40*, 8361–8366.

74. Mahltig, B.; Jerome, R.; Stamm, M. *J. Polym. Res., Taiwan* **2003**, *10*, 219–223.

75. Yao, X. M.; Chen, D. Y.; Jiang, M. *Macromolecules* **2004**, *37*, 4211–4217.

76. Peng, H. S.; Chen, D. Y.; Jiang, M. *J. Phys. Chem. B* **2003**, *107*, 12461–12464.

77. Guo, M. Y.; Jiang, M.; Pispas, S.; Yu, W.; Zhou, C. X. *Macromolecules* **2008**, *41*, 9744–9749.

78. Fournier, D.; Hoogenboom, R.; Thijs, H. M. L.; Paulus, R. M.; Schubert, U. S. *Macromolecules* **2007**, *40*, 915–920.

79. Kang, H.; Liu, R.; Sun, H.; Zhen, J.; Li, Q.; Huang, Y. *J. Phys. Chem. B* **2011**, *116*, 55–62.

Downloaded by NORTH CAROLINA STATE UNIV on August 28, 2012 | http://pubs.acs.org
Publication Date (Web): August 17, 2012 | doi: 10.1021/bk-2012-1107.ch006

Downloaded by OHIO STATE UNIV LIBRARIES on August 28, 2012 | http://pubs.acs.org
Publication Date (Web): August 17, 2012 | doi: 10.1021/bk-2012-1107.ch007

Chapter 7

Diblock Copolymers of Cellulose and Poly(methyl methacrylate) Initiated by Radicals Produced by Mechanical Scission of Cellulose

M. Sakaguchi,*,[1] T. Ohura,[2] and T. Iwata[3]

[1]Institute for Environmental Sciences, University of Shizuoka, 52-1, Yada, Suruga-ku, Shizuoka 422-8526, Japan
[2]Faculty of Agriculture, Meijo University, 1-501, Tempaku-ku, Nagoya 468-8502, Japan
[3]Department of Biomaterial Sciences, Graduate School of Agricultural and Life Sciences, The University of Tokyo, 1-1-1 Yayoi, Bunkyo-ku, Tokyo 133-8657, Japan
***E-mail: sakaguchi@u-shizuoka-ken.ac.jp**

A diblock copolymer of bacterial cellulose (BC) and poly(methyl methacrylate) (BC-*block*-PMMA) was produced by the mechanical fracture of BC in the presence of methyl methacrylate (MMA) in vacuum at 77 K. The radical polymerization of MMA was initiated by chain-end-type radicals of BC (BC mechano-radicals) that were produced by mechanical scission of d-1,4 glycosidic linkages of BC. The BC surface was covered with PMMA chains. Furthermore, a diblock copolymer of microcrystalline cellulose (MCC) and PMMA (MCC-*block*-PMMA) was produced in a similar way. The MCC nanoparticles were fully covered with PMMA chains, *i.e.*, MCC core and PMMA shell nanoparticles were obtained. The core/shell nanoparticles were dispersed in chloroform, and resulted in an optically transparent liquid. The average diameter of the core/shell nanoparticles in chloroform was estimated to be 52 nm. The particles were studied by ESR, FTIR, ^{1}H NMR, GPC and DLS spectroscopy.

Downloaded by OHIO STATE UNIV LIBRARIES on August 28, 2012 | http://pubs.acs.org
Publication Date (Web): August 17, 2012 | doi: 10.1021/bk-2012-1107.ch007

Introduction

Cellulose is the most abundant biological resource on earth, and it has been used to manufacture paper, building materials, textiles, etc. Furthermore, cellulose is a carbon-neutral material and a renewable resource. Thus, the widespread use of cellulose can help to realize a sustainable society. Chemical modification of cellulose can facilitate this goal. Block copolymerization of cellulose may open up novel uses of this compound. We aimed at synthesizing a diblock copolymer of cellulose by radical polymerization initiated by the radicals located at the end of the cellulose chains, which were produced by the mechanical scission of the β-1,4 glycosidic linkage and located on the cellulose surface.

Many workers have reported (*1–4*) that mechanical destruction of cellulose in air at room temperature produces radicals. In these experiments, the radicals were unstable in air at room temperature and, subsequently, were converted to other chemical species through side reactions (*5*). The highly reactive radicals react easily with oxygen, and can be converted to peroxide radicals. Unfortunately, the electron spin resonance (ESR) spectrum of any peroxide radical indicates a characteristic amorphous pattern at 77 K, the temperature at which molecular motion reaches the rigidity limit (*6–9*). Therefore, the original radical species giving rise to subsequently formed peroxide radicals cannot be identified from the ESR spectrum. Thus, the scission mechanism of the β-1,4 glycosidic linkages that occurs upon mechanical fracture of cellulose cannot be directly demonstrated.

In this study, we used bacterial cellulose (BC) as the variant of cellulose. To reveal the scission mechanism of cellulose and the production of chain-end-type radicals, we carried out the mechanical fracture of BC in vacuum at 77 K, which produced chain-end-type radicals of BC (BC mechano-radicals), induced by scission of β-1,4 glycosidic linkages. Furthermore, the diblock copolymer of BC and PMMA (BC-*block*-PMMA) was synthesized on the BC surface starting from the BC mechano-radicals, and BC particles were covered with PMMA chains, giving BC-*block*-PMMAs (*10*). In addition, we applied this technique to microcrystalline cellulose (MCC) and MMA, and obtained diblock copolymer of MCC and PMMA (MCC-*block*-PMMA). The MCC nano particles were fully covered with PMMA chains *i.e.*, MCC core/PMMA shell nanoparticles were obtained.

Experimental

Bacterial Cellulose

Gluconacetobacter xylinus (Acetobacter xylinum) JCM9730 was used as a strain for the production of BC. Culture conditions and purification were as previously reported (*10*).

Mechanical Destruction of BC

BC (0.5 g) was dried in a glass ball mill vessel and evacuated under 0.6 Pa at 373 K for 7 h, sealed off, and placed in a Dewar filled with liquid nitrogen. The

BC was mechanically fractured by a homemade vibration ball mill apparatus for 7 h at 77 K in vacuum (*11*). After milling, the fractured BC was dropped into the ESR sample tube attached to the top of the glass ball mill by turning it over into the liquid nitrogen within 1 s.

Synthesis of BC-*block*-PMMA

MMA was purified by distilling it twice in a vacuum line before use. Oxygen gas incorporated in MMA was eliminated by performing the freeze-pump-thaw cycles four times. The purified MMA was introduced into the glass ball mill containing the vacuum-dried BC, and the mill vessel was sealed off from the vacuum line, set to the homemade vibration ball mill, and milled in vacuum at 77 K for 7 h.

Acetylation of Fractured BC and BC-*block*-PMMA

Acetic acid (0.570 mol) and trifluoroacetic acid anhydride (0.436 mol) were mixed at 323 K for 20 min, BC (0.023 mol glucosyl units) was introduced, and the solution was acetylated at 323 K for 12 h. Acetylated BC (BCTA) was precipitated with methanol, filtered, and dried under vacuum at 343 K for 6 h. Acetylated BC-*block*-PMMA (BCA-block-PMMA) was produced by the same procedure.

^{1}H NMR Measurement

^{1}H NMR spectra were recorded on a JEOL ALPHA-500 NMR spectrometer at 500 MHz with $CDCl_3$. TMS was used as the internal reference for chemical shifts.

ESR Measurement

ESR spectra were observed at a microwave power level of 2 μW to avoid power saturation and with 100 kHz field modulation using a Bruker EMX Plus spectrometer (X-band) equipped with a helium cryostat (Oxford ESR 900) and a temperature controller (Oxford ITC4).

ESR Spectral Simulation

ESR spectral simulation was carried out by a homemade computer programto calculate the line shape equation of the ESR spectrum in solid state, having anisotropic g and hyperfine splitting tensor A, as shown in previous studies (*8*, *9*).

BET Measurement

The nitrogen adsorption isotherm at 77 K was obtained on a Quantachrome Autosorb-1 system. All samples were degassed at 298 K over 5 h before measurement. Surface areas were calculated according to the BET method in the 0.13 to 0.27 relative pressure (P/P_0) range.

Downloaded by OHIO STATE UNIV LIBRARIES on August 28, 2012 | http://pubs.acs.org
Publication Date (Web): August 17, 2012 | doi: 10.1021/bk-2012-1107.ch007

Downloaded by OHIO STATE UNIV LIBRARIES on August 28, 2012 | http://pubs.acs.org
Publication Date (Web): August 17, 2012 | doi: 10.1021/bk-2012-1107.ch007

GPC Measurement

The molecular weights of samples were observed by using GPC (Shimazu 10A GPC system) with column Shodex K802 and K806M.

Dynamic Light Scattering Measurement

Dynamic light scattering (DLS) measurements were performed on a nano Partica SZ-100 (HORIBA Co. Ltd.) in chloroform at 298 K.

Results and Discussion

Mechanical Fracture of BC

BC in a glass ball mill was fractured in vacuum at 77 K for 7 h. Figure 1a shows the ESR spectrum of the fractured BC observed at 77 K, which is a broad signal with humps. After ESR measurement, the fractured BC was annealed at 250 K. The humps were decreased by annealing (Figure 1b, shown with arrows). Subsequently, after annealing at 290 K, the humps disappeared from the spectrum (Figure 1c), and a broad singlet spectrum appeared. The ESR line shape of the spectrum was unaltered by annealing at 350 K, but the ESR intensity decreased. These results indicate that the spectrum of fractured BC annealed at 290 K (Figure 1c) consist of a single radical species, whereas the spectrum before annealing (Figure 1a) is a superposition of several radical species.

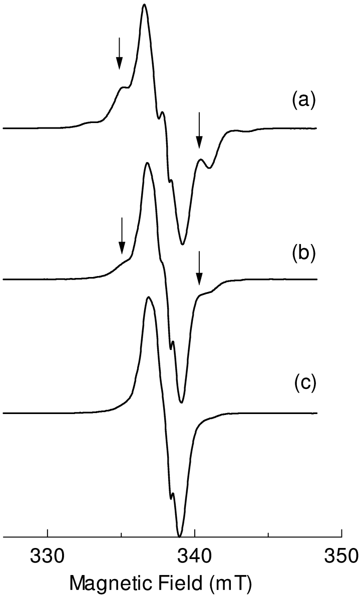

Figure 1. ESR spectra of (a) fractured BC, (b) annealed at 250 K, and (c) annealed at 290 K. All ESR spectra were observed at 77 K. (Reproduced with permission from reference (10). Copyright 2010 American Chemical Society.)

To elucidate the stability of radicals, the fractured BC was annealed at elevated temperatures for 10 min and measured again at 77 K. Figure 2 shows that the radical intensity did not change below 150 K. Above 150 K, it decayed as the annealing temperature increased. The radical intensity was synchronized with the height of the humps in the ESR spectrum (Figure 1a). The humps disappeared at 290 K, and a singlet appeared (Figure 1c) with 58% intensity. These results indicate that the singlet spectrum (Figure 1c) consists of a single radical species and its intensity is about half of that of the fractured BC.

Downloaded by OHIO STATE UNIV LIBRARIES on August 28, 2012 | http://pubs.acs.org
Publication Date (Web): August 17, 2012 | doi: 10.1021/bk-2012-1107.ch007

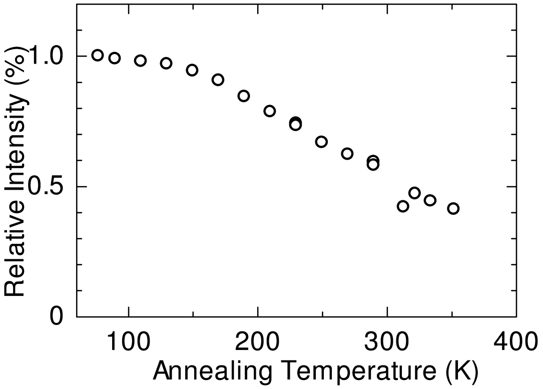

Figure 2. Relative intensities of radicals of fractured BC versus annealing temperatures. The intensity was obtained by double integration of the ESR spectrum and normalized to the intensity of the fractured BC. (Reproduced with permission from reference (10). Copyright 2010 American Chemical Society.)

When mechanical energy was applied to BC, its β-1,4 glycosidic linkages were broken according to two types of scission mechanisms: scissions I and II (shown with wavy lines in Figure 3). Scissions I and II produced pairs of radicals: Ia and Ib as well as radicals IIa and IIb. Radicals Ib and IIa are alkoxyl radicals.

The simulated spectrum of the alkoxyl radicals was calculated (*8*, *9*) with an isotropic *g* value (g_{iso} = 2.0045 ± 0.005) and isotropic hyperfine splitting (A_{iso} = 1.20 ± 0.08 mT) of one β-H. The simulated spectrum of the alkoxyl radicals (broken line in Figure 4) is quite close to the observed spectrum of the fractured BC annealed at 290 K. This result indicates that the fracture of β-1,4 glycosidic linkages produced the alkoxyl radicals Ib and IIa.

Radical Ia produced by scission I has one α proton (α-H) and one β proton (β-H). Assuming the isotropic *g* value (g_{iso} = 2.0043 ± 0.005), the principal value of the anisotropic hyperfine splitting (A_x, A_y, A_z) = (2.10 ± 0.08, 3.10 ± 0.08, 1.10 ±

Downloaded by OHIO STATE UNIV LIBRARIES on August 28, 2012 | http://pubs.acs.org
Publication Date (Web): August 17, 2012 | doi: 10.1021/bk-2012-1107.ch007

0.08 mT) of α-H and the isotropic hyperfine splitting ($A_{\mathrm{iso}} = 2.80 \pm 0.08$ mT) of β-H, the simulated spectrum was obtained as a triplet (shown in Figure 5 as thin solid line). Radical IIb produced by scission II has one α-H and two β-Hs. Assuming the isotropic g value ($g_{\mathrm{iso}} = 2.0034 \pm 0.005$), the principal value of anisotropic hyperfine splitting (A_x, A_y, A_z) = (2.30 ± 0.08, 3.40 ± 0.08, 1.20 ± 0.08 mT) of α-H and, incidentally, the nearly identical isotropic hyperfine splitting ($A_{\mathrm{iso}} = 3.20 \pm 0.08$ mT) of the two β-Hs, the simulated spectrum was obtained as a quartet (shown in Figure 5 as the thin dash double-dotted line). The simulated singlet spectrum of the alkoxyl radicals (Ib and IIa) is shown in Figure 5 as the bold dash-dotted line. We assumed the relative intensity of each radical on the ESR spectrum of the fractured BC as follows: Ib and IIa (0.50), Ia (0.25), and IIb (0.25). The simulated spectrum (Figure 5, bold dashed line) is nearly indistinguishable from the observed spectrum (Figure 5, bold solid line). From these results, we conclude that the β-1,4 glycosidic linkages in BC were fractured mechanically. This fracture produced pair formations of chain-end-type radicals: Ia and IIb and alkoxyl radicals IIa and Ib. The ratio of scissions I and II may be nearly equal, which is based on the relative intensity ratio of each radical. The chain-end-type radicals Ia and IIb are called BC mechano-radicals in the following.

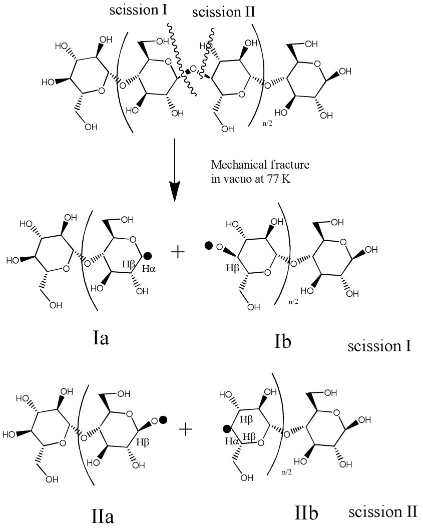

Figure 3. Chemical structure of mechano-radicals Ia and IIb and alkoxyl radicals Ib and IIa produced by the mechanical scission of β-1,4glycosidic linkages of BC. (Reproduced with permission from reference (10). Copyright 2010 American Chemical Society.)

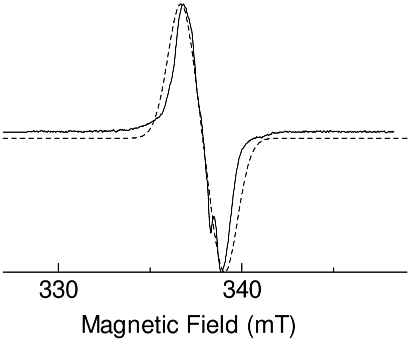

Figure 4. ESR spectrum of fractured BC annealed at 290 K (solid line) and the simulated spectrum of the alkoxyl radicals (dashed line). (Reproduced with permission from reference (10). Copyright 2010 American Chemical Society.)

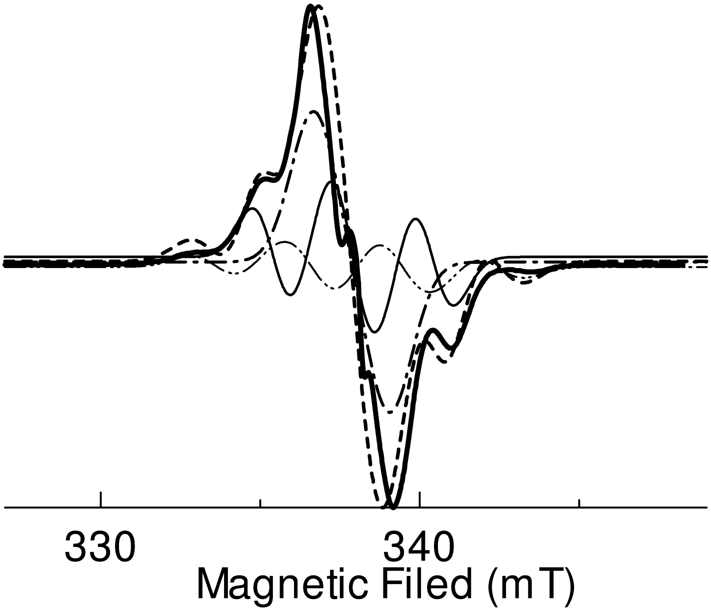

Figure 5. Observed ESR spectrum of the as-fractured BC (bold solid line) and the simulated spectrum (bold dashed line) consisting of Ia (thin solid line), IIb (thin dash double-dotted line), and alkoxyl radicals (bold dash-dotted line). (Reproduced with permission from reference (10). Copyright 2010 American Chemical Society.)

Downloaded by OHIO STATE UNIV LIBRARIES on August 28, 2012 | http://pubs.acs.org
Publication Date (Web): August 17, 2012 | doi: 10.1021/bk-2012-1107.ch007

Downloaded by OHIO STATE UNIV LIBRARIES on August 28, 2012 | http://pubs.acs.org
Publication Date (Web): August 17, 2012 | doi: 10.1021/bk-2012-1107.ch007

Block Copolymerization of BC with MMA

BC with MMA was fractured in vacuum at 77 K. The ESR spectrum (Figure 6, solid line) observed at 77 K seems to be a superposition of characteristic PMMA propagating radicals, -CH_2-C• (CH_3)($COOCH_3$) (*12–14*) as the major part and alkoxyl radicals (thin dash-dotted line) as the minor part of the spectrum.

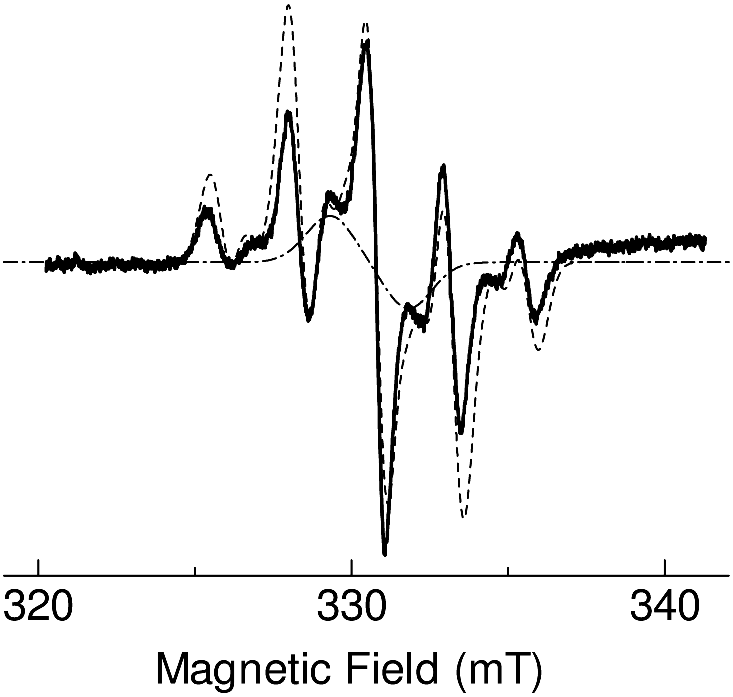

Figure 6. Observed ESR spectrum of BC fractured in the presence of MMA (solid line) and simulated spectrum of alkoxyl radicals (dashed line). The simulated spectrum consisted of PMMA propagating radicals with a relative intensity of 0.8 and alkoxyl radicals with a relative intensity of 0.2 (dash-dotted line line). (Reproduced with permission from reference (10). Copyright 2010 American Chemical Society.)

The simulation spectrum of the PMMA propagating radical was calculated with $A_{\mathrm{iso,CH3}}$ = 2.22 mT for the freely rotating CH_3 group and $A_{\beta,\mathrm{H1}}$ = 1.51 mT and $A_{\beta,\mathrm{H2}}$ = 0.82 mT. The line shape of the simulation spectrum is close to the spectrum reported by Iwasaki and Sakai (*15*, *16*). Furthermore, the simulated spectrum (shown in Figure 6, dashed line) was calculated as superposition of the PMMA propagating radicals with a relative concentration of 0.8 and the simulated spectrum of alkoxyl radicals with a relative concentration of 0.2. The simulated spectrum is fairly indistinguishable from the observed spectrum. By contrast, no ESR signal was observed from the unfractured BC with MMA. Therefore, we can conclude that the BC mechano-radicals Ia and IIb, which were produced by

Downloaded by OHIO STATE UNIV LIBRARIES on August 28, 2012 | http://pubs.acs.org
Publication Date (Web): August 17, 2012 | doi: 10.1021/bk-2012-1107.ch007

scissions of β-1,4 glycosidic linkages and were initiating a radical polymerization of MMA and produced the BC-*block*-PMMA on the BC surface. The reaction scheme of Ia with MMA is shown in Figure 7. IIb has the same reaction fate as Ia.

Figure 8a shows the Fourier transform infrared (FT-IR) spectrum of the BC fractured without MMA in vacuum at 77 K, showing a characteristic cellulose pattern. No peak was observed at around 1729 cm^{-1}. The BC-*block*-PMMA was washed by Soxhlet extract with chloroform for 24 h, and the residue was dried in vacuum at 343 K for 6 h. The FT-IR spectrum of the residue (Figure 8b) shows a similar pattern to that of the BC fractured without MMA, except at the 1729 cm^{-1} peak due to the carbonyl group on the PMMA chain. Because the MMA monomer was removed from the residue by the Soxhlet extract treatment, these results are additional evidence for the production of BC-*block*-PMMA by the mechanochemical reaction of BC with MMA.

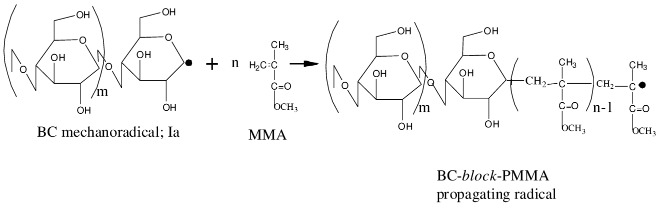

Figure 7. Reaction scheme for the formation of BC-block-PMMA, in which polymerization of MMA is initiated by radical Ia. (Reproduced with permission from reference (10). Copyright 2010 American Chemical Society.)

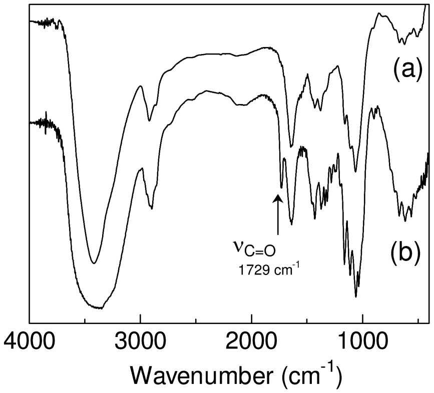

Figure 8. FT IR spectrum of (a) the fractured BC and (b) the BC-block-PMMA. (Reproduced with permission from reference (10). Copyright 2010 American Chemical Society.)

The PMMA homopolymer (weight-averaged molecular weight, M_w = 2.72×10^5 g/mol, number-averaged molecular weight, $M_n = 1.48 \times 10^5$g/mol; M_w/M_n = 1.84) was synthesized by the radical polymerization of MMA with azobisisobutyronitrile as the initiator at 373 K for 2 h. The ^{1}H NMR spectrum

Downloaded by OHIO STATE UNIV LIBRARIES on August 28, 2012 | http://pubs.acs.org
Publication Date (Web): August 17, 2012 | doi: 10.1021/bk-2012-1107.ch007

(Figure 9a) of PMMA shows a characteristic pattern (*17*, *18*). The signals at δ = 0.85-1.24 (peak c), 1.81-2.07 (peak b), and 3.60 ppm (peak a) were assigned to the methyl protons (c), methylene protons (b), and methoxy protons (a), respectively.

The ^{1}H NMR spectrum (Figure 9b) of BCTA shows the characteristic resonances of cellulose triacetate (*19*, *20*). The signals at δ = 1.94-2.12 ppm were assigned to the protons of the acetyl groups. In the region from 3.4 to 5.3 ppm, the signals at δ = 4.42, 4.79, 5.07, 3.71, 3.54, 4.38, and 4.06 ppm were assigned to the protons on the glucopyranose ring at positions 1-H, 2-H, 3-H, 4-H, 5-H,6-H, and 6′-H, respectively.

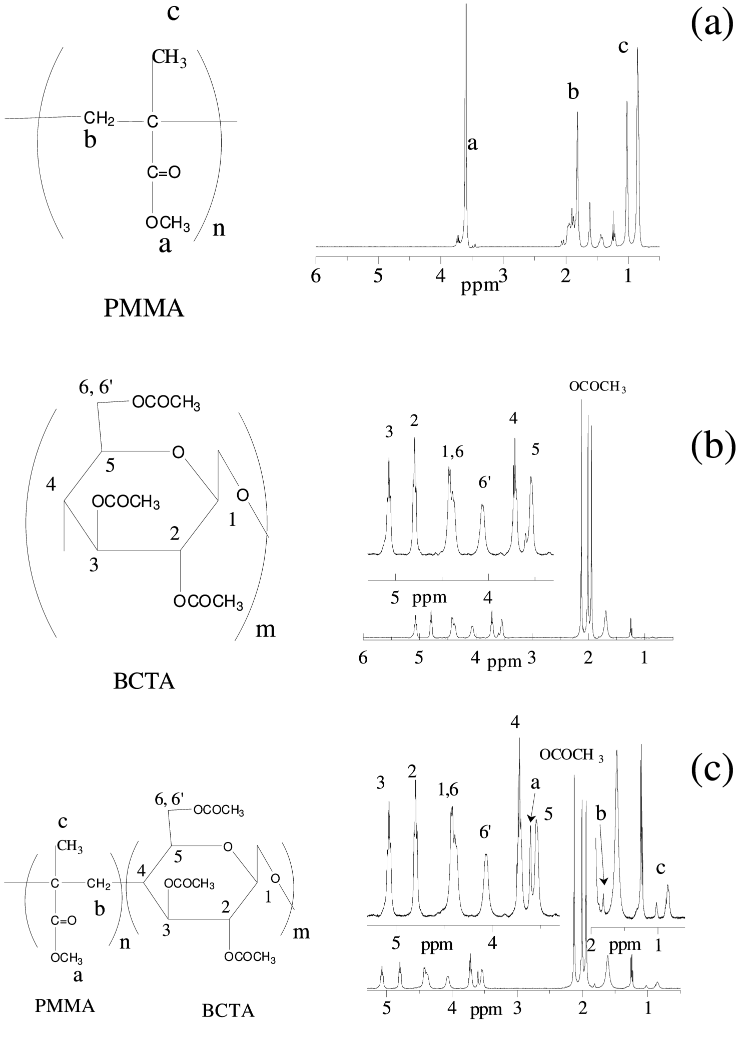

Figure 9. ^{1}H NMR spectra of (a) PMMA, (b) BCTA, and (c) BCA-block-PMMA. (Reproduced with permission from reference (10). Copyright 2010 American Chemical Society.)

The washed and the dried residue, BC-*block*-PMMA, was acetylated with trifluoroacetic acid/acetanhydride and resulted in acetylated BC-*block*-PMMA (BCA-*block*-PMMA). The ^{1}H NMR spectra (Figure 9c) of the BCA-*block*-PMMA reveals two proton groups: one arises from the glucopyranose ring of acetylated BC: 1-H ($\delta = 4.42$ ppm), 2-H (4.79 ppm), 3-H (5.07 ppm), 4-H (3.71 ppm), 5-H (3.54 ppm), 6-H (4.39 ppm), and 6′-H (4.06 ppm), whereas the other arises from the protons of the PMMA chains. It is reasonable to assume that the main chain that consists of BCA-*block*-PMMA is unaltered by acetylation.

Surface Modification of BC with BC-*block*-PMMA

To reveal the profile of the surface modification of BC with BC-*block*-PMMA, the following experiments were performed. To estimate the molecular weights of PMMA in BC-*block*-PMMA, the BC-*block*-PMMA was acetylated with acetic acid and trifluoroacetic acid/acetanhydride, and resulted in BCA-*block*-PMMA, of which the GPC data were as follows: $M_w = 5.15 \times 10^5$ g/mol, $M_n = 1.63 \times 10^5$ g/mol, and $M_w/M_n = 3.15$. The molar ratios of BCTA and PMMA in BCA-*block*-PMMA, calculated based on the ^{1}H NMR spectrum, were 86.4 and 13.6 mol%, respectively. Thus, the M_n values of BCTA and PMMA can be calculated as 1.53×10^5 g/mol (degree of polymerization [DP] = 609, acetylated cellulose unit = 252 g/mol) and 9.59×10^3 g/mol (DP = 95.8, MMA unit = 100.12g/mol), respectively.

Assuming that the DP of PMMA is unaltered by the acetylation of BC-*block*-PMMA, the M_n of the PMMA chain of BC-*block*-PMMA is 9.59×10^3 g/mol (DP = 95.8). The specific surface area of the fractured BC (12.0 m^2/g) was obtained according to the BET method. The concentration of radicals in BC fractured in vacuum at 77 K for 7 h was 1.73×10^{18} spins/g. The occupied surface area per spin was calculated to be 6.94 nm^2/spin. Assuming the occupied surface area to be a circle, the radius (R_t) per tethered point (PMMA stem base) is 1.49 nm. The schematic illustration is shown in Figure 10.

The radius of gyration ($R_{g,0} = [C_\infty (2\mathrm{DP} - 1)a_b{}^2/6]^{0.5}$) of the PMMA chains on the BC-*block*-PMMA was calculated as 2.27 nm based on a DP of 95.8, a carbon-carbon bond length of ab = 0.15351 nm (*21*), and the characteristic ratio ($C_\infty = 6.9$) of *atactic* PMMA (*22*). The relative radius ($R_L = R_{g,0}/R_t$) of PMMA was 1.52 > 1.0. Thus, a tethered PMMA chain is in contact and entangles with the neighboring PMMA chains (illustrated in Figure 10). BC particles are fully covered with PMMA chains of BC-*block*-PMMA.

Mechanical Fracture of MCC

MC was fractured in vacuum at 77 K for 7 h. The observed ESR spectrum of fractured MCC is shown in Figure 11 (bold solid line). From the fracture scheme of cellulose (Figure 3), radical Ia, which is produced by scission pathway I, has H_α and one H_β. The simulated spectrum was obtained by using ESR parameters; g_{iso} (2.0034 ± 0.005), (A_x, A_y, A_z) = (2.10 ± 0.08, 3.10 ± 0.08, 1.10 ± 0.08 mT) for H_α and A_{iso} (3.10 ± 0.08 mT) for H_β: a triplet (shown in Figure 11 with dotted line). The radical IIb, which is produced by scission path II, has one H_α and two H_β atoms. The simulated spectrum was obtained by using ESR parameters;

Downloaded by OHIO STATE UNIV LIBRARIES on August 28, 2012 | http://pubs.acs.org
Publication Date (Web): August 17, 2012 | doi: 10.1021/bk-2012-1107.ch007

g_{iso} (2.0034 ± 0.005), (A_x, A_y, A_z) = (2.30 ± 0.08 mT, 3.40 ± 0.08 mT, 1.20 ± 0.08 mT) for H_α and A_{iso} values of 4.00 ± 0.08 mT and 3.400 ± 0.08 mT for $H_{\beta 2}$ and $H_{\beta 1}$, respectively: a quartet (shown in Figure 11 with thin dash-dotted line). The simulated doublet spectrum arising from the alkoxyl radicals (Ib and IIa) is also shown in Figure 11 (thin solid line).

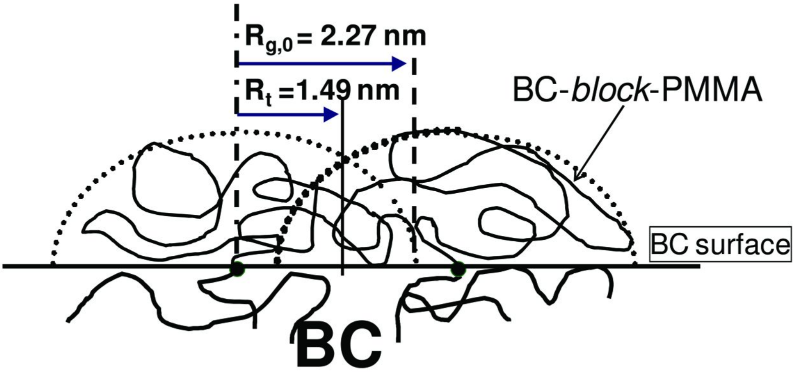

Figure 10. Schematic drawing of BC-block-PMMA on the BC surface. (Reproduced with permission from reference (10). Copyright 2010 American Chemical Society.)

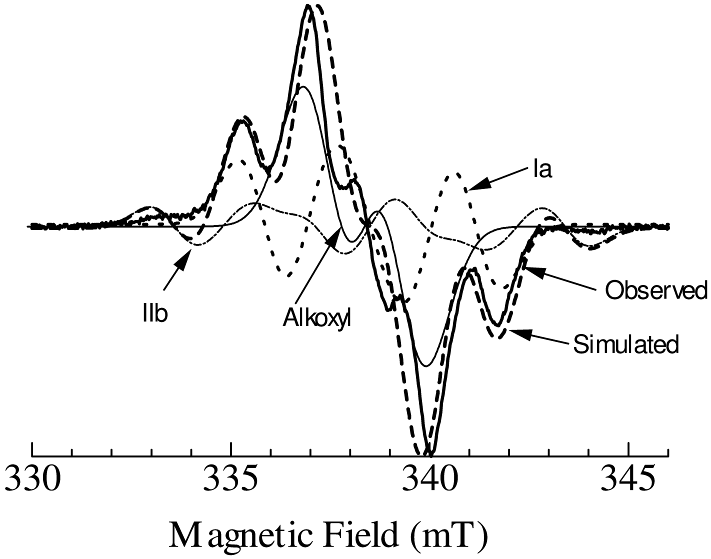

Figure 11. Observed ESR spectrum of the fractured MCC (bold solid line) and the simulated spectrum (bold dashed line) consisting of Ia (triplet: bold dotted line), IIb (quartet: thin dash-dotted line), and alkoxyl radicals (doublet: thin solid line).

Downloaded by OHIO STATE UNIV LIBRARIES on August 28, 2012 | http://pubs.acs.org
Publication Date (Web): August 17, 2012 | doi: 10.1021/bk-2012-1107.ch007

Downloaded by OHIO STATE UNIV LIBRARIES on August 28, 2012 | http://pubs.acs.org
Publication Date (Web): August 17, 2012 | doi: 10.1021/bk-2012-1107.ch007

The simulated spectrum is almost identical to the observed spectrum. Therefore, it can be said that the β-1,4 glycosidic linkages that comprise the MCC main chain were fractured by mechanical energy and resulted in MCC mechano radicals, Ia and IIb, and alkoxyl radicals, IIa and Ib, similar to the behavior of BC described above.

Block Copolymerization of MCC with MMA

MCC was fractured in the presence of MMA in vacuum at 77 K. The ESR spectrum of the fractured sample revealed the similar pattern as shown in Figure 6, which has characteristicsof PMMA propagating radicals.

The fractured sample was evacuated at 300 K for 6 h to eliminate non- reacted MMA. The sample was then washed by Soxhlet extraction with chloroform for 21 h. We obtained two samples: one is "MCC-*block*-PMMA residue", the remainder after Soxhlet extraction, and the second is "MCC-*block*-PMMA filtrate", which was extracted. Both samples were acetylated according to the same procedure described in previous section. The acetylated MCC-*block*-PMMA residue (MCCA-*block*-PMMA residue) and the acetylated MCC-*block*-PMMA filtrate (MCCA-*block*-PMMA filtrate) were obtained.

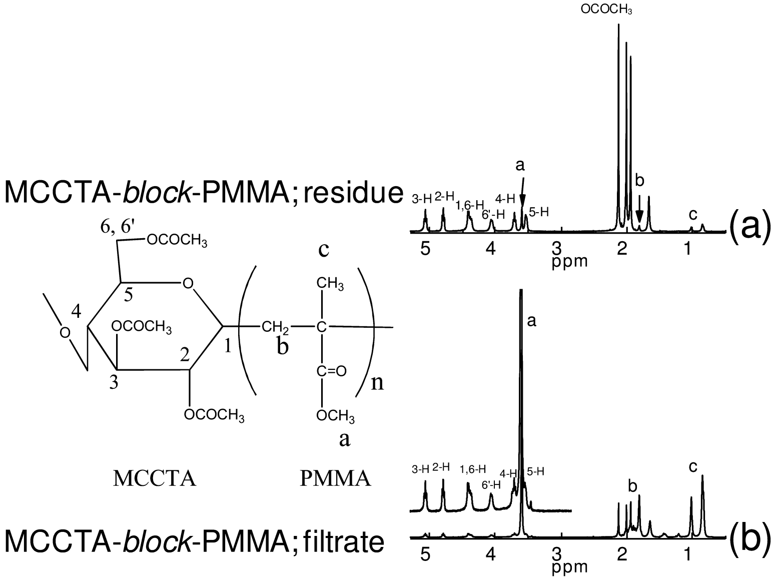

Figure 12. ^{1}H NMR spectra of (a) MCCA-block-PMMA residue and (b) MCCA-block-PMMA filtrate.

The ^{1}H NMR spectrum (Figure 12a) of the MCCA-*block*-PMMA residue in *d*-chloroform reveals two proton groups: one from the protons of the glucopyranose rings of MCCA; 1-H (4.42 ppm), 2-H (4.79 ppm), 3-H (5.07 ppm), 4-H (3.71 ppm), 5-H (3.54 ppm), 6-H (4.38 ppm), and 6′-H (4.06 ppm), and the other from the methyl protons (0.86–1.02 ppm), methylene protons (1.81 ppm), and methoxy protons (3.60 ppm) of the PMMA chains. The ^{1}H NMR spectrum (Figure 12b) of the MCCA-*block*-PMMA filtrate in *d*-chloroform reveals strong peaks from the proton groups of PMMA and weak peaks from the glucopyranose rings.

These results indicate that MCC behaved similarly to BC in the fracture and copolymerization experiments. The MCC-*block*-PMMA was located on the MCC surface, forming MCC core/PMMA shell nanoparticles.

Nanoparticles of MCC Fully Covered with PMMA from the MCC-*block*-PMMA Filtrate: MCC Core/PMMA Shell Nanoparticles

The core-shell nanoparticles were dispersed in chloroform, and resulted in a transparent liquid. The average diameter of the core/shell nanoparticles in chloroform was estimated at 52 nm by DLS. The transparency was kept over one month.

Downloaded by OHIO STATE UNIV LIBRARIES on August 28, 2012 | http://pubs.acs.org
Publication Date (Web): August 17, 2012 | doi: 10.1021/bk-2012-1107.ch007

Conclusions

Modification of cellulose involving diblock copolymerization may provide a novel usage of cellulose. We intended to synthesize diblock copolymer of cellulose by initiating the radical polymerization with by mechano-radicals from the fracture of cellulose.

Here, we used bacterial cellulose (BC) and microcrystalline cellulose (MCC). The mechanical fracture of BC (or MCC) in vacuum at 77 K produced mechano-radicals by scissions of the β-1,4 glycosidic linkage. The BC-*block*-PMMA was synthesized on the BC surface by radical polymerization of MMA initiated by the BC mechano-radicals. The BC surface was fully covered with the PMMA chains of BC-*block*-PMMA. MCC showed the same behavior.

The MCC nanoparticles were fully covered with PMMA chains thus forming MCC core/PMMA shell nanoparticles, dispersable in chloroform as clear liquid.

References

1. Herman, P. H.; Weidinger, A. *J. Am. Chem. Soc.* **1946**, *68*, 2547–2552.
2. Nakai, Y.; Fukuoka, E.; Nakajima, S.; Yamamoto, K. *Chem. Pharm. Bull.* **1977**, *25*, 3340–3346.
3. Hon, D. N.-S.; Srinivasan, K. S. V. *J. Appl. Polym. Sci.* **1983**, *28*, 1–10.
4. Ikekawa, A.; Hayakawa, S. *Bull. Chem. Soc. Jpn.* **1983**, *56*, 3566–3570.
5. Sasai, Y.; Yamauchi, Y.; Kondo, S.; Kuzuya, M. *Chem. Pharm. Bull.* **2004**, *52*, 339–344.
6. Shimada, S.; Suzuki, A.; Sakaguchi, M.; Hori, Y. *Macromolecules* **1996**, *29*, 973–977.
7. Sakaguchi, M.; Yamamoto, K.; Shimada, S. *Macromolecules* **1998**, *31*, 7829–7834.
8. Sakaguchi, M.; Yamamoto, K.; Miwa, Y.; Shimada, S.; Sakai, M.; Iwamura, T. *Macromolecules* **2007**, *40*, 1708–1712.

9. Sakaguchi, M.; Iwamura, T.; Yamamoto, K.; Miwa, Y.; Shimada, S.; Sakai, M. *Macromolecules* **2008**, *41*, 253–257.
10. Sakaguchi, M.; Ohura, T.; Iwata, T.; Takahashi, S.; Akai, S.; Kan, T.; Murai, H.; Fujiwara, M.; Watanabe, O.; Narita, M. *Biomacromolecules* **2010**, *11*, 3059–3066.
11. Sakaguchi, M.; Sohma, J. *J. Polym. Sci., Polym. Phys. Ed.* **1975**, *13*, 1233–1245.
12. Iwasaki, M.; Nunome, K.; Ichikawa, T.; Toriyama, K. *Bull. Chem. Soc. Jpn.* **1971**, *44*, 1522–1526.
13. Iwasaki, M.; Nunome, K.; Ichikawa, T.; Toriyama, K. *Chem. Phys. Lett.* **1971**, *54*, 1839–1840.
14. Lin, Y.-S.; Lee, S.; Lin, B. C.; Cheng, C. P. *Mater. Chem. Phys.* **2003**, *78*, 847–851.
15. Iwasaki, M.; Sakai, Y. *J. Polym. Sci., Part A-1* **1969**, *7*, 1537–1547.
16. Sakai, Y.; Iwasaki, M. *J. Polym. Sci., Part A-1* **1969**, *7*, 1749–1764.
17. Berger, P. A.; Kotyk, J. J.; Resen, E. E. *Macromolecules* **1992**, *25*, 7227–7233.
18. Carriere, P.; Grohens, Y.; Spevacek, J.; Schultz, J. *Langmuir* **2000**, *16*, 5051–5053.
19. Gagnaire, D. Y.; Taravel, R.; Vignon, M. R. *Macromolecules* **1982**, *15*, 126–129.
20. Rao, V. S.; Sauriol, F.; Perlin, A. S. *Can. J. Chem.* **1985**, *63*, 2507–2511.
21. *CRC Handbook of Chemistry and Physics*, 76th ed.; Lide, D. R., Ed.; CRC Press: Boca Raton, FL, 1995−1996; pp 9−31.
22. Boyer, R. F. *Macromolecules* **1992**, *25*, 5326–5330.

Downloaded by OHIO STATE UNIV LIBRARIES on August 28, 2012 | http://pubs.acs.org
Publication Date (Web): August 17, 2012 | doi: 10.1021/bk-2012-1107.ch007

Downloaded by PENNSYLVANIA STATE UNIV on August 28, 2012 | http://pubs.acs.org
Publication Date (Web): August 17, 2012 | doi: 10.1021/bk-2012-1107.ch008

Chapter 8

Super-Hydrophobic Cotton Fabric Prepared Using Nanoparticles and Molecular Vapor Deposition Methods

N. Abidi,* P. Aminayi, L. Cabrales, and E. Hequet

Fiber and Biopolymer Research Institute,
Department of Plant and Soil Science, Texas Tech University,
P.O. Box 45019, Lubbock, Texas 79403, USA
***E-mail: n.abidi@ttu.edu**

Cotton fabric was functionalized with nanoparticles vapor deposition (NVD) of Al_2O_3 followed by molecular vapor deposition (MVD) of (tridecafluoro-1,1,2,2,-tetrahydrooctyl)-trichlorosilane (FOTS). The nanoparticles deposition increased the surface roughness, leading to higher contact angles. The morphology of the treated surfaces was observed with scanning electron microscopy. Fourier-transform infrared (FT-IR) analysis of the functionalized surfaces showed the presence of peaks corresponding to C-F, CF_2, Al-O, and O-Al-O. Dynamic water contact angles were measured in order to assess the hydrophobic properties of the functionalized surface. Dynamic contact angles higher than 150° were obtained for water. In addition, samples treated with nanoparticles and FOTS layer showed low hysteresis when measuring advancing and receding contact angles.

In Functional Materials from Renewable Sources; Liebner, F., et al.;
ACS Symposium Series; American Chemical Society: Washington, DC, 2012.

Downloaded by PENNSYLVANIA STATE UNIV on August 28, 2012 | http://pubs.acs.org
Publication Date (Web): August 17, 2012 | doi: 10.1021/bk-2012-1107.ch008

Introduction

Interests in super-hydrophobic surfaces have been increasing in recent years. There are numerous surfaces in nature which possess hydrophobic characteristics. In general, surfaces with a static contact angle higher than 150° and low contact angle hysteresis are defined as super-hydrophobic surfaces. Highly hydrophobic surfaces have many industrial applications; some of these can be in solar panels, architectural glass, heat transfer surfaces, piping, boat hulls, and microfluidics. Two approaches are commonly used to produce super-hydrophobic surface. In the first approach, a coating is applied to a rough surface using low-surface-energy materials. In the second approach, a low surface energy material is roughened in order to achieve this remarkable property (*1*). Compounds based on silicones (*2–4*), and fluorocarbons (*5–10*) are most used for this purpose.

Processes to impart water repellency to substrates are commonly carried out in liquid phase. Liquid processes have many disadvantages when compared to gas phase processes such as: disposal of organic solvents, incomplete wetting of high aspect ratio structures, diffusion limited transport of reactants, and poor control of reactant supply among others (*11*). In this study, a vapor phase treatment was used to impart super-hydrophobic properties to cotton fabric surfaces. Chemical vapor deposition (CVD) is a gas phase process where the gas molecules react to create thin films (*12*). In the past, CVD has been used to create hydrophobic surfaces (*13*). A special type of gas phase treatment is atomic layer deposition (ALD). In ALD, binary sequential gas reactions occur. Each chemical is introduced in the chamber separately after the other reactant has been removed. One of the advantages of ALD process is the precise thickness (Angstrom scale) and high uniformity of the resultant coating. This is due to the self-limiting surface reactions used in ALD. Since the process is done under gas phase, the reaction can take place even in the pores of the substrate (*14*). Because of the ability of the sequential reaction, the coating thickness is not limited to one layer; hence the thickness is controllable depending on the number of sequences. ALD has been used in the past to produce conformal hydrophobic surfaces by first adding a seed layer onto substrates by ALD and then reacting the seed layer with non-chlorinated alkylsilanes (*15*).

Hyde et al. reported on the use of ALD to perform inorganic nanoscale coatings on three-dimensional natural fibers (*16*). Cotton fabric was treated with chlorine to remove unwanted contaminants and to whiten the fabric, and subjected to a mercerization process. The authors used a hot-wall viscous-flow tube reactor to perform ALD of Al_2O_3 using trimethyl aluminum and H_2O (*17*). The authors measured the thickness of Al_2O_3 film on cotton fabrics and reported a growth rate of 5 Å per cycle initially and 3 Å per cycle as the growth proceeds. The static water contact angle measurements after 100 cycles of Al_2O_3 showed 127°. However, the treated fabric did not show a good dynamic contact angle. The authors reported a decrease of the water contact angle to 53° after 60 min. Jur et al. reported on the use of ALD of conductive coatings on cotton, paper, and synthetic fibers (*18*). Using this technique, ZnO films were formed at 115 °C on fiber and planar silicon substrates. The authors concluded that the conductivity values are consistent with the values expected from the respective thin film conductivity. Hyde et al. reported that ALD of Al_2O_3 on nonwoven

Downloaded by PENNSYLVANIA STATE UNIV on August 28, 2012 | http://pubs.acs.org
Publication Date (Web): August 17, 2012 | doi: 10.1021/bk-2012-1107.ch008

polypropylene and woven cotton fabric materials can be used to transform and control fiber surface properties (*19*). The results showed that the transition between non-wetting to wetting depends on the ALD process variables such as the number of ALD coating cycles and deposition temperature.

The layer-by-layer deposition technique was reported to be suitable to create multilayer thin films on different surfaces (*20–25*). Super-hydrophobic cotton fabric was fabricated by electrostatic layer-by-layer assembly of polyelectrolyte/silica nanoparticle multilayers followed with fluoroalkylsilane treatment (*26*). The results showed that cotton fabric treated with 5 multilayers or more achieved slippery hydrophobicity with a contact angle hysteresis lower than 10°.

The deposition of Al_2O_3 is a model system for ALD because the surface reactions were reported to be very efficient and self-limiting (*14*). Al_2O_3 is deposited by the sequential reaction of trimethyl aluminum (TMA) and water (H_2O) as shown in the following reaction (*14*, *27*):

$$2Al(CH_3)_3 + 3H_2O \rightarrow Al_2O_3 + 3CH_4 \qquad (\Delta H) = -376\ \text{kcal}$$

The effect of surface roughness and heterogeneity on wettability and water contact angle has been the subject of numerous studies (*28*, *29*). Ogawa et al. reported that a glass plate can be made "ultrahydrophobic" with a contact angle of 155° by roughening it at submicron level followed by a hydrophobization step using a fluoroalkyltrichlorosilane (*30*).

In this paper, the same reactants for ALD of Al_2O_3 are used to create ALD-like films and to deposit nanoparticles with a method called Nanoparticle Vapor Deposition (NVD). In NVD, a binary sequential reaction was also used, just as in ALD. The only difference was that the second reactant was introduced without removing the first reactant from the chamber. By doing this, aluminum oxide nanoparticles were deposited on the substrate instead of a conformal coating, leading to an increase of the surface roughness. Then, by using a CVD method, called Molecular Vapor Deposition (MVD), a thin fluorocarbon layer is deposited on the nanoparticles. With the increased roughness of the substrate surface and the addition of the fluorocarbon layer, super-hydrophobic properties are imparted to a material. In this work, we were interested to have a surface with very low contact angle hysteresis (which is defined as the difference between the advancing and receding contact angles). Previous studies reported the results only of the static contact angle. These studies have considered super-hydrophobic fabrics based essentially on the results of the static contact angle larger than 150° (*26*). This has been reported not to be sufficient to guarantee a low sliding angle for self-cleaning properties (*26*). Therefore, the main objective of this first phase of the work is to create super-hydrophobic surface with very low contact angle hysteresis.

Downloaded by PENNSYLVANIA STATE UNIV on August 28, 2012 | http://pubs.acs.org
Publication Date (Web): August 17, 2012 | doi: 10.1021/bk-2012-1107.ch008

Experimental Section

Materials

Microscope slides from Fisher Scientific (Houston, TX) served as a control substrate. Distilled water was deionized in a Milli-Q plus system from Millipore (Billerica, MA) to reach final resistivity of 18.2 MΩ-cm.

The fabric used in this study was desized, scoured, and bleached 100% cotton fabric obtained from Testfabrics, Inc. (West Pittiston, PA). The fabric characteristics were as follows: 95 ends, 100 picks, yarn count of 36 x 40 Ne, and a weight of 118.7 g/m^2 (3.5 oz/yard^2).

The chemicals used for all the treatments were: H_2O, trimethyl aluminum ($Al(CH_3)_3$), and (tridecafluoro-1,1,2,2,-tetrahydrooctyl)-trichlorosilane (FOTS).

Methods

Pre-Treatment

Microscope glass slides were first thoroughly washed with ethanol to remove any surface contaminants. Both glass slides and cotton fabrics were subjected to additional surface cleaning with N_2 microwave plasma (PLASMAtech Inc Erlanger, KY). Samples were exposed to N_2-plasma for 120 s at 500 W (N_2 flow = 60 ml/min).

NVD and MVD Treatments

The system used for vapor phase deposition was a RPX-550 from Integrated Surface Technologies (Menlo Park, CA). The system consists of 5 containers for chemical reactants with independent controlled temperature, a vacuum pump, and sample chamber. Inside the chamber there is a perforated plate to deliver the gases over the samples. This configuration enhances the deposition of nanoparticles on the substrate. N2 is used to transfer the reactants from the containers to the chamber in vapor phase through heated delivery lines. The system chamber was maintained at 55 °C during all the processes. The temperature of the chemical containers was held at 40 °C and the transfer lines at 45 °C to avoid condensation. Due to the low vapor pressure of FOTS, the container for this reactant was held at 90 °C and the transfer line at 95 °C. The chamber was purged with N_2 and vacuumed to 0.13 mbar at the beginning of all processes. Three replications were performed for each treatment and all samples were rinsed in distilled water and were air-dried before any further testing.

Downloaded by PENNSYLVANIA STATE UNIV on August 28, 2012 | http://pubs.acs.org
Publication Date (Web): August 17, 2012 | doi: 10.1021/bk-2012-1107.ch008

Nanoparticles Vapor Deposition of Al_2O_3 (NVD-Al_2O_3)

The NVD of Al_2O_3 was performed as follows: after the initial purging, TMA vapor was added to the chamber to reach a pressure of 0.50 mbar. Subsequently, water vapor (without any previous purging) was introduced to reach a pressure of 1.06 mbar. After 30 seconds of reaction, the chamber was evacuated and purged. The process was repeated 4 times.

Nanoparticles Vapor Deposition of Al_2O_3 Followed by Molecular Vapor Deposition of Bifunctional Trichlorosilane and Molecular Vapor Deposition of (Tridecafluoro-1,1,2,2,-tetrahydrooctyl)-trichlorosilane (FOTS)

The NVD of Al_2O_3 process was performed first as detailed above. Then, a chemical mixture of bifunctional trichlorosilanes (such as bis(trichlorosilyl)-ethane, bis(trichlorosilyl)-butane, and bis(trichlorosilyl)-hexane) was introduced in the chamber to reach a pressure of 0.37 mbar. After 5 s, water vapor was introduced in the chamber to reach a pressure of 2.66 mbar. After 3 s, the chamber was evacuated to 0.13 mbar. The purpose to add the bifunctional trichlorosilanes blend was to increase the wear resistance of the Al_2O_3 nanoparticles coating. The MVD of FOTS was performed as follows: after evacuating the chamber, water vapor was introduced to reach a pressure of 0.11 mbar. Thereafter, the FOTS vapor was introduced to reach a pressure of 0.18 mbar. The reaction was left to take place for 300 s, then the chamber was purged and vented.

Characterization

Morphology of the Nanocoatings

Scanning electron microscopy (SEM) and transmission electron microscopy (TEM) were used to investigate the morphology of the coatings. SEM and TEM images were acquired with S-3400N and H-7650 models (Hitachi High-Technologies America, Pleasanton, CA) respectively. For the SEM images, the samples were coated with gold. SEM images were recorded with the secondary electrons detector at 5 kV accelerating voltage. For TEM experiments, the coating on the glass slides containing aluminum oxide nanoparticles was scratched off and a drop of water was placed on it and collected on a copper grid. The drop was left to dry and images were taken.

Downloaded by PENNSYLVANIA STATE UNIV on August 28, 2012 | http://pubs.acs.org
Publication Date (Web): August 17, 2012 | doi: 10.1021/bk-2012-1107.ch008

FTIR Analysis of the Nanocoatings

Fourier transform infrared (FTIR) spectra of the samples were recorded using Spectrum-One equipped with a universal attenuated total reflectance (UATR) device (Perkin Elmer, Waltham, MA). The UATR-FTIR was equipped with a ZnSe-diamond crystal composite that allows the FTIR spectra collection without any special sample preparation. The UATR accessory has a "pressure arm", which is used to apply a constant pressure to the samples positioned on top of the crystal to ensure good contact between the crystal and the sample. FTIR spectra were collected at a spectra resolution of 4 cm^{-1}, with 32 accumulated scans over the range from 4000 to 650 cm^{-1}. The spectra were baseline-corrected and normalized to the highest absorption peak. A background scan of the clean crystal was acquired before scanning the samples.

Hydrophobic Properties Assessment

Contact angle measurements were performed with a FTA 1000 instrument (First Ten Angstroms, Portsmouth, VA). For static and dynamic contact angles, a drop between 5 and 8 µL of water was placed on the surfaces. A 26 gauge needle was used for this purpose. A Laplace fit method was used to calculate the contact angles. Advancing and receding contact angles were measured to calculate contact angle hysteresis. In order to measure these angles, the needle was brought close to the sample surface and the liquid rest was pumped out for 20 seconds until the drop reached a size of approximately 30 µl. After this volume was reached, the liquid was pumped in at the same rate until the drop detached from the needle (hydrophobic) or the whole amount of liquid was back in the syringe (super-hydrophobic).

Results and Discussion

Scanning Electron Microscopy and Transmission Electron Microscopy

To illustrate the surface roughness introduced by NVD of Al_2O_3, the SEM micrographs of untreated and functionalized glass slides are shown in figures 1-a and 1-b, respectively. The comparison of the two micrographs indicates substantial surface roughness of the functionalized glass slide. Figures 2-a and 2-b show SEM micrographs of untreated and functionalized cotton fabric surfaces. The surface of single cotton fibers appears rough compared to the untreated single cotton fiber.

Downloaded by PENNSYLVANIA STATE UNIV on August 28, 2012 | http://pubs.acs.org
Publication Date (Web): August 17, 2012 | doi: 10.1021/bk-2012-1107.ch008

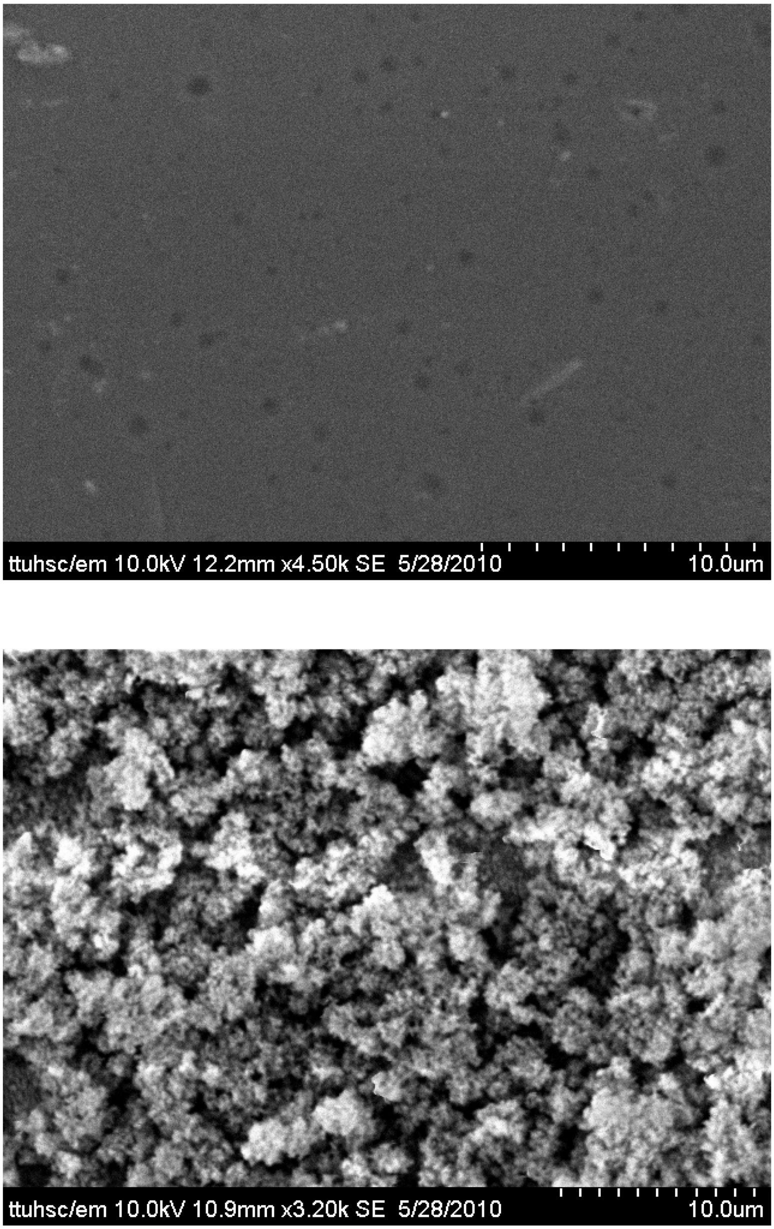
ttuhsc/em 10.0kV 12.2mm x4.50k SE 5/28/2010
10.0um
ttuhsc/em 10.0kV 10.9mm x3.20k SE 5/28/2010
10.0um

Figure 1. (a) SEM image of the untreated glass surface. (b) SEM image of the functionalized glass surface with NVD of Al_2O_3.

Downloaded by PENNSYLVANIA STATE UNIV on August 28, 2012 | http://pubs.acs.org
Publication Date (Web): August 17, 2012 | doi: 10.1021/bk-2012-1107.ch008

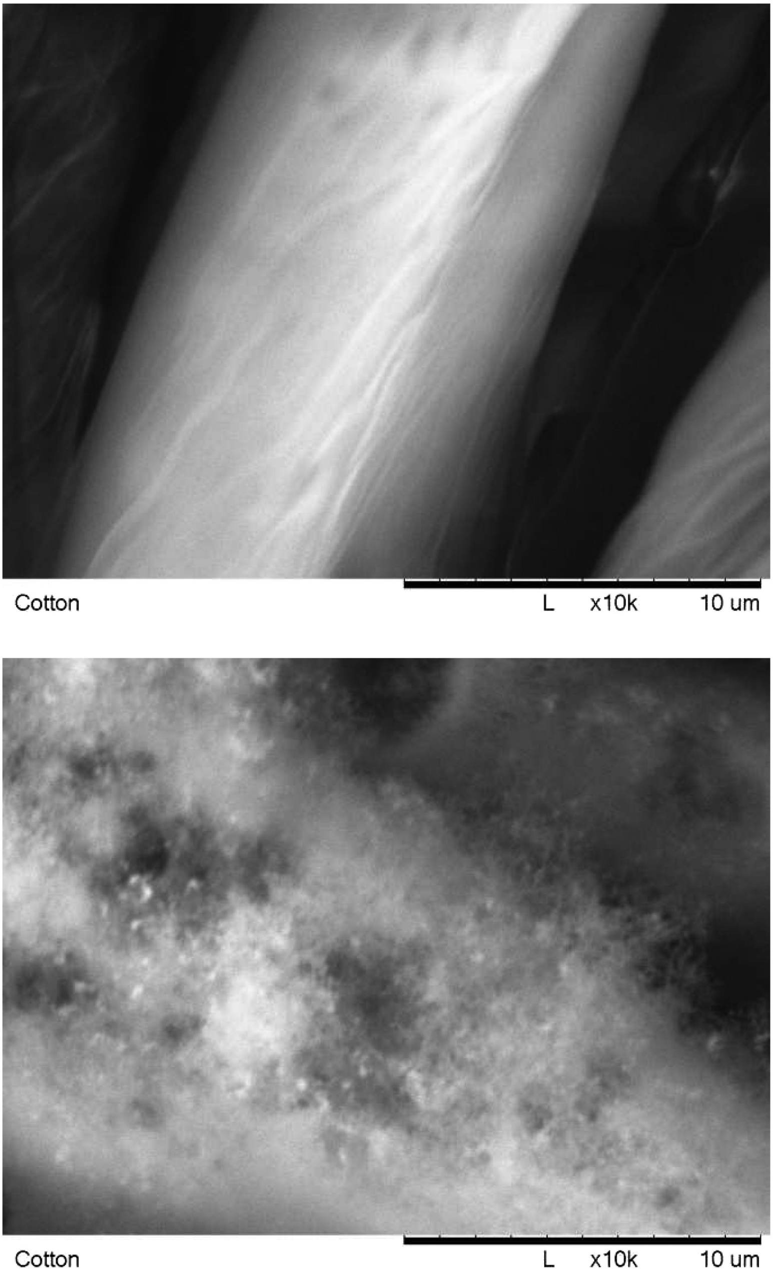

Figure 2. (a) SEM image of an untreated cotton fabric surface. (b) SEM image of the functionalized cotton fabric surface.

Figure 3 shows the TEM image of Al_2O_3 nanoparticles deposited on a microscopy glass slide which was subjected to one cycle of NVD of Al_2O_3. To perform TEM analysis, Al_2O_3 film deposited on the glass slide was scratched and transferred to the TEM sample holder. The size of the particles deposited is between 29.4 and 50.7 nm.

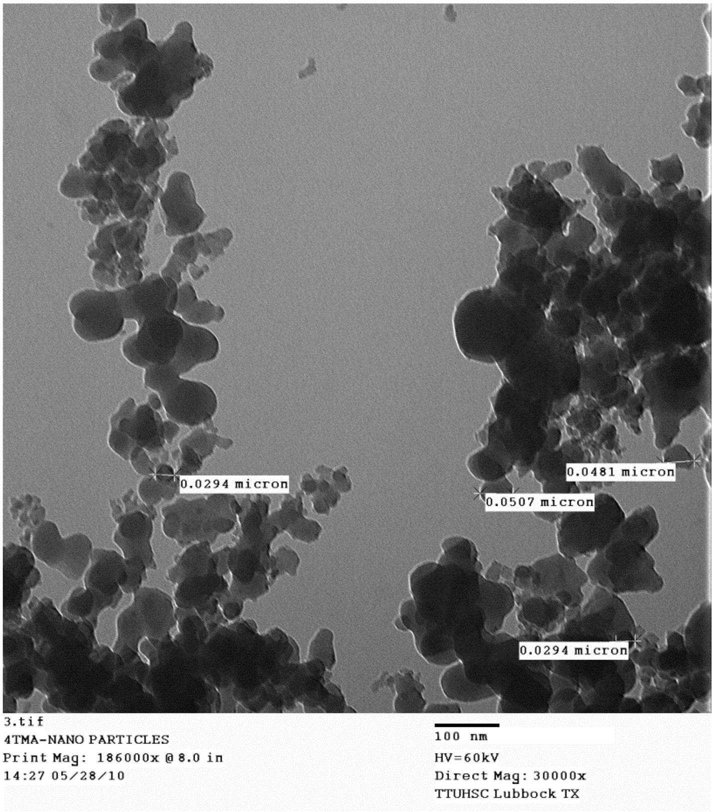
0.0294 micron
0.0481 micron
0.0507 micron
0.0294 micron
3.tif
4TMA-NANO PARTICLES
Print Mag: 186000x @ 8.0 in
14:27 05/28/10
100 nm
HV=60kV
Direct Mag: 30000x
TTUHSC Lubbock TX

Figure 3. TEM image of Al_2O_3 nanoparticles deposited on a glass slide.

Fourier Transform Infrared Spectroscopy

The FTIR spectra of the untreated glass slide and the glass slide functionalized with NVD of Al_2O_3 followed by MVD of FOTS are shown in figure 4. Several additional peaks are present in the FTIR spectrum of the functionalized glass slide. The vibration at 3425 cm^{-1} is attributed to OH groups, which could originate from Al-OH groups. The vibration located at 1630 cm^{-1} is assigned to adsorbed

Downloaded by PENNSYLVANIA STATE UNIV on August 28, 2012 | http://pubs.acs.org
Publication Date (Web): August 17, 2012 | doi: 10.1021/bk-2012-1107.ch008

water on OH hydroxyl groups through hydrogen bonding. The vibrations located at 2920 and 2850 cm^{-1} are attributed to asymmetric and symmetric C-H stretching, respectively, of the FOTS . The vibration located at 1239 cm^{-1} is C-F stretching. The bands located at 1212 and 1145 cm^{-1} are attributed to asymmetric and symmetric CF_2 stretching, respectively (*31*), those at 878 and 705 cm^{-1} to Al-O stretching and O-Al-O bending, respectively (*32*, *33*). The presence of these vibrations is indicative of the successful functionalization of the glass slide substrate with NVD of Al_2O_3 and MVD of FOTS.

Downloaded by PENNSYLVANIA STATE UNIV on August 28, 2012 | http://pubs.acs.org
Publication Date (Web): August 17, 2012 | doi: 10.1021/bk-2012-1107.ch008

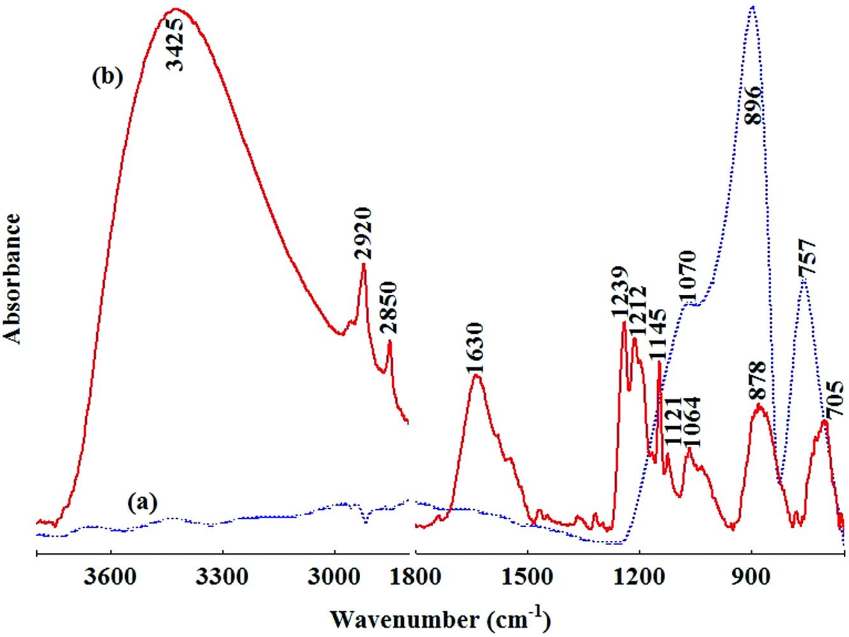

Figure 4. FTIR spectra of (a) a control glass slide and (b) a glass slide functionalized with NVD of Al_2O_3 and MVD of FOTS.

The FTIR analysis of the functionalized cotton fabric with NVD of Al_2O_3 followed by MVD of FOTS shows the presence of additional peaks (Figure 5). The most important bands are those located at 1239 cm^{-1} (attributed to C-F stretching), 1145 cm^{-1} (attributed to symmetric CF_2 stretching), and 705 cm^{-1} (attributed to O-Al-O bending). It is important to note that the intensities of the vibrations located at 3335 and 1620 cm^{-1} are very high compared to the control. This indicates a high amount of physisorbed H_2O on the surface of the functionalized cotton fabric.

Downloaded by PENNSYLVANIA STATE UNIV on August 28, 2012 | http://pubs.acs.org
Publication Date (Web): August 17, 2012 | doi: 10.1021/bk-2012-1107.ch008

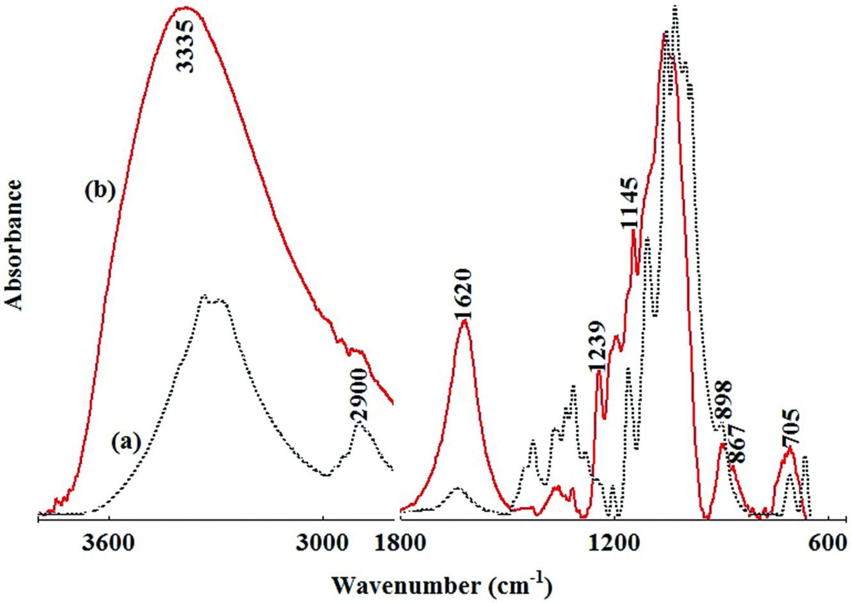

Figure 5. FTIR spectra of (a) a control cotton fabric and (b) a cotton fabric functionalized with NVD of Al_2O_3 and MVD of FOTS.

Dynamic Contact Angle Measurements

In this study, the Young's equation was used to determine the contact angle, θ, of the control and the functionalized surfaces. The Young's equation states that on a flat, smooth, and chemically heterogeneous surface the contact angle is given by (*34*):

$$\delta_{LV}\ \cos\theta = \delta_{SV} - \delta_{SL}$$

where γ_{LV} is the liquid-vapor surface tension, γ_{SL} and γ_{SV} are the solid-liquid and solid vapor interfacial tensions, respectively (*34*). In general, when the static water contact angle is below 90°, a surface is termed hydrophilic. However, when the contact angle is between 90° and 150°, a surface is classified as hydrophobic. A surface is called super-hydrophobic when the water contact angle is larger than 150°.

We consider only water contact angles here. The glass slide substrate with no treatment has a static water contact angle of 18°, which is typical of a hydrophilic surface. The functionalization of this substrate with NVD of Al_2O_3 followed by MVD of bifunctional trichlorosilane and MVD of FOTS leads to a static water contact angle of 168°, which is typical of super-hydrophobic surface. Previously, super-hydrophobic surfaces have been considered only based on the criterion of static contact angles higher than 150°. The dynamic water contact angle measurements give a good indication of the wettability of a surface. A super-hydrophobic surface may have very high initial (static) contact angle. However, over time the water can diffuse and wet the surface. The measurements of the dynamic contact angles allow us only evaluation of the hydrophobicity of a surface, but also determination of the contact angle hysteresis. Figure 6 shows the dynamic contact angles of the control and the functionalized glass slide. The control glass slide has an initial static water contact angle of 18°, which then drops to 0 (the water wets the sample quickly). However, the functionalized glass slide has a static water contact angle of 168°, which does not change with time.

Downloaded by PENNSYLVANIA STATE UNIV on August 28, 2012 | http://pubs.acs.org
Publication Date (Web): August 17, 2012 | doi: 10.1021/bk-2012-1107.ch008

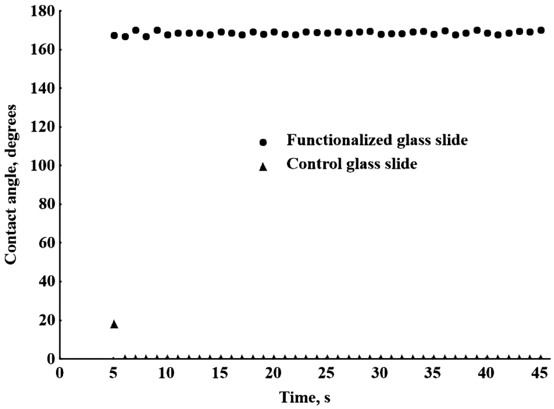

Figure 6. Dynamic contact angle of the control and the functionalized glass slide.

Figure 7 shows the advancing and receding water contact angles of a functionalized glass slide with NVD of Al_2O_3 followed by MVD of bifunctional trichlorosilane and MVD of FOTS. As the volume of the sessile drop increases or decreases, the advancing and receding angles remain the same. The advancing contact angle (θ_a) is measured after the front of the settled drop has progressed, while the receding contact angle (θ_r) is measured when the front has receded (*35*). The hysteresis (*H*) is defined as the difference between the advancing contact angle and the receding contact angle (H = θ_a - θ_r). The contact angle hysteresis of the functionalized glass slide substrate is 1°. This low contact angle hysteresis indicates that only small tilting angle is necessary to roll off the water droplet from the surface of the glass substrate.

Downloaded by PENNSYLVANIA STATE UNIV on August 28, 2012 | http://pubs.acs.org
Publication Date (Web): August 17, 2012 | doi: 10.1021/bk-2012-1107.ch008

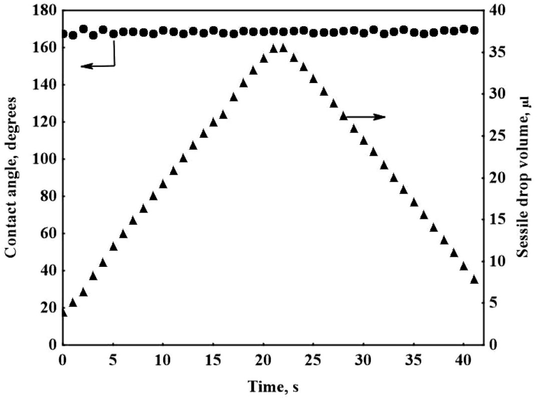

Figure 7. Advancing and receding water contact angle of the functionalized glass slide with NVD of Al_2O_3 followed by MVD of bifunctional trichlorosilane and MVD of FOTS.

The dynamic water contact angle of the control and the functionalized cotton fabric are shown in Figure 8. The control cotton fabric used in this study was initially desized, scoured, and bleached. This fabric was completely hydrophilic (contact angle = 0°). The static contact angle of the functionalized fabric is 161°. The dynamic water contact angle of the functionalized cotton fabric did not show any change. Measurements of the water contact angle performed after 20 min did not show any significant change, the contact angle remained > 150°.

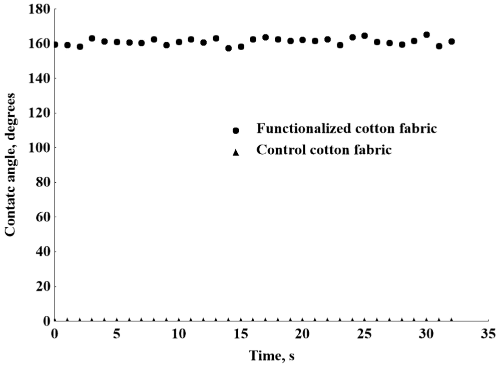

Figure 8. Dynamic contact angle of the control and the functionalized cotton fabric.

Advancing and receding water contact angles of functionalized cotton fabric with NVD of Al_2O_3 followed by MVD of bifunctional trichlorosilane and MVD of FOTS were also measured (Figure 9). The functionalization with Al_2O_3 followed by FOTS imparts super-hydrophobic properties on the cotton fabric. The advancing contact angle is 161° and the receding contact angle is 160°. The very low hysteresis (1°) allows rolling off water droplets at very low tilting angle.

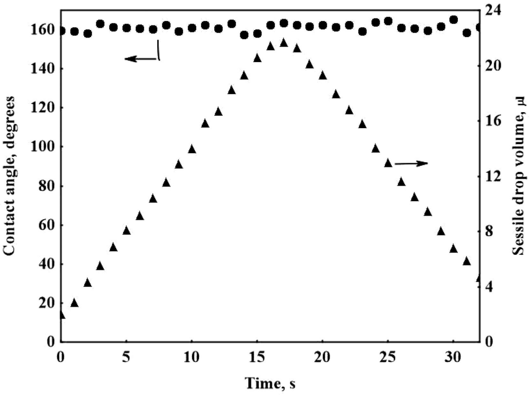

Figure 9. Advancing and receding water contact angle of the cotton fabric functionalized with NVD of Al_2O_3 followed by MVD of bifunctional trichlorosilane and MVD of FOTS.

The determination of the contact angle hysteresis allows calculating the force needed to start rolling off a drop of liquid sitting on the surface (*28*). The following equation has been proposed (*28*):

$$F = \gamma_{LV}(\cos\theta_R - \cos\theta_A)$$

where F is the critical line force per unit length of the drop perimeter, γ_{LV} is the surface tension of the liquid. θ_A and θ_R are the advancing and receding contact angles, respectively. For the functionalized slide substrate, the force calculated is 0.27 mN/m, while for the functionalized cotton fabric this force is 0.09 mN/m. For these super-hydrophobic surfaces, a very small force is needed to roll off a droplet of water.

Figure 10 shows a picture of a water droplet on the surface of functionalized cotton fabric. The droplet has a static water contact angle of 161°. Dynamic contact angle measurements show that the droplet does not diffuse inside the fibers. This imparts very good super-hydrophobic properties to the cotton fabric.

Downloaded by PENNSYLVANIA STATE UNIV on August 28, 2012 | http://pubs.acs.org
Publication Date (Web): August 17, 2012 | doi: 10.1021/bk-2012-1107.ch008

Downloaded by PENNSYLVANIA STATE UNIV on August 28, 2012 | http://pubs.acs.org
Publication Date (Web): August 17, 2012 | doi: 10.1021/bk-2012-1107.ch008

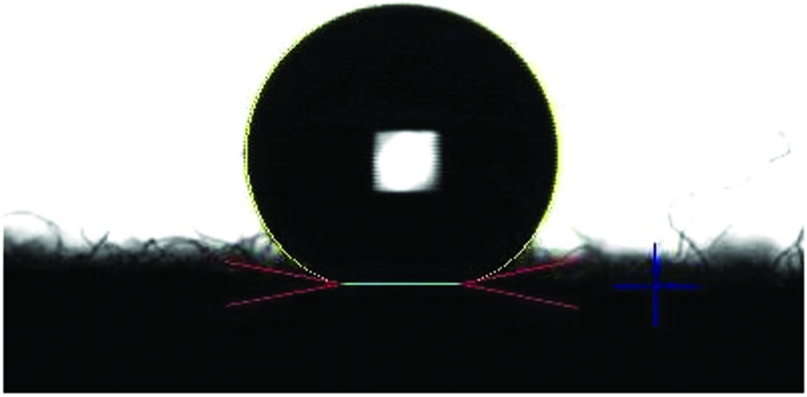

Figure 10. Picture of a water droplet on the functionalized cotton fabric surface.

Conclusions

The use of the nanoparticles vapor deposition method allowed us creating a rough surface through the vapor phase reaction. The addition of a layer of tridecafluoro-1,1,2,2,-tetrahydrooctyl)-trichlorosilane to the roughened surface imparted super-hydrophobic properties on the cotton fabric. The glass slide in this study was used as a control (flat surface). Very low contact angle hysteresis was obtained which allows rolling off a water droplet at very low force and very low tilting angles.

Acknowledgments

The authors would like to thank the Texas Department of Agriculture, Food and Fibers Research Grant Program for providing the financial support for this project (Project # FF-d-1011-03).

References

1. Ma, M.; Hill, R. M. *Curr. Opin. Colloid Interface Sci.* **2006**, *11* (4), 193–202.
2. Khorasani, M. T.; Mirzadeh, H.; Kermani, Z. *Appl. Surf. Sci.* **2005**, *242* (3−4), 339–345.
3. Sun, M.; Luo, C. L.; Xu, H.; Ji, Q.; Ouyang, D. Yu; Chen, Y. *Langmuir* **2005**, *21* (19), 8978–8981.
4. Oner, D.; McCarthy, T. J. *Langmuir* **2000**, *16* (20), 7777–7782.
5. Liu, Y. H.; Wang, X. K.; Luo, J. B.; Lu, X. C. *Appl. Surf. Sci.* **2009**, *255* (23), 9430–9438.
6. Hsieh, C.-T.; Cheng, Y.-S.; Hsu, S.-M.; Lin, J.-Y. *Appl. Surf. Sci.* **2010**, *256* (16), 4867–4872.

7. Di Mundo, R.; De Benedictis, V.; Palumbo, F.; d'Agostino, R. *Appl. Surf. Sci.* **2009**, *255* (10), 5461–5465.
8. Favia, P.; Cicala, G.; Milella, A.; Palumbo, F.; Rossini, P.; d'Agostino, R. *Surf. Coat. Technol.* **2003**, *169-170*, 609–612.
9. Kulinich, S. A.; Farzaneh, M. *Vacuum* **2005**, *79* (3-4), 255–264.
10. Liu, D.; Li, W.; Feng, Z.; Tan, X.; Chen, B.; Niu, J.; Liu, Y. *Surf. Coat. Technol.* **2009**, *203* (9), 1231–1236.
11. Mayer, T. M.; de Boer, M. P.; Shinn, N. D.; Clews, P. J.; Michalske, T. A. *J. Vac. Sci. Technol., B: Microelectron. Process. Phenom.* **2000**, *18* (5), 2433–2440.
12. Gates, S. M. *Chem. Rev.* **1996**, *96* (4), 1519–1532.
13. Nakajima, A.; Hashimoto, K.; Watanabe, T. *Monatsh. Chem.* **2001**, *132* (1), 31–41.
14. George, S. M. *Chem. Rev.* **2009**, *110* (1), 111–131.
15. Herrmann, C. F.; DelRio, F. W.; Bright, V. M.; George, S. M. *J. Micromech. Microeng.* **2005**, *15* (5), 984–992.
16. Hyde, G. K.; Park, K. J.; Stewart, S. M.; Hinestroza, J. P.; Parsons, G. N. *Langmuir* **2007**, *23* (19), 9844–9849.
17. Peng, Q.; Sun, X. Y.; Spagnola, J. C.; Hyde, G. K.; Spontak, R. J.; Parsons, G. N. *Nano Lett.* **2007**, *7* (3), 719–722.
18. Jur, J. S.; Weet, W. J. S; Oldham, C. J.; Parsons, G. N. *Adv. Funct. Mater.* **2011**, *21* (11), 1993–2002.
19. Hyde, G. K.; Scarel, G.; Spagnola, J. C.; Peng, Q.; Lee, K.; Gong, B.; Roberts, K. G; Roth, K. M.; Hanson, C. A.; Devine, C. K.; Stewart, S. M.; Hojo, D.; Na, J. S.; Jur, J. S.; Parsons, G. N. *Langmuir* **2010**, *26* (4), 2550–2558.
20. Hyde, K.; Dong, H.; Hinestroza, J. P. *Cellulose* **2007**, *14* (6), 615–623.
21. Decher, G. *Science* **1997**, *277* (5330), 1232–1237.
22. Lvov, Y.; Ariga, K.; Onda, M.; Ichinose, I.; Kunitake, T. *Colloids Surf., A* **1999**, *146* (1−3), 337–346.
23. de Villiers, M. M.; Otto, D. P.; Strydom, S. J.; Lvov, Y. M. *Adv. Drug Delivery Rev.* **2011**, *63* (9), 701–715.
24. Lvov, Y.; Price, R.; Gaber, B.; Ichinose, I. *Colloids Surf., A* **2002**, *198*, 375–382.
25. Wagberg, L.; Forsberg, S.; Johansson, A.; Juntti, P. *J. Pulp Pap. Sci.* **2002**, *28* (7), 222–228.
26. Zhao, Y.; Tang, Y. W.; Wang, X. G.; Lin, T. *Appl. Surf. Sci.* **2010**, *256* (22), 6736–6742.
27. Dillon, A. C.; Ott, A. W.; Way, J. D.; George, S. M. *Surf. Sci.* **1995**, *322* (1−3), 230–242.
28. Chen, W.; Fadeev, A. Y.; Hsieh, M. C.; Öner, D.; Youngblood, J.; McCarthy, T. J. *Langmuir* **1999**, *15* (10), 3395–3399.
29. Wenzel, R. N. *Ind. Eng. Chem.* **1936**, *28* (8), 988–994.
30. Ogawa, K.; Soga, M.; Takada, Y.; Nakayama, I. *Jpn. J. Appl. Phys., Part 2* **1993**, *32* (4B), L614–L615.
31. Kim, S. H.; Kim, J.-H.; Kang, B.-K.; Uhm, H. S. *Langmuir* **2005**, *21* (26), 12213–12217.

Downloaded by PENNSYLVANIA STATE UNIV on August 28, 2012 | http://pubs.acs.org
Publication Date (Web): August 17, 2012 | doi: 10.1021/bk-2012-1107.ch008

32. Chowdhuri, A. R.; Takoudis, C. G.; Klie, R. F.; Browning, N. D. *Appl. Phys. Lett.* **2002**, *80* (22), 4241–4243.
33. Catherine, Y.; Talebian, A. *J. Electron. Mater.* **1988**, *17* (2), 127–134.
34. McHale, G.; Shirtcliffe, N. J.; Newton, M. I. *Langmuir* **2004**, *20* (23), 10146–10149.
35. Chibowski, E.; Ontiveros-Ortega, A.; Perea-Carpio, R. *J. Adhes. Sci. Technol.* **2002**, *16* (10), 1367–1404.

Downloaded by PENNSYLVANIA STATE UNIV on August 28, 2012 | http://pubs.acs.org
Publication Date (Web): August 17, 2012 | doi: 10.1021/bk-2012-1107.ch008

Downloaded by NORTH CAROLINA STATE UNIV on August 28, 2012 | http://pubs.acs.org
Publication Date (Web): August 17, 2012 | doi: 10.1021/bk-2012-1107.ch009

Chapter 9

Production of Dissolving Grade Pulps from Wood and Non-Wood Paper-Grade Pulps by Enzymatic and Chemical Pretreatments

Dongfang Li, David Ibarra, Viviana Köpcke, and Monica Ek*

**Department of Fiber and Polymer Technology,
KTH Royal Institute of Technology, Teknikringen 56-58,
SE 10044 Stockholm, Sweden
*E-mail: monicaek@kth.se**

A raw material with high cellulose content and low content of hemicelluloses, residual lignin, extractives and minerals is required for many important applications in the pharmaceutical, textile, food and paint industries i.e. cotton and dissolving grade pulp are used. However, the high costs for the production of dissolving grade pulps has triggered interest in upgrading paper-grade pulps into dissolving pulps by selective removal of hemicelluloses and subsequent activation of the pulps. This study reports the feasibility to produce dissolving grade pulps from different wood and non-wood paper-grade pulps employing enzymatic and chemical pre-treatments. The results were compared to those of commercial bleached dissolving pulps.

Introduction

The application of regenerated cellulose and cellulose derivatives in pharmaceutical, textile, food, and painting industries results from their specific solubilities, flexibility, and softness. Cellulose, as a raw material, is thought to be nearly inexhaustible in nature, with prominent environmentally friendly and biocompatible properties compared with petroleum-based products (*1*). Cellulose can be used to produce a number of derivatives, including esters and ethers. Regenerated cellulose is produced in largest amount through viscose

In Functional Materials from Renewable Sources; Liebner, F., et al.;
ACS Symposium Series; American Chemical Society: Washington, DC, 2012.

processes and sometimes through the precipitation of dissolved cellulose from *N*-methylmorpholine-*N*-oxide monohydrate (NMMO) (Lyocell process) (*2*).

To make products with high quality and homogeneity in a way that can compete with fossil-based products, raw materials with high purity, reactivity and consummate quality control during manufacture are required. Moreover, the recovery of processing chemicals, reagents, and the exploration of suitable purification methods are still difficulties that hamper the production of cellulosic materials in completely replacing fossil fuel-based products.

The starting material for producing the regenerated cellulose and cellulose derivatives is normally dissolving pulp, due to the high purity and reactivity of cellulose. Since the 2000s, the world's demand for dissolving pulp has increased, resulting in a continual and dramatic rise in its price from 300 USD in the 1970s to 1900 USD currently (*3*). To obtain the highest profits, industries need to find a less expensive alternative as a starting material, acknowledging that this replacement must fulfill certain requirements, such as a high purity of cellulose, a high reactivity, and a suitable degree of polymerization (DP).

Cotton has been used for decades as pure cellulose for the manufacture of cellulose derivatives and products. However, the consumption of cotton has been increasing significantly as a result of heavy needs in textile industries. In addition, the cultivation of cotton requires more water and pesticides than that of trees, which causes problems for the environment (*4*).

The viscose process was introduced in the 1900s, and it has been developed and applied in modern-day uses despite the fact that the use of carbon disulfide in production flow is a significant disadvantage. For the production of regenerated cellulose, Baksheev and Butyagin (*5*) reported a decrease in the world production of cellulose fibers in 1997. However, viscose fiber production and consumption has increased in a larger increment than forecasted. Cellulose fibers, mainly rayon, produced by the viscose process play an important role in textile industries. In addition, it is also used in feminine hygiene products, baby wipes, computer disk liners and surgical swabs (*6*).

This chapter will focus on the optimization of regenerated cellulose for the conventional viscose process.

Downloaded by NORTH CAROLINA STATE UNIV on August 28, 2012 | http://pubs.acs.org
Publication Date (Web): August 17, 2012 | doi: 10.1021/bk-2012-1107.ch009

Cellulose Structure in Different Levels

Cellulose is the main component of plant cell walls (*7*). The content of cellulose in wood varies according to tree species, growing conditions and age; however, most wood species are composed of 40–47% cellulose, and non-wood plant species contain 60–70%. One of the purest sources of cellulose that can be found in nature is cotton, which consists of more than 95% cellulose (*8*).

Cellulose has many interesting properties, including high strength, water insolubility, resistance towards chemical derivatization, and a remarkable efficiency of interaction with aromatic compounds (*7*). These properties make cellulose valuable for many applications. For many applications, such as paper, textiles, pharmaceuticals, membranes, polymers, and paints, cellulose must be isolated from accompanying raw materials, and for some products it has to be converted into derivatives. Nevertheless, there are several obstacles arising from cellulose's structure that hinder these processes due to the limited accessibility and reactivity of native cellulose (*9*).

The structure of cellulose is complex and has not yet been completely elucidated. Generally, this structure can be considered from three levels: the molecular level, the supramolecular level, and the morphological level.

Cellulose consists of straight and non-branched polymer chains (Figure 1). The average degree of polymerization (DP) of a cellulose molecule is approximately 10.000 in natural wood and 15.000 in cotton (*10*).

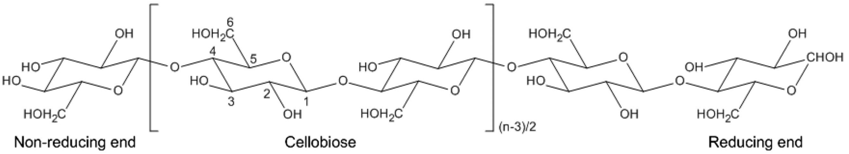

Figure 1. Cellulose structure at the molecular level.

Each glucose unit in a cellulose molecule has the chair formation $^4C_1$ and contains three hydroxyl groups in equatorial positions that form intramolecular hydrogen bonds that are responsible for its high rigidity. At the supramolecular level, the intermolecular bonds are constructed between adjoining cellulose molecules, which gives cellulose its insolubility in water and its stable conformation. Consequently, aggregated molecules are assembled through hydrogen bonds, covalent bonds, and van der Waals forces into microfibrils containing the crystalline regions (*11*). However, cellulose consists not only of highly-ordered crystallites, but also of more disturbed regions with a lower degree of order (amorphous or non-crystalline cellulose). Moreover, the crystalline and amorphous states are not the only two possible states of order; there are also other structures, such as intermediate or para-crystalline states (*12*, *13*).

Different polymorphs of cellulose have been identified (cellulose Iα, Iβ, II, III_I, III_{II}, IV_I, and IV_{II}) with the help of analytical techniques, such as ^{13}C cross polarization/magic angle spinning nuclear magnetic resonance (^{13}C CP/MAS NMR), infrared spectroscopy (IR), and diffraction analysis (*14*, *15*). These polymorphs present different physical properties, such as density, solubility, and optical properties (*7*).

Generally, cellulose I is the native form of cellulose, and this polymorph can be converted into cellulose II by either regeneration or mercerization with concentrated alkaline solutions. Cellulose Iα is normally found in primitive organisms, such as bacteria and algae, while cellulose Iβ is produced in higher plants, such as cotton and wood. Cellulose Iα and cellulose Iβ have different hydrogen bonding patterns. Moreover, cellulose Iα has been reported to have higher reactivity in comparison with cellulose Iβ. (*11*).

Cellulose II can be generated from cellulose I by either mercerization or regeneration. In the process of mercerization, cellulose is first submitted to alkalization, where it swells in a strong alkali solution (18% NaOH). In this

Downloaded by NORTH CAROLINA STATE UNIV on August 28, 2012 | http://pubs.acs.org
Publication Date (Web): August 17, 2012 | doi: 10.1021/bk-2012-1107.ch009

Downloaded by NORTH CAROLINA STATE UNIV on August 28, 2012 | http://pubs.acs.org
Publication Date (Web): August 17, 2012 | doi: 10.1021/bk-2012-1107.ch009

step, the strong inter- and intramolecular bonds among cellulose molecules are partially broken and alkali cellulose is produced. This process is terminated by neutralization to remove the alkali and generate cellulose II. Additionally, cellulose can also be regenerated from various solutions, such as acids, chelating agents, organic solvents, and ionic liquids, to generate cellulose II. The method of regeneration was described to exhibit higher efficiency in the conversion of cellulose I to cellulose II when compared with the mercerization method (*16*).

In addition to crystalline cellulose, less ordered or non-crystalline cellulose is also of great interest (*12*, *13*). A two-phase model of cellulose (highly ordered and less ordered regions) was developed in the late 1950s, and the theory was supported by X-ray diffraction patterns (*17*, *18*). In 1982, it was discovered that solid state ^{13}C CP/MAS NMR can comprehensively elucidate the cellulose crystallinities of different samples (*19*).

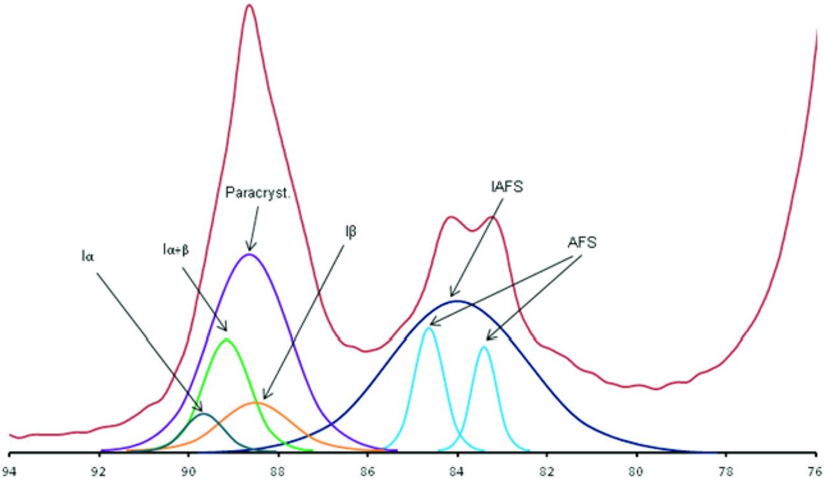

Figure 2. The deconvolution of ^{13}C CP/MAS NMR spectra of cellulose I in the C4 region with Paracryst.=paracrystalline cellulose, IAFS=inaccessible fibril surfaces, AFS=accessible fibril surfaces. (Reproduced with permission from reference (12). Copyright 1997.)

The complicated structure of cellulose results in high analytical complexity. For example, the ^{13}C CP/MAS NMR spectrum is very intricate due to overlapping signals that belong to different conformations. For this reason, a deconvolution method was developed to separate and elucidate those signals in the C4 region of the spectra (Figure 2) so that the different cellulose forms found in the fibril could be quantified.

In the analysis of cellulose morphology with X-ray diffraction, light areas in the diffractogram were attributed to crystalline cellulose and dark areas were attributed to non-crystalline cellulose (*20*). However, to date, it remains difficult to define the limit between crystalline and non-crystalline cellulose due to the additional occurrence of paracrystallinity, shown by Larsson's and Wickholm's models, where the fibrils were thought to be uniform (Figure 3). It is worth to mention that these models are different from Hearle's, which is a structure model containing non-uniform fringed fibrils and more voluminous non-crystalline regions (*17*).

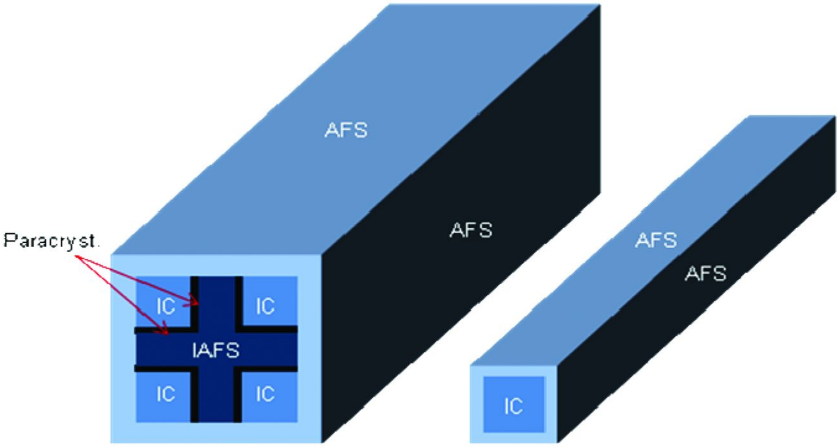

Figure 3. The model for the fibril aggregates (left) and cellulose fibrils (right) with IC=inner crystalline cellulose, Paracryst.=paracrystalline cellulose, IAFS=inaccessible fibril surfaces, AFS=accessible fibril surfaces. (Reproduced with permission from reference (12). Copyright 1997.)

Downloaded by NORTH CAROLINA STATE UNIV on August 28, 2012 | http://pubs.acs.org
Publication Date (Web): August 17, 2012 | doi: 10.1021/bk-2012-1107.ch009

Cellulose Accessibility and Reactivity

As mentioned above, due to the compact and complex structure of cellulose, its accessibility to chemicals and solvents is restricted. In fact, Krässig (*21*) has demonstrated that the accessibility and reactivity of cellulose depend strongly on the cellulose structure and morphology. Fahmy and Mobarak (*22*) also suggested that cellulose reactivity depends more on the disintegration of fibril aggregates than on crystallinity.

The arrangement of cellulose chains in fibrils and fibril aggregates is not uniform, and this creates two morphologically different regions from the superfibrillar level point of view, including highly ordered (crystalline) and less ordered (semi-crystalline or even amorphous) regions. It has been suggested that the less ordered cellulose regions tend to be located on the fibril surface or on the amorphous position in fibrils (*12*). The accessibility of crystalline cellulose to chemicals or other reagents is limited. The ordered regions with high crystallinity that are packed tightly together in fibrils and aggregates are normally hard to access, while the less ordered or amorphous regions located on fibril surfaces can be reached more readily (*23*).

In both native and artificial cellulose, the random arrangement of cellulose fibrils creates differences in size and amount of free volume elements throughout the network, which also defines the accessibility of cellulose. Moreover, the accessibility of cellulose is affected by the size of the chemicals and reagents (*24*).

Downloaded by NORTH CAROLINA STATE UNIV on August 28, 2012 | http://pubs.acs.org
Publication Date (Web): August 17, 2012 | doi: 10.1021/bk-2012-1107.ch009

Larger biological reagents, such as enzymes, might be blocked from reaching the fibrils due to their size (*25*). In addition to the structure of cellulose (at the molecular level), the number of accessible hydroxyl groups also affects cellulose's overall accessibility. Consequently, expansion of pores or spaces among cellulose fibrils and the modification of cellulose structures to expose more reachable regions and functional groups are of great importance in increasing cellulose's accessibility (*21*).

Previous studies have reported several ways of increasing cellulose's accessibility and reactivity. These techniques have focused mainly on chemical degradation (such as hydrolysis and oxidation of raw materials), thermal degradation, mechanical treatments (such as wet/dry milling), and on the swelling of cellulosic materials through the breakage of interfibrillar and intrafibrillar bonds to expose more active surface areas (*21*). The mixing of cellulose and sodium hydroxide to form alkali cellulose is a typical example of water-based swelling techniques (*26*). Kunze and Fink (*27*) described another method based on the combination of sodium hydroxide and urea. One promising method in development uses a relatively new family of solvents, ionic liquids, to increase cellulose's accessibility and reactivity by reassembling cellulose's inner structure (*28*). In addition, the enzymatic treatment of various cellulose materials has recently gained increased attention. Köpcke et al. reported the use of mono-component endoglucanases to increase the reactivity of various paper-grade and dissolving grade pulps (*9*). This method of improving cellulose's accessibility and reactivity has clear advantages because enzymes are selective, non-toxic and environmentally friendly.

However, the improvement of the cellulose's accessibility and reactivity may be negatively affected by the hornification effect, especially for dried cellulose materials such as pulp sheets (*25*). Hornification is caused by the removal of water during the drying of cellulose, causing the formation of new hydrogen bonds between the fibrils and an irreversible shrinking of internal space. This results in decrease of pore size and conversion of accessible regions of the structure into inaccessible ones (*29*, *30*). The existence of hemicelluloses in cellulose-based materials may help to reduce hornification (*31*). Nevertheless, for certain production needs, such as the manufacture of dissolving grade pulps, hemicelluloses must be substantially decreased or totally removed. In this case, hornification becomes a significant issue.

Enzymes Used for Activation of Cellulose

The increased application of enzymes in various industries is stimulated by the need to decrease environmental impacts. Enzymes present many advantages, such as high performance, high selectivity on substrates, and little to no toxicity compared with conventional chemical reagents.

Enzymes can be used to improve cellulose's accessibility (*25*). These enzymes include cellulases and hemicellulases. Under certain conditions, cellulases catalyze the hydrolysis of the 1-4-glucosidic bond between two adjacent glucose units. These cellulases include endoglucanases (EC.3.2.1.4), cellobiohydrolases or exoglucanases (EC. 3.2.1.91), and glucosidases (EC.3.2.1.21) (Figure 4).

Endoglucanases (EG) are a type of enzyme that catalyzes the random hydrolysis of glucosidic bonds in cellulose chains in the less ordered or amorphous regions, generating shorter chains with lower degrees of polymerization or even oligosaccharides. Among these EGs, the endoglucanase derived from *Humicola insolens* has been reported to be the most active toward many cellulose derivatives, as it reacts specifically with cellulose and prefers to attack the amorphous region (*32*, *33*). Engström et al. (*34*), Henriksson et al. (*35*) and Ibarra et al. (*36*) have reported the high efficiency of this enzyme in improving the cellulose reactivity of dissolving pulps. In the same way, Ibarra et al. (*25*, *37*), Köpcke et al. (*38–40*), Li (*41*), and Najar (*42*) have used both mono-component endoglucanase and xylanase enzymes together with alkaline treatments to improve the cellulose reactivity of several raw materials, including both wood and non-wood paper-grade pulps. The potential of converting paper-grade pulps into dissolving grade pulps for viscose processes was also described in these studies.

The catalysis reaction of exoglucanase, however, occurs at the reducing and non-reducing ends of cellulose chains through the so-called “peeling” mechanism. It has been reported that this type of cellulase can also degrade microcrystalline cellulose (*43*). The product from the hydrolysis is mainly cellobiose, which can be further hydrolyzed into glucose units with the help of glucosidase (*44*). Cellulases can be used individually or cooperatively with other enzymes for different needs.

The catalytic domain determines the catalyst function of cellulases. Differences in shape among the catalytic domains distinguish cellulases and give them specific properties. The “cleft-shaped” hydrolysis functional region is specific for endoglucanases, while exoglucanases have a “tunnel-shaped” domain that helps them react with the ends of cellulose molecules. Some cellulases possess a second domain, called the cellulose-binding domain (CBD), which works as a “hand” to catch the substrate, thereby facilitating binding to the cellulose molecules. Ibarra et al. have reported that endoglucanases with CBDs are the most effective endoglucanase enzymes for increasing cellulose’s reactivity (*36*). The catalytic domain and the cellulose-binding domain are connected through an inter-domain linker (*45*).

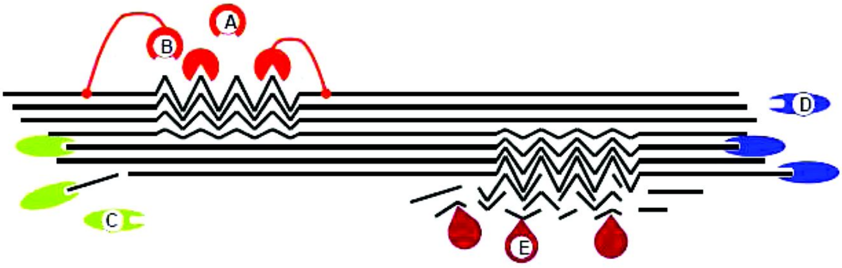

Figure 4. Types of cellulases: A: endoglucanases without cellulose-binding domain; B: endoglucanases with cellulose-binding domain; C and D: cellobiohydrolases. E: glucosidases.

Downloaded by NORTH CAROLINA STATE UNIV on August 28, 2012 | http://pubs.acs.org
Publication Date (Web): August 17, 2012 | doi: 10.1021/bk-2012-1107.ch009

Downloaded by NORTH CAROLINA STATE UNIV on August 28, 2012 | http://pubs.acs.org
Publication Date (Web): August 17, 2012 | doi: 10.1021/bk-2012-1107.ch009

The mechanism of the activation of cellulose by enzymes has yet to be fully elucidated. One hypothesis states that endoglucanase-catalyzed hydrolysis causes breakage of glucosidic bonds in less ordered regions, which are located between and on the surface of fibrils. This process enhances the separation of the fibrils from one another, increasing the inner space between them. Consequently, the accessible areas of cellulose are available for the reaction with chemicals and other reagents, improving cellulose's reactivity (*35*). Nevertheless, the effects of hydrolysis are influenced by other factors, such as the crystallinity, the specific surface area and the degree of polymerization of cellulose (*46*).

In enzymatic treatments, the incubation time, temperature, and pH value are three parameters that directly affect the improvement of cellulose's accessibility and reactivity. It is difficult to find the most suitable conditions for certain types of enzymes with a particular substrate to obtain the best performance (*25*, *36–42*). It is notable that for different types of substrates and sizes of cellulases, the efficiency of their function may be different. It has been described, for example, that cellulose reactivity could be improved to only a certain level with an endoglucanase treatment. Beyond this level, the reactivity could not be further improved, irrespective of how the conditions and doses of enzymes were changed. Ibarra et al. (*25*) demonstrated that the existence of higher content of hemicelluloses in raw materials negatively affected the efficiency of endoglucanases, as they might work as a barrier to hinder the enzyme's ability to connect with the accessible cellulose substrates.

To increase cellulose reactivity, xylanases are used to catalyze the hydrolysis of long xylan chains into shorter chains. Köpcke et al. (*38*) reported the usage of an endoxylanase from a genetically modified *Bacillus* species in combination with an endoglucanase for the treatment of wood pulps. The results showed that the xylanase worked effectively to remove the xylan that may block the reaction between endoglucanase and cellulose, significantly improving cellulose's reactivity. However, it is worth noting that the size of pores among fibrils and the portion of accessible areas of hemicellulose may influence the function of xylanases through a mechanism similar to that which was previously described for cellulases (*25*).

Reactivity Measurements

The reactivity of cellulose is theoretically dominated by the three reactive hydroxyl groups (C2, C3, C6) of each glucose unit (*9*). However, as mentioned above, cellulose reactivity depends highly on the accessibility of the cellulose. There are several methods that can be used to determine cellulose reactivity. Among them, the Fock method (*47*) is usually applied (*25*, *36–42*) for determining reactivity for fibers to be used in the viscose process. This method is a lab-scale simulation of the viscose process that uses cellulose in the reaction with carbon disulfide after swelling in sodium hydroxide solution. The dissolved cellulose is then regenerated with diluted sulfuric acid and oxidized by concentrated sulfuric acid and potassium dichromate. The reactivity of cellulose (in percentage) is calculated by measuring the amount of thiosulfate used to titrate the iodine formed by the oxidation of iodide with the remaining dichromate. In addition, there are several other methods that are commonly used for the determination of cellulose reactivity. Hopner et al. introduced the oldest method, determination of the water retention value, in 1955 (*48*), and Nelson et al. (*49*) reported a method called "iodine sorption analysis" in 1970. Spectroscopic methods, such as FT Raman spectroscopy and ^{31}P NMR spectroscopy, can also be applied for the measurement of reactivity (*50*, *51*). In 2002, Christoffersson et al. reported a method of determination that is carried out by calculating the viscose filter value (*52*).

Downloaded by NORTH CAROLINA STATE UNIV on August 28, 2012 | http://pubs.acs.org
Publication Date (Web): August 17, 2012 | doi: 10.1021/bk-2012-1107.ch009

Dissolving Grade Pulp

Unlike paper-grade pulp, dissolving grade pulp has a low amount of hemicelluloses, lignin, extractives and minerals (less than 10% in total) and contains much higher amounts of cellulose (over 90%). In addition, compared with paper pulp, dissolving pulp exhibits higher brightness and more uniform molecular weight distributions. The high cellulose content of dissolving pulp makes it suitable for the manufacture of regenerated celluloses, such as rayon, and for cellulose derivatives.

Acidic sulfite pulping and prehydrolysis kraft pulping are the main processes used for manufacturing dissolving grade pulp. The former is applied in approximately 65% of the total production and the latter takes approximately 25% of the production worldwide (*53*). Organosolv pulping is another promising method for the manufacture of dissolving pulps, and it has been reported to be more environmentally friendly because the process is sulfur-free, producing dissolving pulp with higher strengths than that produced by conventional techniques. However, the high expenses and low reactivity of some product celluloses limit the generalization of organosolv pulping into larger production (*54*, *55*).

To produce regenerated cellulose and cellulose derivatives, one of the most important parameters of dissolving pulp is the processability, which is characterized by cellulose reactivity. High reactivity helps to lower the demand for processing chemicals during both the derivation and the regeneration of cellulose, reducing environmental impact. More importantly, it ensures the homogeneity and quality of final products (*37*). As mentioned above, cellulose reactivity depends on its accessibility to chemicals, where the accessibility is affected by several factors, including the content of hemicelluloses. Therefore, a dissolving pulp should maintain low levels of hemicelluloses (2–4%). The presence of hemicelluloses decreases the cellulose processability, especially during xanthation in the viscose process, affecting the quality of the end products (*56*). However, the concept that hemicelluloses are impurities and must be removed causes, as a consequence, a relatively low yield compared to common kraft pulping, making the manufacture of these pulps a costly process (*57*).

Concerning the reactivity, it has been reported that the commercially available (dried) hardwood and softwood dissolving pulps possess cellulose reactivities, according to the Fock method, of 65% and 70%, respectively (*36*).

Downloaded by NORTH CAROLINA STATE UNIV on August 28, 2012 | http://pubs.acs.org
Publication Date (Web): August 17, 2012 | doi: 10.1021/bk-2012-1107.ch009

Henriksson et al., Engström et al., and Ibarra et al. have reported the activation of commercial dissolving pulp through enzymatic treatment by a CBD-containing mono-component endoglucanase. Ibarra et al. has demonstrated that the reactivity of both hardwood and softwood dissolving pulp could reach 85% according to the Fock method after treatment with a relatively low dose of 30 ECU/g (ECU: endocellulase units - one unit of endocellulase is defined as the amount of enzyme needed to release 1 μmol of glucose per min under the given reaction conditions). This result would be a consequence of the swelling of cellulose fibrils and the reduction of cellulose II (*36*). Engström et al. have reported that for dissolving pulp that has never been dried, the cellulose reactivity could be elevated to 100% according to the Fock method with a short reaction time with a lower enzyme dose of 27 ECU/g (*34*). The limited accessibility of the dried dissolving pulp compared with the never-dried pulp arises from the hornification effect that was discussed above.

Viscosity is another important parameter to be considered in the production of dissolving pulps, as it can determine the quality of the final product. For example, the viscosity of dissolving pulp should be in the range of 200–300 dm^3/kg to produce viscose rayon of high quality (*38*). Engström et al. (*34*) and Ibarra et al. (*36*) have reported a decrease of viscosity in the dissolving pulp after the endoglucanase treatment. This results from the enzyme helping to cleave the cellulose polymer by catalyzing the hydrolysis of less ordered regions within the fibrils, a theory that is supported by the lower degree of polymerization that was obtained and the relatively smoother surface of cellulose fibers that was observed by scanning electron microscopy (SEM). Moreover, Engström et al., Ibarra et al., and Köpcke et al. have also demonstrated that the increase in cellulose reactivity is not directly related to the decrease in viscosity (*38*).

The Production of Regenerated Cellulose

Regenerated cellulose is mainly produced by the viscose process. One of the most important steps during the production of viscose fibers is the formation of cellulose xanthate, in which alkali cellulose reacts with carbon disulfide (CS_2). To obtain a homogeneous product of high quality, the homogeneity and filterability of the viscose upon regeneration in the acid bath must be ensured. This step, however, depends on the solubility of cellulose xanthate in aqueous sodium hydroxide. An easy way to maximize the solubility of cellulose xanthate is to increase the amount of CS_2 in the reaction with alkali cellulose. However, CS_2 is a reagent with a well-known and high toxicity in humans and in the environment. It has been reported that the emission of pollutants into the surroundings can arise from CS_2 used in many ways during the viscose process (*6*). For humans, carbon disulfide has been described to be a risk factor for many illnesses (*58*). As a result, it is important to develop new means to decrease the use of this reagent. One possible way to achieve this goal is to find alternatives that effectively dissolve cellulose, of which the dissolution of cellulose in NMMO is an example. In this process, cellulose is directly dissolved in an NMMO/water mixture and regenerated into filaments through spinning. The cellulose filaments produced by this method are called Lyocell fibers. Similar to rayon, Lyocell fiber is mostly used in textiles (*2*).

High loop tenacity is one of the advantages of Lyocell. More importantly, the production of Lyocell is more environmentally friendly due to the absence of CS_2. However, several studies have described problems with this method, including the fibrillation tendency of Lyocell fibers, side reactions and the yellowing of end products caused by chromophores that were generated during production (*59*). These issues hamper the application of Lyocell fibers in textile industries over the use of viscose rayon (*60*).

Another alternative is to dissolve cellulose in ionic liquids (ILs). These liquids, containing both cations and anions, are a relatively new family of non-volatile solvents. They are normally found in the liquid state at room temperature because of the low melting temperature (below 100°C). Swatloski et al. (*61*) have reported that ILs are convenient and inert solvents for lignocellulosic materials. ILs are claimed to be green solvents (*62*, *63*). Cellulose dissolved in ILs can be regenerated with common anti-solvents, such as water, ethanol, or acetone, which makes the precipitation and the production of regenerated cellulose in many forms, such as powder, tube, fiber, and film, relatively facile (*61*). However, several problems of using ILs have been described, as the complete removal of ILs from regenerated cellulose and the control of the DP of the final product remain challenging (*64*, *65*).

Consequently, to date, the viscose process continues to dominate the production of regenerated cellulose, leaving the use of CS_2 as a cumbersome issue. As discussed above, the accessibility of cellulose to chemicals is limited, especially for paper-grade pulps. Their correspondingly lower accessibility and lower reactivity compared to dissolving pulp makes these pulps difficult to be used as a starting material for producing regenerated cellulose. However, the higher costs arising from dissolving pulp and overcharging of CS_2 remain a problem. Thus, to decrease the amount of CS_2 needed during the production, to increase quality and homogeneity of the end product, and to save costs, several studies have been conducted to modify cellulose for better accessibility and reactivity, including activation of traditional dissolving grade pulps and upgrading of paper-grade pulps into dissolving grade pulps (*25*, *36–42*).

Downloaded by NORTH CAROLINA STATE UNIV on August 28, 2012 | http://pubs.acs.org
Publication Date (Web): August 17, 2012 | doi: 10.1021/bk-2012-1107.ch009

Upgrading Paper-Grade Pulps into Dissolving Grade Pulps

The conversion of paper-grade pulps into dissolving grade pulps aims at increasing the cellulose´s accessibility and reactivity, controlling the DP, and decreasing the amount of hemicelluloses. As mentioned earlier, the low yield resulting from the removal of hemicelluloses and the relatively strict demands on storage and transportation elevate the price of dissolving grade pulp. Consequently, upgrading a relatively cheaper material, such as paper-grade pulps, through a cost-effective and industrially friendly way to meet worldwide production demands has become an attractive topic for researchers pulps (*25*, *36–42*).

Downloaded by NORTH CAROLINA STATE UNIV on August 28, 2012 | http://pubs.acs.org
Publication Date (Web): August 17, 2012 | doi: 10.1021/bk-2012-1107.ch009

Several studies have focused on the modification of carbohydrate compositions in pulps, as hemicelluloses are considered to be impurities in this circumstance. Other studies have tried to develop new methods for controlling carbohydrate composition, including nitren and cuen extraction, alkaline extraction and enzymatic treatments (*66–70*). Others have worked to change cellulose's structure with chemical treatments. Stephens, for example (*71*), has reported a method of swelling kraft pulp in aqueous suspensions to decrease the DP of cellulose and increase cellulose's accessibility, upgrading the original material into dissolving pulp.

Other authors have described series of conversions that transform paper-grade pulp from both wood and non-wood materials into dissolving pulp through combined procedures based on alkaline treatment and enzymatic treatment (*25*, *37–42*). The effect of these treatments on various paper-grade pulps was determined by measuring the cellulose reactivity according to the Fock method, the pulp viscosity, carbohydrate composition, molecular weight distribution, morphology and supramolecular structure. Based on the use of mono-component endoglucanases as effective reagents to increase the accessibility and reactivity and to decrease the viscosity of both hardwood and softwood dissolving pulps, EGs were used in the conversion of paper-grade pulps to dissolving pulps.

CBD-containing mono-component endoglucanases, such as Novozyme 476 (N476), have shown a strong potential as activating reagents for paper-grade pulps. Two common hardwood paper-grade pulps derived from birch and eucalyptus possess much higher cellulose reactivities according to the Fock method after treatment with N476. Initially, the pulps presented a cellulose reactivity of 40% and 36%, respectively. After treatment, values of approximately 60% were observed. In addition, the viscosity decreased significantly from approximately 700 and 800 dm^3/kg to approximately 500 and 700 dm^3/kg, respectively (Figure 5), as a result of the cleavage of cellulose chains aided by the endoglucanase. It is also worth noting that the most significant effects occurred at low enzyme doses, approximately 50 ECU/g dry weight pulp, though further increases were observed up to an enzyme load of 250 ECU/g dry weight pulp.

For a paper-grade pulp from softwood (a mixture of spruce and pine), a similar trend was observed (Figure 6). The initial cellulose reactivity was elevated from approximately 50% to above 70% according to the Fock method, which is close to that of a commercial dissolving pulp (*36*). The strongest enhancement of reactivity occurred at enzyme doses of approximately 50 ECU/g dry weight pulp.

The effect of the endoglucanase on non-wood paper-grade pulps was also reported. The behavior of these materials was similar to that of wood pulps, especially for sisal pulps. For this pulp, the cellulose reactivity was significantly improved from 36% to approximately 60% by the enzymatic treatment. For other samples, the endoglucanase failed to raise cellulose reactivity to this level. The enzyme did not affect the reactivities of some non-wood pulps, including flax and hemp. The effect on the viscosity, however, was higher for abaca and flax. For the sisal pulp, no significant change in the viscosity was observed (Figure 7). These results imply that there is no direct correlation between the decrease in viscosity and the increase in cellulose reactivity (*34*).

Downloaded by NORTH CAROLINA STATE UNIV on August 28, 2012 | http://pubs.acs.org
Publication Date (Web): August 17, 2012 | doi: 10.1021/bk-2012-1107.ch009

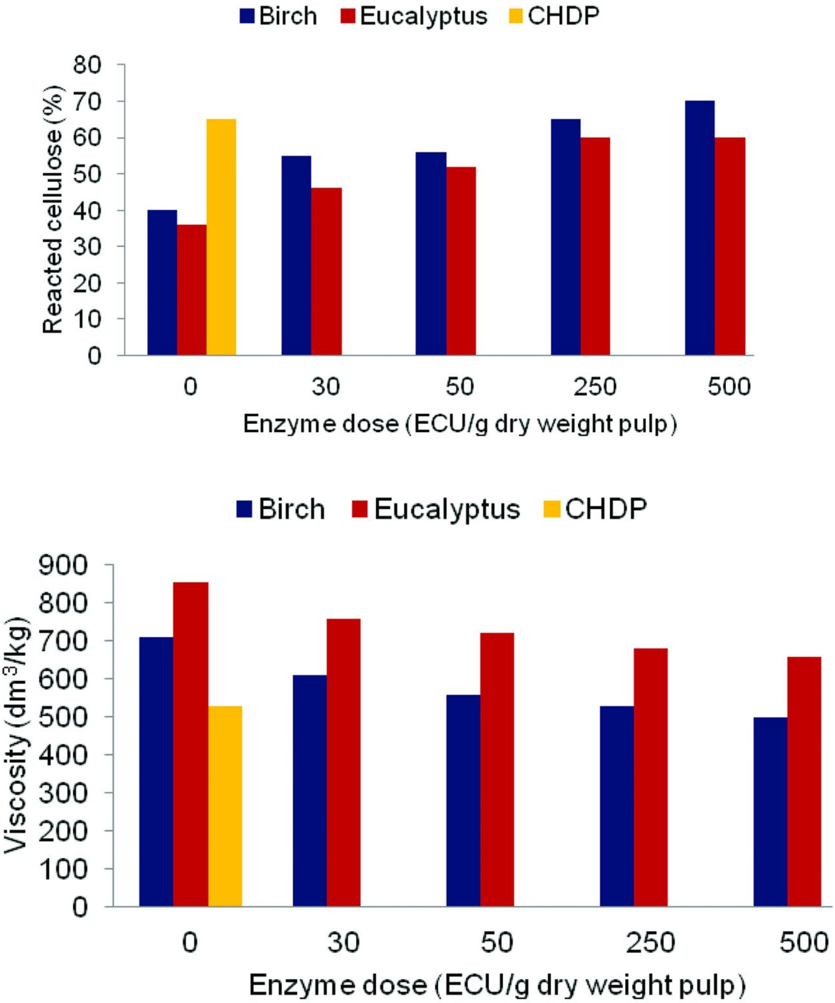

Figure 5. Fock's reactivity (up) and viscosity (down) of birch and eucalyptus paper-grade pulps as a function of enzyme dose and comparison with commercial hardwood dissolving pulp (CHDP). (Reproduced with permission from reference (38). Copyright 2008.)

Downloaded by NORTH CAROLINA STATE UNIV on August 28, 2012 | http://pubs.acs.org
Publication Date (Web): August 17, 2012 | doi: 10.1021/bk-2012-1107.ch009

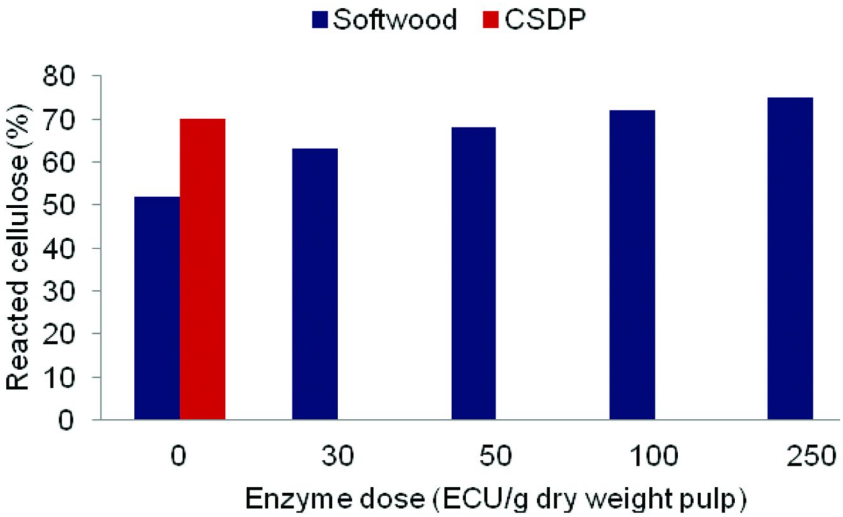

Figure 6. Fock's reactivity of softwood paper-grade pulp as a function of enzyme dose and comparison with commercial softwood dissolving pulp (CSDP).

The reaction time of the enzymatic treatment was also reported to be an important factor that influenced the efficiency of the treatment. For hardwood, softwood, and non-wood paper-grade pulps, the optimal reaction time for endoglucanase treatment was found to be 1 h (*37*, *38*, *41*).

However, from these studies, the cellulose reactivity of different paper-grade pulps could not be further improved after the enzyme dose reached a certain point. The hemicelluloses that cover or precipitate on the surface of cellulose might limit its accessibility. To further enhance the cellulose reactivity and meet the requirements for use as dissolving grade pulps, the content of hemicelluloses within these paper-grade pulps must be lowered. Hemicellulase treatment is thought to be an effective and selective way for removing hemicelluloses. Köpcke et al. reported several trials using a xylanase treatment on paper-grade pulps from birch, eucalyptus, and sisal (*25*, *37*, *38*). The results showed that the contents of xylan, which was the main hemicellulose in these pulps, all significantly decreased to 13–14% (based on the carbohydrate analysis result) after treatment using an enzyme dose of 500 EXU/g of dry weight pulp (EXU: endoxylanase units - one unit of endoxylanase is defined as the needed amount of enzyme to release 1 μmol of xylose per min under the given reaction conditions). The xylan content, however, could not be further decreased even with higher doses of xylanase. This was explained by the limited accessibility of the residual xylan and the size of xylanase itself (*72*).

Downloaded by NORTH CAROLINA STATE UNIV on August 28, 2012 | http://pubs.acs.org
Publication Date (Web): August 17, 2012 | doi: 10.1021/bk-2012-1107.ch009

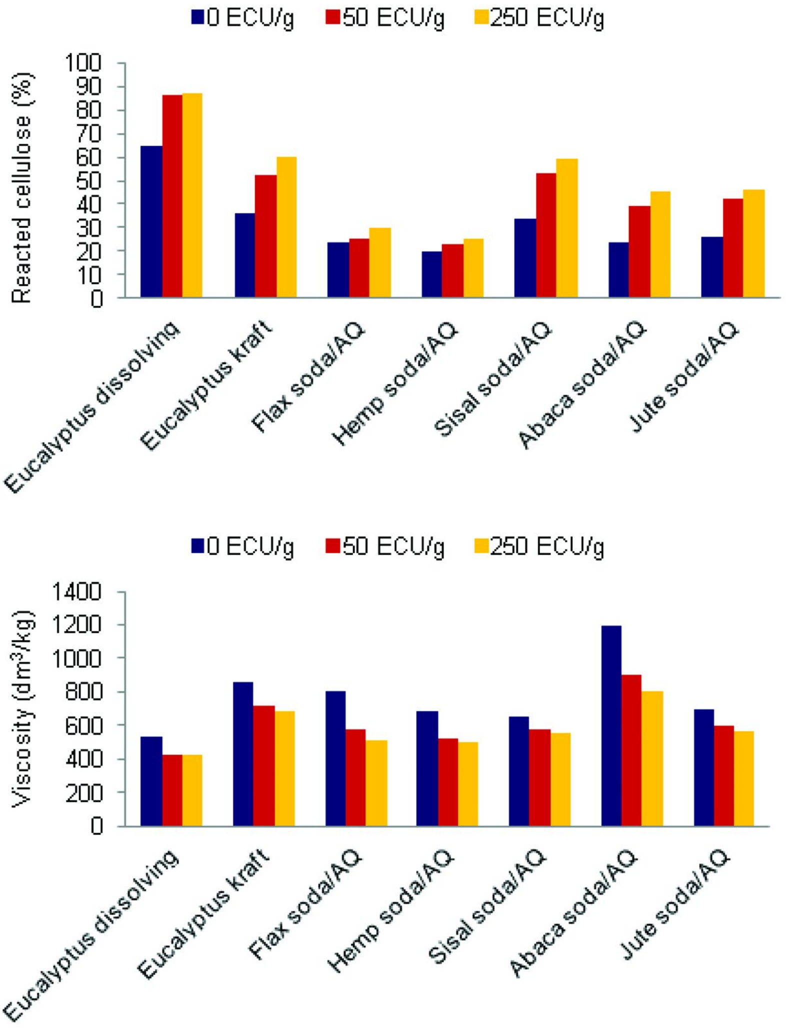

Figure 7. Fock's reactivity (up) and viscosity (down) of different endoglucanase-treated wood and non-wood pulp compared with eucalyptus dissolving pulp. ECU/g: endocellulase units per gram of dry pulp. (Reproduced with permission from reference (37). Copyright 2010.)

Commercial dissolving grade pulps require the content of hemicelluloses to be lower than 10% (*9*). Paper grade pulps treated only with xylanase could not meet this requirement. As a result, alkali treatment, a less selective (this treatment hydrolyzes cellulose as well) but cheaper and very effective method can be applied to these paper-grade pulps to further remove hemicelluloses. Several studies have described trials of alkali treatments on paper-grade pulps (*25*, *37*,

Downloaded by NORTH CAROLINA STATE UNIV on August 28, 2012 | http://pubs.acs.org
Publication Date (Web): August 17, 2012 | doi: 10.1021/bk-2012-1107.ch009

39, *40*, *42*). The treatments were carried out with an alkaline loading of 9 wt%. Ibarra et al. and Köpcke et al. demonstrated that the content of xylan was further decreased to a value of approximately 5% after the treatment. However, the cellulose reactivity also decreased as a result of hornification after drying. As discussed earlier, hornification can be hindered by the presence of hemicelluloses (*73*). After removing the majority of the xylan, hornification might occur more easily and might therefore lower the accessibility and reactivity of cellulose. These authors tried to solve this problem by combining xylananase, alkali, and endoglucanase treatments and testing several sequences of modification (*25*, *37*, *39*, *40*, *42*). Because the most suitable condition for xylanase treatment (dose: 500 EXU/g dry weight pulp, incubation time: 2 h, temperature: 60°C) was already established, optimizing the sequence of treatments on different pulps started by determining the best conditions for alkali treatment to remove the maximum amount of hemicelluloses. The alkaline load was reported be most effective at 7%, as the formation of cellulose II was detected by ^{13}C CP/MAS NMR if the pulps were treated with higher alkaline concentrations (9%). The amount of hemicelluloses could be limited to below 10%. In addition, the best reaction time of alkali treatment was reported to be 10 min (*9*). As with the endoglucanase treatment, the most favorable enzyme dose was found to be 250 ECU/g of dry weight pulp, and the most suitable incubation time and temperature were 1 h and 50°C, respectively (*9*).

The optimized sequences of combined treatment on birch, eucalyptus, and sisal soda/AQ pulps were reported to be different. The best modification sequence for birch pulp was two series of alkali treatments followed by the endoglucanase treatment, with the most favorable conditions as discussed above. In contrast, for eucalyptus and sisal soda/AQ pulps, the best sequence was a xylanase treatment prior to alkali extraction and then an endoglucanase treatment as the last step. The changes in these sequences were based on the evaluation of carbohydrate composition, reactivity of cellulose, and viscosity (Table 1 and 2), where reactivity was primarily considered. The xylanase treatment together with the alkali extraction could fulfill the requirements for the upgraded paper-grade pulps to be used as dissolving grade pulps in terms of their hemicellulose content. The addition of the endoglucanse treatment as the last step was of great importance to achieve high cellulose reactivity. It was also observed that the endoglucanase treatment prevented hornification effects produced by the removal of hemicellulose. This was explained by the hypothesis that the short cellulose chains created by hydrolysis possibly precipitated onto the pores that were generated after removal of hemicelluloses from the previous steps. This effect may hinder the formation of new hydrogen bonds, which causes the cellulose fibrils to be farther apart and therefore limits the hornification effects (*38*). Although the upgraded paper-grade pulps had lower viscosity than the commercial dissolving pulp (530 dm^3/kg), the value was still acceptable. During the viscose process, the viscosity of the original dissolving pulp normally decreases to 160–200 dm^3/kg to give better filterability (*9*). This part of the process takes a significant period of time (0.5-5 h). The upgraded pulps, with a viscosity of approximately 200–300 dm^3/kg, could avoid this step and still meet the needs for the manufacture of cellulose products of high quality (*36*).

Downloaded by NORTH CAROLINA STATE UNIV on August 28, 2012 | http://pubs.acs.org
Publication Date (Web): August 17, 2012 | doi: 10.1021/bk-2012-1107.ch009

Table 1. Carbohydrate composition (glucose and xylose) of eucalyptus, birch and sisal soda/AQ paper pulps after different sequences of treatments[a]

	Commercial eucalyptus dissolving pulp		*Eucalyptus*		*Birch*		*Sisal soda/AQ*	
Treatment	*Glu (%)*	*Xyl (%)*	*Glu (%)*	*Xyl (%)*	*Glu (%)*	*Xyl (%)*	*Glu (%)*	*Xyl (%)*
N/A	97.6	2.4	81.7	18.3	73.4	25.5	81.0	18.1
X+AE	N/A	N/A	N/A	N/A	N/A	N/A	95.6	3.6
X+EG	N/A	N/A	N/A	N/A	N/A	N/A	85.0	14.2
X+AE+EG	N/A	N/A	94.4	4.8	94.5	4.6	95.5	3.9
AE+AE+EG	N/A	N/A	94.5	4.8	92.2	5.5	N/A	N/A
AE+AE+AE+EG	N/A	N/A	95.2	4.2	94.1	4.4	N/A	N/A

[a] X: xylanase treatment (500 EXU/g dry weight pulp, 2 h, 60°C; EXU: endoxylanase units); AE: alkali treatment (7% NaOH, 10 min, 20°C for wood pulps; 9% NaOH, 1 h, room temperature for sisal soda/AQ pulp); EG: endoglucanase treatment (250 ECU/g dry weight pulp, 1 h, 50°C; ECU: endocellulase units); N/A: data are not available.

Table 2. Fock's reactivity (R) and viscosity (V) of eucalyptus, birch and sisal soda/AQ paper pulps after different sequences of treatments[a]

	Commercial eucalyptus dissolving pulp		*Eucalyptus*		*Birch*		*Sisal soda/AQ*	
Treatment	*R (%)*	*V (dm^3/kg)*	*R (%)*	*V (dm^3/kg)*	*R (%)*	*V (dm^3/kg)*	*R (%)*	*V (dm^3/kg)*
N/A	64.8	530	36.1	855	40	712	34.8	655
X+AE	N/A	N/A	N/A	N/A	N/A	N/A	31.1	725
X+EG	N/A	N/A	N/A	N/A	N/A	N/A	65.4	440
X+AE+EG	N/A	N/A	67	335	68	370	66.2	290
AE+AE+EG	N/A	N/A	58	330	69	330	N/A	N/A
AE+AE+AE+EG	N/A	N/A	40	300	60	285	N/A	N/A

[a] X: xylanase treatment (500 EXU/g dry weight pulp, 2 h, 60°C; EXU: endoxylanase units); AE: alkali treatment (7% NaOH, 10 min, 20°C for wood pulps; 9% NaOH, 1 h, room temperature for sisal soda/AQ pulp); EG: endoglucanase treatment (250 ECU/g dry weight pulp, 1 h, 50°C; ECU: endocellulase units); N/A: data are not available.

Downloaded by NORTH CAROLINA STATE UNIV on August 28, 2012 | http://pubs.acs.org
Publication Date (Web): August 17, 2012 | doi: 10.1021/bk-2012-1107.ch009

The paper-grade pulps from birch, eucalyptus, and sisal after the combined treatments have been shown to exhibit characteristics similar to those of a commercial dissolving grade pulp. The molecular weight distribution (MWD) was analyzed by size exclusion chromatography (Table 3). The treated paper pulps had a lower polydispersity index (PDI) than those of commercial dissolving pulps, which implies that these upgraded pulps have better homogeneity and are suitable for the manufacture of uniform cellulose products (*25*). The upgraded birch and eucalyptus paper pulps presented proportions of high-molecular weight cellulose (DP>2000) similar to those of commercial dissolving pulps, which suggests the possibility of using these upgraded paper pulps in manufacture of cellulose products with high quality (*55*). Finally, these treated wood and non-wood paper pulps showed relatively lower weight-average degrees of polymerization (DPw) compared to those of commercial dissolving pulp, which might arise from the cleavage of long cellulose molecules by endoglucanase (*25*).

Table 3. Comparison of molecular weight distribution among birch, eucalyptus, and sisal soda/AQ paper pulps, upgraded pulps, and commercial eucalyptus dissolving pulp[a]. Adapted from permission from references (*25*, *37*, *39*, *40*). Copyright 2009, 2010, 2010, 2010.

Pulp	*DPw*	*PDI*	*DP<50 (%)*	*DP<200 (%)*	*DP>2000 (%)*
Commercial eucalyptus dissolving pulp	2390	7.4	7.9	15.9	26.8
Birch kraft pulp	6213	27.9	N/A	N/A	N/A
AE+AE+EG treated birch pulp	1733	4.5	4.8	17.7	21.5
Eucalyptus kraft pulp	6055	20.5	N/A	N/A	N/A
X+AE+EG treated eucalyptus pulp	1545	7.4	4.9	13.8	21.2
Sisal soda/AQ pulp	3575	9.6	N/A	N/A	N/A
X+AE+EG treated sisal pulp	1200	5.3	3.9	17.9	14.5

[a] AE: alkali treatment (7% NaOH, 10 min, 20°C for wood pulps; 9% NaOH, 1 h, room temperature for sisal soda/AQ pulp); EG: endoglucanase treatment (250 ECU/g dry weight pulp, 1 h, 50°C; ECU: endocellulase units); X: xylanase treatment (500 EXU/g dry weight pulp, 2 h, 60°C; EXU: endoxylanase units); DPw: weight average degree of polymerization; PDI: polydispersity index; N/A: data are not available.

The upgrading of softwood paper-grade pulp has also been described. Li (*41*) tried sequential treatments on a dried paper-grade pulp from spruce and pine, but only enzymes (xylanase, mannanase, endoglucanase) were applied. The treated pulps exhibited similar characteristics to commercial softwood dissolving grade pulp (Table 4).

Downloaded by NORTH CAROLINA STATE UNIV on August 28, 2012 | http://pubs.acs.org
Publication Date (Web): August 17, 2012 | doi: 10.1021/bk-2012-1107.ch009

Table 4. Fock's reactivity (R), viscosity (V), and carbohydrate composition (glucose, xylose, and mannose) of softwood paper pulp after different sequences of treatments[a]

Sample	*R (%)*	*V (dm^3/kg)*	*Glu (%)*	*Xyl (%)*	*Man (%)*
Commercial softwood dissolving pulp	70	560	93.0	N/A	N/A
Softwood paper-grade pulp	52	918	85.0	8.7	6.3
EG[a] treated softwood pulp	68	N/A	N/A	N/A	N/A
EG[b] treated softwood pulp	72	569	N/A	N/A	N/A
X+M+EG[a] treated softwood pulp	80	519	87.0	6.5	6.5
X+M+EG[b] treated softwood pulp	80	519	87.1	6.3	6.6
ME[a] treated softwood pulp	73	436	N/A	N/A	N/A
ME[b] treated softwood pulp	73	412	N/A	N/A	N/A

[a] EG: endoglucanase treatment (a: 50 ECU/g dry weight pulp, b: 100 ECU/g dry weight pulp, 1 h, 50°C; ECU: endocellulase units); X: xylanase treatment (500 EXU/g dry weight pulp, 2 h, 60°C; EXU: endoxylanase units); M: mannanase treatment (500 VHCU/g dry weight pulp, 2 h, 40°C; VHCU: viscosity hemicellulase units); ME: multi-component enzyme treatment (a: 50 EGU/g dry weight pulp, b: 100 EGU/g dry weight pulp, 1 h, 50°C; EGU: endoglucanase units); N/A: data are not available.

The content of xylan decreased as a result of the xylanase treatment. However, a relatively higher amount of hemicelluloses in the upgraded softwood pulp compared with those in the commercial dissolving pulp was observed. As mentioned above, the efficiency of enzymes depends on the accessibility of the substrate, and enzymes that are larger in size than the pores among the fibrils in pulp might be blocked, and therefore only the accessible hemicelluloses were attacked. Moreover, the content of glucomannan (reflected by mannose here) was not affected by the mannanase treatment, which might be caused by a hindrance effect arising from the arrangement of xylan and glucomannan in this softwood pulp (*74*). Nevertheless, the sequential treatment succeeded in removing the hemicelluloses to some extent, and the purity of cellulose in the upgraded paper pulp was close to that of the dissolving pulp.

Furthermore, Li described another method of upgrading paper pulp (*41*). In these experiments, a multi-component enzyme was used as the reagent, which was reported to have various activities as both cellulase and hemicellulase (*75*). The paper-grade pulp treated by this enzyme showed an obvious increase in its cellulose reactivity and a decrease of viscosity, which could be attributed to the synergic function of the multi-component enzyme (Table 4). Moreover, unlike the xylanases and endoglucanases with high enzyme purities (mono-component), the multi-component enzyme has an advantage of being lower in cost.

Finally, for the forest industry, the feasibility of enzymatic treatments on paper-grade pulps depends highly on the economic aspects. Kvarnlöf demonstrated the possibility of decreasing the production cost of viscose fibers by the activation of cellulose materials (dissolving grade pulps) with enzymes in advance (*76*). The total cost was predicted to be reduced by 3%-16% in comparison with the conventional method, with the consideration of investments on enzymes and corresponding reactors. As to the current method, the lower cost of paper-grade pulps is another advantage from the economical point of view.

Downloaded by NORTH CAROLINA STATE UNIV on August 28, 2012 | http://pubs.acs.org
Publication Date (Web): August 17, 2012 | doi: 10.1021/bk-2012-1107.ch009

Conclusions

Enzymatic treatments demonstrated a strong potential for the improvement of cellulose accessibility and reactivity and for the conversion of paper-grade pulps to dissolving grade pulps in a selective, effective, and environmentally friendly manner. This method is of great significance for the fabrication of cellulose fibers, especially for viscose manufacturing, where enzymatic treatment could help to reduce the load of carbon disulfide and therefore lower production expenses.

The upgraded pulps from different sources (hardwood, softwood, and sisal) exhibited characteristics similar to those of dissolving pulps. The efficiency of treatments depended on the type of enzymes used, the structure of these enzymes, the reaction conditions, the treatment sequences (in combination with alkali extraction), and the cellulose substrates. However, the feasibility of this method in industry for the large-scale production of pure cellulose has yet to be evaluated.

References

1. Klemm, D.; Heublein, B.; Fink, H-P.; Bohn, A. *Angew. Chem., Int. Ed.* **2005**, *44*, 3358–3393.
2. Shen, L.; Patel, M. K. *Lenzinger Ber.* **2010**, *88*, 1–59.
3. Patrick, K. Dissolving Pulp Gold Rush in High Gear. *Paper360°*, September/ October, 2011.
4. *Cotton Impact Assessment. Internet Consultation of Stakeholders' View on the EU Cotton Regime: An Overview of the Results*; European Commission, 2007.
5. Baksheev, I. P.; Butyagin, P. A. *Fiber Chem.* **1997**, *29* (4).
6. Beach, R. H.; Van Houtven, G. L.; Buckley, M. C.; Depro, B. M. *Economic Analysis of Air Pollution Regulations: Miscellaneous Cellulose Manufacturing Industry--Industry Profile*; U.S. Environmental Agency, 2000.
7. Henriksson, G.; Lennholm, H. Wood Chemistry and Biotechnology. In *Pulp and Paper Chemistry and Technology*; Ek, M., Gellerstedt, G., Henriksson, G., Eds.; Walter de Gruyter: Berlin, Germany, 2009; Vol. 1, pp 71−99.

Downloaded by NORTH CAROLINA STATE UNIV on August 28, 2012 | http://pubs.acs.org
Publication Date (Web): August 17, 2012 | doi: 10.1021/bk-2012-1107.ch009

8. Klemm, D.; Schmauder, H-P.; Heinze, T. *Cellulose*; Biopolymers Online; Wiley-VCH Varlag: Weinheim, Germany, 2005.
9. Köpcke, V. Ph.D. Thesis, Royal Institute of Technology, Stockholm, Sweden, 2010.
10. Sjöström, E. *Wood Chemistry: Fundamentals and Applications*, 2nd ed.; Academic Press: San Diego, CA, 1993; p 59.
11. O'Sullivan, A. C. *Cellulose* **1997**, *4*, 173–207.
12. Larsson, P. T.; Wickholm, K.; Iversen, T. *Carbohydr. Res.* **1997**, *302*, 19–25.
13. Wickholm, K.; Larsson, P. T.; Iversen, T. *Carbohydr. Res.* **1998**, *312*, 123–129.
14. Sugiyama, J.; Persson, J.; Chanzy, H. *Macromolecules* **1991**, *24*, 2461–2466.
15. Atalla, R. H.; Van der Hart, D. L. In *Cellulose and Wood: Chemistry and Technology, Proceedings of the Tenth Cellulose Conference*; Schuerch, C., Ed.; John Wiley and Sons: Hoboken, NJ, 1984; pp 169−187.
16. Kolpak, F. J.; Blackwell, J. *Macromolecules* **1976**, *9*, 273–278.
17. Hearle, J. W. S. *J. Polymer Sci.* **1958**, *28*, 432–435.
18. Zuckerstätter, G.; Schild, G.; Wollboldt, P.; Röder, T.; Weber, H. K.; Sixta, H. *Lenzinger Ber.* **2009**, *87*, 38–46.
19. Horii, F.; Hirai, A.; Kitamaru, R. *Polym. Bull.* **1982**, *8*, 160–170.
20. Fink, H-P.; Philipp, B.; Paul, D.; Serimaa, R.; Paakkari, T. *Polymer* **1987**, *28*, 1265–1270.
21. Krässig, H. A. Polymer Monographs. In *Cellulose: Structure, Accessibility and Reactivity*; Huglin, M. B., Ed.; Gordon and Breach Science Publishers: Yverdon, Switzerland, 1993; Vol. 11, pp 1−375.
22. Fahmy, Y.; Mobarak, F. *Cellul. Chem. Technol.* **1971**, *6*, 61–65.
23. Fengel, D.; Wegener, G. *J. Polymer Sci.* **1985**, *23* (11), 601–602.
24. Hiett, L. A. *Tappi J.* **1985**, *68* (2), 42–48.
25. Ibarra, D.; Köpcke, V.; Ek, M. *Holzforschung* **2009**, *63*, 721–730.
26. Iovleva, M. M.; Smirnova, V. N.; Belousova, T. A.; Banduryan, S. I.; Kalashnik, A. T.; Rudinskaya, G. Y. *Fibre Chem.* **1996**, *28* (5), 347–350.
27. Kunze, J.; Fink, H-P. *Macromol. Symp.* **2005**, *223*, 175–187.
28. Zhao, H.; Jones, C. L.; Baker, G. A.; Xia, S.; Olubajo, O.; Person, V. N. *J. Biotechnol.* **2009**, *139*, 47–54.
29. Ye, D.; Farriol, X. *Cellulose* **2005**, *12*, 507–515.
30. Fernandes Diniz, J. M. B.; Gil, M. H.; Castro, J. A. A. M. *Wood Sci. Technol.* **2004**, *37*, 489–494.
31. Oksanen, T.; Buchert, J.; Viikari, L. *Holzforschung* **1997**, *51*, 355–360.
32. Zhang, Y. H. P.; Lynd, L. R. *Biotechnol. Bioeng.* **2004**, *88* (7), 797–824.
33. Rabinovich, M. L.; Melnick, M. S.; Bolobova, A. V. *Appl. Biochem. Microbiol.* **2002**, *38* (4), 305–321.
34. Engström, A. C.; Ek, M.; Henriksson, G. *Biomacromolecules* **2006**, *7*, 2027–2031.
35. Henriksson, G.; Christiernin, M.; Agnemo, R. *J. Ind. Microbiol. Biotechnol.* **2005**, *32* (5), 211–214.
36. Ibarra, D.; Köpcke, V.; Ek, M. *Enzyme Microb. Technol.* **2010**, *47*, 355–362.
37. Ibarra, D.; Köpcke, V.; Larsson, P. T.; Jääskeläinen, A-S.; Ek, M. *Bioresour. Technol.* **2010**, *101*, 7416–7423.

38. Köpcke, V.; Ibarra, D.; Ek, M. *Nord. Pulp Pap. Res. J.* **2008**, *23* (4), 363–368.
39. Köpcke, V.; Ibarra, D.; Larsson, P. T.; Ek, M. *Nord. Pulp Pap. Res. J.* **2010**, *25* (1), 191–198.
40. Köpcke, V.; Ibarra, D.; Larsson, P. T.; Ek, M. *Polym. Renewable Resour.* **2010**, *1* (1), 17–34.
41. Li, D. Master Thesis, Royal Institute of Technology, Stockholm, Sweden, 2010.
42. Najar, H. Master Thesis, Royal Institute of Technology, Stockholm, Sweden, 2009.
43. Carrard, G.; Koivula, A.; Söderlund, H.; Béguin, P. *Proc. Natl. Acad. Sci.* **2000**, *97* (19), 10342–10347.
44. Lynd, L. R.; Weimer, P. J.; van Zyl, W. H.; Pretorius, I. S. *Microbiol. Mol. Biol. Rev.* **2002**, *66* (3), 506–577.
45. Rabinovich, M. L.; Melnick, M. S.; Bolobova, A. V. *Biokhimiya (Moscow, Russian Federation)* **2002**, *67* (8), 850–871.
46. Eremeeva, T.; Bikova, T.; Eismonte, M.; Viesturs, U.; Treimanis, A. *Cellulose* **2001**, *8* (1), 69–79.
47. Fock, W. *Papier* **1959**, *13*, 92–95.
48. Hopner, T.; Jayme, G.; Urich, J. C. *Papier* **1955**, *9*, 476–482.
49. Nelson, M. L.; Rousselle, M. A.; Cangemi, S. J.; Trouard, P. *Text. Res. J.* **1970**, *40* (10), 872–880.
50. Fischer, S.; Schenzel, K.; Fischer, K.; Diepenbrock, W. *Macromol. Symp.* **2005**, *223*, 41–56.
51. Filpponen, I.; Argyropoulos, D. S. *Ind. Eng. Chem. Res.* **2008**, *47* (22), 8906–8910.
52. Elg Christoffersson, K.; Sjöström, M.; Edlund, U.; Lindgren, Å.; Dolk, M. *Cellulose* **2002**, *9*, 159–170.
53. Sixta, H. Chemical Pulping. In *Handbook of Pulp*; Wiley-VCH Verlag: Weinheim, Germany, 2006; pp 3−19.
54. Vila, C.; Santos, V.; Parajo, J. C. *J. Chem. Technol. Biotechnol.* **2004**, *79*, 1098–1104.
55. Sixta, H.; Harms, H.; Dapia, S.; Parajo, J. C.; Puls, J.; Saake, B.; Fink, H-P.; Röder, T.*Cellulose* **2004**, *11* (1), 73−83.
56. Christov, L. P.; Prior, B. A. *Biotechnol. Lett.* **1993**, *15* (12), 1269–1274.
57. Hillman, D. *Paper Asia* **2006**, 12–18.
58. Drexler, H.; Ulm, K.; Hubmann, M.; Hardt, R.; Göen, T.; Mondorf, W.; Lang, E.; Angerer, J.; Lehnert, G. *Int. Arch. Occup. Environ. Health* **1995**, *67*, 243–252.
59. Rosenau, T.; Potthast, A.; Sixta, H.; Kosma, P. *Prog. Polym. Sci.* **2001**, *26* (9), 1763–1837.
60. Hermanutz, F.; Meister, F.; Uerdingen, E. *Chem. Fibers Int.* **2006**, *6*, 342–344.
61. Swatloski, R. P.; Rogers, R. D.; Holbrey, J. D. U.S. Patent 6,824,599, 2003.
62. Dadi, A. P.; Varanasi, S.; Schall, C. A. *Biotechnol. Bioeng.* **2006**, *95*, 904–910.

Downloaded by NORTH CAROLINA STATE UNIV on August 28, 2012 | http://pubs.acs.org
Publication Date (Web): August 17, 2012 | doi: 10.1021/bk-2012-1107.ch009

63. Zhu, S.; Wu, Y.; Chen, Q.; Yu, Z.; Wang, C.; Jin, S.; Ding, Y.; Wu, G. *Green Chem.* **2006**, *8*, 325–327.
64. Ebner, G.; Schiehser, S.; Potthast, A.; Rosenau, T. *Tetrahedron Lett.* **2008**, *49*, 7322–7324.
65. Liu, Z.; Wang, H.; Li, Z.; Lu, X.; Zhang, X.; Zhang, S.; Zhou, K. *Mater. Chem. Phys.* **2011**, *128*, 220–227.
66. Janzon, R.; Puls, J.; Saake, B. *Holzforschung* **2006**, *60* (4), 347–354.
67. Janzon, R.; Puls, J.; Bohn, A.; Potthast, A.; Saake, B. *Cellulose* **2008**, *15* (5), 739–750.
68. Puls, J.; Janzon, R.; Saake, B. *Lenzinger Ber.* **2006**, *86*, 63–70.
69. Jackson, L. S.; Heitmann, J. A.; Joyce, T. W. *Tappi J.* **1998**, *81* (3), 171–178.
70. Hyatt, J. A.; Fengel, R. W.; Edgar, K. J.; Alvarez-Wright, M. T. U.S. Patent 6,057,438, 2000.
71. Stephens, R. S. Patent WO/1999/016960, 1999.
72. Gübitz, G. M.; Lischnig, T.; Stebbing, D.; Saddler, J. N. *Biotechnol. Lett.* **1997**, *19* (5), 491–495.
73. Oksanen, T.; Pere, J.; Buchert, J.; Viikari, L. *Cellulose* **1997**, *4* (4), 329–339.
74. Salmén, L.; Olsson, A. M. *J. Pulp Pap. Sci.* **1998**, *24*, 99–103.
75. Sykes, M.; Klungness, J. H.; Abubakr, S.; Tan, F. *Prog. Pap. Recycl.* **1996**, 39–46.
76. Kvarnlöf, N. Ph.D. Thesis, Karlstad University, Karlstad, Sweden, 2007.

Downloaded by NORTH CAROLINA STATE UNIV on August 28, 2012 | http://pubs.acs.org
Publication Date (Web): August 17, 2012 | doi: 10.1021/bk-2012-1107.ch009

Downloaded by COLUMBIA UNIV on August 28, 2012 | http://pubs.acs.org
Publication Date (Web): August 17, 2012 | doi: 10.1021/bk-2012-1107.ch010

Chapter 10

Molecular Dynamics Simulations of the Thermal Stability of Crystalline Cellulose Surfaces Coated with Oleic Acid

**Mir A. A. R. Quddus,[1,2] Orlando J. Rojas,[1,2]
and Melissa A. Pasquinelli*,[2]**

[1]Forest Biomaterials, North Carolina State University, 2820 Faucette Drive, Raleigh, North Carolina 27695
[2]Fiber and Polymer Science/TECS, North Carolina State University, 2401 Research Drive, Raleigh, North Carolina 27695
***E-mail: melissa.pasquinelli@gmail.com**

The thermal stability of different types of oleic acid films on a crystalline cellulose surface has been investigated through molecular dynamics simulations. The thin film was observed to become disordered upon heating, resulting in the evaporation of oleic acid molecules. This effect is expected to contribute to the performance of cellulose, for example in packaging, where food contamination can be facilitated. In contrast, double layers and annealed coatings remained stable over the temperature range tested in this simulation.

Introduction

Interactions between cellulose and organic fluids, such as fatty acids, are of high importance in various fields, such as food packaging, pharmaceuticals, textiles, and paper. The adhesion and subsequent stability of the organic liquids on cellulose surfaces are driven by the interactions occurring between these components. These interactions include hydrogen bonding, van der Waals forces, hydrophobicity, etc. which occur within cellulose and between cellulose and fatty acid molecules. These forces are expected to affect the stability of the cellulose substrate and adsorbed fatty acid molecules. The stability of the cellulose-fatty acid combined structure depends on the attractive forces within each individual

In Functional Materials from Renewable Sources; Liebner, F., et al.;
ACS Symposium Series; American Chemical Society: Washington, DC, 2012.

Downloaded by COLUMBIA UNIV on August 28, 2012 | http://pubs.acs.org
Publication Date (Web): August 17, 2012 | doi: 10.1021/bk-2012-1107.ch010

component as well as their interactions. Oleic acid (OA), a common type of fatty acid, is liquid at room temperature. Thus its behavior at elevated temperatures is most relevant to its stability and of crucial importance in a variety of applications. For example, for eco-friendly packaging materials, fatty acids are sometimes used to coat cellulose. These packages are often referred to as "edible" packaging, which refers to thin continous layer of edible material formed on or between food goods or food components (*1–3*).

Edible food packaging materials are of interest due to their moisture barrier property, given hydrophilicity (*4*) and biodegradability (*5–9*). Bicomponent films with polysaccharides and lipids can provide functional properties that are otherwise difficult to obtain. These coatings are defined as thin, continuous layers of edible material used as a coating or as a film placed between food components to provide a barrier to mass transfer (*e.g.*, humidity) between the environment and food (*10*). These coatings are applied either directly on the food product, or via liquid film or by molten compounds. It can be applied by emulsion (*11*), spraying (*12*), or vapor deposition (*13*, *14*). The applied coating can be as thin as a monolayer to thick (*1*, *3*, *15*). The polysaccharide component of the material can be from sources such as cellulose and its derivatives, alginates, pectins, starches, and chitosan. The lipids can be fatty acids or waxes (*10*). Due to its low melting temperature, fatty acid coatings can become unstable at high temperatures and cause problems such as change in food odor and color and product quality (*16*).

The thermal stability of fatty acid coatings can be compromised due to processing, transportation, storage and consumer usage. The effect of thermal instability of food packaging has been investigated by many researchers (*1*, *17–20*). For example, in a recent experimental study with Nisin, an edible protein film, Giovanna and coworkers indicated that the thermal instability was affected by temperature, thickness and pH due to increased kinetics of the molecules. Among these factors, thickness and pH critically impacted Nisin desorption (*18–20*). Finally, the cohesion between fatty acid molecules define their stability under heating; for example, it is expected that a film with high molecular cohesion is highly stable.

The thermal stability of fatty acid coatings on a typical cellulosic surface depends on the properties of both components. Cellulose does not display a melting point because its degradation starts around 500 K due to disruption of interchain hydrogen bonding (*16*, *21–25*). It has been suggested that complete disruption of the hydrogen bonding network occurs above 500 K (*26–28*). On the other hand, fatty acids tend to possess a much lower thermal degradation temperature compared to that of cellulose. Generally, the saturated fatty acids have higher melting and boiling temperatures compared to unsaturated ones. For example, palmitic acid has a melting temperature of 336 K and a boiling temperature of 535 K, whereas oleic acid possesses melting and boiling points of 287 and 496 K, respectively (*29*). An understanding of the temperature effects on the stability of fatty acid coatings on polysaccharides could provide guiding principles in the advancement of food packaging technologies. The results from this study can be used as gauge of the durability of the edible film coatings under the wide range of temperatures that occur during processing, transportation, storage and consumption or use.

Downloaded by COLUMBIA UNIV on August 28, 2012 | http://pubs.acs.org
Publication Date (Web): August 17, 2012 | doi: 10.1021/bk-2012-1107.ch010

In this study, we have chosen cellulose as the solid substrate and oleic acid to represent the organic coating layer. Both of these components are central in consumer products of food packagings due to their biodegradability and non-toxicity (*30*, *31*). The properties of the crystalline cellulose surface has been characterized previously both in experiment (*32*, *33*) and simulation (*26*, *27*, *34–36*). These studies indicated that the cellulose structure is held together through inter- and intra-chain hydrogen bonding; however, both types of hydrogen bonding start to degrade above 475 K, and so the structure is stable between 300 and 450 K. Films of oleic acid have also been studied experimentally (*37–39*) and by simulation (*36*). It has been observed that oleic acid films have an affinity toward cellulose and form hydrogen bonds with cellulose (*38*). The stability of the three types of oleic acid (OA) films on a crystalline cellulose surface was investigated, representing various types of coatings that can be applied as edible bicomponent materials on food products. We refer to a *thin film* to represent a monolayer coating on the cellulose surface; *thick film* to represent a multilayer coating, and the *annealed film* to indicate a coating deposited from the vapor phase (*40*). This latter case has been addressed in reports that have indicated that vapor deposited films have a high degree of orientation and packing and thus could provide high thermal stability (*41*).

Methodology

The system setup and the molecular dynamics (MD) simulations were conducted with Accelrys' Materials Studio® software, version 5.5 (*42*). We used Forcite Plus® for geometry optimization, parameterization, dynamics and analysis. The simulations were run on a Dell computer with an Intel Core-i7 processor at 2.79 GHz and with 8 GB RAM.

Preparation of the Molecular Model of the OA-Cellulose System

A crystalline cellulose surface was built from a crystal unit cell obtained from X-ray diffraction studies conducted by Nishiyama and coworkers (*43*). The monoclinic 1β unit cell structure was optimized after adding hydrogens within the Materials Studio visualizer. This unit cell was then cleaved along the [110] plane following the protocol of Mazeau (*35*). Then, a supercell was built by replicating the cleaved 2-dimensional structure three times. This structure was converted into 3 dimensions by forming a slab. This slab was then annealed for 500 ps with the peak temperature of 500 K, after removing all of the structural constraints. The annealed structure was then subjected to 500 ps of NVT dynamics.

Three types of fatty acid coatings were built with the Amorphous Builder® utility from the coordinates obtained for OA from PubChem database (*44*). The density of the all these coatings were set to 0.895 g/cm^3. The *thin* film was built from 25 OA molecules with the specified density. The *thick* film was built from 50 OA molecules and same density as the *thin* film. Both of these films were optimized for 20 ps at 300 K. The *annealed* film was built in several steps. First, a thin film was built according to the same procedure as mentioned above. This

Downloaded by COLUMBIA UNIV on August 28, 2012 | http://pubs.acs.org
Publication Date (Web): August 17, 2012 | doi: 10.1021/bk-2012-1107.ch010

thin film was then annealed at 500 K, upon which the film disintegrated into individual molecules, which is comparable to a vaporized state. Then the system was optimized for 20 ps at 298 K.

In the MD box the [110] crystalline cellulose surface was placed at the bottom of the MD box, and each oleic acid film was placed within 9.5 Å (Lennard-Jones cutoff distance) from it. The thin and thick films were incorporated into the MD box with layer builder utility, and the annealed film was added to the box according to the docking method. A 100 Å vacuum space was kept on top of each OA film to avoid interaction with bottom surface of the periodic image. The final dimensions of the combined system is 31 x 35 x Z, where the Z height varies based on the type of film used (Table I).

Table I. Dimensions of the MD boxes used in the simulations

Dimension	*Thin*	*Thick*	*Annealed*
x (Å)	31.1	31.4	31.9
y (Å)	35.8	35.8	36.6
z (Å)	150.2	165.0	172.1

MD Simulations

All of the simulations were conducted using the NPT (isothermal-isobaric) ensemble. The temperature of the system was controlled with the Nose-Hoover thermostat (*45*), and pressure was maintained at 1 atm with the Berendsen barostat (*46*). An integration time step of 1 fs was used, and the Verlet algorithm was used to integrate the equations of motion for all of the simulations. The PCFF force field was used to configure atoms of both the fatty acid and cellulose atoms, which is a second generation force field that was originally developed for the simulation of condensed phase materials such as polymers (*47*, *48*). This force field has been validated previously for use with both fatty acids (*49*) and cellulose (*35*, *50*).

Results and Discussion

We investigated the thermal stability of the different OA films on a cellulose substrate. This MD simulation study was conducted in vacuum at a range of temperatures, mimicking the heating of this coated surface inside a microwave or oven. The temperature was varied from 300 to 450 K in 50 K increments based on temperatures used in handling packaged food products; Table II reflects the food warming temperatures recommended by the FDA for the safe use of food packaging. According to this table, 400 K is a safe temperature for warming a food packaging, and 450 K can be considered as an unsafe temperature for handling. Thus this temperature (450 K) is considered as “misuse” temperature, i.e., if used, it can damage the coating. Thus, the stability at the misuse temperature of a cellulose surface that is coated with a fatty acid is a good indicator of the packaging's thermal stability since this temperature is also close to the boiling point of the fatty acid such as OA. In addition, there is a possibility for the films to be released from the cellulose surface and cause unwanted contamination. The misuse temperature can also cause damage to the base cellulose surface. Thus in this study, we also evaluated the stability of the cellulose surface at this temperature.

Table II. Temperature set points for warming food packages

Temperature (K)	*Set Point Description*
300	Room temperature (*51*)
350	Recommended temperature for cooked meat products (*52*, *53*)
400	FDA recommended temperature for food packaging (*52*)
450	Consumer misuse temperature for food packaging (*52*)

With MD simulations, we investigated the thermal stability of the cellulose substrate coated with OA films, as well as the substrate and OA films separately. As indicated in the introduction, the thickness and formation mechanism is of critical concern related to thermal stability of the coating films. These two factors were selected based on the previous studies where it was found that protein film desorption increased with the decrease in film thickness (*17*, *53*) and vapor deposited films possessed higher orientation and packing compared to thin films (*41*). Thus, we expect to observe higher stability in the case of the thick film (double layer) and the annealed film over the thin film. In the following sections, we evaluate the stability of the cellulose surface, OA films and OA-cellulose assembly, through MD simulations.

Downloaded by COLUMBIA UNIV on August 28, 2012 | http://pubs.acs.org
Publication Date (Web): August 17, 2012 | doi: 10.1021/bk-2012-1107.ch010

Validation of the Molecular Models

The results of the optimization of the [110] crystalline cellulose surface are given in Figure 1, obtained after 500 ps of NPT dynamics at 500 K. The system was minimized for 20 ps at 300 K. The image indicates that the crystalline unit cells within the cellulose structure reorganized from its original structure due to heating. As a result of this reorganization, the surface area of the cellulose structure increased, as is indicated in Figure 1c and 1d. (The surfaces were obtained by a Connolly probe of 1.5 Å diameter and a 0.75 Å grid spacing.) With the reorganization of the structure, the cellulose surface area increased 17% from 1459 to 1703 Å^2. According to Matthews and coworkers, this increase in disorder can lead to diffusion of water molecules into its structure, which is otherwise difficult for cellulose crystal structure (*34*). In addition, heating caused the rearrangement of the inter- and intra-residue hydrogens within the cellulose structure, as depicted in Figure 1a and 1b. But no disruption of the structure occurred at the misuse temperature. The hydrogen bonds were calculated between the oxygen - oxygen and oxygen - hydrogen atoms within the cellulose structure. A close up view of the hydrogen bonding within the cellulose structure can be observed in Figure 2a. There is an increase in inter-residue hydrogen bonding due to rearrangement of the cellulose chains. This observation qualitatively correlate with the study done by Matthews and coworkers in their high temperature simulation of cellulose (*33*). This structure and the hydrogen bonding network is also qualitatively similar to the one indicated by Nishiyama and others (*26*, *27*, *33*, *54*). The results also indicate that the hydrogen bonds remained stable at the misuse temperature, in agreement with Zhang and Bergenstrahle (*25*, *26*).

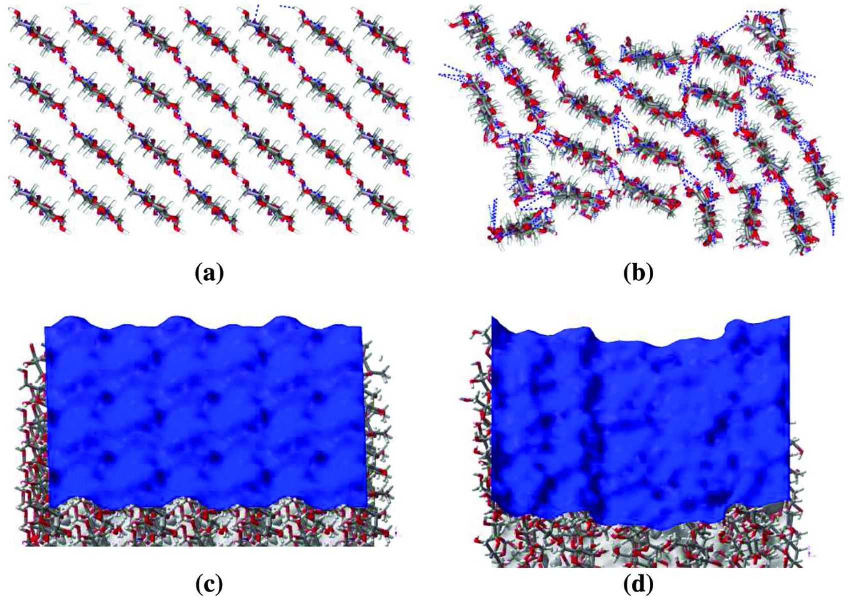

Figure 1. Snapshots of the crystalline [110] cellulose surface a) initial structure at 300 K, b) final structure after 500 ps of NPT at 500 K, c) Connolly surface at 300 K and d) Connolly surface at 500 K. The colors (consistent in all figures) represent the following atoms: carbon is gray, oxygen is red and hydrogen is white. Hydrogen bonds are indicated by blue dashed lines. (see color insert)

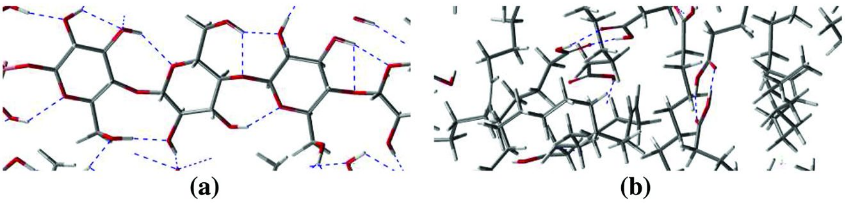

Figure 2. Zoomed-in view of the hydrogen bonding network within the a) cellulose and b) oleic acid structures. (see color insert)

Downloaded by COLUMBIA UNIV on August 28, 2012 | http://pubs.acs.org
Publication Date (Web): August 17, 2012 | doi: 10.1021/bk-2012-1107.ch010

Downloaded by COLUMBIA UNIV on August 28, 2012 | http://pubs.acs.org
Publication Date (Web): August 17, 2012 | doi: 10.1021/bk-2012-1107.ch010

The final structures for the three OA films are depicted in Figure 3. These images represent the aggregated OA molecules in the form of films after geometry optimization and subsequent NPT MD simulation. This figure also suggests that OA molecules within the *thin* and *annealed* films have lower compactness and higher orientation compared to those of the *thick* film, which impact the strength of these films on the cellulose surface.

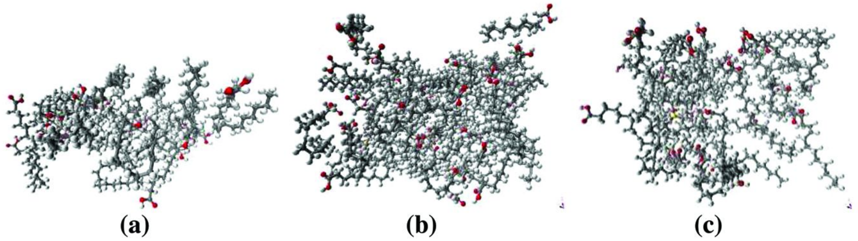

Figure 3. Snapshots of the types of OA films that were created in this simulation: a) thin, b) thick and c) annealed films. (see color insert)

The combined system of cellulose with the *thin* OA film is given in Figure 4. Figure 4a presents the initial state of the combined system, where the OA film has already been optimized prior to placing within the box with the cellulose. At this state, the OA molecules are initially mostly separated from the cellulose surface. Figure 4b is a snapshot from the final frame after 1.1 ns of NPT simulation at 1 atm pressure, which suggests that the OA molecules within the *thin film* adhered onto the cellulose surface. In addition, some hydrogen bonds (indicated by the dashed blue line) formed between OA molecules and the cellulose. Besides increased thickness, no distinguishable difference can be observed for the *thick* film after completion of the NPT simulation. As hypothesized in the previous section, the figure indicates higher orientation of the OA molecules for both *annealed* and *thin* films compared to the *thick* (images of the thick and annealed results are not shown).

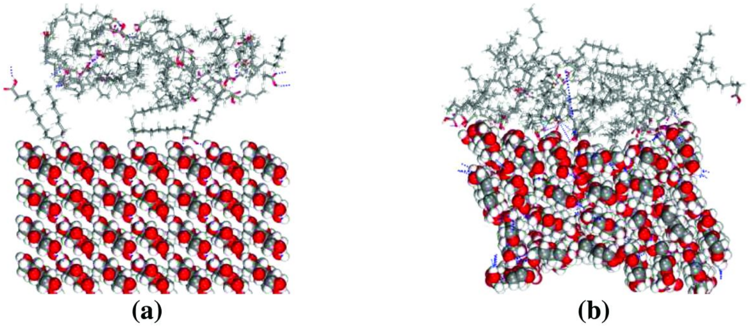

Figure 4. Snapshots of the combined system of crystalline cellulose and the thin OA film at 300 K, for the a) initial and b) final structures. (see color insert)

In the following sections, we analyze how the film thickness and their formation mechanism can impact the thermal stability of the OA films on the cellulose surface. We first extract the individual components from the simulation and evaluate how their structures and interactions are impacted by elevated temperatures.

Effect of Temperature on the Structure of Crystalline Cellulose

Thermal stability of the cellulose at high temperatures has been studied by both experimental (*32*, *55*, *56*) and computational (*26*, *27*, *34*, *35*) techniques. From the experimental studies performed by Wada, it was observed that the cellulose 1β diffraction peaks widened at 473 K without decomposition (*56*). A significant change in the crystal structure was observed, indicating the crystalline phase transition was beyond 500 K (*56*). Kim and coworkers, working with cellulose 1β, observed that it starts to degrade above 573 K. Additionally, at 633 K, the cellulose crystal crystallites produced spectra similar to amorphous cellulose materials, which indicates loss of order (*32*). Nada and coworkers, using viscose pulp, observed that cellulose starts to degrade at 588 K; the cellulose had lost 80% of its original weight (*55*). In addition, the glass transition temperature for cellulose has been estimated to also be within this temperature range, 490 K (*23*).

We evaluated the integrity of the cellulose structure at elevated temperatures from the MD simulations performed at the temperature ranges given in Table II. The radial distribution function (RDF) which provides information about the structural order of the system, was used to evaluate the integrity of the cellulose surface at elevated temperatures. To evaluate the RDF, we used a 0.1 Å integration step and 15 Å cutoff, and the pairwise distribution function was calculated between all pair of atoms within the cellulose structure that are indicated in Figure 5a. An overall observation is that of no or negligible difference in the RDF beween 300 and 450 K. There is only slight increase in the height of the peaks observed at the 500 K temperature. According to Mazeau, the peaks at 1.44 and 1.55 Å are due to C-O and C-C atoms respectively, and the peaks beyond 2 Å are due to non-bonded atoms. Similarly, Chen and co-workers found that C-H, O-H, C-C and C-O bonds within cellulose I occurs between 1.0 - 1.5 Å. Whereas the hydrogen bonding occurs between 2.0 - 3.0 Å (*57*). Figure 6 indicates that the first non-bonding peak appears within 3 Å, which can be considered as a hydrogen bonding distance (*58*). It has been indicated that the crystalline microstructure peaks fluctuate at larger distances beyond 5 Å, which is also observed in Figure 6. These observations suggest that the cellulose structure has retained its crystalline order even after rearrangement along with non-bonded interactions at the misuse temperature, which correlates with earlier experimental findings (*55*, *56*). Thus our results coincide with the experimental findings that the cellulose surface remains stable below 500 K (*26*).

Downloaded by COLUMBIA UNIV on August 28, 2012 | http://pubs.acs.org
Publication Date (Web): August 17, 2012 | doi: 10.1021/bk-2012-1107.ch010

Downloaded by COLUMBIA UNIV on August 28, 2012 | http://pubs.acs.org
Publication Date (Web): August 17, 2012 | doi: 10.1021/bk-2012-1107.ch010

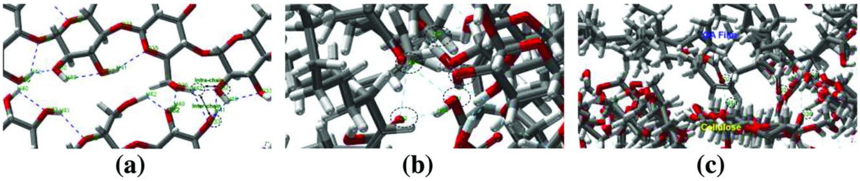

Figure 5. Atoms (indicated by the dashed lines and circles) that are used for RDF calculation for the a) cellulose chains, b) OA molecule and c) OA-cellulose interaction. (see color insert)

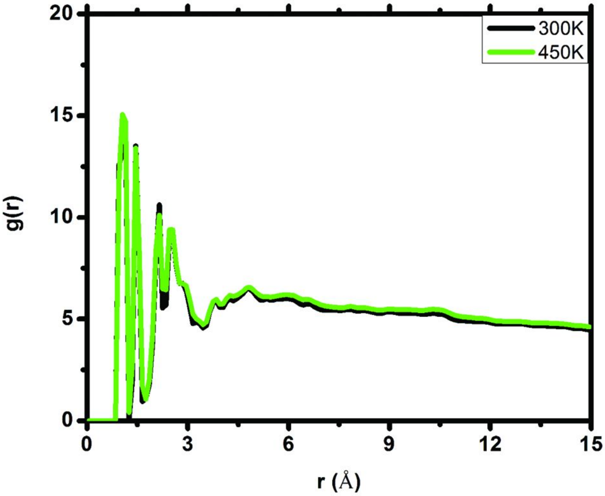

Figure 6. Radial distribution function (RDF) of crystalline cellulose at 300 K and 450 K temperatures, calculated over the entire trajectory. (see color insert)

Effect of Temperature on the OA Film Structure

The RDF was also evaluated between all of the atom pairs within the OA films that are indicated in Figure 6b using the same integration step and cutoff as for cellulose, and the results are displayed in Figure 7. The peaks below 2 Å are due to atom connectivity within the OA molecules, and these peaks remained stable with the increase in temperature. The first peak that appears above 2 Å is due to non-bonded interactions. These peaks are lower in magnitude and almost non-existent beyond 3 Å, suggesting that there are few hydrogen bonds within the OA film and the structure is disordered at longer distances. At misuse temperature, these peaks shift to smaller distances for the *thick* film, which suggests that the OA molecules become more ordered than initial. On the other hand, the location of the non-bonded peaks within the *thin* and *annealed* films becomes smooth at longer distances. This indicates the increase in structural order for both of these films.

The overall trends for all three of the films are similar but their degree of order differs based on their thickness. Thus, there is some possibility at the misuse

Downloaded by COLUMBIA UNIV on August 28, 2012 | http://pubs.acs.org
Publication Date (Web): August 17, 2012 | doi: 10.1021/bk-2012-1107.ch010

temperature of film disruption due to loss of hydrogen bonding. Using FTIR, Proctor and coworkers found the presence of of strong hydrogen bonding between OA molecules (*38*). The loss of hydrogen bonding at higher temperatures can also be due to increased mobility of the OA molecules (to be discussed later), which enables the cohesive forces to be overcome, and leading to instability of the OA molecules especially in the *thin* and *annealed* films.

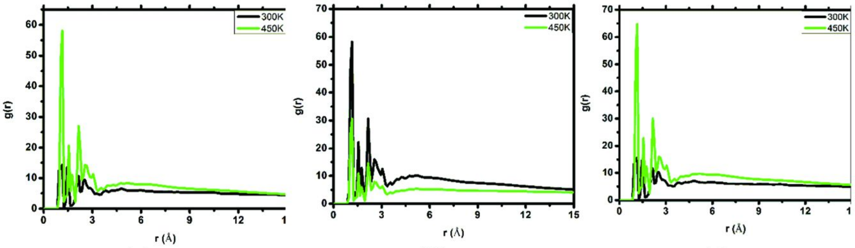

(a) **(b)** **(c)**

Figure 7. The RDF at the 300 K and 450 K tempteratues for the (a) thin, (b) thick, and (c) annealed OA films. These plots were calculated from the entire MD trajectory. (see color insert)

Figure 8 provides the average torsion angle along the OA double bond (depicted in Figure 9). These plots indicate that OA prefers torsional angles of 120° with the backbone for all three types of films. This value was obtained by previous simulations (*59*) and closer to the experimental value obtained for crystalline oleic acid (*60*). The probability of finding that angle (indicated by the height of the peaks) slightly decreases with an increase in temperature for all three types of OA films. This observation is likely due to the increased movement of the atoms from the elevated temperatures; a decrease in torsion angle is directly associated with heating and related expansion of chains. At 450 K, the highest expansion of the chains is observed to occur. Thus, the loss of hydrogen bonding within the fatty acid film in Figure 7 can be inferred to be due to the increase in the conformational freedom of the OA molecules. However, the effect is most prominent in the *thin* film compared to *thick* and *annealed*. This can affect its stability on the cellulose surface.

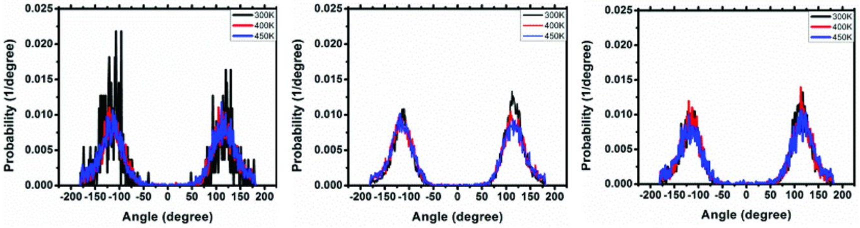

(a) **(b)** **(c)**

Figure 8. The torsion angle averaged over the entire trajectory for the (a) thin, (b) thick, and (c) annealed OA films. (see color insert)

Downloaded by COLUMBIA UNIV on August 28, 2012 | http://pubs.acs.org
Publication Date (Web): August 17, 2012 | doi: 10.1021/bk-2012-1107.ch010

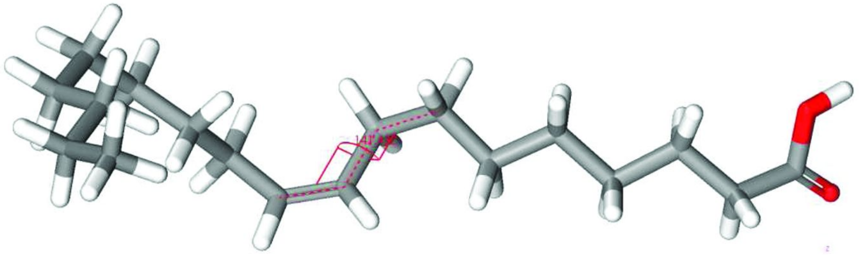

Figure 9. Definition of the torsion angle (-C-C-C=C-) for oleic acid. (see color insert)

Effect of Temperature on Interaction between the OA Film and the Cellulose Surface

In a recent study with cellulose microfibril faces, Mazeau noted that adhesion can be impacted by the accessibility of the OH groups located on the cellulose surface, and that the [110] crystalline cellulose surface has intermediate accessibility of the hydrophilic OH group (*35*). In order for the OA films to adhere onto the cellulose surface, the OH group accessibility is of primary importance. The integrity of the OA film can also be maintained through the cohesive hydrogen bond formation through its carboxylic acid group (*37*). These groups can also interact with cellulose hydroxyl groups to form hydrogen bonding. For example, Figure 4b indicates that there is hydrogen bonding between oleic acid and the cellulose surface.

In order to better quantify this effect, we have evaluated the number of hydrogen bonds between the cellulose hydroxyl group (OH) and the carboxylic acid oxygen atoms. The results in Figure 10 suggest that the number of hydrogen bonds increases slightly with the increase in temperature. Between the carbonyl oxygen (C=O) and hydroxyl oxygen (OH) with the cellulose OH groups, a higher number of hydrogen bonds can be observed with C=O. Among the three films, the highest number of OH – OH hydrogen bonds is present in the *thin* and the lowest in the *thick* one at the misuse temperature. However, in the case of *thin* films, the OH – OH hydrogen bonding reduces at the misuse temperature, which may lead to some desorption of OA molecules attracted through hydrogen bonding.

Further evaluation of order in these films was conducted by applying RDF between the OA films and the cellulose surface. We have taken the difference in RDF profiles for both OA and the cellulose between the atom pairs of cellulose and the OA film that are indicated in Figure 5c to understand their interactions, and the results are given in Figure 11. In this case, every change in slope of the respective curve is associated with a difference in peak height between the two systems. It can be observed from this graph that a peak shift between the covalent bonded atoms of both surfaces (under 2 Å) does not deviate and thus the difference is negligible. But on the other hand, the non-bonded atoms slightly deviate between 2-3 Å due to the increase in the number of hydrogen bonds. Beyond 5 Å, the peaks deviate further due to disorder within the structure, which increased with the increase in temperature. Among the three films, the magnitude of this trend is lowest for the

Downloaded by COLUMBIA UNIV on August 28, 2012 | http://pubs.acs.org
Publication Date (Web): August 17, 2012 | doi: 10.1021/bk-2012-1107.ch010

thick film, which could be due to the lowest degree of hydrogen bonding and order within the structure. On the other hand, the structural order increases for both *thin* and *annealed* films at the misuse temperature. In case of the *annealed* film, the increase in structural order at the misuse temperature is slightly higher than the *thin* film. The loss of order for the *thin* film can be due to potential disruption of some of the hydrogen bonds between the OA film and the cellulose at this temperature.

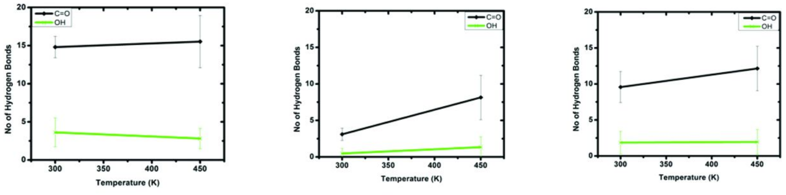

(a) **(b)** **(c)**

Figure 10. Difference between the number of hydrogen bonds formed at 300 K and 450 K for the cellulose hydroxyl group (OH) and the carbonyl groups (C=O, green, and OH, black) of (a) thin, (b) thick, and (c) annealed OA films. The error bars indicate deviation of hydrogen bond formation within a given temperature. (see color insert)

The density of the three OA-cellulose systems is given in Figure 12. This figure indicates that the density of the *thin* film decreased with an increase in temperature. The steep reduction in system density of the thin film can be an indication of large structural changes, including OA molecule desorption from the film. In case of the *thick* film, the density increased up to 350 K and then decreased slightly thereafter, which could be due to formation of hydrogen bonds and subsequent increase in order within the structure. Density of the *annealed* film remained nearly unchanged at the misuse temperature, with some decrease between 350 and 400 K temperatures.

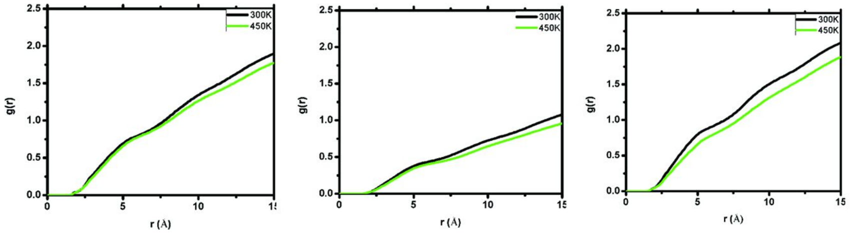

(a) **(b)** **(c)**

Figure 11. Difference between the RDF between the cellulose surface at 300 K and 450 K indicating interaction of the (a) thin, (b) thick, and (c) annealed OA films. (see color insert)

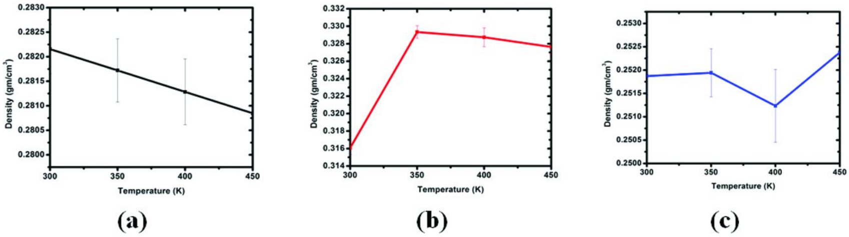

Figure 12. Density of the cellulose-OA system surface between 300 to 450 K temperatures of the (a) thin, (b) thick, and (c) annealed OA films. (see color insert)

Downloaded by COLUMBIA UNIV on August 28, 2012 | http://pubs.acs.org
Publication Date (Web): August 17, 2012 | doi: 10.1021/bk-2012-1107.ch010

The changes due to hydrogen bonding between OA molecules and the cellulose surface influence the interfacial interaction energy (E_{inter}), given by:

$$E_{inter} = \frac{E_{tot} - (E_{cell} + E_{OA})}{A} \qquad (1)$$

where E_{tot} is the total potential energy of the combined system, E_{cell} is the potential energy of the cellulose surface, E_{OA} is the potential energy of the OA film, and A is the area of the interface (in this case, the cellulose surface). A decrease in this quantity can suggest a decrease in the OA film adhesion on the cellulose surface, thus leading to instability, while a positive change indicates a favorable interaction, leading to greater film stability (*61*).

The E_{inter} as a function of temperature for the three films considered in this study is given in Figure 13. The results suggest that there is an initial increase in the interaction energy for *thick* and *annealed* films between 300 and 350 K, likely due to an increased number of hydrogen bonds between the OA films and the cellulose surface. Between 350 to 400 K, the interaction energy of the *annealed* surface increased further due to structural ordering and formation of C=O – OH hydrogen bonding. However, between 400 to misuse temperature, there might be some loss of OH – OH hydrogen bonds but reformation of C=O – OH hydrogen bonds due to increased structural ordering beyond 5 Å distance. In case of the *thick* film, the potential energy decreased slightly between 350 and 400 K due to lower formation of C=O – OH hydrogen bond formation. But it increased slightly at the misuse temperature due to higher increase in OH – OH hydrogen bonding. On the other hand, the potential energy of the *thin* film decreased with the decrease in the C=O – OH hydrogen bonding. There is a steep decrease in potential energy for this film at the misuse temperature close to zero, indicating OA molecule desorption (evaporation) from the surface. These results indicate that the *thick* and *annealed* films are able to withstand the temperatures considered in this study, but not necessarily the *thin* one.

The snapshots of the final trajectory frame of the three films can provide some insights on their stability. Figure 14 provides the final frame snapshots of the three films. This figure indicate that all the three films remained adsorbed at the misuse temperature. The OA molecules have slightly diffused into the cellulose surface due to increased surface area (indicated in Figure 1d). Furthermore, an OA molecule is being desorbed (evaporated) from the *thin* film at the misuse temperature. On the other hand, no desorption can be observed for the *thick* and *annealed* films. The thick film structure looks more disordered than the *thin* and *annealed* ones.

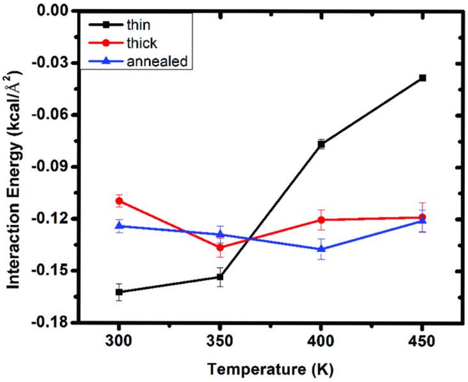

Figure 13. The interfacial energy between the [110] crystalline cellulose surface and the OA molecules as a function of temperature for thin, thick, and annealed OA films (as indicated). The values have been averaged over the 100 final ps of the MD trajectories. (see color insert)

The mean squared displacement (MSD) can provide information about molecular diffusion; as such, the dynamics of the OA molecules within the fatty acid film toward the cellulose surface can be estimated by the MSD. The diffusion coefficient (D) can be calculated from the MSD from the following equation,

$$D = \frac{1}{6N} \lim_{t\to 0} \left\langle \sum_{i}^{N} \left[r_i(t) - r_i(0) \right]^2 \right\rangle \tag{2}$$

where N is the number of atoms, and $r(t)$ is the displacement at time t. The summation term in the brackets is the MSD.

The MSD calculated from the entire production trajectory for each of the OA films relative to the cellulose surface is given in Figure 15. The MSD is calculated by considering the carbonyl oxygen atoms as the penetrating atoms within the OA film, which diffuse towards the cellulose surface. As illustrated in Figure 14, for each OA film system, the mobility of the carbonyl oxygen atoms increased with the increase in temperature. In case of the *thin* film, the highest increase can be observed at 450 K (*62*). The MSD plot for the *thick* film (Figure 14b) also reveals some other interesting features. At 400 and 450 K, there is an initial steep slope followed by a reduced one due to a reduction of mobility of the carbonyl atoms away from the surface. This type of trend is observed in systems where a phase transition occurs, for example, from liquid to gaseous phase (*63*). In this system, it can be inferred that this transition is due to the formation of cohesive interactions within the coating, and this stability reduces the possibility of desorption of the OA molecules from the *thick* surface. The *annealed* film

Downloaded by COLUMBIA UNIV on August 28, 2012 | http://pubs.acs.org
Publication Date (Web): August 17, 2012 | doi: 10.1021/bk-2012-1107.ch010

Downloaded by COLUMBIA UNIV on August 28, 2012 | http://pubs.acs.org
Publication Date (Web): August 17, 2012 | doi: 10.1021/bk-2012-1107.ch010

exhibits features similar to both the thick and the thin films. It too has a initial steep slope, which gradually decreases at higher temperatures (450 K). This trend indicates that the *annealed* film was stabilized by the continuous rearrangement of the molecules on the cellulose surface. The overall magnitude of the displacement of the molecules is highest for the *thin* followed by *annealed* and *thick* films.

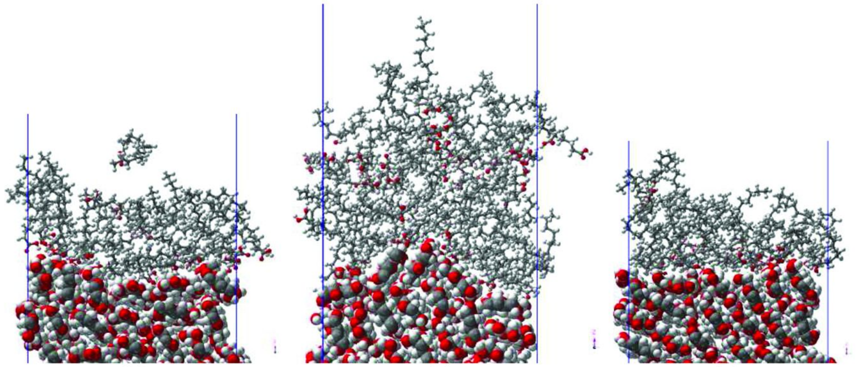

(a) (b) (c)

Figure 14. Snapshots from the 1 ns timestep of the MD simulation trajectory of crystalline [110] cellulose (bottom) coated with a (a) thin, (b)thick and (c) annealed OA film (top) heated at 450 K. (see color insert)

The calculated diffusivity values from Eqn. 2 are given in Table III and indicate that the *thin* film has the highest diffusivity among the three films, which is indicative of its higher mobility. The *annealed* film has the intermediate diffusivity. These observations suggest that both the *thick and annealed* films might be a a good choice for cellulose surfaces compared to *thin*. Considering the cost of manufacturing, the *annealed* might be a more prudent option for edible food packaging that is made from cellulose.

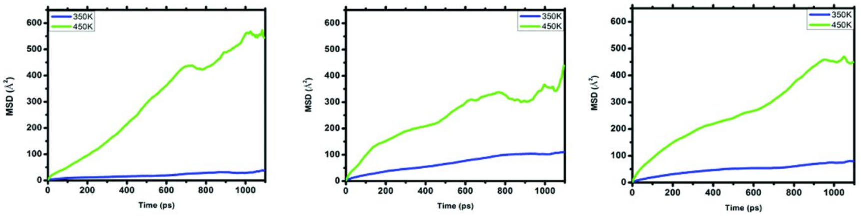

(a) (b) (c)

Figure 15. Mean square displacement (MSD) in a (a) thin, (b) thick, and(c) annealed OA film. (see color insert)

Downloaded by COLUMBIA UNIV on August 28, 2012 | http://pubs.acs.org
Publication Date (Web): August 17, 2012 | doi: 10.1021/bk-2012-1107.ch010

Table III. Diffusion coefficients calculated with Eqn. 2 at various temperatures for the three OA films systems calculated over the first 500 ps of the MD trajectory

Temperature (K)	*Thin (10^{-6} cm²/s)*	*Thick (10^{-6} cm²/s)*	*Annealed (10^{-6} cm²/s)*
300	0.8	0.4	0.6
400	1.3	2.9	2.8
450	10.1	6.1	7.9

Conclusion

We investigated the thermal stability of fatty acid films coating cellulose substrates as a model of edible food packaging materials. The results from molecular dynamics simulations indicate that both components of the system are stable up to the misuse temperature recommended by FDA.

The use of a *thick and annealed* coating over the *thin* one is preferred due to their stability up to the misuse temperature. The results found in our MD simulations correlated with results from experimental evidence and therefore it is suggested that the computational methods used can be used to predict, screen or troubleshoot the performance of related systems, for example, in cellulose-based packaging applications.

Acknowledgments

The authors would like to thank Whirlpool Corporation for funding this work through a graduate fellowship to MAQ.

References

1. Debeaufort, F.; Voilley, A.*Lipid-Based Edible Films and Coatings*; Springer: New York, 2009; pp 135−168.
2. Kamper, S.; Fennema, O. *J. Food Sci.* **1984**, *49* (6), 1482–1485.
3. Torres, J. A. *Protein Funct. Food Syst.* **1994**, 467–507.
4. Janjarasskul, T.; Krochta, J. M. *Annu. Rev. Food Sci. Technol.* **2010**, *1*, 415–448.
5. Tome, L. C.; Brandao, L.; Mendes, A. M.; Silvestre, A. J. D.; Neto, C. P.; Gandini, A.; Freire, C. S. R.; Marrucho, I. M. *Cellulose* **2010** (0969-0239), 1–9.
6. Ghanbarzadeh, B.; Almasi, H. *Int. J. Biol. Macromolecules* **2010** (0141-8130).
7. Zahedi, Y.; Ghanbarzadeh, B.; Sedaghat, N. *J. Food Eng.* **2010**, *100* (1), 102–108.
8. Lacroix, M.*Edible Films and Coatings for Food Applications*; Springer: New York, 2009; pp 347366

Downloaded by COLUMBIA UNIV on August 28, 2012 | http://pubs.acs.org
Publication Date (Web): August 17, 2012 | doi: 10.1021/bk-2012-1107.ch010

9. Quintero-Salazar, B.; Ponce-Alquicira, E. *Edible Packaging for Poultry and Poultry Products*.
10. Sorrentino, A.; Gorrasi, G.; Vittoria, V. *Trends Food Sci. Technol.* **2007**, *18* (2), 84–95.
11. McClements, D.; Decker, E.; Weiss, J. *J. Food Sci.* **2007**, *72* (8), R109–R124.
12. Suppakul, P.; Jutakorn, K.; Bangchokedee, Y. *J. Food Eng.* **2010**, *98* (2), 207–213.
13. Andersson, C. *Packag. Technol. Sci.* **2008**, *21* (6), 339–373.
14. Haas, K. H.; Amberg-Schwab, S.; Rose, K.; Schottner, G. *Surf. Coat. Technol.* **1999**, *111* (1), 72–79.
15. Kamper, S.; Fennema, O. *J. Food Sci.* **1984**, *49* (6), 1482–1485.
16. Barreto, P.; Pires, A.; Soldi, V. *Polym. Degrad. Stab.* **2003**, *79* (1), 147–152.
17. Rossi-Marquez, G.; Han, J. H.; Garcia-Almendarez, B.; E., C.-T.; Regalado-Gonzalez, C. *J. Sci. Food Agric.* **2009**, *89* (14), 2492–2497.
18. Robertson, G. L. *Food Packaging: Principles and Practice*; CRC Press: Boca Raton, FL, 2006.
19. Siracusa, V.; Rocculi, P.; Romani, S.; Rosa, M. D. *Trends Food Sci. Technol.* **2008**, *19* (12), 634–643.
20. Kim-Kang, H. *Crit. Rev. Food Sci. Nutr.* **1990**, *29* (4), 255–271.
21. Kokoszka, S.; Debeaufort, F.; Lenart, A.; Voilley, A. *Int. Dairy J.*, *20* (1), 53–60.
22. Plackett, D. V. *Biopolymers: New Materials for Sustainable Films and Coatings*; Wiley Online Library: 2011.
23. Szczesniak, L.; Rachocki, A.; Tritt-Goc, J. *Cellulose* **2008**, *15* (3).
24. Bergenstrahle, M.; Mazeau, K.; Berglund, L. A. *Eur. Polym. J.* **2008**, *44* (11), 3662–3669.
25. Liu, H.; Li, Y.; Krause, W. E.; Rojas, O. J.; Pasquinelli, M. A. *J. Phys. Chem. B* **2012**.
26. Zhang, Q.; Bulone, V.; Agren, H.; Tu, Y. *Cellulose* **2011**, 1–15.
27. Bergenstrahle, M.; Berglund, L. A.; Mazeau, K. *J. Phys. Chem. B* **2007**, *111* (30), 9138–9145.
28. Liu, H. a. L. Y. V.; Krause, W. E.; Pasquinelli, M. A.; Rojas, O. J. *ACS Appl. Mater. Interfaces* **2011**.
29. Arpe, H. J.; Ullmann, F.; Gerhartz, W.; Yamamoto, Y. S.; Campbell, F. T.; Pfefferkorn, R.; Rounsaville, J. F. *Ullmann's Encyclopedia of Industrial Chemistry*; Wiley-VCH: Weinheim, Germany, 1985.
30. Chiellini, E.; Solaro, R. *Adv. Mater.* **1996**, *8* (4), 305–313.
31. Bertrand, Y.; Hoang, L. In *Vegetal Oils As Substitute for Mineral Oils*; IEEE: 2003; pp 491−494 vol. 2.
32. Kim, D. Y.; Nishiyama, Y.; Wada, M.; Kuga, S.; Okano, T. *Holzforschung* **2001**, *55* (5), 521–524.
33. Dumitriu, S. *Polysaccharides: Structural Diversity and Functional Versatility*. CRC Press: Boca Raton, FL, 2005.
34. Matthews, J. F.; Bergenstrahle, M.; Beckham, G. T.; Himmel, M. E.; Nimlos, M. R.; Brady, J. W.; Crowley, M. F. *J. Phys. Chem. B* **2011**.
35. Mazeau, K. *Carbohydr. Polym.* **2010**.

36. Quddus, M. *A Systematic Study of Fatty Acids Interacting with Crystalline Cellulose Surfaces via Molecular Dynamics Simulations*. Dissertation, North Carolina State University, NCSU Institutional Repository, 2011.
37. Vargas, M.; Albors, A.; Chiralt, A.; Gonzalez-Martinez, C. *Food Hydrocolloids* **2009**, *23* (2), 536–547.
38. Proctor, A.; Adhikari, C.; Blyholder, G. *J. Am. Oil Chem. Soc.* **1995**, *72* (3), 331–335.
39. Garland, E. R.; Lee, A. D.; Baer, T.; Clarke, L. I. *J. Phys. Chem. C* **2008**, *113* (6), 2141–2148.
40. Dou, Y.; Zhigilei, L. V.; Winograd, N.; Garrison, B. J. *J. Phys. Chem. A* **2001**, *105* (12), 2748–2755.
41. Gaffo, L.; Cordeiro, M. R.; Freitas, A. R.; Moreira, W. C.; Girotto, E. M.; Zucolotto, V. *J. Mater. Sci.* **2010**, *45* (5), 1366–1370.
42. *Materials Studio*; Accelrys, Inc.: San Diego, CA, 2010.
43. Nishiyama, Y.; Langan, P.; Chanzy, H. *J. Am. Chem. Soc* **2002**, *124* (31), 9074–9082.
44. Bolton, E. E.; Wang, Y.; Thiessen, P. A.; Bryant, S. H. *Annu. Rep. Comput. Chem.* **2008**, *4* (8), 217–241.
45. Hoover, W.; Posch, H.; Holian, B. L.; Gillan, M.; Mareschal, M.; Massobrio, C. *Mol. Simul.* **1987**, *1*, 79–86.
46. Berendsen, H. *Comput. Simul. Mater. Sci.* **1991**, *205*, 139.
47. Sun, H. *Macromolecules* **1995**, *28* (3), 701–712.
48. Pavel, D.; Lagowski, J. *Polymer* **2005**, *46* (18), 7528–7542.
49. Montanari, L.; Frigerio, F. S *J. Colloid Interface Sci.* **2010**.
50. Mazeau, K.; Rivet, A. *Biomacromolecules* **2008**, *9* (4), 1352–1354.
51. Cedeno, F. O.; Prieto, M. M.; Espina, A.; Garcia, J. R. *Thermochim. Acta* **2001**, *369* (1-2), 39–50.
52. Hollifield, H. C. *Food Packag. Interact.* **1991** (22-36).
53. Zimmermann, W. *J. Food Sci.* **1983**, *48* (3), 856–860.
54. Nishiyama, Y.; Johnson, G. P.; French, A. D.; Forsyth, V. T.; Langan, P. *Biomacromolecules* **2008**, *9* (11), 3133–3140.
55. Nada, A.; Hassan, M. L. *Polym. Degrad. Stab.* **2000**, *67* (1), 111–115.
56. Wada, M.; Hori, R.; Kim, U. J.; Sasaki, S. *Polym. Degrad. Stab.* **2010**, *95* (8), 1330–1334.
57. Chen, W.; Lickfield, G. C.; Yang, C. Q. *Polymer* **2004**, *45* (3), 1063–1071.
58. Jeffrey, G. A. *An Introduction to Hydrogen Bonding*; Oxford University Press: New York, 1997; Vol. 303.
59. Rich, M. R. *Biochim. Biophys. Acta, Mol. Cell Res.*, *1178* (1), 87–96.
60. Kaneko, F.; Yamazaki, K.; Kitagawa, K.; Kikyo, T.; Kobayashi, S. *J. Phys. Chem. B* **1997**, *101* (10), 1803–1809.
61. Murphy, M.; Hodgson, A. *J. Chem. Phys.* **1998**, *108*, 4199.
62. Haile, J. *Molecular Dynamics Simulation, Elementary Methods*; John Wiley & Sons: New York, 1992.
63. Shao, Y. H.; Li, Y.; Cao, X. L.; Shen, D. Z.; Ma, B. M.; Wang, H. Y. *Sci. China, Ser. B: Chem.* **2008**, *51* (10), 918–927.

Downloaded by COLUMBIA UNIV on August 28, 2012 | http://pubs.acs.org
Publication Date (Web): August 17, 2012 | doi: 10.1021/bk-2012-1107.ch010

Downloaded by STANFORD UNIV GREEN LIBR on August 28, 2012 | http://pubs.acs.org
Publication Date (Web): August 17, 2012 | doi: 10.1021/bk-2012-1107.ch011

Chapter 11

Highly Swellable Lignin Hydrogels: Novel Materials with Interesting Properties

Lars Passauer*

**Institute of Plant and Wood Chemistry, Technische Universitaet Dresden,
Pienner Str. 19, 01737 Tharandt, Germany
*E-mail: Passauer.Lars@ihd-dresden.de
Current affiliation: Institut für Holztechnologie Dresden gGmbH,
Zellescher Weg 24, 01217 Dresden, Germany**

Cross-linking of kraft and organosolv lignin with poly(ethylene glycol) diglycidyl ether in alkaline media was found to give water-swellable chemical networks with hydrogel character. In the present chapter, some general aspects on hydrogels and novel pathways to prepare lignin hydrogels and the corresponding xerogels are given. In order to characterize the materials obtained, selected analytical methods such as light, polarized light and scanning electron microscopy, swelling/shrinking and oscillation measurements, as well as FTIR ATR spectroscopy and phenolic OH group determination by selective aminolysis were applied.

Introduction

Properties of Hydrogels

Hydrogels are water absorbing polymeric materials with a wide range of application. When they come into contact with water or aqueous liquids, dry xerogel material which normally forms powders, granulates or beads, changes into a gel-like substance due to the liquid sorption. Besides surface adsorption, the swelling phenomenon is caused 1) by capillary pressure of the open porous structure of the cross-linked polymer network which induces the physical filling of the pores with water (*1*), and 2) by osmotic pressure which is the major driving force in the water absorption and swelling of gels. It is caused by differences in the chemical potential inside and outside of the absorbing polymer particles (*2*).

Downloaded by STANFORD UNIV GREEN LIBR on August 28, 2012 | http://pubs.acs.org
Publication Date (Web): August 17, 2012 | doi: 10.1021/bk-2012-1107.ch011

The extend and rate of absorption depend on the wettability, strongly influenced by hydrophobic vs. hydrophilic properties of the polymer, and furthermore on pore volume, pore length and radius, as well as external forces, such as gravitation and pressure load (*1*).

Hydrogels can be obtained from synthetic polymers (*3*) and biopolymers (*4–7*). They are synthesized by cross-linking of branched or unbranched polymer chains to a three-dimensional network (*4–7*) or by cross-linking polymerization which is simultaneously synthesizing polymer chains and cross-linking them (*3*). Hydrogel-forming polymers have hydrophilic properties and are normally water soluble. Due to cross-linking they become water-insoluble, but swell by solvent absorption (*2*).

In view of the swelling phenomenon of hydrogels, the contribution of the electrostatic interaction between water-swellable polymers to the equilibrium with the osmotic pressure has to be considered as an expansive pressure. This so-called polyelectrolyte effect is caused by ionic functional groups of the polymer (*2*). For example, gels with weakly acidic groups are deprotonated in alkaline media. Consequently, the density of negatively charged groups within the network strongly increases, connected with an increase of mobile counterions inside the gel, and phase transition due to electrostatic repulsion of polymer chains is induced. In acidic media, the acidic groups of the gel are protonated and both, charge density and concentration of mobile counterions within the hydrogel decrease, causing gel shrinking (*5*, *6*).

Hydrogel-Forming Polymers and Cross-Linking Procedures

Most of the commercial hydrogels featuring superabsorbent properties are based on acrylic acid. They are obtained by solution radical polymerization (*3*). Such cross-linked polyacrylates play an important role as absorbants in sanitary products and diapers. Other gel-forming polymers, such as poly(vinyl pyrrolidones) (*8*) and poly(vinyl alcohols) (*9–11*), are used in technical or biomedical applications. Since the late 1970s, besides polymerization, grafting of polymerizable ethylene-type monomers (e.g. acrylic acid, methacrylic acid, acrylamide, maleic anhydride) on to polysaccharides, such as starch or cellulose as graft base has been accomplished, yielding hydrogels with suberabsorbant properties (*12–14*). Synthetic superabsorbent polymers and hydrogels are also used in food packaging, in agriculture (*15*, *16*) or as so-called stimuli-responsive smart hydrogels which are applied as sensors, actuators and valves in microsystems technology (*2*).

In the last two decades, much efforts have been made in research and development of hydrogels based on biopolymers. Such biobased materials, which are an environmentally friendly alternative to synthetic hydrogels and superabsorbants, can be obtained by derivatization and chemical cross-linking of polysaccharides, such as cellulose (*17*), hemicelluloses (*18*), and starch (*4–6*, *19*, *20*) forming covalently bonded chemical networks after chemical modification. The swelling properties and rheological characteristics of such chemical networks can be controlled by adjusting the cross-linking density and the cross-linking agent employed (*4*). Such materials are preferably used

Downloaded by STANFORD UNIV GREEN LIBR on August 28, 2012 | http://pubs.acs.org
Publication Date (Web): August 17, 2012 | doi: 10.1021/bk-2012-1107.ch011

in biomedical applications (e.g. tissue engineering, ultrasonic contact gels) (*4*), pharmacy (drug delivery / carrier systems), food technology (thickening agents, stabilizer), and technical applications such as waste water treatment (*7*). Most swellable and stable gels can be obtained from carboxymethyl (*4*, *7*), hydroxypropyl (*21*) and phosphate derivatives (*5*, *6*, *19*) of cellulose and starch which can be cross-linked with diamines (*22*), dicarboxylic acids (*4*, *19*), diepoxides (*17*), or multifunctional sulfur compounds (*23*). Alternative approaches are thermal (*24*, *25*) or electron-beam induced cross-linking (*26*). Some of the polysaccharides such as carrageenans, alginates, and pectins which possess polyelecrolytic properties caused by carboxyl groups (polyuronides: alginates, low-methylated pectins) or sulphate groups (carrageenans) form thermo-irreversible ionotropic gels with divalent ions e.g. calcium (pectins, alginates, ι-carrageenans) (*27*, *28*). Cross-linking of ionotropic gels is realized by the formation of ionic bonds between carboxylate anions of the polysaccharide and corresponding multivalent counterions (*27*).

Lignin-Based Hydrogels

In comparison with the multiplicity of approaches dealing with polysaccharide-based hydrogels, the chemical modification of lignin - the most abundant biopolymer next to cellulose - for the preparation of hydrogels is less widely used. This is due to the hydrophobic nature and the complex and heterogeneous structure which make a chemical utilization of lignin difficult. Nevertheless, in the last three decades few attempts have been made to modify technical lignins in order to obtain water-swellable lignin-based materials. Just as other polymers used for gel synthesis, preparation of lignin hydrogels requires a certain degree of chemical modification and cross-linking. Some authors report chemical cross-linking of kraft lignin, water-soluble lignosulfonates, or chemically modified lignin e.g. hydroxypropyl lignin (*29*) with formaldehyde (*30*, *31*), glutaraldehyde (*32*), α–epichlorhydrin (*33–35*), or diepoxy compounds (*29*). Other approaches deal with the copolymerization of lignin with poly(acrylamide) and poly(vinyl alcohol) (*36*). All materials obtained had comparatively low water swelling capacities $< 10\ g_{H2O}\ g_{gel}^{-1}$ (*33–35*). Some of them are reported to be potentially used as encapsulating materials for slow release of bioactive compounds or fertilizers in agricultural applications (*30*).

Besides Lindström′s approach which described cross-linking of milled wood (*33*) and kraft lignin (*34*, *35*) with epichlohydrin, a promising work concerning lignin-based hydrogels was communicated by Nishida et al. (*37*, *38*) who reported chemical cross-linking of birch hydrolysis lignin (BHL) with poly(ethylene) glycol diglycidyl ether (PEGDGE). The BHL-PEGDGE gels obtained had comparatively low water swelling capacities ($8.5\ g_{H2O}\ g_{gel}^{-1}$) which was found to be temperature dependend and strongly influenced by cross-linking density and the average number of ethylene oxide groups of PEGDGE used. Interestingly, the gels were reported to be swellable in aqueous EtOH with a maximum swelling ($14.5\ g_{aq.EtOH}\ g_{gel}^{-1}$) at a concentration of 50% EtOH(v/v).

Following Nishida′s approach, Passauer et al. (*39–43*) investigated strongly water absorbing lignin hydrogels with significantly increased free swelling capacities up to 75 g_{H2O} g_{gel}^{-1}which were obtained by cross-linking of different either unmodified or oxidatively pre-activated technical lignins with PEGDGE. Such lignin hydrogels could be potentially used as water storing soil conditioners which not only enhance the soil water retention but also could contribute to soil fertility as natural source of soil humic substances (*42*). In the following, some novel and fundamental results concerning the preparation and characterization of such oligo(oxyethylene)-lignin hydrogels and the corresponding xerogel counterparts - the latter were obtained by different drying techniques - are summarized.

Downloaded by STANFORD UNIV GREEN LIBR on August 28, 2012 | http://pubs.acs.org
Publication Date (Web): August 17, 2012 | doi: 10.1021/bk-2012-1107.ch011

Materials and Methods

Preparation of Lignin Hydrogels

Materials Pine kraft lignin Indulin AT (IND, MeadWestvaco, Charleston, USA). Spruce organocell lignin, in the following referred to as organosolv (OS) lignin (organocell pulping: MeOH/ NaOH/ anthraquinone [AQ]), lignin precipitated with sulfuric acid at pH 4; former Organocell GmbH Munich, pilot plant Munich – Pasing, Germany). H_2O_2 (Merck, Darmstadt, Germany). Poly(ethylene) glycol diglycidyl ether (MW~526 g mol^{-1}; Sigma Aldrich, Steinheim, Germany).

Oxidation of OS lignin was accomplished with hydrogen peroxide in alkaline media as described in (*39*, *42*): 5 g of lignin was dissolved in 8 ml of 3.3 M aqueous NaOH solution at ambient temperature. After 24 h of stirring, 1 ml aqueous hydrogen peroxide (5 %, v/v) was added drop-wise and the reaction mixture was stirred for another 24 h at r.t.

IND was pre-activated by Fenton-oxidation (*39*, *42*). For this, 5 g of lignin was suspended in 10 ml of de-ionized water. After 30 min stirring, 0.11 mmol of $FeCl_2·4H_2O$ g_{lig}^{-1} was added and the suspension was stirred for another 30 min. 1 ml of aqueous hydrogen peroxide (5 %, v/v) was subsequently added dropwise. The suspension was stirred for 24 h at r.t. and was air-dried at r.t. Pre-activated lignins are indicated as OSox and INDox, respectively.

Cross-linking of unmodified lignins and oxidized OS lignin was performed with PEGDGE (see below) according to Nishida et al. (*37*, *38*) as described in (*39*, *42*). Briefly, 5 g of unmodified or Fenton-oxidized IND was dissolved either in 8 ml (OS lignin) or 10 ml of 3.3 M aqueous sodium hydroxide solution (IND, INDox). After 24 h of vigorous stirring at r.t., 0.5 mmol of PEGDGE g_{lig}^{-1} were added drop-wise until the viscosity was drastically increased by gel formation. H_2O_2-oxidized OS was cross-linked by adding the same amount of PEGDGE immediately after oxidative treatment. The resulting gels were thoroughly washed and neutralized with de-ionized water. Xerogels were obtained by different drying techniques.

Preparation of lignin xerogels was conducted as decribed in (*39*): *Air drying* of hydrogel granules was conducted at 80°C in a drying chamber UM-300 (Memmert, Schwabach, Germany). For *film formation*, swollen gel samples were coated on microscope slides and were air-dried either at r.t., 50°C, or 80°C.

Lyophilization was performed in a self-built system (high vacuum pump Edwards E2M5, Doucaster, UK; cooling trap Bachofer, Reutlingen, Germany; dessicator) at ambient temperature and 4 Pa after freezing swollen hydrogel samples at 253 K in a freezer.

Critical point drying (CPD) of swollen gel samples was carried out with a POLARON E3000 critical point dryer (POLARON Equipment Ltd, Watford, UK). For dehydration of swollen samples, EtOH and acetone were used as intermediate fluids and supercritical carbon dioxide ($scCO_2$) as transitional fluid (T_{crit} = 31°C, P_{crit} = 7.39 MPa).

Material Characterization

Light microscopic (LMi) images of swollen hydrogel and dried xerogel particles were recorded with a reflected-light stereoscopic zoom microscope (RLMi) Nikon SMZ-U (Nikon Corp., Tokyo, Japan) connected with a TSO digital CMOS microscope camera (Thalheim-Spezial-Optik, Pulsnitz, Germany) and a transmitted-light microscope (TLMi) Jenamed variant (Carl Zeiss, Jena, Germany).

Polarized light microscopy (PolMi) of OS-PEGDGE-films and xerogels was performed with a Zeiss AXIOPLAN microscope (Carl Zeiss, Göttingen, Germany) connected with a Zeiss digital camera AXIOSAM MRc5 (Carl Zeiss MicroImaging, Göttingen, Germany).

Scanning electron microscopic (SEM) images of the surface of xerogel samples were obtained with a scanning electron microscope unit JEOL T330A (JEOL Ltd., Tokyo, Japan), operating at 15 kV acceleration voltage. For SEM analysis, dried xerogel samples were double-coated by vaporizing their surface with a 40 nm carbon layer under high vacuum (vaporizing unit Emitech K950 carbon coater, Emitech Ltd., Ashford, UK) and finally sputter-coating with a 30 nm gold layer (ion sputter Jeol JFC 1100E, Jeol Ltd., Tokyo, Japan).

Free (re-)swelling capacity (FSC_{aq}, $FReSC_{aq}$; [$g_{H2O}\ g_{gel}^{-1}$]) values of lignin hydrogels were calculated according to Equation 1 from the amount of de-ionized water (aq) a certain amount of the dry gel granulate (m_{XG}; XG: xerogel) can absorb and retain against gravitation in fully swollen state (m_{HG}; HG: hydrogel):

$$F(\mathrm{Re})SC_{aq} = \frac{m_{HG} - m_{XG}}{m_{XG}} \qquad \text{(eq. 1)}$$

m_{XG} corresponds to the solid content of the swollen hydrogel which was determined after drying the swollen gels at 105°C.

Cyclic swelling/ shrinking and associated determination of $FReSC_{aq}$ were conducted by fivefold repeating of swelling/ shrinking procedures. For this, swollen gels were initially air-dried at 80°C in a drying chamber until constant weight was reached and then re-swollen with de-ionized water. $FReSC_{aq}$ values were determined just as FSC_{aq} gravimetrically.

Rheology: Dynamic measurements were carried out at 20°C with an oscillation rheometer ARES (TA Instruments; Newcastle, DE, USA) using the plate-plate geometry (Ø 25 mm). In order to determine the linear viscoelastic

Downloaded by STANFORD UNIV GREEN LIBR on August 28, 2012 | http://pubs.acs.org
Publication Date (Web): August 17, 2012 | doi: 10.1021/bk-2012-1107.ch011

region, strain sweep tests were conducted in a range from $\gamma = 0.01$-1. Frequency sweeps were measured in a range from $\omega = 0.1$-100 rad s^{-1}. For the measurements partially (water content 50 % of FSC_{aq}) and fully swollen hydrogel samples from alkaline granulates (particle size 50 µm – 1,000 µm) were used.

Chemical Characterization of Parent and PEGDGE-Modified Lignin

Determination of phenolic OH groups: Acetylation of parent and PEGDGE-modified lignins was accomplished according to (*44*) (Scheme 1a). *Phenolic OH groups* of lignins were determined by selective aminolysis of peracetylated lignin samples with pyrrolidine and quantification of the resulting 1-acetylpyrrolidine by gas chromatography (*45*) see Scheme 1b; internal standard: propionylpyrrolidine, synthesized according to (*46*). GC conditions: GC/ FID autosystem Perkin-Elmer; column: Roticap®-5 MS (0.25 µm x 30 m x 0.25 mm); carrier gas: He (2 ml min^{-1}); combustion gases: H_2 (30 ml min^{-1}), synthetic air (310 ml min^{-1}), temperature program 160°C, 4 min; injector temperature: 230°C, detector temperature 250°C; software: TotalChrom Workstation 6.3.1 (Perkin-Elmer, Waltham, MA, USA).

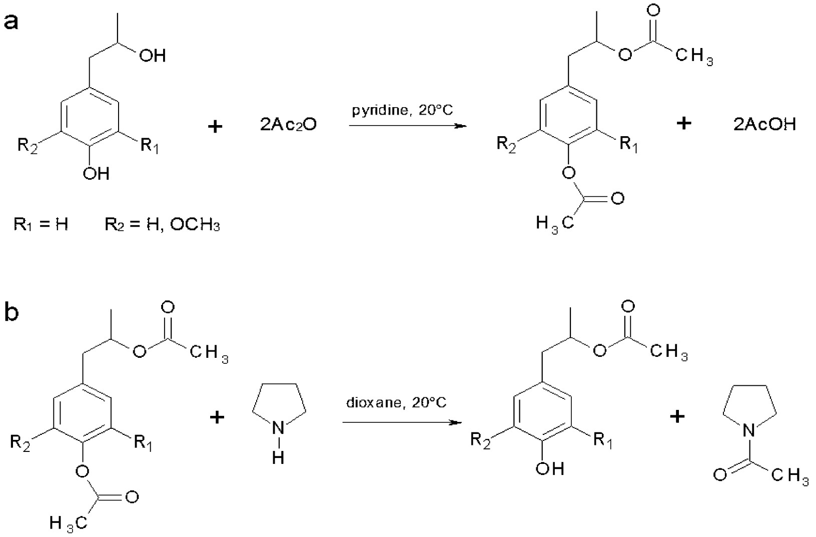

Scheme 1. (a) Acetylation of lignin structures with acetic anhydride in pyridine and (b) aminolysis of phenylacetates with pyrrolidine in dioxane with formation of 1-acetylpyrrolidine (45).

FTIR ATR spectroscopy: FTIR ATR spectra of parent and PEGDGE-cross-linked lignin samples as well as corresponding acetylated counterparts were recorded with a Thermo Scientific Nicolet iS5 MIR FT IR spectrometer (Thermo Fischer Scientific Inc., Waltham, MA, USA) equipped with a deuterated triglycin sulphate (dTGS) detector using the ATR accessory id5. The spectra were measured in a spectral range from 4,000 to 500 cm^{-1} and at a spectral resolution

Downloaded by STANFORD UNIV GREEN LIBR on August 28, 2012 | http://pubs.acs.org
Publication Date (Web): August 17, 2012 | doi: 10.1021/bk-2012-1107.ch011

of 4 cm^{-1}. For each spectrum, 32 scans were added. Base-line correction and vector-normalization of spectra was carried out using the OPUS software version 6 (Bruker Instruments, Billerica, MA, USA).

Results and Discussion

Morphology and Swelling Properties

Cross-linking of both parent and oxidatively modified IND as well as OS lignin with PEGDGE were found to afford hydrogels that have typical gel morphology (Figures 1a and b).

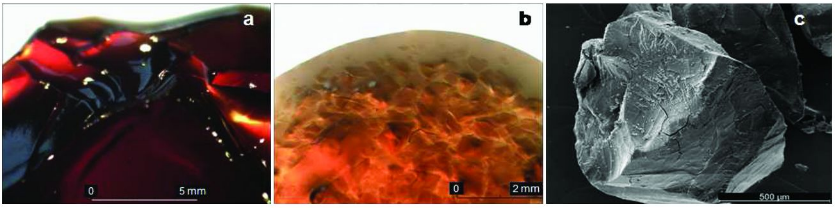

Figure 1. Light-microscopic images from swollen OSox-PEGDGE hydrogel particles: (a) never-dried gel bloc, (b) re-swollen gel granulate, (c) SEM-micrograph of an alkaline OSox-PEGDGE gel granulate after air-drying at 80°C.

In comparison with hydrogels based on epichlorhydrin-cross-linked kraft and milled wood lignin ((*33–35*); $FSC_{aq} < 10\ g_{H2O}\ g_{gel}^{-1}$), PEGDGE-cross-linked birch hydrolysis lignin ((*37*, *38*); BHL-PEGDGE; $FSC_{aq} = 8.5\ g_{H2O}\ g_{gel}^{-1}$) or pine kraft lignin Indulin AT ((*39*, *40*, *42*); IND-PEGDGE; $FSC_{aq} = 8.0\ g_{H2O}\ g_{gel}^{-1}$), cross-linking of unmodified OS lignin yielded hydrogels with strongly increased FSC_{aq} values up to 27.4 $g_{H2O}\ g_{gel}^{-1}$ (Figure 2). Hence, despite a similar functionality of kraft and OS lignin (*47*), cross-link ability with PEGDGE and swelling properties of the corresponding PEGDGE-cross-linked products strongly differ. This is supposed to be caused by different polymeric properties of the lignins used. For instance, spruce OS lignin possesses a significantly diminished average molecular weight ((*47*); $M_{w\ OS} = 2.25\ 10^3\ g\ mol^{-1}$) and polydispersity ($M_w/M_{n\ OS} = 3.75$; (*47*)) compared with kraft lignin Indulin AT ((*48*); $M_{w\ IND} = 19.8\ 10^3\ g\ mol^{-1}$, $M_w/M_{n\ IND} = 9.0$, $M_w/M_{n\ OS} = 3.75$). In that context it was observed that OS lignin was much better soluble in aq. NaOH than IND and, therefore, one may assume that OS lignin is more accessible for the etherification with PEGDGE than Indulin AT.

Oxidation of OS lignin with aq. H_2O_2 in alkaline medium and subsequent cross-linking with PEGDGE further promoted the gel formation and enhanced the FSC_{aq} values significantly up to 72.5 $g_{H2O}\ g_{gel}^{-1}$ compared with their non-activated counterpart that reached values up to 27.4 $g_{H2O}\ g_{gel}^{-1}$ (Figure 2).

Downloaded by STANFORD UNIV GREEN LIBR on August 28, 2012 | http://pubs.acs.org
Publication Date (Web): August 17, 2012 | doi: 10.1021/bk-2012-1107.ch011

Downloaded by STANFORD UNIV GREEN LIBR on August 28, 2012 | http://pubs.acs.org
Publication Date (Web): August 17, 2012 | doi: 10.1021/bk-2012-1107.ch011

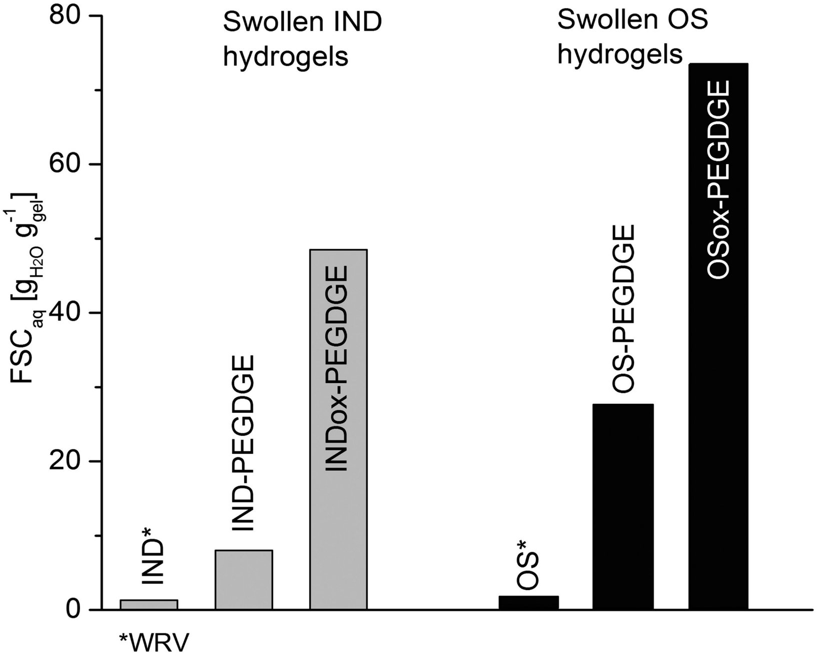

Figure 2. Water retention capacity (WRC) of Indulin AT (IND) and organosolv lignin (OS) and FSC_{aq} values of PEGDGE-cross-linked unmodified and pre-oxidized (ox) lignins.

This should be due to the oxidatively induced structural changes of lignin, e.g. hydroxylation of aromatic rings and the formation of secondary hydroxyl groups in the side chain and was verified for oxidized Indulin AT which was modified in terms of a Fenton-type pre-oxidation step (*43*). The corresponding PEGDGE-cross-linked hydrogels (INDox-PEGDGE) possessed significantly increased FSC values compared with gels from non-pre-activated Indulin AT (IND-PEGDGE) ((*42*); Figure 2). Thus, in terms of cross-linking lignin with PEGDGE and the properties of the resulting hydrogels, both phenolic and aliphatic OH groups play a key role.

The improved swelling ability of PEGDGE-modified lignins compared with alternative types of lignin hydrogels, e.g. gels cross-linked with epichlorhydrin (*33–35*), is mainly caused chemically by 1) the hydrophilicity of the ether oxygen of oligo(oxyethylene) (OOE) substituents which were introduced by PEGDGE-mediated cross-linking of lignin, 2) the formation of new secondary hydroxyl groups which are formed during the oxirane ring opening of PEGDGE (Scheme 2) and 3) physically by the microstructure of PEGDGE-modified lignin which is much more loosened and porous (Figures 3b, c) than those of parent lignin (Figure 3a). The latter form aggregates with dimensions in the range from 10 - 50 µm (Figure 3a). These lignin aggregates are composed of spherical particles with diameters < 600 nm due to self-association of lignin fragments acting as

Downloaded by STANFORD UNIV GREEN LIBR on August 28, 2012 | http://pubs.acs.org
Publication Date (Web): August 17, 2012 | doi: 10.1021/bk-2012-1107.ch011

colloidal seed points in alkaline lignin solutions and grow in number and size during precipitation of lignin from spent liquor (*49*). In contrast, SEM images of OS-PEGDGE xerogel which was obtained after CPD of the swollen gel, reveal a nanoscaled (particle Ø 50 - 100 nm), loosened and porous fractal cluster structure (*49*) which strongly promotes water absorption and swelling of the material.

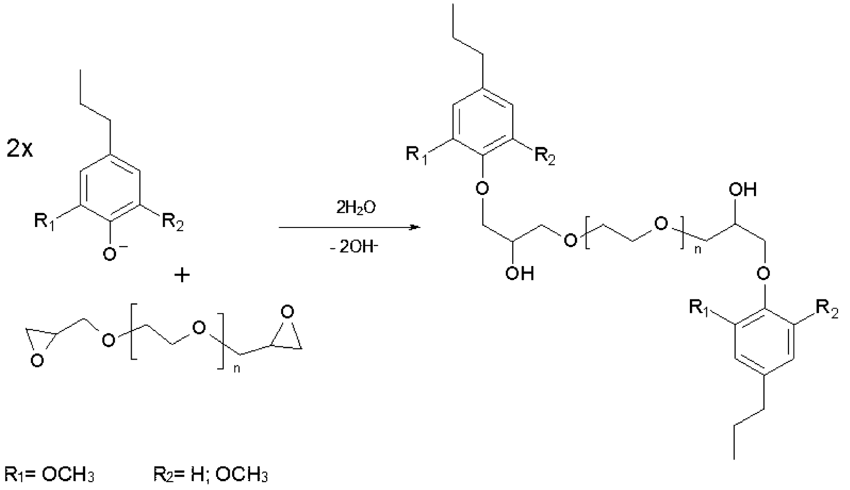

Scheme 2. Proposed reaction scheme of PEGDGE-mediated cross-linking of phenolic lignin substructures under alkaline conditions.

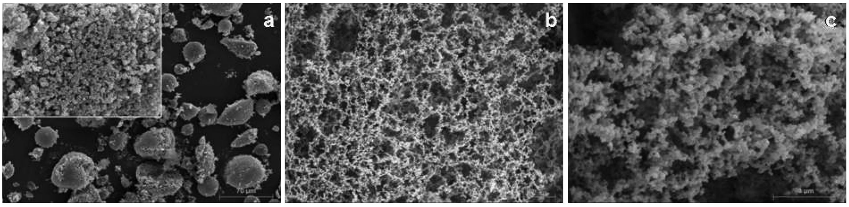

Figure 3. SEM micrographs of (a) parent OS lignin and OS-PEGDGE hydrogel after CPD (b, c).

As is shown in Figure 4, both lyophilized OSox-PEGDGE xerogels and samples which were air-dried under comparatively harsh conditions (80°C) are, nevertheless, well re-swellable in water (swelling/ shrinking cycle 1) and possess $FReSC_{aq}$ values of 43.3 $g_{H2O}\ g_{gel}^{-1}$ and 38.4 $g_{H2O}\ g_{gel}^{-1}$, respectively. The corresponding alkaline granulate which was obtained by air-drying of the alkaline gel bloc at 80°C possesses a drastically decreased absorption capacity $< 20\ g_{H2O}\ g_{gel}^{-1}$ which could be indicative of 1) a thermal post-cross-linking reaction between PEGDGE and lignin substructures which causes a increased cross-linking density which lowers the swelling ability, 2) a collapse of the porous structure of the material due to the drying procedure, and 3) intermolecular interactions between adjacent OOE substituents. The morphology of such an alkaline gel granule is shown in Figure 1c.

Downloaded by STANFORD UNIV GREEN LIBR on August 28, 2012 | http://pubs.acs.org
Publication Date (Web): August 17, 2012 | doi: 10.1021/bk-2012-1107.ch011

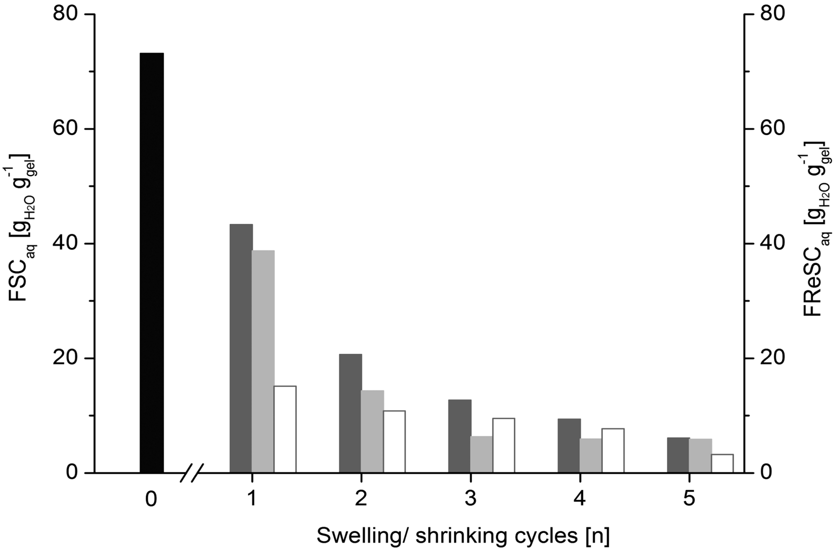

Figure 4. FSC value of a never-dried OSox-PEGDGE hydrogel (black bar) and FReSC values of the corresponding lyophilized (dark gray bar) and air-dried xerogel (light gray bar) as well as alkaline xerogel granulate (white bar). Air-drying of swollen/ re-swollen hydrogels was conducted at 80°C.

Cyclic swelling/ shrinking measurements reveal decreasing $FReSC_{aq}$ values (Figure 4) for each lyophilized and air-dried xerogels as well as alkaline gel granulate. In comparison with the never-dried OSox-PEGDGE hydrogel which absorbs 72.5 g_{H2O} g_{gel}^{-1}, $FReSC_{aq}$ values of both lyophilized and air-dried xerogel were almost halved after the 1st (43.3 vs. 38.74 g_{H2O} g_{gel}^{-1}), 2nd (20.68 vs. 14.32 g_{H2O} g_{gel}^{-1}) and 3rd (12.70 vs. 6.32 g_{H2O} g_{gel}^{-1}) swelling/ shrinking cycle and converge against 6.0 g_{H2O} g_{gel}^{-1} after the 5th re-swelling. The water absorption of the alkaline xerogel counterpart is much lower after the 1st re-swelling (15.15 g_{H2O} g_{gel}^{-1}) and possesses only 3.22 g_{H2O} g_{gel}^{-1} after the 5th swelling/ shrinking cycle, which is probably caused again by 1) thermal post-cross-linking of lignin with PEGDGE during air-drying of the alkaline gel bloc at 80 °C, and 2) a collapse of the microporous structure due to the drying procedure (Figure 1c). In contrast, lyophilization seems to be the gentlest method to convert lignin hydrogels into re-swellable xerogel structures (Figure 5).

Air-drying of lignin gels which were coated on microscope slides at ambient and elevated temperatures (50, 80°C) effects the formation of glassy and brittle films which are hardly or not at all re-swellable in water (*41*). The reasons suggested for the swelling inhibition of air-dried OS(ox)-PEGDGE xerogels and films are 1) the local collapse of microporous structures, 2) the formation of lamellar, semicrystalline structures and 3) association complexes between introduced OOE substituents, both caused by the formation of hydrogen bonds between OOE substituents (*50*). Chatterjee and Sethi (*51*) reported the formation

Downloaded by STANFORD UNIV GREEN LIBR on August 28, 2012 | http://pubs.acs.org
Publication Date (Web): August 17, 2012 | doi: 10.1021/bk-2012-1107.ch011

of interpolymer association complexes between OOE and polyphenolic structures which could contribute to swelling inhibition of lignin-based xerogels.

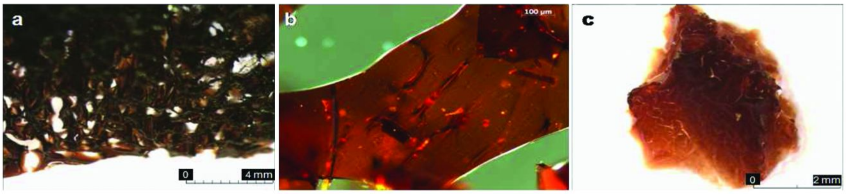

Figure 5. OS-PEGDGE xerogel after lyophilization; (a) light-microscopic image, (b) polarized-light-microscopic image. (c) Hydrogel particle after re-swelling in de-ionized water.

Examination of lignin gel films with different light-microscopic techniques points to the formation of such highly ordered semicrystalline structures: Between cross-polarizers, lamellar and banded interference patterns along drying cracks (bright reflexes) which are concentrically arranged around amorphous parts (dark regions) are visible (Figures 6b and c). Such lamellar and banded structures were also observed with transmission light-microscopy (Figure 6a). In contrast to air-dried films, lyophilized xerogels possess only minor proportions of such banded interference patterns between cross-polarizers (Figure 5b) indicating an amorphous structure and diminished interactions between OOE substituents and phenolic substructures of lignin.

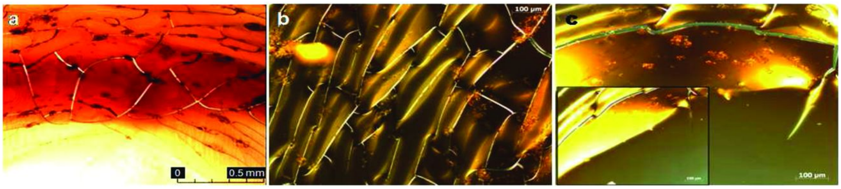

Figure 6. OS-PEGDGE xerogel film after air-drying at 50°C; (a) light-microscopic image, (b) under polarized light and (c) under polarized light (after air-drying at 80°C).

Mechanical Properties

A dynamic oscillatory measurement is the most suitable method for describing polymer networks and allows a calculation of the viscous and elastic properties of the materials investigated (*52*). The variation of the rheological parameters determined, i.e. the storage modulus G′, the loss modulus G′′, the loss factor tan δ (ratio G′′/G′), and the dynamic viscosity η* with the frequency of oscillation, provides a mechanical spectrum which is typical for each diluted polymer solution, concentrated polymer solution, and strong gel (*53*). Exemplarily, two rheo-mechanical spectra of G′, G′′, tan δ and η* for a OSox-PEGDGE hydrogel are shown in Figure 7.

Downloaded by STANFORD UNIV GREEN LIBR on August 28, 2012 | http://pubs.acs.org
Publication Date (Web): August 17, 2012 | doi: 10.1021/bk-2012-1107.ch011

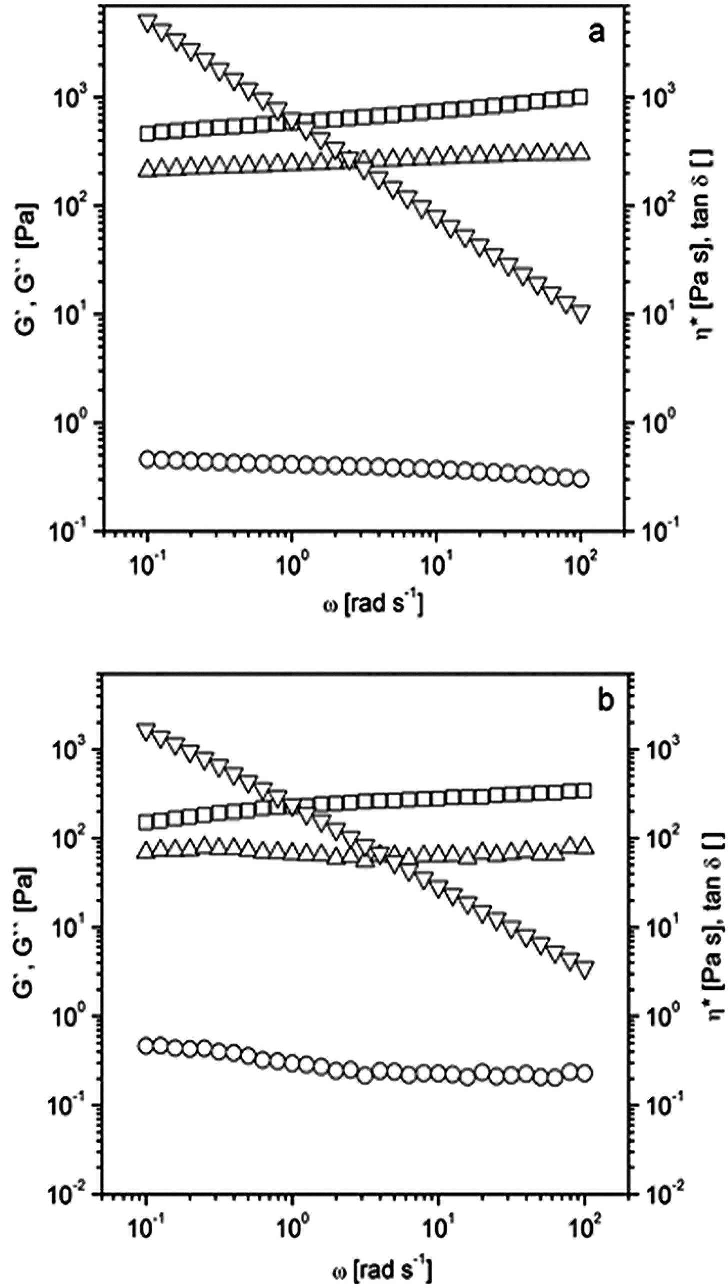

Figure 7. Dynamic viscosity η, storage (G') and loss modulus (G''), and loss factor tan δ of an OSox-PEGDGE hydrogel in (a) partially (50% FSC$_{aq}$) and (b) fully swollen state (100% FSC$_{aq}$).*

Downloaded by STANFORD UNIV GREEN LIBR on August 28, 2012 | http://pubs.acs.org
Publication Date (Web): August 17, 2012 | doi: 10.1021/bk-2012-1107.ch011

For η*, a linear decrease of about three orders of magnitude within the measured frequency range (0.08-100 rad s^{-1}) was observed for both the partially (Figure 7a) and the fully swollen sample (Figure 7b), revealing the typical rheological behavior of a polymer network and hydrogel structure, respectively (*4*, *52*, *53*). Both, G′ and G′′ slightly increase linearly, and G′ was half an order of magnitude higher than G′′. This shows that with increasing shear frequency more energy is dissipated (viscous part) and stored (elastic part). Such a behavior is also typical for cross-linked gel structures which possess a dominating elastic component (*52*, *53*), and it indicates a certain mechanical sturdiness of the materials. This is supported by the loss factor tan δ. At tan δ < 1.0, G′ is the dominating material function which is of particular importance concerning different potential applications of lignin hydrogels, e.g. as water storing material for soil improvement (*42*, *54*) which requires an enhanced resistance of the gel material to compressive and shear forces occurring in soil, particularly by soil cultivation. In further investigations it was shown that the rheological material functions could be adjusted by different amounts of PEGDGE and it was pointed out that swelling in terms of FSC_{aq} and hydrogel′s stiffness are opposing parameters (*42*).

Chemical Structure of PEGDGE-Modified Lignins

A comparison of the FTIR ATR spectra of OS lignin (Figure 8a) with the cross-linked counterpart (Figure 8b) clearly reveals differences in the frequency range 3.000-2.800 cm^{-1} and the finger print region 1.750-750 cm^{-1} of the spectra, which is the result of the cross-linking reaction of lignin with PEGDGE.

The unmodified spruce OS lignin shows typical and intense signals which are related to aromatic skeletal vibrations (1.595 cm^{-1}), aromatic skeletal vibrations of non-conjugated guajacyl units (1.510 cm^{-1}), aromatic in-plane C-H deformation vibrations (1.030 cm^{-1}), and aromatic C-H out-of-plane deformation vibrations in 2,6-positions (855 cm^{-1}; syringyl units) and in 2,5,6-positions (815cm^{-1}; guajacyl units). Signals at 1.463 and 1.452cm^{-1} are related to δ_{as}(C-H) in methyl and methylene groups of the lignin side chain and methoxy groups, respectively (*55*, *56*).

The appearance of very intense bands at 1.125 and 1.085 cm^{-1} which were assigned to υ(C-O-C) and δ(C-O) clearly indicates the introduction of OOE groups ($-CH_2-CH_2-O-$) due to the cross-linking reaction of OS lignin with PEGDGE (Figure 8b). This is supported by the increased intensity of the bands at 2.930, 2.870, and 2.835 cm^{-1} which are related to υ_{as}(C-H) and υ_{s}(C-H) in methylene groups of OOE. The decreased intensities of the signals at 1.510 and 815cm^{-1} which are typical for guajacyl units (*55*, *56*) would be indicative of cross-linking by the etherification of phenolic OH groups of guajacyl units - which dominate in conifer lignins - with PEGDGE. Secondary OH groups which are formed due to the ring-opening of the epoxide groups of PEGDGE (Scheme 2) were verified by the band at 1.085 cm^{-1} which is not only related to δ(C-O) of OOE but also to secondary alcohols (*57*). Because both signals overlap, the contribution of each is hard to evaluate.

Downloaded by STANFORD UNIV GREEN LIBR on August 28, 2012 | http://pubs.acs.org
Publication Date (Web): August 17, 2012 | doi: 10.1021/bk-2012-1107.ch011

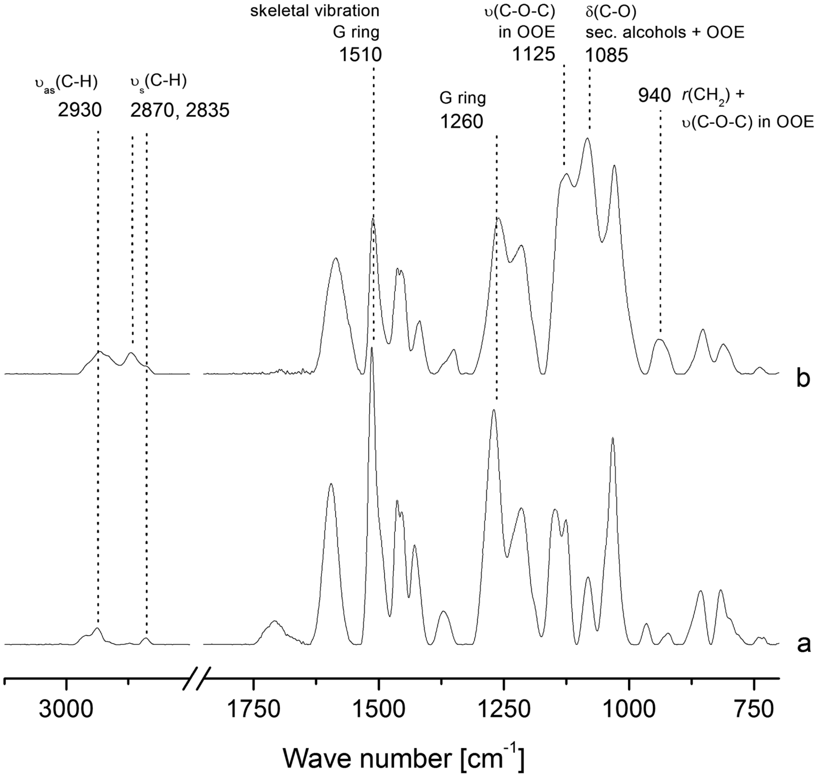

Figure 8. FTIR ATR spectra of (a) OS lignin and (b) OSox-PEGDGE lignin; G: guajacyl, OOE: oligo(oxyethylene) substituent.

The FTIR ATR spectra of the acetylated counterparts allow a more detailed consideration of the structural differences between OS lignin (Figure 9a) and the PEGDGE-modified sample (Figure 9b).

It is clearly visible that the intensities of the very strong bands at 1.765 and 1.740 cm^{-1} which are related to υ(C=O) of phenolic (OAc_{phen}) and aliphatic acetates (OAc_{aliph}) (*58*, *59*) changed after PEGDGE-cross-linking of lignin. Both, the decreasing intensity of υ(C=O) of OAc_{phen} at 1.765 cm^{-1} and the increasing strength of υ(C=O) of OAc_{aliph} at 1.740 cm^{-1} after PEGDGE-modification of lignin are indicative of the etherification of phenolic OH groups with PEGDGE and the formation of new secondary OH groups due to the ring-opening of the epoxide groups of PEGDGE (Scheme 2). This is supported by wet-chemically determined values of OH_{phen} which amounts to 5.96 % for parent OS lignin and 2.4-2.8 % for lignin counterparts cross-linked with 0.5 mmol PEGDGE g_{lig}^{-1}. Hence, 55-60 % of OH_{phen} were etherified in the course of cross-linking OS lignin with PEGDGE under the selected reaction conditions. A correlation between wet-chemically determined OH group contents of PEGDGE-modified lignins based on acetylated samples with FTIR spectroscopic data, which is extensively described for technical lignins (*58–60*), is the subject of current investigations.

Downloaded by STANFORD UNIV GREEN LIBR on August 28, 2012 | http://pubs.acs.org
Publication Date (Web): August 17, 2012 | doi: 10.1021/bk-2012-1107.ch011

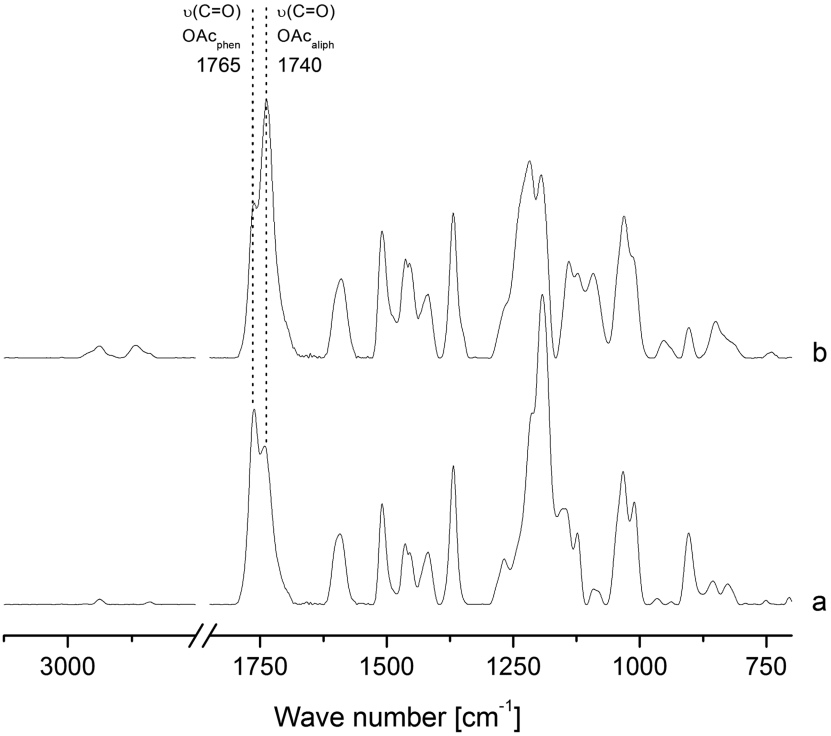

Figure 9. FTIR ATR spectra of per-acetylated samples of (a) OS lignin and (b) OSox-PEGDGE lignin.

Conclusions

Simultaneous derivatization and chemical cross-linking of pine kraft and spruce organosolv lignin with PEGDGE was shown to be a suitable means of preparing water-swellable and mechanically stable lignin hydrogels featuring rheological properties of typical polymer networks. Hydrogels have been usually obtained by polymerization of hydrophilic acryl derivatives (e.g. acrylic acid or acryl amide) or subsequent cross-linking of water-soluble or at least hydrophilic polymers. The present method describes an unconventional pathway to obtain swellable materials with hydrogel character from hydrophobic kraft or organosolv lignin. FTIR ATR spectroscopic investigations and selective aminolysis of peracetylated lignin and PEGDGE-modified samples pointed out that the cross-linking reaction mainly occurred by an etherification reaction between the phenolic OH groups of lignin and PEGDGE. It was shown that the resulting oligo(oxyethylene) lignin hydrogels which absorb more than 70 g_{H2O} g_{gel}^{-1} (FSC_{aq}) are well re-swellable in water after converting them into the xerogel form reaching $FReSC_{aq}$ values < 40 g_{H2O} g_{gel}^{-1}. Several repetitions of swelling/ shrinking cycles revealed a successive diminishment of $FReSC_{aq}$ values of each air-dried, lyophilized and alkaline xerogels. Microscopic investigations suggest that this phenomenon is most likely caused by the local collapse of microporous structures and morphological changes, which occurred during the dehydration of the lignin hydrogels and which are assumed to be mainly induced by the formation of hydrogen bonds between OOE substituents as well as between OOE substituents and phenolic substructures of lignin.

Acknowledgments

The author would like to thank M. Struch (TU Dresden) for the preparation of selected gel samples, N. Herold (University of Applied Science, Eberswalde, Germany) for conducting FTIR ATR spectroscopy measurements, and J. Appelt (TU Dresden) for supporting GC measurements and the synthesis of propionylpyrrolidine. E. Bäucker (TU Dresden) is acknowledged for conducting SEM analyses, B. Günther (TU Dresden) for recording light-microscopic images, Prof. H. Siedel (TU Dresden) and Dr. F. Haubrich (formerly TU Dresden) for conducting polarization microscopy measurements, and Dr. D. Jaros (TU Dresden) for supporting oscillatory measurements. Finally, I would like to express my cordial thanks to Prof. K. Fischer (TU Dresden) who initiated the research activities on lignin hydrogels and to Ass.Prof. F. Liebner (BOKU, Vienna, Austria) for his continued support and encouragement.

Downloaded by STANFORD UNIV GREEN LIBR on August 28, 2012 | http://pubs.acs.org
Publication Date (Web): August 17, 2012 | doi: 10.1021/bk-2012-1107.ch011

References

1. Frank, M. Superabsorbants. In *Ullmanns's Encyclopedia of Industrial Chemistry*; Wiley-VCH: Weinheim, Germany, 2005.
2. Richter, A.; Paschew, G.; Klatt, S.; Lienig, J.; Arndt, K.-F.; Adler, H.-J. P. *Sensors* **2008**, 561–581.
3. Brandt, K.; Goldman, S.; Inglin, T. U.S. Patent 32,649, 1988.
4. Seidel, C.; Kulicke, W.-M.; Heß, C.; Hartmann, B.; Lechner, W.; Lazik, W. *Starch* **2004**, *56*, 157–166.
5. Kulicke, W. M.; Aggour, Y. A.; Nottelmann, H.; Elsabee, M. Z. *Starch* **1989**, *41*, 140–146.
6. Kulicke, W.-M.; Aggour, Y. A.; Elsbee, M. Z. *Starch* **1990**, *42*, 134–141.
7. Chang, C.; Zhang, L. *Carbohydr. Polym.* **2011**, *84*, 40–53.
8. Chen, J.; Park, H.; Park, K. *J. Biomed. Mater. Res.* **1999**, *44*, 53–62.
9. Arndt, K.-F.; Richter, A.; Ludwig, S.; Zimmermann, J.; Kressler, J.; Kuckling, D.; Adler, H.-J. *Acta Polym.* **1999**, *50*, 383–390.
10. Paradossi, G.; Cavalieri, F.; Chiessi, E.; Ponassi, V.; Martorana, V. *Biomacromol.* **2002**, *3*, 1255–1262.
11. Purss, H. K.; Caulfield, M. J.; Solomon, D. H.; Sommer-Knudsen, J. *Electrophoresis* **2003**, *24*, 12–19.
12. Mashuda, F.; Nishida, K.; Nakamura, A. U.S. Patent 4,076,663, 1976.
13. Athawale, V. D.; Vidyagauri, M. *Starch* **1998**, *50*, 421–426.
14. Zhang, J.; Li, A.; Wang, A. *Carbohydr. Polym.* **2006**, *65*, 150–158.
15. Johnson, M. S. *J. Sci. Food Agric.* **1984**, *35*, 1063–1066.
16. Johnson, M. S.; Leah, R. T. *J. Sci. Agric. Food Chem.* **1990**, *52*, 431–434.

17. Marsano, E.; Bianchi, E.; Sciutto, L. *Polymer* **2003**, *44*, 6835–6842.
18. Söderquist Lindlbad, M.; Albertson, A.-C.; Ranucci, E.; Laus, M.; Giani, E. *Biomacromolecules* **2005**, *6*, 684–690.
19. Passauer, L.; Liebner, F.; Fischer, K. *Starch* **2009**, *61*, 621–627.
20. Passauer, L.; Liebner, F.; Fischer, K. *Starch* **2009**, *61*, 628–633.
21. Wach, R. A.; Mitomo, H.; Yoshii, F.; Kume, T. *Macromol. Mater. Eng.* **2002**, *287*, 285–295.
22. Magnani, R.; Rappuoli, R.; Lamponi, S.; Barbucci, R. *Polym. Adv. Technol.* **2000**, *11*, 488–495.
23. Stachetzki, J. Ph.D. Thesis, University of Stuttgart, Germany, 2003.
24. Elliot, E. W. U.S. Patent 2,639,239, 1953.
25. Gross, J. R.; Greuel, M. P. U.S. Patent 5,079,354, 1992.
26. Abd El-Rehim, H. A.; Hegazy, E.-S. A.; Dia, D. A. *J. Macromol. Sci.* **2006**, *43*, 101–103.
27. Grant, G. T.; Morris, E. R.; Rees, D. A.; Smith, P. J. C.; Thom, D. *FEBS Lett.* **1973**, *32*, 195–198.
28. Campo, V. L.; Kawano, D. F.; Braz da Silva, D., Jr.; Carvalho, I. *Cabohydr. Polym.* **2009**, *77*, 167–180.
29. Brown, W. U.S. Patent 4,131,573, 1978.
30. Dellicolli, H. T.; Dilling, P.; Falkehag, S. U.S. Patent 4,244,728, 1976.
31. Johansen, S. DE Patent 198,28,438 A1, 1998.
32. Yamamoto, H.; Amaike, M.; Saito, H.; Sano, Y. *Mat. Sci. Eng.* **2000**, *C7*, 143–147.
33. Lindström, T.; Wallis, A.; Tulonen, J.; Kolseth, P. *Holzforschung* **1988**, *42*, 225–228.
34. Lindström, T.; Westman, L. *Colloid Polym. Sci.* **1982**, *260*, 594–598.
35. Lindström, T.; Westman, L. *Colloid Polym. Sci.* **1980**, *258*, 390–397.
36. El-Zawawy, W. K. *Polym. Adv. Technol.* **2005**, *16*, 48–54.
37. Nishida, M.; Uraki, Y.; Sano, Y. *11th International Symposium on Wood and Pulp Chemistry 2001*, Proceedings Vol. 2, pp 43−46
38. Nishida, M.; Uraki, Y.; Sano, Y. *Bioresour. Technol.* **2003**, *88*, 81–83.
39. Passauer, L. Ph.D. Thesis, TU Dresden, Germany, 2008.
40. Passauer, L.; Fischer, K.; Liebner, F. *European Workshop on Lignocellulosic and Pulp 2010*, Proceedings, pp 595−598.
41. Passauer, L.; Günther, B.; Bäucker, E. *Nordic Wood and Biorefinery Conference 2011*, Book of Abstracts, pp 382−385.
42. Passauer, L.; Fischer, K.; Liebner, F. *Holzforschung* **2011**, *65*, 309–317.
43. Passauer, L.; Fischer, K.; Liebner, F. *Holzforschung* **2011**, *65*, 319–326.
44. Glasser, W. G.; Jain, K. J. *Holzforschung* **1993**, *47*, 225–233.
45. Månsson, P. *Holzforschung* **1983**, *87*, 143–146.
46. Koch, C. J. Ph.D. Thesis, LMU Munich, Germany, 2002.
47. Zier, N. Ph.D. Thesis, TU Dresden, Germany, 1996.
48. Glasser, W. G.; Davé, V.; Frazier, C. H. *J. Wood Chem. Technol.* **1993**, *13*, 545–559.
49. Norgren, M.; Eklund, H.; Wågberg, L. *Langmuir* **2002**, *18*, 2859–2865.
50. Bailey, F. E.; Koleske, V. *Alkylene Oxides and Their Polymers*; Marcel Dekker: New York, Basel, 1992.

Downloaded by STANFORD UNIV GREEN LIBR on August 28, 2012 | http://pubs.acs.org
Publication Date (Web): August 17, 2012 | doi: 10.1021/bk-2012-1107.ch011

51. Chatterjee, S. K.; Sethi, K. R. *J. Macromol. Sci.* **1983**, *A-21*, 1045–1052.
52. Kulicke, W.-M. *Fließverhalten von Stoffen und Stoffgemischen*; Hüthig & Wepf: Basel, Switzerland, 1986.
53. Robinson, G. *Rheology* **1991**, *1*, 93–101.
54. Passauer, L.; Liebner, F.; Fischer, K.; Katzur, J. WO Patent 2011,098,078 A1, 2011.
55. Hergert, H. L. *J. Org. Chem.* **1960**, *25*, 405–413.
56. Faix, O. *Holzforschung* **1991**, *45*, 21–27.
57. Socrates, G. *Infrared and Raman Characteristic Group Frequencies*; Wiley & Sons: Chichester, U.K., 2001.
58. Wegener, G.; Strobel, C. *Holz Roh- Werkst.* **1992**, 417–420.
59. Faix, O.; Argyropoulos, D.; Robert, D.; Neirinck, V. *Holzforschung* **1994**, 387–394.
60. Faix, O.; Böttcher, J. H. *Holzforschung* **1993**, *47*, 45–49.

Downloaded by STANFORD UNIV GREEN LIBR on August 28, 2012 | http://pubs.acs.org
Publication Date (Web): August 17, 2012 | doi: 10.1021/bk-2012-1107.ch011

Downloaded by OHIO STATE UNIV LIBRARIES on August 28, 2012 | http://pubs.acs.org
Publication Date (Web): August 17, 2012 | doi: 10.1021/bk-2012-1107.ch012

Chapter 12

Lignin Model Compound Studies To Elucidate the Effect of "Natural" Mediators on Oxidoreductase-Catalyzed Degradation of Lignocellulosic Materials

P. Nousiainen,*,[1] J. Kontro,[1] P. Maijala,[2] E. Uzan,[3]
A. Hatakka,[2] A. Lomascolo,[3] and J. Sipilä[1]

[1]Department of Chemistry, Laboratory of Organic Chemistry,
University of Helsinki, P.O. Box 55 (A.I. Virtasen aukio1),
Helsinki 00014, Finland
[2]Department of Food and Environmental Sciences,
University of Helsinki, P.O.Box 56 (Viikinkaari 9),
Helsinki 00014, Finland
[3]Aix-Marseille Univ., UMR 1163 Fungal Biotechnology,
163 avenue de Luminy, Case 925, 13009 Marseille, France
***E-mail: paula.nousiainen@helsinki.fi**

Eco-efficient biotechnological applications are important innovations for modern industrial developments. Oxidoreductases, e.g. laccases and manganese peroxidases (MnPs), provide interesting possibilities. In many cases these enzymes require low molecular weight co-substrates to mediate oxidation. In this study, various types of lignin model compounds were investigated both as mediators and as final targets to find out their effect and potential in oxidation reactions, catalyzed by laccases and MnPs. Especially acetosyringone and methyl syringate mediated the laccase-catalyzed oxidation. These phenolics were also found to facilitate MnP-catalyzed reactions of non-phenolic compounds. Oxidation potentials, pH and chemical stability of the mediator affected the oxidation efficiency.

In Functional Materials from Renewable Sources; Liebner, F., et al.;
ACS Symposium Series; American Chemical Society: Washington, DC, 2012.

Downloaded by OHIO STATE UNIV LIBRARIES on August 28, 2012 | http://pubs.acs.org
Publication Date (Web): August 17, 2012 | doi: 10.1021/bk-2012-1107.ch012

One of the most important challenges in modern industrial development is the advancement of eco-efficient and eco-friendly applications. This challenge also requires the use of plant biomass as feedstock of fuels, chemicals and energy, to reduce our dependence on fossil-originated materials (*1–3*). Attributed to the rapid advancement of modern biotechnology and genetic engineering, enzymes are studied as economically feasible and environmentally friendly industrial biocatalysts, to hone the required chemical conversions in future biorefineries (*4–6*).

Plant biomass is a complex arrangement of biomolecules. It is generally considered to consist of polymers with variable chemical labilities, from relatively labile (e.g. sugars, starch, pectin, hemicellulose, and cellulose) to more recalcitrant materials (e.g. lignin, suberin, and cutin) (*7*, *8*). Cellulose and starch are already thoroughly exploited and found in several technical applications in the chemical industry. In the cases of hemicelluloses and lignin, the utilization of these raw materials has been much more cumbersome. Although produced in large quantities, i.e. in wood pulping, so far these polymers have been utilized as a source of energy, rather than being further refined to a chemical feedstock. In vascular plants hemicelluloses and lignin make up roughly half of the dry weight of the cell walls, in approximately equal proportions. The particular technical interest in lignin is that, contrary to (hemi)celluloses, lignin is a polyphenol and thus a potential natural source of aromatics, for the chemical industry. Lignin has the potential role as a raw material, for example, in the production of renewable fuels, adhesives, binders, antioxidants, carbon fibers and bulk chemicals in general (*9*, *10*). However, its widespread industrial utilization still awaits the relevant breakthroughs.

The significant problem with the utilization of lignin is its heterogenous, polydisperse and complex three-dimensional structure and its location in the cell wall interwoven with the carbohydrate matrix (*11*, *12*). The lignin macromolecule is formed through enzymatically initiated oxidative radical polymerization, with the main building blocks of three monolignols; p-coumaryl alcohol, coniferyl alcohol and sinapyl alcohol. According to their relative proportions lignins can be identified as softwood, hardwood and grass lignins. Monolignols are mainly linked by arylglycerol-β-aryl-ether (β-O-4′), phenylcoumaran (β-5′) and resinol (β-β′) linkages, with numerous other substructures in smaller amounts, but the actual mechanism of the polymerization process in cell tissues has not been completely established (*11*, *13*, *14*). The molecular weight, structural features and amount of lignin vary between different plant species and also on how the lignin material is isolated. Despite the combination of modern analytical techniques, used for structural elucidation, the exact structure of processed and native lignins remains undefined. Due to these difficulties in separation and analysis of lignin, simpler model compounds are commonly applied in matters of lignin structure identification and reactivity.

Oxidative enzymes, such as peroxidases and laccases, intimately participate in lignin biosynthesis but they are also key catalysts in lignin biodegradation. They are therefore a potential source for industrial ligninolytic biocatalysts (*5*, *6*). Wood decaying white-rot fungi secrete extracellular ligninolytic enzymes (lignin-degrading oxidative enzymes), including lignin peroxidases

(LiP, EC 1.11.1.14), manganese peroxidases (MnP, EC 1.11.1.13), versatile peroxidases (VP, EC 1.11.1.16) and laccases (EC 1.10.3.2 *p*-diphenol:oxygen oxidoreductases). Peroxidases show the ability to degrade and even mineralize lignin to carbon dioxide and water, through intermediate formation of organic radicals and diffusible, oxidative mediators (*15–17*). Most ligninolytic fungi secrete the peroxidase enzymes LiP or MnP that have stronger oxidation capacity than laccases. The expression of MnP together with laccase is more common than that of LiP, but there are also some fungi, e.g. *Pycnoporus cinnabarinus*, which appear to produce mainly laccase, and degrade lignin even without apparent peroxidase activity (*18*).

Ligninolytic basidiomycetes (white-rot fungi) produce laccases with the highest redox potentials, but often the wild-type enzymes do not meet the demands of industrial applications in regard to stability or thermotolerance. The enzyme production levels also remain unsatisfactory. For the generation of tailor-made laccases the preliminary step includes screening of the promising enzymes from natural sources, with subsequent purification and characterization, followed by gene cloning and molecular breeding (*19–22*). While the focus in lignin degradation has been on basidiomycetes and their enzymes, ascomycetes have not been studied intensively. In these fungi, the ability to produce laccase seems to be more common than the ability to produce peroxidases. Genetic engineering and heterologous production of the ascomycete enzymes has so far been more straightforward than that of basidiomycetes (*23*).

Laccases belong to a superfamily of multi-copper oxidases forming therein a phylogenetically divergent group of the so-called “blue oxidases”. They are extracellular glycoproteins of about 500 amino acid in length (typically 55–85 kDa) and contain four copper atoms, distributed in one mononuclear (T1) and one trinuclear (T2/T3) domain, in the active site of the enzyme. The substrate is oxidized monoelectronically at the T1 copper domain. The electron is transferred intramolecularly to the trinuclear center, which accepts the electron at the oxygen-binding site, thus reducing molecular oxygen altogether, by four electrons with concomitant excretion of water (*24*, *25*). Laccases are capable of catalyzing the oxidation of a wide range of organic substrates, such as phenols and polyphenols, aromatic amines, thiols, heterocyclic compounds and even inorganic salts (*26*). Most oxidative biochemical applications have focused on laccases that can already be produced on an industrial scale and can be tailored by modern biotechnological means. The wide substrate spectrum, stability of laccases towards chemical solvent systems, thermostability and the lack of significant substrate inhibition has made laccases feasible for industrial applications (*27*).

Ligninolytic extracellular peroxidases have the advantage of having higher redox potentials and thus also broader substrate range than laccases. Ligninolytic peroxidases contain a heme prostethic group (iron(III) protoporphyrin IX) at their active sites. Their catalytic cycle involves the two-electron oxidation of iron(III) porphyrin IX by hydrogen peroxide, to give the highly reactive oxoiron(IV) porphyrin IX π-cation radical (compound I). This returns to its resting state after two consecutive one-electron reductions via the compound II-intermediate, by electron donating substrates (*28*). Manganese peroxidases oxidize Mn(II) to reactive Mn(III), which acts as diffusible mediator. Mn(III) requires organic

Downloaded by OHIO STATE UNIV LIBRARIES on August 28, 2012 | http://pubs.acs.org
Publication Date (Web): August 17, 2012 | doi: 10.1021/bk-2012-1107.ch012

Downloaded by OHIO STATE UNIV LIBRARIES on August 28, 2012 | http://pubs.acs.org
Publication Date (Web): August 17, 2012 | doi: 10.1021/bk-2012-1107.ch012

acids, such as oxalic or malonic acid, to provide stabilization by chelation. It oxidizes phenolic compounds directly, or in turn oxidizes a second mediator, e.g. thiols or unsaturated fatty acids and their derivatives, for the degradation of non-phenolic compounds (*29*, *30*). The drawbacks of lignolytic peroxidases are their limited commercial availability and problematic activity. They require hydrogen peroxide, but are also inhibited by excess of peroxide (*31*). This means that the control of constant peroxide production is essential to carry out effective oxidation (*32–34*). In the case of MnP also the requirement of manganese chelators and suitable co-oxidants restricts their use in biotechnical applications.

Both peroxidases and laccases exhibit low substrate specificity and catalyze substrate oxidation by a mechanism involving free radicals. Reactions catalysed by laccases and peroxidases produce organic radicals through one-electron abstractions from organic substrates. These radicals can undergo various spontaneous follow-up reactions independent of enzyme activity, such as polymerization by radical coupling, aromatic ring cleavage, or C–C bond cleavage (*35*). Laccases and manganese peroxidase/Mn(III)-chelates, accompanied with their low redox potential characteristics, are capable of initial oxidation/cleavage of phenolic lignin units that often comprise less than 10% of the polymer (*22*). Laccase enzymes must be in direct contact with their substrate molecules to carry out oxidation. As lignins on average are high-molecular weight polymers with complex 3D structures and the access of the enzyme is further restricted by the compact structure of the plant cell wall, laccases need low-molecular weight compounds to transfer the oxidation further (*27*).

The lively research on laccases and laccase mediators has revealed that combined with a co-catalyst, acting as so called redox mediators or enhancers, the range of laccase substrates may be considerably extended to more recalcitrant materials, e.g. non-phenolic lignin moieties and environmental xenobiotics. As a consequence, potential biotechnical applications of laccases now include a wide spectrum of applications, such as decolorization and detoxification of effluents from the textile and dyestuff industries, in the pulp and paper industries, treatment of olive mill wastes, coffee pulp, the degradation and detoxification of recalcitrant waste water pollutants (chlorophenols, endocrine disrupting compounds (EDCs), polycyclic aromatic hydrocarbons (PAHs), pesticides and insecticides) and immobilization of soil pollutants, as well as various other applications, such as wood fiber modification, biosensors and organic synthesis (*6*, *36–39*).

Most of the mediators studied so far have been synthetic compounds, based on nitrogen heterocycles, such as TEMPO (2,2,6,6-tetramethyl-1-piperidinyloxyl) or HBT (1-hydroxybenzotriazole). The mediator–substrate oxidation has been reported to occur either according to an ionic mechanism, e.g. TEMPO and its analogues, or a radical mechanisms. The radical mechanisms proceed by electron transfer (ET) with e.g. ABTS [2,2-azinobis-(3-ethylbenzothiazoline-6-sulphonic acid)], or hydrogen atom abstraction (HAT) with e.g. HBT (*40*, *41*). The exploitation of laccase mediators in industrial processes has been limited, since they are expensive in the amounts required for oxidation processes and they mostly are problematic from an environmental perspective. Recently, it has been found that some natural substances, derived from syringyl-type plant phenolics, can be good substrates for laccases. They produce radicals with sufficiently long life-times and abilities to mediate the oxidation to substances which are recalcitrant towards oxidation by laccases (*28–30*). Simple syringyl-type phenolics are potentially cheap and readily available in down-streams from hardwood pulping industry wastes (*42*, *43*). Natural phenolics react further in laccase-catalyzed reactions, resulting in environmentally sustainable processes. Thus, several lignin-related natural phenols have been investigated as laccase mediators for pulp bleaching (*42*, *44*) and removal of lipophilic extractives from pulp (*45*, *46*). In this work, we have compared the effect and potential of several phenolic compounds as laccase mediators in reactions with simple lignin model compounds. Syringyl-type phenolics mediate oxidation reactions even by laccases with low redox potential. The efficiency of mediators was significantly enhanced by high redox potential *Pycnoporus* laccases when the pH of the reaction medium was adjusted to retain the stability of the mediator. Interestingly, we also found that phenolic mediators clearly boosted the manganese peroxidase-catalyzed oxidations in a reaction system with no external addition of hydrogen peroxide.

Downloaded by OHIO STATE UNIV LIBRARIES on August 28, 2012 | http://pubs.acs.org
Publication Date (Web): August 17, 2012 | doi: 10.1021/bk-2012-1107.ch012

Experimental

Myceliophthora thermophila laccase (NS 51003, redox potential of T1 Cu of 0.46 V; pH 4-9), kindly provided by Novozymes, Bagsvaerd, Denmark, was used as commercial feedstock without further purification. The high redox *Pycnoporus cinnabarinus* ss3 laccase, from the monokaryotic hyperproducing strain ss3 (0.75 V, optimal pH 4.0 with pH range 3.5-6), *Pycnoporus coccineus* BRFM 938, *Pycnoporus sanguineus* BRFM 902 and *P. sanguineus* BRFM 66 were from INRA Marseille, France. Laccase activity and stability were determined as previously described (*47*)**,** determining the oxidation of 2,6-dimethoxyphenol to the corresponding dimeric product (*48*), and ABTS (*49*), respectively. Lignin model compounds and mediators (Figures 1 and 2) were synthesized according to methods described in the literature (*47*).

Veratryl alcohol **(1)**, veratraldehyde, syringaldehyde **(**SA**, 11)**, acetosyringone **(**AS, **10)**, HBT **(14)** and 1,3,5-trimethoxybenzene were of commercial grade. Typically, the oxidation of non-phenolic model compounds was performed at room temperature (22 ºC) in vials that contained 50 mM succinate buffer and 20% (v/v) 1,4-dioxane. The solution was 12 mM in respect to substrate, mediator and 1,3,5-trimethoxybenzene as internal standard. Laccase activity in the reaction was 5, 20 or 200 nkat/ml. Samples of the reaction mixture were collected at 0 h, 2-3 h, 24 h and 48 h. The conversion of the model compounds was monitored onan HPLC Agilent 1200 with quantification on a detection wavelength of 270 nm.

Manganese peroxidase (MnP) activity was measured at 270 nm by the formation of Mn(III)-malonate complexes, as described by Wariishi et al. (1992) (*50*). In experiments with MnP, each reaction mixture (1 ml) was 3 mM of substrate (lignin model compound), 3 mM of phenolic mediator, 10 mM of $MnSO_4$, 12 mM of 1,3,5-trimethoxybenzene (TMB, internal standard) and 13 nkat manganese peroxidase *Phlebia* sp. *Nf* b19 (*Nematoloma frowardii* b19) (*51*). The solvent system consisted of 50 mM malonic acid/25 mM oxalic acid buffered

Downloaded by OHIO STATE UNIV LIBRARIES on August 28, 2012 | http://pubs.acs.org
Publication Date (Web): August 17, 2012 | doi: 10.1021/bk-2012-1107.ch012

to pH 4.5, 5.0 and 5.5, containing 20% (v/v) 1,4-dioxane. The lipid peroxidation system was 30 mM of linoleic acid and 3% Tween 80 in 50 mM acetate buffer of pH 4.5.

All reactions were performed in buffered organic solutions to keep both the initial substrate and non-phenolic target substrate dissolved in the solvent system, in order to efficiently catalyze enzymatic oxidations.

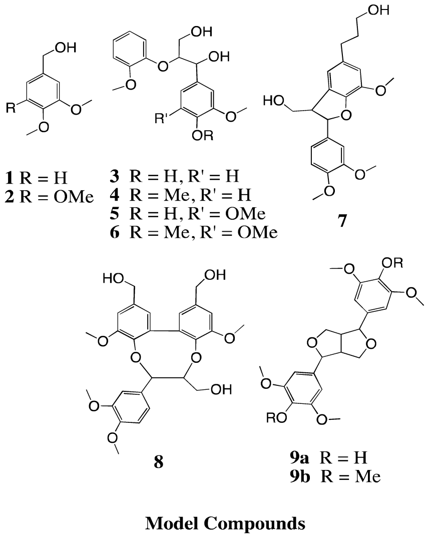
1 R = H
2 R = OMe
3 R = H, R' = H
4 R = Me, R' = H
5 R = H, R' = OMe
6 R = Me, R' = OMe
7
8
9a R = H
9b R = Me
Model Compounds

Figure 1. Phenolic and non-phenolic lignin model compounds studied as mediators and final targets for reactions by oxidoreductases.

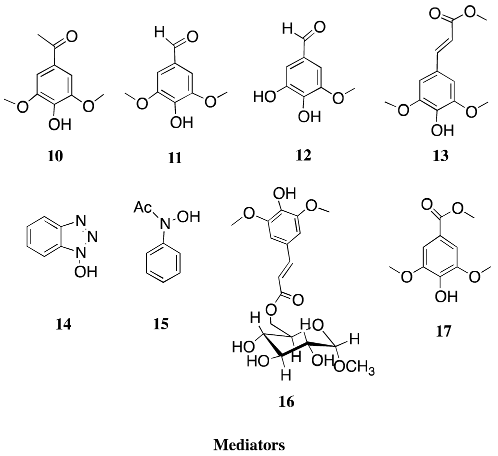
10
11
12
13
14
15
16
17
Mediators

Figure 2. Phenolic and synthetic compounds studied as mediators for reactions by oxidoreductases.

Downloaded by OHIO STATE UNIV LIBRARIES on August 28, 2012 | http://pubs.acs.org
Publication Date (Web): August 17, 2012 | doi: 10.1021/bk-2012-1107.ch012

Results and Discussion

Effect of Laccase Redox Potential

Laccases from different sources exhibit a wide range of redox potentials differing from typical plant laccases around 0.4 V to wood rotting fungal laccases with up to 0.7-0.8 V redox potentials. *M. thermophila* laccase belongs to ascomycete low-redox potential laccases, with a T1 redox-potential of 0.48 V and *P. cinnabarinus* ss3 represents high-redox laccases, with a T1 redox potential of 0.75 V. The substrate oxidation step involves the electron transfer from the reductant to the T1 Cu site in the protein active site. The substrate specificity is conferred by structure–activity relationships near this site and not at the trinuclear cluster. According to Xu (1997) the catalytic efficiency (k_{cat}/K_m) of laccases for some reducing substrates depends linearly on the redox potential of the T1 copper, meaning that the higher the potential difference between the T1 site acceptor and the substrate donor the higher the catalytic efficiency (*52*). Other factors, such as solvent accessibility, dipole orientation, and H-bonding, also contribute to the tuning of reduction potentials (*53*). Syringyl-type phenolic compounds possess an aromatic ring with two electron-donating methoxy substituents *ortho* to the phenolic position. These electron-donor substituents lower the redox potential of the phenols thereby making the enzymatic oxidation easier (*54*).

In our earlier paper (*47*), the mediating capacity of ten simple syringyl-type phenolics, of plant origin, was examined and compared with the common synthetic hydroxylamine mediators HBT **(14)** and *N*-hydroxyacetanilide **(**NHA**, 15),** with regard to their ability to act as mediators in the low redox potential *M. thermophila* laccase oxidation of non-phenolic lignin model compounds (Figure 1). The oxidation of veratryl alcohol **(1)** to veratraldehyde in aqueous dioxane was monitored by HPLC (Table I). Acetosyringone **(**AS, **10)** and methyl syringate **(**MeS, **17**) especially demonstrated the ability to mediate the oxidation of high oxidation potential substrates by a low redox potential laccase, even at low mediator concentration levels (1:10, mediator to substrate ratio). Importantly, at low mediator to substrate ratio they seemed to be more effective than the commonly used commercial hydroxylamines NHA and HBT (*47*). This is also in accordance with Babot et al. (2011) who applied low laccase and phenolic mediator doses in pilot-scale trials for pulp delignification and pitch removal, obtaining good results with moderate and low mediator concentration, thus enabling cost-efficient pulping (*46*).

The most common structural unit in lignin, arylglycerol β-ether (β-O-4′; **3-6**), represented by the non-phenolic guaiacylglycerol β-guaiacyl ether, adlerol (**4**), was oxidized by a *M. thermophila* laccase-mediator system. With acetosyringone, methyl syringate and HBT as mediators and a substrate:mediator ratio of 1:1, the system gave less than 5% of adlerone, the corresponding α-carbonyl derivative. The most effective mediator in experiments with *M. thermophila* laccase proved to be NHA, capable of producing 15% adlerone from adlerol (Table I).

Downloaded by OHIO STATE UNIV LIBRARIES on August 28, 2012 | http://pubs.acs.org
Publication Date (Web): August 17, 2012 | doi: 10.1021/bk-2012-1107.ch012

Table I. Oxidation of veratryl alcohol to veratraldehyde and adlerol to adlerone (substrate:mediator ratio 1:1) by *M. thermophila* laccase (NS 51003)

	Veratraldehyde yield % *Reaction time, hours*		*Adlerone yield %* *Reaction time, hours*	
Mediator	*24*	*48*	*24*	*48*
No mediator	0	0	0	0
14 HBT pH 6.0	13	20	2	<5
15 NHA pH 6.0	33	40	9	13
10 AS pH 6.0	18	23	3	4
17 MeS pH 6.0	22	28	3	<5

The condensed units phenylcoumaran (β-5′; **7**) and syringaresinol (β-β′; **9b**) were much more resistant to mediated oxidation by the low-redox potential laccase-mediator-system. An interesting reactivity was found with the condensed biphenyl 4-O-methylated dibenzodioxocine structure **(8)**, considered to be the main branching point in softwood lignin with comparatively high abundance (*11*, *55*). This compound was easily oxidized by all mediators at its biphenylic benzyl position with 30-80% conversion, depending on the mediator. The product was isolated from the reaction mixture and verified by NMR.

The HAT oxidation mechanism has been proposed to be involved for hydroxylamine–type mediators, where oxidation of the target non-phenolic compound occurs when it possesses moderately weak C-H bond in benzylic α-position (*41*), thus omitting the redox restrictions of non-phenolic substrates. This mechanism was proposed to be involved also for phenolic mediators (*56*, *57*). The results obtained from the electrochemical oxidation of benzyl alcohols, by several phenolic compounds, support this mechanism (*58*). In the same study was observed that the redox potentials of the phenolic compounds seem to have a negligible effect on their catalytic efficiency.

Syringaldehyde **(**SA, **11)**, acetosyringone **(**AS, **10)** and also NHA (**15**) were oxidatively degraded or coupled during the five day period that the reactions were followed. According to findings by Kawai *et al.* (1989), a considerable amount of syringaldehyde is oxidized to 2,6-dimethoxyhydroquinone and eventually 2,6-dimethoxy-*p*-benzoquinone, in laccase-catalyzed mediated reactions (*59*). This can be attributed to the ability of syringyl radical species to undergo concurrent reaction by disproportionation, leading to the corresponding stabilized cation (phenoxonium ion). Nucleophilic attack on these arylcations produce the corresponding quinones. In the case of syringaldehyde, used in 10:1 substrate:mediator ratio, undesirable secondary reactions took place consuming syringaldehyde in a few hours, which explains the low mediating effect of this phenol. Even when a higher mediator ratio (1:1 substrate:mediator) was used, only a 5% conversion was achieved. Significant differences were found between mediators in their stability and mediating efficiency. The observed stabilities of the syringyl-type mediators in the reaction system with the *M. thermophila* laccase were from the highest to lowest: methyl syringate ≫ acetosyringone >

syringaldehyde. Other compounds tested, such as the 5-hydroxy vanillin (12) and two sinapic acid esters (13,16), proved to be unstable under the applied conditions, with less than 5% mediating capacity.

The oxidation of veratryl alcohol to veratraldehyde by the *high redox potential* laccase *P. cinnabarinus* ss3 was effectively mediated by HBT, NHA, AS and MeS resulting in 40-100% conversion. HBT was clearly the most effective of the mediators studied (Table II). The efficiency of HBT was even more pronounced in the oxidation of adlerol to adlerone, with 90% conversion, whereas the other mediators mentioned above gave only 5-10% conversion. The oxidation of adlerol by *P. cinnabarinus* ss3 with HBT as a mediator produced solely the α-carbonyl product adlerone, without any α-β cleavage of the side chain.

Downloaded by OHIO STATE UNIV LIBRARIES on August 28, 2012 | http://pubs.acs.org
Publication Date (Web): August 17, 2012 | doi: 10.1021/bk-2012-1107.ch012

Table II. Oxidation of veratryl alcohol to veratraldehyde and adlerol to adlerone with substrate:mediator ratio 1:1 by *P.cinnabarinus* laccase ss3

	Veratraldehyde yield % Reaction time, hours			*Adlerone yield % Reaction time, hours*		
Mediator	*2-3*	*24*	*48*	*3*	*24*	*48*
No mediator	0	0	0	0	0	0
14 HBT pH 4.5	22	98	100	10	63	90
15 NHA pH 4.5	25	36	40	7	9	11
15 NHA pH 6.0	ND	ND	ND	1	5	13
10 AS pH 4.5	6	6	7	ND	ND	ND
10 AS pH 6.0	1	17	40	0.5	3	5
17 MeS pH 4.5	5	9	9	ND	ND	ND
17 MeS pH 6.0	1	18	40	0	2	6
11 SA pH 6.0	1	1	3	0	0	0.5

ND=not determined

The laccases from the species *P. coccineus* and *P. sanguineus,* originating from subtropical and tropical environments (strains BRFM 938, BRFM 66 and BRFM 902), were studied in Uzan et al. (*21*). It was found that HBT, AS and MeS efficiently mediated the oxidation of veratryl alcohol (32–100%) by these laccases. The synthetic mediator HBT was the most effective in the oxidation of both veratryl alcohol (100%) and adlerol (86%), using BRFM 66 laccase. AS was as effective as MeS, with oxidation of veratryl alcohol 30–40%, after 48 h of incubation with all three laccase systems. Adlerol was significantly oxidized only by laccase-HBT systems, yielding 33–86% adlerone, which was 10- to17-fold more than using laccase-“natural” mediator systems. Marked differences were thus found in oxidation of veratryl alcohol and adlerol by the three enzymes. The reactivities were in the order: BRFM 66 > BRFM 938 > BRFM 902 for veratryl alcohol, and BRFM 66 > BRFM 902 > BRFM 938 for adlerol, suggesting that the substrate specificities of the three laccases might have some effect on mediated oxidation of non-phenolic substrates (*21*).

The Effect of pH on Mediating Power and Stability of Syringyl-Type Laccase Mediators

Fungal laccases usually show pH optima in acidic media. The pH optimum depends on the substrate used, e.g. for the oxidation of ABTS they are generally lower than 4.0, while with phenolic compounds like guaiacol and syringaldazine they exhibit higher values between 4.0 and 7.0 (*60*). Many ascomycete laccases with pH optima close to neutral (pH 6-8) have been described. The ascomycete *M. thermophila* laccase has a wide working pH range with a pH optimum around pH 6 and *P. cinnabarinus* ss3 is a typical fungal laccase with optimal pH of 4 and pH range of 3.5-6. The inhibitory effect generated by the binding of a hydroxide ion to the type 2/type 3 coppers of laccase (which inhibits the activity at higher pH), contributes to the pH activity profile of the fungal laccases (*52*). On the other hand, phenol oxidation to a phenoxy radical is favored in presence of the phenolate form, meaning that higher pH favors the initial oxidation process. The pKa values for methyl syringate, syringaldehyde and acetosyringone are 8.7, 7.0 and 7.8, respectively (*52*).

Based on the results received by high redox potential laccase *P. cinnabarinus,* on oxidation of veratryl alcohol (Table II), the mediating effectivity of acetosyringone was further studied in a system using veratryl alcohol and *P. cinnabarinus* ss3 enzyme in solutions of 50 mM buffered sodium succinate pH 4.5, 5.0, 5.5 and 6.0. In Figure 3 the amount of veratraldehyde formed in the oxidation is presented as a function of reaction time. The results show that acetosyringone performed best at pH 6, during the 48 h reaction time, with 30% yield of veratraldehyde. At pH 5.5 the reaction was faster giving the oxidation product in 25% yield, during a 24 h period, after which the reaction did not proceed further.

Downloaded by OHIO STATE UNIV LIBRARIES on August 28, 2012 | http://pubs.acs.org
Publication Date (Web): August 17, 2012 | doi: 10.1021/bk-2012-1107.ch012

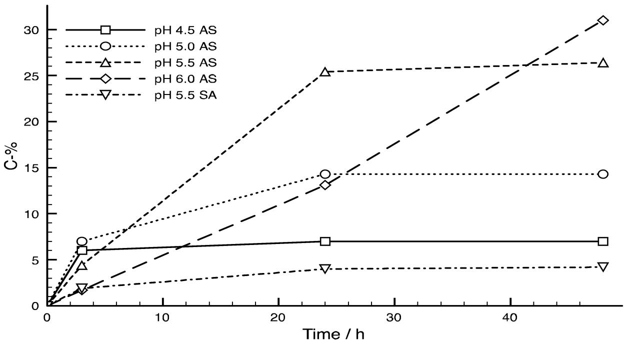

Figure 3. Oxidation of veratryl alcohol to veratraldehyde (%) by Pycnoporus cinnabarinus laccase ss3 with acetosyringone (AS, ***10****) or syringaldehyde (SA,* ***11****) as a mediator (substrate:mediator ratio 1:1) at different pH, followed over 48 h at 22 ºC.*

Syringaldehyde deteriorated even faster at all tested pHs, mediating only 4% conversion of veratryl alcohol to veratraldehyde under the optimum pH 5.5 conditions. The side reactions were accelerated under acidic conditions where the mediator was consumed to give the corresponding *p*-benzoquinone and most likely dimers and polymerized polymeric products as well. The results show that the optimum pH for the oxidation of the target substrate was influenced by the stability of the oxidized mediator, rather than the optimal pH for laccase.

Oxidation Reactions by Manganese Peroxidase (MnP)

In order to study the effect of different mediators in the MnP-induced oxidation reactions, by *Phlebia* sp. *Nf* b19 (*Nematoloma frowardii* b19), three oxidation systems were studied: lipid peroxidation (*29*), Mn(III) malonate chelate with *in situ* peroxide production by glucose oxidase (*61*) and a system with phenolic mediators where hydrogen peroxide was generated directly from oxalic acid (*62*) in malonate buffer. The results in Table III show that the lipid-MnP-system, which already possessed a mediator in the form of lipid radical, readily oxidized veratryl alcohol to veratraldehyde with ca. 4.5% conversion. Interestingly, the systems with syringyl-type mediators oxidized the non-phenolic model compound veratryl alcohol, much more efficiently than the lipid-MnP-systems.

Downloaded by OHIO STATE UNIV LIBRARIES on August 28, 2012 | http://pubs.acs.org
Publication Date (Web): August 17, 2012 | doi: 10.1021/bk-2012-1107.ch012

Table III. The oxidation of veratryl alcohol to veratraldehyde by manganese peroxidase *Phlebia* sp. *Nf* b19 (*Nematoloma frowardii* b19) in lipid and phenolic mediator systems, over 48 h

Mediator system	*Veratraldehyde (%)*
Linoleic acid	4.5
10 AS pH 5.0	9.2
10 AS pH 5.5	5.5
17 MeS pH 5.0	9.9
17 MeS pH 5.5	7.3

Conclusions

The results demonstrate that the oxidation efficiency of laccases is enhanced by lignocellulose-derived syringyl-type aromatic mediators: in particular acetosyringone and methyl syringate effectively mediate the oxidation of comparatively high oxidation potential substrates, even with a low redox potential *M. thermophila* laccase. The results also show that the efficiency of these mediators can still be enhanced by high redox potential laccase, e.g. *P. cinnabarinus* ss3. The high performance of synthetic mediator HBT under the same reaction conditions clearly demonstrates that further improvement on the stability of these natural-type mediators is required. Also, the side products formed by oxidation of phenolic mediators should be studied further. The study shows that the effect of pH for the reaction is crucial when exploiting phenolic mediators. For example, the critical pH for the oxidation reaction catalyzed by *Pycnoporus* laccase is around 5.5. A lower pH in the reaction medium leads the mediated oxidation reactions towards degradation of the mediator by acid-catalyzed side reactions. In addition, the results suggest that reactions catalyzed by MnP of the white-rot fungus *Phlebia* sp. *Nf* b19 are likewise facilitated by the presence of syringyl-type mediators.

Acknowledgments

This work was supported by the EU contract NMP2-CT-2006-026456 (BIORENEW), and the Academy of Finland contract 1133022, which are gratefully acknowledged.

References

1. Ragauskas, A. J.; Williams, C. K.; Davison, B. H.; Britovsek, G.; Cairney, J.; Eckert, C. A.; Frederick, W. J.; Hallett, J. P.; Leak, D. J.; Liotta, C. L.; Mielenz, J. R.; Murphy, R.; Templer, R.; Tschaplinski, T. *Science* **2006**, *311*, 484–489.
2. Clark, J. H. *J. Chem. Technol. Biotechnol.* **2007**, *82*, 603–609.
3. Bozell, J. J. *Clean* **2008**, *36*, 641–647.
4. Wohlgemuth, R. *Curr. Opin. Biotechnol.* **2010**, *21*, 713–724.
5. Martínez, A. T.; Ruiz-Dueñas, F. J.; Martínez, M. J.; del Río, J. C.; Gutiérrez, A. *Curr. Opin. Biotechnol.* **2009**, *20*, 348–357.
6. Xu, F. *Ind. Biotechnol.* **2005**, *1*, 38–50.
7. Aneja, M. K.; Sharma, S.; Fleischmann, F.; Stich, S.; Heller, W.; Bahnweg, G.; Munch, J. C.; Schloter, M. *Microb. Ecol.* **2006**, *52*, 127–135.
8. Theuerl, S.; Buscot, F. *Biol. Fertil. Soils* **2010**, *46*, 215–225.
9. Zakzeski, J.; Bruijnincx, P. C. A.; Jongerius, A. L.; Weckhuysen, B. M. *Chem. Rev.* **2010**, *110*, 3552–3599.
10. Rex, E. Future Use of Lignin in Value Added Products, LigniMatch, 2010, pp 1–16. https://document.chalmers.se/download?docid=128138106.
11. Ralph, J.; Lundquist, K.; Brunow, G.; Lu, F.; Kim, H.; Schatz, P. F.; Marita, J. M.; Hatfield, R. D.; Ralph, S. A.; Christensen, J. H.; Boerjan, W. *Phytochem. Rev.* **2004**, *3*, 29–60.
12. Adler, E. *Wood. Sci. Technol.* **1977**, *11*, 169–218.
13. Vanholme, R.; Morreel, K.; Ralph, J.; Boerjan, W. *Curr. Opin. Plant Biol.* **2008**, *11*, 278–285.
14. Boerjan, W.; Ralph, J.; Baucher, M. *Annu. Rev. Plant Biol.* **2003**, *54*, 519–546.
15. Tuor, U.; Winterhalter, K.; Fiechter, A. *J. Biotechnol.* **1995**, *41*, 1–17.
16. Kirk, T. K.; Farrell, R. L. *Annu. Rev. Microbiol.* **1987**, *41*, 465–501.
17. Hatakka, A.; Hammel, K. In *Mycota X, A Comprehensive Treatise on Fungi as Experimental Systems for Basic and Applied Research*, 2nd ed.;

Downloaded by OHIO STATE UNIV LIBRARIES on August 28, 2012 | http://pubs.acs.org
Publication Date (Web): August 17, 2012 | doi: 10.1021/bk-2012-1107.ch012

Hofrichter, M., Ed.; Springer-Verlag: Berlin, Heidelberg, 2010; Vol. 10, Industrial Applications, pp 319–340.

18. Eggert, C.; Temp, U.; Eriksson, K. *FEBS Lett.* **1997**, *407*, 89–92.
19. Otterbein, L.; Record, E.; Longhi, S.; Asther, M.; Moukha, S. *Eur. J. Biochem.* **2000**, *267*, 1619–1625.
20. Ayala, M.; Pickard, M. A.; Vazquez-Duhalt, R. *J. Mol. Microb. Biotechnol.* **2008**, *15*, 172–180.
21. Uzan, E.; Nousiainen, P.; Balland, V.; Sipilä, J.; Piumi, F.; Navarro, D.; Asther, M.; Record, E.; Lomascolo, A. *J. Appl. Microbiol.* **2010**, *108*, 2199–2213.
22. Martínez, A. T.; Speranza, M.; Ruiz-Dueñas, F. J.; Ferreira, P.; Camarero, S.; Guillén, F.; Martínez, M. J.; Gutiérrez, A.; del Río, J. C. *Int. Microbiol.* **2005**, *8*, 195–204.
23. Rodgers, C. J.; Blanford, C. F.; Giddens, S. R.; Skamnioti, P.; Armstrong, F. A.; Gurr, S. J. *Trends Biotechnol.* **2010**, *28*, 63–72.
24. Solomon, E. I.; Augustine, A. J.; Yoon, J. *Dalton Trans.* **2008**, 3921–3932.
25. Ferraroni, M.; Myasoedova, N. M.; Schmatchenko, V.; Leontievsky, A. A.; Golovleva, L. A.; Scozzafava, A.; Briganti, F. *BMC Struct. Biol.* **2007**, *7*, 60.
26. Xu, F. *Biochemistry* **1996**, *35*, 7608–7614.
27. Kunamneni, A., Ballesteros, A., Plou, F. J.; Alcade, M. In *Communicating Current Research and Educational Topics and Trends in Applied Microbiology*; Méndez-Vilas, A., Ed.; Microbiology Book Series; 2007, pp 233–245, Formatex 2007, Badajoz.
28. Ruiz-Dueñas, F. J.; Martinez, M. J.; Martinez, A. T. *Mol. Microbiol.* **1999**, *31*, 223–235.
29. Kapich, A. N.; Steffen, K. T.; Hofrichter, M.; Hatakka, A. *Biochem. Biophys. Res. Commun.* **2005**, *330*, 371–377.
30. Hofrichter, M. *Enzyme Microb. Technol.* **2002**, *30*, 454–466.
31. Taboada-Puig, R.; Lú-Chau, T.; Eibes, G.; Moreira, M. T.; Feijoo, G.; Lema, J. M. *Biotechnol. Prog.* **2011**, *27*, 668–676.
32. Bockle, B.; Martínez, M. J.; Guillén, F.; Martínez, A. T. *Appl. Environ. Microb.* **1999**, *65*, 923.
33. Timofeevski, S.; Reading, N.; Aust, S. *Arch. Biochem. Biophys.* **1998**, *356*, 287–295.
34. Valderrama, B.; Ayala, M.; Vazquez-Duhalt, R. *Chem. Biol.* **2002**, *9*, 555–565.
35. Wong, D. W. S. *Appl. Biochem. Biotechnol.* **2008**, *157*, 174–209.
36. Tuomela, M.; Hatakka, A. In *Comprehensive Biotechnology, Vol. 6, Environmental Biotechnology and Safety*, 2nd ed.; Moo-Young, M., Ed.; Elsevier, 2011; pp 183–196.
37. Wells, A.; Teria, M.; Eve, T. *Biochem. Soc. Trans.* **2006**, *34*, 304–308.
38. Widsten, P.; Kandelbauer, A. *Enzyme Microb. Technol.* **2008**, *42*, 293–307.
39. Riva, S. *Trends Biotechnol.* **2006**, *24*, 219–226.
40. Fabbrini, M.; Galli, C.; Gentili, P. *J. Mol. Catal. B: Enzym.* **2002**, *16*, 231–240.
41. Cantarella, G.; Galli, C.; Gentili, P. *J. Mol. Catal. B: Enzym.* **2003**, *22*, 135–144.

Downloaded by OHIO STATE UNIV LIBRARIES on August 28, 2012 | http://pubs.acs.org
Publication Date (Web): August 17, 2012 | doi: 10.1021/bk-2012-1107.ch012

42. Camarero, S.; Ibarra, D.; Martínez, A. T.; Romero, J.; Gutiérrez, A.; del Río, J. C. *Enzyme Microb. Technol.* **2007**, *40*, 1264–1271.
43. Canas, A. I.; Camarero, S. *Biotechnol. Adv.* **2010**, *28*, 694–705.
44. Aracri, E.; Colom, J. F.; Vidal, T. *Bioresour. Technol.* **2009**, *100*, 5911–5916.
45. Gutiérrez, A.; Rencoret, J.; Ibarra, D.; Molina, S.; Camarero, S.; Romero, J.; del Río, J. C.; Martínez, A. T. *Environ. Sci. Technol.* **2007**, *41*, 4124–4129.
46. Babot, E. D.; Rico, A.; Rencoret, J.; Kalum, L.; Lund, H.; Romero, J.; del Río, J. C.; Martínez, A. T.; Gutiérrez, A. *Bioresour. Technol.* **2011**, *102*, 6717–6722.
47. Nousiainen, P.; Maijala, P.; Hatakka, A.; Martínez, A. T.; Sipilä, J. *Holzforschung* **2009**, *63*, 699–704.
48. Jaouani, A.; Guillen, F.; Penninckx, M.; Martinez, A.; Martínez, M. *Enzyme Microb. Technol.* **2005**, *36*, 478–486.
49. Lomascolo, A.; Cayol, J.; Roche, M.; Guo, L.; Robert, J.; Record, E.; Lesage-Meessen, L.; Ollivier, B.; Sigoillot, J.; Asther, M. *Mycol. Res.* **2002**, *106*, 1193–1203.
50. Wariishi, H.; Valli, K.; Gold, M. H. *J. Biol. Chem.* **1992**, *267*, 23688–2368823695.
51. Hildén, K. S.; Bortfeldt, R.; Hofrichter, M.; Hatakka, A.; Lundell, T. K. *Microbiology* **2008**, *154*, 2371–2379.
52. Xu, F. *J. Biol. Chem.* **1997**, *272*, 924–928.
53. Quintanar, L.; Stoj, C.; Taylor, A. B.; Hart, P. J.; Kosman, D. J.; Solomon, E. I. *Acc. Chem. Res.* **2007**, *40*, 445–452.
54. Tadesse, M. A.; D'Annibale, A.; Galli, C.; Gentili, P.; Sergi, F. *Org. Biomol. Chem.* **2008**, *6*, 868–878.
55. Heikkinen, S.; Toikka, M. M.; Karhunen, P. T.; Kilpeläinen, I. A. *J. Am. Chem. Soc.* **2003**, *125*, 4362–4367.
56. Baiocco, P.; Barreca, A. M.; Fabbrini, M.; Galli, C.; Gentili, P. *Org. Biomol. Chem.* **2003**, *1*, 191–197.
57. Calcaterra, A.; Galli, C.; Gentili, P. *J. Mol. Catal. B: Enzym* **2008**, *51*, 118–120.
58. Díaz González, M.; Vidal, T.; Tzanov, T. *Electroanalysis* **2009**, *21*, 2249–2257.
59. Kawai, S.; Umezawa, T. *Wood Res.* **1989**, *76*, 10–16.
60. Baldrian, P. *FEMS Microbiol. Rev.* **2006**, *30*, 215–242.
61. Lopez, C.; Cavaco-Paulo, A. *Eng. Life Sci.* **2008**, *8*, 315–323.
62. Hofrichter, M.; Ziegenhagen, D.; Vares, T.; Friedrich, M.; Jäger, M.; Fritsche, W.; Hatakka, A. *FEBS Lett.* **1998**, *434*, 362–366.

Downloaded by OHIO STATE UNIV LIBRARIES on August 28, 2012 | http://pubs.acs.org
Publication Date (Web): August 17, 2012 | doi: 10.1021/bk-2012-1107.ch012

Downloaded by UNIV OF GUELPH LIBRARY on August 28, 2012 | http://pubs.acs.org
Publication Date (Web): August 17, 2012 | doi: 10.1021/bk-2012-1107.ch013

Chapter 13

Novel Functions of Non-Ionic, Amphiphilic Lignin Derivatives

**Yasumitsu Uraki,[1] Keiichi Koda,*,[1] Tatsuhiko Yamada,[2]
Chihiro Oikawa,[3] and Tomohiro Aso[3]**

**[1]Research Faculty of Agriculture, Hokkaido University, Kita 9 Nishi 9,
Kita-ku, Sapporo, 060-8589 Hokkaido, Japan
[2]Department of Biomass Chemistry, Forestry and Forest Products Research
Institute, 1 Matsunosato, Tsukuba, Ibaraki 305-8687, Japan
[3]Graduate School of Agriculture, Hokkaido University, Kita 9 Nishi 9,
Kita-ku, Sapporo, 060-8589 Hokkaido, Japan
*E-mail: cody@for.agr.hokudai.ac.jp**

Technical lignins including water-insoluble isolated lignins were easily converted to water-soluble derivatives by the reaction with several types of epoxidized polyethylene glycol derivatives. The resulting lignin-based derivatives were soluble in water and organic solvents, thus having amphiphilic property. We found novel functions of the amphiphiles, such as the uses as cellulase-aid agent and cement dispersant in addition to the surfactant action. This article reviews the functions in relation to the development of biorefining processes for Japanese woody biomass.

Introduction

An amphiphile is defined as a substance which is soluble both in water and organic solvents, sometimes including a substance having just affinity for both solvents without being soluble. An amphiphile is composed of a hydrophobic moiety and a hydrophilic moiety. In solution it forms an aggregate, for example a micelle, by intermolecular interaction. In aqueous environment, such micelle may surround droplets of oil, and allows oil to be dispersed in water. This micelle formation is referred to as self-assembly of molecules in the case of an amphiphilic polymer. Self-assembly becomes self-organization, when it shows a

In Functional Materials from Renewable Sources; Liebner, F., et al.;
ACS Symposium Series; American Chemical Society: Washington, DC, 2012.

definite orientation of molecules. Self-organization of molecules has a variety of applications, and it draws attention as an important technique to fabricate novel materials, because it saves costs and energy (*1*).

Woody biomass has received much attention as an alternative resource, with regard to the public perception of the depletion of fossil resources, their environmental impact, and the risk of nuclear power generation. Conversion of lignin to a value-added material is a key process to achieve a complete biorefining system of woody biomass. Lignin is a phenolic macromolecule biologically synthesized according to an enzymatically mediated, dehydrogenative radical coupling process (*2*). A considerable amount of lignin is produced worldwide as a byproduct by pulp and paper industries and bioethanol production plants that require exclusively cellulose from woody biomass. These lignins produced this way are called technical lignins, and they are generally used by combustion for heat and energy production. Kraft pulping, a major chemical pulping process employed worldwide today, is the most important contributor to the production of lignin.

The authors have focused on the utilization of technical lignins with regard to biorefining of woody biomass. We have developed a technique to convert technical lignins to amphiphilic derivatives with self-assembling ability for a wide variety of applications. This review will give an overview of our studies, dealing with functions and applications of amphiphilic lignin derivatives.

Downloaded by UNIV OF GUELPH LIBRARY on August 28, 2012 | http://pubs.acs.org
Publication Date (Web): August 17, 2012 | doi: 10.1021/bk-2012-1107.ch013

Water Solubility of Isolated Lignins and Their Conversion to Amphiphiles

Lignin consists of C_9-phenylpropanoid units connected at different positions which give the inter-unit linkages their name. The β-O-4 type ether bond are the major (50 % and more) linkage type (*2*). The β-O-4 bonds are cleaved effectively upon kraft pulping. As a result of the ether cleavage, considerable amounts of phenolic hydroxyl groups are formed which render the resulting lignin (kraft lignin; KL) soluble in aqueous alkali (Figure 1) (*3*). Organosolv pulping, performed in an organic solvent, produced lignin, termed organosolv lignin that is soluble in the organic solvent used in the pulping process. Thus, those isolated lignins from wood are generally not soluble in water under acidic or neutral conditions.

By contrast, lignosulfonate (LS), produced according to the sulfite pulping process that uses aqueous bisulfite solution, is a rare exception and it is soluble in water at neutral pH. This is because sulfonic acid groups are introduced into lignin during this pulping process. Accordingly, LS can be classified as a water soluble, anionic polyelectrolyte. LS is also an anionic surfactant because it is composed of aromatic groups as hydrophobic moieties and sulfonic acid groups as hydrophilic functional groups. Based on these unique properties, only LS - among technical lignins - is utilized as a cement dispersant (*4*) and as an electrode environment in lead batteries (*5*) on a commercial basis.

Downloaded by UNIV OF GUELPH LIBRARY on August 28, 2012 | http://pubs.acs.org
Publication Date (Web): August 17, 2012 | doi: 10.1021/bk-2012-1107.ch013

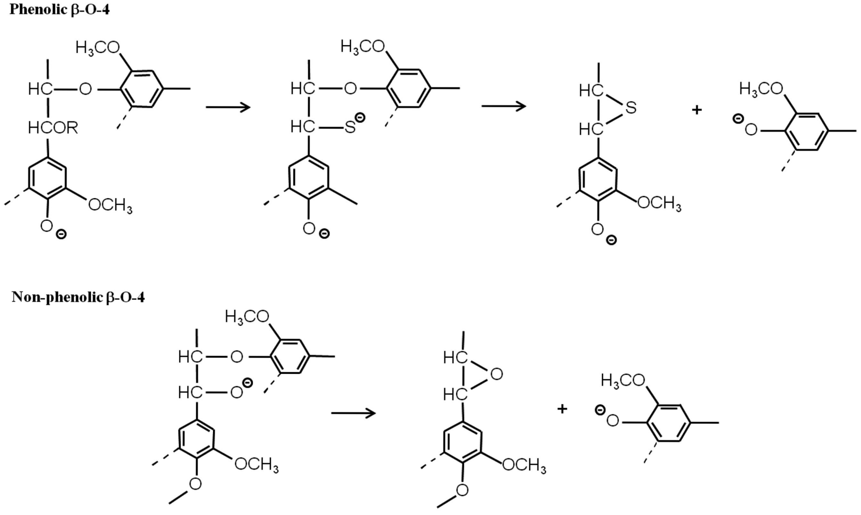

Phenolic β-O-4

Non-phenolic β-O-4

Figure 1. Cleavage of β-O-4 type lignin interunitary linkages and formation of phenolic hydroxy groups during kraft pulping.

Although some researchers already tried to solubilize lignin in water by carboxymethylation (*6*) and hydroxypropylation (*7*), mimicking conventional derivatization approaches of cellulose, the yields of the resulting water-soluble derivatives were not satisfactory. Furthermore, sulfonation was also investigated by at least two research groups (*8*, *9*).

We made an attempt to solubilize KL and organosolv lignin in water, by introducing polyethylene glycols (PEGs) as a hydrophilic moiety to the lignins, instead of introducing small hydrophilic functional groups.

Figure 2 illustrates PEG derivatives used in our studies, which are epoxidized PEGs. Compounds A (PEGDE) and C (DAEO) were commercially available and were kindly provided from a chemical company (Nagase ChemTech Co. Ltd., Japan). Compound B (EPEG) was prepared in our laboratory, by reacting compound A with sodium ethoxide (*10*).

A general procedure of derivatization of isolated lignins was as follows. Isolated lignin (10 g) was dissolved in 100 mL of aqueous 1 M NaOH. To the solution, a given amount of an epoxidized PEG was added. The mixture was heated at 70 °C for 2 h. The completion of the reaction was confirmed by observing that no precipitation was formed under acidic condition after the addition of glacial acetic acid. The reaction mixture was neutralized with glacial acetic acid and the non-reacted matter was removed by ultrafiltration. A purified lignin derivative was then collected by lyophilization (*10*). The resulting lignin derivatives are soluble in water, chloroform, and alcohols, but sparingly soluble in tetrahydrofuran, suggesting that they are amphiphilic.

Downloaded by UNIV OF GUELPH LIBRARY on August 28, 2012 | http://pubs.acs.org
Publication Date (Web): August 17, 2012 | doi: 10.1021/bk-2012-1107.ch013

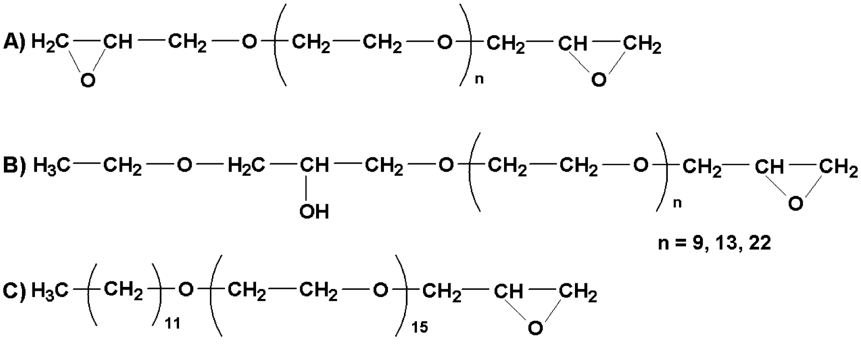
A)
B)
C)
n
n = 9, 13, 22
11
15

Figure 2. Epoxylated polyethylene glycols (PEGs). A), polyethylene glycol diglycidylether (PEGDE); B), ethoxy (2-hydroxy)propoxy polyethylene glycol glycidylether (EPEG); C), dodecyloxy-polyethylene glycol glycidylether (DAEO).

We finally prepared such amphiphilic derivatives from softwood and hardwood kraft lignin (KL) (*11*), acetic acid lignin (AL) as an organosolv lignin (*10*), and soda lignin (SL) obtained by the soda pulping of Japanese cedar wood (*12*). A typical amphiphilic lignin derivative is schematically shown in Figure 3.

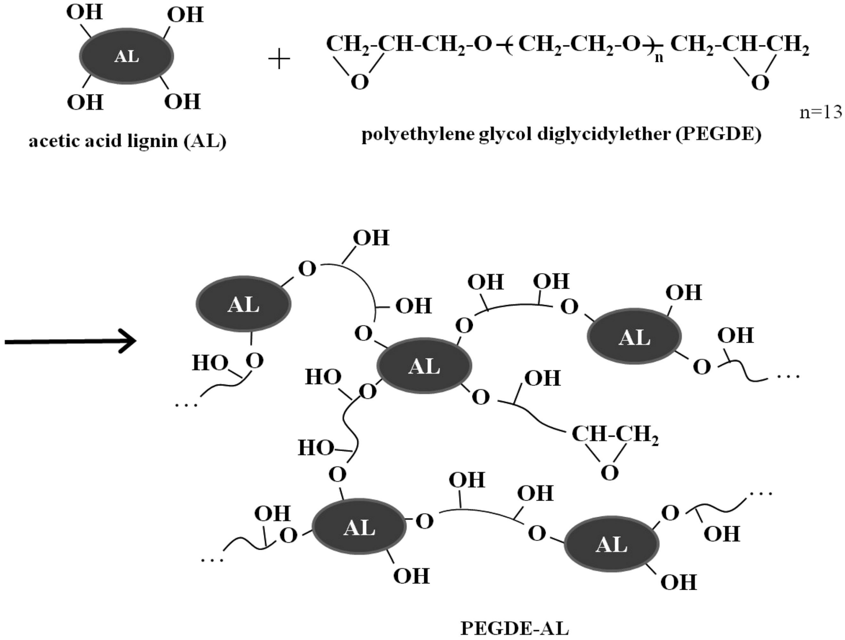
AL
acetic acid lignin (AL)
polyethylene glycol diglycidylether (PEGDE)
n=13
PEGDE-AL

Figure 3. Schematic image of PEGDE-AL as a typical amphiphilic lignin derivative.

Downloaded by UNIV OF GUELPH LIBRARY on August 28, 2012 | http://pubs.acs.org
Publication Date (Web): August 17, 2012 | doi: 10.1021/bk-2012-1107.ch013

Surface Activity of Amphiphilic Lignin Derivatives

Surface activity is the most important property of amphiphiles. It can be evaluated by measuring the surface tension of the aqueous solution at the water-air interface. Critical micelle concentration (CMC) and surface tension at CMC are important indicators of surface activity. Surface tension of water vs. concentration of various amphiphilic lignin derivatives is shown in Figure 4. The PEGs (typically shown as PEG 20,000 in Figure 4) and epoxidized PEGs such as PEGDE and EPEG on their own (only EPEG data shown in Figure 4) did not give clear CMC values, thus not showing any significant surface activity, although they lowered surface tension very slightly. Amphiphilic lignin derivatives, on the other hand, significantly lowered surface tension of water, giving distinct CMC values. It was concluded that derivatization of hydrophobic lignins with hydrophilic PEGs added high surface activity to the lignins.

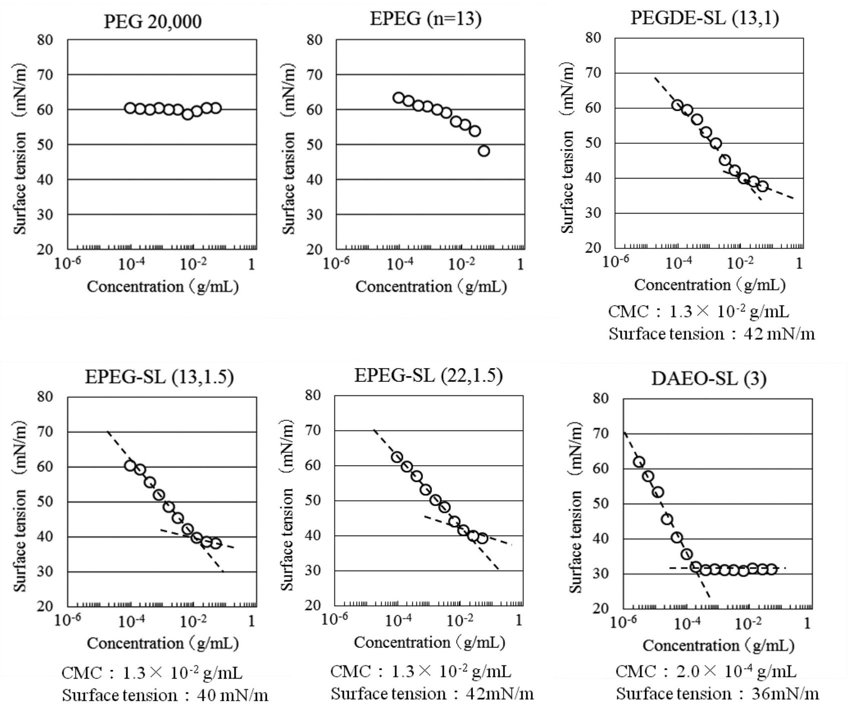

CMC：1.3× 10^{-2} g/mL
Surface tension：42 mN/m

CMC：1.3× 10^{-2} g/mL
Surface tension：40 mN/m

CMC：1.3× 10^{-2} g/mL
Surface tension：42mN/m

CMC：2.0× 10^{-4} g/mL
Surface tension：36mN/m

Figure 4. Isotherms of surface tension of water plotted against concentration of amphiphilic lignin derivatives. Surface tensions of water at CMC are indicated in caption. Numbers on left in parentheses indicate frequency of repeating units of ethylene oxide, while numbers on right indicate weight ratio of PEGs to lignin.

Downloaded by UNIV OF GUELPH LIBRARY on August 28, 2012 | http://pubs.acs.org
Publication Date (Web): August 17, 2012 | doi: 10.1021/bk-2012-1107.ch013

DAEO (compound C in Figure 2) has a surface activity on its own, as was expected from its structure which is composed of repeating units of hydrophilic ethylene oxide and hydrophobic methylene moieties. An amphiphilic lignin derivative from DAEO showed the highest surface activity among the three types of lignin derivatives examined. This result proved that technical lignin can successfully be converted to a surfactant with high surface activity by derivatization with DAEO, without losing surface activity of original DAEO (*11*).

Amphiphilic Lignin Derivatives as Cellulase-Aid Agents for Bioethanol Production

Amylase, a hydrolytic enzyme specifically cleaving α-1,4-glucan, is used for the production of first-generation bioethanol from food crops, such as maize and rice, as feedstock. Amylases are quite inexpensive enzymes. Second-generation bioethanol is produced from woody biomass (lignocellulosics). As first step of the bioethanol production, two saccharification options for cellulose are proposed; one is acidic hydrolysis, the other is enzymatic hydrolysis. In this century, the latter process based on cellulases, hydrolytic enzymes cleaving β-1,4-glucan, has drawn much attention (*13*, *14*). However, cellulases are still much more expensive than amylases. Therefore, improvement of cellulase activity and/or its reuse are matters of concern.

Immobilization is one of the possible ways to achieve repeated use of cellulase. However, a conventional enzymatic digestion system, where the enzyme is immobilized onto solid polymer support, is not suitable for cellulase, since the hydrolysis does not proceed efficiently, due to the solid-solid reaction between immobilized cellulase and a solid substrate like lignocellulosics. To solve that problem, a concept of water-soluble immobilized cellulase was proposed in 1980s to enhance the hydrolysis rate of a solid substrate (*15*). Furthermore, one of the main hindrances to use cellulase continuously over a long time at constantly high activity levels lies in an irreversible adsorption of cellulase onto the substrate. If woody biomass, consisting of the three major components cellulose, hemicellulose, and lignin, is used as a feedstock for enzymatic saccharification, careful attention should be paid to the adsorption behavior of cellulase not only onto cellulose, but also onto lignin. Cellulase strongly adsorbs on cellulose by their specific interaction, and on lignin by non-specific interactions (hydrophobic interactions) (*16*), which makes cellulase liberation from lignin-containing substrates very difficult.

We expected amphiphilic lignin derivatives to act as a water-soluble, immobilizing support of cellulase that enables repeated use of cellulase and to hinder the interaction between cellulase and substrate lignin. Our hypothetical mechanism is illustrated in Figure 5.

We have already reported the changes in the rate of enzymatic hydrolysis in the course of time (*17*), using Meicelase™ as a representative cellulase, unbleached pulp as a lignin-containing substrate, and an amphiphilic lignin derivative (PEGDE-AL) (*18*) as a cellulase-aid agent. Upon addition of the amphiphilic lignin derivative, the rate of hydrolysis was maintained at more than 80 % of the initial value after five times of usage. Without addition, the rate of hydrolysis was only 20 % or less. The initial hydrolysis rate in the presence of the lignin derivative was slightly larger than that without additives (*19*).

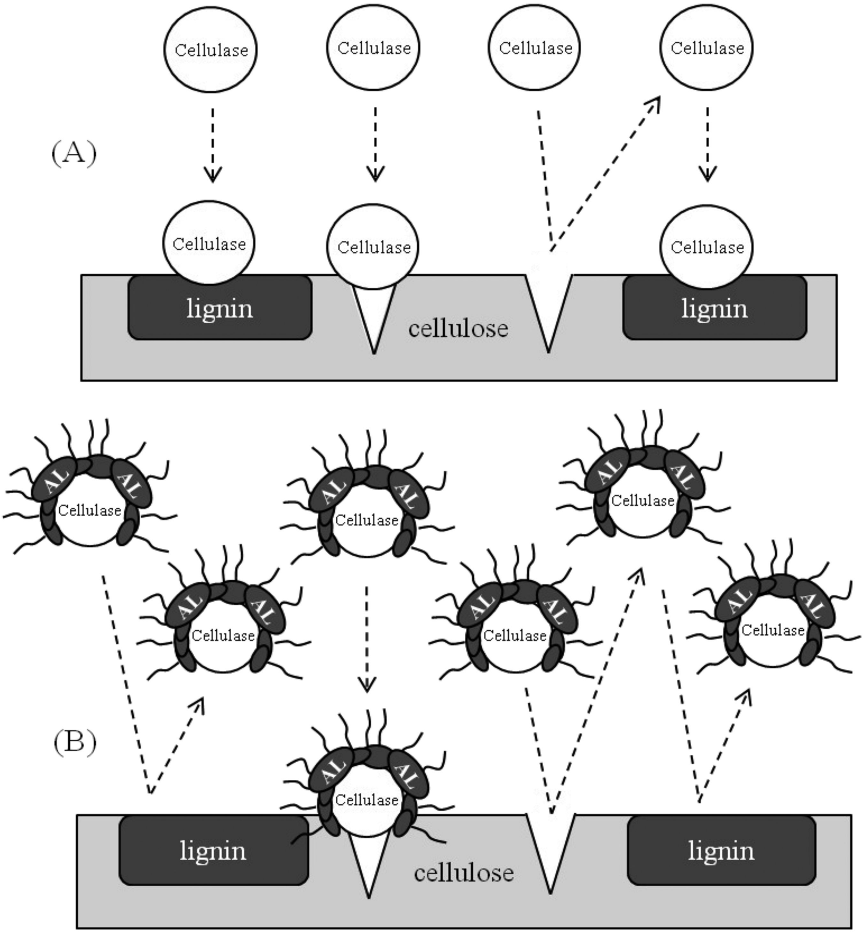

Figure 5. Mechanism of how an amphiphilic lignin derivative works as a cellulase-aid agent. (A); without addition, (B); with addition of PEGDE-AL.

We thought that the rate of enzymatic hydrolysis could be improved by using another lignin derivative having a higher surface activity and investigated the effect of other derivatives. In this research, unbleached cedar pulp prepared by soda pulping was used as a substrate. The pulp was furnished as a feedstock for bioethanol production by a project of Forest and Forest Products Research Institute, Tsukuba, Japan, under the sponsorship of Ministry of Agriculture,

Downloaded by UNIV OF GUELPH LIBRARY on August 28, 2012 | http://pubs.acs.org
Publication Date (Web): August 17, 2012 | doi: 10.1021/bk-2012-1107.ch013

Downloaded by UNIV OF GUELPH LIBRARY on August 28, 2012 | http://pubs.acs.org
Publication Date (Web): August 17, 2012 | doi: 10.1021/bk-2012-1107.ch013

Forestry and Fisheries Japan. Genencor GC220™ was used as the cellulase. Results are shown in Table 1. Both EPEG- and DAEO-based lignin derivatives showed significantly higher rates of hydrolysis than PEGDE-based derivative and control (no additive). Residual enzymatic activity is a more important factor in evaluation of repeated usage of cellulase. The residual activity was greatly improved by the addition of lignin derivatives, whereas it remained only at about 20 % without addition. The EPEG-based derivative caused the highest remaining activity (78.4 %). While the DAEO-based lignin derivative showed higher surface activity than EPEG-based lignin derivative (typically shown as in Figure 4), the latter had a larger effect on cellulosic hydrolysis. Our result thereby indicated that the effect of amphiphilic lignin derivatives on the enhancement of cellulase activity was not simply dependent upon their surface activities.

Table 1. Enzymatic hydrolysis of unbleached cedar pulp with a cellulase (Genencor GS220)

Additives	*Rate of hydrolysis*[1)] *(%)*	*Rate of hydrolysis*[2)] *(%)*	*Residual activity (%)*
PEGDE	54.8	61.2	24.9
PEGDE-AL	55.2	61.6	74.0
EPEG-AL	63.2	70.5	78.4
DAEO-AL	63.7	71.1	59.1
PEG 4.000	69.1	77.1	43.8
No additive	53.2	59.3	20.5

Table 1 also lists the result with PEG 4.000 as additive. A research paper reported in 2007 that a PEG with a molecular weight over 4.000 remarkably enhanced enzymatic hydrolysis (*16*). We examined PEG 4.000 in order to compare its effect with those of amphiphilic lignin derivatives. PEG 4.000 improved the rate of hydrolysis more significantly than the amphiphilic lignin derivatives we developed, but it also gave a lower residual activity than the amphiphilic lignin derivatives. This result suggests that PEG 4.000 and PEG-based lignin derivatives have different mechanisms in improving cellulase activity (*20*). In conclusion, we have successfully developed amphiphilic lignin derivatives to provide cellulase-aid agents that maintain hydrolytic activity of cellulase for a long period of time.

Cement Dispersants

LS, an anionic polyelectrolyte, is mainly used as a cement dispersant, which reduces water content of concrete, as described so far. It is considered that LS surrounds small particles of cement, and that electrostatic repulsion of anionic moiety of LS enables the cement particles to disperse effectively even at relatively low moisture content.

Downloaded by UNIV OF GUELPH LIBRARY on August 28, 2012 | http://pubs.acs.org
Publication Date (Web): August 17, 2012 | doi: 10.1021/bk-2012-1107.ch013

We investigated a variety of amphiphilic lignin derivatives in terms of cement dispersing capacity, and compared them with LS. We used soda lignin (SL) as a source for amphiphiles, which was recovered by spray drying of black liquor produced during soda pulping of Japanese cedar wood, as described in the former section.

Flow value (*Γ*) was used for evaluating the dispersing capacity. A typical procedure of flow value measurement was as follows: To an aqueous solution containing a given amount of a lignin derivative and other additives, cement was added and mixed vigorously for a prescribed time. The mixture was transferred to a cylindrical vessel on a glass plate. After the forming process, the vessel was removed and the mixture was allowed to develop on a glass plate. The diameter of the developed, round-shaped cement was measured and the flow value was calculated according to Japanese Industrial Standard (JIS R5201). The effect of cement admixture (dispersant) is typically shown in Figure 6.

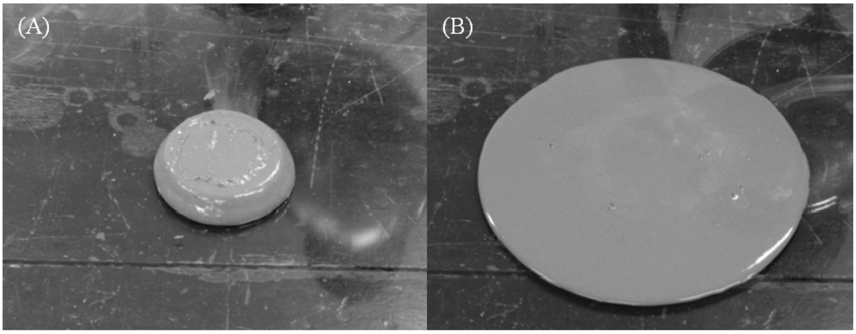

Figure 6. Effect of an amphiphilic lignin derivative as cement admixture on the flow behavior of cement paste. (A); without admixture, (B); with admixture.

Figure 7 gives flow values of lignin derivatives and LS at 20°C. The LS used was SANX P201™, kindly provided from Nippon Paper Chemicals Co. Ltd., Japan. EPEG-SL gives a higher flow value than LS. It is clear that EPEG-SL has an excellent dispersing capacity, although it is a non-ionic surfactant, but not an anionic surfactant like LS. DAEO-SL, however, shows even a lower dispersing capacity than LS. This result suggests that the surface activity of amphiphilic lignin derivatives does not directly correlate to their cement dispersing capacity.

Finally, the usefulness of the amphiphilic lignin derivatives in a cold region is discussed. In Hokkaido (northern part of Japan), daily highs are less than 10°C from late October to early May. It is important to develop cement dispersants that work in a cold environment, since house building is carried out in any season these days. We investigated the dispersing capacity at 6°C (Figure 8).

The dispersing capacity of LS did not depend on its concentration at low temperature, suggesting that LS cannot work effectively as cement dispersant under cold conditions. DAEO-based lignin derivatives did not work either, whereas EPEG-based lignin derivatives exhibited a dispersing capacity at 6°C which was just as high as at 20°C.

Downloaded by UNIV OF GUELPH LIBRARY on August 28, 2012 | http://pubs.acs.org
Publication Date (Web): August 17, 2012 | doi: 10.1021/bk-2012-1107.ch013

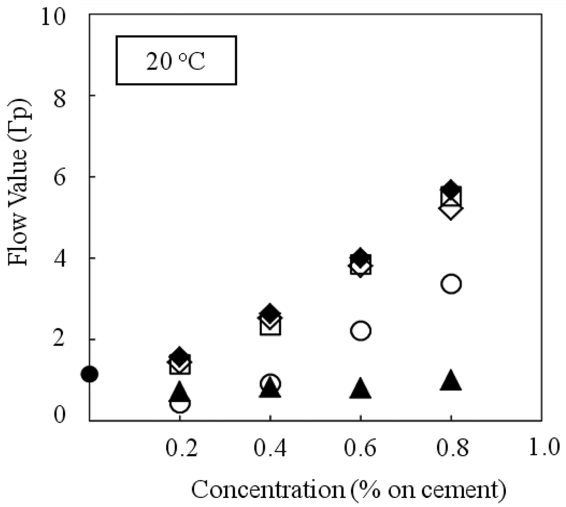

○; LS (SANX P201), □; PEGDE-SL (13,1), ◇; EPEG-SL (13,1.5), ◆; EPEG-SL (22,1.5), ▲; DAEO-SL (3).

Figure 7. Flow values at different concentrations of lignin-based cement dispersants at 20°C. Numbers on left in parentheses indicate frequency of repeating units of ethylene oxide, while numbers on right indicate weight ratio of PEGs to lignin.

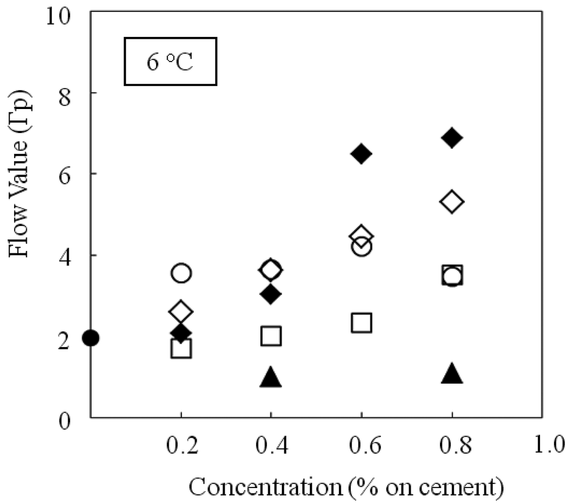

○; SANX P201, □; PEGDE-SL (13,1), ◇; EPEG-SL (13,1.5), ◆; EPEG-SL (22,1.5), ▲; DAEO-SL (3).

Figure 8. Flow values at different concentrations of lignin-based cement dispersants at 6°C. Numbers on left in parentheses indicate frequency of repeating units of ethylene oxide, while numbers on right indicate weight ratio of PEGs to lignin.

Conclusion

Amphiphilic lignin derivatives have several functions that conventional surfactants never exhibit. It is especially surprising that non-ionic EPEG-based lignin derivatives show a high cement dispersing capacity. It is our next target to investigate in more detail the interaction between amphiphilic lignin derivatives and cement particles, and the interaction between the amphiphiles and protein. In other words, it is important to clarify the host-guest chemistry pertaining to amphiphilic lignin derivatives, in order to fabricate lignin-derived materials carrying even higher functionality.

In our studies so far, the effectiveness of SL as a cellulase-aid agent has not been elucidated. But it is expected that SL-based lignin derivatives would probably exhibit positive effects on hydrolysis rate and/or residual activity of cellulase, as observed in AL- and KL-based lignin derivatives. Therefore, also SL, a wasteful by-product produced from soda pulping process as a pretreatment of cedar wood for ethanol production, could be converted to useful, multifunctional materials, which may reduce costs in the production of bioethanol significantly. We believe that these research works will help to establish a biorefining system to fully utilize woody biomass.

Downloaded by UNIV OF GUELPH LIBRARY on August 28, 2012 | http://pubs.acs.org
Publication Date (Web): August 17, 2012 | doi: 10.1021/bk-2012-1107.ch013

References

1. Shimomura, M. *NIPTEC Quarterly Review* 2010, No. 37, pp 54−75. http://www.nistep.go.jp/achiev/ftx/eng/stfc/stt037e/qr37pdf/STTqr3704.pdf (accessed October 14, 2011).
2. Henriksson, G. In *Pulp and Paper Chemistry and Technology, Vol. 1, Wood Chemistry and Wood Biotechnology*; Ek, M., Gellerstedt, G., Henriksson, G., Eds.; de Gruyter: Berlin, 2009; Ch. 6, pp 121−145.
3. Gierer, J. *Wood Sci. Technol.* **1980**, *14*, 241–266.
4. Gellerstedt, G. In *Pulp and Paper Chemistry and Technology, Vol. 1, Wood Chemistry and Wood Biotechnology*; Ek, M., Gellerstedt, G., Henriksson, G., Eds.; de Gruyter: Berlin, 2009; Ch. 8, pp 173−193.
5. Moseley, P. J.; Nelson, R. F.; Hollenkamp, A. F. *J. Power Sources* **2006**, *157*, 3–10.
6. Brezny, R.; Paszner, L.; Micho, M. M.; Uhrin, D. *Holzforschung* **1988**, *42*, 369–373.
7. Glasser, W. G.; Barnett, C. A.; Rials, T. G.; Saraf, V. P. *J. Appl. Polym. Sci.* **1984**, *29*, 1815–1830.
8. Matsushita, Y.; Yasuda, S. *Bioresour. Technol.* **2005**, *96*, 465–470.
9. Watanabe, M.; Meshitsuka, G.; Ishizu, A. *Mokuzai Gakkaishi* **1990**, *36*, 876–882.
10. Homma, H.; Kubo, S.; Yamada, T; Matsushita, Y.; Uraki, Y. *J. Wood Chem. Technol.* **2008**, *28*, 270–282.
11. Homma, H.; Kubo, S.; Yamada, T; Koda, K.; Matsushita, Y.; Uraki, Y. *J. Wood Chem. Technol.* **2010**, *30*, 164–174.
12. Magara, K.; Ikeda, T.; Nojiri, M. *Kami Pa Gikyoshi* **2010**, *64*, 493–499.
13. Nguyen, Q A. *Biotechnol. Agric. Ser.* **1993**, *9*, 321–340.

14. von Sivers, M.; Zacchi, G. *Bioresour. Technol.* **1996**, *56*, 131–140.
15. Wongkhalaung, C.; Kashiwagi, Y.; Magae, Y.; Ohta, T.; Sasaki, T. *Appl. Microbiol. Biotechnol.* **1985**, *21*, 37–41.
16. Börjesson, J.; Peterson, R.; Tjerneld, F. *Enzyme Microb. Technol.* **2007**, *40*, 754–762.
17. Uraki, Y.; Ishikawa, N.; Nishida, M.; Sano, Y. *J. Wood Sci.* **2001**, *47*, 301–307.
18. Uraki, Y.; Sano, Y.; Sasaya, T. *Kami Pa Gikyoshi* **1991**, *45*, 1018–1024.
19. Koda, K.; Kubo, S.; Uraki, Y. In *Sustainable Production of Fuels, Chemicals, and Fibers from Forest Biomass*; Zhu, J. Y., Zhang, X., Pan X., Eds.; ACS Symposium Series 1067, American Chemical Society: Washington, DC, 2011; Ch. 10, pp 261−277.
20. Bardant, T. B.; Oikawa, C.; Nojiri, M.; Koda, K.; Sudiyani, Y.; Yamada, T.; Uraki, Y. *Mokuzai Gakkaishi* **2010**, *56*, 420–426, in Japanese with English abstract.

Downloaded by UNIV OF GUELPH LIBRARY on August 28, 2012 | http://pubs.acs.org
Publication Date (Web): August 17, 2012 | doi: 10.1021/bk-2012-1107.ch013

Downloaded by STANFORD UNIV GREEN LIBR on August 28, 2012 | http://pubs.acs.org
Publication Date (Web): August 17, 2012 | doi: 10.1021/bk-2012-1107.ch014

Chapter 14

A Facile Approach for the Synthesis of Xylan-Derived Hydrogels

**Teresa C. Fonseca Silva,[1,2] Ilari Filpponen,[3] Youssef Habibi,[2]
Jorge Luiz Colodette,[1] and Lucian A. Lucia[*,2]**

**[1]Departamento de Química, Universidade Federal de Viçosa,
Viçosa, Minas Gerais 36570-000, Brazil
[2]Laboratory of Soft Materials & Green Chemistry, Department of Forest
Biomaterials (Wood & Paper Science), North Carolina State University,
Campus Box 8005, Raleigh, North Carolina 27695-8005
[3]Department of Forest Products Technology, School of Chemical Technology,
Aalto University, P.O. Box 16300, 00076 Aalto, Finland
[*]E-mail: lucian.lucia@ncsu.edu**

Xylan polysaccharides from *Eucalyptus urograndis* wood were obtained by controlled extraction processes to provide xylans with and without acetyl groups. Xylans extracted were characterized by NMR and subsequently used without previous modification to prepare xylan/poly(2-hydroxyethylmethacrylate)-based hydrogels in one-step by radical polymerization of hydroxyethylmethacrylate (HEMA). Heteronuclear NMR (HSQC) confirmed traces of lignin that were likely remnants of the LCC (Lignin Carbohydrate Complexes). The availability of double bounds localized in the remnant lignin functionalities from the delignification step with peracetic acid under mild conditions was the justification for the crosslinking. The hydrogels were produced at two composition ratios of xylan to HEMA (60:40 and 40:60) and further characterized by means of their morphology, swelling, and rheological properties. All hydrogels showed great homonogeneity, elasticity and softness, whereas the presence of acetyl groups caused reduced capacity for water uptake.

In Functional Materials from Renewable Sources; Liebner, F., et al.;
ACS Symposium Series; American Chemical Society: Washington, DC, 2012.

Keywords: xylans; hardwoods; hydrogels; renewable resources

Downloaded by STANFORD UNIV GREEN LIBR on August 28, 2012 | http://pubs.acs.org
Publication Date (Web): August 17, 2012 | doi: 10.1021/bk-2012-1107.ch014

Introduction

Hydrogels are three-dimensional stable networks formed from physically or chemically cross-linked hydrophilic polymers, forming insoluble polymeric materials that can absorb and retain water in a multiple-fold excess of the hydrogel mass (*1*, *2*). They have gained increasing attention over the last several years because of their attractive physico-chemical properties such as hydrophilicity, soft and rubbery consistency, high permeability to metabolites and oxygen, and resilience. Hydrogels closely resemble living tissues making them extremely suitable for a variety of applications in the pharmaceutical and biomedical fields. Furthermore, hydrogels have been exploited for diverse applications: in cartilage or tendons, in bio-adhesives, in membranes, as scaffolds for tissue engineering, as ocular lenses, and as drug delivery vehicles (*3–5*).

Natural polysaccharide-based hydrogels are currently showing potential application in the biomaterials field because of their tunable functionality, safety, biocompatibility, biodegradability, and high degree of swelling (*6*). We have demonstrated recently the overall richness and tunability of the delivery system based on the chemical functionality of xylan-based polysaccharides (*7*). Moreover, the morphological, rheological and swelling properties of this polysaccharide-based hydrogel biomaterial have been influenced by the acetyl groups present on the xylan backbone.

Although a number of polysaccharides have been investigated for hydrogel formulations, hemicelluloses have shown significant potential as a material resource for hydrogels preparation (*7*, *8*). Xylans are the most common hemicelluloses and are considered to be the major non-cellulosic cell wall polysaccharide component of angiosperms (*9*). Indeed, xylans' intrinsic structure exhibits a β-(1→4) linked D-xylosyl backbone with various side groups or chains anchored to the *O*-2 and/or *O*-3 of the xylosyl residues depending on the species and/or the extraction method. A sampling of the natural variety of xylan structures is shown in Figure 1. The side chains mainly consist of α-D-glucuronic acid, 4-*O*-methyl-α-D-glucuronic acid and several neutral sugar units (α-L-arabinofuranose, α-D-xylopyranose or α-D-galactopyranose). Among the common side groups are also acetyl groups, phenolic, ferulic and coumaric acids (*10*). Moreover, it has already been demonstrated that hemicelluloses associate with lignin (the famous Lignin-Carbohydrate Complexes or LCCs) by covalent linkages (*11–14*) which confers versatile physical and chemical characteristics to the xylans. Recent studies found that all lignin in wood exists chemically linked to polysaccharides, and chemical treatments are not always able to completely separate it from the LCC linkage and so the material properties of the polymeric hemicelluloses have not yet been fully exploited (*15*, *16*).

Downloaded by STANFORD UNIV GREEN LIBR on August 28, 2012 | http://pubs.acs.org
Publication Date (Web): August 17, 2012 | doi: 10.1021/bk-2012-1107.ch014

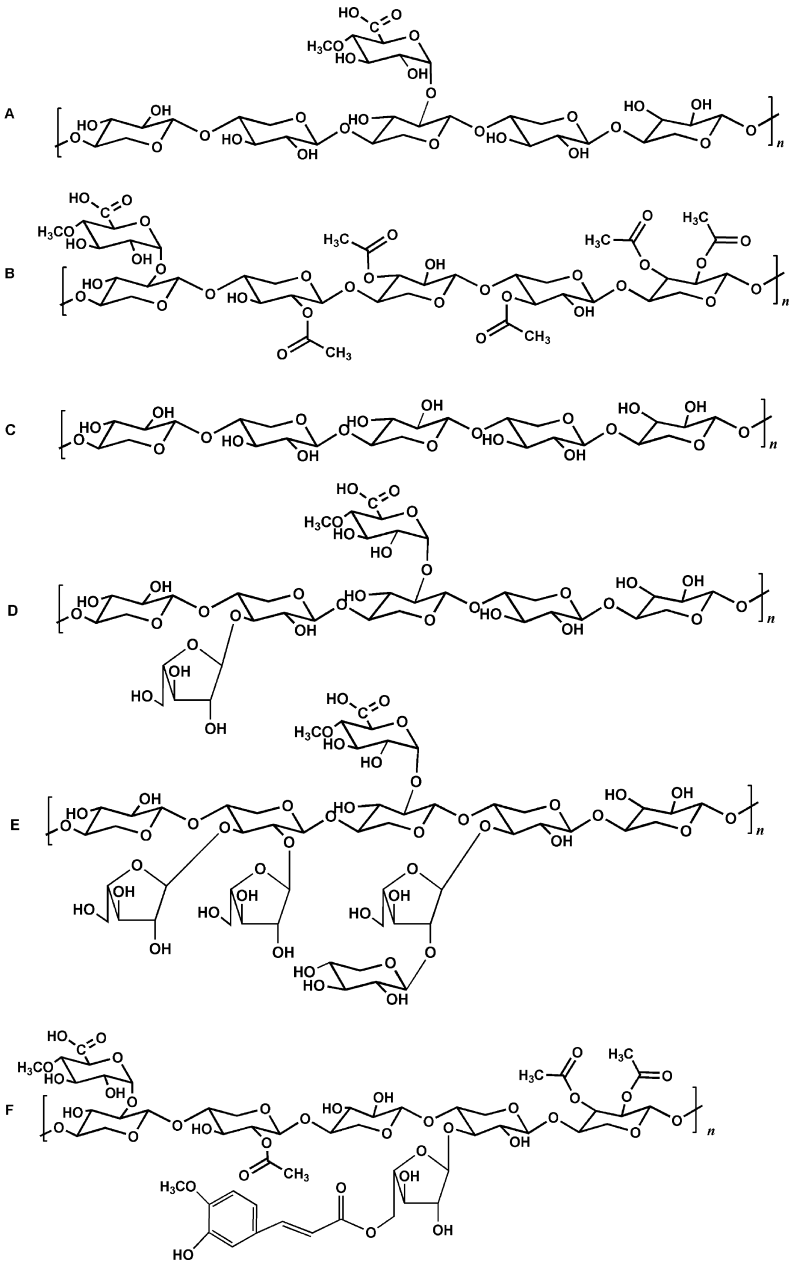

Figure 1. Examples of xylan structures presenting different side groups composition: A) methylglucuronic acid (MeGlcA), B) MeGlcA and acetyl groups, C) no side groups, D) MeGlcA and α-L-arabinofuranose (α-L-Araf), E) MeGlcA and α-L-Araf and β-D-Xylp-(1→2)-α-L-Araf and F) MeGlcA, acetyl groups and ferulic acid (FA) 5-linked to α-L-Araf.

Downloaded by STANFORD UNIV GREEN LIBR on August 28, 2012 | http://pubs.acs.org
Publication Date (Web): August 17, 2012 | doi: 10.1021/bk-2012-1107.ch014

Whereas many approaches to modify polymers or even use various synthetic polymers to develop advanced gels with tailored properties have been considered, xylans themselves appear to satisfy the requirement to produce advanced hydrogels because of their multi-branched structural architecture and water solubility, thus avoiding long and tedious processes to impart such functionality, as well as the necessity to employ organic solvents sometimes under severe conditions.

Based on the above considerations, a facile one-step hydrogel synthesis exploiting xylan, one of the most available renewable resources on the globe and a typical by-product from the wood industry, was performed without *a priori* grafting of vinyl groups applied in case of spruce hemicellulose by Lindblad et al. (*8*) by radical polymerization of 2-hydroxylethylmethacrylate (HEMA).

The aim of this work was therefore to produce xylan-based hydrogels in a facile approach, using as a raw material xylans extracted from *Eucalyptus urograndis*, by two different approaches to give xylans-based hydrogels with different structural features and potential functionality. The obtained hydrogels were characterized in terms of their morphology, swelling, and rheological properties.

Experimental Part

Materials

2-Hydroxyethylmethacrylate (HEMA, 99%), ammonium peroxodisulfate (98%), sodium perodisulfate (98%), sodium sulfate (99%), potassium hydroxide (99%), and hydrogen peroxide (30%) were all purchased from Sigma-Aldrich and used as received. Acetic acid (99.5%) was purchased from Acros Organics. Organic solvents (ethanol (99%), methanol (99%), and acetone (99.9%)) were all purchased from Sigma-Aldrich and used as received.

Isolation and Characterization of Xylan

The xylans used in this work were extracted from the hardwood *Eucalyptus urograndis*. First, extractives-free sawdust of wood samples was subject to delignification under the mild condition of 5% v/v peracetic acid (PAA) solution (pH 4.5) at 65°C for 30 minutes to yield *holocellulose*. PAA solution was prepared from acetic acid and hydrogen peroxide under cooling with an ice bath. Acetylated xylans were solvent-extracted under stirring from the holocellulose by DMSO for 12 hours at 50°C. Non-acetylated xylans were alkali-extracted with KOH solution 24% (w/v) for 24 hours at room temperature according to the literature (*7*).

Isolated xylans were characterized by sugar composition and HSQC NMR. Sugar compositions were determined by high performance liquid chromatography (HPLC) analysis after acid hydrolysis of the polymers. Xylans were first pre-hydrolyzed by 72% (w/v) sulfuric acid at room temperature for 2 hours followed by sulfuric acid-catalyzed (4% w/v) hydrolysis at 120°C for 1 hour (*17*). The resulting solutions were diluted to the desired concentration and filtered through a 0.2 μm nylon filter before chromatographic analysis. They were analyzed on a Dionex ICS 3000 IC system equipped with a CarboPac PA1 cartridge, an eluent generator (EG50), and an electrochemical detector (ED50). The mobile phase was 18 mM sodium hydroxide and all analyses were conducted at a column temperature of 25°C.

^{1}H and HSQC NMR spectra were recorded on an AC 500 MHz Bruker spectrometer at 30°C in a 5 mm tube in D_2O. Sodium 3-(trimethylsilyl)propionate-*d*4 was used as the internal standard (δ 0.00) and the operational parameters for the NMR acquisitions were set as reported previously (*18*, *19*).

Downloaded by STANFORD UNIV GREEN LIBR on August 28, 2012 | http://pubs.acs.org
Publication Date (Web): August 17, 2012 | doi: 10.1021/bk-2012-1107.ch014

Hydrogel Synthesis and Characterization

Xylan-based hydrogels were prepared from HEMA as the co-monomer and varying the weight ratio of xylan to HEMA (60:40 and 40:60). In a typical experiment, 225 or 100 mg of xylan was dissolved in 1.4 mL of deionized water. Then, 150 μL of HEMA was added and the resulting mixture was then thoroughly stirred for 2-3 minutes. 30 μL of water solutions of ammonium peroxodisulfate and sodium pyrosulfite, both at 2% (w/v) were added to initiate the cross-linking reaction and the solution was later transferred quickly to a cylindrical mold before gelation. The mold was sealed with Parafilm™ and the mixture was left at room temperature for at least 6 h before analysis. Scheme 1 represents the steps used for hydrogel production.

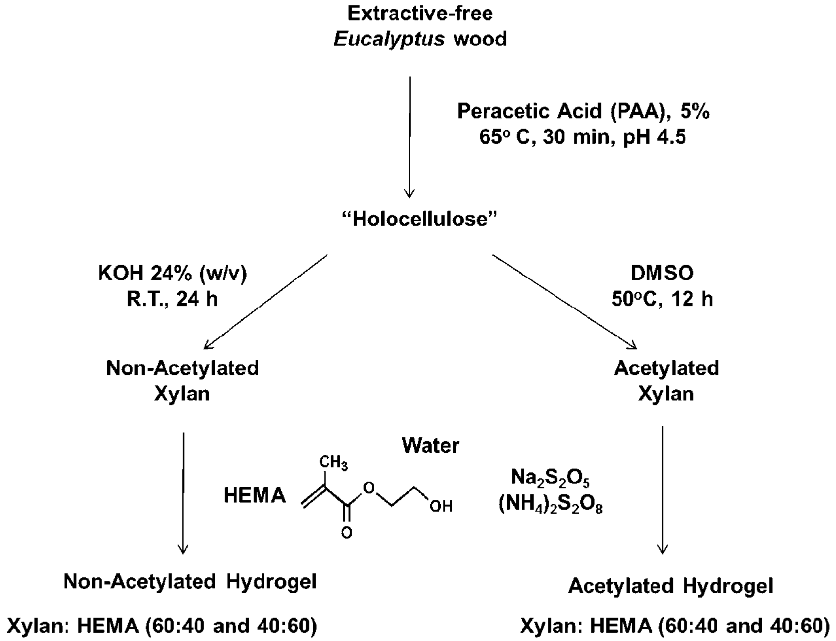
Extractive-free
Eucalyptus wood
Peracetic Acid (PAA), 5%
65° C, 30 min, pH 4.5
"Holocellulose"
KOH 24% (w/v)
R.T., 24 h
DMSO
50°C, 12 h
Non-Acetylated Xylan
Acetylated Xylan
Water
HEMA
CH3
O
OH
O
Na2S2O5
(NH4)2S2O8
Non-Acetylated Hydrogel
Xylan: HEMA (60:40 and 40:60)
Acetylated Hydrogel
Xylan: HEMA (60:40 and 40:60)

Scheme 1. Isolation of xylans from eucalyptus wood and preparation of xylan-based hydrogels.

Downloaded by STANFORD UNIV GREEN LIBR on August 28, 2012 | http://pubs.acs.org
Publication Date (Web): August 17, 2012 | doi: 10.1021/bk-2012-1107.ch014

The formed hydrogels were characterized according to their rheological properties, morphology, and swelling. Rheological measurements were performed on a StressTech model rheometer (Reologica Instruments) for determination of G' (shear storage modulus) and G" (shear loss modulus). Cylindrical discs (diameter = 8 mm and height = 4 mm) were cut from the hydrogels as prepared and the rheological properties of the formed hydrogels were tested at parallel plate geometry with a diameter of 8 mm. Dynamic frequency sweep test was performed at 25°C with each sample at 5% of strain within a frequency range from 10 to 0.1 Hz for both types of xylan-based hydrogels produced.

The morphology of the hydrogels was examined by field emission scanning electron microscopy (FE-SEM) using a JEOL 6400F microscope operated with an accelerating voltage of 5 kV, a working distance of 15 mm, and a 30 µm objective aperture. A small hydrogel sized sample was affixed onto a conductive carbon tape, mounted on the support, and then sputtered with an approximately 25 nm thick layer of gold/palladium (60/40).

Hydrogel swelling ratio measurements were performed by freeze-drying the gels and immersing them in deionized water at 37°C. At various times, the samples were withdrawn from the water medium and weighed. The swelling (Q_S), was calculated from: $Q_S=(W_s-W_d)/W_d$, where W_d is the weight of the dry gel before swelling and W_s is the swollen state weight.

Results and Discussion

Isolation and Characterization of Xylans

First, carbohydrate-rich material or *holocellulose* was extracted from *Eucalyptus urograndis* by treatment with PAA 5% for 30 minutes at 65°C and pH 4.5 as shown in Scheme 1. Mild delignification conditions were used to enable the isolation of xylans having preserved lignin-xylan bonds that can provide lignin double bonds to serve as an initiating point for hydrogel production. After the PAA delignification step, acetylated and non-acetylated xylans were obtained with DMSO at 50°C and potassium hydroxide 24% (w/v) at room temperature, respectively.

Xylans obtained were characterized by structure (^{1}H NMR and HSQC NMR) and sugar composition. As expected, the sugar composition showed a predominance of xylose for both types of extracts and minor amounts of other monosaccharides such as glucose, mannose, rhamnose, and galactose. In fact, the molar ratio of xylose to the other minor sugars detected was 0.82:0.18 for non-acetylated xylan and 0.87:0.13 for acetylated xylans, which is similar to previous results for xylans isolated from eucalyptus wood (*18*, *20*). The xylans obtained presented evidence of lignin contamination confirmed by NMR even after extensive purification from solubilization-reprecipitation and dialysis. Both the degree of acetylation and 4-*O*-methylglucuronic acid (MeGlcA) contents were determined by ^{1}H NMR to yield values that were approximately 0.61 and 0.10, respectively, which corroborated the values already published for other hardwood species (*21*). The value for MeGlcA was approximately the same for both xylans.

HSQC spectra are presented in Figure 2. Figure 2A refers to non-acetylated xylan as the acetyl group signal at ~ δ 2.0/20 ppm is absent. In both spectra, xylan main chains have shown characteristic signals between ~ δ 3.2 and 5.0 ppm in ^{1}H NMR, in accordance with previous work (*18*, *20*). The H/C cross-peaks in Figure 1A for the xylan backbone can be clearly identified together with the typical C-1, C-4 and MeO signals of MeGlcA in accordance with previous work (*18*, *22*). The variations in the spectrum (2B) are mainly due to presence of acetylated sugar units in accordance with the data of the former reported acetylated methylglucuronoxylan from eucalyptus wood (*18*, *19*). However, the signals between ~ 5.7 and 7.0 ppm clearly indicate olefinic protons likely due to the presence of lignin fragments attached to the xylan chain preserved and/or modified during the mild PAA delignification.

Indeed, the reaction between PAA and wood is relatively selective for lignin. As stated before, the spectra of both xylans differed in the carbohydrate region. However, differences were also seen between both spectra in the non-carbohydrate region. It is possible to detect the typical signals for guaiacyl (G) and syringyl (S) lignin units, which are typical of hardwood lignins. Several of the believed types of the linkage in lignin-carbohydrates complexes isolated from wood are presented in Figure 3 (*14*, *23*). These xylan structures are most likely found as components of the holocellulose; as such, their linkages persist once they are extracted with exception of ester linkages upon use of KOH 24% (w/v) as the extractant.

Modification of the side chain group of lignin by PAA is similar to that with hydrogen peroxide (α,β-unsaturated aldehydes, conjugated double bonds and α-carbonyl groups). Even though the mechanisms of the reactions between PAA and lignin have not yet been completely elucidated, it is known that double bonds can be created by reacting lignin substructures with PAA. Oxidative cleavage of the aromatic rings of the lignin generates lactones (Figure 4A) and open quinoid structures, such as muconic acid derivatives (Figure 4B) as well as maleic acids derivatives (Figure 4C). The latter may likely be formed from *p*-quinones generated by oxidation of syringyl and guaiacyl units (*24*). The formation of double bonds in the open quinoid structures are essential for the cross-linking when HEMA is used to produce xylan-based hydrogels.

Previous study on lignin compounds has identified vinyl-guaiacol and vinyl-benzene (Figure 4D) as products of a reaction in acidic reaction with hydrogen peroxide (*25*, *26*). Random reactions of carbohydrates with hydroxyl radicals also generate a degree of unsaturation and ketone thus promoting fragmentation of the carbohydrate main chain (Figure 4E).

HSQC spectra (Figure 2) corroborate the formation of unsaturated fragments as proposed in Figure 4. Signals observed at 5.9/100 ppm, 6.3/112 ppm for non-acetylated xylan (Figure 2A) and 5.9/100 ppm, 6.2/118 ppm for acetylated xylan (Figure 2B) were attributed to hydrogen linked to the double bond carbon.

Downloaded by STANFORD UNIV GREEN LIBR on August 28, 2012 | http://pubs.acs.org
Publication Date (Web): August 17, 2012 | doi: 10.1021/bk-2012-1107.ch014

Downloaded by STANFORD UNIV GREEN LIBR on August 28, 2012 | http://pubs.acs.org
Publication Date (Web): August 17, 2012 | doi: 10.1021/bk-2012-1107.ch014

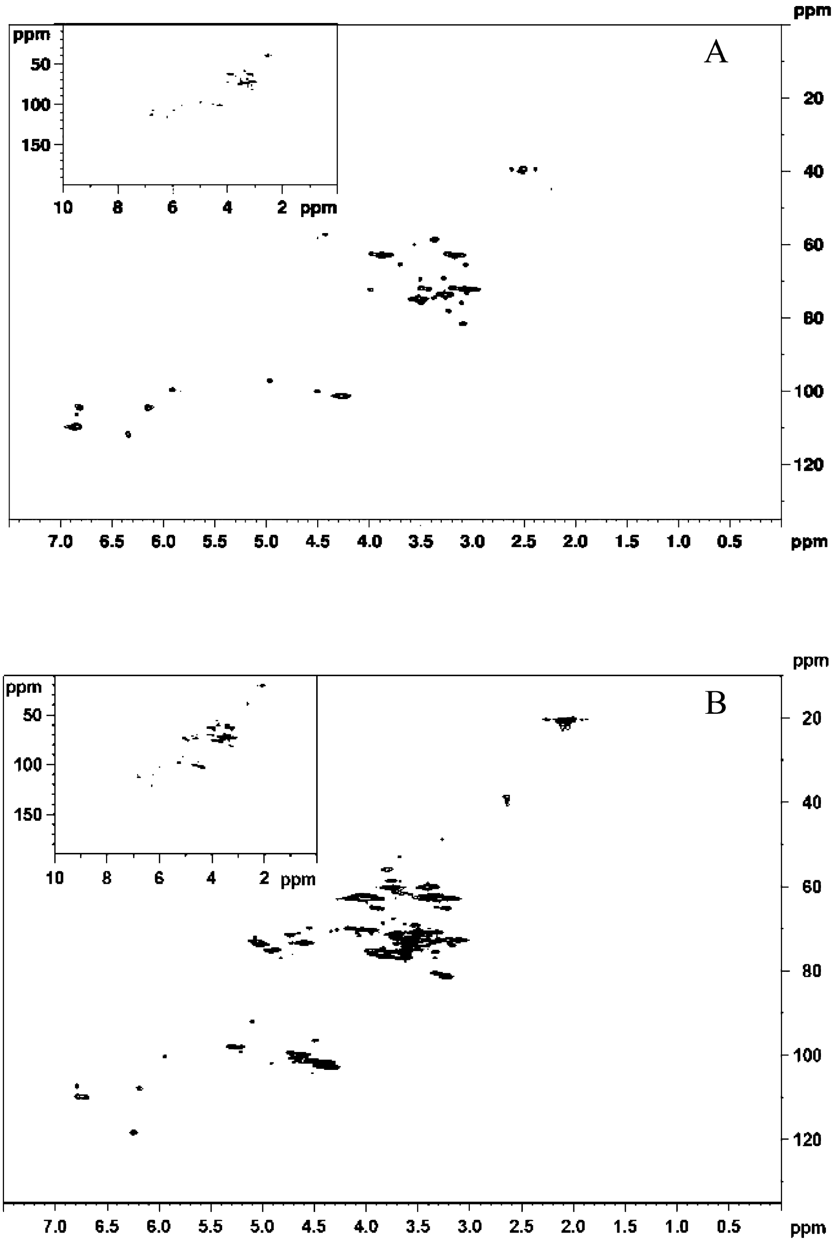

Figure 2. HSQC NMR spectra of xylans extracted from eucalyptus under mild conditions with PAA. A) non-acetylated xylan and B) acetylated xylan.

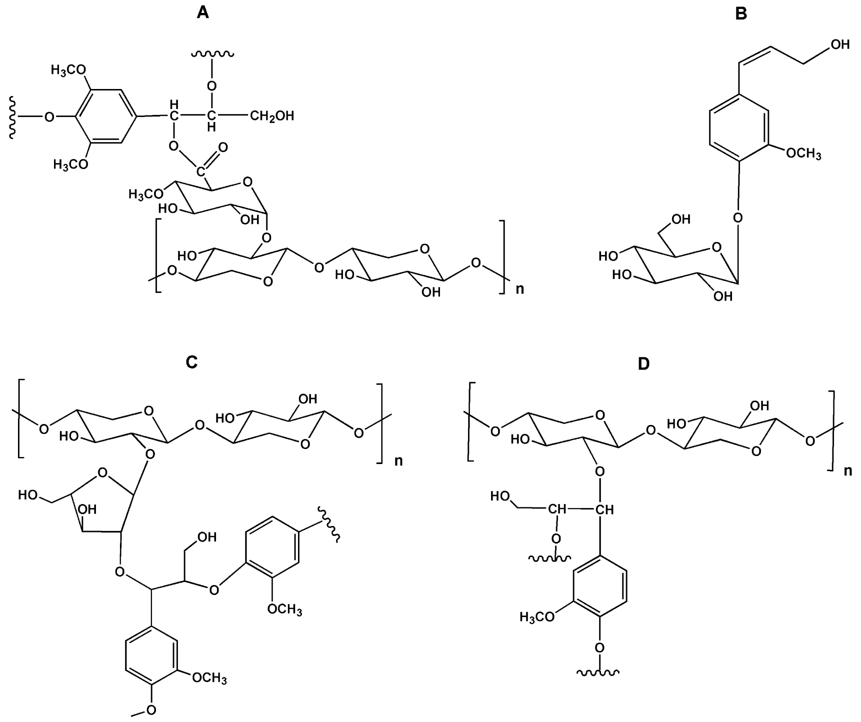

Figure 3. Main lignin-carbohydrate linkages: A) ester, B) phenyl glycoside, C) and D) benzyl ether.

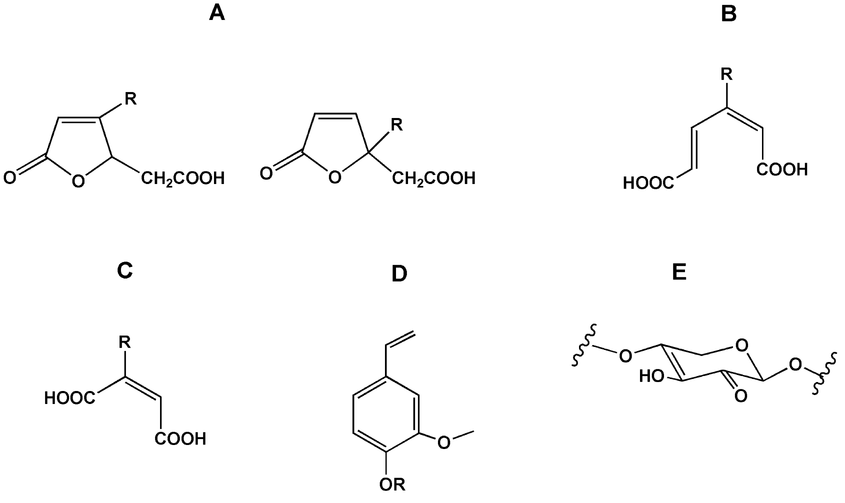

Figure 4. Conjectured products of the reaction of lignin (A-D) and carbohydrate (E) with PAA.

Downloaded by STANFORD UNIV GREEN LIBR on August 28, 2012 | http://pubs.acs.org
Publication Date (Web): August 17, 2012 | doi: 10.1021/bk-2012-1107.ch014

Downloaded by STANFORD UNIV GREEN LIBR on August 28, 2012 | http://pubs.acs.org
Publication Date (Web): August 17, 2012 | doi: 10.1021/bk-2012-1107.ch014

Preparation and Characterization of Xylan-Based Hydrogel

Both acetylated and non-acetylated xylans extracted from eucalyptus wood were used to produce four hydrogel samples with two weight ratios of xylan to HEMA (60:40 and 40:60). In general, hydrogels can be defined as a class of polymeric-based materials prepared by covalent and/or physical cross-links of polymers to form a 3D network (*26*). Furthermore, the presence of the additional reactive sites would be beneficial for further crosslinking. Therefore, the covalently linked fragments of lignin in the xylan chain would serve as junction points for subsequent use of HEMA as a co-monomer to further enhance the cross-linking and finally form a hydrogel without any modification in the xylan structure.

Morphology and Rheological Properties

The morphology of the produced hydrogels is presented in Figure 5. Both xylans (acetylated and non-acetylated) provide a rather homogeneous network, thus contributing to the elasticity of the network (*27*). The trapped water molecules are believed to hydrate and bind most of the hydrophilic sites, thus providing homogenous water distribution throughout the polymer matrix (*28*). Acetylated hydrogels provided more open structures with larger pores than their non-acetylated counterparts. It can be seen from Figure 5 that the network of the non-acetylated hydrogels contains rather small pores and agglomerates. One possible explanation might be the contribution of water molecules to such an entanglement-driven gelation in the case of more hydrophilic non-acetylated xylan (*7*). The ratio xylan:HEMA did not affect the morphology of the hydrogels and so, the ratio xylan:HEMA of 60:40 is displayed in Figure 5 in both cases.

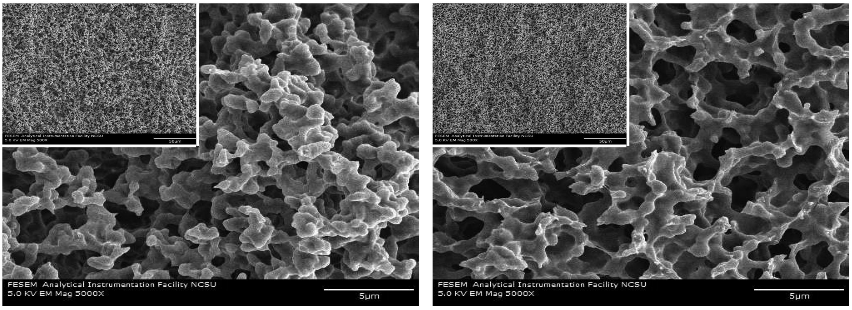
FESEM Analytical Instrumentation Facility NCSU
5.0 KV EM Mag 500X
50μm
FESEM Analytical Instrumentation Facility NCSU
5.0 KV EM Mag 5000X
5μm
FESEM Analytical Instrumentation Facility NCSU
5.0 KV EM Mag 500X
50μm
FESEM Analytical Instrumentation Facility NCSU
5.0 KV EM Mag 5000X
5μm

Figure 5. SEM images of xylan-based hydrogels with xylan to HEMA ratio of 60:40. (Left: non-acetylated xylans and right: acetylated xylans).

Rheological properties of the resulting hydrogels were studied as obtained from the reaction media at all different compositions (Figure 6). Results revealed higher values for the storage modulus G' than for the shear modulus G''over the entire frequency range. Therefore, all the prepared hydrogels have a more pronounced elastic versus viscous response. It is also important to note here that a frequency-independent behavior at lower frequencies was observed for all the hydrogels. This is a clear indication for the stable, cross-linked network. At higher frequencies, acetylated xylan-based hydrogels maintained this frequency-independent behavior, whereas hydrogels fabricated with non-acetylated xylans displayed an increase in the modulus, especially at xylan:HEMA ratio of 60:40. A s previously reported by our group (*7*), the reason for such behavior is related to a highly cross-linked polymer which would fail under stress and rapidly stiffen. Therefore, is reasonable to suggest that the extraction of xylans with sodium hydroxide may better maintain and/or form more available unsaturated sites compared to the extraction carried out with DMSO at 50°C.

Rheological properties of the xylan-based hydrogels are highly dependent on the presence of the acetyl groups on xylan. Hydrogels from acetylated xylan rendered approximately 10-fold increase in storage modulus at both ratios studied (40:60 and 60:40). One possible explanation might be the more open morphology of the acetylated xylan-based hydrogels enabling the formation of a mildly cross-linked network and a large free volume. Such structures are capable of instant and reversible response against external stresses with concomitant rapid rearrangement of the polymer segments. Consequently, acetylated hydrogels provided slightly higher stiffness when compared to their non-acetylated counterpart and therefore, more solid-like structures were obtained.

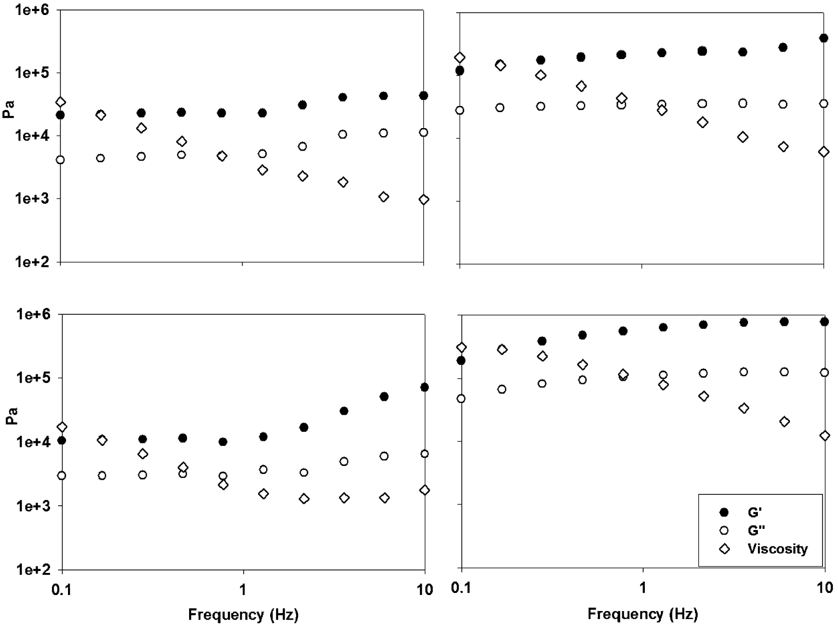

Figure 6. Rheological behavior of hydrogels based on non-acetylated (left) and acetylated xylans (right) with different xylan:HEMA ratios (top 40:60 and bottom 60:40).

Downloaded by STANFORD UNIV GREEN LIBR on August 28, 2012 | http://pubs.acs.org
Publication Date (Web): August 17, 2012 | doi: 10.1021/bk-2012-1107.ch014

Downloaded by STANFORD UNIV GREEN LIBR on August 28, 2012 | http://pubs.acs.org
Publication Date (Web): August 17, 2012 | doi: 10.1021/bk-2012-1107.ch014

Swelling Behavior

The cross-linking density of the network played an important role on the water uptake (swelling) of the hydrogels. Open structures, with elevated free volume contained more trapped water. The swelling ratio of the produced hydrogels was monitored from 0.25 to 24 hours of immersion in water at 37°C. Very stable hydrogels were obtained and no dissolution was observed for any of them. The swelling behavior of all the hydrogels produced from different types of xylans is presented in Figure 7. It can be seen that the swelling occurs very quickly with all the hydrogels (approximately in one hour) after immersion in water. Hydrogels based on the non-acetylated xylans trapped more water than their acetylated counterparts. In fact, the swelling ratio (Q_S) of the non-acetylated hydrogels is almost 2-fold those of the acetylated hydrogels. It can be postulated that the hydrophobicity induced by the acetyl groups to the hydrogels contributed to their diminished water uptake. In addition, the swelling is also affected by different xylan:HEMA ratios of the hydrogels. In both cases, a lesser amount of xylan (40%) in the hydrogels induced greater water uptake. However, this effect is more pronounced in the case of non-acetylated xylan-based hydrogels.

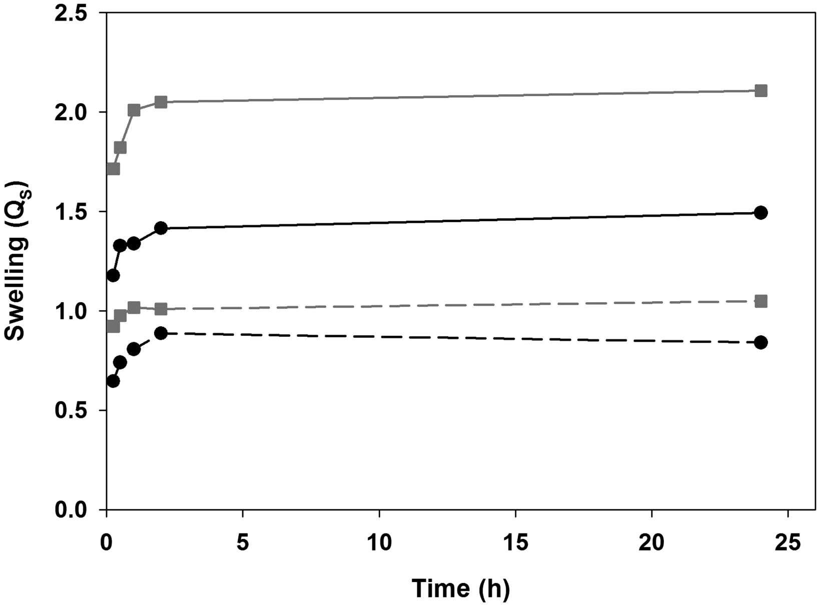

Figure 7. Variation of swelling ratios versus time of hydrogels based on non-acetylated (gray) and acetylated (black) xylans (solid line 40:60 and dashed line 60:40 of xylan:HEMA).

Conclusions

Hydrogels were successfully prepared from eucalyptus xylan (with and without acetyl groups) in a facile approach with methacrylic monomers in a standard radical polymerization. The presence of acetyl groups provided a more open hydrogel network, slightly stiffer hydrogels, and reduced their water swelling capacity.

A delignification step that was performed with PAA under mild conditions would likely generate double bonds in the lignin moieties present within the xylans previously extracted. Double bonds are essential for the formation of radicals which might act as the active sites for the cross-linking with HEMA as a co-monomer.

Downloaded by STANFORD UNIV GREEN LIBR on August 28, 2012 | http://pubs.acs.org
Publication Date (Web): August 17, 2012 | doi: 10.1021/bk-2012-1107.ch014

Acknowledgments

We would like to sincerely thank the *CNPq (Conselho Nacional de Desenvolvimento Científico e Tecnológico)* of Brazil for the generous provision of a research fellowship to TCFS that enabled large portions of this work to be completed. We would also like to thank Dr. Hanna S. Gracz for the expert assistance in executing the NMR experiments.

References

1. Jagur-Grodzinski, J. *Polym. Adv. Technol.* **2010**, *21*, 27.
2. Cai, W.; Gupta, R. B. Hydrogels. In *Kirk-Othmer Encyclopedia of Chemical Technology*, 5th ed.; Arza, S., Ed.; John Wiley & Sons, Inc: Hoboken, NJ, 2005; p 729.
3. Hoare, T. R.; Kohane, D. S. *Polymer* **2008**, *49*, 1993.
4. Pal, K.; Banthia, A. K.; Majumdar, D. K. *Des. Monomers Polym.* **2009**, *12*, 197.
5. Slaughter, B. V.; Khurshid, S. S.; Fisher, O. Z.; Khademhosseini, A.; Peppas, N. A. *Adv. Mater.* **2009**, *21*, 3307.
6. Oh, J. K.; Lee, D. I.; Park, J. M. *Prog. Polym. Sci.* **2009**, *34*, 1261.
7. Silva, T. C. F.; Habibi, Y.; Colodette, J. L.; Lucia, L. A. *Soft Matter* **2011**, *7*, 1090.
8. Lindblad, M. S.; Ranucci, E.; Albertsson, A.-C. *Macromol. Rapid Commun.* **2001**, *22*, 962.
9. Stephen, A. M. Other Plant Polysaccharides. In *The Polysaccharides*; Aspinall, G. O., Ed.; Academic Press: Orlando, FL, 1983; p 98.
10. Wilkie, K. C. B. *Adv. Carbohydr. Chem. Biochem.* **1979**, *36*, 215.
11. Gellerstedt, G.; Majtnerova, A.; Zhang, L. *C. R. Biol.* **2004**, *327*, 817.
12. Takahashi, N.; Koshijima, T. *Wood Sci. Technol.* **1988**, *22*, 231.
13. Laine, C.; Tamminen, T.; Hortling, B. *Holzforschung* **2005**, *58*, 611.
14. Fengel, D.; Wegener, G. *Wood Chemistry, Ultrastructure, Reactions*; Walter De Gruyter, Inc.: Berlin, 1984; p 167.
15. Lawoko, M.; Henriksson, G.; Gellerstedt, G. *Holzforschung* **2006**, *60*, 162.
16. Gabrielii, I.; Gatenholm, P. *J. Appl. Polym. Sci.* **1998**, *69*, 1661.

17. Ehrman, T. Method for Determination of Acid-Soluble Lignin in Biomass. In *Laboratory Analytical Procedures*; National Renewable Energy Laboratory: Golden, CO, 1996; p 004.
18. Evtuguin, D.; Tomás, J.; Silva, A. S.; Neto, C. *Carbohydr. Res.* **2003**, *338*, 597.
19. Shatalov, A. A.; Evtuguin, D. V.; Pascoal Neto, C. *Carbohydr. Res.* **1999**, *320*, 93.
20. Magaton, A. S.; Piló-Veloso, D.; Colodette, J. L. *Quím. Nova* **2008**, *31*, 1085.
21. Teleman, A.; Lundqvist, J.; Tjerneld, F.; Stålbrand, H.; Dahlman, O. *Carbohydr. Res.* **2000**, *329*, 807.
22. Balakshin, M. Y.; Capanema, E. A.; Chang, H.-m. *Holzforschung* **2007**, *61*, 1.
23. Koshijima, T.; Watanabe, T. *Association between Lignin and Carbohydrates in Wood and Other Plant Tissues*; Springer-Verlag: Berlin, 2003.
24. Brasileiro, L. B.; Colodette, J. L.; Piló-Veloso, D. *Quím. Nova* **2001**, *24*, 819.
25. Zhu, T.; Kadla, J. F.; Chang, H. m.; Jameel, H. *Holzforschung* **2005**, *57*, 44.
26. Kishimoto, T.; Kadla, J. F.; Chang, H. m.; Jameel, H. *Holzforschung* **2005**, *57*, 52.
27. Hoffman, A. S. *Adv. Drug Delivery Rev.* **2002**, *54*, 3.
28. Qu, X.; Wirsén, A.; Albertsson, A. C. *Polymer* **2000**, *41*, 4589.

Downloaded by STANFORD UNIV GREEN LIBR on August 28, 2012 | http://pubs.acs.org
Publication Date (Web): August 17, 2012 | doi: 10.1021/bk-2012-1107.ch014

Downloaded by COLUMBIA UNIV on August 28, 2012 | http://pubs.acs.org
Publication Date (Web): August 17, 2012 | doi: 10.1021/bk-2012-1107.ch015

Chapter 15

Moisture Vapor Barrier Properties of Biopolymers for Packaging Materials

Rashi Grewal, Whitney Sweesy, Jesse S. Jur, and Julie Willoughby*

College of Textiles, Fiber and Polymer Science Program,
The Nonwovens Institute, North Carolina State University,
Campus Box 8301, 2401 Research Drive,
Raleigh, North Carolina 27695-8301
***E-mail: jacrowe@ncsu.edu**

We present a review of current research focused on the use of biopolymers as viable packaging materials. We discuss polysaccharides, proteins, lipids, materials systems comprising edible coatings, and inorganic surface modification processes as they impact moisture barrier permeability properties. We give an overview of the fundamental factors that affect moisture vapor permeability (MVP), provide an overview of barrier properties for typical packaging materials on a common unit basis, and the MVP improvements made with evolving techniques. We explore some challenges and unknowns with surface modifications specific to altering the barrier properties of polymers derived from renewable resources. We provide some of the future directions in our own work to improve materials with inherently poor moisture vapor properties using the insights from this review as a road map.

Introduction

The advancements in packaging materials have afforded protection, freshness, extended shelf life, and convenience for food industry products. Food packaging platforms comprise flexible plastics, durable plastics, paperboard, synthetic coating systems, foil, and combinations thereof. The material selection depends on shelf life requirements and storage conditions as dictated by the industry sector.

In Functional Materials from Renewable Sources; Liebner, F., et al.;
ACS Symposium Series; American Chemical Society: Washington, DC, 2012.

Components of a packaging system comprise the substrate, or materials of construction, and the conversion to final form (such as bag, cup, box, or jug). Packaging systems for consumable goods are divided into flexible or durable goods with function dependent of serving either primary (direct food contact) or secondary protection. The focus of this chapter lies in an assessment of the current state of research for polymers from renewable resources targeted for use in food/ or consumable goods primary packaging.

Understanding the potential of renewable polymers for primary food packaging requires integration of both the shelf life of a package and the product performance requirements. Barrier properties of interest are grease or oil resistance, oxygen transfer rates, moisture resistance or impermeability, and UV protection. Moving into the realm of sustainable packaging, however, requires the use of materials with inherently poor moisture vapor barrier properties. We seek to give an understanding of the state-of-the-art in new materials and techniques to eliminate this challenge for sustainable packaging. In addition, we provide an overview of testing methodology and governing factors for moisture vapor permeability properties in materials.

Downloaded by COLUMBIA UNIV on August 28, 2012 | http://pubs.acs.org
Publication Date (Web): August 17, 2012 | doi: 10.1021/bk-2012-1107.ch015

Requirements of the Consumable Good Products Food Packaging

With the trend towards environmentally friendly products comes a desire for such materials to be used for packaging. Typical commercial polymers that are used for packaging, such as polyethylene terephthalate (PET), are not so environmentally friendly, but are very good packaging materials because of their low moisture vapor permeability (MVP). MVP and oxygen permeability (OP) are key packaging parameters for protecting the product contents. For food packaging, products need to be able to last from their initial creation to shelves in a store to customer purchase to consumption. Shelf life (*1*)θ_s is defined as

$$\theta_s = \frac{b}{\Omega p_o} ln\left(\frac{m_e - m_i}{m_e - m_c}\right) \qquad (1)$$

where m_e is the equilibrium moisture of the food at the RH outside the package, m_i is the initial moisture within the food, m_c is the critical moisture at which the food has reached its shelf life, Ω is a constant from packaging parameters, p_0 is the vapor pressure at storage temperature, and θ_s is the time elapsed or shelf life.

MVP and OP affect the Ω value specific to package design. Flat substrate testing of MVP and OP barrier properties are normally implemented to screen new materials for a given application. This is especially true in lack of a converting facility to trial the material in a package. Ultimately, the true shelf life of a material needs to be determined in package format with respect to barrier properties.

Benchmark Packaging Systems

Sustainable packaging includes the use of recyclable materials such as laminated flexible packaging and coated paperboard. The plastics industry is seeing a growth spurt from investors and research, largely because of the versatility of plastics. They can be molded into various shapes, which is beneficial from both a practical and commercial standpoint (*2*). Also a plus for plastics are their thermal stability at high temperatures, and coating methods, such as plasma treatment, that are used to make them stronger (*3*). The flexible packaging industry has been doing well despite difficult economic times, largely because of environmental concerns. Flexible packaging materials do not take up as much space in landfills thus help to alleviate the growing concern about excess packaging (*4*). Current research is focused on designing laminated foils and films that allow food to have extended shelf lives; a plus for flexible packaging and food industries (*4*). Figure 1 depicts the barrier properties for commonly used packaging materials both from synthetic resources and renewable resources (*5–9*). Barrier coatings on materials such as paperboard are becoming more popular enabling lower extruded "plastic" coat weights with more rigidity than the plastic layer alone. While coating paperboard involves an extra processing step, coatings enhance the overall package through appearance and protection (*10*). Specific to paperboard packaging, its construction comprises approximately 80% of materials from renewable resources. Figure 2 shows the cross-section of barrier paperboard where the polymer layers are poly(lactic acid) (PLA) instead of traditional low-density poly(ethylene) (LDPE). The substrate in Figure 2 is the bottom-stock of a EcoProducts® hot cup, a paperboard cup lined with approximately 33 microns of PLA. Replacing packaging materials with "greener" materials, such as PLA, has resulted in widespread evaluation for improving its mechanical and physical properties.

While PLA is a good choice for food packaging as any of the residual monomer, lactide, hydrolyzes into FDA-approved lactic acid (*11*), has acceptable mechanical properties at appropriate levels of crystallinity (*12*), it also has inherently high MVP properties and is brittle. Yang et al. attempted to improve tensile modulus by compounding PLA with triallyl isocyanurate and dicumyl peroxide. As Figure 3 depicts this material modification resulted in increased brittleness, or lower fracture toughness (*13*).

The problem with most polymers from renewable resources is that while they are "green" materials with low oxygen permeability, their moisture vapor permeability is an order of magnitude higher than those of commercial polymers such as PE and PET (*14*). This has resulted in utilizing PLA in applications which do not have extended shelf-life requirements (*15*). Thus it becomes necessary to determine ways to decrease the MVP of such polymers so that they can be of the same caliber as their current commercial counterparts. The exception to this rule is for the emerging "bio"-polyesters, poly(hydroxyalkanoate) (PHA) and especially poly(glycolic acid) (PGA), which have barrier properties equivalent to poly(ethylene terephthalate) (PET). Due to the absent pendant methyl group in PGA as compared to PLA, it has better OP and MVP properties due to its

Downloaded by COLUMBIA UNIV on August 28, 2012 | http://pubs.acs.org
Publication Date (Web): August 17, 2012 | doi: 10.1021/bk-2012-1107.ch015

inherently better intermolecular chain packing ability. When the price-volume point for PGA or PHA is the equivalent of PLA, they will be serious contenders for use in packaging applications (*7*, *9*, *16*).

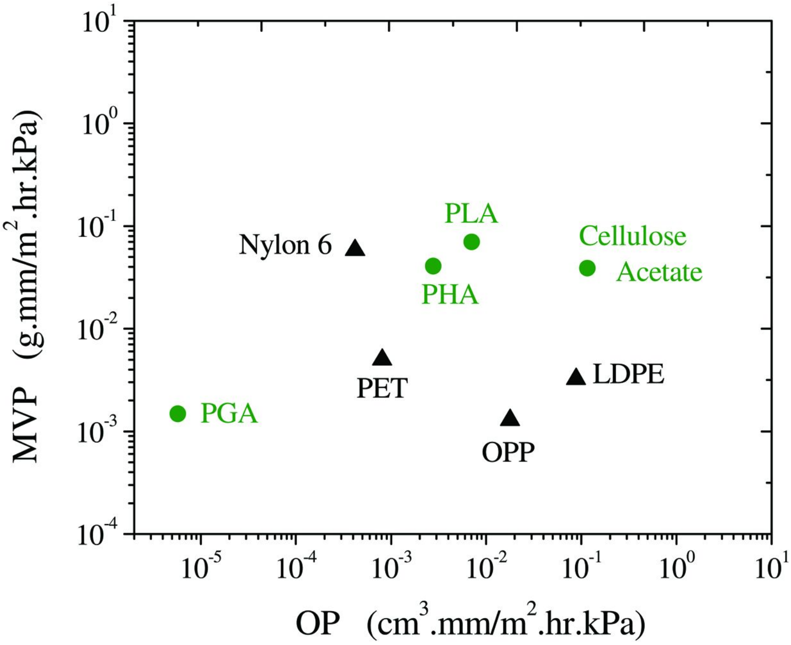

Figure 1. Moisture vapor (MVP) and oxygen (OP) permeability of common packaging polymers where polymers from renewable resources (green circle) have higher MVP, except PHA, than the synthetic polymers (black triangle). MVP tested at 90% RH and 38°C for all polymers and OP at 23°C and 0% RH, except for Cellulose Acetate at 35 °C and 0% RH. Data from references (5–9).

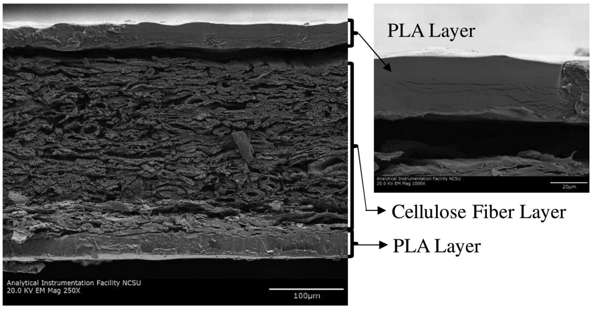
PLA Layer
Cellulose Fiber Layer
PLA Layer
Analytical Instrumentation Facility NCSU
20.0 KV EM Mag 250X
100μm
Analytical Instrumentation Facility NCSU
20.0 KV EM Mag 1000X
20μm

Figure 2. Scanning electron microscopy (SEM) cross-section of extrusion coated paperboard at 250X and 1000X magnification. The paperboard sample was EcoProducts® coffee cup bottom stock. The polymer layer(s) are poly(lactic acid) (PLA).

Downloaded by COLUMBIA UNIV on August 28, 2012 | http://pubs.acs.org
Publication Date (Web): August 17, 2012 | doi: 10.1021/bk-2012-1107.ch015

Downloaded by COLUMBIA UNIV on August 28, 2012 | http://pubs.acs.org
Publication Date (Web): August 17, 2012 | doi: 10.1021/bk-2012-1107.ch015

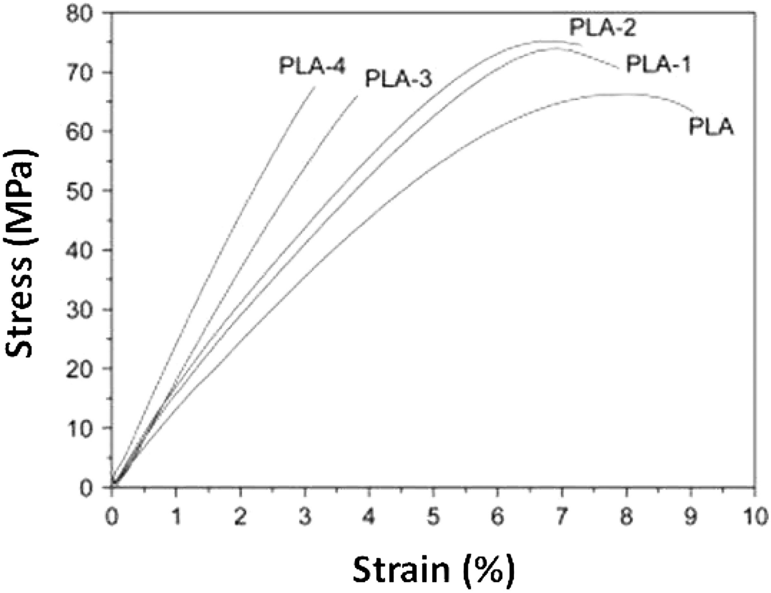

Figure 3. Stress-strain curves of PLA samples containing different amounts of crosslinker. Crosslinker content for samples PLA-4, PLA-3, PLA-2, PLA-1 are 3 wt%, 1.0 wt%, 0.5 wt %, and 0.15wt % as compared to non-crosslinked PLA. Reproduced with permission from reference (13). Copyright 2011 Elsevier.

Fundamentals of Moisture Vapor Permeability

Terminology and Units

Moisture vapor transport is the movement of moisture, or water, vapor through a material or medium. The moisture vapor permeability (MVP) of a material is determined by measuring its moisture vapor transfer rate (MVTR). Throughout this chapter we will invoke both MVP and MVTR terms for materials. As MVP is normalized for thickness, it is the MVTR of a packaging structure which really dictates its shelf life. It is a measurement used intensively in the field of packaging and barrier design, such as for packaging and containers for food, or military equipment. MVTR is of high importance because it allows one to determine the rate of moisture flow, and of even more significance, how this rate can be altered or controlled depending on storage conditions. For instance, one may choose a moderate MVTR for contact lenses, so that the eyes can remain moisturized, but a lower MVTR for firefighter clothing, to ensure dryness under the intense conditions of putting out a fire. MVTR is defined below by Equation 2 (*17*).

$$MVTR\ (\frac{\mathrm{g}}{\mathrm{m}^2 \cdot \mathrm{hr}}) \equiv \frac{mass}{surface\ area \cdot time} \qquad (2)$$

Downloaded by COLUMBIA UNIV on August 28, 2012 | http://pubs.acs.org
Publication Date (Web): August 17, 2012 | doi: 10.1021/bk-2012-1107.ch015

where *mass* is the weight pickup of water absorbed by a medium at any given *time*. The *surface area* is the amount of sample exposed to the permeating moisture vapor. Moisture vapor permeability *MVP* is defined as

$$MVP\ (\mathrm{g} \cdot \frac{\mathrm{mm}}{\mathrm{m}^2 \cdot \mathrm{hr} \cdot \mathrm{kPa}}) = MVTR \cdot \frac{l}{\Delta p} \qquad (3)$$

where l is the sample thickness and Δp is the pressure drop across the sample or

$$\Delta p\ (kPa) = V^{sat} \cdot (RH_2 - RH_1) \qquad (4)$$

where V^{sat} is the saturation pressure at test conditions, RH_2 is the relative humidity in the test chamber, and RH_1 is the relative humidity in the sample container.

Governing Factors of MVTR

There are several factors that determine the MVTR of a material. In a review by Morillon et al., the importance of film thickness was explained to dictate the transfer rate of moisture vapor as for thinner films there is shorter travel distance. The works of various groups were described in this review, and if the thickness of a film is increased between a certain range, on the order of microns, the transfer rate and permeability will both decrease (*18*). Hu et al. found that beyond a critical film thickness for poly(ethylene oxide) MVTR was unaffected (*19*). Another study obtained results showing that for methylcellulose films up to 100 microns thick, the MVTR decreased noticeably as the thickness of the films increased (*20*). These results were also shown by Martin-Polo et al., who found that for hydrophobic paraffins, their ability to act as a moisture barrier largely depended on film homogeneity and thickness (*21*)

A study by Debeaufort et al. found that the polarity and homogeneity of a material influence its MVTR. In their work, they found that hydrophilic, heterogeneous materials had a higher MVTR (*20*, *22*). The hydrophilic material attracts water increasing the MV solubility and enhancing permeability. The influence of heterogeneity allows for high moisture transport through material defects or hydrophilic regions.

Due to their hydrophilicity, certain plasticizers have been shown to increase MVTR (*23*). Figure 4 depicts a study where starch-based nanocomposites comprised thermal transitions dependent on the plasticizer type (*23*). The plasticizers under evaluation were sorbitol, glycerol and Polysorb® brand. At any given clay loading in the composite, the use of sorbitol resulted in a higher glass transition temperature. In addition, thermo-mechanical testing indicated a slight decrease in mechanical properties due to poor dispersion or exfoliation of the nanoclays in the sorbitol formulations. This conversely related to phase separation. It would be expected that these discontinuities in the nanocomposite would have an adverse effect on barrier properties. Two separate groups, led by Laohakunjit and Cao, found that glycerol, a hydrophilic plasticizer of small molecular size, increased the MVTR of rice films and gelatin films, respectively.

While the plasticizer increased the non-recoverable deformation of the films, it also increased their affinity for water, thus increasing MVTR (*24*, *25*). Film crystallinity affects MVTR as crystallites impede the transport of moisture. It was shown in one study that the MVTR of crystalline poly(lactic acid) was over 50% lower than its amorphous counterpart. It was also demonstrated that hydrophobic polymers, such as polyester, had a lower MVTR than did the more hydrophilic ones such as cellulose (*26*). The crystalline regions in a film are denser than the amorphous regions and more resistant to the passage of water. Hence high film density decreases MVTR (*27*).

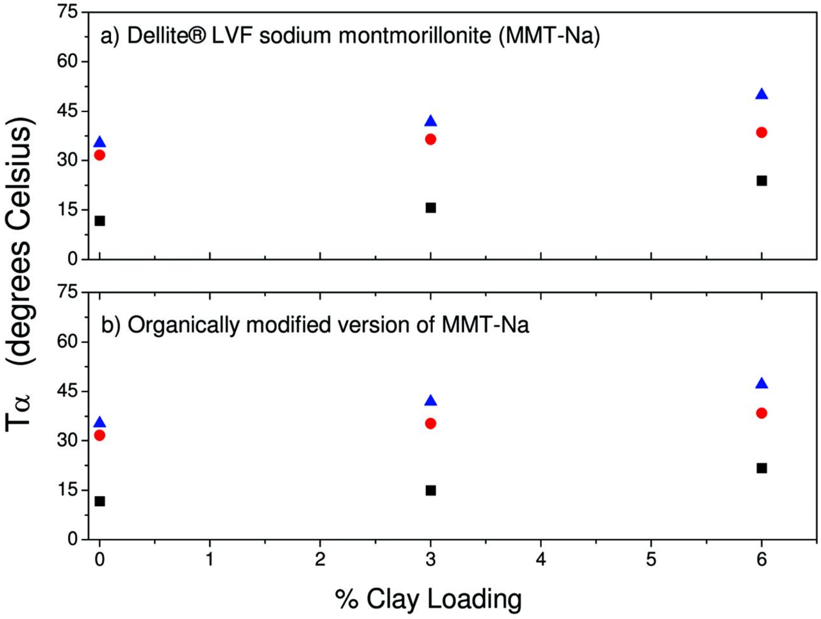

Figure 4. Effect of plasticizer on temperature transition T_α of wheat starch/ clay nanocomposites with various plasticizers; (black square, glycerol; red circle, Polysorb ®; and blue triangle, sorbitol). Data from reference (23).

Test Methodology

Different experiments will use different conditions, depending on the type of environment in which a barrier material is supposed to survive. Since the test is to see how well a barrier can keep out moisture, we implement standard tropical conditions of 38°C and 90% relative humidity (RH) (*28*). With Equation 1 given above, we use a Mason jar apparatus to measure MVTR through a given material (cf. Figure 5). We evaluated two types of desiccant; $CaSO_4$ and silica gel. The $CaSO_4$ was a size 8 mesh from Drierite, and the silica gel was a size 4 mesh bead from Delta Adsorbents. Both were coated with cobalt chloride as a color-changing indicator of the saturation point. When dry, it is blue, and turns pink when fully saturated with water. Our technique was first validated by putting

Downloaded by COLUMBIA UNIV on August 28, 2012 | http://pubs.acs.org
Publication Date (Web): August 17, 2012 | doi: 10.1021/bk-2012-1107.ch015

Downloaded by COLUMBIA UNIV on August 28, 2012 | http://pubs.acs.org
Publication Date (Web): August 17, 2012 | doi: 10.1021/bk-2012-1107.ch015

100 g of each desiccant type in a Mason jar uncovered in the humidity chamber. The true absorption of each desiccant was found by observing the weight gain of each desiccant under evaluation. The majority of absorption occurred at initial exposure, with saturation being reached after 5 days at steady state. Silica gel and $CaSO_4$ had respective weight gains of 30.71 (+/- 0.106) and 25.2 (+/- 0.223) g before saturation. Due to their similar absorbance capability, either desiccant is a suitable medium for testing.

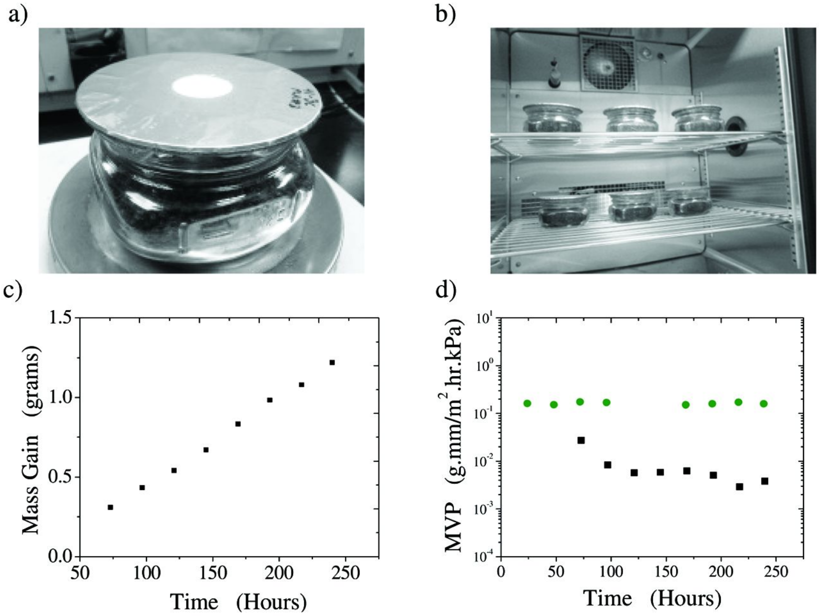

Figure 5. MVP apparatus where a) the foil mask insures an impervious seal for the white LDPE coated paperboard sample (sample area exposed to humidity is 510 mm^2). The entire sample apparatus is placed into the b) humidity chamber where spacing between samples is essential for adequate air circulation. The data collected over discrete time intervals is c) the mass gain over time (example data is for a 18.5 micron extrusion-coated LDPE paperboard and d) is converted to MVP per Equation 2 for LDPE (black square) and PLA (green circle) coated paperboard.

The aluminum foil disc shown in Figures 5a, b is used to seal the test substrate to the jar. The test material is exposed to moisture vapor through the exposed sample area in the foil mask. Vapor penetrates the film from the high humidity side (90% RH) to the desiccant side (0% RH). Since water is being amassed by this process, the weight gain of the entire apparatus was measured daily (or at regular intervals). We used equations 1-3 to calculate the resultant MVP of LDPE and PLA (.cf Figure 5c, d). Our results were consistent with previously reported values (*5*, *9*).

Any testing method has possible sources of error. For this method, the air flow within the humidity chamber needs to be controlled uniformly throughout testing. During the initial exposure to humidity, there is an initial spike in moisture vapor adsorption for each sample. Thus samples with drastically different MVTRs could create variation in air flow throughout the chamber. It is important to minimize this possibility by only testing similar materials at one time and to space appropriately in the chamber as shown in Figure 5b. In addition, once the samples reach steady state, new samples should not be introduced to the chamber. Another challenge is the quality of the seal between the mask and the sample as any leakage would result in an erroneous higher MVTR values (*29*).

Downloaded by COLUMBIA UNIV on August 28, 2012 | http://pubs.acs.org
Publication Date (Web): August 17, 2012 | doi: 10.1021/bk-2012-1107.ch015

Current Research

Nanoclay Coatings and Composites

Current research in nanoclay coating and composites has focused on reducing barrier layer thickness enabled by a tortuous path mechanism. This mechanism is governed by exfoliated high aspect ratios, clays sufficiently dispersed in polymer melts or solvent-based coatings. For coating systems, the solvent of choice is predominately water, ethanol or combinations of both. The coating system will depend on the manufacturing point of application, for instance an on-machine coating for a 2000 ton/day paper machine will have different rheology requirement than a 200 ton/day toll manufacture with off-machine coating capabilities such as gravure, off-set printing or rod coating. The polymer binder in the coatings can be derived from synthetic or renewable resources. For coatings applied onto existing biodegradable webs such as paperboard or PLA sheets, the biodegradability of the final product is enhanced for coatings comprising higher clay content with coating thicknesses less than one micron. This is in sharp contrast to extruded barrier polymer layers with thicknesses ranging from 0.5 to 2 mils (or 10 to 50 microns). Challenges for these coatings include cost equivalency per square area of product and converting robustness to the finished product. Ultimately, the barrier coatings need to provide acceptable shelf life in a finished product for its given application and costs equal or lower to existing technology.

Aqueous Coatings in Traditional Synthetic Latexes

Polymer-clay nanocomposites prepared in aqueous systems for application to web substrates such as paperboard have advantages for on-machine coating to reduce costs. For an environmental benefit as compared to extrusion coatings, the following criteria include

- energy neutral (or savings) for application/ processing methods, drying time, and transportation costs,
- lower coat weights (or thickness) of the barrier layer,
- and better biodegradability of the final substrate.

Downloaded by COLUMBIA UNIV on August 28, 2012 | http://pubs.acs.org
Publication Date (Web): August 17, 2012 | doi: 10.1021/bk-2012-1107.ch015

Figure 6 illustrates a typical packaging structure comprising paperboard or other web substrate and associated barrier layers. Nanocomposites under high study involve highly exfoliated clays, such as vermiculite, montmorillonite, and talc (cf. Figure 7) (*30–32*). Although the initial surge of interest in nanocomposites stemmed from materials produced by Nanocor where the moisture vapor and oxygen transmission rates of amorphous nylon were improved 10-fold (*33*), there is heightened attempts of using the same strategies to improve the resistance to moisture vapor permeation in biopolymer systems. As outlined above the permeation of moisture vapor is more complex than oxygen as often the inherent nature of the polymer will swell in the presence of moisture enabling higher diffusivity and enhanced solubility. The reader is referred to several excellent and comprehensive reviews on nanocomposite fundamentals (*32*, *34–38*).

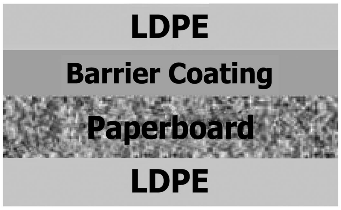

Figure 6. Illustration of a paperboard packaging structure. The barrier coating could be several applications of a solvent-based coating. These laminate structures are typically produced in converting facilities versus during the paperboard manufacture. The paperboard and LDPE layers can be replaced with other substrates.

Cloisite 30B clay, a modified montmorillonite surface modified with tallow, methyl and bis(2-hydroxyethyl) groups, and cetyltrimethylammonium bromide (CTAB) saponite clay were ultrasonically dispersed with water and acrylic resin emulsions for durations less than two minutes (*39*). To achieve colloidal stability, the nanoclay must be compatible with both the hydrophobic polymer system and the aqueous solvent system. After screening several dispersing agents, the researchers found homogenous and stable suspensions of the clay types with two surfactants, Tween-85 and poly(acrylic acid). The approximate 30 weight% coating formulations were rod-coated by hand onto paper linerboard with a basis weight of 160 g/m^2 comprising a 50/50 blend of soft and hardwoods. Through x-ray diffraction and differential scanning calorimetry, they showed effective exfoliation of the nanoclay formulations despite the lack of rigorous delamination. This was especially true for the CTAB-saponite clay where ideal compatibility of the stabilizers, high surface area of the clay and mechanical force provided by ultrasonification had the necessary synergy to fully exfoliate the clay. The exfoliation of the clay provided a tortuous path for the diffusing moisture vapor leading to a reduction in MVTR in the latex coating from 9.2 g/m^2·day to 5.0 g/m^2·day. The clay content was tested between 3-15 w-% in the formulation with no discernible MVTR difference between the different loading amounts. We note that the conditions for MVTR testing were at 23°C and 50% RH.

Downloaded by COLUMBIA UNIV on August 28, 2012 | http://pubs.acs.org
Publication Date (Web): August 17, 2012 | doi: 10.1021/bk-2012-1107.ch015

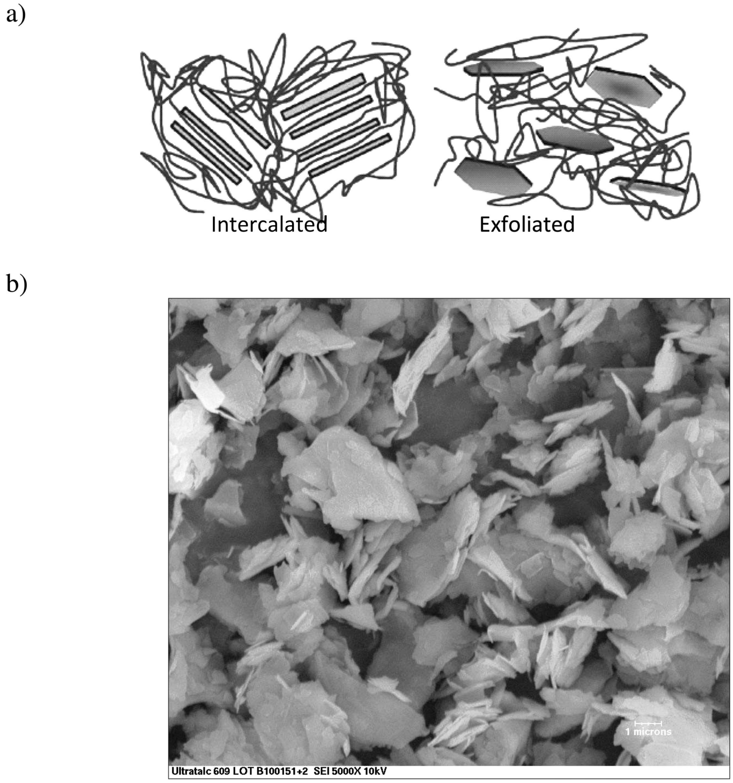

Figure 7. Nanoclays (or high aspect ratio clays) used in packaging composites for improved barrier properties can comprise a) intercalated or exfoliated clays. or b) high efficiency talc produced by Specialty Minerals. FESEM provided by Specialty Minerals. Reproduced with permission from reference (30). Copyright 2005 Elsevier.

Incorporation of Nanoclays into Renewable Polymers

Agar is of interest as a renewable source-based biodegradable packaging material. Agar, a complex mixture of polysaccharides, is derived from algae. Essentially a non-food crop, its use in packaging comprises foams, films and coatings. From Figure 8a it is apparent that with the high degree of hydrogen bonding it follows suit to be a good oxygen barrier. Obviously, its water sensitivity will reduce its performance as an oxygen barrier at higher temperatures and humidity where the favored energy state would be to complex with water versus intermolecular interactions between polymer chains. Active research to improve both barrier properties and mechanical properties of agar and other natural biopolymers such as carbohydrates and proteins includes the addition of highly exfoliated high aspect ratio nanoclays. Specifically for agar, a study varying the amount unmodified natural montmorillonite (Cloisite Na+) for the improvement in MVP resulted in over a 50% reduction from 2.22 to 1.07 g·mm/m^2·hr·kPa (*40*,

Downloaded by COLUMBIA UNIV on August 28, 2012 | http://pubs.acs.org
Publication Date (Web): August 17, 2012 | doi: 10.1021/bk-2012-1107.ch015

41). The solution intercalation method utilized temperature, a homogenizer, and ultrasonic mixer for adequate nanoclay exfoliation. The results are summarized in Figure 8b where inspection of the data reveals 20% w/w of clay was needed for the reduction in MVP (*40*). Of notable importance is that the relative humidity and temperature implemented for the MVTR testing was less stringent than tropical conditions yet the MVP is still significantly higher as compared to LDPE (three orders of magnitude). Thus nanocomposite technology for natural biopolymers has yet to meet the criteria for food packaging applications with this specification or the overall impact of shelf life.

An important study examined how water diffuses through bio-based nanocomposite materials. They used transmission electron microscopy (TEM), wide angle x-ray diffraction (WAXD) and dynamic mechanical analysis (DMA) for structure properties (*42*). Correlating structure properties to barrier properties (characterized with permeability, water sorption, and diffusivity measurements), they concluded amorphous regions within the nanocomposite were the dominate mode of transport for water vapor. The nanocomposite comprised starch, sodium montmorillonite, and glycerol as the plasticizer. Phase separation in the nanocomposite was induced by high contents of glycerol, greater than 23 w-% of the formulation. As the nanoclay induced processing problems due to rheology and interactions with the inherent properties of the starch, the high amount of glycerol was necessary for contiguous film formation. However, as Figure 9 illustrates, the hydrophilic glycerol regions were incompatible with the starch and montomorillonite regions (*42*). The absence of nanoclay in the glycerol regions allows facile transport of moisture vapor though the composite.

It is important to note that the study above was relevant for nanocomposites derived from melt processing where intercalation of the high aspect ratio clay was absent. Other studies showed that where the surface chemistry of the clay and the chemical nature of the diluent (monomer, plasticizer, or solvent) were adequately compatible, intercalated structures were possible.

Edible Coatings

Biodegradable materials would be a great way to go as far as packaging; for foods, however, it would be even better if the packaging could be edible. Food packaging is especially important because it largely determines the shelf life and freshness of such products for consumption. The problem, though, is that edible coating, such as polysaccharides, milk proteins, and lipids, are poor moisture vapor barriers compared to those industrially-produced, such as PE and BOPP. The questions remain of whether or not to continue researching such materials for packaging, and if so, how to engineer them to do better.

Polysaccharides have been examined for their use as edible cheese coatings. A study by Cerqueira, et al. evaluated three polysaccharides: chitosan, galactomannan, and agar, with respect to their effect on MVP. Various formulations of glycerol and sorbitol were used with each and the barrier properties determined using a modified ASTM E96 method, at 20°C and 100% RH. The results showed that the coating with 1.5% galactomannan, 2.0% glycerol, and 0.5% sorbitol was the best barrier to moisture (*43*). This likely demonstrates that galactomannan

Downloaded by COLUMBIA UNIV on August 28, 2012 | http://pubs.acs.org
Publication Date (Web): August 17, 2012 | doi: 10.1021/bk-2012-1107.ch015

is a competent moisture barrier as a cheese coating. Martins et al. measured properties of galactomannan coatings for cheeses over the course of a month. The results of the study showed that galactomannan coatings did increase the shelf of life of cheeses, as the MVP reduced with increased galactomannan (*44*). It is likely that galactomannans create a stronger, more coherent network where molecules are more closely packed (*43*).

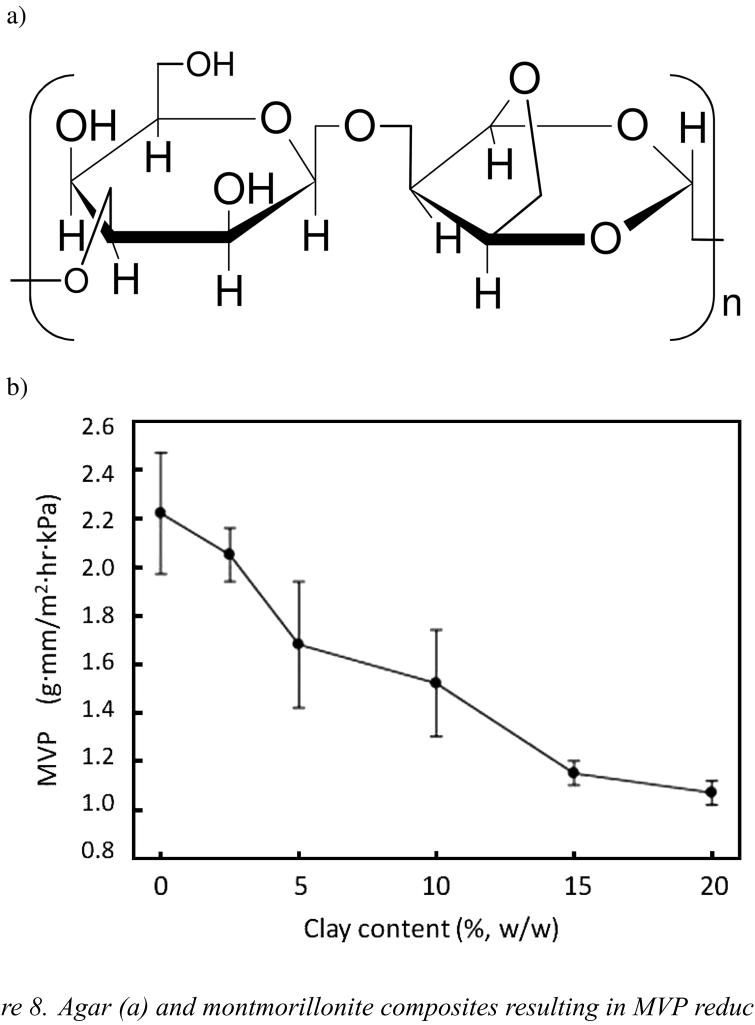

Figure 8. Agar (a) and montmorillonite composites resulting in MVP reductions (b). Reproduced with permission from reference (40). Copyright 2011 Elsevier.

The use of plasticizers, such as glycerol and sorbitol, is needed for polysaccharide films due to their stiff and brittle nature. Plasticizers effectively increase polymer chain mobility and free volume allowing for higher diffusion rates and solubilities of both gases and moisture vapor in the film (*45*). As previously mentioned, including glycerol in a coating formulation can increase MVP with respect to barrier attributes. One study found that increasing the

Downloaded by COLUMBIA UNIV on August 28, 2012 | http://pubs.acs.org
Publication Date (Web): August 17, 2012 | doi: 10.1021/bk-2012-1107.ch015

glycerol content of galactomannan coatings for tropical fruits increased the MVP attributed to the hydrophilic nature of glycerol (*46*). Work by others with plasticized whey protein isolate and starch films concurred with this result (*47*). One study found that MVP (tested at 30°C and 52% RH) linearly increased with additional plasticizer content. Another study showed that while glycerol increased MVP at 75% RH for starch/leaf gum films, its negative effect on MVP can be counterbalanced with increases in the polysaccharide leaf gum concentration. There also seemed to be a critical glycerol concentration of 40%, at which MVP rose drastically (*48*).

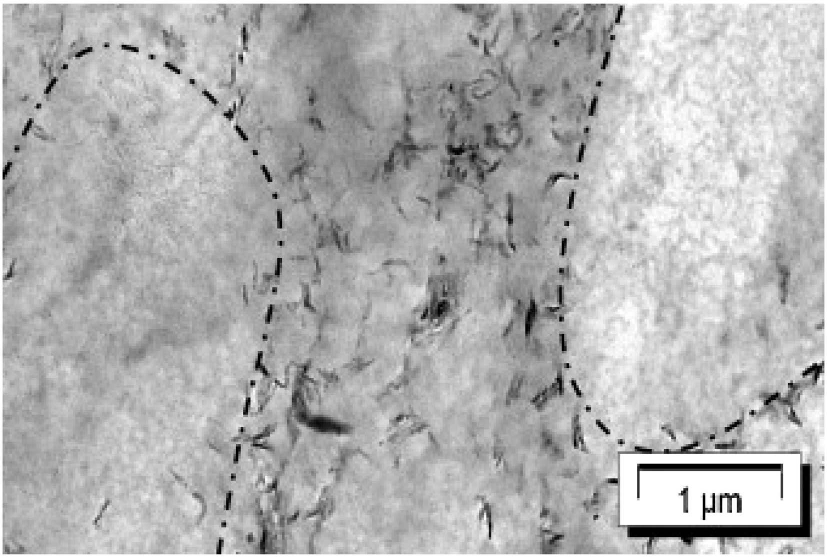

Figure 9. Transmission Electron Microscopy (TEM) picture of wheat starch, organo-modified montmorillonites (OMMT) and glycerol composites. The OMMT phase segregated in the wheat starch rich phase resulting in amorphous regions of OMMT-free glycerol phases. This phase separation is attributed to higher MVP throughout the composites. Reproduced with permission from reference (42). Copyright 2010 Elsevier.

In the instance of casein, a milk protein, adding glycerol produces an anomaly. Casein is currently used in food supplements, adhesives, and finishes. Since it is from milk, it is edible, and its structure allows for the formation of an effective biodegradable food coating. One major problem is that moisture dissolves casein; however, its combination with glycerol and water creates a flexible, moisture-resistant film. This is probably due to the decrease in defects with the addition of plasticizer, which allows for greater flexibility and prevention of surface defects ultimately in more controllable MVTR or permeability. There is likely an optimum ratio of casein to glycerol that should be used, as too much glycerol as mentioned above would be expected to increase the film hydrophilicity, thus increasing MVTR (*49–51*).

Lipids have been studied for their use as edible food coatings, to increase the shelf life of food. Although they do not form films easily, they are used as coatings because they are nonpolar or hydrophobic (*12*). One study showed that lipids were an effective moisture vapor barrier as a coating for rice (*52*). However, a study involving films containing milk fat found that the fat globules large in size created aggregates increasing film heterogeneity and water diffusion rates, hence higher MVP values (cf. Figure 10) (*53*). It has been shown that smaller globules results in a more homogeneous profile and consequently, a lower transfer rate of moisture vapor (*54*).

Beeswax, a naturally-occurring lipid, has been studied by itself as a moisture vapor barrier. Several groups have found that beeswax does reduce the MVP of films to some extent. The group of Bourlieu et al. compared white beeswax with several other lipids, including milk chocolate and dark chocolate, as film coatings, and found that beeswax was the best at blocking out moisture vapor for dry foods (*55*). While Bourlieu's group compared the performance of multiple lipids, there are others that have studied the effect of percent beeswax content of film coatings on MVP. Their results have some similarities and differences. Paulson and Yang produced films with 25% beeswax content had a reduced MVP as compared to those films without beeswax (*56*). The group of Min et al. concluded from their work that the average MVP for their protein-beeswax composite films decreased by 57% when the beeswax content was 40% (*57*). Monedero, et al. found that for protein-lipid composite films, the best combination was 25% lipid, with 30-50% of that portion comprising beeswax (cf. Figure 11) (*58*). Han et al., had very similar findings to Min's group, stating that less than 30 weight percent, beeswax had no considerable effect on MVP. They found that a maximum concentration of 40% beeswax resulted in a 15% reduction in MVP (cf. Figure 12) (*59*). While the results show that increased beeswax content results in a decreased MVP, it is still an order magnitude higher than films of PLA. Its use is best for direct spray coatings onto food requiring only short shelf life or for items receptive to thick barrier layers.

Downloaded by COLUMBIA UNIV on August 28, 2012 | http://pubs.acs.org
Publication Date (Web): August 17, 2012 | doi: 10.1021/bk-2012-1107.ch015

Inorganic Surface Treatments

Aside from inherent material properties, permeation through barrier layers attributed to pinholes and defects on the film, or other substrate imperfections often need another surface treatment to obtain a boost in MVP or OP. As such, inorganic surface modifications at the nano-scale are undergoing significant research as both an additional level of protection or to enable the use of polysaccharides or PLA. Nano-scale materials growth methods for moisture barrier layers on polymer substrates include chemical vapor deposition (CVD) (*60*, *61*), atomic layer deposition (ALD) (*62–67*) and physical vapor deposition (PVD) (*68*).

Downloaded by COLUMBIA UNIV on August 28, 2012 | http://pubs.acs.org
Publication Date (Web): August 17, 2012 | doi: 10.1021/bk-2012-1107.ch015

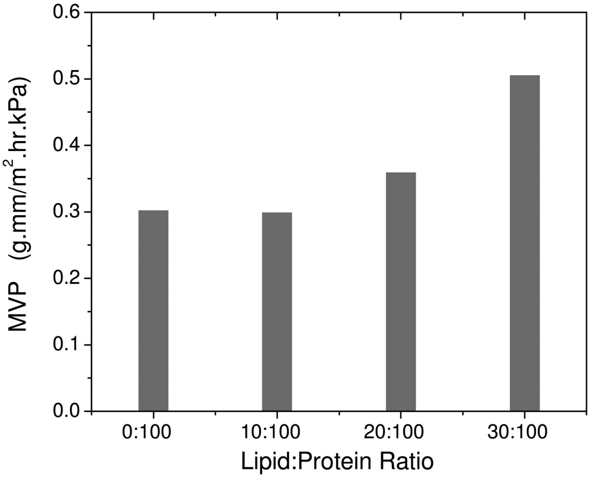

Figure 10. MVP as a function of milk fat (lipid) content in sodium caseinate (protein) films. Data from reference (53).

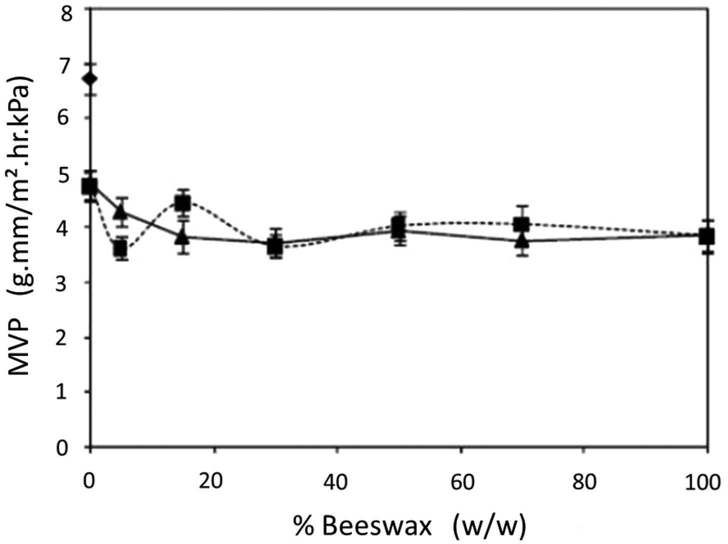

Figure 11. MVP as a function of weight percent beeswax in soy protein isolate films containing various proportions of lipid. Reproduced with permission from reference (54). Copyright 2009 Elsevier.

Downloaded by COLUMBIA UNIV on August 28, 2012 | http://pubs.acs.org
Publication Date (Web): August 17, 2012 | doi: 10.1021/bk-2012-1107.ch015

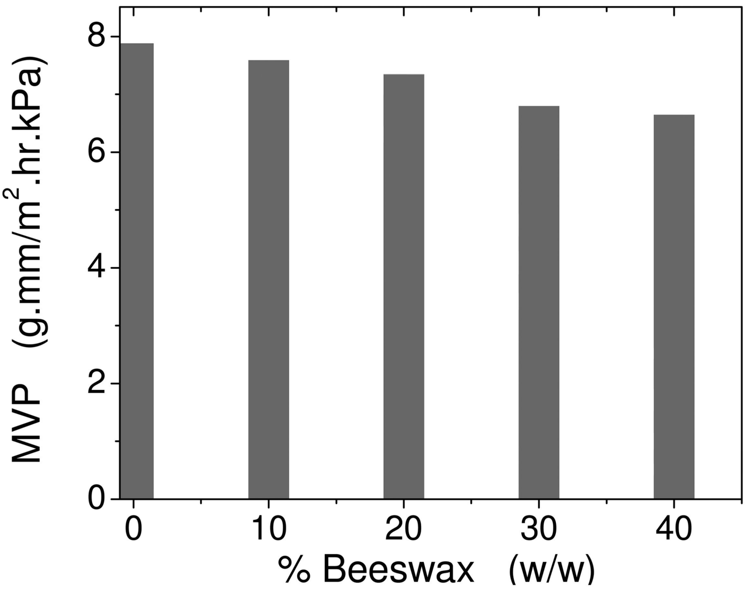

Figure 12. MVP as it depends on weight % beeswax (the main lipid component) in a soy protein isolate film. As beeswax content increases, there is a marginal decrease in MVP. Data from reference (59).

Atomic Layer Deposition

Atomic layer deposition is ideally suited for conformal material growth on a wide range of structured materials, including polymer and polymer fiber, due to its natural self-limiting growth behavior. In an ALD process, precursor vapors are pulsed sequentially to a surface, separated by an inert purge to remove any unreacted vapor. The surface reaction is self-limiting where a single ALD cycle, completed in seconds, results in a thin layer of material growth. Multiple cycles are used to obtain inorganic film thickness of <100nm. ALD is capable of depositing a variety of materials including oxides, nitrides, sulfides, and metals. A number of groups have experimented with ALD barrier layers on organic light emitting diodes (OLED) and measured the efficiency (*69*), luminance (*70*), and moisture vapor transmission rates (*71*).

In particular, ALD aluminum oxide has been explored as MVP barrier encapsulant for both OLED devices (*72*) and food packaging applications (*73*, *74*). OLED devices with the Al_2O_3 coating have been shown to withstand ambient atmosphere for over 6000 hours, while the ones with no encapsulation rapidly degraded after 10 hours of exposure (*69*). ALD deposited Al_2O_3 has reduced the MVTR of polyethylene naphthalene and Kapton® polymers by over three orders of magnitude (*75*). Other ALD materials also show good barrier properties. For example, ALD deposited SiO_2 on polyethersulfone (PES) has shown a reduction in $MVTR_{25C,\ 100\%RH}$ from 50 g/m^2·day for a bare substrate to 0.31 g/m^2·day for the

Downloaded by COLUMBIA UNIV on August 28, 2012 | http://pubs.acs.org
Publication Date (Web): August 17, 2012 | doi: 10.1021/bk-2012-1107.ch015

coated substrate (*71*). Direct ALD coating on active layer of an organic device is not always preferred, as demonstrated in the work published by Ferrari et al. Here the authors use an interlayer between the polymer substrate and the ALD material to prevent a reaction between the ALD precursors and active OLED layer (*72*). The interlayer serves as a sacrificial layer to preserve the barrier property enhancement achievable with ALD, while maintaining the device performance. Research efforts by Spagnola et al. (*76*) and Jur et al. (*77*) revealed that the nucleation behavior of the ALD materials is highly dependent on the ALD precursor chemistry, the polymer chain constituents, and the general processing conditions. For example, ALD processing temperature dependence affects the nucleation behavior of the inorganic film on the polymer (*77*). High temperature processing on polypropylene results in subsurface nucleation, which is decreased substantially at lower temperatures. On the other hand, ALD processing on cellulose has little temperature dependence and no observed sub-surface growth. Johansson et al. determined that processing temperature can also affect the deposition rate of inorganic barrier constituents. For the sample number of deposition cycles, a thicker ALD barrier layer was observed for the samples treated at 65 °C versus at 100 °C (*74*).

Table 1. Resultant MVTR for ALD-modified LDPE and PLA extrusion coated packaging substrates. Data from reference (*73*).

Substrate Description	*ALD Reaction Temp. (°C)*	*ALD Cycle No.*	*Material Deposited*	*MVTR @ 23°C, 50% RH ($g/m^2 \cdot h$)*	*MVTR @ 38°C, 90% RH ($g/m^2 \cdot h$)*
LDPE (19.35 um) Coated Paper Board	65	0	--	--	1.16
		120	10 nm Al_2O_3	--	1.12
		350	25 nm Al_2O_3	--	0.61
		600	40 nm Al_2O_3	--	0.23
PLA (20.16 um) Coated Paper Board	65	0	--	3.00	12.08
		600	65 nm Al_2O_3	0.16	2.29
		1200	110 nm Al_2O_3	0.17	2.21

Downloaded by COLUMBIA UNIV on August 28, 2012 | http://pubs.acs.org
Publication Date (Web): August 17, 2012 | doi: 10.1021/bk-2012-1107.ch015

It has been a natural transition to use this powerful deposition technique for conformal coatings on paperboard and film substrates, particularly biopolymer substrates with inherent poor moisture vapor permeability. Tables 1 and 2 list research done on polymer coated paperboard substrates with the aim of decreasing the MVP of PLA coated boards and packaging film. This data provides insight into the deposition differences with PLA and LDPE paperboard with respect to resultant MVTR and processing conditions. It is clear that more tropical conditions will generate larger transmission rates, but it is surprising to see that the samples with thinner ALD coatings had higher barrier performance. For a smooth substrate, a thin coating is sufficient, but rougher surfaces may require a thicker layer, despite the increased susceptibility to cracking (*73*). In general, PLA substrates responded better than the LDPE to an Al_2O_3 layer. It is unclear if this is due to the deposition temperature or the substrate surface chemistry differences. Although LDPE showed consistently lower MVTR, the PLA shows a more drastic improvement with any number of cycles when compared to the uncoated substrate. The results for PLA reveal that a thin coating is sufficient and additional cycles diminish the barrier enhancement. For the most part, MVTR for LDPE continued to decrease as the coating thickness increased. The poor film growth for LDPE substrates at higher reaction temperatures was attributed to the surface mobility of LDPE as compared to the PLA resulting in Al_2O_3 penetration in the extruded polymer layer versus a more uniform surface layer (*73*).

ALD deposition was recently combined with polyelectrolyte multilayer PEM) films to produce MVTR barriers (*78*). A variety of PEM functional thin films can be produced using the layer-by-layer (LbL) assembly technique (*79*, *80*). LbL-based thin films are currently being evaluated for properties that include antimicrobial (*81–83*), anti-reflection (*84*), electrical conductivity (*85*),anti-flammable (*86–88*), gas barrier (*89–91*), and UV resistance (*92*). These films, typically $< 1\mu m$ thick, are created by alternately exposing a substrate to positively- and negatively-charged molecules, polymer electrolytes, or particles in a series of steps to produce the desired number of “bilayers” (or cationic-anionic pairs of layers). While excellent gas barriers have been achieved via LbL, its moisture sensitivity affects the barrier performance at higher temperatures and humidity. Hirvikorpi et al. merged the attributes of both ALD and LbL deposition techniques in attempt to reduce the MVTR of a PLA film coated with a 20nm PEM film comprising anionic sodium alginate and cationic chitosan (*78*). The objective was to enable the use of moisture-sensitive-PEMs layers comprising inherent antimicrobial and fungicidal properties of chitosan with a moisture vapor barrier layer via ALD. They measured the MVTR of commercial grade PLA film (25 microns) to be 2.2 $g/m^2 \cdot hr$ at 23°C and 75% relative humidity. Upon depositing the sodium alginate- chitosan 20 nm PEM, the MVTR increased almost 100%. Depositing a 25nm Al_2O_3 layer on top of the PEM layer reduced the MVTR to levels 50% lower than the native PLA film.

Downloaded by COLUMBIA UNIV on August 28, 2012 | http://pubs.acs.org
Publication Date (Web): August 17, 2012 | doi: 10.1021/bk-2012-1107.ch015

Table 2. Resultant MVTR for ALD-modified LDPE and PLA extrusion coated paperboard and PLA film packaging substrates. Data from reference (*72*).

Substrate Description	*ALD Reaction Temp. (°C)*	*ALD Cycle No.*	*Material Deposited*	*MVTR @ 23°C, 75 % RH ($g/m^2\cdot h$)*
(PE) (16.13 um) Coated Paper Board	100	0	--	0.29
		500	50 nm Al_2O_3	0.08
	80	0	--	0.35
		500	50 nm	0.19
PLA (28.23 um) Coated Paper Board	100	0	--	2.70
		500	50 nm Al_2O_3	0.08
		1000	100 nm Al_2O_3	1.21
	80	0	--	5.46
		500	50 nm Al_2O_3	0.58
PLA Film (25 um)	100	0	--	3.88
		500	50 nm Al_2O_3	0.14

Physical and Chemical Vapor Deposition

Multilayer films for flexible packaging typically use a vacuum metallization, a physical vapor deposition (PVD) method. In contrast to CVD or ALD, temperatures must be between 1500-1800°C to vaporize the metal, such as aluminum, for deposition onto the film, typically polyester (PET) or oriented polypropylene (OPP) (*1*). Most synthetic films, however, can undergo this process with resulting barrier properties that are 75-98% less of untreated films for aluminum layers between 5-20 nanometers thick. The vaporization of metal results in production of minute particles that must be subjected to vacuum levels of at least 3 kPa to prevent reaction with air molecules and oxidation for subsequent deposition to the substrate. Alternatively, thin glass-like films of SiO_x can be deposited via PVD or plasma-enhanced CVD of organosilanes on formed substrates (such as the inside of beverage bottles) or traditional roll-to-roll processing (*61*). To achieve comparable barrier protection as the metalized aluminum process, thickness of the barrier layer need to be at least an order of magnitude higher. Finally, acetylene can be deposited on film via PVD process in a plasma atmosphere to achieve a 10-fold reduction in O_2 permeability but with little impact on moisture vapor.

Downloaded by COLUMBIA UNIV on August 28, 2012 | http://pubs.acs.org
Publication Date (Web): August 17, 2012 | doi: 10.1021/bk-2012-1107.ch015

Frito-lay North America Inc. launched a replacement of the traditional chip bag (cf. Figures 13a, c) for their SunChip® multigrain chip line in 2009 (*93*). The packaging material comprised biodegradable components in the multi-layers allowing a fully biodegradable claim as illustrated in Figures 13b, d (*68*). Biodegradable is defined as less than 5% of its original weight after exposure to air for 60 days at constant temperature, 35 °C, and 75% relative humidity (*68*). To achieve a MVTR comparable to the original bag, the conjunction of both an aqueous nano-coating comprising exfoliated silicates as described in the previous section and a metalized layer such as aluminum provided acceptable performance requirements. Specifically it was pointed out that upon exposure to moisture, PLA will tend to swell. A metalized coating directly applied to PLA has a tendency to crack thus in high humidity, thus the crack potential is further exasperated upon exposure to moisture defeating the original purpose of the barrier layer. The mechanical properties of PLA caused the first 100% compostable chip bag to be rather loud while handling; quoted to be 80-85 decibels, the level of busy expressway traffic (*94*). This caused less consumer acceptance than anticipated on the new bag despite its biodegradable nature (*68*). Through the incorporation of an elastomeric adhesive for noise reduction the packaging was re-launched in early 2011 with a much better consumer acceptance rate (*68*, *94*).

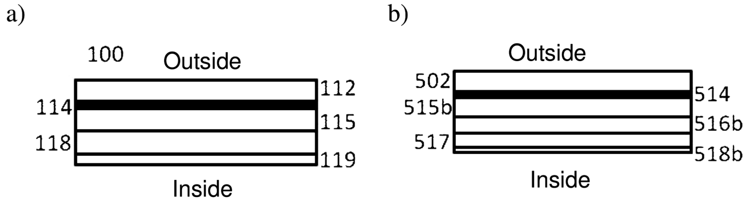

Layer	Description
112	OPP or PET
114	Graphics layer (reverse printed)
115	Glue or laminate layer (PE)
118	Metal deposited layer (on OPP)
119	Heat seal layer

Layer	Description
502	PLA or PHA
514	Graphics layer
515b	Adhesive layer (modified PLA)
516b	Metal deposited coating
517	Nanocoating
518b	PLA or PHA

Figure 13. Multi-layer flexible packaging structures for a) traditional OPP bag for chips and b) SunChips® fully compostable structure. Data from reference (68).

Downloaded by COLUMBIA UNIV on August 28, 2012 | http://pubs.acs.org
Publication Date (Web): August 17, 2012 | doi: 10.1021/bk-2012-1107.ch015

Future Directions

Systematic Studies

With our MVTR technique, we have confirmed the MVTR values of benchmark materials such as polyethylene, poly(lactic acid) and poly(dimethylsiloxane) (PDMS). Although hydrophobic, PDMS is highly permeable to moisture vapor due to its amorphous nature. Using the desiccant method we described in the earlier sections, we measured a MVTR of 25.47 $g/m^2.h$ for a 0.22 mm thick film. Our resultant MVP was 0.992 ($g.mm/m^2.h.kPa$), an order of magnitude higher than that of PLA.

Our next step is to create a superhydrophobic surface on PDMS using the technique of creating mechanically assembled monolayers (MAMs) with nonpolar moieties (*95*). It has been shown that this procedure results in a stable superhydrophobic surface on PDMS films due to densely packed fluorinated alkane chains as verified by contact angle measurements, and near edge X-ray absorption fine structure (NEXAFS). Understanding moisture vapor transport as function of chain packing will enable us to determine the threshold of surface modifications possible to tune permeable substrates. This in turn could be the stepping stone to creating materials that are responsive to their environment based on the factors that can control transport of moisture vapor and other permeants.

Conclusions and Outlook

From this literature review, we now have an appreciation for the factors that drive moisture vapor transport and permeability. We also know of the various techniques that can aid in improving materials as moisture barriers. It will be through increasing the commercial viability of surface modification techniques such as ALD and nanoclay coatings along with availability of emerging biomaterials like PGA that will make biodegradable and renewable materials the norm versus the exception for packaging materials. It remains to be seen if the research will enable a sustainable business model for transitioning packaging materials from dependence on fossil fuel resources to more environmentally-friendly counterparts. Not only are changes in materials of construction for packaging a necessary component but changes in consumer behavior are key to reducing the barriers of entry for a paradigm shift in consumable goods packaging technology.

Acknowledgments

We gratefully acknowledge The Nonwovens Institute and College of Textiles at North Carolina State University for their financial support of this work. The authors also acknowledge Ms. Cynthia Norton and Mr. Charles Harkness of MeadWestvaco for their insights on MVTR testing techniques.

References

1. Robertson, G. L. *Food Packaging: Principles and Practice*; Taylor & Francis/CRC Press: Boca Raton, FL, 2006.
2. *Packaging Digest* **2006**, *43*, 40−42. .
3. Mans, J. *Packaging Digest* **2001**, *38*, 40.
4. Kalkowski, J. *Packaging Digest* **2009**, *46*, 10.
5. Briston, J. H. In *Plastics Films*; Katan, L. L., Ed.; Longman Scientific & Technical, Plastics and Rubber Institute; Wiley: Harlow, Essex, England; New York, 1988, 1989.
6. Thellen, C.; Coyne, M.; Froio, D.; Auerbach, M.; Wirsen, C.; Ratto, J. A. *J. Polym. Environ.* **2008**, *16*, 1–11.
7. Kureha Corporation to Launch New Polyglycolic Acid (PGA) Business in West Virginia. *Drug Week*, 2008, 1996 original.
8. Osborn, K. R. In *Plastic Films: Technology and Packaging Applications*; Jenkins, W. A., Ed.; Technomic Pub. Co.: Lancaster, PA, 1992.
9. Alpha Packaging. http://www.alphap.com/basics/compare.html.
10. Gloor, P. E. Coating Control, quality, & paperboard packaging. *Pap., Film Foil Converter* **2002**, *76*, 46.
11. Ahvenainen, R. *Novel Food Packaging Techniques*; CRC Press; Woodhead Pub. Ltd.: Boca Raton, FL; Cambridge, England, 2003.
12. Chiellini, E. *Environmentally Compatible Food Packaging*; CRC; Woodhead: Boca Raton, FL; Cambridge, England, 2008.
13. Yang, S.; Wu, Z.; Yang, W.; Yang, M. *Polym. Test.* **2008**, *27*, 957–63.
14. Leaversuch, R. *Plast. Technol.* **2002**, *48*, 50.
15. Siracusa, V.; Rocculi, P.; Romani, S.; Rosa, M. D. *Trends Food Sci. Technol.* **2008**, *19*, 634–643.
16. Williams, S. F.; Martin, D. P.; Horowitz, D. M.; Peoples, O. P. *Int. J. Biol. Macromol.* **1999**, *25*, 111–121.
17. ASTM E96: Standard Test Methods for Water Vapor Transmission of Materials.
18. Morillon, V.; Debeaufront, F.; Blond, G.; Capelle, M.; Voilley, A. *Crit. Rev. Food Sci. Nutr.* **2002**, *42*, 67.
19. Hu, Y.; Topolkaraev, V.; Hiltner, A.; Baer, E. *J. Appl. Polym. Sci.* **2001**, *81*, 1624–1633.
20. Debeaufort, F.; Quezada-Gallo, J.; Delporte, B.; Voilley, A. *J. Membr. Sci.* **2000**, *180*, 47–55.
21. Martin-Polo, M. *J. Agric. Food Chem.* **1992**, *40*, 407–412.
22. Debeaufort, F.; Martin-Polo, M.; Voilley, A. *J. Food Sci.* **1993**, *58*, 426–429.
23. Chivrac, F.; Pollet, E.; Dole, P.; Averous, L. *Carbohydr. Polym.* **2010**, *79*, 941–947.
24. Cao, N.; Yang, X.; Fu, Y. *Food Hydrocolloids* **2009**, *23*, 729–735.
25. Laohakunjit, N.; Noomhorm, A. *Starch - Stärke* **2004**, *56*.
26. Shogren, R. *J. Polym. Environ.* **1997**, *5*, 91–95.
27. Todd, W. G. *J. Plast. Film Sheeting* **2003**, *19*, 209–220.
28. ASTM E398: Standard Test Method for Water Vapor Transmission Rate of Sheet Materials Using Dynamic Relative Humidity Measurement.

Downloaded by COLUMBIA UNIV on August 28, 2012 | http://pubs.acs.org
Publication Date (Web): August 17, 2012 | doi: 10.1021/bk-2012-1107.ch015

29. Gennadios, A.; Weller, C. L.; Gooding, C. H. *J. Food Eng.* **1994**, *21*, 395–409.
30. Ray, S.; Bousmina, M. *Prog. Mater. Sci.* **2005**, *50*, 962–1079.
31. Wuu, F.; Rabot, Y. In *High Performance Talc for Water-Based Barrier Coatings*; Tappi: St. Louis, MO, 2009.
32. Pavlidou, S.; Papaspyrides, C. D. *Prog. Polym. Sci.* **2008**, *33*, 1119–1198.
33. Lan, T. *Nanotechnology Platforms for Plastics Commercialization.* http://www.nanocor.com/tech_papers/Nano-2004.pdf (accessed November 4, 2011).
34. Khonakdar, H. A.; Jafari, S. H.; Asadinezhad, A. *Iran Polym. J.* **2008**, *17*, 19–38.
35. Meng, X. Y.; Wang, Z.; Tang, T. *Mater. Sci. Technol.* **2006**, *22*, 780–786.
36. Okamoto, M. *J. Ind. Eng. Chem.* **2004**, *10*, 1156–1181.
37. Sorrentino, A.; Tortora, M.; Vittoria, V. *J. Polym. Sci., Part B: Polym. Phys.* **2006**, *44*, 265–274.
38. Zhang, J.; Manias, E.; Wilkie, C. A. *J. Nanosci. Nanotechnol.* **2008**, *8*, 1597–1615.
39. Sun, Q.; Schork, F. J.; Deng, Y. *Compos. Sci. Technol.* **2007**, *67*, 1823–1829.
40. Rhim, J. *Carbohydr. Polym.* **2011**, *86*, 691–699.
41. Rhim, J.; Lee, S.; Hong, S. *J. Food Sci.* **2011**, *76*, N40–N48.
42. Chivrac, F.; Angellier-Coussy, H.; Guillard, V.; Pollet, E.; Averous, L. *Carbohydr. Polym.* **2010**, *82*, 128–135.
43. Cerqueira, M. A. *J. Agric. Food Chem.* **2009**, *57*, 1456–1462.
44. Martins, J. T.; Cerqueira, M. A; Souza, B.; do Carmo Avides, M.; Vicentea, A. A. *J. Agric. Food Chem.* **2010**, *58*, 1884–1891.
45. Bertuzzi, M. A.; Castro Vidaurre, E. F.; Armada, M.; Gottifredi, J. C. *J. Food Eng.* **2007**, *80*, 972–978.
46. Cerqueira, M. A.; Lima, Á. M.; Teixeira, J. A.; Moreira, R. A.; Vicente, A. A. *J. Food Eng.* **2009**, *94*, 372–378.
47. Kokoszka, S.; Debeaufort, F.; Lenart, A.; Voilley, A. *Int. Dairy J.* **2010**, *20*, 53–60.
48. Chen, C.; Lai, L. *Food Hydrocolloids* **2008**, *22*, 1584–1595.
49. Core, J. Edible. *Agric. Res.* **2005**, *53*, 21.
50. Tomasula, P. M.; Parris, N.; Yee, W.; Coffin, D. *J. Agric. Food Chem.* **1998**, *46*, 4470–4474.
51. Encyclo Online Encyclopedia. http://www.encyclo.co.uk/define/plasticizer (accessed October 27, 2011).
52. Bourtoom, T.; Chinnan, M. S. *Food Sci. Technol. Int.* **2009**, *15*, 149–158.
53. Khwaldia, K.; Banon, S.; Desobry, S.; Hardy, J. *Int. J. Food Sci. Technol.* **2004**, *39*, 403–411.
54. Debeaufort, F.; Voilley, A. *Int. J. Food Sci. Technol.* **1995**, *30*, 183–190.
55. Bourlieu, C.; Guillard, V.; Powell, H.; Vallès-Pàmies, B.; Guilbert, S.; Gontard, N. *Eur. J. Lipid Sci. Technol.* **2006**, *108*, 1007–1020.
56. Paulson, A.; Yang, L. *Food Res. Int.* **2000**, *33*, 571–578.
57. Min, S. C.; Janjarasskul, T.; Krochta, J. M. Te *J. Sci. Food Agric.* **2009**, *89*, 251–257.
58. Monedero, F. *J. Food Eng.* **2009**, 509–515.

Downloaded by COLUMBIA UNIV on August 28, 2012 | http://pubs.acs.org
Publication Date (Web): August 17, 2012 | doi: 10.1021/bk-2012-1107.ch015

59. Han, J. H.; Seo, G. H.; Park, I. M.; Kim, G. N.; Lee, D. S. *J. Food Sci.* **2006**, *71*, E290–E296.

60. Saitoh, K.; Kumar, R. S.; Chua, S.; Masuda, A.; Matsumura, H. *Thin Solid Films* **2008**, *516*, 607–610.

61. Zambov, L.; Shamamian, V.; Weidner, K.; Loboda, M. *Chem. Vap. Deposition* **2011**, *17*, 253–260.

62. Kwak, S.; Jun, J.; Jung, E. *Langmuir* **2009**, *25*, 8051–8055.

63. Jang, C.; Han, B. *J. Appl. Phys.* **2009**, *105*, 093532.

64. Bystrova, S.; Holleman, J.; Aarnink, A.; Wolters, R. *Barrier Properties of ALD $W_{1.5}N$ Thin Films*; Erb, D., Ramm, P., Masu, K., Osaki, A., Eds.; 2004; pp 774.

65. Dameron, A. A.; Davidson, S. D.; Burton, B. B.; Carcia, P. F.; McLean, R. S.; George, S. M. *J. Phys. Chem. C* **2008**, *112*, 4573–4580.

66. Hirvikorpi, T.; Vaha-Nissi, M.; Harlin, A.; Marles, J.; Miikkulainen, V.; Karppinen, M. *Appl. Surf. Sci.* **2010**, *257*, 736–740.

67. Liang, X.; King, D. M.; Groner, M. D.; Blackson, J. H.; Harris, J. D.; George, S. M.; Weimer, A. W. *J. Membr. Sci.* **2008**, *322*, 105–112.

68. Knoerzer, A. R.; Laverdure, K. S.; Rodgers, B. D. US7943218B2, 2011.

69. Potscavage, W. J.; Yoo, S.; Domercq, B.; Kippelen, B. *Appl. Phys. Lett.* **2007**, *90*.

70. Mu, H.; Li, W.; Jones, R.; Steckl, A.; Klotzkin, D. *J. Lumin.* **2007**, *126*, 225–229.

71. Wuu, D. S.; Lo, W. C.; Chang, L. S.; Horng, R. H. *Thin Solid Films* **2004**, *468*, 105–108.

72. Ferrari, S.; Perissinotti, F.; Peron, E.; Fumagalli, L.; Natali, D.; Sampietro, M. *Org. Electron.* **2007**, *8*, 407–414.

73. Hirvikorpi, T.; Vaha-Nissa, M.; Mustonen, T.; Iiskola, E.; Harlan, A.; Karppinen, M. *Thin Inorganic Barrier Coatings for Packaging Materials*; 2010.

74. Johansson, P.; Lahtinen, K.; Kuusipalo, J. *Atomic Layer Deposition Process for Barrier Applications of Flexible Packaging*; 2010.

75. Groner, M. D. *Appl. Phys. Lett.* **2006**, *88*, 051907–3.

76. Spagnola, J. C.; Gong, B.; Arvidson, S. A.; Jur, J. S.; Khan, S. A.; Parsons, G. N. *J. Mater. Chem.* **2010**, *20*, 4213–4222.

77. Jur, J. S.; Spagnola, J. C.; Lee, K.; Gong, B.; Peng, Q.; Parsons, G. N. *Langmuir* **2010**, *26*, 8239–8244.

78. Hirvikorpi, T.; Vaha-Nissi, M.; Harlin, A.; Salomaki, M.; Areva, S.; Korhonen, J. T.; Karppinen, M. *Appl. Surf. Sci.* **2011**, *257*, 9451–9454.

79. Ariga, K.; Hill, J. P.; Ji, Q. *Phys. Chem. Chem. Phys.* **2007**, *9*, 2319–2340.

80. Decher, G. Polyelectrolyte Multilayers, An Overview. In *Multilayer Thin Films: Sequential Assembly of Nanocomposite Materials*; Decher, G., Schlenoff, J. B., Eds.; Wiley-VCH: Weinheim, Germany, 2003.

81. Fu, J. H.; Ji, J.; Yuan, W. Y.; Shen, J. C. *Biomaterials* **2005**, *26*, 6684–6692.

82. Fu, J.; Ji, J.; Fan, D.; Shen, J. *J. Biomed. Mater. Res., Part A* **2006**, *79A*, 665–674.

83. Dvoracek, C. M.; Sukhonosova, G.; Benedik, M. J.; Grunlan, J. C. *Langmuir* **2009**, *25*, 10322–10328.

Downloaded by COLUMBIA UNIV on August 28, 2012 | http://pubs.acs.org
Publication Date (Web): August 17, 2012 | doi: 10.1021/bk-2012-1107.ch015

84. Hiller, J.; Mendelsohn, J. D.; Rubner, M. F. *Nat. Mater.* **2002**, *1*, 59–63.
85. Park, Y. T.; Ham, A. Y.; Grunlan, J. C. *J. Mater. Chem.* **2011**, *21*, 363–368.
86. Li, Y.; Mannen, S.; Schulz, J.; Grunlan, J. C. *J. Mater. Chem.* **2011**, *21*, 3060–3069.
87. Li, Y.; Schulz, J.; Grunlan, J. C. *ACS Appl. Mater. Interfaces* **2009**, *1*, 2338–2347.
88. Carosio, F.; Laufer, G.; Alongi, J.; Camino, G.; Grunlan, J. C. *Polym. Degrad. Stab.* **2011**, in press.
89. Priolo, M. A.; Gamboa, D.; Grunlan, J. C. *ACS Appl. Mater. Interfaces* **2010**, *2*, 312–320.
90. Priolo, M. A.; Gamboa, D.; Holder, K. M.; Grunlan, J. C. *Nano Lett.* **2010**, *10*, 4970–4974.
91. Yang, Y.; Haile, M.; Park, Y. T.; Malek, F. A.; Grunlan, J. C. *Macromolecules* **2011**, *44*, 1450–1459.
92. Dawidczyk, T. J.; Walton, M. D.; Jang, W.; Grunlan, J. C. *Langmuir* **2008**, *24*, 8314–8318.
93. Frito-Lay North America Behind the Scenes. http://www.sunchips.com/healthier_planets.html (accessed October 26, 2011).
94. Mohan, A. M. Sunchips relaunched in quieter compostable bag. *Packaging World* **2011**.
95. Genzer, J.; Efimenko, K. *Science* **2000**, 2130–2133.

Downloaded by COLUMBIA UNIV on August 28, 2012 | http://pubs.acs.org
Publication Date (Web): August 17, 2012 | doi: 10.1021/bk-2012-1107.ch015

Downloaded by NORTH CAROLINA STATE UNIV on August 28, 2012 | http://pubs.acs.org
Publication Date (Web): August 17, 2012 | doi: 10.1021/bk-2012-1107.ch016

Chapter 16

Synthesis and Characterization of Biologically Active Chitosan Sulfates

**Kai Zhang,*,[a,1] Annett Weltrowski,[b] Dieter Peschel,[b]
Steffen Fischer,[a] and Thomas Groth[b]**

**[a]Institute of Plant and Wood Chemistry, Dresden University of Technology,
Pienner Str. 19, D-01737 Tharandt, Germany
[b]Biomedical Materials Group, Department Pharmaceutics and
Biopharmaceutics, Martin Luther University Halle-Wittenberg,
Heinrich-Damerow-Straβe 4, D-06120 Halle (Saale), Germany
[1]Current address: 110 Agricultural Engineering Building,
The Pennsylvania State University,
University Park, Pennsylvania 16802
*E-mail: kzhang@forst.tu-dresden.de**

Synthesis and structural characterization of chitosan sulfates (CHS) showing biological activities are reported. CHS with diverse total degrees of sulfation (DS_S) in the range of 1.1-1.77 and distinct distributions of sulfate groups were synthesized under homogeneous or non-homogeneous conditions. The sulfate groups were located primarily at 6-O-position as well as at 3-O-position. No sulfation at 2-N-position was detected. The measurements of molecular weights of CHS showed that obtained products are polydisperse. Their molecular weights decrease with longer reaction time or higher reaction temperature. The synthesized CHS did not show significant toxicity to 3T3-L1 fibroblast cells. Subsequently, the effects of CHS on the mitogenic activity of FGF2 and osteogenic activity of BMP2 were investigated.

In Functional Materials from Renewable Sources; Liebner, F., et al.;
ACS Symposium Series; American Chemical Society: Washington, DC, 2012.

Downloaded by NORTH CAROLINA STATE UNIV on August 28, 2012 | http://pubs.acs.org
Publication Date (Web): August 17, 2012 | doi: 10.1021/bk-2012-1107.ch016

Introduction

Glycosaminoglycans, such as heparin and heparan sulfate, are naturally occurring sulfated biopolymers and play a pivotal role in regulating cellular proliferation and differentiation (*1*, *2*). The sulfate groups are important for the biological activities (*3*, *4*). Other naturally non-sulfated polysaccharides including cellulose also exhibited biological activities after sulfation, e.g. anticoagulant and antiviral activity (*5*, *6*). Apart from the sulfate groups, other functional groups including carboxyl and acetyl groups are detected in the backbones of heparin and heparan sulfate (*7*, *8*). In spite of the wide use of heparin in medicine and pharmacy, some drawbacks of it including death cases have been reported (*9*, *10*). Thus, possible substitutes for heparin with heparin-analogue activities have been searched for years (*11*, *12*). Diverse biopolymers have been used as starting materials, e.g. fucan, and galactan (*13*, *14*).

Chitosan is a polysaccharide with a degree of acetylation on the amino groups of up to 50%. Chitosan consists of 2-amino-2-deoxy-D-glucopyranose and 2-acetamido-2-deoxy-D-glucopyranose units that are linked through *β*-(1→4)-glycosidic bonds (*15*, *16*). Chitosan has some beneficial properties, such as antimicrobial ones, excellent biocompatibility, low toxicity and good biodegradability that promote its applications in cosmetics, pharmaceutics and other branches (*15*, *17*, *18*).

Chitosan sulfate (CHS) is a water-soluble ester of chitosan which exhibits blood anticoagulant, antiviral, antimicrobial activity and antioxidant activity (*19*, *20*). Furthermore, CHS promoted the bioactivity of BMP2-induced osteoblastic differentiation *in vitro* and *in vivo* (*21*). CHS is prepared with diverse sulfating agents including chlorosulfonic acid, sulfuric acid and SO_3-pyridine/*N,N*-dimethylformamide (DMF)-complex, yielding CHS with low to high DS_S with various sulfation patterns (*20–23*).

Apart from CHS with only sulfate groups along chitosan chains, chitosan derivatives bearing other functional groups in addition to sulfate groups have also been synthesized e.g. sulfated *N*-carboxymethyl chitosan and chitin sulfate (*24–26*). Sulfated carboxymethyl chitosans were prepared through a multi-step reaction and chitin sulfates were obtained by sulfating chitin showing high degrees of acetylation (*25*, *26*). These products with several functional groups display molecular structures more similar to heparin. However, sulfate groups were supposed to play the predominant role for biological activities of sulfated polysaccharides, e.g. sulfated cellulose, chitosan or fucan (*3–6*, *13*, *14*, *21*, *27*).

In this report, novel CHS were prepared through the sulfation of chitosan using sulfamidic acid and chlorosulfonic acid as sulfating agents. The prepared CHS were characterized regarding their total degrees of sulfation (DS), the distribution of sulfate groups, i.e. the substitution patterns, and their molecular weights. Chlorosulfonic acid is a commonly used sulfating agent and the sulfation of polysaccharides including chitosan with chlorosulfonic acid has been often reported (*5*, *6*, *19–21*, *23*). In contrast, the sulfation of chitosan using sulfamidic acid has not yet been published. Therefore, in this report, the focus lies on the sulfation using sulfamidic acid as sulfating agent. Finally, the cytotoxicity of chosen CHS and their effects on FGF2 (fibroblast growth factor)-induced proliferation as well as BMP2 (bone morphogenic protein)-induced osteogenic activity were analyzed.

Experimental

Materials

Chitosan with a degree of deacetylation of 95.7% and a viscosity of 145 mPas (1% in 1% aqueous acetic acid at 20°C) was purchased from Heppe Medical Chitosan GmbH (Halle/Saale, Germany). Heparin from porcine intestinal mucosa was obtained from Calbiochem (Gibbstown, USA). *N,N*-dimethylformamide (DMF) was freshly distilled. Water was demineralized before use. Other chemicals were all of analysis grade and used as received. Dialysis membrane from Spectrum Laboratories Inc. (Rancho Dominquez, USA) has an approximate molecular weight cut-off of maximal 500 Daltons.

Sulfation of Chitosan (Scheme 1)

Chitosan was sulfated homogeneously or non-homogeneously as described before (*23*, *28*). During the homogeneous sulfation, chitosan remained dissolved in the reaction medium throughout the reaction. In contrast, chitosan was not dissolved at the beginning of the non-homogeneous sulfation.

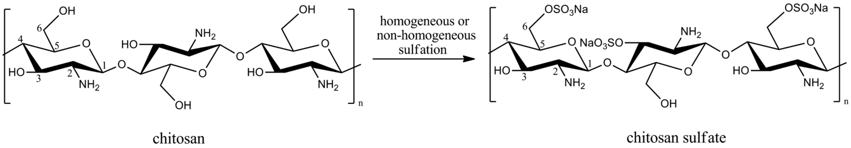

Scheme 1. Schematic representation for sulfation of chitosan.

For the homogeneous sulfation, chitosan (1 g) was dissolved in 20 ml of formic acid and the solution was diluted with 156 ml of DMF. Sulfamidic acid or chlorosulfonic acid in DMF was added into the chitosan solution under vigorous stirring over 30 min. After being kept at 50°C or 70°C for 3 to 24 h, the solution that was cooled down to room temperature (RT) was poured into a saturated ethanolic solution of anhydrous sodium acetate and the product was collected using centrifugation. The product was dissolved in water and the pH value was adjusted to 7.5. Finally, the product was dialyzed against water and obtained after lyophilization. Yield of CHS: up to 76% (w-% of starting chitosan).

The non-homogeneous sulfation of chitosan was realized after the regeneration of chitosan. The regeneration was carried out through dissolving 1 g of chitosan in 100 ml of 1% aqueous acetic acid, precipitating chitosan by adding 100 ml of methanol and 100 ml of an aqueous solution of 4%

Downloaded by NORTH CAROLINA STATE UNIV on August 28, 2012 | http://pubs.acs.org
Publication Date (Web): August 17, 2012 | doi: 10.1021/bk-2012-1107.ch016

Downloaded by NORTH CAROLINA STATE UNIV on August 28, 2012 | http://pubs.acs.org
Publication Date (Web): August 17, 2012 | doi: 10.1021/bk-2012-1107.ch016

sodium hydrogencarbonate and washing with methanol as well as DMF. After the regeneration, chitosan was suspended in 50 ml of DMF for subsequent non-homogeneous sulfation. Sulfamidic acid or chlorosulfonic acid in DMF was added to the chitosan suspension and the mixture was kept at 70°C for 24 h. After the sulfation, the reaction mixture became clear, suggesting that chitosan was dissolved in the reaction mixture. Then, the reaction mixture was precipitated in a saturated ethanolic solution of anhydrous sodium acetate and the product was obtained as described above. Yield of CHS: up to 89% (w-% of starting chitosan).

Characterization of Synthesized CHS

FT Raman spectra of the samples in small metallic discs were recorded on a Bruker MultiRam spectrometer (Bruker, Ettlingen, Germany) with a liquid-nitrogen cooled Ge diode as detector. A cw-Nd:YAG-laser with 1064 nm excitation was applied as light source for Raman scattering. The spectra were recorded over a range of 3500-150 cm^{-1} at a spectral resolution of 3 cm^{-1} and a laser power output of 100 mW.

The ^{13}C NMR spectra in D_2O were recorded at r.t. on a Bruker DFX 400 spectrometer with a frequency of 100.13 MHz, 30° pulse length, and a relaxation delay of 3 s. Up to 20000 scans were accumulated. The CP/MAS ^{13}C NMR spectra were recorded using a Bruker Avance 400 WB spectrometer at r.t. with a frequency of 100.65 MHz, and a relaxation delay of 3 s. Between 5000 and 7000 scans were accumulated. CP/MAS ^{15}N NMR spectroscopy was carried out on the Bruker Avance 400 WB spectrometer at r.t. with a contact time of 1 ms, a relaxation delay of 1 s and an acquisition time of 20 ms. 80.000 scans were accumulated and the chemical shifts were externally referenced to ^{15}N-nitromethane.

The contents of carbon, hydrogen and nitrogen were determined with Elemental Analyser vario EL from Elementar (Hanau, Germany). The content of sulfur was measured with Elemental Analyser Eltra CS 500 (Neuss, Germany). The total DS_S was calculated according to: total $DS_S = (S\%/32)/(N\%/14)$.

Size exclusion chromatography (SEC) was performed on a system containing a Waters 410 reflective index (RI) detector (Waters Corporation, Milford, MA) and PSS Suprema 3000 and 100 columns (Polymer Standards Service GmbH, Mainz, Germany). The columns have been calibrated with pullulan standards (Sigma–Aldrich, Buchs, Switzerland). The elution of the sample solution (0.05-0.07%) was carried out with 0.1 M aqueous NaCl as the mobile phase. Empower Pro software (Waters Corporation) was used for analyzing the data.

Scanning electron microscopy (SEM) images were recorded on a JEOL JSM-T330A scanning microscope (Jeol Ltd, Tokyo, Japan) at RT. Samples were coated with a 30 nm thick carbon and gold layer before the measurement.

Cell Culture

3T3-L1 fibroblast cells obtained from ATCC (Manassas, USA) were cultured in flasks (75 cm^2, Greiner bio-one, Frickenhausen, Germany) in Dulbecco's modified Eagle medium (DMEM, Biochrom AG, Berlin, Germany) supplemented with 10% fetal bovine serum (FBS, Biochrom AG) and 1%

Downloaded by NORTH CAROLINA STATE UNIV on August 28, 2012 | http://pubs.acs.org
Publication Date (Web): August 17, 2012 | doi: 10.1021/bk-2012-1107.ch016

penicillin–streptomycin–fungizone (PSF, Promocell, Heidelberg, Germany) in a humidified atmosphere of 5% CO_2/95% air at 37 °C. Cells were harvested by treatment with trypsin/EDTA (Biochrom). Trypsinization was stopped by addition of FBS, and cells were washed twice with DMEM. The mouse myoblast cell line C2C12 which expresses osteogenic activity in the presence of BMP2 was purchased from the German Collection of Microorganisms and Cell Cultures (Braunschweig, Germany). The cells were cultured in 75 cm^2 culture flasks in DMEM containing 10% fetal bovine serum (Biochrom), antibiotics (100 U/ml penicillin, 100 µg/ml streptomycin; Biochrom) and 2 mM L-glutamine (Biochrom) at 37 °C in a humidified atmosphere of 5% CO_2/95% air until near confluence. The cells were detached with 0.25% trypsin/0.02% EDTA. Trypsinization was stopped after 5 min by the addition of DMEM with 10% FBS.

Cytotoxicity Assay

The cytotoxicity assay was carried out according to (*29*). CHS4 and CHS5 were dissolved in DMEM with 1% PSF (Promocell, Heidelberg, Germany) and 1% insulin-transferrin-selenium A (ITS, Gibco, New York, USA) at a concentrations of 500 µg/ml. 3T3-L1 fibroblast cells were seeded at a density of 40 000 cells/well in 96-well plates (Greiner bio-one) in DMEM supplemented with 10% FBS and 1% PSF, cultured for 48 h. The plates were washed once with DMEM, and then with 200 µl of either CHS-DMEM-solution or DMEM (control). After an incubation of cells for further 24 h, the viability of cells was measured with QBlue assay (BioChain, Hayward, USA). This assay is based on the use of the redox dye resazurin, which is converted into a highly fluorescent product (resorufin) by reductases of metabolically active cells. The fluorescence intensity was measured with an excitation wavelength of 544 nm and an emission wavelength of 590 nm using plate reader Fluostar Optima (BMG Labtech, Offenburg, Germany). The viability was calculated as a ratio of the control. Measurements were carried out in quadruplicates and given as means ± standard deviations.

Investigation of mitogenic effects of CHS on 3T3-L1 fibroblasts 3T3-L1 fibroblast cells were seeded at a density of 10.000 cells/well in 96-well plates (Greiner bio-one) in DMEM supplemented with 10% FBS and 1% PSF and cultured for 24 h. After washing the plates with DMEM only, CHS or heparin were applied to the cells in DMEM without FBS at concentrations of 50 and 500 µg/ml for 48 h in the presence of 10 ng/ml FGF-2. Proliferation was measured on the basis of the total released LDH content using the Cytotoxicity Detection Kit^{PLUS} (LDH) (Roche, Mannheim, Germany). Cells proliferate and at the end of an experiment, lysis reagents supplied with the kit were added to each cell-containing well. To determine the LDH activity, 100 µl of reaction mixture was added and incubated for 30 min. The absorbance of the samples was measured with a wavelength at 490 nm by the Fluostar Optima plate reader. Cell growth was expressed as a ratio of samples to control wells (10 ng/ml FGF2 only). All experiments were carried out with four wells per sample and dilution from which means and standard deviations were calculated.

Downloaded by NORTH CAROLINA STATE UNIV on August 28, 2012 | http://pubs.acs.org
Publication Date (Web): August 17, 2012 | doi: 10.1021/bk-2012-1107.ch016

Quantification of Alkaline Phosphatase (ALP) Activity

The quantification of ALP activity was carried out as previously reported (*30*). The C2C12 cells were seeded at a density of 2 × 10^4/96-wells in normal growth medium. After 18 h, the cells were washed quickly with PBS to remove serum. Then, DMEM containing 2% FBS and different concentrations of BMP-2 (Invitrogen, Karlsruhe, Germany) with or without CHS was added. The measurement of ALP activity was performed after 72 h. At the end of the incubation period, cells were lysed by addition of 50 µl of 0.5% Triton 100 in distilled water for 30 min at RT at 300 rpm on an orbital shaker (IKA, Staufen, Germany). Then, 20 µl of the lysate was transferred to a new 96-well plate and 40 µl of 1 mg p-nitrophenylphosphate/ml (Roth, Karlsruhe, Germany) in 0.5 M 2-amino-2-methyl-1-propanol buffer (Roth) pH 10.3 was added for the determination of ALP activity. The absorbance was measured at a wavelength of 405 nm using an Optima FluoroStar microplate reader (BMG Labtech, Offenburg, Germany) after 15 min incubation of the mixture at 37 °C. The histochemical staining of alkaline phosphatase was done by fixing the cells with 5% glutaraldehyde for 15 min, washing with PBS and subsequent incubation with a mixture of 0.17 mg /ml 5-bromo-4-chloro-3-indolylphosphate (BCIP, Applichem, Darmstadt, Germany) and 0.33 mg/ml nitro blue tetrazolium (NBT; Applichem) in 0.375 M 2-amino-2-methyl-3-propanol buffer (pH = 10.3) for 1 h at RT. The staining reaction was stopped by addition of 20 mM EDTA solution. Micrographs were taken with an inverted light microscope (Axiovert 100, Carl Zeiss, Oberkochen, Germany) equipped with a CCD camera.

Results and Discussion

Synthesis and Characterisation of Chitosan Sulfate (CHS)

Chitosan could be sulfated by sulfamidic acid or chlorosulfonic acid. The sulfation of chitosan proceeded homogeneously in formic acid/DMF-mixture or non-homogeneously in DMF. Figure 1 depicts the FT-Raman spectra of chitosan and obtained CHS. FT-Raman spectroscopy as a rapid and sensitive analytical method does not suffer interference from highly polar compounds including water. Based on FT-Raman spectroscopy, quantification of the DS of CHS has been established before (*23*, *28*).

Comparing the FT-Raman spectrum of chitosan and CHS, new bands are notable at 1069, 1016, 833 and 588 cm^{-1}. The band at 833 cm^{-1} is attributed to stretching vibrations of C-O-S groups. The bands at 1069 and 1016 cm^{-1} are ascribed to the stretching vibrations of O=S=O groups, while the band at 588 cm^{-1} is due to the deformation vibration δ(O=S=O) (*23*, *31*). The presence of these bands suggests the introduction of sulfate groups into chitosan chains (*23*).

Furthermore, it is visible that certain bands attributed to the chitosan backbone change their positions after the introduction of sulfate groups. The signals between 2800 and 3000 cm^{-1} are ascribed to the stretching vibrations of C-H bonds (*31*). The peak at 2885 cm^{-1} within the spectrum of chitosan shifts to 2962 cm^{-1} within the spectrum of CHS. The signal at 1462 cm^{-1} attributed to bending vibrations of

CH_2 groups shifts to 1458 cm^{-1} after the sulfation (*32*). The signals at 1376, 1261 and 898 cm^{-1} due to vibrations of chitosan backbones shift only slightly to 1384, 1274 and 917 cm^{-1}, respectively. Moreover, the bands at 1094 and 1115 cm^{-1} with a shoulder at 1145 cm^{-1} are not observable within the FT-Raman spectrum of CHS with high total DS_S. Besides, the very weak signal between 1570 and 1630 cm^{-1} due to the amide II vibrations of amide groups remains in the same range and its intensity stays almost constant, which implies the non-derivatisation of the amino groups (*10*, *32*).

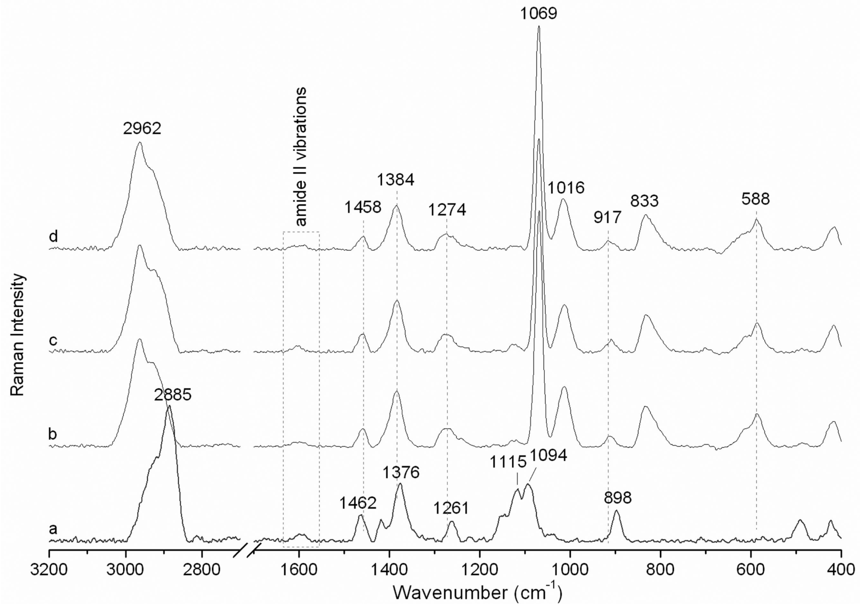

Figure 1. FT-Raman spectra (3200-400 cm^{-1}) of (a) chitosan, (b) CHS4, (c) CHS7 and (d) CHS10 at RT.

The total DS_S of obtained CHS were determined to range between 1.1 and 1.72 (Table 1). It was varied by altering the sulfation status through homogeneous or non-homogeneous sulfation as well as sulfation parameters including the sulfation duration, temperature and the amount of sulfating agent. Under homogeneous or non-homogeneous sulfation conditions, longer sulfation times reduced the total DS_S. Furthermore, higher sulfation temperature decreased the total DS_S upon the non-homogeneous sulfation of chitosan (Table 1).

CHS prepared in this report are all water-soluble. In comparison to the homogeneous sulfation that was realized within 3 h, the non-homogeneous sulfation with sulfamidic acid needed longer sulfation times, e.g. 24 h, for the preparation of water-soluble products. However, the sulfation with chlorosulfonic acid resulted in water-soluble CHS within 3 h. As reported before, the non-homogeneous sulfation by other sulfating agents, e.g. SO_3-DMF complex, also produced water-soluble CHS after a reaction within 3 h at 50°C or 70°C (*20*, *23*). The requirement of longer sulfation durations for sulfamidic acid under non-homogeneous conditions may be due to its low reactivity towards chitosan.

Downloaded by NORTH CAROLINA STATE UNIV on August 28, 2012 | http://pubs.acs.org
Publication Date (Web): August 17, 2012 | doi: 10.1021/bk-2012-1107.ch016

Downloaded by NORTH CAROLINA STATE UNIV on August 28, 2012 | http://pubs.acs.org
Publication Date (Web): August 17, 2012 | doi: 10.1021/bk-2012-1107.ch016

Table 1. Sulfation of chitosan and characterization of synthesized CHS

samples	*molar ratio*[a]	*reaction temperature / duration*	DS_{S6}[b]	*Total* DS_S[b]	DS_{S3}[b]	DP_n	DP_w	DP_w/DP_n
Homogeneous sulfation								
CHS1[c]	15	70°C / 24 h	0.69	1.12	0.43	210	611	2.91
CHS2[c]	15	70°C / 3 h	0.84	1.55	0.71	789	2355	2.98
CHS3[c]	15	70°C / 3 h	0.82	1.4	0.58	809	2604	3.22
CHS4[d]	6	50°C / 5 h	0.85	1.1	0.25	438	1785	4.07
Non-homogeneous sulfation								
CHS5[d]	13	50°C / 3 h	1	1.77	0.77	426	1811	4.25
CHS6	15	50°C / 24 h	1	1.69	0.69	731	3512	4.80
CHS7	6	70°C / 24 h	1	1.33	0.33	565	2375	4.20
CHS8	10	70°C / 24 h	1	1.72	0.72	543	2407	4.43
CHS9	10	70°C / 40 h	1	1.49	0.49	486	1598	3.29
CHS10	15	70°C / 24 h	1	1.59	0.59	331	1048	3.17
CHS11	15	90°C / 24 h	1	1.50	0.5	114	170	1.49

[a] Molar ratio in mol sulfamidic acid per mol GlcN units. [b] Partial DS_S at 6-O-position (DS_{S6}) were estimated by liquid-state ^{13}C NMR spectroscopy (D_2O) and total DS_S determined by elemental analysis. Partial DS_S at 3-O-position (DS_{S3}) is equal to the difference between total DS_S and DS_{S6}. [c] CHS1 and 2 were prepared in 156 ml DMF/20 ml formic acid and CHS3 in 78 ml DMF/20 ml formic acid. [d] CHS4 and 5 were prepared with chlorosulfonic acid as sulfating agent and other CHS were prepared with sulfamic acid as sulfating agent.

CP/MAS ^{15}N NMR spectroscopy was used to characterize chitin/chitosan and chitosan derivatives (*23*, *33*). Figure 2 illustrates the CP/MAS ^{15}N NMR spectrum of CHS10 at r.t. Only one peak at -344.8 ppm attributed to non-derivatised amino groups of GlcN units is visible, suggesting that the 2-N-position of chitosan was not sulfated during the sulfation with sulfamidic acid. Possibly, the amino groups were protonated under the applied sulfation conditions and thus a sulfation of amino groups was not possible. Thus, an alkaline medium would be required for the sulfation at 2-N-position (*22*).

Figure 3 displays characteristic liquid- and solid-state ^{13}C NMR spectra of CHS and chitosan. It has been reported that liquid-state ^{13}C NMR spectroscopy was used to quantitatively analyze chitosan and cellulose derivatives with only small deviations of 1-2%, which makes this method feasible for calculating DS_S of CHS (*34*, *35*). In the ^{13}C NMR spectrum of CHS in D_2O, a new peak at 67 ppm is notable, while the signal at 60.5 ppm in the ^{13}C NMR spectrum of chitosan disappears. The latter signal is attributed to C6 and the former to $C6_S$ with sulfate groups at 6-O-position. The disappearance of the signal at 60.5 ppm suggests the complete sulfation of the 6-O-position. Based on these both signals, the partial DS_S at 6-O-position (DS_{S6}) of CHS was estimated. As shown in Table 1, the homogeneous sulfation of chitosan produced CHS with diverse DS_{S6}, while the DS_{S6} of non-homogeneously prepared CHS was always 1. This difference lies in the distinct sulfation processes: the non-homogeneous process preferred the sulfation of the primary hydroxyl groups because of its high reactivity, while the hydroxyl groups at 3-O-position were highly sulfated under homogeneous conditions (*9*, *10*, *27*). The partial DS_S at 3-O-position (DS_{S3}) was calculated by comparing the total DS_S and DS_{S6} (Table 1). Thus, the sulfation patterns of CHS, i.e. the distribution of the sulfate groups at 6- and 3-O-position, were regulated by applying diverse sulfation statuses or sulfation parameters.

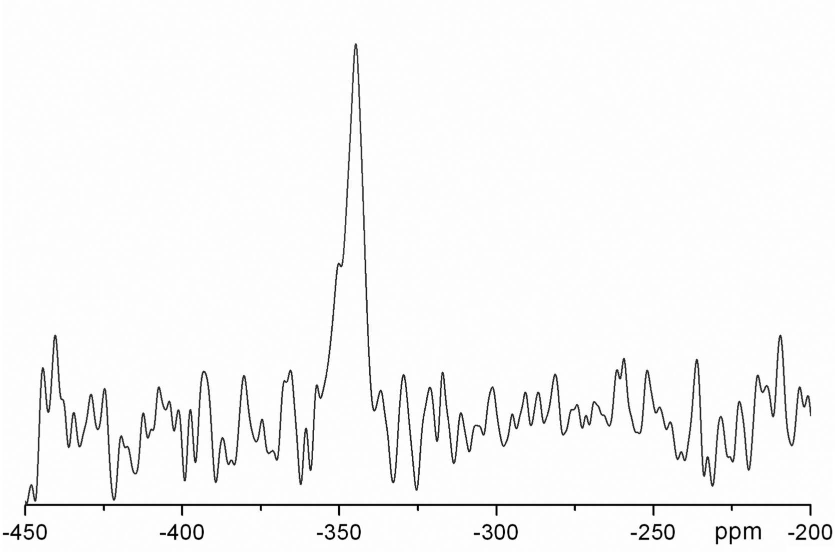

Figure 2. CP/MAS ^{15}N NMR spectrum (-450 – -200 ppm) of CHS10 at r.t.

Moreover, the peak of C2 at 56.7 ppm in the ^{13}C NMR spectrum of chitosan shifts to 55.8 ppm after the sulfation. The signals attributable to C3, 4 and 5 are visible in the range of 70–80 ppm in the ^{13}C NMR spectrum of chitosan. After the sulfation, the peak of C3/$C3_S$ shifts to around 78 ppm, while the signals of C4 and C5 between 72 and 74 ppm overlap strongly.

Apart from the liquid-state ^{13}C NMR spectroscopy, the sulfation of chitosan can also be characterized by CP/MAS ^{13}C NMR spectroscopy as depicted in Figure 3. After the sulfation, the peak of C1 at 106.3 ppm in the solid-state ^{13}C NMR spectrum of chitosan shifts to around 97.3 ppm (*36*). Furthermore, the signal of C4 between 81 and 88 ppm is not observable after the sulfation. As well, the signal of C6 at 61.2 ppm disappears, while a new signal at 69 ppm due to the complete sulfation of primary hydroxyl groups is notable. Moreover, the peak of C2 at 58 ppm shifts slightly to 56.6 ppm, and the peak at 75.8 ppm derived from C3 and 5 shifts to 73.6 ppm after the sulfation. Additionally, the signals in the solid-state ^{13}C NMR spectrum of CHS became broader than those of chitosan, indicating the formation of a more amorphous product than the starting chitosan (*37*).

Downloaded by NORTH CAROLINA STATE UNIV on August 28, 2012 | http://pubs.acs.org
Publication Date (Web): August 17, 2012 | doi: 10.1021/bk-2012-1107.ch016

Downloaded by NORTH CAROLINA STATE UNIV on August 28, 2012 | http://pubs.acs.org
Publication Date (Web): August 17, 2012 | doi: 10.1021/bk-2012-1107.ch016

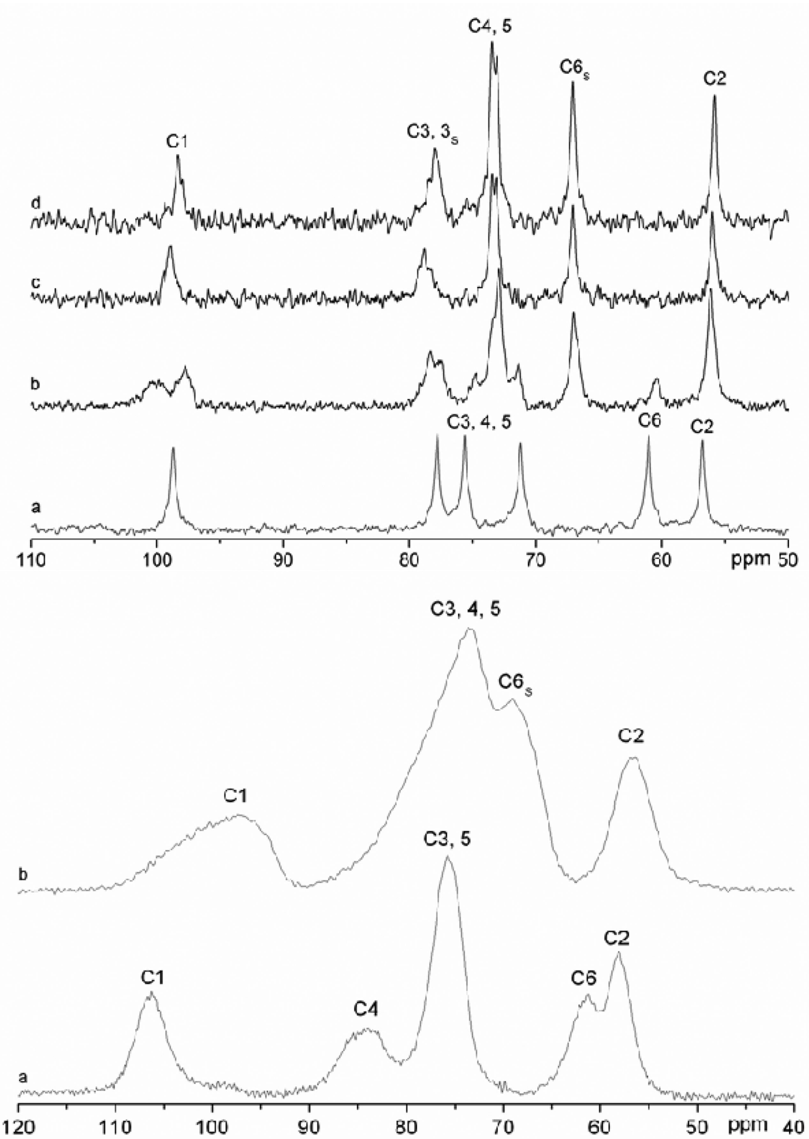

Figure 3. Above: ^{13}C NMR spectra (110-50 ppm) of (a) chitosan in 1% aqueous acetic acid, (b) CHS4, (c) CHS6 and (d) CHS10 in D_2O at RT. Bottom: CP/MAS ^{13}C NMR spectra (120-40 ppm) of (a) chitosan and (b) CHS6 at r.t.

Water-soluble CHS with diverse total $DS_S/DS_{S6}/DS_{S3}$ and therefore distinct sulfation patterns with sulfate groups at 3/6-O-position can be prepared using sulfamidic acid besides chlorosulfonic acid (*23*). By varying the sulfation status and parameters, total and partial DS_S could be regulated. The distribution of the sulfate groups within sulfated polysaccharides was proposed to be important for

Downloaded by NORTH CAROLINA STATE UNIV on August 28, 2012 | http://pubs.acs.org
Publication Date (Web): August 17, 2012 | doi: 10.1021/bk-2012-1107.ch016

their biological activities. As reported before, sulfated cellulose and chitosan demonstrated anticoagulant activities and the sulfate groups at 6-O-position were assumed to be necessary (*38*, *39*). The enhanced bioactivity of BMP2 by CHS was suggested to be primarily attributable to the sulfation at 6-O-position (*21*). Furthermore, the sulfate groups at 6-O-position in heparin played a pivotal role in its interaction with FGF (*4*). Rising contents of sulfate groups among heparin oligosaccharides, i.e. rising total DS_S and especially DS_{S6}, increased FGF2-induced proliferation (*40*, *41*). Moreover, it was found that the distribution of sulfate groups among chondroitin sulfate oligosaccharide was critical for its interaction with growth factors (*42*). Thus, the determination of the distribution of sulfate groups within CHS and the elucidation of their structures are important for subsequent investigations of their biological properties.

Apart from the DS_S, the molecular weight of sulfated polysaccharides is another important feature influencing their properties (*43*, *44*). Figure 4 illustrates typical SEC chromatograms of CHS prepared by sulfamidic acid. The molecular weights in the form of number-average degree of polymerisation (DP_n) as well as mass-average degree of polymerisation (DP_w) were calculated based on the SEC analysis (Table 1). According to the data, the DP_n of obtained CHS decreased with longer sulfation time, comparing CHS1 and 2 or CHS8 and 9. Higher sulfation temperature and larger amount of sulfamidic acid also reduced the DP_n of CHS significantly (Figure 5). Especially, the sulfation temperature decreased the DP_n more strongly than the amount of sulfamidic acid.

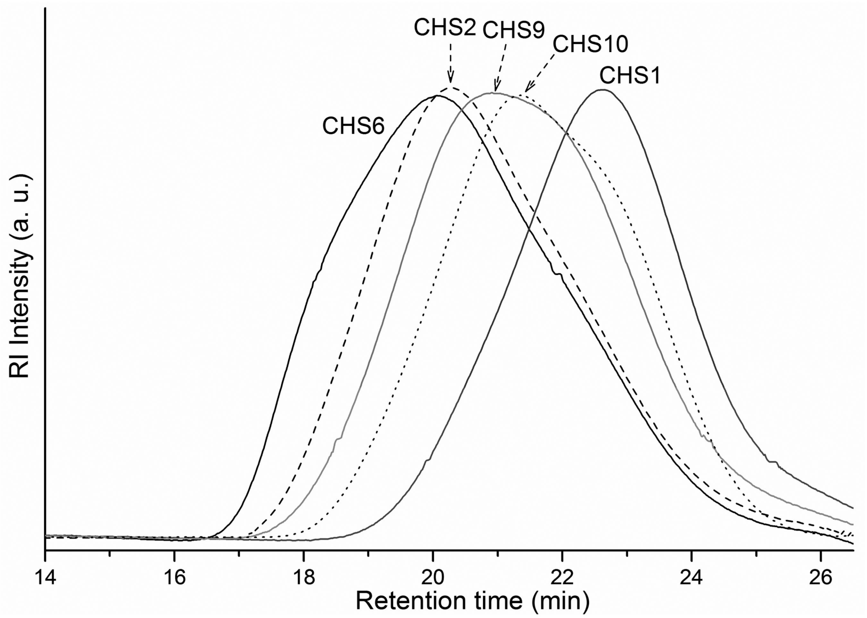

Figure 4. SEC elution patterns of CHS1, 2, 6, 9 and 10.

Downloaded by NORTH CAROLINA STATE UNIV on August 28, 2012 | http://pubs.acs.org
Publication Date (Web): August 17, 2012 | doi: 10.1021/bk-2012-1107.ch016

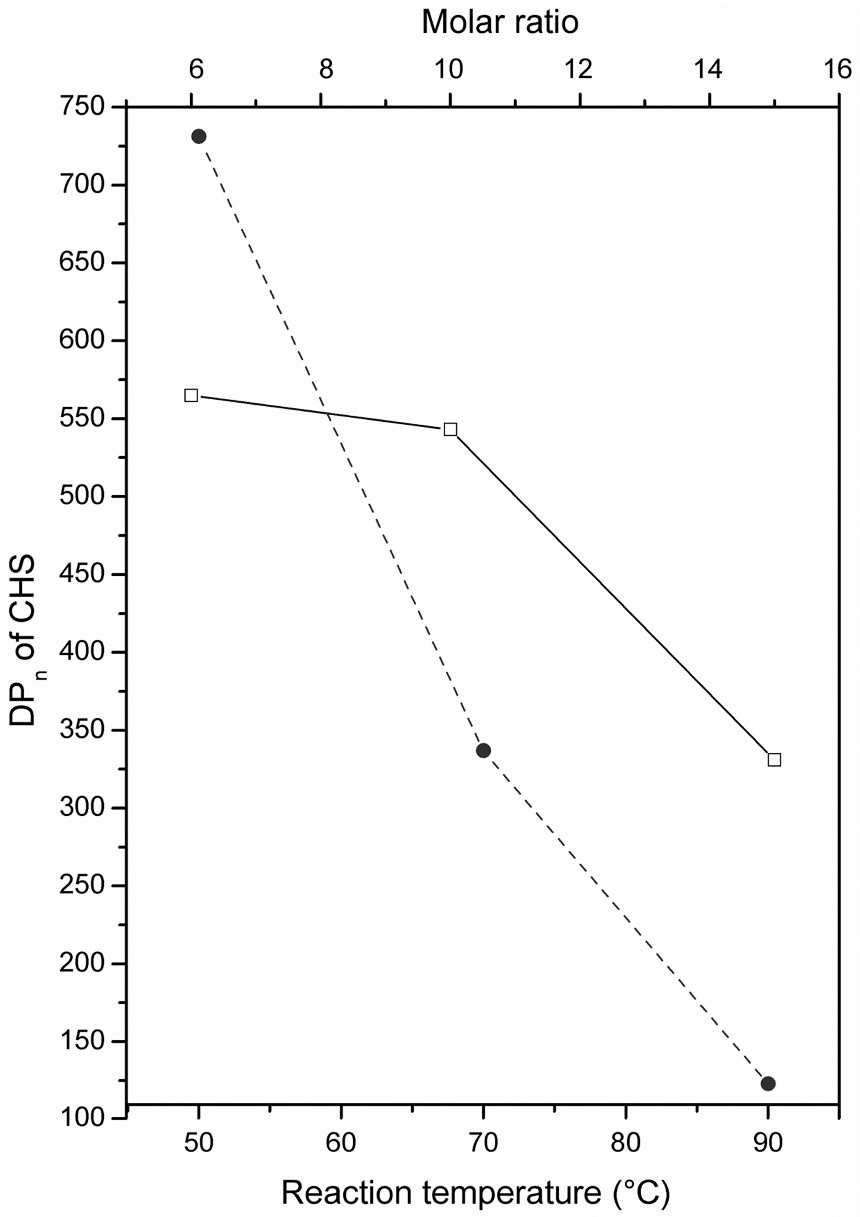

Figure 5. DP$_n$ of non-homogeneously prepared CHS depending on molar ratios in mol sulfamidic acid per mol GlcN units (□) and reaction temperatures in °C (●).

The polydispersities, i.e. DP$_w$/DP$_n$, of obtained CHS were determined to be between 1.49 and 4.8 (Table 1), indicating wide distributions of their molecular weights. Furthermore, the polydispersity decreases with higher sulfation temperature or larger amount of sulfamidic acid (Table 1). A very low polydispersity of 1.49 was determined for the CHS11 which was prepared at high temperatures of 90°C for 24 h. Thus, at high sulfation temperature, chitosan chains should be strongly degraded down to a certain level, and relatively uniform distributions of molecular weights were achieved. The contents of sulfate groups in CHS may also affect the average sizes of the sulfated chitosan chains in an aqueous solution.

Cytotoxicity Measurement

Cytotoxicity measurements of CHS4 and CHS5 were performed to ensure that these CHS for further mitogenic and osteogenic investigations are not toxic for cells. As shown in Figure 6, CHS4 and CHS5 showing low and high total DS_S of 1.1 and 1.77 did not demonstrate significant toxicity to 3T3-L1 fibroblast cells. Therefore, CHS can be used for further mitogenic and osteogenic investigations. As reported before, cellulose sulfate and cellulose sulfate containing carboxyl or carboxymethyl groups also did not exhibit significant cytotoxicity to 3T3-L1 fibroblast cells (*29*).

Downloaded by NORTH CAROLINA STATE UNIV on August 28, 2012 | http://pubs.acs.org
Publication Date (Web): August 17, 2012 | doi: 10.1021/bk-2012-1107.ch016

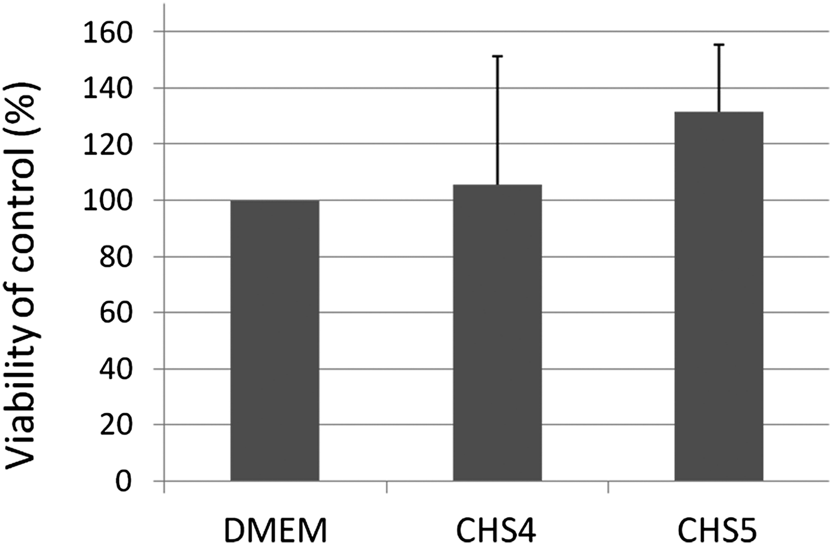

Figure 6. Cytotoxicity measurement of CHS4 and CHS5 in comparison to control (DMEM only). Viability was measured by QBlue assay with 3T3-L1 fibroblast cells treated with CHS4 or CHS5 at a concentration of 500 µg/ml or only with DMEM.

Biological Activity of CHS

Figure 7 shows the effect of heparin, CHS4 and CHS5 at two different concentrations of 50 and 500 µg/ml on the mitogenic activity of FGF2. In comparison to heparin, CHS4 and CHS5 enhanced the mitogenic activity of FGF2 more strongly at low concentration of 50 µg/ml. Moreover, CHS5 with a total DS_S of 1.77 showed a higher effect than CHS4 with a lower total DS_S of

1.1. However, at higher concentration of 500 µg/ml, CHS4 had a similar effect as heparin, while CHS5 exhibited a significantly lower effect.

It has been shown that cellulose sulfates with high total DS_S demonstrated remarkable mitogenic activity compared to heparin. The total DS_S and sulfation pattern of cellulose sulfates are proposed to be relevant to their effects on the mitogenic activity of FGF2. Protection of FGF2 against proteolytic degradation was assumed to be a reason for the prolongation of the mitogenic activity of FGF2 (*29*). However, the effect of cellulose sulfates with total DS_S of less than 1.8 was lower than that of heparin at concentrations of up to 1000 µg/ml. In the present study, CHS showed higher effects than heparin at 50 µg/ml. Possibly, CHS could protect FGF2 against proteolytic degradation more effectively due to the presence of amino groups and therefore higher binding activity to the binding sites in FGF2 (*4*).

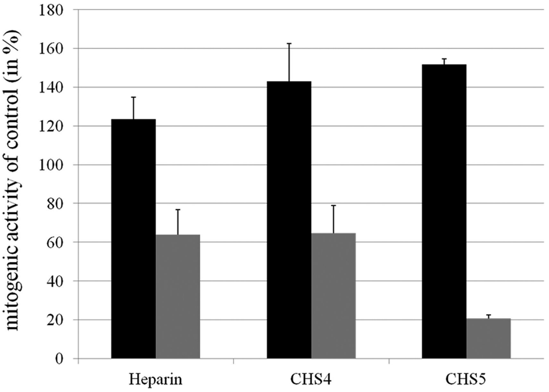

Figure 7. Mitogenic activity of 50 and 500 µg/ml CHS or heparin in the presence of FGF2. Proliferation was measured after incubation of 3T3-L1 fibroblast with CHS or heparin and FGF2. Black for 50 and gray for 500 µg/ml.

CHS with high total DS_S also promoted the effect of BMP2-induced osteogenic activity (*21*). As shown in Figure 8A, CHS5 with a total DS_S of 1.77 caused a significant increase of BMP2-induced ALP activity, but this effect is only very significant at concentrations below 400 ng/ml. At the concentration of 400 ng/ml, CHS5 showed only a slightly higher effect compared to the experiment without CHS5. Moreover, the protein content was measured to quantify amounts of C2C12 cells after incubations (Figure 8B). It is obvious that the amounts of cells were higher after the incubations without CHS5 at higher concentrations of 100, 200 and 400 ng/ml. An inhibitory effect possibly dominated the incubation of cells in the presence of CHS.

Figure 9 visualizes the effect of CHS on the BMP2-induced ALP secretion. BCIP and NBT were used for histochemical staining of C2C12 cells. C2C12 cells demonstrated faint blue staining. It is evident that the application of 2.5 µg/ml CHS5 in the presence of 200 ng/ml BMP2 caused stronger blue staining than the control. However, if a higher concentration of 10 µg/ml CHS5 was used, the ALP expression decreased significantly resulting in weaker staining.

Downloaded by NORTH CAROLINA STATE UNIV on August 28, 2012 | http://pubs.acs.org
Publication Date (Web): August 17, 2012 | doi: 10.1021/bk-2012-1107.ch016

Downloaded by NORTH CAROLINA STATE UNIV on August 28, 2012 | http://pubs.acs.org
Publication Date (Web): August 17, 2012 | doi: 10.1021/bk-2012-1107.ch016

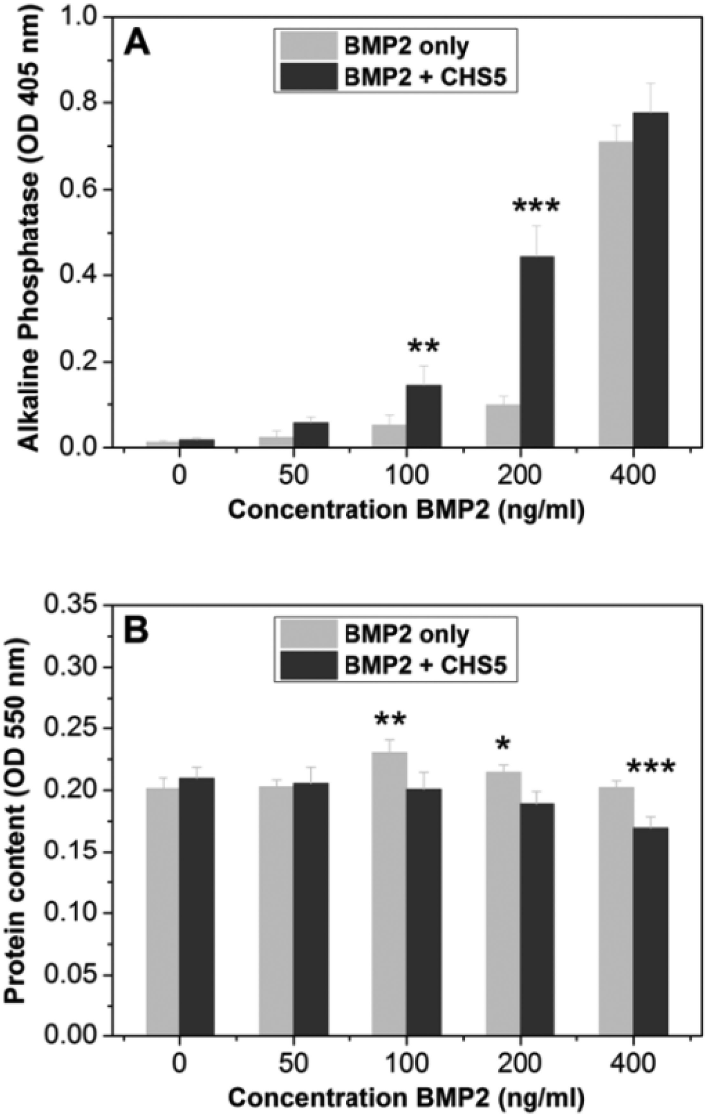

*Figure 8. Effect of different BMP2 concentrations on ALP expression and protein contents. Cells were cultured for three days with 0, 50, 100, 200 or 400 ng/ml BMP2 with or without 0.6 µg/ml of CHS5. (A) ALP activity was measured after 3 days with p-nitrophenylphosphate. (B) Protein content was measured after 3 days with BCA + $CuSO_4$. The values represent means ± standard deviations (n = 8), *p < 0.01, **p < 0.001, ***p < 0.0001 calculated by Student's test. For ALP: significant difference between the samples with and without CHS5 for different BMP2 concentrations, respectively. Protein content: significant difference compared to the control without BMP2/without CHS5. (Reproduced with permission from reference (30), Copyright 2011 Elsevier).*

Downloaded by NORTH CAROLINA STATE UNIV on August 28, 2012 | http://pubs.acs.org
Publication Date (Web): August 17, 2012 | doi: 10.1021/bk-2012-1107.ch016

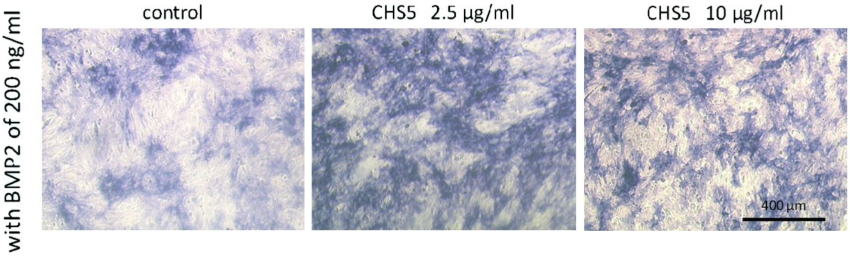

Figure 9. Expression of ALP activity by C2C12 cells. Cells were cultured for 3 days in the presence of 200 ng/ml BMP2 and 2.5 or 10 μg/ml CHS5. Control with 200 ng/ml BMP2 only ALP was visualized by histochemical staining with NBT and BCIP. (Reproduced with permission from reference (30), Copyright 2011 Elsevier).

Conclusion

Various CHS with distinct contents of sulfate groups as well as sulfation patterns were synthesized with sulfamidic acid or chlorosulfonic acid as sulfating agents. The sulfation proceeded homogeneously or non-homogeneously, producing CHS with total DS_S between 1.1 and 1.77. The DS_{S6} were determined to be in the range of 0.69-1, while no sulfation at 2-N-position was detectable. The obtained CHS are polydisperse and demonstrate big aggregates after lyophilization. CHS did not show significant cytotoxicity. At a concentration of 50 μg/ml, CHS enhanced the mitogenic activity of FGF2 more strongly than heparin. However, at a higher concentration of 500 μg/ml, both lowly and highly sulfated CHS showed lower effect on the mitogenic activity of FGF2 than heparin. Moreover, CHS5 with high total DS_S of 1.77 promoted of BMP2-induced ALP expression at concentrations up to 400 μg/ml, but the protein contents decreased at concentrations higher than 100 μg/ml.

Acknowledgments

The financial support by German Research Foundation (Deutsche Forschungsgemeinschaft, grants: FI755/4-1 and FI755/4-2, GR1290/7-1 and GR1290/7-2) is gratefully acknowledged.

References

1. Capila, I.; Lindardt, R. J. *Angew. Chem., Int. Ed.* **2002**, *41*, 391–412.
2. Hacker, U.; Nybakken, K.; Perrimon, N. *Nat. Rev. Mol. Cell Biol.* **2005**, *6*, 530–541.
3. Pye, D. A.; Vives, R. R.; Turnball, J. E.; Gallagher, J. T. *J. Biol. Chem.* **1998**, *273*, 22936–22946.
4. Schlessinger, J.; Plotnikov, A.; Ibrahimi, O. A.; Eliseenkova, A. V.; Yeh, B. K.; Yayon, A.; et al. *Mol. Cell* **2000**, *6*, 743–750.

5. Groth, T.; Wagenknecht, W. *Biomaterials* **2001**, *22*, 2719–2729.
6. Wang, Z.; Li, L.; Xiao, K.; Wu, J. *Bioresour. Technol.* **2009**, *100*, 1687–1690.
7. Gandhi, N. S.; Mancera, R. L. *Chem. Biol. Drug Des.* **2008**, *72*, 455–482.
8. Sasisekharan, R.; Shriver, Z.; Venkataraman, G.; Narayanasami, U. *Nat. Rev. Cancer* **2002**, *2*, 521–528.
9. Capila, I.; Linhardt, R. J. *Angew. Chem.* **2002**, *114*, 426–50.
10. Mulloy, B.; Forster, M. J. *Glycobiology* **2000**, *10*, 1147–1156.
11. Liu, H.; Zhang, Z.; Linhardt, R. J. *Nat. Prod. Rep.* **2009**, *26*, 313–321.
12. Laremore, T.; Zhang, F.; Dordick, J. S.; Liu, J.; Linhardt, R. J. *Curr. Opin. Chem. Biol.* **2009**, *13*, 633–640.
13. Nishino, T.; Aizu, Y.; Nagumo, T. *Thromb. Res.* **1991**, *62*, 765–773.
14. Farias, W. R. L.; Valente, A-P.; Pereira, M. S.; Mourão, P. A. S. *J. Biol. Chem.* **2000**, *275*, 29299–29307.
15. Muzzarelli, R. A. A.; Muzzarelli, C. *Adv. Polym. Sci.* **2005**, *186*, 151–209.
16. Rinaudo, M. *Prog. Polym. Sci.* **2006**, *31*, 603–632.
17. Kumar, M. N. V. R.; Muzzarelli, R. A. A.; Muzzarelli, C.; Sashiwa, H.; Domb, A. J. *Chem. Rev.* **2004**, *104*, 6017–6084.
18. Muzzarelli, R. A. A. *Mar. Drugs* **2010**, *8*, 292–312.
19. Huang, R.; Du, Y.; Zheng, L.; Liu, H.; Fan, L. *React. Funct. Polym.* **2004**, *59*, 41–51.
20. Xing, R.; Liu, S.; Yu, H.; Guo, Z.; Li, Z.; Li, P. *Carbohydr. Polym.* **2005**, *61*, 148–154.
21. Zhou, H.; Qian, J.; Wang, J.; Yao, W.; Liu, C.; Chen, J.; et al. *Biomaterials* **2009**, *30*, 1715–1724.
22. Holme, K. R.; Perlin, A. S. *Carbohydr. Res.* **1997**, *302*, 7–12.
23. Zhang, K.; Helm, J.; Peschel, D.; Gruner, M.; Groth, T.; Fischer, S. *Polymer* **2010**, *51*, 4698–4705.
24. Ho, Y.; Wu, S.; Mi, F.; Chiu, Y.; Yu, S.; Panda, N.; Sung, H. *Bioconjugate Chem.* **2010**, *21*, 28–38.
25. Muzzarelli, R. A. A.; Tanfani, F.; Emanuell, M.; Pace, D. P.; Chiurazzi, E.; Piani, M. *Carbohydr. Res.* **1984**, *126*, 225–231.
26. Zou, Y.; Khor, E. *Carbohydr. Polym.* **2009**, *77*, 516–525.
27. Kunou, M.; Hatanaka, K. *Carbohydr. Polym.* **1995**, *28*, 107–112.
28. Zhang, K.; Peschel, D.; Helm, J.; Groth, T.; Fischer, S. *Carbohydr. Polym.* **2011**, *83*, 60–65.
29. Peschel, D.; Zhang, K.; Aggarwal, N.; Brendler, E.; Fischer, S.; Groth, T. *Acta Biomater.* **2010**, *6*, 2116–2125.
30. Peschel, D.; Zhang, K.; Fischer, S.; Groth, T. *Acta Biomater.* **2012**, *8*, 183–193.
31. Socrates, G. *Infrared and Raman Characteristic Group Frequencies: Table and Charts*, 3rd ed.; Wiley: England, 2001.
32. Focher, B.; Naggi, A.; Torri, G.; Cosani, A.; Terbojevich, M. *Carbohydr. Polym.* **1992**, *17*, 97–102.
33. Yu, G.; Morin, F. G.; Nobes, G. A. R.; Marchessault, R. H. *Macromolecules* **1999**, *32*, 518–520.
34. Nehls, I.; Wagenknecht, W.; Philipp, B.; Stscherbina, D. *Prog. Polym. Sci.* **1994**, *19*, 29–78.

Downloaded by NORTH CAROLINA STATE UNIV on August 28, 2012 | http://pubs.acs.org
Publication Date (Web): August 17, 2012 | doi: 10.1021/bk-2012-1107.ch016

35. Baumann, H.; Faust, V. *Carbohydr. Res.* **2001**, *331*, 43–57.
36. Heux, L.; Brugnerotto, J.; Desbrières, J.; Versali, M. F.; Rinaudo, M. *Biomacromolecules* **2000**, *1*, 746–751.
37. Tanner, S. F.; Chanzy, H.; Vincendon, M.; Roux, J. C.; Gaill, F. *Macromolecules* **1990**, *23*, 3576–3583.
38. Baumann, H.; Richter, A.; Klemm, D.; Faust, V. *Macromol. Chem. Phys.* **2000**, *201*, 1950–1962.
39. Nishimura, S.; Kai, H.; Shinada, K.; Yoshida, T.; Tokura, S.; Kurita, K.; Nakashima, H.; Yamamoto, N.; Uryu, T. *Carbohydr. Res.* **1998**, *306*, 427–433.
40. Pye, D. A.; Vivès, R. R.; Turnball, J. E.; Callagher, J. T. *J. Biol. Chem.* **1998**, *273*, 22936–22946.
41. Pye, D. A.; Vivès, R. R.; Hyde, P.; Gallagher, J. T. *Glycobiology* **2000**, *10*, 1183–1192.
42. Gama, C. I.; Tully, S. E.; Sotogaku, N.; Clark, P. M.; Rawat, M.; Vaidehi, N.; Goddard, W. A., III; Nishi, A.; Hsieh-Wilson, L. C. *Nature Chem. Biol.* **2006**, *2*, 467–473.
43. Barbucci, R.; Lamponi, S.; Magnani, A.; Renier, D. *Biomaterials* **1998**, *19*, 801–806.
44. Rezaie, A. R. *Thromb. Res.* **2007**, *119*, 481–488.

Downloaded by NORTH CAROLINA STATE UNIV on August 28, 2012 | http://pubs.acs.org
Publication Date (Web): August 17, 2012 | doi: 10.1021/bk-2012-1107.ch016

Downloaded by PENNSYLVANIA STATE UNIV on August 28, 2012 | http://pubs.acs.org
Publication Date (Web): August 17, 2012 | doi: 10.1021/bk-2012-1107.ch017

Chapter 17

Sulfated Glycosaminoglycan Building Blocks for the Design of Artificial Extracellular Matrices

**Jana Becher,[1] Stephanie Möller,[1] Thomas Riemer,[2]
Jürgen Schiller,[2] Vera Hintze,[3] Susanne Bierbaum,[3]
Dieter Scharnweber,[3] Hartmut Worch,[3]
and Matthias Schnabelrauch*,[1]**

**[1]INNOVENT e. V., Biomaterials Department,
Prüssingstrasse 27B, D-07745 Jena, Germany
[2]University of Leipzig, Institute of Medical Physics and Biophysics,
Härtelstrasse 16-18, D-04107 Leipzig, Germany
[3]Technical University of Dresden, Institute of Material Science,
Max Bergmann Center of Biomaterials, D-01069 Dresden, Germany
*E-mail: ms@innovent-jena.de**

Sulfated glycosaminoglycans are important constituents of the natural extracellular matrix (ECM) of mammals offering a promising potential to design bioactive materials for tissue repair and reconstruction. The biological properties of these biomacromolecules are strongly influenced by the degree of sulfation and the sulfate group distribution in the polymer. We report on new synthesis pathways for the sulfation of hyaluronan and chondroitin sulfate enabling control of the degree of sulfation and regioselectivity. In addition, first results on the formation of artificial ECM based materials and their interaction with protein-based growth factors are presented.

Introduction

The natural extracellular matrix (ECM) in mammalian tissues is the optimum medium nature has created to surround and support cells. Due to its complex composition, architecture and functionality, ECM is not only able to support cells, but also to mediate important cellular processes such as cell proliferation,

Downloaded by PENNSYLVANIA STATE UNIV on August 28, 2012 | http://pubs.acs.org
Publication Date (Web): August 17, 2012 | doi: 10.1021/bk-2012-1107.ch017

differentiation and cellular signalling. Structurally, native ECM is an interlocking polymer mesh mainly formed from fibrous proteins such as collagens, elastin, fibronectin and laminin, and protein-linked glycosaminoglycans (GAGs), so-called proteoglycans.

Driven by the superior properties of ECM with regard to cell hosting, various strategies have been proposed to use main components of the natural ECM as biomaterials in implantology and regenerative medicine (*1–3*). Examples of those potential applications are matrices for tissue development after cell seeding (*4*, *5*) and bioactive implant coatings to improve implant integration into the surrounding tissue (*6*, *7*). Compared to synthetic materials, ECM-containing polymers have several advantages including a high cytocompatibility, a complete degradability in the body and the ability to directly interact with cell receptors. In addition, it has been known for several years that proteoglycans derived from high-sulfated GAGs such as heparan sulfate (HS) or heparin are able to bind to certain secreted protein growth factors by ionic interactions between basic residues in the protein and negatively charged sulfate groups of GAG (*8*, *9*). As a result of this GAG-growth factor interaction macromolecular complexes might be formed protecting growth factors in their active conformation against proteolytic attacks and generating local depot forms for growth factors to act on a restricted number of cells. Therefore, the systematic exploration of those growth factor-GAG interactions offers promising access to new innovative biomaterials able to actively stimulate tissue repair or implant ingrowth.

Lacking effective synthesis procedures, the reproducible availability of complex high-sulfated GAG such as HS in larger quantities is difficult. By contrast, both non-sulfated hyaluronan (HA) available from an industrial-scale fermentation process and also chondroitin sulfate (CS), a low-sulfated GAG, which is isolated from different animal sources, can be easily produced in large amounts. The use of HA or CS as starting materials for the synthesis of high-sulfated GAG represents an interesting approach to provide building blocks for the construction of artificial ECM materials mimicking not only the structure but also selected cell-relevant properties of natural ECM. Taking into account that the biological activity of sulfated GAGs is determined not only by the degree of sulfation (DS_S) but also by the position of sulfate groups and the presence of additional substituents in the anhydrosugar repeating unit (ASU) (*10*), the major challenge of this approach is to establish regioselective sulfation procedures enabling effective control of the substitution pattern in the resulting GAG sulfates. While those regioselective reactions for homopolysaccharides such as cellulose (*11*) or chitosan (*12*) have been known for many years, only very few examples are reported for the introduction of sulfate groups at a pre-determined position within the ASU of heteropolysaccharides like complex GAGs (*13*, *14*).

This chapter aims at surveying our recent work on synthetic routes to obtain sulfated HA and CS derivatives with both an adjustable degree of sulfation and a pre-determined distribution of sulfate groups within the ASU. In addition, first results are presented to test the potential of the synthesized sulfated GAG derivatives mimicking natural ECM-containing GAG components. For this purpose, the use of sulfated HA and CS to construct artificial ECM and the ability of sulfated GAG to interact with selected growth factors were studied.

Downloaded by PENNSYLVANIA STATE UNIV on August 28, 2012 | http://pubs.acs.org
Publication Date (Web): August 17, 2012 | doi: 10.1021/bk-2012-1107.ch017

Conventional Sulfation of Glycosaminoglycans

Hyaluronan (HA), the only non-sulfated GAG, and chondroitin sulfate (CS), the most abundant GAG, have already been used as starting materials for sulfation for many decades (*15–17*). While these early attempts mainly used sulfuric acid or chlorosulfonic acid as reagents, today's sulfation agents of choice are complexes of SO_3 with organic amines and amides (*17–19*). The diverse SO_3 complexes are relatively mild reagents that cause less degradation, and they feature different reactivities. Hence, they allow a controlled synthesis of derivatives with an adjusted degree of sulfation in the range of 0/1 (for HA and CS, respectively) $\leq DS_S \leq 4$, whereas SO_3/DMF is the preferred reagent for the synthesis of high-sulfated derivatives and SO_3/pyridine for the lower degrees of sulfation (*20–22*). The reactions are usually performed in aprotic solvents such as DMF at room temperature. To increase the solubility of the educts in aprotic solvents and thus also their reactivity, HA and CS were transferred into their corresponding tetrabutylammonium (TBA) salts before sulfation (Figure 1).

Studies on the regioselectivity of this reaction prove that the primary hydroxy group at C_6' reacts preferably. The ^{13}C NMR of a low-sulfated HA with a DS_S = 1 evidences that only the primary hydroxy group is sulfated (*20*, *23*). Since native CS usually occurs as a mixture of a C_4'- and C_6'-sulfate, an oversulfation cannot lead to a product that is only sulfated at C_6'. But also here NMR studies prove that the reaction appears at first at the primary hydroxy group as illustrated in Figure 2. The peak for the non-sulfated C_6' in the native CS (DS_S = 0.9, 70% of the sulfate groups at C_4', 30% at C_6', Figure 2A) at about 62 ppm completely disappears in the sulfated derivative with a DS_S = 1.8 (Figure 2B) and the signal for the sulfated C_6' at 68 ppm increases, while the other signals remain.

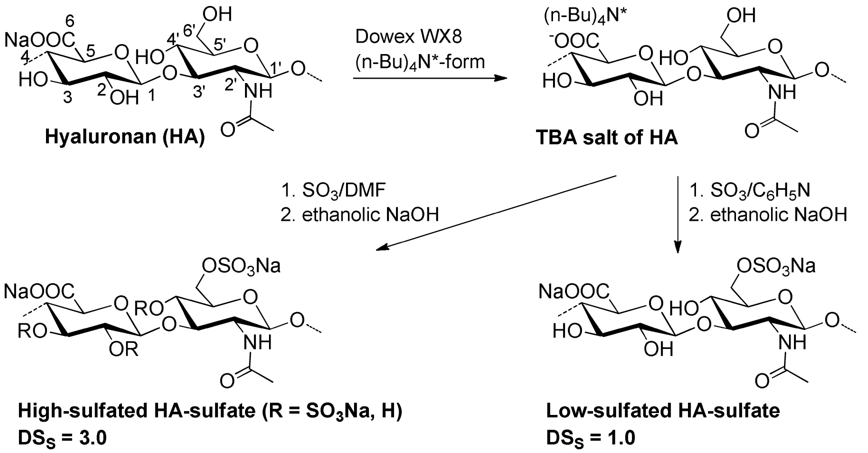

Figure 1. Synthesis of HA sulfates with different degree of sulfation.

Downloaded by PENNSYLVANIA STATE UNIV on August 28, 2012 | http://pubs.acs.org
Publication Date (Web): August 17, 2012 | doi: 10.1021/bk-2012-1107.ch017

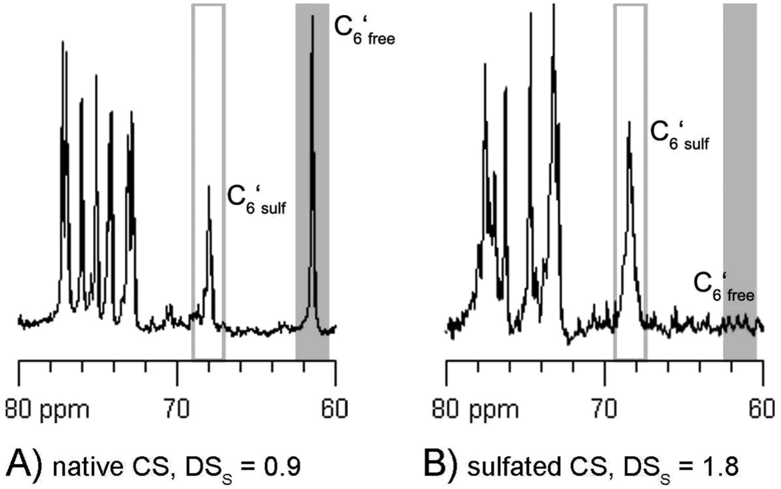

A) native CS, DS_S = 0.9

B) sulfated CS, DS_S = 1.8

Figure 2. Detail of the ^{13}C NMR spectrum of native chondroitin sulfate (DS_S = 0.9; A) and sulfated chondroitin sulfate (DS_S = 1.8; B).

Recent results of a more detailed investigation on the regioselectivity of the sulfation of HA by comparative ^{13}C NMR suggest a reactivity sequence as follows: $C_6' \gg C_2 / C_3 > C_4'$ (Figure 3).

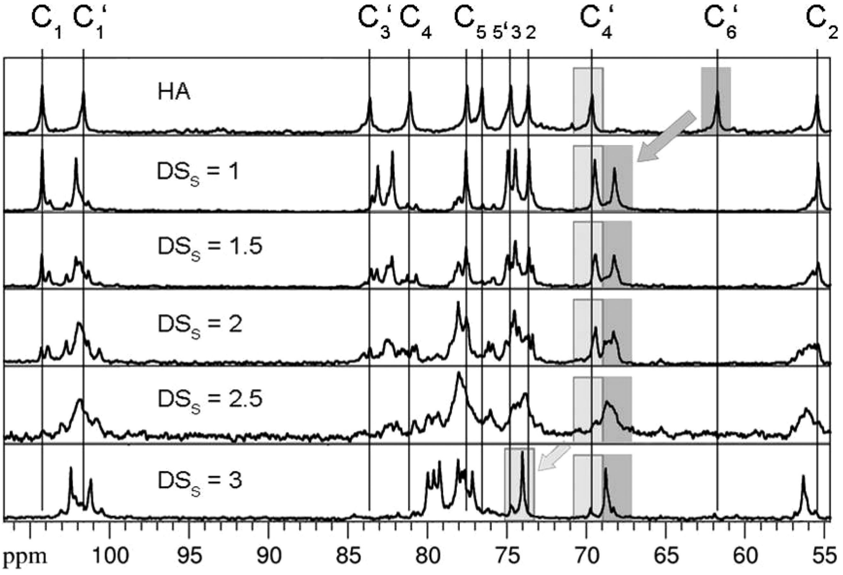

Figure 3. Comparative ^{13}C NMR study on the regioselectivity of HA sulfation.

To allow a coupling of linker molecules, bioactive agents or proteins or to activate the sulfated GAGs for an immobilization to surfaces, an introduction of further substituents can be useful. Very suitable for the mentioned applications are carboxymethyl groups that can easily be introduced with a low degree of substitution ($DS_{CM} \approx 0.5$) into the HA backbone before sulfation with varying DS_S.

Synthesis Strategies for the Controlled Regioselective Sulfation of Glycosaminoglycans

As already mentioned, not only the degree of sulfation, but also the distribution of the sulfate groups over the ASU strongly influences the biomedical properties of the sulfated GAGs (*24*, *25*). That's why we focus on the synthesis of sulfated GAGs with a well-defined regiochemistry that allows a detailed investigation of the effect of the position of the sulfate groups on the biomedical properties. Since the conventional sulfation preferably occurs at the primary hydroxy group, synthetic routes for derivatives with sulfate groups mainly or exclusively at the secondary ones are of particular interest.

One approach to obtain derivatives with the desired regiochemistry is the selective desulfation of high-sulfated GAGs by means of silylating agents such as *N*-methyl-*N*-(trimethylsilyl)trifluoroacetamide (MSTFA) and *N*,*O*-bis(trimethylsilyl)acetamide (BTSA, see Figure 4).

This method has already been described for some sulfated monosaccharides and heparin (*26–28*) and was adapted by our group for the desulfation of sulfated HA and CS. Therefore, a high-sulfated HA or CS derivative is transferred into the corresponding pyridinium or tributylammonium salt, respectively, and then reacted with one of the above silylation agents (*23*).

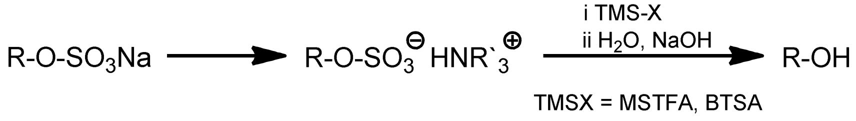

Figure 4. Reaction scheme for the desulfation of high-sulfated GAGs.

Investigations of the sulfur content in the elemental analysis of the products reveal that already after 4 h treatment with BTSA the DS_S of a sulfated HA can be reduced from $DS_S = 3.1$ to $DS_S = 2.6$. When the reaction is continued for 24 h the DS_S even decreases to 2.3. A comparison of the different educts and reagents shows that the pyridinium salts react faster than the tributylammonium salt of the starting sulfated GAGs and that there is no significant difference between BTSA and MSTFA as desulfation agent concerning the effectiveness of the reaction.

For an investigation of the regioselectivity of the reaction the ^{13}C-APT NMR spectra of the products were consulted. Figure 5 shows exemplarily details of the ^{13}C NMR spectra of a high-sulfated HA (Figure 5A) and the above-mentioned desulfation products with BTSA after 4 h at 60 °C (5B) and 24 h at 60 °C (5C) reaction time, respectively. After 4 h C_6' is partially desulfated (new peak at 62 ppm) and all other signals remain. However, after 24 h reaction time C_6' is not yet

Downloaded by PENNSYLVANIA STATE UNIV on August 28, 2012 | http://pubs.acs.org
Publication Date (Web): August 17, 2012 | doi: 10.1021/bk-2012-1107.ch017

Downloaded by PENNSYLVANIA STATE UNIV on August 28, 2012 | http://pubs.acs.org
Publication Date (Web): August 17, 2012 | doi: 10.1021/bk-2012-1107.ch017

completely desulfated, but a signal of the free hydroxy group at C4′ appears at 69 ppm. When the reaction is performed at 80 °C, C6′ is completely desulfated after 24 h and C4′ is desulfated to 80%. Thus, the reaction proceeds regioselectively at the primary hydroxy group, but the sulfate group there cannot be completely cleaved without also desulfating secondary ones. Similar reaction courses were found for all starting materials and reaction conditions examined.

A second approach to obtain sulfated HA and CS, respectively, with the desired regioselectivity is a sulfation with prior introduction of protecting groups. The benzoyl ester group turned out to be most applicable to protect the primary hydroxy group at C6′ of the HA backbone from a subsequent sulfation, because it is sterically demanding enough to allow regioselective functionalization and is stable under the acidic sulfation conditions (Figure 6).

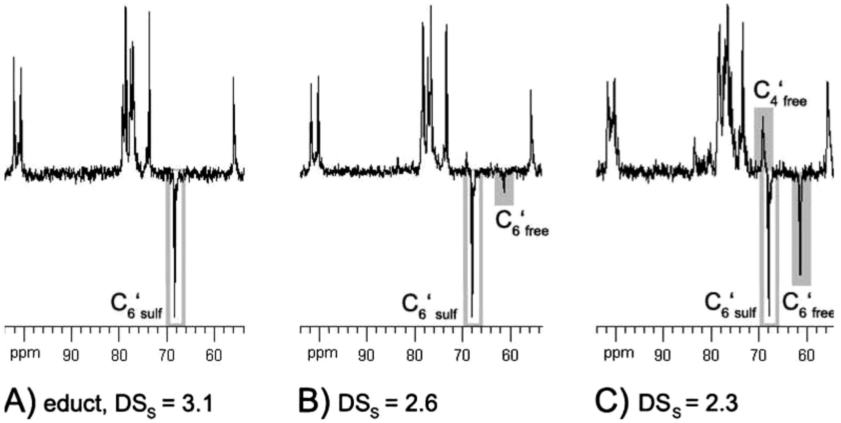

Figure 5. Details of ^{13}C-APT NMR spectra of high-sulfated HA (A) and desulfated products after 4 h (B) and 24 h (C), respectively, with BTSA.

Afterwards, the protecting group can easily be cleaved under basic conditions and a high-sulfated HA with DS_S = 2.6 is obtained (*23*). The ^{13}C-APT NMR (detail shown in Figure 7A) proves that the primary hydroxy group at C6′ remains completely unsulfated.

When native CS (DS_S = 0.9, 70% of the sulfate groups at C4′, 30% at C6′) is treated the same way, a sulfated product with a similar DS_S is obtained. However, the regioselectivity is considerably lower. More than 60% of the primary hydroxy groups at C6′ are sulfated, as can be seen in Figure 7B. The reason for this is probably the sterical hindrance of C6′ by C4′, which is axially oriented in contrast to HA in CS. That's why we exchanged the benzoic ester in the synthesis pathway for a smaller protecting group, an acetic ester, which should be able to access C6′ more easily. The final sulfated and deprotected product features a similar DS_S as that obtained by the original protocol. However, the ^{13}C-APT NMR proves that the regioselectivity is much higher (Figure 7C). The ratio between the sulfated C6′ and the unsulfated one is found to be similar to the native CS (see Figure 5C), which means that the protection was successful and no further sulfation of the primary hydroxy group occurred.

Downloaded by PENNSYLVANIA STATE UNIV on August 28, 2012 | http://pubs.acs.org
Publication Date (Web): August 17, 2012 | doi: 10.1021/bk-2012-1107.ch017

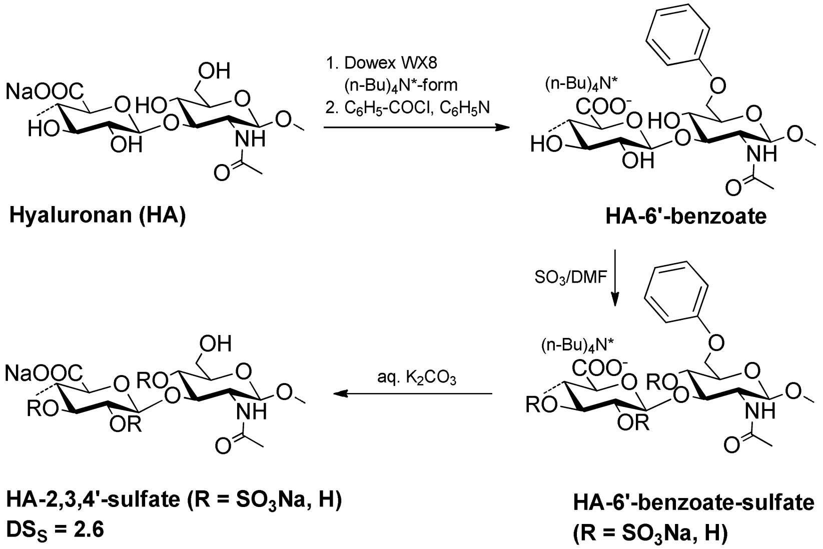
NaOOC
OH
HO
OH
O
NH
1. Dowex WX8
(n-Bu)4N*-form
2. C6H5-COCl, C6H5N
(n-Bu)4N*
COO-
Hyaluronan (HA)
HA-6'-benzoate
SO3/DMF
aq. K2CO3
RO
OR
HA-2,3,4'-sulfate (R = SO3Na, H)
DSS = 2.6
HA-6'-benzoate-sulfate
(R = SO3Na, H)

Figure 6. Synthesis of HA sulfate with free primary hydroxyl group by using a benzoyl protecting group.

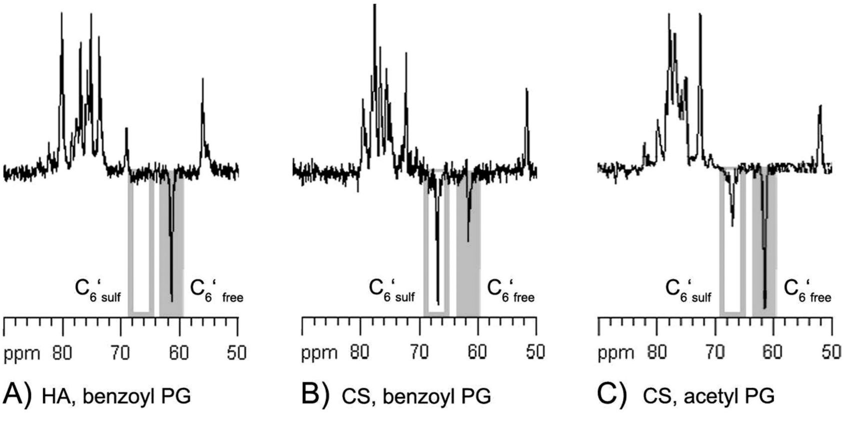

Figure 7. Details of ^{13}C-APT NMR spectra of a high-sulfated HA (A) and CS (B, C) synthesized using different protecting groups (PG).

Formation of Artificial ECMs from Sulfated GAGs

The integration of an implant is determined by the interaction of cells at the interface with the surrounding tissue. One promising strategy to improve the biological acceptance of implants is to employ biological implant coatings consisting of ECM components to mimic the natural surroundings of cells and to make use of its biological features. *In vivo* the ECM provides not only a scaffold for cell adhesion, but also influences cellular functions either directly through the interaction with cells or indirectly via capturing and presenting growth factors (*29–32*). The ECM is a complex network consisting of a number of different collagens, proteoglycans and glycoproteins. The exact composition is depending on the tissue type. In bone, about 90% of the protein matrix is collagen type I, forming banded triple-helical fibrils self-aggregation. The resulting fibrillar architecture is influenced, for example, by the interaction with proteoglycans (*33*). The process of self-aggregation can also be observed *in vitro* being sensitive to the experimental conditions chosen (*34*).

Several reports demonstrated that matrix coatings of collagen type I improved not only cellular attachment in *in vitro* experiments, but also induced bone apposition in animal experiments (*35–37*).

To create artificial ECM coatings with a potentially wider range of functions, non-collagenous components with specific functionalities were integrated into the collagen matrices. One obvious group of candidates, the proteoglycans, is found in the bone matrix, for which decorin is an example (*38*). It consists of a core protein that is glycosylated with a chondroitin sulfate (CS) chain. It is thought to promote the calcification of the matrix (*39*) and is expressed by differentiated osteoblasts before mineralization (*40*). Decorin is also reported to bind TGF-β, an important growth factor in the metabolism of bone (*41*).

Other promising candidates are the GAGs, since sugars without core protein may be less immunogenic. Some of their members, such as HS and heparin, are well known to interact with ECM components (collagen, fibronectin), influencing their affinity for integrins (*42*). Equally important is that they function as co-receptors for growth factors including fibroblast growth factor (FGF) and vascular endothelial growth factor (VEGF) and interact with interleukins possibly modulating the inflammatory response (*43–45*).

Artifical ECM were created from collagen type I and decorin or native CS (associated with decorin in bone) in different buffer systems at 37 °C using the natural self-assembly potential of collagen. They were then characterized for the integration of collagen monomers, the association of non-collagenous components and the fibrillar morphology. In general, the effect of ionic strength in the fibrillogenesis buffer (buffer A: 30 mM sodium phosphate buffer, buffer B: like buffer A, but with 135 mM sodium chloride, both buffers pH = 7.4) on collagen monomer integration was rather small.

Adding decorin prior to fibrillogenesis started to negatively affect the integration of collagen into fibrils at decorin to collagen ratios of 1:10 in both buffer systems. The presence of 1:10 native CS also reduced the integration of collagen, but to a lower extent than decorin. However, the integration of collagen monomers was not severely hampered, since more than 90% of the original amount of employed monomers were still integrated in the presence of non-collagenous components. It is noteworthy that the amount of monomers integrated was depending on the collagen type I preparation and the effect of non-collagenous components can be more pronounced with different preparations (*6*). Decorin and CS were associated with collagen fibrils, with higher amounts when buffer A was used (*6*).

The fibrillar morphology was influenced by the ionic strength and the presence of non-collagenous components. However, the general fibrillar structure was not

Downloaded by PENNSYLVANIA STATE UNIV on August 28, 2012 | http://pubs.acs.org
Publication Date (Web): August 17, 2012 | doi: 10.1021/bk-2012-1107.ch017

disrupted and the typical binding pattern was preserved (Figure 8). The fibril diameter increased with ionic strength (Figure 8, A and D), while it decreased again in the presence of decorin and CS (Figure 8, D and E and F). A more heterogeneous distribution of fibril diameters with some larger aggregates was apparent in the presence of CS in buffer A (Figure 8, A and C).

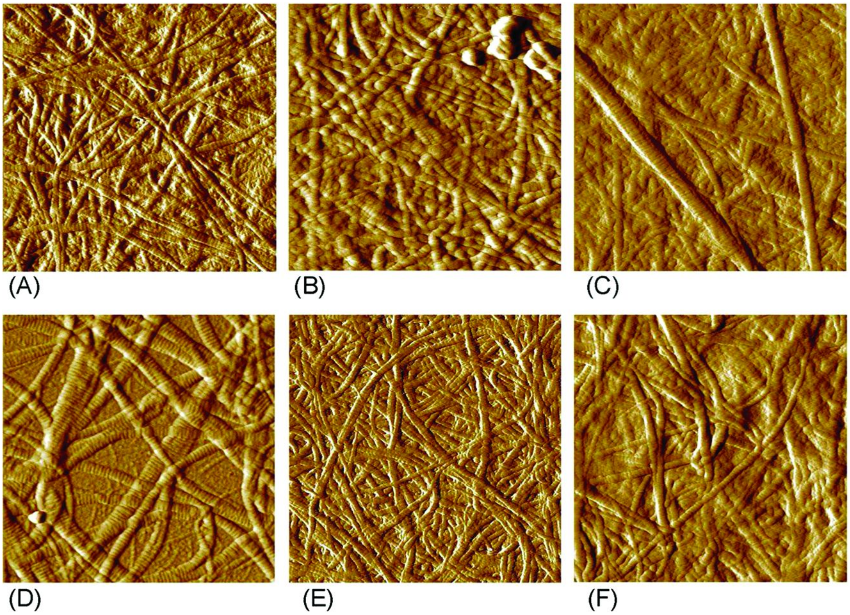

Figure 8. Collagen fibrils adsorbed to titanium (Ti6Al4V) discs. AFM contact mode, (A) collagen buffer A, (B) collagen with 25 µg/mL decorin buffer A, (C) collagen with 25 µg/mL CS buffer A, (D) collagen buffer B, (E) collagen with 25 µg/mL decorin buffer B, (F) collagen with 25 µg/mL CS buffer B. Represented area 5 µm × 5 µm. Reproduced with permission from reference (32). © 2006 John Wiley and Sons.

In summary, it was possible to assemble artificial ECM from collagen type I and decorin/CS without severely disrupting the fibrillar architecture.

Investigations on Interactions of Glycosaminoglycan Sulfates with Cellular Growth Factors

Heparin and heparan sulfate (HS), but also high-sulfated CS, are known to interact with a variety of proteins including growth factors and chemokines (*8*, *46*, *47*). The interactions are of importance in stabilizing proteins from denaturation or proteolysis, in preventing diffusion and allowing local storage of proteins, which enable them to act on a restricted number of cells and in stabilizing growth factor receptor complexes, thereby facilitating signal transduction (*8*). The naturally occurring sulfate groups in GAGs were identified to be of major

Downloaded by PENNSYLVANIA STATE UNIV on August 28, 2012 | http://pubs.acs.org
Publication Date (Web): August 17, 2012 | doi: 10.1021/bk-2012-1107.ch017

importance in protein binding. The interaction can be highly specific to a defined sulfation pattern. Miyazaki et al., for example, showed that the sulfation of C_4' and C_6' in the galactosamine unit of CS was of special importance for high affinity binding of CS-E to BMP-4 (*46*). The strongly anionic sulfate groups interact with basic amino acid side chains found, for example, in the *N*-termini of bone morphogenetic protein-2 and -4 (BMP-2 and -4) (*48*).

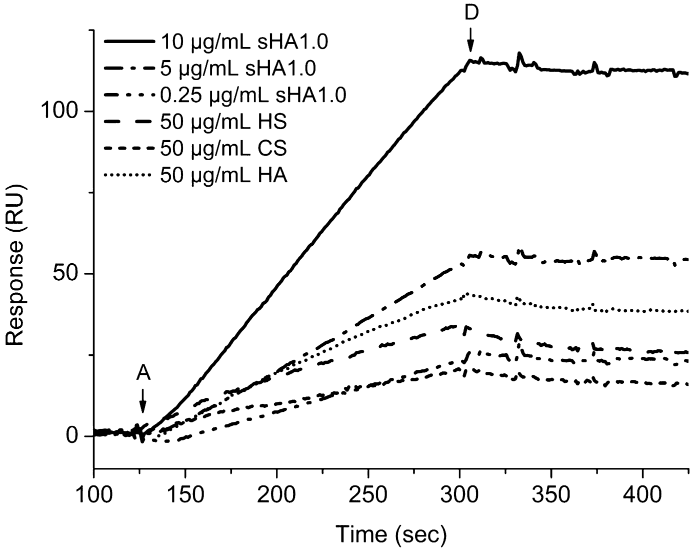

Figure 9. SPR sensorgrams of the interactions of different GAGs with immobilized BMP-4. Arrow A indicates the starting point of the GAG injection. Arrow D indicates the end of the sample injection. Adapted with permission from reference (20). © 2009 American Chemical Society.

Consequently, we investigated GAG derivatives with different degrees of sulfate groups and varying regioselectivity to identify new forms of HA and CS with defined modification patterns and interaction profiles for biomedical application.

The interaction between sulfated HA and CS with growth factors was analyzed by surface plasmon resonance (SPR) at 25 °C recording mass-based changes due to interaction at a sensor chip surface and enzyme-linked immunosorbent assay (ELISA). In both cases, one interaction partner was immobilized while the other was free in solution. Figure 9 displays a comparison of the interaction response levels of different GAGs at certain concentrations with immobilized BMP-4 as derived by SPR. The responses for 50 μg/ml HA, CS and HS were significantly smaller than for a five times smaller amount of low sulfated HA (sHA1.0) with $DS_S = 1.0$.

A quantification of the affinity of different GAGs for BMP-4 by the overall dissociation constant K_D revealed that high-sulfated HA with $DS_S = 2.8$ (sHA2.8) was about 2000 times more affine than the low-sulfated HA (sHA1.0, $DS_S = 1.0$)

Downloaded by PENNSYLVANIA STATE UNIV on August 28, 2012 | http://pubs.acs.org
Publication Date (Web): August 17, 2012 | doi: 10.1021/bk-2012-1107.ch017

Downloaded by PENNSYLVANIA STATE UNIV on August 28, 2012 | http://pubs.acs.org
Publication Date (Web): August 17, 2012 | doi: 10.1021/bk-2012-1107.ch017

which in turn was up to 700 times more affine than HS, CS and HA (not shown) (*20*).

To verify these findings, the interaction between GAGs and BMP-4 was also analyzed by ELISA assay. The amount of bound BMP-4 was calculated from the amount of non-bound BMP-4 as determined in the supernatant after incubation of immobilized GAG with different concentrations of growth factor for 16 h at 4 °C (Figure 10). Again, high-sulfated sHA2.8 and low-sulfated sHA1.0 retained significantly more BMP-4 than HS, CS and HA. Importantly, as in SPR, sHA2.8 retained significantly more growth factor than sHA1.0.

In summary, we confirmed with two independent assays that the modification of HA with sulfate groups gave macromolecules with significantly higher binding affinities in comparison to the native GAGs HS, CS and HA.

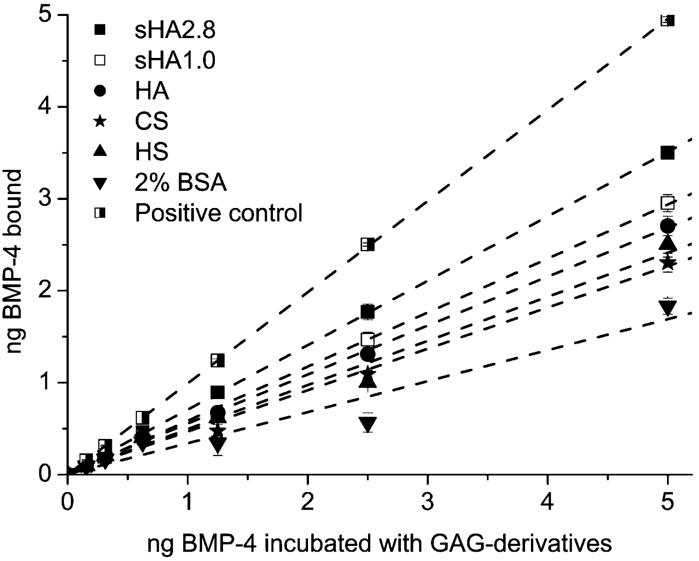

Figure 10. Sandwich-ELISA of the interaction of BMP-4 with immobilized GAGs. Adapted with permission from reference (20). © 2009 American Chemical Society.

Conclusion

The conventional sulfation of HA and CS usually produces GAG derivatives in which the primary OH-group is preferentially sulfated. Due to the proposed influence of the sulfation pattern of the repeating saccharide unit of GAGs on their biological properties there is a special interest in products with different sulfation patterns. Hence, regioselective GAG sulfation pathways, namely the desulfation of high-sulfated HA and CS, respectively, and a protecting group strategy to block the primary OH-group of HA during sulfation, were established. According to the latter strategy, a high-sulfated HA completely unsulfated at the primary OH-group was synthesized.

First investigations to create artificial ECM coatings have demonstrated that it is possible to assemble artificial ECMs from collagen type I and decorin/CS without severely disrupting the fibrillar architecture. In addition, it was shown by SPR and ELISA techniques that sulfated HA had a higher binding affinity to the growth factor BMP-4 in comparison to native HA and even sulfated GAGs such as CS and HS. Readily available sulfated GAGs based on HA or CS are therefore promising candidates to be incorporated in artificial ECM to add growth factor attracting features to collagenous matrices as bioengineered coating of biomaterials.

Downloaded by PENNSYLVANIA STATE UNIV on August 28, 2012 | http://pubs.acs.org
Publication Date (Web): August 17, 2012 | doi: 10.1021/bk-2012-1107.ch017

Acknowledgments

This work was supported by the German Research Council (DFG TR 67).

References

1. Burdick, J. A.; Prestwich, G. D. *Adv. Mater.* **2011**, *23*, H41–56.
2. Ferdous, Z.; Grande-Allen, K. J. *Tissue Eng.* **2007**, *13*, 1893–1904.
3. Lutolf, M. P.; Hubbell, J. A. *Nat. Biotechnol.* **2005**, *23*, 47–55.
4. Fedorovich, N. E.; Alblas, J.; de Wijn, J. R.; Hennink, W. E.; Verbout, A. J.; Dhert, W. J. *Tissue Eng.* **2007**, *13*, 1905–1925.
5. Tibbitt, M. W.; Anseth, K. S. *Biotechnol. Bioeng.* **2009**, *103*, 655–663.
6. Bierbaum, S.; Douglas, T.; Hanke, T.; Scharnweber, D.; Tippelt, S.; Monsees, T. K.; Funk, R. H.; Worch, H. *J. Biomed. Mater. Res., Part A* **2006**, *77*, 551–562.
7. von der Mark, K.; Park, J.; Bauer, S.; Schmuki, P. *Cell Tissue Res* **2010**, *339*, 131–153.
8. Kreuger, J.; Spillmann, D.; Li, J. P.; Lindahl, U. *J. Cell Biol.* **2006**, *174*, 323–327.
9. Vlodavsky, I.; Miao, H. Q.; Medalion, B.; Danagher, P.; Ron, D. *Cancer Metastasis Rev.* **1996**, *15*, 177–186.
10. Habuchi, H.; Habuchi, O.; Kimata, K. *Glycoconjugate J.* **2004**, *21*, 47–52.
11. Baumann, H.; Richter, A.; Klemm, D.; Faust, V. *Macromol. Chem. Phys.* **2000**, *201*, 1950–1962.
12. Nishimura, S. I.; Kai, H.; Shinada, K.; Yoshida, T.; Tokura, S.; Kurita, K.; Nakashima, H.; Yamamoto, N.; Uryu, T. *Carbohydr. Res.* **1998**, *306*, 427–433.
13. Kovensky, J.; Cirelli, A. F. *Carbohydr. Res.* **1997**, *303*, 119–122.
14. Liu, Z.; Perlin, A. S. *Carbohydr. Res.* **1992**, *236*, 121–133.
15. Wolfrom, M. L.; Juliano, B. O. *J. Am. Chem. Soc.* **1960**, *82*, 2588–2592.
16. Barbucci, R.; Benvenuti, M.; Casolaro, M.; Lamponi, S.; Magnani, A. *J. Mater. Sci.: Mater. Med.* **1994**, *5*, 830–833.
17. Nagasawa, K.; Uchiyama, H.; Wajima, N. *Carbohydr. Res.* **1986**, *158*, 183–190.
18. Magnani, A.; Albanese, A.; Lamponi, S.; Barbucci, R. *Thromb. Res.* **1996**, *81*, 383–395.

19. Nadkarni, V. D.; Toida, T.; VanGorp, C. L.; Schubert, R. L.; Weiler, J. M.; Hansen, K. P.; Caldwell, E. E. O.; Linhardt, R. J. *Carbohydr. Res.* **1996**, *290*, 87–96.
20. Hintze, V.; Moeller, S.; Schnabelrauch, M.; Bierbaum, S.; Viola, M.; Worch, H.; Scharnweber, D. *Biomacromolecules* **2009**, *10*, 3290–3297.
21. Kunze, R.; Rosler, M.; Moller, S.; Schnabelrauch, M.; Riemer, T.; Hempel, U.; Dieter, P. *Glycoconjugate J.* **2010**, *27*, 151–158.
22. Schiller, J.; Becher, J.; Moeller, S.; Nimptsch, K.; Riemer, T.; Schnabelrauch, M. *Mini-Rev. Org. Chem.* **2010**, *7*, 290–299.
23. Becher, J.; Möller, S.; Weiss, D.; Schiller, J.; Schnabelrauch, M. *Macromol. Symp.* **2010**, *296*, 446–452.
24. Gama, C. I.; Hsieh-Wilson, L. C. *Curr. Opin. Chem. Biol.* **2005**, *9*, 609–619.
25. Schmidtke, M.; Wutzler, P.; Makarov, V. *Lett. Drug Des. Discovery* **2004**, *1*, 293–299.
26. Kariya, Y.; Kyogashima, M.; Suzuki, K.; Isomura, T.; Sakamoto, T.; Horie, K.; Ishihara, M.; Takano, R.; Kamei, K.; Hara, S. *J. Biol. Chem.* **2000**, *275*, 25949–25958.
27. Takano, R. *Trends Glycosci. Glycotechnol.* **2002**, *14*, 343–351.
28. Takano, R.; Takashige; Hayashi, K.; Yoshida, K.; Hara, S. *J. Carbohydr. Chem.* **1995**, *14*, 885–888.
29. Kanematsu, A.; Marui, A.; Yamamoto, S.; Ozeki, M.; Hirano, Y.; Yamamoto, M.; Ogawa, O.; Komeda, M.; Tabata, Y. *J. Controlled Release* **2004**, *99*, 281–292.
30. Lee, J. W.; Juliano, R. *Mol. Cells* **2004**, *17*, 188–202.
31. Schneiderbauer, M. M.; Dutton, C. M.; Scully, S. P. *Cell. Signalling* **2004**, *16*, 1133–1140.
32. Taipale, J.; Keski-Oja, J. *FASEB J.* **1997**, *11*, 51–59.
33. Garg, A. K.; Berg, R. A.; Silver, F. H.; Garg, H. G. *Biomaterials* **1989**, *10*, 413–419.
34. Williams, B. R.; Gelman, R. A.; Poppke, D. C.; Piez, K. A. *J. Biol. Chem.* **1978**, *253*, 6578–6585.
35. Becker, D.; Geissler, U.; Hempel, U.; Bierbaum, S.; Scharnweber, D.; Worch, H.; Wenzel, K. W. *J. Biomed. Mater. Res.* **2002**, *59*, 516–527.
36. Bernhardt, R.; van den Dolder, J.; Bierbaum, S.; Beutner, R.; Scharnweber, D.; Jansen, J.; Beckmann, F.; Worch, H. *Biomaterials* **2005**, *26*, 3009–3019.
37. Geissler, U.; Hempel, U.; Wolf, C.; Scharnweber, D.; Worch, H.; Wenzel, K. *J. Biomed. Mater. Res.* **2000**, *51*, 752–760.
38. Robey, P. G. *Connect. Tissue Res.* **1996**, *35*, 131–136.
39. Mochida, Y.; Duarte, W. R.; Tanzawa, H.; Paschalis, E. P.; Yamauchi, M. *Biochem. Biophys. Res. Commun.* **2003**, *305*, 6–9.
40. Kamiya, N.; Shigemasa, K.; Takagi, M. *J. Oral Sci.* **2001**, *43*, 179–188.
41. Takeuchi, Y.; Kodama, Y.; Matsumoto, T. *J. Biol. Chem.* **1994**, *269*, 32634–32638.
42. Ruoslahti, E.; Engvall, E. *Biochim. Biophys. Acta* **1980**, *631*, 350–358.
43. Cross, M. J.; Claesson-Welsh, L. *Trends Pharmacol. Sci.* **2001**, *22*, 201–207.
44. Mummery, R. S.; Rider, C. C. *J. Immunol.* **2000**, *165*, 5671–5679.

Downloaded by PENNSYLVANIA STATE UNIV on August 28, 2012 | http://pubs.acs.org
Publication Date (Web): August 17, 2012 | doi: 10.1021/bk-2012-1107.ch017

45. Shintani, Y.; Takashima, S.; Asano, Y.; Kato, H.; Liao, Y.; Yamazaki, S.; Tsukamoto, O.; Seguchi, O.; Yamamoto, H.; Fukushima, T.; Sugahara, K.; Kitakaze, M.; Hori, M. *EMBO J.* **2006**, *25*, 3045–3055.
46. Miyazaki, T.; Miyauchi, S.; Tawada, A.; Anada, T.; Matsuzaka, S.; Suzuki, O. *J. Cell. Physiol.* **2008**, *217*, 769–777.
47. Pichert, A.; Samsonov, S. A.; Theisgen, S.; Thomas, L.; Baumann, L.; Schiller, J.; Beck-Sickinger, A. G.; Huster, D.; Pisabarro, M. T. *Glycobiol.* **2011**.
48. Ruppert, R.; Hoffmann, E.; Sebald, W. *Eur. J. Biochem.* **1996**, *237*, 295–302.

Downloaded by PENNSYLVANIA STATE UNIV on August 28, 2012 | http://pubs.acs.org
Publication Date (Web): August 17, 2012 | doi: 10.1021/bk-2012-1107.ch017

Downloaded by PENNSYLVANIA STATE UNIV on August 28, 2012 | http://pubs.acs.org
Publication Date (Web): August 17, 2012 | doi: 10.1021/bk-2012-1107.ch018

Chapter 18

Advances in the Application of Oxidative Enzymes in Biopolymer Chemistry and Biomaterial Research

Gibson S. Nyanhongo, Endry Nugroho Prasetyo,*
Enrique Herrero Acero, and Georg M. Guebitz

Graz University of Technology, Institute of Environmental Biotechnology,
Petersgasse 12/1, A-8010 Steiermark, Graz, Austria
***E-mail: nugrohoprasetyo@tugraz.at**

Enzymatic polymer synthesis is fast emerging as an alternative tool to chemical catalysts driven by advances in enzyme molecular engineering, increasing knowledge in enzyme reaction engineering and the desire to fulfill the goals of sustainable development. Among the enzymes actively exploited in polymer chemistry are oxidative enzymes, especially fungal laccases and peroxidases. The most fascinating features of these enzymes are their ability to generate reactive species which undergo non-enzymatic coupling and polymerization reactions. This chapter therefore summarizes the different approaches and strategies used in order to produce the desired functional polymers with oxidative enzymes. This is important given the multidisciplinary nature of enzyme polymer synthesis, which requires the integration of chemical engineering principles and enzyme catalysis. This chapter will therefore provide scientists from different backgrounds with an enzyme-based platform for developing functional polymers.

Downloaded by PENNSYLVANIA STATE UNIV on August 28, 2012 | http://pubs.acs.org
Publication Date (Web): August 17, 2012 | doi: 10.1021/bk-2012-1107.ch018

Introduction

The process for the synthesis of functional polymers has evolved through distinct phases with acids and bases as catalysts dominating the production processes until the 1920s (*1*), followed by metal catalysts which became popular in the 1950s. Advances in biotechnology have witnessed increased interests in enzymes as catalysts. Enzymatic polymer synthesis methods are fast evolving as an alternative tool to chemical catalysts, driven by advances in enzyme molecular engineering, increasing knowledge in enzyme reaction engineering as well as the desire to fulfill the goals of sustainable development. In addition to being environmentally friendly, enzymes as catalysts provide the opportunity to synthesize a well-defined structure with controlled stereochemistry, regio-selectivity and chemo-selectivity. Among the enzymes increasingly being applied in polymer chemistry are oxidative enzymes especially, fungal peroxidases and laccases. These enzymes are widely investigated for many biotechnological applications including personal care, organic synthesis, biosensors, textile industry, waste remediation, synthesis of biomedical functional polymers etc.

Although several authors have reviewed the different biotechnological applications of oxidative enzymes, according to our knowledge there is hardly any work which summarizes the evolving strategies for the successful synthesis, modification or functionalization of polymers by oxidative enzymes. It has become clear that successful development of functional polymers requires careful reaction engineering skills, drawing expertise from many disciplines (biochemistry, organic chemistry, material science, nanotechnology, chemical/process engineering etc.) as well as knowledge of the different possible experimental setup strategies. This chapter therefore tries to summarize the different approaches and strategies that are employed for the successful synthesis, modification or functionalization of polymers. It should be noted, however, that given the multitude of studies conducted so far, only a few selected examples can be discussed.

Attractive Features of Peroxidases and Laccases for Application in Polymer Chemistry

Besides their robustness and easiness in handling, the most fascinating features of oxidative enzymes include their ability to generate reactive species and their wide substrate specificity. Enzymatic synthesis or polymer modifications processes with oxidases mimic the same natural processes of these enzymes, converting substrates into reactive species which can cross-couple non-enzymatically.

For example, laccases (benzenediol: oxygen oxidoreductase, EC 1.10.3.2) catalyze the oxidation of various phenolic substrates (phenols, polyphenols, anilines, aryl diamines, methoxy-substituted phenols, hydroxyindols, benzenethiols, inorganic/organic metal compounds and many others) (Figure 1) with the simultaneous reduction of molecular oxygen to water (*2–4*). In insects these enzymes participate in the synthesis of protective pigments while in plants they participate in the synthesis of lignin and other secondary metabolites (*5*).

Laccases have four copper atoms in the active site (T1, T2, T3) and a redox potential between 0.45 – 0.8 V against the normal hydrogen electrode (NHE) (*6–8*). The T1 copper abstract electrons from the substrate (AH) which are transferred to the trinuclear T2/T3 cluster were they reduce molecular oxygen to water and a substrate radical (A·) (Figure 1).

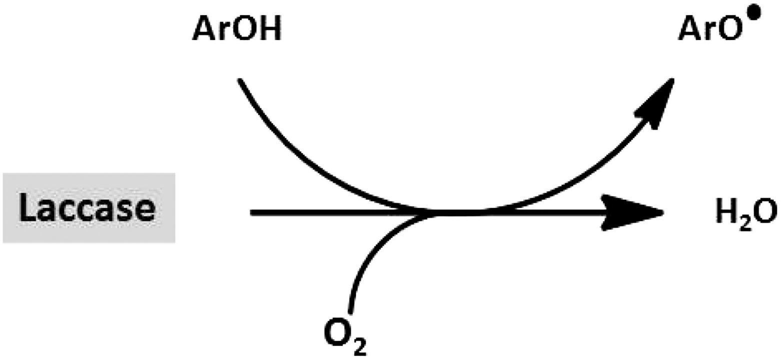

Figure 1. Laccase reaction action mechanism.

Unlike laccases which contain copper at their active site, peroxidases (EC 1.11.1.7) are oxidative enzymes with a ferric protoheme group at the redox center. Generally, peroxidases require hydrogen peroxide and their catalytic cycle is characterized by electron transfer from an oxidizable substrate, formation and reduction of compound I (a porphyrin π-cation radical containing Fe^{IV}) and compound II intermediates (oxyferryl center coordinated to a normal porphyrin ligand) (Figure 2). The resting enzyme reacts with H_2O_2 to produce the two-electron oxidized intermediate, compound I, which in turn oxidizes the substrate (AH) to yield the one-electron oxidized intermediate compound II and a substrate radical (A·). Compound II returns to the resting enzyme by oxidizing a second substrate molecule. The free radical can undergo a variety of reactions.

The most widely used peroxidases in polymer chemistry include plant peroxidases, soybean peroxidases, fungal peroxidases (lignin peroxidases, manganese peroxidases and versatile peroxidases). The redox potential of lignin peroxidases is approximately 1.4 V vs NHE (*9*), horseradish peroxidase is 0.95 V (*10*) while Mn^{3+} produced by manganese peroxidase has a redox potential of 1.51 V (*11*). Manganese peroxidases [EC 1.11.1.13] unlike lignin peroxidases, oxidizes Mn^{2+} to Mn^{3+}, which acts as a diffusible oxidizer attacking both phenolic and non-phenolic lignin units inside the polymer. Versatile peroxidases (EC 1.11.1.16) have been described as a third type of lignolytic peroxidase produced by fungi, which combines the catalytic properties of peroxidases and manganese (*12*). Molecular characterization of versatile peroxidase enzymes reveals structures closer to lignin peroxidase than to the manganese peroxidase (*12*).

Downloaded by PENNSYLVANIA STATE UNIV on August 28, 2012 | http://pubs.acs.org
Publication Date (Web): August 17, 2012 | doi: 10.1021/bk-2012-1107.ch018

Downloaded by PENNSYLVANIA STATE UNIV on August 28, 2012 | http://pubs.acs.org
Publication Date (Web): August 17, 2012 | doi: 10.1021/bk-2012-1107.ch018

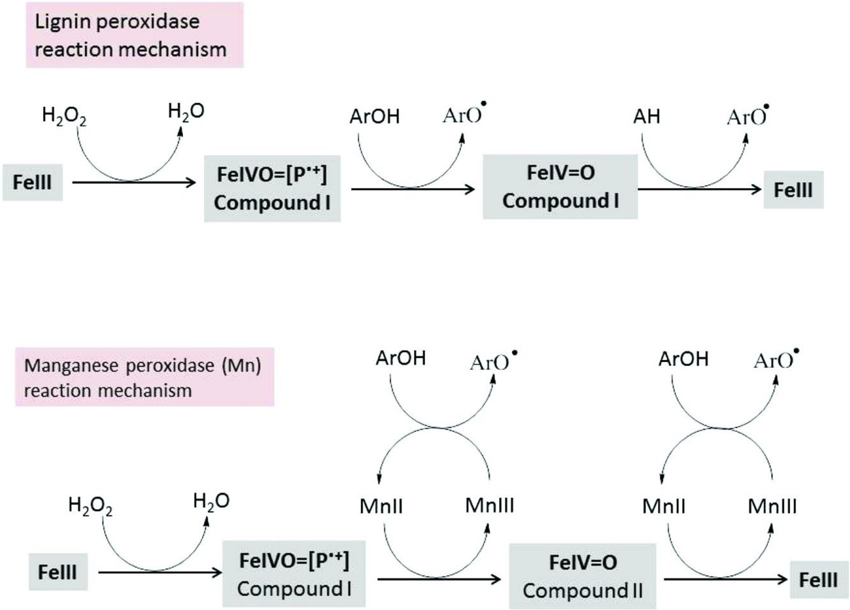
Lignin peroxidase reaction mechanism
H2O2
H2O
FeIII
FeIVO=[P•+] Compound I
ArOH
ArO•
FeIV=O Compound I
AH
ArO•
FeIII
Manganese peroxidase (Mn) reaction mechanism
H2O2
H2O
FeIII
FeIVO=[P•+] Compound I
ArOH
ArO•
MnII
MnIII
FeIV=O Compound II
ArOH
ArO•
MnII
MnIII
FeIII

Figure 2. General reaction mechanism of lignin peroxidase and manganese peroxidase (Mn).

Although the major substrates of peroxidases and laccases are phenolic compounds, these enzymes have proved to be versatile biocatalysts with abilities to oxidize even wider varieties of natural and synthetic molecules (*13*). The generated reactive species are able to attack other molecules as well as polymers (*14*) thereby indirectly extending the activity of these enzymes.

Reaction Engineering Strategies for Production of Functional Polymers

Successful production of functional polymers based on laccases and peroxidases depends on a number of factors, including reactivity of substrates with enzymes, reactivity of oxidized substrates to each other or with the target molecule, solvent compositions, pH and many other reaction conditions which require optimization. These factors influence the choice of the process conditions for polymer functionalization. Various strategies have been investigated and applied during the production of functional polymers including:

- simultaneous direct oxidation of both substrates leading to cross-coupling and formation of novel functional polymers,
- the use of cross-linkers molecules (bifunctional reactive molecules e.g. phenolic amines) to facilitate the binding of polymers or functional molecules,

Downloaded by PENNSYLVANIA STATE UNIV on August 28, 2012 | http://pubs.acs.org
Publication Date (Web): August 17, 2012 | doi: 10.1021/bk-2012-1107.ch018

- the use of small, highly reactive molecules (mediators) which oxidize either the target polymer or functional molecule for subsequent coupling or grafting reactions,
- grafting reactive molecules which act as anchor groups for coupling functional molecules
- and the use of templates.

Strategies for the Synthesis of Functional Polymers

Direct Oxidation of Substrates Causing Cross-Coupling and Formation of New Functional Polymers

This is one of the most commonly used approaches. The functional molecules or the target polymer is oxidized by laccases or peroxidases resulting in the generation of reactive species which in turn cross-react. A typical example of this strategy include laccase-catalyzed coupling of fluorophenols onto wood veneers to increase hydrophobicity (*15*, *16*). The wood veneers were incubated with fluorophenols in the presence of laccase. Laccase oxidized both the wood veneers and the fluorophenols leading to the grafting of the fluorophenols onto the surface of the veneers and subsequent increase in hydrophobicity. *In vitro* mechanistic studies performed with complex lignin model compounds showed the ability of laccase to mediate the coupling of fluorophenol, e.g. 4-[4-(trifluoromethyl)-phenoxy]-phenol, onto different complex lignin models, such as syringylglycerol-β-guaiacyl ether (G-S-β-ether), guaiacylglycerol-β-guaiacyl ether (erol) and dibenzodioxocin (*15*, *16*), present in the wood as shown in (Figure 3).

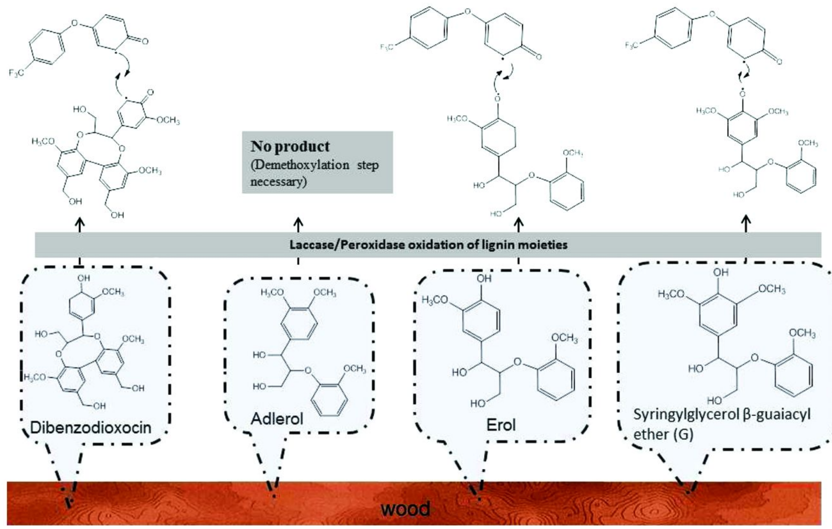
No product
(Demethoxylation step necessary)
Laccase/Peroxidase oxidation of lignin moieties
Dibenzodioxocin
Adlerol
Erol
Syringylglycerol β-guaiacyl ether (G)
wood

Figure 3. Schematic representation of Laccase- or peroxidase-mediated grafting of functional molecules onto different lignin moieties at a wood surface.

For example, 4-[4-(trifluoromethyl)-phenoxy]-phenol was coupled onto sinapyl units through 4-*O*-5 linkages and through 5-5 linkages onto guaicyl units (Figure 3). The important role played by laccases in activating the lignin model compounds was further confirmed by the fact that no coupling product was detected during incubation of adlerol (no laccase substrate) with laccase-oxidized 4-[4-(trifluoromethyl)-phenoxy]-phenol (Figure 3). The presence of the methoxy groups decreases the number of reactive sites on the aromatic ring of lignin moieties available for cross-coupling reactions. This means that successful modification of these highly methoxylated lignocellulose materials therefore requires an intermediate demethoxylation step in order to increase oxidation by oxidative enzymes. Direct oxidation of substrates leading to cross-coupling and formation of new functional polymers is applied and has been successfully used for synthesis of phenol-based adhesives or coating materials, processing of fiberboards, and synthesis of several polymers as summarized in Table 1.

Downloaded by PENNSYLVANIA STATE UNIV on August 28, 2012 | http://pubs.acs.org
Publication Date (Web): August 17, 2012 | doi: 10.1021/bk-2012-1107.ch018

Table 1. Examples of direct oxidation leading to cross-coupling and formation of functional polymers

Examples	*References*
Synthesis of lignin-based adhesives	(*17–19*)
Bonding of wood chips	(*20–23*)
Grafting of hydrophobicity enhancers, such as lauryl gallate, fluorophenols long-chain alkylamines onto lignocellulose materials	(*24–26*)
Grafting of antimicrobial compounds onto target polymers	(*27–34*)
Synthesis of biocatalytically active hydrogel-based polymers	(*35–39*)
Synthesis of high-molecular weight radical-scavenging antioxidant polymer	(*40*, *41*)
Functionalization of flax fibers with phenolic compounds	(*42*)

Cross-Linker and Reactive Anchor Group Assistance for Development of Functional Polymers

Cross-linkers are molecules with at least two reactive groups, e.g. reactive amino groups and hydroxyl groups in phenolic amines. Cross-linkers are widely used for bonding many different polymers as summarized in Table 2. For example, Nimz et al. (*43*, *44*) were among the first to successfully use technical lignins modified with oxidative enzymes as cross-linkers for the production of particle boards. Similarly, when Kühne and Dittler (*45*) incubated a whole culture fermentation broth containing phenolics with rape-straw fibers, they obtained medium-density fiberboards superior to those produced by incubating with a purified *Trametes versicolor* laccase, indicating that the phenolic molecules acted as cross-linkers. Different cross-linkers have also been used to increase the mechanical strength and other properties of pulps. For example, the addition of lignin-rich extractives as cross-linkers to laccase treated high-yield Kraft pulp

(*46*) and addition of a low-molecular-weight ultra-filtered lignin fraction (*47*) improved the mechanical properties of the pulps. Similarly incubation of different pulps with low-molecular weight phenolic and cationic dyes (*48–51*), methyl syringate (*52*) and aromatic amino acids (*53*) as cross-linkers also resulted in improved strength of the pulp or paper. The enhanced improvement in mechanical properties results from a combination of factors including grafting of oxidized phenolic molecules onto the fibers, increase in carboxyl and hydroxyl groups which promote hydrogen bonding and also the crosslinking of phenoxy radicals inside the paper sheet. Widsten et al. (*54*) also produced superior fibers boards in terms of mechanical strength by incorporating tannins as cross-linkers in the presence of laccase.

Table 2. Functional polymers by cross-linker and reactive anchor group assistance

Examples	***References***
Production of particle boards with technical lignins as cross-linkers	(*43*, *44*)
Medium-density fiber boards produced from rape-straw fibers incubated with whole fungal culture fermentation	(*21*, *45*)
Pulp and paper: low-molecular-weight ultra-filtered lignin fraction, phenolics and aromatic amino acids as cross-linkers	(*46–53*)
Fiber boards prepared by incorporating tannins in the presence of oxidative enzymes	(*54*)
Use of chemo-enzymatically produced oxiranes for modifying lignocellulose polymers	(*55*)
Phenolic cross-linkers during the synthesis of hydrogels for tissue engineering, drug delivery and wound healing	(*56–62*)
Coupling of phenolic amines for subsequent functionalization	(*63*)
Activation of inert polymers e.g. tosylated cellulose	(*64*, *65*)
Functionalization of polyethersulphonate membrane	(*66*)

Grönqvist et al. (*67*) reported a 90% loss of radicals formed on laccase-bleached thermo-mechanical pulp after an hour. In an effort to avoid the loss of generated radicals in complex lignin polymers without coupling, Kudanga et al (*68*) developed a novel strategy for creating a stable, reactive surface based on grafting various structurally different laccase-oxidizable phenolic amines onto lignocellulose material to act as anchor groups (Figure 4). The authors provided *in vitro* evidence for the covalent binding of aromatic amines onto different lignin model compounds (syringylglycerol-guaiacyl ether, erol and dibenzodioxocin) (*68*), involving the hydroxyl group and leaving the –NH_2 group free for further coupling reactions as shown in Figure 4. Regardless of the chemical structure, all the phenolic amines underwent C-C coupling with dibenzodioxocin and 4-O-5 coupling with syringylglycerol-guaiacyl ether, leaving the –NH_2 group free to act as an anchor group (Figure 4).

Downloaded by PENNSYLVANIA STATE UNIV on August 28, 2012 | http://pubs.acs.org
Publication Date (Web): August 17, 2012 | doi: 10.1021/bk-2012-1107.ch018

Downloaded by PENNSYLVANIA STATE UNIV on August 28, 2012 | http://pubs.acs.org
Publication Date (Web): August 17, 2012 | doi: 10.1021/bk-2012-1107.ch018

Grafting of these reactive aromatic amines onto beech veneers resulted in increased coupling of antifungal molecules onto the reactive surface as compared to the control (*68*). Kudanga et al. (*55*) also developed a novel non-selective chemo-enzymatic process for the functionalization of polymers based on the generation of oxiranes from unsaturated oils (Figure 5). Unlike the current enzymatic processes which mostly target lignin in lignocellulose polymers, this method is relatively non-selective (*55*) and therefore can react with many different molecules. This means that this approach can also be used to modify many other different polymers.

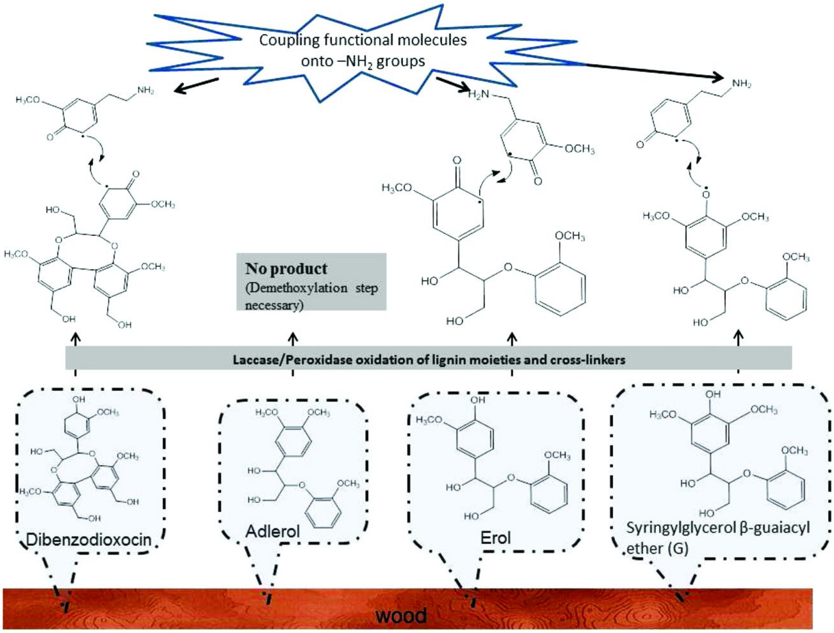
Coupling functional molecules onto –NH$_2$ groups
No product
(Demethoxylation step necessary)
Laccase/Peroxidase oxidation of lignin moieties and cross-linkers
Dibenzodioxocin
Adlerol
Erol
Syringylglycerol β-guaiacyl ether (G)
wood

Figure 4. Laccase- or peroxidase-mediated grafting of a stable reactive surface which can be used to further couple molecules of interest.

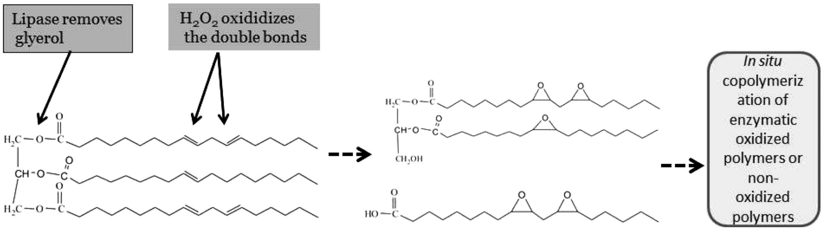
Lipase removes glyerol
H$_2$O$_2$ oxididizes the double bonds
In situ copolymerization of enzymatic oxidized polymers or non-oxidized polymers

Figure 5. Chemo-enzymatic process for generating oxiranes to mediate the development of functional polymers.

Downloaded by PENNSYLVANIA STATE UNIV on August 28, 2012 | http://pubs.acs.org
Publication Date (Web): August 17, 2012 | doi: 10.1021/bk-2012-1107.ch018

Mediator-Assisted Polymer Functionalization

Mediators (small molecules which when oxidized by oxidative enzymes form highly reactively molecules) are increasingly used to oxidize complex substrates which are no direct substrates for oxidative enzymes. This is because enzymes such as laccase have a rather low redox potential (E°) between 0.45 V- 0.8 V vs. NHE. Mediators therefore enable laccase to oxidize substrates which would normally be not its substrate, enable oxidation of bulky substrates which cannot enter the active site of the enzyme or oxidize molecules inside complex substrates where the enzyme itself has no access. There are two main types of mediators currently being used: N–OH type (e.g. 1-hydroxybenzotriazole, *N*-hydroxyphthalimide, violuric acid, *N*-hydroxyacetanilide and 2,2,6,6-Tetramethyl-1-piperidinyloxy and ArOH type (acetosyringone, syringaldehyde, vanillin, acetovanillone, sinapic acid, ferulic acid, *p*-coumaric acid, etc). Basically, these mediators, as shown in Figure 6, are oxidized by oxidative enzymes, e.g. laccases, under formation of radicals which in turn oxidize the functional molecules or the target polymers, the mediators thus undergoing reduction and subsequent re-oxidation by oxidative enzymes (Figure 6). The oxidized functional molecules and /or target polymer cross-react leading to the formation of polymers with new properties (Figure 6).

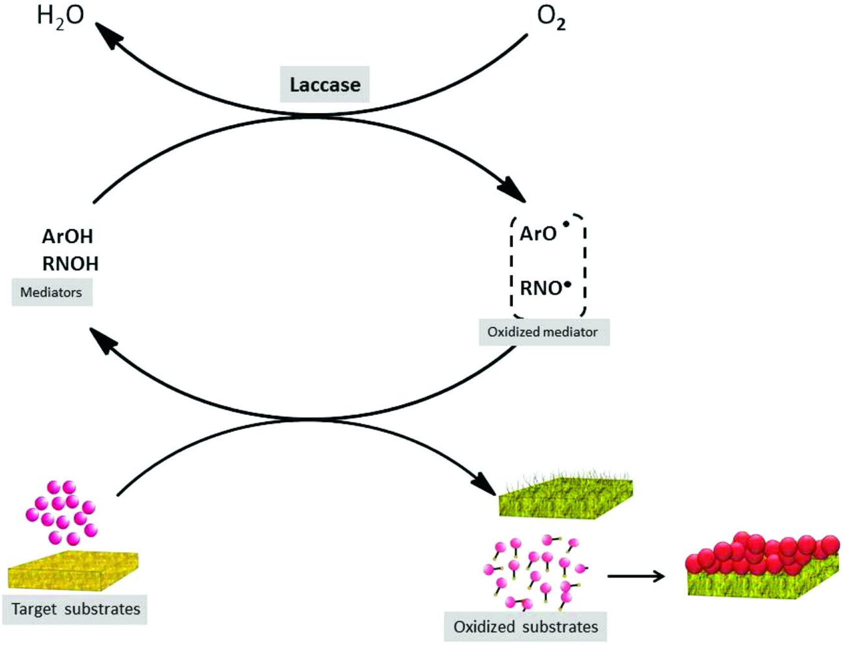

Figure 6. Laccase/mediator-assisted oxidation of functional molecules and/or target polymers.

Downloaded by PENNSYLVANIA STATE UNIV on August 28, 2012 | http://pubs.acs.org
Publication Date (Web): August 17, 2012 | doi: 10.1021/bk-2012-1107.ch018

Mediators are widely investigated mainly to boost laccase degradation of residual lignin in the pulp and paper industry (*70*), textile processing, cellulose oxidation, polymer synthesis and degradation of notorious environmental pollutants from many industrial processes (*71*). Many laccase-mediator formulations are already on the market for industrial application including Laccase/phenothiazinylpropionate developed by Novozymes (Denmark) used for bleaching indigo on jean fabrics to give nice fastness color, Suberash® used for cork modification and a Laccase/mediator system capable of bleaching textile fibers developed by Zytex Mumbai, India (*71*). Codexis Inc., United States, patented a binary mediator system, which, in combination with laccase, selectively performs oxidation of 6-hydroxy groups of cellulose to carbonyl and carboxyl groups which can be further modified by compounds bearing amino or other reactive groups (*71*). Laccase-TEMPO formulations are also increasingly used to mediate the oxidation of cellulose aimed at introducing functional molecules. Further, laccase-TEMPO mediated system is used to catalyze the largely regioselective oxidation of the primary hydroxyl groups of sugar derivatives, starch, pullulan and cellulose, preparing these compounds for subsequent functionalization (*72*).

Template-Assisted Synthesis of Functional Polymers

In polymer chemistry, the synthesis of well-defined structures is crucial. Several strategies are used including template-assisted synthesis of polymers. As shown in Figure 7, functional molecules are oxidized in the presence of a template. The oxidized molecules polymerize and adopt the geometry of the template which is then removed after the reaction.

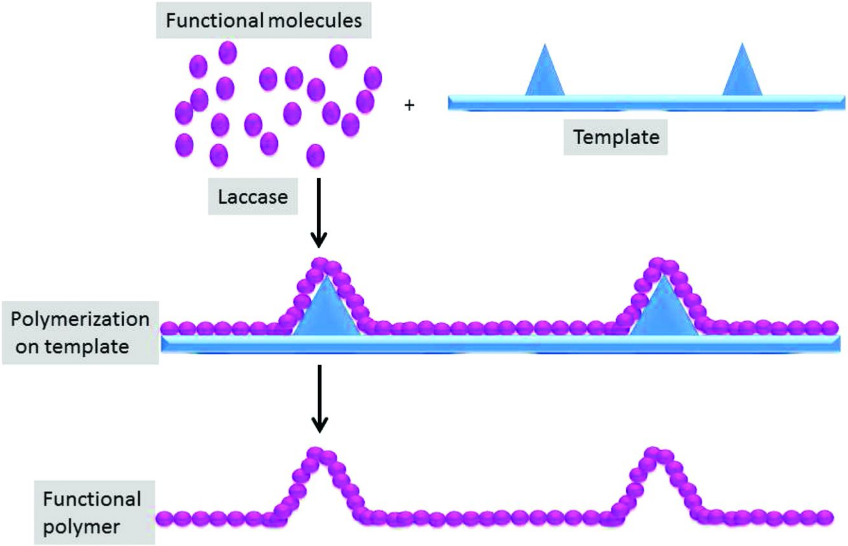

Figure 7. Schematic representation of template-assisted synthesis of functional polymers.

Downloaded by PENNSYLVANIA STATE UNIV on August 28, 2012 | http://pubs.acs.org
Publication Date (Web): August 17, 2012 | doi: 10.1021/bk-2012-1107.ch018

The synthesis of electric conducting polymers based on polyaniline, mediated by oxidative enzymes, is one example which demonstrates evolution of reaction engineering processes directed towards refining reaction conditions. Several strategies including the use of different solvent mixtures, reverse micellar systems and different templates (Table 3) among other conditions have been investigated.

Table 3. Template-assisted synthesis of functional polymers

Examples	***References***
Templates for synthesis of polyaniline	(*73–77*)
A template of a borate-containing electrolyte or lignin sulphonate template	(*78*)
Anionic polymeric templates	(*79*)
Amphiphilic triblock copolymers of poly(ethylene glycol), (PEG)-poly(propylene glycol), (PPG)-poly(ethylene glycol) (PEG) (pluronic), with pluronic F68 (EG76-PG29-EG76)	(*80–82*)
Polyelectrolyte like sulfonated polystyrene	(*83*)

For example, anionic polymeric templates were used to promote the *para*-directed head-to-tail coupling of aniline radicals in order to obtain a well-defined electrically conducting polyaniline (*73–80*). Template-assisted synthesis of functional polymers has also been pursued for other applications such polymerization of phenol on poly(ethylene glycol) monododecyl ether a as a template in the presence of horseradish peroxidase, resulting in increased regioselectivity close to 90% attributed to oriented alignment due to hydrogen bonding interaction of phenolic OH groups and ether oxygen atoms of the template (*80–82*). Similarly, ultrahigh-molecular weight ($Mw> 10^6$) polyphenol were produced when phenol was polymerized in the presence of amphiphilic triblock copolymers of poly(ethylene glycol) (PEG), poly(propylene glycol) (PPG), and poly(ethylene glycol) (PEG) (pluronic), with pluronic F68 (EG_{76}-PG_{29}-EG_{76}) as template (*80–82*). The use of pluronic with high PEG content also improved the regioselectivity of the polymerization of phenol. The use of templates therefore provides a platform for the synthesis of functional polymers with a well-defined structure. This is very important given the fact that oxidative enzyme-generated radicals tend to react randomly.

Advances in Solvent Reaction Engineering for Development of Functional Polymers

Another complication related to polymer synthesis with laccases and peroxidase is related to the solubility of the involved reagents. Generally, laccase and peroxidase substrates are not soluble in aqueous solutions, requiring the use of buffer/organic solvents mixtures, surfactants, reverse micelles, dispersive colloidal systems, ionic liquids, supercritical fluids and at certain

Downloaded by PENNSYLVANIA STATE UNIV on August 28, 2012 | http://pubs.acs.org
Publication Date (Web): August 17, 2012 | doi: 10.1021/bk-2012-1107.ch018

times solvent-free reaction conditions. However, as biological catalysts, enzymes operate under defined optimal conditions with a certain degree of hydration. Although studies of enzymatic reactions in non-aqueous media started more than 100 years ago (*83*), this strategy became popular only as from the 1970s thanks to the pioneering works of Klyosov et al. (*84*), Klibanov et al. (*85*) and Martinek et al. (*86*). Subsequent progress in solvent reaction engineering has led to the development of many different solvent reaction systems, namely:

(a) aqueous buffer systems,
(b) monophasic aqueous-organic systems (water-miscible organic solvents),
(c) biphasic aqueous-organic systems (an aqueous phase plus non-polar organic solvent).
(d) reverse micelles (emulsions of water and immiscible solvents stabilized by surfactants)
(e) ionic liquids (molten salts, i.e., mixtures of cations and anions that melt below 100°C (*87*, *89*).
(f) supercritical fluids (substance above its critical temperature (T_C) and critical pressure (P_C) where vapor and liquid form of the substance become indistinguishable) as solvents for enzymatic reactions. Supercritical fluids rely on the fact that the solubility behavior is altered in the supercritical state, resulting in increased solubility properties.

Aqueous/Organic Solvent and Their Mixtures as Media for the Synthesis of Functional Polymers

Many aromatic substrates oxidized by oxidoreductases are not soluble in aqueous solutions and require an organic co-solvent. Nevertheless, increasing the content of a hydrophilic organic solvent in an aqueous mixture removes the water around the enzyme leading to enzyme aggregation and precipitation. This implies that careful studies have to be carried out to define the best conditions. Thanks to advances in enzyme reaction engineering it was demonstrated that enzyme activity and reactivity can be manipulated in organic solvents leading to the production of novel products not possible under conventional conditions (*90*). For example, by manipulating the reaction solvent conditions, lignin peroxidase can more easily oxidize aromatic amines than phenolic compounds in 70% aqueous ethylene glycol medium although it failed to oxidize veratryl alcohol in the same medium (*91*). This means that by carefully manipulating the solvent it is possible to selectively target certain molecules for modification. This observation has produced the most impressive achievements in solvent reaction engineering studies, leading to enhanced enzyme selectivity (stereo-, regio- and chemoselectivity) in organic solvents (*90*). For example, the oxidative polymerization of 4-hexyloxyphenol was designed to enhance the production of ortho−ortho C−C coupling products (*92*) while laccase oxidation of 2,6-dimethoxyphenol in water-organic solvent system produced the para-coupling product 3,3′,5,5′- tetramethoxy,1,1′-biphenyl-4,4′-diol only (*93*). Advances in solvent reaction engineering are also providing solutions for producing polymers with increased molecular weight. For example, yields of radical polymerization of styrene and its derivatives (4-methylstyrene, 2-vinylnaphthalene) were raised from 41% to 59% by using tetronic acid and 1,3-cyclopentanedione, respectively (*94*). Similarly, polymerization yields of methyl methacrylate were increased when low-dielectric co-solvents, such as dioxane and THF, were used (*95*). The use of organic solvents/buffer mixtures suppressed unwanted hydrolytic side reactions (*90*, *96*).

The catalytic efficiency of laccase for catechin and epicatechin was three times higher in hexane as compared to that obtained in aqueous media, whereas that for catechol was eight times higher in toluene (*97*). The use of a biphasic system consisting of ethyl acetate and sodium phosphate buffer during the Laccase-mediated synthesis of phenolic colorants facilitated separation of products from reactants with the yellow intermediate product accumulating in the organic phase and also prevented its polymerization (*98*). The antioxidant activity of naringenin, an abundant flavonoid in citrus fruits, was enhanced by coupling simple phenolic molecules rich in hydroxyl groups and/or methoxyl groups with laccases (*99*). In all cases, up to two catechol, guaiacol, ferulic and sinapic acid molecules were covalently coupled onto naringenin. The type of solvent used had an impact on the coupling efficiency, with highest yields obtained for ethyl acetate compared to methanol and acetonitrile (*99*). Hence, aqueous/organic solvent reaction engineering is extremely important since it affects reactivity, product yield, regioselectivity, product recovery and size of the produced polymers.

Reverse Micelles as Micro-Environments for Development of Functional Polymers

Reverse micelles have been widely used in organic synthesis because they provide a microenvironment for enzymes similar to that within cells (*100*). Reverse micelle systems are also important for increasing product recovery as demonstrated by Cruz-Silva et al (*101*) during the recovery of polyaninile produced through the catalytic activities of peroxidases. Rao et al. (*102*) showed that it was possible to control polymer chain growth (molecular weight) by manipulating the ability of the reverse micelles-based anionic surfactant, bis(2-ethylhexyl) sodium sulfosuccinate, to sustain chain solubility in the presence of peroxidases. Similarly, oxidative polymerization of 2-naphthol with cyclodextrins as carrier resulted in a polymer with fluorescence characteristics of the 2-naphthol chromophore (*103*). Michizoe et al. (*104*) showed that laccase activity towards bisphenol A dramatically increased when 4% of water was (v/v) is included in the reaction media, compared with pure isooctane. These studies indicate that it is possible to designed reverse micelle systems in order to obtain the desired polymers, to modulate polymer size, to provide conditions for optimal enzyme activity, as well as to increase product recovery.

Ionic Liquids as Medium for Development of Functional Polymers

The most attractive feature of ionic liquids is the existence of these salts in liquid form at ambient and even below ambient temperatures (*105*). The biotechnological application of enzymes in ionic liquids medium is very attractive

Downloaded by PENNSYLVANIA STATE UNIV on August 28, 2012 | http://pubs.acs.org
Publication Date (Web): August 17, 2012 | doi: 10.1021/bk-2012-1107.ch018

Downloaded by PENNSYLVANIA STATE UNIV on August 28, 2012 | http://pubs.acs.org
Publication Date (Web): August 17, 2012 | doi: 10.1021/bk-2012-1107.ch018

since they increase the solubility of organic substrates. Magnuson et al. (*106*) were among the first to use enzymes in ionic liquids (aqueous mixtures of ethylammonium nitrate [$EtNH_3$][NO_3]. Since then the application of enzymes in ionic liquids has been increasing as evidenced by increased numbers of literature reports (*104*, *107–114*). This is driven by the observed attractive properties of ionic liquids such as no vapor formation, providing stable environment for the enzyme, ability to dissolve a wide range of different substrates including polymeric compounds, and ability to manipulate their physical and chemical properties (polarity, hydrophobicity, viscosity, and solvent miscibility). Laccases and peroxidases in ionic liquids were able to oxidize veratryl alcohol, anthracene and guaiacol in 1-butyl-3-methylimidazolium tetrafluroborate [4-mbpy][BF4] (*115*, *116*) and achieve 100 % polymerization of phenol in [bmim][BF4] (*117*). Application of oxidative enzymes in ionic liquids has been shown to improve enzyme stability and also enable repeated reuse. For example, horseradish peroxidase was 3 times more stable at 80 °C in 5-10% BMIM(BF_4) (*118*, *120*) and could be reused 5 times as compared to only 2 times in water for the oxidation of veratryl alcohol (*120*). Laccase in 25% ionic liquid 4-methyl-*N*-butylpyridinium tetrafluoroborate BMPyr(BF4) has shown a 30-fold higher substrate conversion rate than in 20% butanol (*121*). These remarkable properties have witnessed increasing applications of ionic liquids during the production of biosensors based on laccases and peroxidases (*18*, *121–124*). Examples include the development of a new biosensor for the determination of the pesticide based on laccase immobilized on platinum nanoparticles dispersed in 1-butyl-3-methylimidazolium tetrafluoroborate (Pt–[BMIM][BF_4]) ionic liquid (*125*), a biosensor for the determination of adrenaline in pharmaceutical formulations dispersed in 1-butyl-3-methylimidazolium hexafluorophosphate (Pt-[BMIM][PF_6]) (*126*) and a biosensor based on cellulose acetate and 1-butyl-3-methylimidazolium bis(trifluoromethylsulfonyl)imide ([BMIM][$N(Tf)_2$]) for the detection of methyldopa (*127*). This latter sensor demonstrated acceptable stability (ca. 60 days; at least 350 determinations), good repeatability and reproducibility (relative standard deviations of 1.5 and 4.3%, respectively) (*127*). Therefore, ionic liquids in combination with oxidative enzymes are gaining popular in organic synthesis, polymer synthesis and biosensors.

Supercritical Fluids as Solvents for the Development of Functional Polymers

Among the advantages of supercritical fluids is their non-toxicity, provision of ideal temperatures for heat-sensitive enzymes or reactions and also easy product recovery. The critical point for carbon dioxide is 31.1 °C at 73.8 bar conditions which is very good for many industrial enzymes. A polymer of acrylamide was produced by peroxidase-mediated free radical polymerization in an inverse emulsion of water-in-supercritical carbon dioxide (*128*). Polyphenol oxidases in supercritical fluids have been applied for the oxidation of *p*-cresol and *p*-chlorophenol (*129*) and removal of phenol from aqueous solutions using tyrosinase (*130*). Supercritical fluids have also been shown to enhance enantio-selectivity during the synthesis of polymers (*131*, *132*).

Downloaded by PENNSYLVANIA STATE UNIV on August 28, 2012 | http://pubs.acs.org
Publication Date (Web): August 17, 2012 | doi: 10.1021/bk-2012-1107.ch018

Importance of Redox Potential Control during the Development of Functional Polymers

Solvent effects are directly linked to pH effects. The pH value has a direct bearing on both the redox potential of the enzyme and substrate. For example, increasing the pH increases the ionization of phenolic substrates. However, increasing pH increases hydroxide anions (OH^-) in the system which in turn interferes with the activity of oxidative enzymes, such as laccases, by disrupting the internal flow of electrons between the T1 and T2/T3 sites. The pH also affects the redox potential of lignin peroxidase as demonstrated by the decrease in the redox potential of lignin peroxidase when the pH was increased from pH 3 to 7 (*133*). To successfully produce functional polymers the interplay between effects of pH on the enzyme and substrates has to be carefully optimized. It has been recommended to use enzymes recovered through lyophilization or precipitation from their aqueous pH optimum solutions (*134*, *135*).

In summary, advances in solvent reaction engineering have made it possible to perform reactions originally thought impossible in aqueous medium (e.g. esterification and trans-esterification reactions), produce desired polymers through engineering selectivity (region, enantioselectivity and chemoselectivity), increase overall yields of products, increase product recovery, recycling the enzymes, increase enzyme stability, modify enzyme reactivity and suppress side reactions (e.g. racemization, decomposition or precipitation due to rapid polymerization).

Concluding Remarks

Several strategies in terms of reaction engineering approaches have been developed for the production of functional polymers based on oxidative enzymes and many more are being developed. The selection of any particular strategy or reactions conditions requires detailed knowledge of the desired products, enzymes reaction mechanisms, available strategies, chemical composition of substrates etc. It is evident that a multidisciplinary approach combining knowledge from biotechnology, polymer chemistry, chemical engineering, organic synthesis is extremely important for successful development of functional polymers.

Acknowledgments

The authors are grateful to the assistance offered by Seventh Framework Programme FP7-SME-EU-CottonBleach, Austrian Centre of Industrial Biotechnology (ACIB), the MacroFun project and the COST Action 868, the Federal Ministry of Economy, Family and Youth (BMWFJ), the Federal Ministry of Traffic, Innovation and Technology (bmvit), the Styrian Business Promotion Agency SFG, the Standortagentur Tirol and ZIT - Technology Agency of the City of Vienna through the COMET-Funding Program managed by the Austrian Research Promotion Agency FFG.

References

1. Kobayashi, S.; Makino, A. *Chem. Rev.* **2009**, *109*, 5288–5353.
2. Nyanhongo, G. S.; Aichernig, N.; Ortner, M.; Steiner, W.; Guebitz, G. M. *J. Hazard. Mater.* **2009**, *165* (1−3), 285–290.
3. Riva, S. *Trends Biotechnol.* **2006**, *24*, 219–226.
4. Morozova, O. V.; Shumakovich, G. P.; Gorbacheva, M. A.; Shleev, S. V.; Yaropolov A. I.*Biochemistry (Moscow)* **2007**,*72* (10), 136−1150.
5. Arora, D. S.; Sharma, R. K. *Appl. Biochem. Biotechnol.* **2010**, *160* (6), 1760–1788.
6. Reinhammar, B. R. M. *Biochim. Biophys. Acta.* **1972**, *275*, 245–259.
7. Xu, F.; Berka, R. M.; Wahleithner, J. A.; Nelson, B. A.; Shuster, J. R.; Brown, S. H.; Palmer, A. E.; Solomon, E. I. *Biochem. J.* **1998**, *334*, 63–70.
8. Alcalde, M. In *Industrial Enzymes: Structure, Function and Applications*; Polaina, J., MacCabe, J., Eds.; Springer: New York, 2007; pp 459−474.
9. Wong, D. W. S. *Appl. Biochem. Biotechnol.* **2009**, *157*, 174–209.
10. Hayashi, Y.; Yamazaki, I. *J. Biol. Chem.* **1979**, *254*, 9101–9106.
11. Martínez, A. T.; Speranza, M.; Ruiz-Dueñas, F. J.; Ferreira, P.; Camarero, S.; Guillén, F.; Martínez, M. J.; Gutiérrez, A.; Del Rio, J. C. *Int. Microbiol.* **2005**, *8* (3), 195–204.
12. Martinez, A. T. *Enzyme Microb. Technol.* **2002**, *30*, 425–444.
13. Nyanhongo, G. S.; Kudanga, T.; Nugroho Prasetyo, E.; Guebitz, G. M. In *Biofunctionalization of Polymers and Their Applications*; Nyanhongo, G. S., Steiner, W., Guebitz, G. M., Eds.; Springer−Verlag: Berlin, 2011.
14. Nyanhongo, G. S.; Kudanga, T.; Nugroho Prasetyo, E.; Guebitz, G. M. In *Biocatalysis Based on Heme Peroxidase*; E. Torres, E., Ayala, M., Eds.; Springer−Verlag Berlin, 2010.
15. Kudanga, T.; Nugroho Prasetyo, E.; Widsten, P.; Kandelbauer, A.; Jury, S.; Heathcote, C.; Sipilä, J.; Weber, H.; Nyanhongo, G. S.; Guebitz, G. M. *Bioresour. Technol.* **2010**, *101*, 2793–2799.
16. Kudanga, T.; Nugroho Prasetyo, E.; Sipilä, J.; Nyanhongo, G. S.; Guebitz, G. M. *Enzyme Microb. Technol.* **2010**, *46*, 272–280.
17. Milstein, O.; Huttermann, A.; Frund, R.; Ludemann, H. -D. *Appl. Microbiol. Biotechnol.* **1994**, *40*, 760–767.
18. Eker, B.; Zagorevski, D.; Zhu, G.; Linhardt, R. J.; Dordick, J. S. *J. Mol. Catal. B: Enzym.* **2009**, *59*, 177–184.
19. Li, K.; Geng, X. *Macromol. Rapid Commun.* **2005**, *26*, 529–532.
20. Unbehaun, H.; Wolff, M.; Kühne, G.; Schindel, K.; Hüttermann, A.; Cohen, R.; Chet, I. *Holz Roh- Werkst.* **1999**, *57*, 92.
21. Unbehaun, H.; Dittler, B.; Kühne, G.; Wagenführ, A. *Acta Biotechnol.* **2000**, *20*, 305–312.
22. Felby, C.; Pedersen, L. S.; Nielsen, B. R. *Holzforschung* **1997**, *51*, 281–286.
23. Felby, C.; Olesen, P. O.; Hansen, T. T. Laccase Catalyzed Bonding of Wood Fibers. In Enzyme Applications in Fiber Processing; Eriksson K.-E. L., Cavaco-Paulo, A., Eds.; ACS Symposium Series 687; American Chemical Society: Washington, DC 1998, pp 88–98:

Downloaded by PENNSYLVANIA STATE UNIV on August 28, 2012 | http://pubs.acs.org
Publication Date (Web): August 17, 2012 | doi: 10.1021/bk-2012-1107.ch018

Downloaded by PENNSYLVANIA STATE UNIV on August 28, 2012 | http://pubs.acs.org
Publication Date (Web): August 17, 2012 | doi: 10.1021/bk-2012-1107.ch018

24. Kudanga, T.; Nugroho Prasetyo, E.; Sipilä, J.; Nyanhongo, G. S.; Guebitz, G. M. *Enzyme Microb. Technol.* **2010**, *46*, 272–280.
25. Suurnäkki, A.; Mikkonen, H.; Immonen, K. In *Biotechnology for Lignocellulose Biorefineries*; The Final Workshop of COST FP0602, Poster presentation, 2011.
26. Kudanga, T.; Nyanhongo, G. S.; Guebitz, G. M.; Burton, S. *Enzyme Microb. Technol.* **2011**, *48* (3), 195–208.
27. Schroeder, M.; Pereira, L.; Rodríguez Couto, S.; Erlacher, A.; Schoening, K.-U.; Cavaco-Paulo, A.; Guebitz, G. M. *Biotechnol J.* **2007**, *2*, 334.
28. Elegir, G.; Kindl, A.; Sadocco, P.; Orlandi, M. *Enzyme Microb. Technol.* **2008**, *43*, 84–92.
29. Widsten, P.; Heathcote, C.; Kandelbauer, A.; Guebitz, G. M.; Nyanhongo, G. S.; Nugroho Prasetyo, E.; Kudanga, T. *Proc. Biochem.* **2010**, *45* (7), 1072.
30. Shin, H.; Gübitz, G. M.; Cavaco-Paulo, A. *Macromol. Mater. Eng.* **2001**, *286*, 691–694.
31. Tzanov, T.; Silva, C.; Zille, A.; Oliveira, J.; Cavaco-Paulo, A. *Appl. Biochem. Biotechnol.* **2003**, *111*, 1–14.
32. Barfoed, M.; Kirk, O. Method for Dyeing a Material with a Dyeing System Which Contains an Enzymatic Oxidizing Agent. U.S. Patent 5972042,1999.
33. Calafell, M.; Díaz, C.; Hadzhiyska, H.; Gibert, J. M.; Dagá, J. M.; Tzanov, T. *Biocatal. Biotransform.* **2007**, *25*, 336–340.
34. Kim, Y.-J.; Shibata, K.; Uyama, H.; Kobayashi, S. *Polymer* **2008**, *49*, 4791.
35. Govar, C. J.; Chen, T.; Liu, N.-C.; Harris, M. T.; Payne, G. F. Grafting Renewable Chemicals to Functionalize Chitosan. In Biocatalysis in Polymer Science; Gross, R. A., Cheng H. N., Eds.; ACS Symposium Series 840; American Chemical Society: Washington, DC, 2002; pp 231− 242.
36. Chen, T. H.; Vazquez-Duhalt, R.; Wu, C. F.; Bentley, W. E.; Payne, G. F. *Biomacromolecules* **2001**, *2*, 456–462.
37. Chen, T. H.; Embree, H. D.; Wu, L. Q.; Payne, G. F. *Biopolymers* **2002**, *64*, 292–302.
38. Chen, T. H.; Small, D. A.; Wu, L. Q.; Rubloff, G. W.; Ghodssi, R.; Vazquez-Duhalt, R.; Bentley, W. E.; Payne, G. F. *Langmuir* **2003**, *19*, 9382–9386.
39. Chen, T. H.; Embree, H. D.; Brown, E. M.; Taylor, M. M.; Payne, G. F. *Biomaterials* **2003**, *24*, 2831–2841.
40. Desentis-Mendoza, R. M.; Hernández-Sánchez, H.; Moreno, A.; Rojas del C, E; Chel-Guerrero, L.; Tamariz, J.; Jaramillo-Flores, M. E. *Biomacromolecules* **2006**, *7*, 1845–1854.
41. Nugroho Prasetyo, E.; Nyanhongo, G. S.; Guebitz, G. M. *Process Biochem.* **2011**, *46* (4), 1019–1024.
42. Aracri, E.; Fillat, A.; Colom, J. F.; Gutiérrez, A.; del Río, J. C.; Martínez, A. T.; Vidal, T. *Bioresour. Technol.* **2010**, *101*, 8211–8216.
43. Nimz, H.; Razvi, A.; Mogharab, I.; Clad, W. German Patent DE2221353, 1972.
44. Nimz, H.; Ludemann, H.-D. *Holzforschung* **1976**, *30*, 33.
45. Kühne, G.; Dittler, B. *Holz Roh- Werkst.* **1999**, *57*, 264.
46. Lund, M.; Felby, C. *Enzyme Microb. Technol.* **2001**, *28*, 760–765.

Downloaded by PENNSYLVANIA STATE UNIV on August 28, 2012 | http://pubs.acs.org
Publication Date (Web): August 17, 2012 | doi: 10.1021/bk-2012-1107.ch018

47. Elegir, G.; Bussini, D.; Antonsson, S.; Lindström, M. E.; Zoia, L. *Appl. Microbiol. Biotechnol.* **2007**, *77* (4), 809–817.
48. Chandra, R. P.; Ragauskas, A. J. *Tappi Pulping Conf.* **2001**, 1041–1051.
49. Chandra, R. P.; Ragauskas, A. J. *Enzyme Microb. Technol.* **2002**, *30*, 855–861.
50. Chandra, R. P.; Ragauskas, A. J. *Prog. Biotechnol.* **2002**, *21*, 165–172.
51. Chandra, R. P.; Wolfaardt, A. J. Biografting of Celestine Blue onto a High Kappa Kraft Pulp. In Applications of Enzymes to Lignocellulosics; Mansfield, S. D., Saddler, J. N., Eds.; ACS Symposium Series 855; American Chemical Society: Washington, DC, 2003; pp 66− 80.
52. Liu, N.; Shi, S.; Gao, Y.; Qin, M. *Enzyme Microb. Technol.* **2009**, *44* (2), 89–95.
53. Witayakran, S.; Ragauskas, A. *Enzyme Microb. Technol.* **2009**, *44*, 176–181.
54. Widsten, P.; Hummer, A.; Heathcote, C.; Kandelbauer, A. *Holzforschung* **2009**, *63* (5), 545–550.
55. Kudanga, T.; Nugroho Prasetyo, E.; Sipilä, J.; Nyanhongo, G. S.; Guebitz, G. M. *Process Biochem.* **2010**, *45* (9), 1557–1562.
56. Kurisawa, M.; Chung, J. E.; Yang, Y. Y.; Gao, S. J.; Uyama, H. *Chem. Commun.* **2005**, 4312–4314.
57. Jin, R.; Hiemstra, C.; Zhong, Z.; Feijen, J. *J. Biomater.* **2007**, *28*, 2791–800.
58. Sakai, S.; Kawakami, K. *Acta Biomater.* **2007**, *3*, 495–501.
59. Ogushi, Y.; Sakai, S.; Kawakami, K. *Macromol. Biosci.* **2009**, *9*, 262–267.
60. Ogushi, Y.; Sakai, S.; Kawakami, K. *J. Biosci. Bioeng.* **2007**, *104*, 30–33.
61. Sakai, S.; Yamada, Y.; Zenke, T.; Kawakami, K. *J. Mater. Chem.* **2009**, *19*, 230–235.
62. Chung, J. E.; Kurisawa, M.; Uyama, H.; Kobayashi, S. *Biotechnol. Lett.* **2003**, *25*, 1993–1997.
63. Nyanhongo, G. S.; Gomes, J.; Gubitz, G. M.; Zvauya, R.; Read, J. S.; Steiner, W. *Water Res.* **2002**, *36*, 1449–1456.
64. Rodríguez Couto, S.; Toca Herrera, J. L. *Biotechnol. Adv.* **2006**, *24*, 500–513.
65. Wong, K. K. Y.; Richardson, J. D.; Mansfield, S. D. *Biotechnol. Prog.* **2000**, *16*, 1025–1029.
66. Wong, K. Y.; Signal, F. A.; Campion, S. H. *Appita J.* **2003**, *56*, 308–311.
67. Grönqvist, S.; Rantanen, K.; Alén, R.; Mattinen, M. L.; Buchert, J.; Viikari, L. *Holzforschung* **2006**, *60*, 503–50.
68. Kudanga, T.; Prasetyo, E. N.; Sipilä, J.; Nousiainen, P.; Widsten, P.; Kandelbauer, A.; Nyanhongo, G. S.; Guebitz, G. *Eng. Life Sci.* **2008**, *8*, 297–302.
69. Kudanga, T.; Nugroho Prasetyo, E.; Sipila, J.; Eberl, A.; Nyanhongo, G. S.; Guebitz, G. M. *J. Mol. Catal. B: Enzym.* **2009**, *61*, 143–149.
70. Call, H. P.; Mücke, I. *J. Biotechnol.* **1997**, *53*, 163–202.
71. Osma J. F; Toca-Herrera J. and Rodríguez-Couto S.*Enzyme Res.*. doi:10.4061/2010/918761
72. Marzorati, M.; Danieli, B.; Haltrich, D.; Riva, S. *Green Chem.* **2005**, *7*, 310–315.
73. Flores-Loyola, E. *Eur. Polym. J.* **2005**, *41*, 1129–1135.

74. Liu, W.; Cholli, A. L.; Nagarajan, R.; Kumar, J.; Tripathy, S.; Bruno, F. J.; Samuelson, L. *J. Am. Chem. Soc.* **1999**, *121*, 11345–11355.
75. Cruz-Silva, R.; Escamilla, A.; Nicho, M. E.; Padron, G.; Ledezma-Perez, A.; Arias-Marin, E.; Moggio, I.; Romero-Garcia, J. *Eur. Polym. J.* **2007**, *43*, 3471–3479.
76. Liu, W.; Kumar, J.; Tripathy, S. *Langmuir* **2002**, *18*, 9696–9704.
77. Karamyshev, AV.; Shleev, S. C; Koroleva, O. V.; Yaropolov, A. I.; Sakharov, I. Y *Enzyme Microb. Technol.* **2003**, *33*, 556–564.
78. Bruno, F. F.; Nagarajan, R.; Stenhouse, P.; Yang, P.; Tripathy, S.; Kumar, J.; Samuelson, L. *Macromolecules* **2001**, *12*, 1417–1426.
79. Choli, A. L.; Thiyagarajan, M.; Kumar, J.; Parmar, V. S. *Pure Appl. Chem.* **2005**, *77*, 339–344.
80. Kim, Y.; Shibata, K.; Uyama, H.; Kobayashi, S. *Polymer* **2008**, *49*, 4791–4795.
81. Kim, Y.; Uyama, H.; Kobayashi, S. *Macromolecules* **2003**, *36* (14), 5058–5060.
82. Kim, Y.; Uyama, H.; Kobayashi, S. *Macromol. Biosci.* **2004**, *4*, 497–502.
83. Peng, Y.; Liu, H. W.; Zhang, X. Y.; Li, Y. S.; Liu, S. Y. *J. Polym. Sci., Part A: Polym. Chem.* **2009**, *47*, 1627.
84. Klyosov, A. A.; Van Viet, N.; Berezin, I. V. *Eur. J. Biochem.* **1975**, *59*, 3–7.
85. Klibanov, A. M.; Samokhin, G. P.; Martinek, K.; Berezin, I. *Biotechnol Bioeng.* **2000**, *19*, 1351–1361.
86. Martinek, K.; Levashov, A. V.; Klyachko, N. L.; Pantin, V. I.; Berezin, I. V. *Biochim. Biophys. Acta* **1981**, *657*, 277–294.
87. Yang, Z.; Pan, W. *Enzyme Microb. Technol.* **2005**, *37*, 19–28.
88. Cantone, S.; Hanefeld, U.; Basso, A. *Green Chem.* **2007**, *9*, 954–971.
89. Klibanov, A. M. *Nature* **2001**, *409*, 241–246.
90. Yoshida, S.; Watanabe, T.; Honda, Y.; Kuwahara, M. *J. Mol. Catal. B: Enzym.* **1997**, *2*, 243–251.
91. Angerer, P. S.; Studer, A.; Witholt, B.; Li, Z. *Macromolecules* **2005**, *38*, 6248–6250.
92. Singh, A.; Ma, D. C.; Kaplan, D. L. *Biomacromolecules* **2000**, *1*, 592–596.
93. Wan, Y. Y.; Du, Y. M.; Miyakoshi, T. *Chin Chem. Lett.* **2008**, *19*, 333–336.
94. Kalra, B.; Gross, R. A. *Biomacromolecules* **2000**, *1*, 501–505.
95. Azevedo, M.; Prazeres, D. M. F.; Cabral, J. M. S.; Fonseca, L. P. *J. Mol. Catal. B: Enzym.* **2001**, *5*, 147.
96. Krieger, N.; Bhatnagar, T.; Baratti, J. C.; Baron, A. M.; de Lima, V . M.; Mitchell, D. *Food Technol. Biotechnol.* **2004**, *42* (4), 279–286.
97. Ma, H-J.; Kermasha, S.; Gao, J. M.; Morales Borges, R.; Yu, X. *J. Mol. Catal. B: Enzym.* **2009**, *57*, 89–95.
98. Mustafa, R.; Muniglia, L.; Rovel, B.; Girardin, M. *Food Res. Int.* **2005**, *38*, 995–1000.
99. Nugroho Prasetyo, N.; Nyanhongo, G. S.; Guebitz, G. M. *Proc. Biochem.* **2011**, *46*, 1019–1024.
100. Cruz-Silva, R.; Romero-García, J.; Angulo-Sánchez, J. L.; Ledezma-Pérez, A.; Arias-Marín, E.; Moggio, I.; Flores-Loyola, E. *Eur. Polym. J.* **2005**, *41*, 1129–1135.

Downloaded by PENNSYLVANIA STATE UNIV on August 28, 2012 | http://pubs.acs.org
Publication Date (Web): August 17, 2012 | doi: 10.1021/bk-2012-1107.ch018

Downloaded by PENNSYLVANIA STATE UNIV on August 28, 2012 | http://pubs.acs.org
Publication Date (Web): August 17, 2012 | doi: 10.1021/bk-2012-1107.ch018

101. Madhusudhan Rao, A.; John, V. T.; Gonzalez, R. D. *Biotechnol. Bioeng.* **1993**, *41*, 531–540.
102. Premachandran, R. S.; Banerjee, S.; Wu, X.-K.; John, V. T.; McPherson, G. L.; Akkara, J.; Ayyagari, M.; Kaplan, D. *Macromolecules* **1996**, *29* (20), 6452–6460.
103. Michizoe, J.; Ichinose, H.; Kamiya, N.; Maruyama, T.; Goto, M. *J. Biosci. BioEng.* **2005**, *99*, 642–647.
104. Moniruzzaman, M.; Nakashima, K.; Kamiya, N.; Goto, M. *Biochem. Eng. J.* **2010**, *48*, 295–314.
105. Magnuson, D. K.; Bodley, J. W.; Evans, D. F. *J. Solution Chem.* **1984**, *13*, 583–587.
106. Kragl, U.; Eckstein, M.; Kaftzik, N. *Curr. Opin. Biotechnol.* **2002**, *13*, 565–571.
107. Sheldon, R. A.; Lau, R. M.; Sorgedrager, M. J.; van Rantwijk, F.; Seddon, K. R. *Green Chem.* **2002**, *4*, 147–151.
108. van Rantwijk, F.; Madeira Lau, R.; Sheldon, R. A. *Trends Biotechnol.* **2003**, *21*, 131–138.
109. van Rantwijk, F.; Sheldon, R. A. *Chem. Rev.* **2007**, *107*, 2757.
110. Park, S.; Kazlauskas, R. J. *Curr. Opin. Biotechnol.* **2003**, *14* (4), 432–437.
111. Zhao, H. *J. Mol. Catal. B: Enzym.* **2005**, *37*, 16–25.
112. Yang, Z. *J. Biotechnol* **2009**, *144*, 12–22.
113. Lozano, P. *Green Chem.* **2010**, *12*, 555–569.
114. Hinckley, G.; Mozhaev, V. V.; Budde, C.; Khmelnitsky, Y. L. *Biotechnol. Lett.* **2002**, *24*, 2083–2087.
115. Rodriguez, O.; Tavares, A. P.-M.; Cristóvão, R.; Macedo, E. A. In *Ionic Liquids: Applications and Perspectives*; Kokorin, A., Ed.; InTech: Rijeka, 2011; Vol. 2, pp 499−516.
116. Zaragoza-Gascaa, P.; Villamizar-Galveza, O. J; García-Arrazolaa, R.; Gimenoa, M.; Bárzana, E. *Polym. Adv. Technol.* **2010**, *21*, 454–456.
117. Franzoi, A. C.; Migowski, P.; Dupont, J.; Vieira, I. C. *Anal. Chim. Acta* **2009**, *639*, 90–95.
118. Tee, K. L.; Roccatano, D.; Stolte, S.; Arning, J.; Jastorff, B.; Schwaneberg, U. *Green Chem.* **2008**, *10*, 117–123.
119. Hinckley, G.; Mozhaev, V. V.; Budde, C.; Khmelnitsky, Y. L. *Biotechnol. Lett.* **2002**, *24*, 2083–2087.
120. Kumar, A.; Jain, N.; Chauhan, S. M. *Synlett* **2007**, *3*, 411–414.
121. Franzoi, A. C.; Dupont, J.; Spinelli, A.; Vieira, I. C. *Talanta* **2009**, *77*, 1322–1327.
122. Okrasa, K.; Guibé-Jampel, E.; Therisod, M. *Tetrahedron: Asymmetry* **2003**, *14*, 2487–2490.
123. Brondani, D.; Scheeren, C. W.; Dupont, J.; Vieira, I. C. *Sens. Actuators, B* **2009**, *140*, 252–259.
124. Sgalla, S.; Fabrizi, G.; Cacchi, S.; Macone, A.; Bonamore, A.; Boffi, A. *J. Mol. Catal. B: Enzym* **2007**, *44*, 144–148.
125. Zapp, E.; Brondania, D.; Vieiraa, I. C. W.; Scheeren, W. C.; Dupont, J.; Barbosa, A. M. J.; Ferreira, V. S. *Sens. Actuators* **2011**, *B 155*, 331–339.

126. Brondani, D.; Weber Scheeren, C.; Dupont, J.; Cruz Vieira, I. *Sens. Actuators, B* **2009**, *140*, 252–259.
127. Moccelini, S. K.; Franzoi, A. C.; Vieira, I. C.; Dupont, J.; Scheeren, C. W. *Biosens. Bioelectron.* **2011**, *26*, 3549–54.
128. Matsuda, T.; Kanamaru, R.; Watanabe, K.; Harada, T.; Nakamura, K. *Tetrahedron Lett.* **2001**, *42*, 8319–8321.
129. Matsuda, T.; Kanamaru, R.; Watanabe, K.; Harada, T.; Nakamura, K. *Tetrahedron: Asymmetry* **2003**, *14*, 2087–2091.
130. Villarroya, S.; Thurecht, K. J.; Howdle, S. M. *Green Chem.* **2008**, *10*, 863–867.
131. Hammond, D. A.; Karel, M.; Klibanov, A. M.; Krukonis, V. J. *Appl. Biochem. Biotechnol.* **1985**, *11*, 393–400.
132. Amaral, P.; Garcia, D.; Cardoso, M.; Mendes, M.; Coelho, M. A.; Pessoa, F. *Int. J. Mol. Sci.* **2009**, *10*, 5217–5223.
133. Kersten, P. J.; Kalyanaraman, B.; Hammel, K. E.; Reinhammar, B.; Kirkp, T. K. *Biochem. J.* **1990**, *268*, 475–480.
134. Zaks, A.; Klibanov, A. M. *Science* **1984**, *224* (4654), 1249–1251.
135. Zaks, A.; Klibanov, A. M. *J. Biol. Chem.* **1988**, *263* (7), 3194–3201.

Downloaded by PENNSYLVANIA STATE UNIV on August 28, 2012 | http://pubs.acs.org
Publication Date (Web): August 17, 2012 | doi: 10.1021/bk-2012-1107.ch018

Subject Index

A

Amphiphilic lignin derivatives
  bioethanol production, 248
  cellulase-aid agents, 248, 249*f*
  cement dispersants, 250, 251*f*, 252*f*
  enzymatic hydrolysis, 250*t*
  overview, 243
  surface activity, 247, 247*f*
  water solubility, 244, 245*f*

B

Bacterial cellulose aerogels
  active substance release, 69*f*
  apparent density, 67*f*, 67*t*
  application potential, 60
  cellulose I aerogels, 60
  cellulose II aerogels, 60
  depressurized, 68*f*
  D-panthenol release, 69*f*
  E-modulus, 67*f*
  fluorescent, 71*f*
  mechanical properties, 63
  overview, 57
  porosity, 63
  porous scaffolds, 68
  preparation, 61
  properties, 62
  reinforcement, 66
  shrinkage, 63*f*
  solvent exchange, 63*f*, 64*f*
  stress-strain curves, 65*f*
  yield strength, 67*t*
  Young's modulus, 67*t*
Bacterial cellulose (BC), 134
  acetylation, 135
  BET measurement, 135
  block copolymerization, 140
  chemical structure, 138*f*
  dynamic light scattering measurement, 136
  ESR measurement, 135
  ESR spectral simulation, 135
  fractured, 136*f*, 137*f*, 139*f*, 140*f*, 141*f*
  GPC measurement, 136
  ^{1}H NMR measurement, 135
  ^{1}H NMR spectra, 142*f*
  mechanical destruction, 134
  mechanical fracture, 136
  surface modification, 143, 144*f*
  synthesis, 135
BC. *See* bacterial cellulose (BC)
Biopolymers, packaging materials
  benchmark packaging systems, 273
  moisture vapor permeability
    fundamentals, 274*f*, 278*f*, 286*f*, 287*f*
    agar, 283*f*
    aqueous coatings, 279
    atomic layer deposition, 287, 288*t*, 290*t*
    chemical vapor deposition, 290
    edible coatings, 282
    inorganic surface treatments, 285
    montmorillonite, 283*f*, 284*f*
    multi-layer flexible packaging structures, 291*f*
    MVTR governing factors, 276
    nanoclay coatings, 279, 281*f*
    paperboard packaging structure, 280*f*
    physical vapor deposition, 290
    plasticizer effect, 277*f*
    renewable polymers, 281
    terminology, 275
    test methodology, 277
    units, 275
  overview, 271
  oxygen permeability, 274*f*
  requirements, 272
  SEM, 274*f*
  stress-strain curves, 275*f*

C

CDA. *See* diacetate cellulose (CDA)
Cellulose-based honeycomb-patterned films
  overview, 37
  synthesis
    film preparation, 42
    honeycomb film formation, 50
    2,3-O-(2-bromoisobutyryl)-2,6-O-TDMS-cellulose, 41, 46, 47*t*, 48*t*, 49*f*, 50*f*, 51*f*, 52*f*, 53*f*
    3-O-(2-bromoisobutyryl)-2,6-O-TDMS-cellulose, 41, 43, 43*s*, 44*t*, 45*f*, 51*f*
    2,6-O-TDMS-cellulose, 40, 43*f*, 46*f*
    surface-initiated ATRP, 42, 52, 52*t*

Downloaded by 217.66.152.26 on August 23, 2012 | http://pubs.acs.org
Publication Date (Web): August 17, 2012 | doi: 10.1021/bk-2012-1107.ix002

Cellulose graft copolymers
  applications, 122
  controllable synthesis, ATRP, 111
    monomer conversion, 112*f*
    reaction time, 112*f*
    synthesis route, 111*s*
  cyclic voltammograms, 127*f*
  EC, 114*f*, 124*t*
  HPC, 115*f*, 116*f*, 117*f*, 118*f*, 119*f*, 120*f*, 121*f*, 122*f*, 127*f*
  micelle size distribution, 119*f*
  overview, 109
  porous films, 123*f*, 124*f*
  pyrene release, 126*f*
  pyrene-loaded micelle, 125*f*
  self-assembled blank micelle, 125*f*
  self-assembly, 112, 113*f*
  stimuli-responsive properties, 112
  temperature dependence, 116*f*, 117*f*
Cellulose nanocrystals (CNC), 4
Cellulose nanofibrils (CNF), 4, 7*f*, 8*f*, 8*t*, 9*f*, 10*f*, 12*f*, 14*f*
Cellulose nanowhiskers (CNW)
  composite preparation
    AC electric field force effect, 27*f*
    aqueous solution, 20
    birefringent pattern, 20*f*
    CNC, 31*f*
    co-electrospinning apparatus, 29*f*
    experimental setup, 23*f*
    films, 22
    fingerprint texture, 20*f*
    microfibers, 27
    optical micrograph, 26*f*
    overview, 17
    parabolic focal conics, 22*f*
    self assembly, 20
    SEM, 31*f*
    TEM, 19*f*, 26*f*, 29*f*
  electrochemical applications
    composite films, 79*f*, 80*f*, 81, 83*f*, 86*f*, 87*f*
    electrocatalysis, 93
    electronically conducting polymer composites, 88
    metal electrocatalysts, 93, 94*f*
    overview, 75
    platinum electrocatalysts, 95, 96*f*
    polyaniline conducting networks, 88, 89*f*
    polypyrrole supercapacitor materials, 89, 90*f*, 91*f*, 95*f*
    pure cellulose nanocrystal films, 80
    silver electrocatalysts, 93, 95*f*
    ultrathin carbon films, 97, 98*f*, 99*f*, 100*f*, 101*f*
  sisal derived, 78*f*, 82*f*, 86*f*
Chitosan sulfates (CHS)
  alkaline phosphatase activity quantification, 302, 311*f*, 312*f*
  biological activity, 309
  ^{13}C NMR spectra, 306*f*
  cell culture, 300
  characterization, 300, 302
  CP/MAS ^{15}N NMR spectrum, 305*f*
  cytotoxicity assay, 301
  cytotoxicity measurement, 309, 309*f*
  DP_n, 308*f*
  FT-Raman spectra, 303*f*
  mitogenic activity, 310*f*
  overview, 297
  protein content, 311*f*
  SEC elution patterns, 307*f*
  sulfation, 299, 299*s*, 304*t*
  synthesis, 302
CHS. *See* chitosan sulfates (CHS)
CNC. *See* cellulose nanocrystals (CNC)
CNF. *See* cellulose nanofibrils (CNF)
CNW. *See* cellulose nanowhiskers (CNW)
Composite films, 79*f*, 80*f*, 81, 83*f*, 86*f*, 87*f*
Crystalline cellulose surfaces
  diffusion coefficients, 206*t*
  hydrogen bonds, 202*f*
  interfacial energy, 204*f*
  MD simulations, 194, 194*t*, 205*f*
  mean square displacement, 205*f*
  molecular model validation, 195
  OA-cellulose system, 193
  overview, 191
  radial distribution function, 199*f*, 200*f*, 202*f*
  temperature effect
    cellulose structure, 196*f*, 198
    OA film structure, 197*f*, 199
    OA film vs. cellulose surface, 197*f*, 201
  temperature set points, warming food packages, 195*t*
  torsion angle, 200*f*, 201*f*

D

DAEO. *See* dodecyloxy-polyethylene glycol glycidylether (DAEO)
Diacetate cellulose (CDA), 111
Diblock copolymers
  BC, 134
    acetylation, 135
    BET measurement, 135
    block copolymerization, 140

Downloaded by 217.66.152.26 on August 23, 2012 | http://pubs.acs.org
Publication Date (Web): August 17, 2012 | doi: 10.1021/bk-2012-1107.ix002

Downloaded by 217.66.152.26 on August 23, 2012 | http://pubs.acs.org
Publication Date (Web): August 17, 2012 | doi: 10.1021/bk-2012-1107.ix002

    - dynamic light scattering measurement, 136
    - ESR measurement, 135
    - ESR spectral simulation, 135
    - GPC measurement, 136
    - ^{1}H NMR measurement, 135
    - mechanical destruction, 134
    - mechanical fracture, 136
    - surface modification, 143
    - synthesis, 135
  - MCC
    - block copolymerization, 145
    - mechanical fracture, 143
    - nanoparticles, 146
  - overview, 133
- Dissolving grade pulps
  - ^{13}C CP/MAS NMR spectra, 170*f*
  - carbohydrate composition, 183*t*
  - cellulases, 173*f*
  - cellulose
    - accessibility, 171
    - fibrils, 171*f*
    - reactivity, 171
    - structure, 168, 169*f*
  - enzymes, 172
  - fibril aggregates, 171*f*
  - Fock's reactivity, 179*f*, 180*f*, 181*f*, 183*t*, 185*t*
  - molecular weight distribution, 184*t*
  - overview, 167
  - paper-grade pulp upgrading, 177
  - reactivity measurements, 174
  - regenerated cellulose, 176
  - viscosity, 179*f*, 181*f*, 183*t*, 185*t*
- Dodecyloxy-polyethylene glycol glycidylether (DAEO), 246*f*

E

- EC. *See* ethyl cellulose (EC)
- Electrocatalysis, 93
- Electrochemical applications, CNW
  - composite films, 79*f*, 80*f*, 81, 83*f*, 86*f*, 87*f*
  - electrocatalysis, 93
  - electronically conducting polymer composites, 88
  - metal electrocatalysts, 93, 94*f*
  - overview, 75
  - platinum electrocatalysts, 95, 96*f*
  - polyaniline conducting networks, 88, 89*f*
  - polypyrrole supercapacitor materials, 89, 90*f*, 91*f*, 95*f*
  - pure cellulose nanocrystal films, 80
  - silver electrocatalysts, 93, 95*f*
  - ultrathin carbon films, 97, 98*f*, 99*f*, 100*f*, 101*f*
  - *See also* cellulose nanowhiskers (CNW)
- Electronically conducting polymer composites, 88
- EPEG. *See* ethoxy (2-hydroxy)propoxy polyethylene glycol glycidylether (EPEG)
- Epoxylated polyethylene glycols (PEG), 246*f*
- Ethoxy (2-hydroxy)propoxy polyethylene glycol glycidylether (EPEG), 246*f*
- Ethyl cellulose (EC), 111, 114*f*, 124*t*

F

- Food package warming, temperature set points, 195*t*
- Fritz Wotruba's Church, Holy Trinity, Vienna, 71*f*

H

- High-modulus oriented cellulose nanopaper
  - CNF, 7*f*, 8*f*, 8*t*, 9*f*, 10*f*, 12*f*, 14*f*
  - mechanical characterization, 6
  - overview, 3
  - preferred orientation, 11
  - preparation, 5
  - properties, 7
  - stretching, 6
  - structural characterization, 6
  - structure, 7
  - TEMPO, 7*f*, 8*f*, 9*f*, 10*f*, 11*f*, 12*f*, 14*f*
- Honeycomb film formation, 50
- HPC. *See* hydroxypropyl cellulose (HPC)
- Hydroxypropyl cellulose (HPC), 111, 115*f*, 116*f*, 117*f*, 118*f*, 119*f*, 120*f*, 121*f*, 122*f*, 127*f*

L

- Laccase redox potential, 235
- Laccases, 330, 331*f*, 333*f*, 336*f*, 337*f*
- Lignin hydrogels
  - acetylation, 216*s*
  - aminolysis, 216*s*
  - chemical characterization, 216
  - cross-linking, 212, 219*s*
  - hydrogel-forming polymers, 212

In Functional Materials from Renewable Sources; Liebner, F., et al.;
ACS Symposium Series; American Chemical Society: Washington, DC, 2012.

Downloaded by 217.66.152.26 on August 23, 2012 | http://pubs.acs.org
Publication Date (Web): August 17, 2012 | doi: 10.1021/bk-2012-1107.ix002

  material characterization, 215
  mechanical properties, 221
  morphology, 217
  overview, 211
  PEGDGE-modified lignin, 216, 217*f*, 219*f*, 220*f*, 221*f*, 222*f*, 224*f*, 225*f*
    chemical structure, 223
  preparation, 214
  properties, 211
  swelling properties, 217
  water retention capacity, 218*f*

M

Manganese peroxidase oxidation, 239
MCC. *See* microcrystalline cellulose (MCC)
Metal electrocatalysts, 93, 94*f*
Micelle size distribution, 119*f*
Microcrystalline cellulose (MCC)
  block copolymerization, 145
  fractured, 144*f*
  ^{1}H NMR spectra, 145*f*
  mechanical fracture, 143
  nanoparticles, 146
Moisture vapor permeability fundamentals, biopolymer packaging materials, 274*f*, 278*f*, 286*f*, 287*f*
  agar, 283*f*
  aqueous coatings, 279
  atomic layer deposition, 287, 288*t*, 290*t*
  chemical vapor deposition, 290
  edible coatings, 282
  inorganic surface treatments, 285
  montmorillonite, 283*f*, 284*f*
  multi-layer flexible packaging structures, 291*f*
  MVTR governing factors, 276
  nanoclay coatings, 279, 281*f*
  paperboard packaging structure, 280*f*
  physical vapor deposition, 290
  plasticizer effect, 277*f*
  renewable polymers, 281
  terminology, 275
  test methodology, 277
  units, 275

O

2,3-O-(2-bromoisobutyryl)-2,6-O-TDMS-cellulose, 41, 46, 47*t*, 48*t*, 49*f*, 50*f*, 51*f*, 52*f*, 53*f*
3-O-(2-bromoisobutyryl)-2,6-O-TDMS-cellulose, 41, 43, 43*s*, 44*t*, 45*f*, 51*f*
Oriented cellulose nanowhiskers composite preparation. *See* cellulose nanowhiskers (CNW)
2,6-O-TDMS-cellulose, 40, 43*f*, 46*f*
Oxidative enzymes
  laccases, 330, 331*f*, 333*f*, 336*f*, 337*f*
  overview, 329
  peroxidases, 330, 332*f*, 333*f*, 336*f*
  reaction engineering strategies, 332
  redox potential control, 343
  solvent reaction engineering, 339
    aqueous solvent, 340
    ionic liquids, 341
    organic solvent, 340
    reverse micelles, 341
    supercritical fluids, 342
  synthesis strategies
    chemo-enzymatic process, 336*f*
    cross-linker, 334, 335*t*
    direct oxidation, 333, 334*t*
    mediator-assisted polymer functionalization, 337
    reactive anchor group assistance, 334
    template-assisted synthesis, 338, 338*f*, 339*t*
Oxidoreductase-catalyzed degradation
  laccase redox potential, 235
  manganese peroxidase oxidation, 239
  non-phenolic lignin model compounds, 234*f*
  overview, 229
  pH effect, 238
  phenolic lignin model compounds, 234*f*
  synthetic compounds, 234*f*
  veratryl alcohol oxidation, 236*t*, 237*t*, 238*f*, 239*t*

P

PEG. *See* epoxylated polyethylene glycols (PEG)
PEGDE. *See* polyethylene glycol diglycidylether (PEGDE)
Peroxidases, 330, 332*f*, 333*f*, 336*f*
Platinum electrocatalysts, 95, 96*f*
Polyaniline conducting networks, 88, 89*f*
Polyethylene glycol diglycidylether (PEGDE), 246*f*
Polypyrrole supercapacitor materials, 89, 90*f*, 91*f*, 95*f*
Porous films, 123*f*, 124*f*
Pure cellulose nanocrystal films, 80

Downloaded by 217.66.152.26 on August 23, 2012 | http://pubs.acs.org
Publication Date (Web): August 17, 2012 | doi: 10.1021/bk-2012-1107.ix002

Pyrene-loaded micelle, 125*f*

S

Self-assembled blank micelle, 125*f*
Silver electrocatalysts, 93, 95*f*
Sulfated glycosaminoglycan building blocks
  artificial ECM formation, 321
  ^{13}C NMR spectrum, 318*f*
  ^{13}C-APT NMR spectra, 320*f*, 321*f*
  cellular growth factors, 323
  collagen fibrils, 323*f*
  overview, 315
  sandwich-ELISA, 325*f*
  SPR sensorgrams, 324*f*
  sulfation, 317, 319*f*
  synthesis, 317*f*, 319, 321*f*
Super-hydrophobic cotton fabric
  dynamic contact angle measurements, 159, 160*f*, 161*f*
  FTIR, 157, 158*f*, 159*f*
  hydrophobic properties assessment, 154
  MVD treatment, 152
  nanocoatings, 153
  NVD treatment, 152
  NVD-Al_2O_3, 153, 161*f*, 162*f*
  overview, 149
  pre-treatment, 152
  SEM, 154, 155*f*, 156*f*
  TEM, 154, 157*f*
  water droplet, 163*f*
Surface-initiated ATRP, 42, 52, 52*t*

T

Temperature set points, warming food packages, 195*t*
TEMPO. *See* 2,2,6,6-tetramethylpiperidinyl-1-oxyl (TEMPO)
2,2,6,6-tetramethylpiperidinyl-1-oxyl (TEMPO), 5, 7*f*, 8*f*, 9*f*, 10*f*, 11*f*, 12*f*, 14*f*

U

Ultrathin carbon films, 97, 98*f*, 99*f*, 100*f*, 101*f*

V

Veratryl alcohol oxidation, 236*t*, 237*t*, 238*f*, 239*t*

X

Xylan-derived hydrogels
  characterization, 260, 262, 266
  HSQC NMR spectra, 264*f*
  isolation, 260, 261*s*, 262
  lignin reaction, 265*f*
  lignin-carbohydrate linkages, 265*f*
  morphology, 266
  overview, 257
  preparation, 266
  rheological properties, 266, 267*f*
  SEM, 266*f*
  structures, 259*f*
  swelling behavior, 268, 268*f*
  synthesis, 261